Impact of mitochondrial alterations on prostate cancer progression

Ashwin Sachdeva

Wellcome Centre for Mitochondrial Research

& Northern Institute for Cancer Research

Faculty of Medical Sciences

Thesis submitted to Newcastle University in candidature for the degree of

Doctor of Philosophy

September 2019

Author's Declaration

This thesis is submitted for the degree of Doctor of Philosophy at Newcastle University. The research was conducted at the Wellcome Centre for Mitochondrial Research and Northern Institute for Cancer Research (Newcastle University). All research is my own unless stated otherwise.

I certify that none of the material offered in this thesis has been previously submitted by me for a degree of any other qualification at this or any other university.

Abstract

Cancer metabolism is characterised by a 'Warburg shift' to aerobic glycolysis with decreased mitochondrial oxidative phosphorylation (OXPHOS), feasibly mediated by alterations in mitochondrial DNA (mtDNA). However, despite recent advances in our understanding of nuclear genomic alterations in prostate cancer, there remains a paucity of data evaluating the impact of mitochondrial alterations in prostate cancer progression.

Therefore, using publicly available genomic datasets, the mitochondrial molecular landscape of aggressive prostate cancer was characterized. This revealed a spectrum of mtDNA mutations under clonal selection pressures, reduced mtDNA copy number, and a transcriptomic profile composed of reduced mitochondrial and increased nuclear OXPHOS gene expression.

In order to assess the downstream impact of these alterations and aid clinical translation, I developed an automated assay to evaluate proteomic OXPHOS defects in archived prostate cancer tissue microarrays at the single cell level. Upon unpicking widespread multi-faceted heterogeneity in OXPHOS protein expression, patients with low complex I abundance and increased mitochondrial mass appeared to be at increased risk of all-cause mortality at 20-year follow-up.

The prognostic value of both mitochondrial molecular alterations and proteomic OXPHOS defects was enriched in patients with *PTEN*-loss and *TMPRSS2:ERG* fusion. Given that mitochondrial alterations and prostate cancer risk features are also associated with advancing age, transgenic models were generated to elucidate the impact of age-related systemic mitochondrial dysfunction on *PTEN*-deficient prostate cancer progression. Despite early mortality due to accelerated age-related phenotypes, attenuated tumour progression was observed, suggesting a tumour suppressive effect of systemic mitochondrial dysfunction.

In conclusion, mitochondrial alterations exert diverse systemic and local effects on prostate cancer progression. Leveraging mitochondrial tissue biomarkers and mitochondrial-targeted systemic therapies may provide a novel approach for identifying aggressive prostate cancer and suppressing progression to lethal disease.

Acknowledgements

PTEN and *ERG* data for the Manchester TMA in Chapter 5 was based on previous experimental work undertaken by Mrs Claire Hart and Mr Ahmad Al-Sukaini, as part of a collaboration with Professor Noel Clarke and Dr Mick Brown at the Genito-urinary Cancer Research Group, University of Manchester.

Ki67 staining for the *Polg* mouse prostate tissue in Chapter 6 was performed by Miss Karolina Habrajska as part of her MRes thesis.

CD8 and CD11b staining of *Polg* mouse prostate tissue in Chapter 6 was performed by Dr Debayan Mukherjee at the University of Manchester.

Bioinformatic analysis of RNA sequencing data from *Polg* mouse prostate tissue in Chapter 6 was performed by Dr Rebecca Steele (Queen's University Belfast) under the supervision of Professor Ian Mills.

The mouse models described in Chapter 7 were established at Cardiff University in collaboration with Dr Boris Shorning, Professor Matthew Smalley and Professor Alan Clarke. Mouse dissection and histopathological evaluation of mouse prostate tissue sections was performed by Dr Boris Shorning. Dr Amira El-Sherif, Consultant Histopathologist at Newcastle-upon-Tyne NHS Foundation Trust advised on the interpretation of mouse and human prostate tissue samples.

Bioinformatic analysis of mtDNA sequencing data in the Appendix was performed by Dr Helen Tuppen (Wellcome Centre for Mitochondrial Research, Newcastle University).

Publications

1. **Sachdeva A***, Veeratterapillay R, Voysey A, Kelly K, Johnson MI, Aning J, Soomro NA. *Positive surgical margins and biochemical recurrence following minimally invasive radical prostatectomy – An analysis of outcomes from a UK tertiary referral centre.* BMC Urology. 2017 Oct 2; 17(1): 91.
2. Canfarotta F, Czulak J, Betlem K, **Sachdeva A**, Eersels K, Van Grinsven B, Cleij T, Peeters M. *A novel thermal detection method based on molecularly imprinted nanoparticles as recognition elements*. Nanoscale 2018 Jan 25; 10(4): 2081-2089.
3. Stamp C, Anze A, **Sachdeva A**, Stoll EA, Shanley DP, Mathers JC, Kirkwood TBL, Heer R, Simons BD, Turnbull DM, Greaves LC. *Predominant asymmetrical stem cell fate outcome limits the rate of niche succession in human colonic crypts*. EBioMedicine. 2018 May; 31: 166-173.
4. **Sachdeva A*,** Dalton MD, Lees TA. *Graduated compression stockings for prevention of deep vein thrombosis.* Cochrane Database of Systematic Reviews. 2018 Nov 3; 11: CD001484.

Grants secured

- *Impact of mitochondrial alterations on prostate cancer progression*
    - Cancer Research UK Clinician Bursary (2014-15). Principal Investigator, £25,000.
    - The Urology Foundation Research Scholarship (2015-16). Principal Investigator, £50,000.
    - The Urology Foundation and The Rosetrees Trust Research Scholarship (2017-19). Principal Investigator, £100,000.
    - JGW Patterson Research Foundation (2017-19). Principal Investigator, £44,640.
- *Influence of metformin on metabolic changes associated with androgen deprivation therapy: Analysing samples from the prospective STAMPEDE trial.*
    - Prostate Cancer UK. Co-Investigator, £341,990.

Awards

- The Urology Foundation Research Medal (2015)
- Runners-up, Best Oral Presentation, British Association of Urological Surgeons Section of Academic Urology Meeting (2015)
- Best Oral Presentation Prize, North of England Urological Society Annual Meeting (2016)
- Best Young Researcher Presentation Prize, Newcastle Academic Health Partners Research Day (2016)

Table of contents

List of figures

List of tables

Chapter 1 Introduction

1.1 The prostate gland

1.1.1 Structure

The prostate is an accessory exocrine sex organ of the male reproductive system. It is cone-shaped with its apex lying inferiorly, abutting the urogenital diaphragm, and its broad base lying below the bladder neck. Anatomically, the rectum is separated posteriorly by the double layers of Denonvilliers' fascia and the pouch of Douglas; a layer of extra-peritoneal fat and the dorsal venous plexus lie anteriorly, separating the prostate from the pubic symphysis; and circumferentially the prostate surrounds part of the urethra, known as the prostatic urethra. The prostate is encased within a fibromuscular band of tissue, inseparable from the prostatic stroma, and referred to as the 'capsule' (Ayala *et al.*, 1989).

1.1.2 Zonal anatomy of the prostate gland

The zonal anatomy of the human prostate described by John McNeal (McNeal, 1981) is most widely accepted and has since been extensively revised (Selman, 2011). Though the surface of the prostate appears grossly homogenous, the prostate may be divided into four zones based on subtle histological differences and variation in incidence of various prostatic diseases – central, transitional, peripheral and anterior zones (**Figure 1-1**). About 70% of the prostate is composed of secretory glands, with the remainder accounted for by the anterior zone, also referred to as anterior fibromusclar stroma, a thick non-glandular region in continuity with the prostatic capsule.

The peripheral zone accounts for approximately 75% of glandular elements and has the highest incidence of prostate adenocarcinomas and prostatitis, whereas the transitional zone, accounting for 5-10% of glandular elements, is most often implicated in benign prostatic hyperplasia (BPH), a non-malignant enlargement of the prostate (McNeal *et al.*, 1988). The medial and lateral 'lobes' observed in BPH emerge from the central and transitional zones, respectively. Nodular expansion of these zones is associated with compression of the urethra and account for the partial bladder outlet obstruction and lower urinary tract symptoms frequently observed in BPH (Aaron *et al.*, 2016). With advancing age, the whole prostate gland size increases, largely due to an increase in the size of the central zone. However, the volume of the peripheral zone does not change with age (Turkbey *et al.*, 2012).

A growing body of literature suggests that tumour location within McNeal's zones of the prostate differ in molecular features (Sinnott *et al.*, 2015), cell types (Henry *et al.*, 2018), and disease aggressiveness. In comparison to peripheral zone tumours, transitional tumours are more indolent (Lee *et al.*, 2015), whereas central zone tumours, though rarely observed, are most aggressive (Cohen *et al.*, 2008).

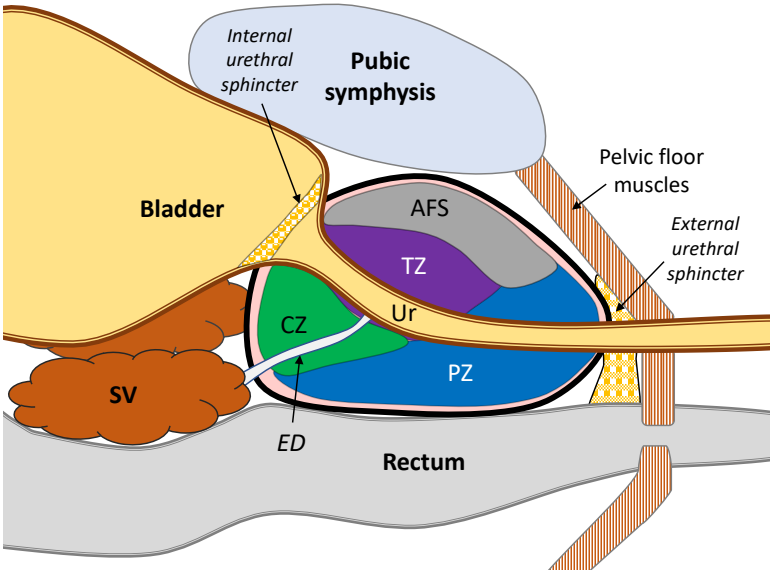

Figure 1-1: Zonal anatomy of the prostate and adjacent structures. CZ: Central zone; TZ: transitional zone; PZ: peripheral zone; ED: ejaculatory duct; SV: seminal vesicle; AFS: anterior fibromuscular stroma.

1.1.3 Function

The key functions of the prostate gland are based upon its two functional components: the glandular component comprising of a complex branching structure of epithelial cells which produces prostatic fluid, and the fibromuscular component comprising of smooth muscle cells which assists in expelling semen at ejaculation. Prostatic fluid is mildly alkaline and merges with secretions brought by the ejaculatory ducts from the seminal vesicles to form 30% of the volume of semen, which drains into the prostatic urethra at the verumontanum. Prostatic fluid contains strong proteolytic enzymes including prostate specific antigen (PSA). PSA is an androgen-regulated serine protease produced by prostate epithelial cells and secreted directly into the prostatic lumen. PSA forms a major protein in the semen, where it cleaves semenogelins I and II in the seminal coagulum into low molecular weight proteins (Balk *et al.*,

2003). Semenogelins are proteins that mediate gel formation in semen to maintain spermatozoa in a quiescent phase (Lilja *et al.*, 1987). At ejaculation, alkalinisation of semen by prostatic fluid and liquefaction of seminal coagulum is believed to play an important role in spermatozoa survival and motility in the acidic environment of the female reproductive tract, enabling spermatozoa to reach and subsequently fertilize ova (Hamamah and Gatti, 1998).

1.1.4 Embryological development

The development of the prostate occurs over a period spanning two decades, with generation of rudimentary structures during embryonic development, followed by a quiescent period postnatally, and subsequent re-emergence of cell proliferation and branching during puberty to result in the formation of a mature gland. During embryonic development, the prostate gland develops from the growth of prostatic buds from the urogenital sinus, the anterior division of the cloaca, with a small contribution from the mesonephric or Wolffian duct at 10 weeks of gestation, as the urogenital endoderm invaginates into the surrounding urogenital mesenchyme. Under the influence of androgens produced by foetal testes and other signalling factors, the prostate gland enlarges and matures, with progressive branching of the prostatic ducts, through an interplay between the urogenital mesenchyme and the endoderm (Cunha *et al.*, 2004; Cunha, 2008; Meeks and Schaeffer, 2011; Moad *et al.*, 2017).

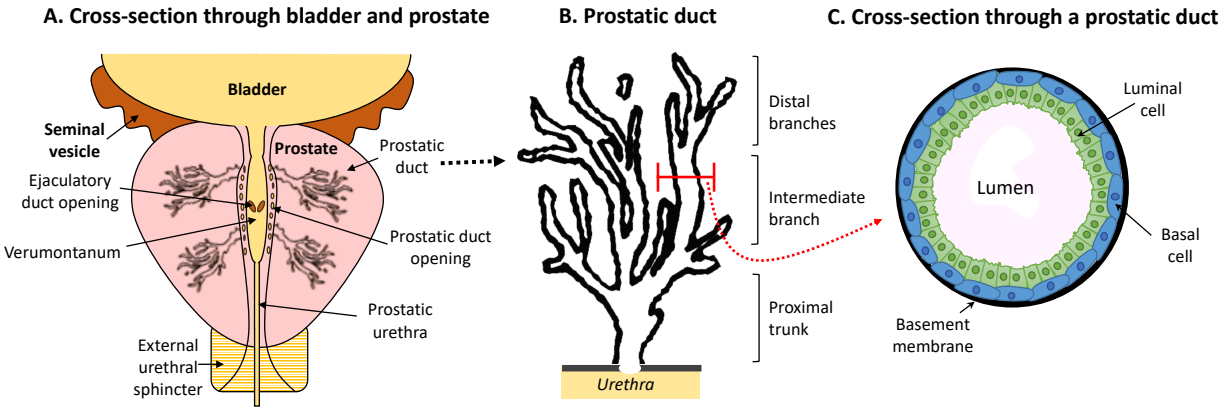

Figure 1-2: Cross-sectional anatomy of the human prostate. **(A)** Schematic cross-section through bladder and prostate showing drainage of seminal fluid through ejaculatory duct opening and prostatic fluid from the prostatic ducts into the verumontum at the prostatic urethra. **(B)** Schematic of a prostatic duct. **(C)** Cross-section of a prostatic duct.

1.1.5 Histology

The prostate is primarily composed of the following cellular components: epithelial, stromal (fibroblasts and myofibroblasts), smooth muscle, endothelial, and immune cells (**Figure 1-3**).

Prostate epithelium composes of three main cell types: luminal cells, basal cells and neuroendocrine cells. Luminal cells form a continuous layer of cells surrounding the gland lumen and produce proteinaceous prostatic secretions which drain into the lumen of the prostatic ducts. These cells express cytoplasmic markers including cytokeratin (CK) 8 and 18, as well as high levels of androgen receptor (AR)(Shen and Abate-Shen, 2010). Basal cells line the basement membrane and express cytoplasmic markers CK8, CK14 and p63. These cells are thought to maintain ductal integrity and support differentiation of luminal cells (Kurita *et al.*, 2004). Neuroendocrine cells, characterised by expression of cytoplasmic markers synaptophysin and chromogranin-A, are rare and their role remains unclear. In addition, there is emerging evidence supporting the presence of multipotent stem cells in the adult prostate, which have the ability to proliferate, self-renew and generate both basal and luminal cells (Moad *et al.*, 2017). These are thought to reside in a peri-urethral niche though definitive markers to reliably identify these cells in the human prostate are currently lacking. Acellular components of the stroma include a network of collagen fibres forming an extracellular matrix intervening between prostate acini (or glands), proteolytic enzymes, and minerals including high levels of zinc and citrate.

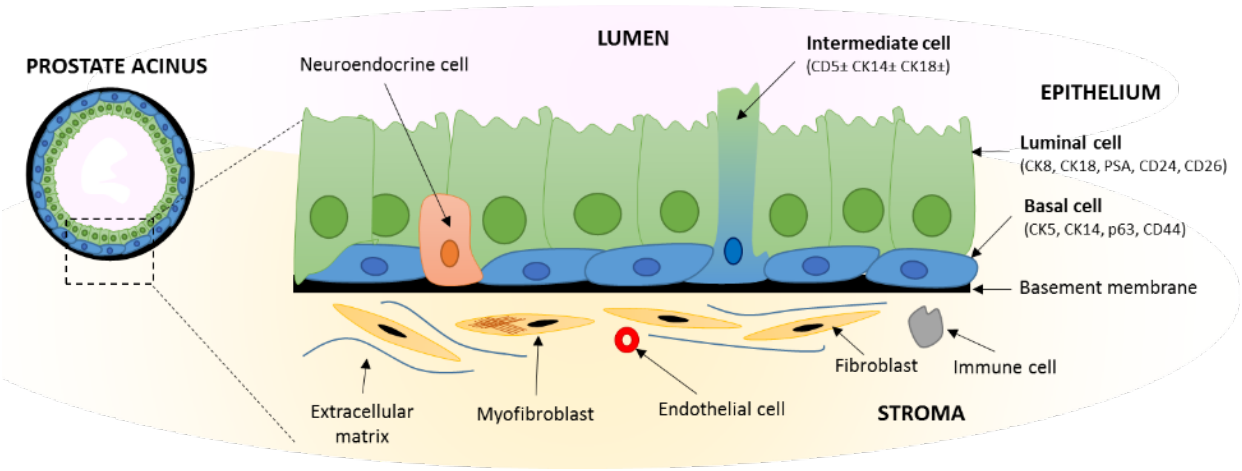

Figure 1-3: Cellular organisation of the human prostate epithelium. Immunophenotypes of epithelial cell subtypes are annotated. Adapted from Rybak *et al.* (2015).

1.1.6 Endocrinology

Androgens are sex hormones that play a key role in prostate growth, development and maturation, in addition to contributing to the development of male secondary sex characteristics. Testosterone is the most predominant androgen. It is produced by Leydig cells in the testes from 8 weeks of gestation, and accounts for 95% of androgen synthesis. The remainder 5% of androgens are produced by zona reticularis of the adrenal gland as dehydroepiandrosterone (DHEA).

Testosterone levels are maintained by a complex interplay across the hypothalamus-pituitary-gonadal axis. At low circulating androgen levels, pulsatile release of the luteinising hormone release hormone (LHRH) by the hypothalamus acts on the anterior pituitary gland to release luteinising hormone (LH). Circulating LH leads to the release of testosterone from the Leydig cells within the testes. When androgen levels are replete, a negative feedback loop results in suppression of LHRH release and a consequent reduction in circulating LH resulting in reduced testosterone release.

The prostate reduces circulating testosterone to the more potent AR ligand, dihydrotestosterone (DHT), by the action of the enzyme 5-alpha reductase. This allows a high concentration of androgens to be maintained within the prostate, thereby supporting the luminal cell activity. The functional impact of testosterone in cellular processes is mediated by the androgen receptor (AR). Upon binding to testosterone, AR translocates to the nucleus and regulates gene transcription. AR therefore plays a fundamental role in prostate homeostasis, with aberrations in AR activity frequently being implicated in prostate pathology. This will be discussed further in section 1.4.

1.1.7 Comparative mouse prostate anatomy and histology

Transgenic rodent models are frequently employed in the study of human disease since a variety of basic processes are conserved amongst all mammals. An understanding of comparative prostate anatomy and histology is therefore necessary. The mouse prostate has four distinct paired lobes (anterior, ventral, dorsal and lateral; **Figure 1-4**), whereas the human prostate is a more homogenous organ divided into four zones (as described in section 1.1.2). The dorsal and lateral lobes in the mouse prostate are often grouped together as the dorso-lateral prostate (DLP) since these lobes are closely located. The dorsal lobe is butterfly shaped

and surrounds the urethra. The ventral lobe is leaf shaped and located at the midline above the urethra. The lateral lobes flank the ventral lobes and incompletely wrap around the urethra ventrally. The anterior lobes are the largest in size and are closely attached to the lesser curvature of the seminal vesicles.

Unlike humans, the mouse prostate has an outpouching of the proximal vas deferens lying dorsal to the bladder neck called the ampullary gland. This structure contributes to the formation of semen. Due to the histological similarity with prostate tissue, careful attention must be paid to the histological appearance of the ampullary gland, which is characterised by a surrounding dense, fibromuscular stroma. Furthermore, the glands contain eosinophilic secretions with characteristic holes that impart a "swiss cheese" appearance (Knoblaugh and True, 2012).

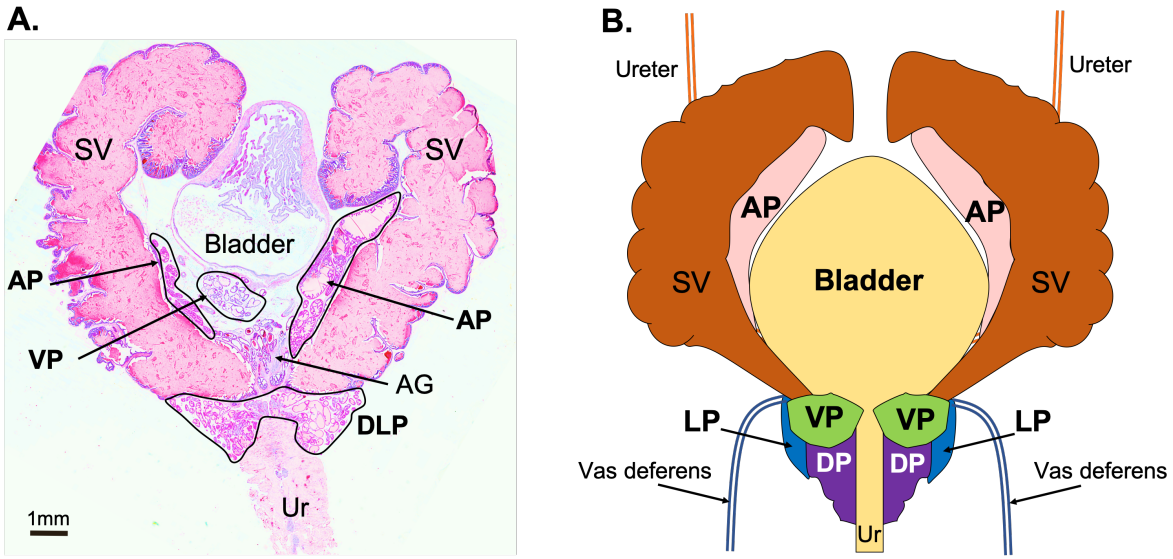

Figure 1-4: Anatomy of the mouse urogenitus. Haematoxylin and eosin stained cross-section of a 11-month mouse urogenitus, and **(B)** schematic diagram (anterior view). AP: anterior prostate; VP: ventral prostate; DP: dorsal prostate; LP: lateral prostate; DLP: dorso-lateral prostate; Ur: urethra; AG: ampullary gland; SV: seminal vesicle. Note: the ampullary gland lies dorsally at the level of the bladder neck and is therefore obscured in the schematic diagram.

Histologically, human and mouse prostate tissue share a similar ductal architecture, except mouse prostates contain fewer basal, neuroendocrine and smooth muscle cells, and have looser and less dense fibromuscular stroma (Parisotto and Metzger, 2013) in comparison to human prostates. There are marked histological differences between each of the lobes of the mouse prostate (Shappell *et al.*, 2004; Ittmann *et al.*, 2013), which are important to consider when interpreting architectural changes associated with PCa.

	DP	LP	VP	AP
Acini	Small	Small to large	Moderate to large	Moderate to large
Stroma	Dense	Thin	Thin	Prominent connective tissue with smooth muscle
Secretions	homogenous eosinophilic	amorphous slightly basophilic	Homogenous pale serous	abundant homogenous eosinophilic
Epithelial cells	Columnar	Cuboidal to columnar	Cuboidal to columnar	Columnar
Basal layer folding	Moderate infolding	Sparse focal folding	many mucosal folds projecting into the gland lumen	Enlarged infoldings with projections
Nuclei	Small, round, central	Small, round, basal	Oval, basal	Round central nuclei

Table 1-1: Histology of mouse prostate lobes. Adapted from Knoblaugh and True (2012).

1.2 Prostate cancer

1.2.1 Epidemiology

Prostate cancer (PCa) is the most common cancer amongst men in the UK, accounting for approximately 47,700 new cases and 11,500 cancer deaths annually (Cancer Research UK, 2019). Incidence of PCa is increasing and is projected to continue rising to 233 cases per 100,000 men by 2035. Overall, 84% of men with PCa survive their disease for 10 years or more, with an ongoing trend of improving survival outcomes, likely associated with increased use of PSA screening and associated detection of a greater proportion of men with slow-growing indolent early stage PCa.

Early diagnosis and treatment of PCa is associate with excellent long-term survival. Unfortunately, PCa is diagnosed at a late stage in 4 in 10 cases in England and Northern Ireland, and 6 in 10 cases in Scotland, which is associated with 33% mortality at 5-year follow-up.

1.2.2 Risk factors

Only 10-15% of all cases are hereditary in nature, with the vast majority associated with somatic alterations. The main risk factors associated with development of PCa are advancing age, ethnicity, and family history (Bostwick *et al.*, 2004). Of these, advancing age is most strongly associated with the development of PCa. However, PCa is not clearly linked to any modifiable risk factors (Cancer Research UK, 2019).

1.2.2.1 Ageing

Amongst all age-related cancers, the risk of development of prostate cancer is most strongly associated with advancing age (**Figure 1-5**)(Siegel *et al.*, 2019). Autopsy studies have noted an increasing frequency of histopathological evidence of PCa in men, with prevalence of up to 60% in men above the age of 79 years and an odds ratio of 1.71 (95% confidence interval 1.62-1.81) for each increasing decade (Bell *et al.*, 2015). HGPIN and invasive PCa may emerge in men in as early as their 20s and 30s and have a long latent period (Sakr *et al.*, 1994; Sakr *et al.*, 1996). Other age-related changes seen in ageing prostate tissue, including development of an inflammatory microenvironment (Begley *et al.*, 2008), altered autonomic innervation (White *et al.*, 2013), and methylation (Kwabi-Addo *et al.*, 2007) have also been implicated in age-related development of both BPH and PCa.

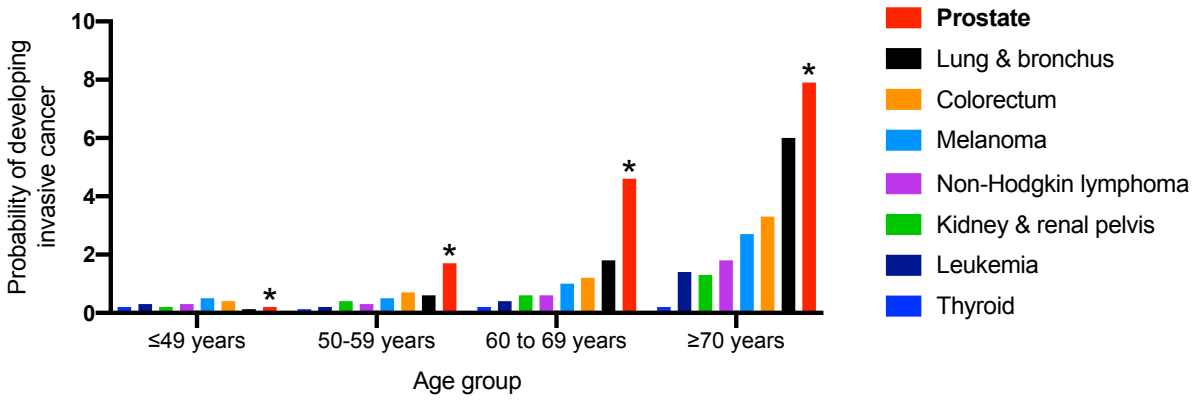

Figure 1-5: Probability of men developing various invasive age-related cancers stratified by age groups. Adapted from 2013-15 data from Siegel *et al.* (2019).

Older men with PCa are also found to have more advanced disease at presentation, representing nearly 50% of cases with metastatic disease and increased cancer-specific mortality (Scosyrev *et al.*, 2012). Despite higher-risk disease in elderly men, the use of radical therapy is lower in this cohort, perhaps due to associated toxicity, multi-morbidity and paucity of clinical trials including men above the age of 75 years (Bechis *et al.*, 2011; Jha *et al.*, 2014; Vernooij *et al.*, 2019). Therefore, there is a growing unmet clinical need to develop less toxic therapies for older men with PCa. Furthermore, accelerated progression of PCa with ageing suggests that physiological changes associated with ageing may also contribute to disease progression. However, such data may be at risk of lead time bias (Assel *et al.*, 2018), whereby older patients may be more likely to be diagnosed at a late stage upon seeking medical attention once they are symptomatic resulting in relative upstaging and upgrading of their

disease, as compared to younger patients who may be more likely to be offered opportunistic PSA screening (Drummond *et al.*, 2009; Jessen *et al.*, 2013).

1.2.2.2 Family history

Family history of PCa influences both risk of a PCa diagnosis (Kicinski *et al.*, 2011) and aggressive PCa features (Bratt *et al.*, 2016), with increasing number of first degree relatives being associated with greatest lifetime risk of PCa (**Table 1-2**).

Relative with PCa	Kicinski et al 2001	Bratt et al 2016 (by 65 years)	
	Relative risk (95% CI)	% Any PCa (95% CI)	% High-risk PCa (95% CI)
None	1	4.8 (4.8 to 4.9)	1.4 (1.3 to 1.4)
Father	2.35 (2.02-2.74)	n.r.	n.r.
Brother	3.14 (2.37-4.15)	14.9 (14.1 to 15.8)	3.0 (2.6 to 3.4)
2 Brothers	4.39 (2.61-7.39)	34.4 (28.1 to 40.1)	2.7 (0.8 to 4.5)
Father & brother		29.8 (27.0 to 32.5)	5.6 (4.4 to 6.7)
Father & 2 brothers		43.9 (33.7 to 52.5)	11.4 (3.6 to 18.5)
2nd degree relative	2.52 (0.99-6.46)	n.r.	n.r.

Table 1-2: Family history and risk of prostate cancer incidence and mortality. Relative risk of a diagnosis of prostate cancer is associated family history of prostate cancer, with number and relatedness influence prostate cancer incidence (Kicinski *et al.*, 2011) and aggressiveness (Bratt *et al.*, 2016).

Germline *BRCA1* and *BRCA2* mutation carrier status is observed in 0.44% and 1.2% of PCa cases (Kote-Jarai *et al.*, 2011; Leongamornlert *et al.*, 2012), respectively, and increases lifetime risk of developing PCa (Nyberg *et al.*, 2019). As compared to the general population, *BRCA2* carriers, particularly those with a family history of PCa, are at higher risk of a diagnosis of PCa, a stronger association with Gleason >7, and a higher risk of death from PCa (**Table 1-3**), with 5-year cancer specific survival estimated at 68%. The association between *BRCA1* carrier status and PCa is relatively weaker (Nyberg *et al.*, 2019). Furthermore, PCa in *BRCA1/2* carriers is associated with aggressive features including higher Gleason score, tumour stage, nodal involvement, de novo metastases and cancer-specific mortality, as compared to non-carriers (Castro *et al.*, 2013). Given that *BRCA2*-mutant PCa harbours increased genomic instability and a molecular profile more akin to metastatic, rather than localised PCa (Taylor *et al.*, 2017), these cancers may be amenable to treatment with PARP inhibitors (Mateo *et al.*, 2015).

In light of these findings, PSA screening has also been proposed for early detection of PCa in *BRCA2* carriers (Page *et al.*, 2019). Notably, localised PCa in *BRCA1/2* carriers is also more likely to progress (Castro *et al.*, 2015), due to which early radical treatment should be considered in this cohort, over an active surveillance approach (Taylor *et al.*, 2019).

Gene	Standardised Incidence Rate		Standardised mortality rate
	Any PCa	Gleason >7 PCa	Any PCa
BRCA1	2.35 (1.43-3.88)	1.80 (0.89-3.65)	1.75 (0.44-6.90)
BRCA2	4.45 (2.99-6.61)	5.07 (3.20-8.02)	3.85 (1.44-10.3)

Table 1-3: BRCA carrier status and risk of prostate cancer incidence and mortality. Data from Nyberg *et al.* (2019).

1.2.2.3 Geography and ethnicity

The incidence of prostate cancer is greater in the western world, as compared to Asia and Africa (Culp *et al.*, 2019). However, PCa mortality is highest in Latin America, the Caribbean and Africa (**Table 1-4**). Autopsy studies have revealed that the prevalence of PCa is greatest amongst both American white and black men, and lowest amongst men of Mediterranean origin (Haas *et al.*, 2008), which may be associated with both ethnicity and environmental factors.

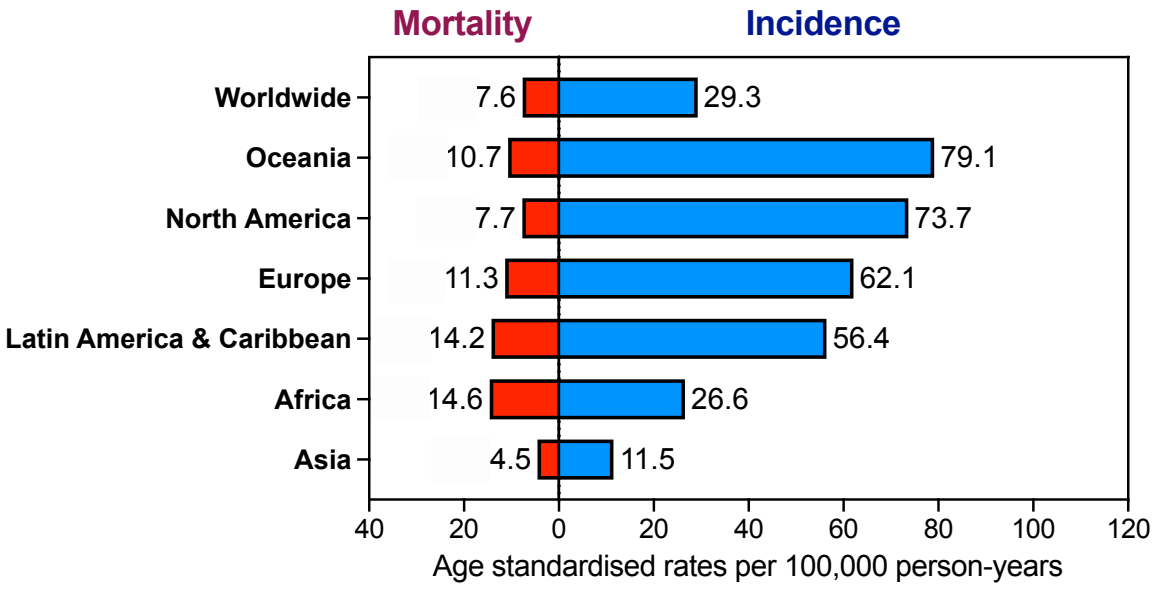

Table 1-4: Geographical variation in prostate cancer incidence and mortality. Adapted from Culp *et al.* (2019).

African American (AA) men have the highest reported PCa incidence and mortality rates, which is markedly higher than that of European American (EA) men (Williams and Powell, 2009). Conversely, Hispanic and American men with Asian, Pacific Islander, Indian and Alaskan ancestry have lower incidence and mortality rates as compared with EA men. AA men are also more likely to present with advanced or de novo metastatic PCa (Powell *et al.*, 2010; Akinyemiju *et al.*, 2018). These differences persist despite adjustment for previously hypothesised variation in factors including socioeconomic disparity, dietary fat intake, and access to care (Alexander and Brawley, 1998; Hoffman *et al.*, 2001), suggesting potential biological differences accounting for ethnic variation in PCa outcomes (Khani *et al.*, 2014).

1.2.3 Natural history of prostate cancer

The natural history of prostate cancer is thought to traverse in a stepwise manner, emerging as a precursor lesion and initially progress in an indolent manner over many decades. Subtle early histopathological changes may include focal hyperplasia, reduction in basal cells, pleomorphic hyperchromatic nuclei, and prominent nucleoli, which are classified as prostate intra-epithelial neoplasia (PIN) (McNeal and Bostwick, 1986), and are not considered pre-malignant. In contrast, high-grade PIN (HGPIN), which in addition displays marked elevation of proliferation markers but without invasion of the basement membrane, may precede subsequent development of invasive PCa by up to 10 years, when epithelial cells breach the basement membrane.

Prostate cancer is often multifocal and heterogenous, with individual tumours harbouring diverse genomic alterations and progressing at variables rates. This complicates both initial diagnosis and subsequent management of PCa. Well differential tumours may be indolent, whereas poorly differentiated tumours are at increased risk of dissemination to regional lymph nodes or distant structures, including bone, liver and brain. Local radical therapies including radical prostatectomy and external beam radiotherapy may successfully treat low and intermediate risk prostate cancer with favourable long-term results and low recurrence rates. Since primary untreated prostate cancer cells are androgen-dependent, androgen deprivation therapy has been the mainstay of treatment of advanced and metastatic prostate cancer, which is associated with increased risk of progression to a androgen-independent or castrate-resistant state. Therapeutic options for management of advanced, metastatic and castrate-resistant prostate cancer have expanded in recent years, supported by robust clinical trial data, which is discussed later in section 1.3.

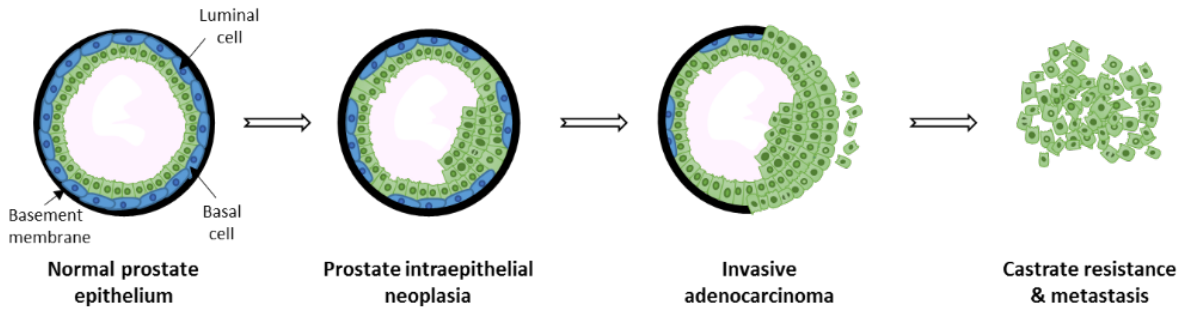

Figure 1-6: Natural history of prostate cancer. Stepwise progression from normal prostate epithelium, through precursor prostate intraepithelial (PIN) lesions characterised by subtle early histopathological changes, including focal hyperplasia and pleomorphic hyperchromatic nuclei. Invasion through the basement membrane results in invasive adenocarcinoma, which may disseminate, and following a period of androgen deprivation therapy, develop castrate resistance. Adapted from Shen and Abate-Shen (2010).

1.2.4 Diagnostic evaluation

The vast majority of patients are asymptomatic at time of presentation, and often diagnosed incidentally or by an elevated prostate serum antigen (PSA) level. Symptomatic patients usually present with voiding difficulties, back pain or haematuria in the early stages, or manifestations of advanced disease including bone pain from skeletal metastasis, neurological deficits due to spinal cord compression, or systemic features associated with cancer (loss of appetite, weight loss, and anaemia). Common sites of metastasis include regional lymph nodes, bone, lungs and liver (Bubendorf *et al.*, 2000).

1.2.4.1 Digital rectal examination

Diagnostic evaluation of patients with suspected PCa includes a detailed history, digital rectal examination (DRE), PSA test and prostate biopsy. Since the vast majority of PCa occurs in the peripheral zone, larger tumours may be palpable at DRE. However, DRE is often subjective, with low sensitivity (28.6%), high specificity (90.7%), and positive and negative predictive value of 42.3% and 84.2%, respectively (Jones *et al.*, 2018). Thus, DRE is supplemented by other diagnostic modalities including PSA, in determining risk of PCa.

1.2.4.2 Serum PSA

As described in section 0, PSA is secreted by prostate luminal cells and plays an important role in liquifying semen. In prostate adenocarcinoma, PSA production is often increased, and disruption of the basal cell layer and basement membrane allows PSA direct access to the peripheral circulation, resulting in a rise in serum PSA levels (Balk *et al.*, 2003). Notably, neuroendocrine prostate cancers are characterised by low PSA levels (Conteduca *et al.*, 2019).

Since PSA increases with advancing age, age-specific thresholds of PSA have been proposed. However, Public Health England have recently updated this guidance and now recommend onward specialist input in men aged 50-69 years with PSA ≥ 3.0 ng/ml and use of clinical judgement for men under 50 years of age suspected to have PCa (Public Health England, 2016). PSA cut off of 3.0 ng/ml has a sensitivity of 59% and specificity of 87% for detection of any prostate cancer (Holmstrom *et al.*, 2009). Though PSA-based screening results in earlier diagnosis of PCa, the use of PSA as a screening strategy remains controversial (Ilic *et al.*, 2018), due to increased risk of diagnosing indolent localised prostate cancer with an associated increase in treatment-related toxicity. Furthermore, at 10-year follow-up, PSA screening results in no impact on overall survival and either an extremely small (Schroder *et al.*, 2014) or no impact (Martin *et al.*, 2018) on reducing disease specific mortality.

1.2.4.3 Prostate biopsy

Men with abnormal DRE or raised PSA may undergo a prostate biopsy. This is performed under ultrasound guidance, traditionally via a transrectal route, though increasingly via a transperineal route, given the reduced risk of sepsis (Grummet *et al.*, 2014), comparable complication rate (Shen *et al.*, 2012) and improved ability to target anterior tumours (Dimmen *et al.*, 2012).

1.2.4.4 Imaging

In light of recent data from PROMIS (Ahmed *et al.*, 2017a) and PRECISION trials (Kasivisvanathan *et al.*, 2018), pre-biopsy multi-parametric MRI (mpMRI) is increasingly performed to target suspicious lesions to increase detection of clinically significant PCa, minimise risk of identifying clinically insignificant PCa, and potentially avoid the need for prostate biopsy in low risk cases altogether (Drost *et al.*, 2019). However, 15-25% of clinically significant PCa lesions (Johnson *et al.*, 2019) including some with high risk genetic alterations (Purysko *et al.*, 2019), may not be visible on mpMRI.

Patients with high risk or suspected metastatic disease are offered computed tomography (CT) of the abdomen and pelvis and technetium-99m diphosphonate scintigraphy bone scan, to assess for metastases.

1.2.5 Histopathology

Histopathological evaluation of prostate biopsy may include benign conditions such as BPH and prostatitis, pre-malignant lesions such as high-grade PIN (HGPIN) and atypical small acinar proliferation (ASAP), or overt malignancy. Amongst patients with HGPIN, the risk of cancer detection on repeat biopsy is 22% (Amin *et al.*, 2007). Similarly, the finding of ASAP, defined as highly suspicious glandular architecture that is insufficient for the diagnosis of PCa warrants repeat extended biopsies, as it is associated with a 40-59% risk of cancer detection (Amin *et al.*, 2007; Abouassaly *et al.*, 2008).

Over 95% of prostate cancers are classified pathologically as prostate adenocarcinomas (PCa), which are of a luminal phenotype, whereas a small minority are neuroendocrine prostate cancers (NEPC), which are associated with rapid disease progression or *de novo* metastases. Prostate adenocarcinomas are often multifocal in origin with distinct clonal hierarchies, and histologically characterised by architectural atypia (invasion through the basement membrane, cribriform pattern, peri-neural invasion) and cellular atypia (enlarged nuclei with prominent nucleoli). This is usually associated with loss of the basal cell layer (absence of immunostaining for p63 and CK5/14 antibodies), increase in the luminal marker alpha-methylacyl-CoA racemace (AMACR), and decrease in zinc and citrate levels.

Histomorphological evaluation of PCa traditionally employs the Gleason scoring system (Macintosh *et al.*, 1998) initially proposed by Donald Gleason, which as subsequently been updated by the International Society for Urological Pathology (ISUP) in 2005, 2014 and most recently in 2016. The Gleason score is the sum of primary and secondary Gleason grades, individually scored on a scale from 1-5, based upon the most and the second most abundant histopathological patterns in the specimen. Thus, the Gleason score ranges from 2-10, with higher scores representing greater loss of tissue architecture and more aggressive disease phenotypes. Notably, Gleason 7 disease may fail to distinguish between Gleason 4+3=7 and Gleason 3+4=7 disease, which are prognostically very different (Epstein *et al.*, 2016b). Furthermore, in clinical practice, the lowest Gleason score is 6, rather than 2, which results in scale of 6-10 and difficulties in accurately communicating histopathological findings to patients' regarding their disease. In light of these issues, ISUP grade groups (also referred to as *Gleason groups*) ranging from 1 to 5 are proposed (Epstein *et al.*, 2016a), which better reflect disease prognosis (**Table 1-5**, Epstein *et al.* (2016b)).

ISUP grade group	Gleason score	Definition	BCR at 5 years
Grade 1	2-6	Only individual discrete well-formed glands	96%
Grade 2	3+4=7	Predominantly well-formed glands with lesser component of poorly formed/fused/cribriform glands	88%
Grade 3	4+3=7	Predominantly poorly formed/fused/cribriform glands with lesser component of well-formed glands	63%
Grade 4	4+4=8	Only poorly formed/fused/cribriform glands	48%
	3+5=8	Predominantly well-formed glands and lesser component lacking glands	
	5+3=8	Predominantly lacking glands and lesser component of well-formed glands	
Grade 5	9-10	Lack of gland formation (or with necrosis) with or without poorly formed/fused/cribriform glands	26%

Table 1-5: Description of Gleason grade groups defined by ISUP. The 5-year biochemical-recurrence free survival in a patient cohort treated with radical prostatectomy and stratified by pathological Gleason group are reported (Epstein *et al.*, 2016b). BCR: Biochemical recurrence.

1.2.6 TNM staging

Like most other cancers, the TNM classification system is used to ascertain disease stage and plan subsequent management in PCa (**Table 1-6**). This is composed of three domains: (a) the primary tumour stage, which ranges from impalpable (T1) tumour incidentally diagnosed at transurethral resection of the prostate (TURP) for obstructive lower urinary tract symptoms or at needle biopsy, through to organ-confined (T2), and locally-advanced disease with invasion beyond the prostate capsule (T3) and into adjacent structures (T4); and presence of metastases in either (b) regional lymph nodes, or (c) distant structures such as non-regional lymph nodes, bone or other organs.

<table>
<tr><th colspan="2">T – Primary tumour stage</th></tr>
<tr><td colspan="2">Tx: Cannot be assessed
T1: Clinically inapparent tumour not palpable or visible by imaging
T1a: Incidental finding in ≤5% of resected tissue
T1b: Incidental finding in >5% of resected tissue
T1c: Tumour identified by needle biopsy (eg due to elevated PSA level)
T2: Tumour confined within the prostate
T2a: Involves one half of one lobe or less
T2b: Involves more than half of one lobe, but not both lobes
T2c: Involves both lobes
T3: Tumour extends into prostate capsule
T3a: Extra-capsular invasion including microscopic bladder neck involvement
T3b: Seminal vesicle invasion
T4: Tumour is fixed or invades adjacent structures other than SV: external sphincter, rectum, levator muscles, and/or pelvic wall</td></tr>
<tr><th>N – Regional lymph nodal status</th><th>M – Distant metastasis</th></tr>
<tr><td>(nodes below bifurcation of common iliac arteries)

Nx: Cannot be assessed
N0: No regional lymph node metastasis
N1: Regional lymph node metastasis</td><td>Mx: Cannot be assessed
M0: No distant metastasis
M1: Distant metastasis
M1a: Non-regional lymph nodes
M1b: Bone(s)
M1c: Other site(s)</td></tr>
</table>

Table 1-6: TNM staging of prostate cancer. Based upon the 7th edition of UICC International Union Against Cancer classification of malignant tumours (Sobin *et al.*, 2009).

1.2.7 Risk stratification

Patients may be divided into low, intermediate and high risk for progression to disseminated disease, based on PSA, Gleason group, tumour stage and presence of lymph node metastasis (Mottet *et al.*, 2018).

Low risk	Intermediate risk	High risk	
PSA < 10 ng/ml	PSA 10-20 ng/ml	PSA > 20ng/ml	Any PSA
and GS < 7 (ISUP grade 1)	**or**, GS 7 (ISUP grade 2/3)	**or**, GS >7 (ISUP grade 4/5)	Any GS (Any ISUP grade)
and cT1-cT2a	**or**, cT2b	**or**, cT2c	cT3-4 or cN+
Localised			***Locally advanced***

Table 1-7: Prostate cancer risk stratification. Based upon European Association of Urology guidelines (Mottet *et al.*, 2018).

1.3 Clinical management of prostate cancer

Risk of progression of prostate cancer to disseminated, potentially lethal disease, is determined by patient characteristics, a combination of histopathological characteristics (ISUP Gleason group), serum PSA and TNM staging. Disease risk, patient characteristics and patient preferences are used to devise a management plan, which may include conservative management (such as watchful waiting, active surveillance or active monitoring for low risk disease), radical treatment including prostatectomy with or without pelvic lymph node dissection, brachytherapy or conformal radiotherapy (for localised or locally advanced disease), and systemic therapies including hormonal or chemotherapy (for advanced or metastatic disease).

Charles Huggins first discovered that prostate cancer progression was testosterone dependent and proposed the use of surgical castration as a treatment modality for prostate cancer (Huggins and Hodges, 1941). Subsequently, Andrew Schally developed the first LHRH agonist for medical castration (Tolis *et al.*, 1982). Surgical castration by bilateral sub-capsular orchidectomy offers permanent androgen suppression, with lower toxicity as compared to medical castration (Sun *et al.*, 2016); however, it is associated with greater cosmetic and psychological concerns. Thus, medical castration is the predominant mode of androgen deprivation therapy (ADT) in western countries, and until recently, considered the mainstay of therapy for metastatic disease. Medical castration uses either anti-androgens such as bicalutamide, LHRH agonists such as leuprorelin, or gonadotrophin releasing hormone (GnRH)

antagonists such as degarelix, for chemical castration to slow the growth of prostate cancer. Though ADT can be used at all stages of prostate cancer, patient and disease factors should be used to carefully consider alternative management strategies.

Novel agents have also been developed to either suppress adrenal androgen synthesis or suppress AR activity. Abiraterone inhibits androgenic steroid synthesis, by targeting cytochrome P450 17A1 (CYP17A1) and blocking 17 alpha-hydoxylase and 17,20 lyase (Potter *et al.*, 1995). This inhibits adrenal and possible tumoural steroid synthesis resulting in upstream mineralocorticoids, if given without glucocorticoids (Attard *et al.*, 2008). Enzalutamide is a novel AR-anatagonist (Tran *et al.*, 2009) by competitively binding against androgens, prevents translocation of AR to the nucleus and prevents AR transcription by inhibiting AR from binding to chromosomal DNA. When used concomitantly with ADT, these therapies have shown promise in advanced and metastatic prostate cancer, with ongoing studies aiming to evaluate the efficacy of these therapies in earlier stages of prostate cancer.

1.3.1 Low and intermediate risk disease

At 10 years follow-up, the ProtecT trial reported comparable oncological outcomes across both surgery and radiotherapy arms amongst 1,643 PSA-screened men with localised PCa with predominantly low (67.6%) and intermediate risk (32.4%) disease, randomised to either active monitoring, radical radiotherapy or radical prostatectomy (Hamdy *et al.*, 2016). As compared to both radical treatment modalities, patients allocated to the active monitoring arm had higher rates of metastasis and disease progression. However, the proportion of patients reaching the primary outcome of prostate-cancer mortality was extremely low (17 patients, 1.03%), irrespective of allocated treatment modality. Notably, early toxicity and quality of life scores varied by treatment modality, with higher rates of erectile dysfunction and urinary incontinence in the prostatectomy cohort, and higher rates of bowel toxicity, urinary voiding dysfunction and nocturia in the radiotherapy cohort. Men in the active monitoring arm avoided these side-effects for longer, until eventually undergoing radical treatments or developing age-related changes (Donovan *et al.*, 2016).

Similar to findings from the ProtecT trial, the PIVOT trial (Wilt *et al.*, 2017) in the early PSA-screening era randomised 731 men with low or intermediate risk PCa to either radical prostatectomy or observation and reported comparable all cause and prostate-specific

mortality at 20 year follow-up. Only the Scandinavian Prostate Cancer Group 4 (SPCG-4) trial (Bill-Axelson *et al.*, 2014), which randomised unscreened 695 men with low and intermediate risk PCa into RP vs watchful waiting, reported reduced prostate-specific (RR 0.56, 95% CI 0.41-0.77, p=0.001) and all-cause mortality (RR 0.71, 95% CI 0.59-0.86, p<0.001) amongst patients undergoing RP.

Patients with low or intermediate risk PCa may also be offered brachytherapy or external beam radiotherapy (EBRT). EBRT may be delivered at a total dose of 76-78Gy with 4-6 months of ADT, or an escalated dose of 76-80Gy for patients unwilling to undergo ADT (Kupelian *et al.*, 2008; Krauss *et al.*, 2011). Current NICE guidelines recommend hypofractionated radiotherapy (60 Gy in 20 fractions) using image-guided intensity modulated radiotherapy (IMRT), or conventional radiotherapy (74 Gy in 37 fractions) for patients who cannot have hypofractionated radiotherapy (National Institute for Health and Care Excellence, 2019). Though level 1 evidence for use of low dose brachytherapy is lacking, it may be offered to patients with prostate volume <50ml, with good voiding function, and without previous TURP (Zaorsky *et al.*, 2017).

1.3.2 High risk prostate cancer

In high risk cases with suspected regional nodal metastasis, radical prostatectomy may be combined with pelvic lymph node dissection and radical radiotherapy may be combined with pelvic radiotherapy to manage nodal disease. However, level 1 evidence for the management of high risk PCa is currently only available for external beam radiotherapy (EBRT) with three trials demonstrating a clear benefit of EBRT with ADT, over ADT alone, in terms of both cancer-specific and overall survival (Widmark *et al.*, 2009; Mottet *et al.*, 2012; Mason *et al.*, 2015). Multimodal therapy combining surgery, radiotherapy, ADT and/or chemotherapeutic regimens is increasingly considered for locally advanced and metastatic PCa.

Non-metastatic castrate-resistant PCa (non-mCRPC) has recently been defined amongst patients harbouring no radiological evidence of metastasis on technetium-99m bone scan and CT, with increasing PSA levels despite castrate testosterone levels (Mateo *et al.*, 2019). Survival benefit with the use of anti-androgens including enzalutamide (Hussain *et al.*, 2018), apalutamide (Smith *et al.*, 2018), and darolutamide (Fizazi *et al.*, 2019) has recently been confirmed in phase III RCTs amongst this cohort of patients.

1.3.3 Metastatic prostate cancer

Recent level 1 evidence supports the role of docetaxel (Sweeney *et al.*, 2015; Sydes *et al.*, 2018), radical radiotherapy (Parker *et al.*, 2018), and novel AR-targeted therapies including abiraterone (Fizazi *et al.*, 2017; James *et al.*, 2017; Sydes *et al.*, 2018; Hoyle *et al.*, 2019) and enzalutamide (Davis *et al.*, 2019) in metastatic PCa; however, the optimal sequencing strategy and efficacy of combination therapies is currently unclear (Lorente *et al.*, 2015). After a median period of 1-2 years, depending on site and burden of metastases (**Table 1-8**), patients with metastatic disease may progress to castrate-resistant or androgen-independent PCa (Gandaglia *et al.*, 2015; James *et al.*, 2015), defined as progression of disease by PSA or radiographic progression despite ADT with adequately suppressed testosterone (<50 ng/dl).

	Failure-free survival (FFS)		Overall survival (OS)	
Cohort	**Median**	**2-year FFS (95% CI)**	**Median**	**2-year OS (95% CI)**
N0M0 + ADT (James *et al.*, 2016)	n/a	68% (54%-78%)	n/a	97% (93%-99%)
N1M0 + ADT (James *et al.*, 2016)		53% (40%-65%)		93% (88%-96%)
M1 + ADT (James *et al.*, 2015)	11 months	29% (25%-33%)	42 months	72% (68%-76%)

Table 1-8: Failure-free and overall survival amongst ADT-treated patients with advanced prostate cancer. Failure free survival defined as time from randomization to the first of the following events: biochemical failure; progression either locally, in lymph nodes, or in distant metastases; or death from prostate cancer (James *et al.*, 2016).

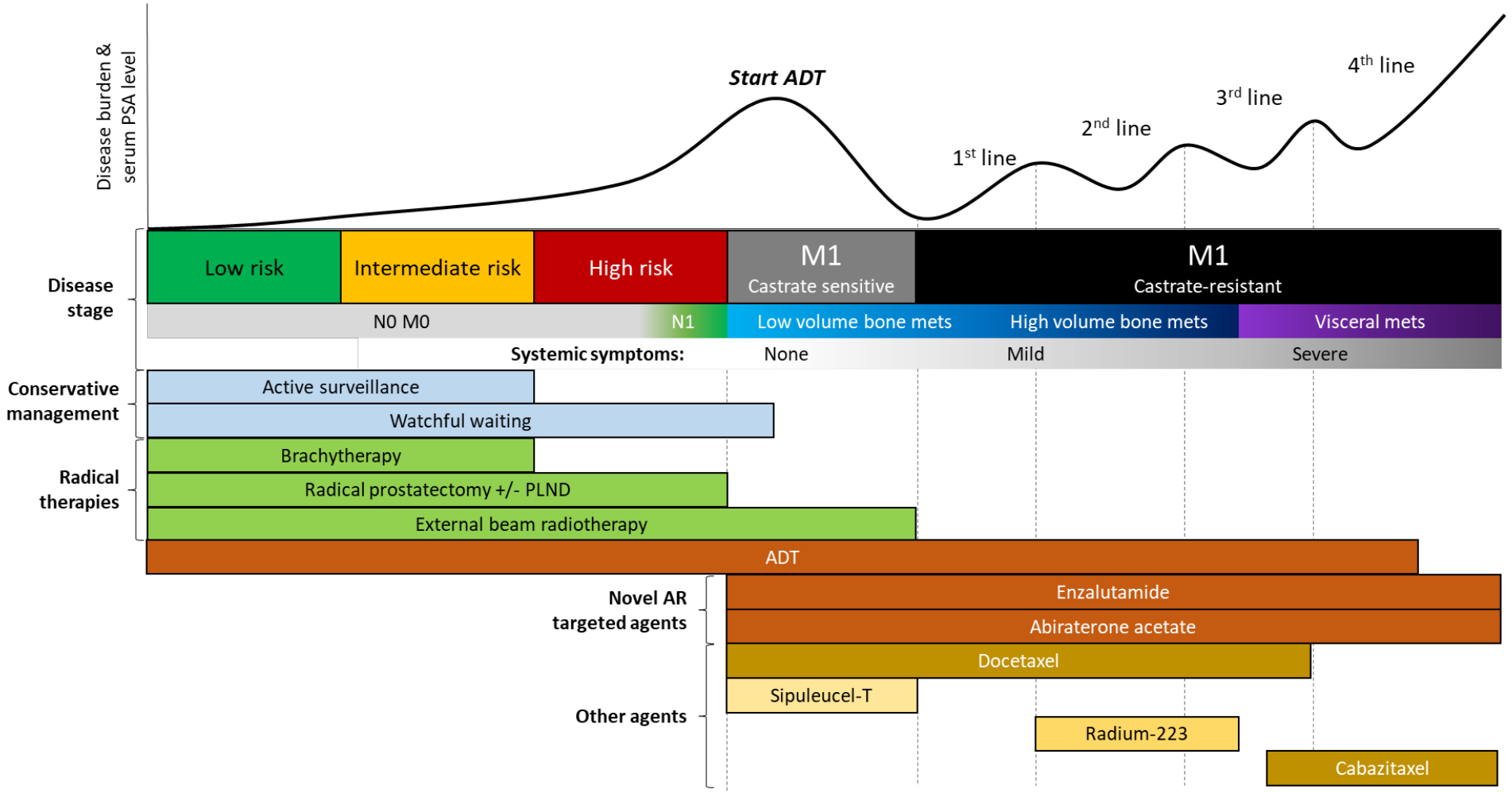

Figure 1-7: Treatment options in the management of prostate cancer. Adapted from Lorente *et al.* (2015). Non-metastatic castrate resistant PCa are not represented in this schematic. Note: Visceral metastasis may also occur concurrently with bone metastases

1.3.4 Follow-up

Following initial treatment of primary PCa, ongoing follow-up aims to assess and manage both treatment-related toxicity and disease progression. Depending on the treatment modality, clinical examination and measurement of serum PSA should be performed at each follow-up visit.

Serum PSA should be undetectable 6 weeks after a successful RP, with measurable serum PSA thought to be due to residual prostate tissue (Stamey *et al.*, 1989) and associated with increased risk of subsequent metastasis, cancer-specific and overall mortality (Preisser *et al.*, 2019a). Rising PSA following RP is considered 'biochemical recurrence' (BCR), which may be defined as two consecutively elevated PSA results greater than 0.2ng/ml (Freedland *et al.*, 2003), however a consensus definition is lacking (Cookson *et al.*, 2007). Amongst patients who develop BCR, 24-34% will progress to metastatic disease within 15 years of RP, and 2-6% will die due to PCa (Pound *et al.*, 1999). A subset of patients with high risk features in addition to development of BCR are at increased risk of overall mortality (Van den Broeck *et al.*, 2019). Thus, time to BCR is considered an early surrogate marker of subsequent disease progression, however, time to development of metastases more accurately predicts PCa mortality amongst patients with non-metastatic PCa (Xie *et al.*, 2017). Patients with who develop BCR or symptoms suggestive of metastatic progression should be restaged.

Positive surgical margins at radical prostatectomy is associated with increased risk of biochemical recurrence (Yossepowitch *et al.*, 2014). Patients with adverse risk features or PSM post-RP may be offered either a watchful waiting approach, ADT, adjuvant or salvage radiotherapy or salvage lymph node dissection (Ploussard *et al.*, 2019). Preliminary results of the RAVES trial (NCT00860652, 'Radiotherapy Adjuvant Versus Early Salvage') suggest comparable time to BCR between adjuvant and salvage radiotherapy amongst patients with high risk features following RP. The ongoing RADICALS trial (NCT00541047, 'Radiotherapy and Androgen Deprivation in Combination After Local Surgery') and GETUG-17 trial (NCT00667069, 'Groupe d'Etude des Tumeurs Uro-Génitales') may help further clarify the impact of radiotherapy and ADT on disease-free survival and progression-free survival in this setting, respectively.

Serum PSA levels fall more slowly following radical radiotherapy, as compared to RP, and may take up to 3 years to reach their lowest ('nadir PSA') level. The Phoenix criteria may be used to determine BCR amongst patients following radical radiotherapy, which is defined as an

increase of 2 ng/ml above the post-treatment nadir PSA (Abramowitz *et al.*, 2008). Such patients may either be offered salvage RP, cryotherapy, interstitial brachytherapy and high intensity focussed ultrasound, though the available evidence for these interventions is of low quality.

In addition to clinical evaluation and measurement of PSA, patients with primary PCa treated with ADT alone should additionally undergo serum testosterone monitoring and evaluation of complications associated with ADT, including development of metabolic syndrome, cardiovascular morbidity, mental health problems and bone resorption (Mottet *et al.*, 2018). Increasing serum PSA despite maximal androgen blockade may herald the development of castrate resistant PCa.

A summary of relevant clinical endpoints is presented in **Table 1-9**.

Endpoint	Definition
Biochemical recurrence	**Post-prostatectomy:** Two consecutively elevated PSA results greater than 0.2ng/ml.
	Post-radiotherapy: A rise by 2ng/ml or more above the nadir PSA (Phoenix criteria).
Disease-free survival (or relapse-free survival)	First evidence of recorded clinical recurrence (local/regional progression and/or distant metastases confirmed by imaging or histological evidence).
Progression-free survival (or event-free survival)	Any documented disease event (same as disease-free survival, plus biochemical failure) or death from any cause.
Metastasis-free survival	Documented metastatic disease or death from any cause.
Prostate cancer specific survival	Death directly attributable to prostate cancer.
Overall survival	Death from any cause.

Table 1-9: Definitions of clinical end points commonly used in prostate cancer trials.

1.4 Molecular biology of prostate cancer

1.4.1 Molecular alterations in prostate cancer

In comparison to other solid organ cancers, the molecular biology of PCa remains poorly understood. Recurrent autosomal genomic alterations occur at low frequencies in early PCa lesions, with higher frequencies of autosomal mutations only seen in advanced or metastatic disease (Armenia *et al.*, 2018).

Copy number alterations (CNA) are observed more frequently than point mutations in prostate cancer, ranging from an average CNA burden of 5% in primary disease to 32% in metastatic samples (Hieronymus *et al.*, 2014). These may frequently be observed in genes including 'Phosphate tensin homologue' (*PTEN*), 'retinoblastoma 1' (RB1), Myelocytomatosis (MYC), NK3 Homeobox 1 (NKX3-1), and Chromodomain Helicase DNA Binding Protein 1 (CHD1). Point mutations may be recurrently observed in approximately 5-15% of cases of localised prostate cancer, including 'speckle-type poxvirus and zinc finger protein' (*SPOP*), 'forkhead box A1' (*FOXA1*), and 'tumour protein 53' (*TP53*) genes (Taylor *et al.*, 2010; Cancer Genome Atlas Research, 2015; Fraser *et al.*, 2017).

The 'transmembrane protease serine 2–v-ets erythroblastosis virus E26 oncogene homolog' (*TMPRSS2-ERG*) gene fusion results in *ERG* overexpression and is observed in up to half of all prostate cancers (Esgueva *et al.*, 2010). It may play a role in tumour initiation with development of PIN lesions (Klezovitch *et al.*, 2008; Tomlins *et al.*, 2008), enriches for *PTEN* loss, and may subsequently cooperate with activated *Pi3k/Akt* signalling pathways to drive progression from HGPIN to invasive adenocarcinoma (Carver *et al.*, 2009). Similarly, NKX3-1 is a tumour suppressor gene on chromomose 8p, which stabilises *p53*, and inhibits *Akt* activation (Lei *et al.*, 2006). It may be downregulated in many high grade PCa lesions and eventually completely lost upon progression to metastatic disease (Bowen *et al.*, 2000; Gurel *et al.*, 2010). *SPOP* mutations alone do not initiate PCa, however, may cooperate with activated *Pi3k/Akt* and androgen receptor signalling pathways (Blattner *et al.*, 2017) to drive PCa progression.

1.4.2 Androgen receptor signalling

The androgen receptor is a nuclear hormone receptor, with AR signalling playing a pivotal role in prostate carcinogenesis. Since primary PCa tumour cells are dependent upon androgens, the binding of testosterone or DHT to the AR results in translocation of AR to the nucleus, where it recruits cofactors and regulates gene expression. AR amplification and point

mutations are observed in 46% and 10% of castrate resistant samples, however these alterations are rarely observed in early localised prostate cancer or without prior use of AR-targeted therapies (Barbieri *et al.*, 2012; Grasso *et al.*, 2012). Thus, aberrations in AR are thought to be mechanisms of resistance to ADT.

1.4.3 The *Pi3k/Akt/m-TOR* pathway and *PTEN*-loss

The *Pi3k/Akt/mTOR* signalling pathway is a signalling transduction pathway that plays an essential role in both anabolic and catabolic cellular processes (Edlind and Hsieh, 2014). A variety of signals may trigger the activation of this pathway, through receptor tyrosine kinases and insulin-like growth factor-1 (IGF-1) receptors. This causes the lipid kinase phosphoinositide 3-kinase (*PI3K*) to phosphorylate phosphatidylinositol-4,5-bisphosphate (*PIP2*) to phosphatidylinositol-3,4,5-triphosphate (*PIP3*). The action of *PTEN* counteracts this phosphorylation step. However, upon *PTEN* inactivation, unopposed action of *PIP3* causes the activation of the *Akt* family of serine/threonine protein kinases which, amongst other effects, stimulates mechanistic target of rapamycin (*mTOR*). *Akt* activation leads to multiple downstream effects to regulate cell growth, cell survival, cell cycle proliferation, metabolism, and angiogenesis (Edlind and Hsieh, 2014).

Importantly, a reciprocal feedback loop exists between *Pi3k/Akt* signalling and AR signalling, whereby AR signalling stabilises *Akt* and downregulates *Pi3k* activity via negative feedback, and Pi3k signalling inhibits AR activity by feedback inhibition of receptor tyrosine kinases (Carver *et al.*, 2011). Thus, both AR-targeted therapies (such as androgen deprivation therapy and castration) and *PTEN* loss, activates the *mTOR* pathway, enabling prostate cancer cells to survive and proliferate in an androgen independent manner. Thus, transgenic *Pten*-deficient mouse models develop castrate resistant PCa.

Though the impact of *PTEN* loss on activation of *Pi3k/Akt* signalling is most well established, *PTEN* loss is also implicated in *MAPK* activation, suppression of senescence and as a metastasis mediator (Conde-Perez *et al.*, 2015). Aberrations resulting in *MAPK* activation may also arise due to overexpression of Ras proto-oncogenes, including *K-ras*, *H-ras*, and *N-Ras*. *Ras* may interact with *Pi3k* by binding to its p110-binding domain, resulting in activation of both *Pi3k/Akt* and *MAPK* signalling pathways (Castellano and Downward, 2011). Thus, mutations in *K-ras* often result in aberrant *Ras* activation, thereby supporting cellular growth, proliferation, and survival.

PTEN loss also activates *p53*-mediated senescence, which halts cell proliferation and promotes immune surveillance (Chen *et al.*, 2005; Parisotto *et al.*, 2018). A reciprocal cooperation between *PTEN* and *p53* is therefore proposed, whereby *Pten* regulates *p53* stability and *p53* in turn enhances *PTEN* transcription. Phenotypes associated with *p53* mutations vary by mutation and exon type (Hartmann *et al.*, 1995). Notably, metabolic profiles, including mitochondrial function, also vary across different p53 mutations (Eriksson *et al.*, 2017).

1.4.4 Crosstalk between tumour signalling pathways in prostate cancer

The *PI3K/Akt/mTOR* signalling pathway is dysregulated in 42% of primary prostate cancers and 100% of metastatic tumours (Taylor *et al.*, 2010), and is often activated through the loss of heterozygosity of *PTEN*, which is a key tumour suppressor of this pathway. PTEN is most frequently altered as a deep deletion (Poluri and Audet-Walsh, 2018), with PTEN alterations observed in 20% primary PCa samples and over 50% castrate-resistant PCa samples (**Figure 1-8**)(Jamaspishvili *et al.*, 2018).

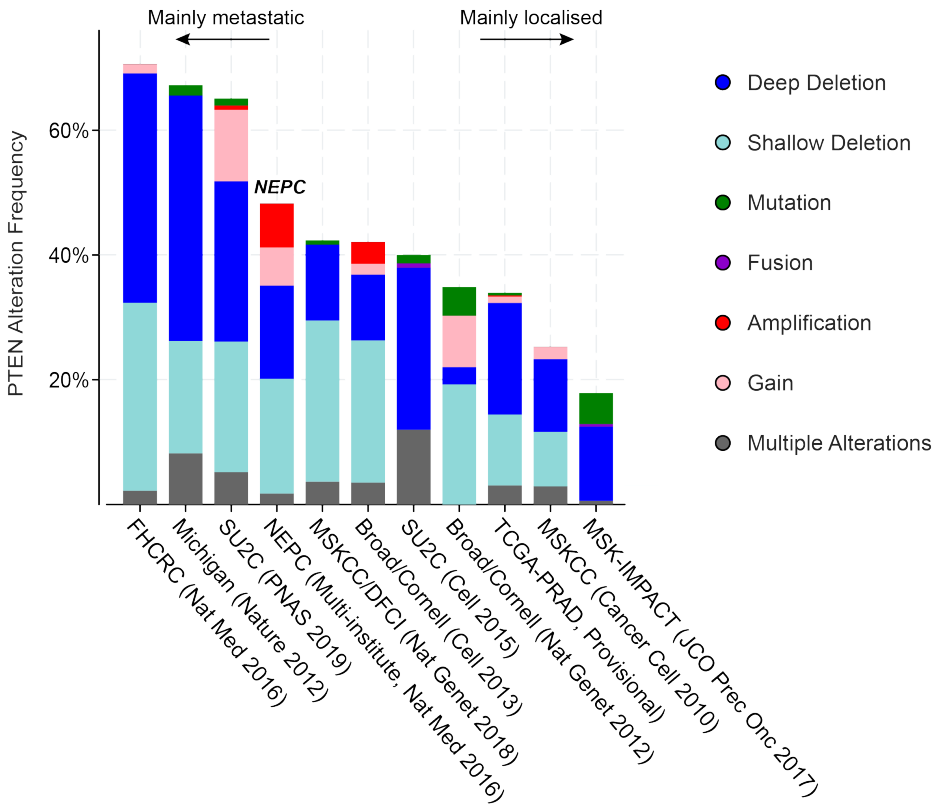

Figure 1-8: Frequency of Pi3k/Akt signalling alterations in PCa. Data from multiple cohorts evaluated using cBioPortal. Cohort names and associated references are annotated. NEPC: neuroendocrine prostate cancer.

Crosstalk between *Pi3k/Akt* and *MAPK* signalling results may accelerate PCa progression, via epithelial-to-mesenchymal transition (Mulholland *et al.*, 2012; Jefferies *et al.*, 2017). Activation of *MAPK* signalling is observed in 40% primary and 80% metastatic samples, and particularly amongst ADT-treated and CRPC specimens (Wang *et al.*, 2011), often with activated *Pi3k/Akt* signalling. In comparison, *TP53* alterations are observed in 24-43% primary and 67-90% metastatic specimens (Taylor *et al.*, 2010). Co-occurrence of *Pi3k/Akt* activation and *p53* alterations is observed in approximately 24% PCa samples (Millis *et al.*, 2019).

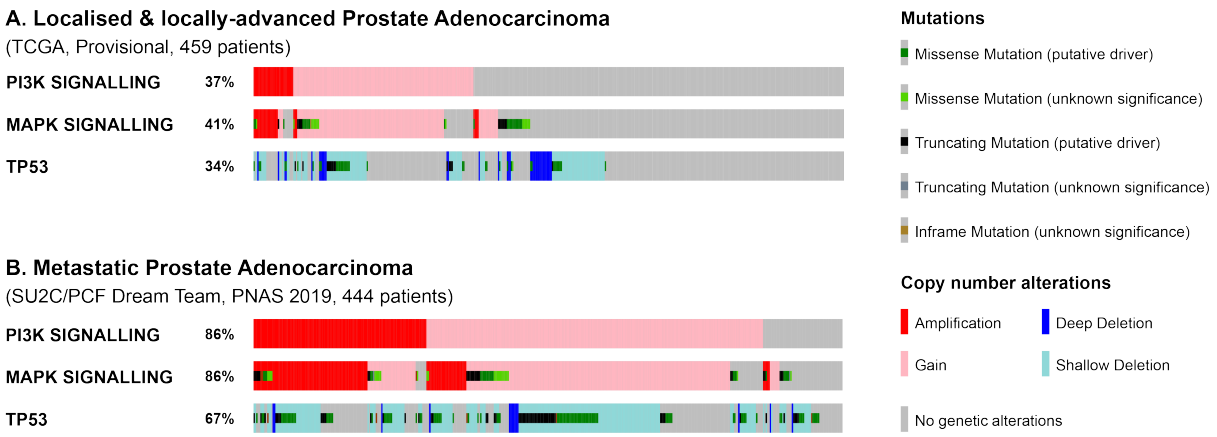

Figure 1-9: Co-occurrence of tumour signalling pathways in prostate cancer. Frequency of mutations and copy number alterations in genes associated with *Pi3k/Akt* signalling, *MAPK* signalling and *TP53* in **(A)** localised and locally advanced patients with prostate cancer in the TCGA-PRAD cohort (n=459), and **(B)** metastatic PCa patients in the SU2C/PCF cohort (n=444). Data were evaluated using cBioPortal.

1.5 Metabolic alterations in prostate cancer

1.5.1 Cellular metabolism

1.5.1.1 Overview

Cellular metabolism is comprised of a series of biochemical reactions that convert nutrients into small molecules called metabolites. These metabolites participate in a variety of cellular processes, where they may serve as energy equivalents (eg ATP), redox cofactors (eg NADH, $FADH_2$), building blocks for biomass, and substrates. Thereby, cellular metabolism pervades every aspect of biology. Consequently, metabolic reprogramming reflects alterations in cancer cell requirements. Key substrates for cancer cell metabolism include carbohydrates, lipids and proteins, which are initially broken down into simpler forms, such as glucose, fatty acids and amino acids. Relevant pathways implicated in PCa metabolism are discussed below.

1.5.1.2 Glycolysis

Glucose enters the cell via glucose transporters (GLUTs) at the cell membrane. It can then participate in glycolysis, comprising 10 enzyme catalysed reactions that breakdown glucose into pyruvate with the simultaneous production of ATP and NADH. This process occurs in the cytosol in both aerobic and anaerobic conditions, with the net reaction summarised as below:

$$\text{Glucose} + 2\text{NAD}^+ + 2\text{ADP} + 2\text{P}_i \rightarrow 2\text{Pyruvate} + 2\text{NADH} + 2\text{H}^+ + 2\text{ATP} + 2\text{H}_2\text{O}$$

1.5.1.3 Pyruvate decarboxylation

Pyruvate released from glycolysis in the cytosol is transported into the mitochondrial matrix by the transport protein pyruvate translocase. Decarboxylation of pyruvate forms acetyl co-enzyme A (CoA), and reduction of NAD to NADH, with the net reaction summarised below:

$$\text{Pyruvate} + \text{CoA} + \text{NAD}^+ \rightarrow \text{Acetyl CoA} + \text{CO}_2 + \text{NADH} + \text{H}^+$$

Acetyl co-enzyme A then participates in the Krebs cycle, whereas NADH is utilised in generation of ATP via the electron transport chain.

1.5.1.4 Fatty acid oxidation

Long chain fatty acids enter the cell via a family of fatty acid transporters (FAT) and are activated in the cytosol by conjugation with co-enzyme A (CoA), catalysed by acetyl CoA synthetase (ACS), to form fatty acyl CoA. Fatty acyl CoA enters the mitochondrial matrix in two steps. It first enters the intermembrane space using the carnitine shuttle, where it is initially converted to acylcarnitine by carnitine palmitoyl transferase I (CPT1) located at the outer mitochondrial membrane. Subsequently, it then enters the mitochondrial matrix by the carnitine-acylcarnitine transporter (CAT), where it is converted back to fatty acyl CoA by CPT2 located at the inner mitochondrial membrane. Breakdown of fatty acids by β-oxidation leads to the formation of a series of two-carbon units which combine with co-enzyme A to form acetyl CoA. This process is associated with the reduction of nicotinamide adenine dinucleotide (NAD) and flavin adenine dinucleotide (FAD) to NADH and $FADH_2$ respectively.

$$C_n\text{-acyl-CoA} + \text{FAD} + \text{NAD}^+ + \text{H}_2\text{O} + \text{CoA} \rightarrow C_{n-2}\text{-acyl-CoA} + \text{FADH}_2 + \text{NADH} + \text{H}^+ + \text{acetyl-CoA}$$

In addition, *de novo* fatty acid synthesis from TCA cycle intermediate is a hallmark of prostate cancer (Poulose *et al.*, 2018) and also results in the production of fatty acids.

1.5.1.5 Tricarboxylic acid (TCA) cycle

The TCA cycle (also known as the Kreb's cycle) consists of eight steps that are catalysed by different enzymes and is initiated when acetyl-coenzyme A joins oxaloacetate to form citrate. This first step is irreversible and is controlled by negative feedback, i.e. accumulation of high energy molecules such as acetyl-CoA inhibits the rate of reaction. The pathway is cyclic but there are several branch points; once acetyl-CoA enters the pathway, instead of completing the full cycle it can also be used for the synthesis of non-essential amino acids or storage of glucose when levels of oxaloacetate are high.

The TCA cycle plays a central role in the biosynthesis of key cellular intermediates for anabolic reactions and catabolism of organic fuel molecules. One molecule of ATP is directly produced in step 5 of the cycle; however, most energy is obtained by generation of NADH and $FADH_2$, which can enter the ETC for ATP production. This is later discussed in section 1.6. The net reaction of the TCA cycle is as follows:

$$\text{Acetyl CoA} + 3NAD^+ + FAD + ADP + P_i + 2H_2O \rightarrow CoA + 3NADH + 2H^+ + FADH_2 + ATP + 2CO_2$$

1.5.1.6 Glutamine metabolism

Glutamine is the most abundant amino acid in circulation, and has long been considered a hallmark of cancer cell metabolism (Cluntun *et al.*, 2017). Upon entering cells via the *SLC1A5* transport, glutamine is used for both nucleotide synthesis and cell metabolism. Glutamine then enters mitochondria via glutamine transports, where its deamination generates glutamate. Glutamate is transformed into glutaminase and subsequently into α-ketoglutarate that is shuttled into the TCA cycle. In prostate cancer, however, the enzyme glutaminase-1 is upregulated, which leads to enhanced cellular uptake of glutamine. Albeit the mechanism is not well-understood, under hypoxic conditions, cells can use reductive metabolism to produce acetyl-CoA from α-ketoglutarate and thereby provide both metabolites and lipids to support rapid cell division (Metallo *et al.*, 2011; Hosios *et al.*, 2016).

1.5.1.7 Oxidative phosphorylation

Transport of cytosolic NADH to the mitochondria via two redox shuttles including the malate/aspartate shuttle and the glycerol 3-phosphate shuttle. NADH and FADH transfer electrons to complexes I and II of the electron transport chain (ETC), which are shuttled across the ETC to create a proton gradient across the IMS and mitochondrial membrane. This proton gradient is eventually used by complex V, ATP synthase, to phosphorylate ADP to ATP. Oxidation of each NADH and $FADH_2$ molecule results in production of 3 and 2 ATP molecules, respectively. Further details regarding the structure and function of the electron transport chain in oxidative phosphorylation are provided in section 1.6.4.

1.5.1.8 *De novo* fatty acid synthesis

Increased cancer cell proliferation is supported by *de novo* synthesis of fatty acids to ensure availability of sufficient lipids for membrane production (Mashima *et al.*, 2009). Two key enzymes involved in this process include acetyl-CoA carboxylase (ACC) and fatty-acid synthase (FASN). ACC carboxylates acetyl-CoA to form malonyl-CoA, which is subsequently converted

into long-chain fatty acids by FASN. In benign cells, FASN is expressed in low levels which suppresses *de novo* fatty acid synthesis. Several studies have reported overexpression of *FASN* in various human cancers, including prostate, stomach, ovary, and lung cancer (Jones and Infante, 2015). The role of *ACC* is relatively less understood; however, its pharmacological inhibition has shown to decrease prostate cancer cell migration and cell proliferation (Singh and Singh, 2017).

1.5.2 Warburg effect

Otto Warburg first observed that cancer cells switch energy metabolism from OXPHOS to aerobic glycolysis, which is now commonly referred to as 'the Warburg effect' (Warburg, 1956). This implies that cancer cells undergo aerobic glycolysis, whereby glucose in the cytoplasm is converted to pyruvate and then to lactate, forming 4 molecules of ATP per molecule of glucose. Whereas during oxidative phosphorylation, glucose molecules are broken down to pyruvate in the cytoplasm which is then transported into the mitochondria where it is broken down to carbon dioxide, releasing 36 molecules of ATP per molecule of glucose. Though aerobic glycolysis is less energy efficient compared to OXPHOS, it provides greater biomass to support cell proliferation. Furthermore, glycolysis causes upregulation of glucose transporters, which increases glucose import into the cytoplasm (Vander Heiden *et al.*, 2009; Hanahan and Weinberg, 2011). Warburg suggested that mitochondrial alterations may account for this phenomenon (Warburg, 1956). These alterations may include mtDNA mutations, altered expression, changes in mtDNA content and altered activity of respiratory chain subunits (Chatterjee *et al.*, 2006).

1.5.3 Normal prostate metabolism

The normal human prostate has a unique metabolism due to increased uptake of zinc via ZIP transporters resulting in inactivation of the aconitase enzyme (Costello *et al.*, 1997; Tsui *et al.*, 2006). Since aconitase is responsible for the conversion of citrate to isocitrate in the TCA cycle, inactivation of aconitase leads to increased mitochondrial citrate levels and truncation of the TCA cycle. Citrate is exported to the cytosol and then into the prostate gland lumen, where it plays an important role in maintaining sperm viability through calcium chelation and as an energy source (Ford and Harrison, 1984).

1.5.4 Bioenergetic theory of prostate cancer

Notably, citrate levels of the prostate are highest in the peripheral zone of the normal prostate (Costello and Franklin, 2006), which correlates with increased *de novo* fatty acid synthesis and increased incidence of prostate cancer in this region (Al Kadhi *et al.*, 2017).

Transformation to PCa results in suppression of ZIP transporters with consequently reduced mitochondrial zinc levels. Thus, aconitase activity is not suppressed, leading to oxidation of citrate to isocitrate in the TCA cycle. With progression to advanced stages of malignancy, mitochondrial zinc levels are further suppressed, resulting in uninhibited progression of the TCA cycle and thereby lower levels of citrate excretion. Thus, there is a shift from citrate producing non-malignant cells to citrate oxidising malignant cells (ie increased TCA cycle turnover) (Costello *et al.*, 1999).

Since the truncated TCA cycle observed in normal prostate tissue is highly inefficient, Franklin and Costello proposed that the dramatic decrease in citrate levels observed in PCa may be an adaptive mechanism to return to a more energy-efficient system, whereby oxidation of citrate to isocitrate helps complete the TCA cycle (Costello and Franklin, 2006). Thus, metabolically inefficient healthy prostate cells are converted to metabolically efficient malignant prostate cells.

The altered zinc and citrate phenotype in early stage PCa has a dual role; by activating the TCA cycle there is more energy available for cell growth and low levels of zinc, which help cells overcome apoptopic regulation (Costello *et al.*, 2005). An alternative mechanism is also proposed, whereby reduced citrate may result from decreased carbon flux from glycolysis to the TCA cycle or increased cytosolic utilisation of citrate to generate downstream products such as lipids and amino acids (Lloyd *et al.*, 2015).

These metabolic changes observed in PCa progression, including reduced citrate levels (as described above) and increased choline (Awwad *et al.*, 2012), are currently being evaluated as potential diagnostic and prognostic markers, using magnetic resonance spectroscopy (Tayari *et al.*, 2017).

1.5.5 Impact of hypoxia on cell metabolism

The Krebs cycle has a number of reversible steps, including the formation of α-ketoglutarate from citrate. These steps include a decarboxylation process resulting in formation of carbon dioxide. However, under hypoxic conditions which implies a low O_2 content and high CO_2 content in tissue, the equilibrium of the reaction shifts towards the reactants and reductive metabolism can occur. This reductive glutamine metabolism can lead to the increased formation of lipids and metabolic programming of the cells, which may positively impact cancer progression (Eidelman *et al.*, 2017).

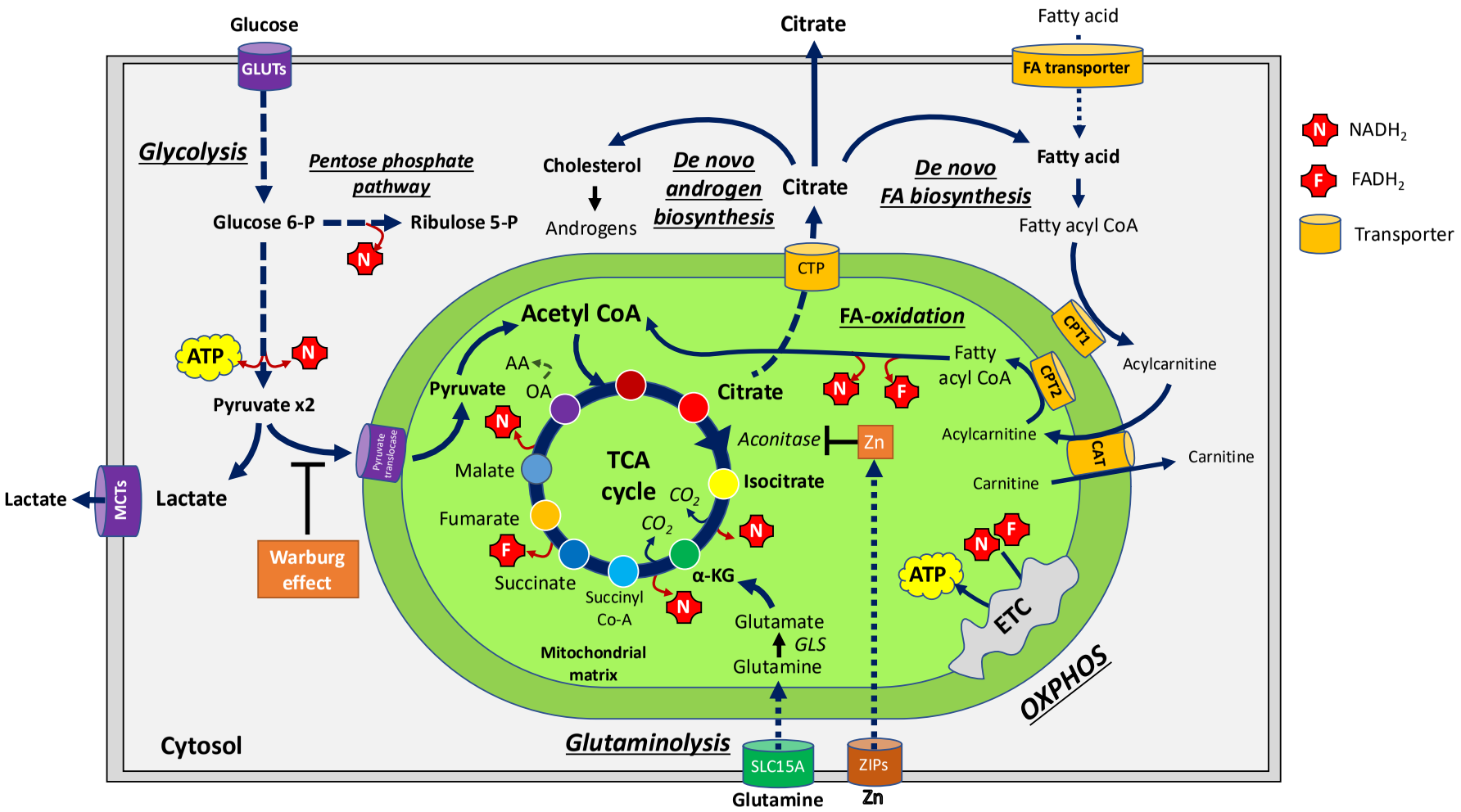

Figure 1-10: Prostate metabolism. FA: Fatty acid, MCT: Monocarboxylate transporters, ZIP: Zinc/iron permease, CTP: citrate transporter protein, CPT: carnitine palmitoyltransferase. ETC: Electron transport chain, ATP: Adenosine triphosphate, GLUT: Glucose transporter; CoA: Co-enzyme A, CAT: Carnitine-acylcarnitine translocase; GLS: Glutaminase.

1.6 Mitochondrial biology

Mitochondria are semi-autonomous dynamic organelles found in all nucleated mammalian cells. They are the only extra-nuclear organelle that contain their own DNA, which encodes key protein subunits for oxidative metabolism. Mammalian somatic cells are estimated to contain 80 to 2000 mitochondria per cell, which varies by tissue type and stage of the cell cycle, in response to stress and across development (Cole, 2016). The main functions of mitochondria include synthesis of adenosine triphosphate (ATP) by oxidative phosphorylation (OXPHOS), calcium homeostasis, regulation of apoptosis, and iron-sulphur cluster biogenesis.

1.6.1 Eukaryotic origin of mitochondria

Lynn Margulis first posited the endosymbiotic hypothesis in 1967, which states that eukaryotic cells emerged from the symbiotic merging of two prokaryotic cells, including an α-proteobacteria endosymbiont and an archaebacteria host (Sagan, 1967). It is estimated that this event occurred nearly two billion years ago, overlapping with the main period of rapid oxygenation of the Earth's atmosphere (Sicheritz-Ponten *et al.*, 1998). Since the α-proteobacteria were capable of respiring oxygen, symbiosis enabled both cytosolic glycolysis and oxidative respiration in the resulting organism (Gabaldon and Huynen, 2003). It is thought that subsequent evolutionary events led to the transfer of a large fraction of original genes in the α-proteobacteria ancestor to the host genome, and a small fraction of genes in the α-proteobacteria endosymbiont were recruited by the host nuclear genome (Karlberg *et al.*, 2000). This corresponds to the dual nature of the mitochondrial proteome, which is encoded by both mitochondrial and nuclear genes.

1.6.2 Mitochondrial structure

Mitochondria are elongated rod-shaped structures approximately measuring 2.5µm in length and 0.5µm in diameter, and with a double membrane surrounding a matrix. This double-membrane system consists of inner and outer mitochondrial membranes, separated by an inter-mitochondrial space (**Figure 1-11**). The inner mitochondrial membrane is organised into numerous folds called 'cristae', which extend into the mitochondrial matrix, and contains complexes of the electron transport chain (ETC). The matrix contains enzymes for the tricarboxylic acid cycle, other than succinate dehydrogenase, which is embedded within the inner mitochondrial membrane as part of the ETC. The inner mitochondrial membrane is impermeable to most ions and small molecules, which helps maintain the proton gradient required to drive oxidative phosphorylation. In contrast, the outer mitochondrial membrane

contains proteins called 'porins', which allow small molecules to permeate into the intermembrane space.

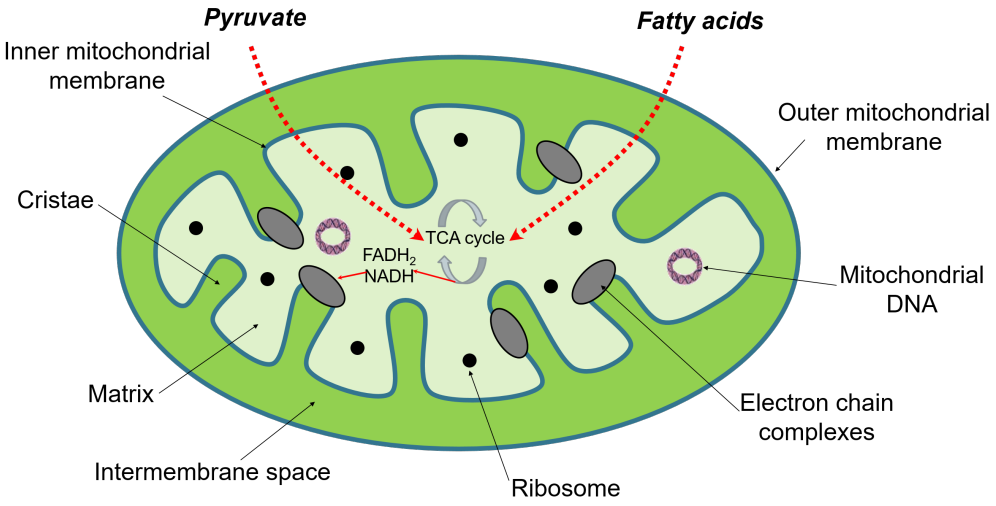

Figure 1-11: Structure of the mitochondria. Adapted from Cooper (2000). Dotted red arrows represent the influx of pyruvate and fatty acids from the cytosol into the mitochondrial matrix, where they enter the TCA cycle to form electron rich NADH and $FADH_2$. These electron rich molecules then enter the ETC on the inner mitochondrial membrane to form ATP via OXPHOS.

1.6.3 Mitochondrial genome

Mitochondria are unique amongst cytoplasmic organelles in that they carry their own compact, circular, double-stranded DNA, which is maternally inherited. There may be 100 to 10,000 copies of mitochondrial DNA (mtDNA) molecules in each cell, in a tissue-specific manner (Clay Montier *et al.*, 2009). Each double-stranded mitochondrial DNA (mtDNA) molecule consists of 16,569 base pairs in a circular genome (**Figure 1-12**). This is organised into a guanine-rich heavy strand (H-strand) and a cytosine-rich light strand (L-strand). Together, these encode 37 genes, including 13 subunits of OXPHOS complexes, 22 transfer RNAs (tRNAs) and 2 ribosomal RNAs (rRNAs) (Anderson *et al.*, 1981). The remaining 77 subunits of the OXPHOS complexes are encoded by nuclear genes. Thus, mitochondria rely on close genetic coordination between nuclear and mitochondrial genomes.

Unlike nuclear DNA, there are no introns or intergenic regions within mtDNA. However, unusually, a 1.1kb triple-stranded displacement loop (D-loop), also referred to as the 'control region', is the major non-coding region. The D-loop also harbours three highly conserved sequence blocks (*CSB1-3*), though its functional relevance is unclear (Nicholls and Minczuk, 2014). It is the site of initiation of mtDNA replication as it contains the origin of H strand

replication, whereas the origin of L-strand replication is located between *MT-TC* and *MT-TN* genes (Montoya *et al.*, 1982). The D-loop is also a site of initiation of transcription since it contains binding sites for mitochondrial transcription factor A (*TFAM*), one H-strand promoter (HSP1) and the L-strand promoter (LSP), though the second heavy strand promoter (HSP2) is located near the 5' end of the *MT-RNR1* gene.

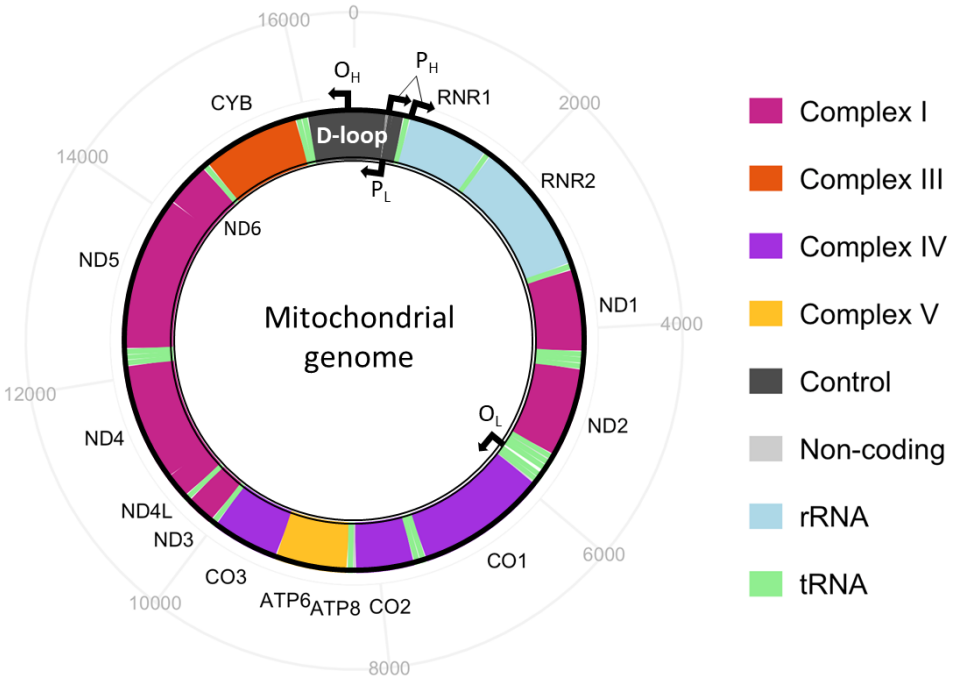

Figure 1-12: The mitochondrial genome. Colours denote genes encoding subunits of individual complexes, rRNA and tRNA genes. Genes encoding OXPHOS complexes are annotated. Origin of replication of heavy (O_H) and light (O_H) strands, and promoter regions of heavy (P_H) and light (P_L) strands are also annotated. Outer numbers represent base pair position.

1.6.3.1 mtDNA replication

The entire mtDNA molecule may replicate in 90 minutes (Clayton, 1982). Unlike nuclear DNA, the mtDNA replication is active throughout the cell cycle (Bogenhagen and Clayton, 1977). MtDNA replication requires nuclear-encoded replication machinery consisting of DNA polymerase γ (*Polγ*, or *Polg*), single stranded DNA binding protein (*mtSSB*), and the mitochondrial DNA helicase *TWINKLE* (Falkenberg, 2018). Mitochondrial *Polg* is comprised of two key subunits, including the catalytic *PolgA* domain and the accessory *PolgB* domain. The 3'-5' exonuclease activity of the catalytic *PolgA* domain plays a principle proofreading function during mtDNA replication, with its catalytic activity further enhanced by the accessory *PolgB*

domain. Replication is initiated at the origin of replication sites for both H and L strands of the mitochondrial genome by the ATP-dependent 5'-3' helicase activity of *TWINKLE* (Korhonen *et al.*, 2003). Unwound single stranded DNA is then stabilised by the mtSSB for uninterrupted replication and increased processivity by *Polg* (Kaguni, 2004).

Two models of mtDNA replication have been proposed: the asynchronous strand displacement model (Clayton, 1982), and the synchronous model (Holt *et al.*, 2000). According to the asynchronous strand displacement model, replication starts at the O_H site and proceeds around the genome until it reaches the O_L site, at which point the leading single stranded mtDNA binds to the light strand and commences replication of the lagging strand, with the mtDNA molecule subsequent circularised by ligation. In contrast, according to the synchronous model, replication at both light and heavy strands occurs simultaneously, assisted by short Okazaki RNA fragments, which are subsequently converted to DNA (Yasukawa *et al.*, 2006).

1.6.3.2 mtDNA transcription

The nuclear-encoded mitochondrial transcription machinery comprises of mitochondrial RNA polymerase (POLMRT), mitochondrial transcription factor A (TFAM) and mitochondrial transcription factor B2 (TBF2M). MtDNA promoter regions are thought to be unwound by TFAM (Fisher *et al.*, 1992). POLMRT and TFB2M form a heterodimer, whereby TFB2M stabilises single stranded DNA (ssDNA) enable subsequent transcription by POLMRT (Falkenberg *et al.*, 2002). Transcription is initiated at two heavy strand promoters (HSP1, HSP2) and the light strand promoter (LSP) regions. Bidirectional transcription of heavy and light strands results in polycistronic transcripts, which are then cleaved by RNA processing enzymes which target tRNA cloverleaf folds (Ojala *et al.*, 1981). The 5' and 3' ends of tRNAs are then cleaved by secondary RNAase enzymes. Once polycistronic mRNA has been transcribed, transcription is terminated by mitochondrial termination factors (mTERF1-4).

1.6.3.3 mtDNA translation

Mammalian mtDNA encodes 22 mitochondrial tRNAs, which form cloverleaf structures with four stems and three loops. The mitochondrial translation machinery, also referred to as the 'mitoribosome', is located in the matrix and consists of two nuclear-encoded subunits (28S and 39S) and two mitochondrial rRNAs (12S and 16S). Similar to bacterial translation, mitochondrial translation is composed of three stages: initiation, elongation and termination. Mitochondrial initiation factors mtIF2 and mtIF3 are require for initiation. MtIF2 selects

initiator methionine tRNA (Suzuki *et al.*, 2011), whereas mtIF3 promotes dissociation of the mitoribosome into subunits, binds the ribosomal initiation complex to the initiator tRNA (Kuzmenko *et al.*, 2014) and also performs a proof-reading function by rejecting initiation complexes lacking mRNA or incorrectly loaded elongator tRNAs (Christian and Spremulli, 2009). Elongation is polypeptides requires factors including *mt-EFTu*, *mt-EFTs*, and *mt-EFG1*, and continues until a stop codon (either UAA or UAG) is reached and recognised by the mitochondrial release factor 1a (*mt-RF1a*), eventually releasing the polypeptide from the 39S subunit (Soleimanpour-Lichaei *et al.*, 2007). The mitoribosome is then dissociated using two mitochondrial recycling factors, *mt-RRF1* and *mt-EFG2* (Rorbach *et al.*, 2007).

1.6.4 Oxidative phosphorylation

The electron transport chain on the inner mitochondrial membrane is the site of oxidative phosphorylation (OXPHOS). The mitochondrial respiratory chain (RC) or 'electron transport chain' (ETC) consists of five complexes embedded within the inner mitochondrial membrane, which participate in oxidative phosphorylation (**Figure 1-13**). Electron-rich NADH and $FADH_2$, primarily produced as a by-product of the TCA cycle and cytosolic glycolysis, enter Complex I of the ETC. Electrons from these carrier molecules, in addition to those from fatty acid ß-oxidation, along with translocation of protons across complexes I, III and IV, results in a chemo-osmotic proton gradient, which is utilised by Complex V to eventually phosphorylate adenosine diphosphate (ADP) to ATP.

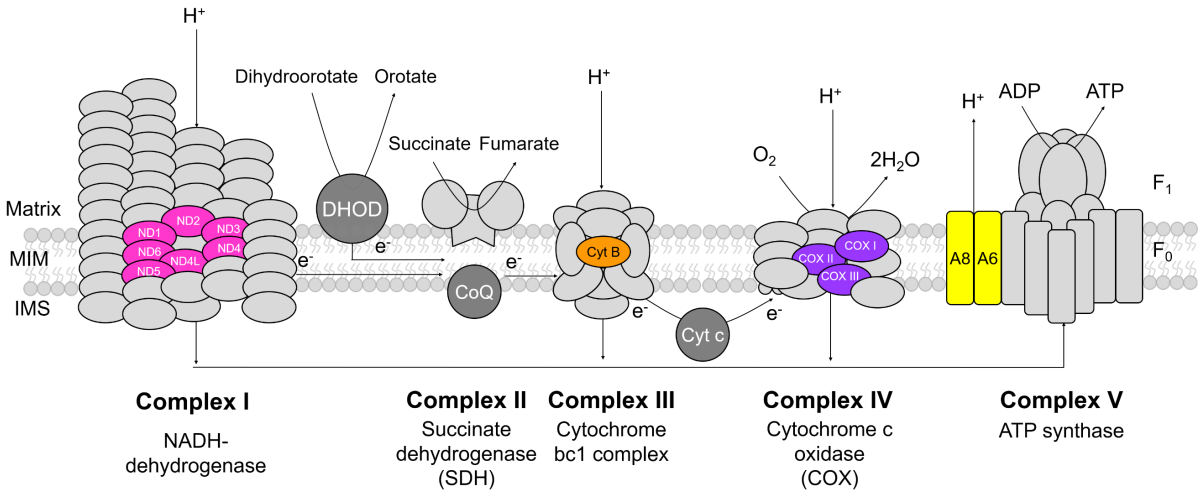

Figure 1-13: Schematic of the mitochondrial respiratory chain. Mitochondrial-encoded subunits are highlighted in colours corresponding to associated protein complex. Adapted from Schon *et al.* (2012). CoQ: co-enzyme Q; DHOD: dihydro-odorate; Cyt c: cytochrome c.

1.6.4.1 Complex I

Complex I, also referred to as NADH-dehydrogenase or NADH:ubiquinone oxioreductase, is the largest respiratory complex, comprising 45 subunits including seven mitochondrial-encoded and 38 nuclear-encoded subunits (Zhu *et al.*, 2016). Amongst these, 14 subunits are core subunits, which are highly conserved across both bacteria and human mitochondria, and essential for enzymatic function. Loss of core subunits results in enzymatic defects in patients with mitochondrial disease (Lazarou *et al.*, 2009). The remaining 31 subunits are accessory subunits, which also play an important role in mitochondrial structure and function (Stroud *et al.*, 2016). Notably, *NDUFAB1* is essential for cell viability (Stroud *et al.*, 2016). The assembly of this large complex is further supported by 13 assembly proteins (*NUBPL*, *NDUFAF1-7*, *TIMMDC1*, *ECSIT*, *ACAD9*, *TMEM126B*, *FOXRED1*)(Sanchez-Caballero *et al.*, 2016). Complex I is the entry point for most electrons into the respiratory chain, and considered a rate limiting step in oxidative metabolism (Sharma *et al.*, 2009). The key function of Complex I involves the oxidation of NADH associated with the release of two electrons, reduction of ubiquinone (Q) to ubiquinol (QH_2), eventually allowing four protons to flow from the matrix to the inter-membrane space (Efremov *et al.*, 2010; Baradaran *et al.*, 2013). The key reaction at Complex I may be summarised using the following equation:

$$NADH + CoQ + 5H^+_{matrix} \rightarrow NAD^+ + CoQH_2 + 4H^+_{ims}$$

1.6.4.2 Complex II

Complex II, succinate ubiquinone oxidoreductase, is comprised of four nuclear-encoded subunits, two of which lie within the matrix (SDHA, SDHB) and two lie within the inner mitochondrial membrane (SDHC, SDHD) (Hagerhall, 1997). Besides Complex I, Complex II is the only other entry point of electrons at the ETC. In addition to its role at the ETC, Complex II also participates in the TCA cycle, where it converts succinate to fumarate, and releases $FADH_2$, which is then oxidised to FAD^+ at the inner mitochondrial membrane. This results in the release of two electrons, which are shuttled across FeS clusters, leading to the reduction of co-enzyme Q. Unlike other ETC complexes, Complex II does not participate in the transfer of protons across the inner mitochondrial membrane. The overall reaction at Complex II may be summarised using the following equation:

$$Succinate + CoQ \rightarrow Fumarate + CoQH_2$$

1.6.4.3 Complex III

Complex III, ubiquinol:cytochrome *c* reductase, is composed of 11 subunits, of which ten are nuclear-encoded and only one, *cytochrome b* (*MT-CYB*), is mitochondrial encoded. Two cycles of reduction of cytochrome *c* (*Cytc*) results in the transfer of four protons from the matrix to IMS, and the uptake of two protons from Complex I at the matrix, which reduce ubiquinol (QH_2) to ubiquinone (Q). The overall reaction at Complex III may be summarised using the following equation:

$$2QH_2 + Q + 2Cytc_{oxidised} + 2H^+_{matrix} \rightarrow 2Q + 2Cytc_{reduced} + 2Cytc + 4H^+_{IMS} + 2e^-$$

1.6.4.4 Complex IV

Complex IV, cytochrome *c* oxidase, is composed of 14 units, including three core mitochondrial encoded subunits (CO1-3), and 11 nuclear-encoded subunits (Tsukihara *et al.*, 1996). As the last enzyme in the ETC, Complex IV is responsible for the reduction of molecular oxygen to water, using electrons delivered by cytochrome c, which is oxidised. This process is associated with the transfer of four protons from the matrix to the IMS, and may be summarised as follows:

$$4Cytc_{reduced} + 8H^+_{matrix} + O_2 + 4e^- \rightarrow 4Cytc_{oxidised} + 2H_2O + 4H^+_{IMS}$$

1.6.4.5 Complex V

Complex V, ATP synthase is comprised of 16 subunits, including two mitochondrial-encoded subunits. It composed of two regions: the F0 section forming a central stalk bound within the IMM and the F1 section forming a peripheral stalk located within the matrix (Yoshida *et al.*, 2001). The transfer of protons across the mitochondrial membrane by Complexes, I, III, and IV of the ETC results in an electrochemical gradient between the inner mitochondrial space and matrix, referred to as the membrane potential ($\Delta\Psi m$). Complex V catalyses the synthesis of ATP from ATP, using inorganic phosphate. The transfer of approximately three protons across the ATP synthase complex is required for the synthesis of one ATP molecule, which may be summarised as follows:

$$ADP + P_i + 3H^+_{IMS} + \tfrac{1}{2}O_2 + 2e^- \rightarrow ATP + H_20 + H^+_{matrix}$$

1.6.5 Calcium homeostasis

Mitochondria act as intracellular Ca^{2+} buffers, via voltage dependent anion channels (VDAC) and ruthenium red-sensitive mitochondrial Ca^{2+} uniporter (MCU) to transport Ca^{2+} across the outer and inner mitochondrial membranes, respectively (Pinton *et al.*, 2008; Baughman *et al.*, 2011; De Stefani *et al.*, 2011; Betz *et al.*, 2013). This enables mitochondria to absorb up to 1000 nmol Ca^{2+}/mg mitochondrial mass (Kirichok *et al.*, 2004). Calcium supports enzymatic activity of TCA cycle, thereby accelerating shuttling of intermediates and reduction of NAD to NADH (McCormack *et al.*, 1990; Jouaville *et al.*, 1999), which results in ATP production at the ETC. Importantly, absence of calcium may lead to reduced ATP production and AMPK-mediated autophagy (Giorgi *et al.*, 2008).

1.6.6 Iron-sulphur cluster formation

Reduced iron is transferred into the mitochondrial matrix by mitoferrins 1 and 2 (Paradkar *et al.*, 2009), where nuclear-encoded mitochondrial proteins including *Isu1/2*, *Grx5* and *Abcb7* are involved in the formation of iron sulphur (Fe-S) clusters (Wang and Pantopoulos, 2011). Fe-S clusters play a crucial role in accepting and donating electrons across OXPHOS complexes I, II, and III (Stehling *et al.*, 2009). For instance, complex I activity depends upon eight iron-sulphur clusters (Sazanov, 2015). Furthermore, Fe-S clusters are also involved in binding of substrates involved in the TCA cycle such as aconitase, which catalyses oxidation of citrate to isocitrate, and conversion of succinate to fumarate catalysed by succinate dehydrogenase (Akram, 2014). Thus, mitochondrial Fe-S cluster formation plays an important role in metabolism.

1.6.7 Apoptosis

Mitochondria play an important role in activation of programmed cell death, also referred to as apoptosis. Apoptosis is used to control the cell population and degrade cells harbouring DNA damage. Cytochrome c is bound to cardiolipin in the inner mitochondrial membrane via electrostatic and hydrophobic interactions and plays a fundamental role in initiating the intrinsic apoptosis pathway (Orrenius and Zhivotovsky, 2005). Upon increase of the mitochondrial ROS production, cardiolipin is oxidized and hence cytochrome c is released into the cytosol (Ott *et al.*, 2007). This causes the activation of caspases, proteases and enzymes

that cleave specific intracellular substrates in order to kill and dismantle cells destined for apoptosis (McIlwain *et al.*, 2013).

The release of cytochrome c from the mitochondria is controlled by the Bcl-2 proteins *Bax* and *Bak*. These proteins have a globular structure and appear as monomers in healthy cells. However, following stress signals, these convert into oligomeric complexes that move to the outer mitochondrial membrane (Westphal *et al.*, 2011). In this process, they create apoptopic pores and promote cell permeabilisation, which in turn leads to caspase activation and cell death.

1.6.8 ROS production

Reactive oxygen species are produced during a variety of biochemical reactions and have an important role in cellular signalling pathways, cell differentiation, proliferation, senescence and apoptosis (Valko *et al.*, 2007). In the ETC, oxygen is normally fully reduced to produce water. However, in 0.1-2% of all cases, incomplete reduction of oxygen leads to the formation of the superoxide radical (O_2^-). This superoxide radical is the precursor of most ROS. The principal sites of production of reactive oxygen species (ROS) are Complexes I & III (Turrens and Boveris, 1980), with dysfunction of complexes I and III being associated with increased ROS production, as a by-product of enzymatic reactions (Murphy, 2009). Under the influence of environmental stress, ROS levels can increase dramatically leading to oxidative stress which can damage macromolecular complexes including DNA, proteins, and lipids (Shadel and Horvath, 2015).

1.6.9 Mutations in mtDNA

The mtDNA mutational rate is thought to be approximately ten-times greater than nuclear DNA due to a lack of “protective” histones, close proximity to site of ROS production at the respiratory chain leading to oxidative damage and limited repair capacity (Alexeyev *et al.*, 2013).

1.6.9.1 Homoplasmy vs heteroplasmy

Each mitochondrial organelle may carry 1-2 mtDNA molecules, and a typical somatic cell contains over 1000 copies of mtDNA (Robin and Wong, 1988), with the mtDNA content linked

with the energy requirements of the cell. As multiple copies of mtDNA exist within each cell, cells may carry multiple variants of mtDNA simultaneously. This is also referred to as variant allele frequency (VAF). Cells with a mixture of mtDNA variants are considered 'heteroplasmic', whereas those purely comprising of multiple copies of mutated mtDNA are termed 'homoplasmic'.

In heteroplasmic states, wild type mtDNA molecules may compensate for mutant mtDNA, allowing mitochondria to function normally up to reasonably low levels of heteroplasmy (60-90% mutant mtDNA, depending on type of mutation). However, functional homoplasmic mtDNA mutations may manifest a mitochondrial dysfunction phenotype. Clonal expansion leads to the expansion of an individual variant of mtDNA, which may eventually cause a heteroplasmic cell to become homoplasmic, and thereby lead to a change in phenotype.

Patients with mitochondrial syndromes have clonal expansion of pathogenic mtDNA mutations often leading to high levels of homoplasmy, whereas ageing is associated with polyclonal expansion of mtDNA mutations and low levels of homoplasmy (Ye *et al.*, 2014).

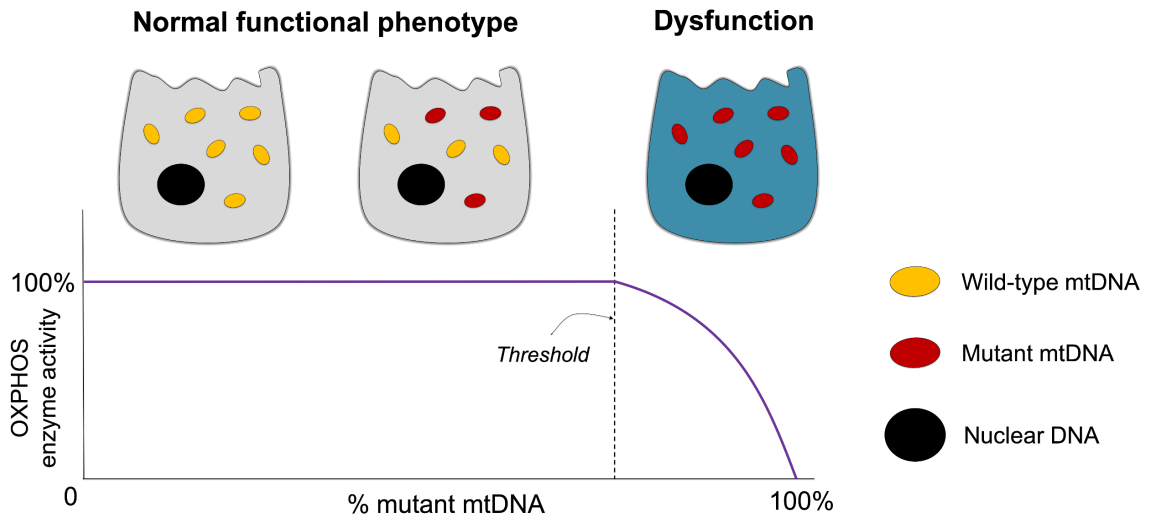

Figure 1-14: Heteroplasmic mutations lead to OXPHOS defects. Depending on the mtDNA mutation and cell type, a cell can tolerate a threshold degree of heteroplasmy whilst maintaining OXPHOS enzyme activity. However, at higher heteroplasmy than this threshold, OXPHOS enzyme activity is lost and enzymatic dysfunction ensues.

1.6.10 Mitochondrial dynamics

Mitochondria are positioned intra-cellularly in regions of high energy demand, typified by their location in the proximal part of the flagellum of mammalian spermatozoa (Fawcett, 1975) to fuel motility. The dynamic nature of mitochondria, via fusion, fission, mitophagy and biogenesis, further serve to optimise mitochondrial function, particularly in response to changing bioenergetic conditions of the cell.

Optimal mitochondrial function is served by fused mitochondria, which engages the entire mitochondrial machinery to work co-ordinately for maximal efficiency. Exposure to metabolic stress or starvation further upregulates mitochondria and results in a hyperfused network. Similarly, fusion allows the cell to compensate for accumulation of mutant mtDNA in heteroplasmic cells. Mitochondrial fusion requires mitofusin proteins, *Mfn1* and *Mfn2*, on the outer mitochondrial membrane, in addition to Opa1 at the inner mitochondrial membrane. Mitochondrial fission, on the other hand, serves to generate heterogeneity and aids in eradicating damaged mitochondria via mitophagy. It only requires Dynamin-related protein, *Drp1*, which constricts mitochondria by forming a ring-like structure and eventually achieving separation (Hoppins *et al.*, 2007).

Similarly, mitochondrial turnover, through a balance between synthesis of new mitochondria (biogenesis) or degradation of damaged mitochondria (mitochondrial autophagy, or mitophagy), also play a crucial role in responding to changing metabolic requirements and quality control. Mitochondrial biogenesis is primarily regulated by peroxisome proliferator activated receptor γ co-activator 1α (*PGC-1α*), by activating a variety of transcription factors, including nuclear respiratory factors, *NRF1* and *NRF2*, which activate *TFAM* and drive transcription and replication of mtDNA (Jornayvaz and Shulman, 2010). Notably, AMP-activated protein kinase (*AMPK*) acts as a key energy sensor and regulates mitochondrial biogenesis. Similarly, overexpression of *Myc*, a proto-oncogene, in the context of cell cycle entry stimulates mitochondrial biogenesis in preparation for cell division, and during metabolic stress (Morrish and Hockenbery, 2014). Conversely, damaged mitochondria may be identified by *PTEN*-induced kinase 1 (*PINK1*) upon overexpression of Parkin (Narendra *et al.*, 2008) and selectively removed through autophagy, in a processed referred to as mitophagy. This may occur subsequent to fission of mitochondrial networks. In addition to its role in mitochondrial quality control, mitophagy also plays an important role in cellular differentiation and metabolic reprogramming (Gustafsson and Dorn, 2019).

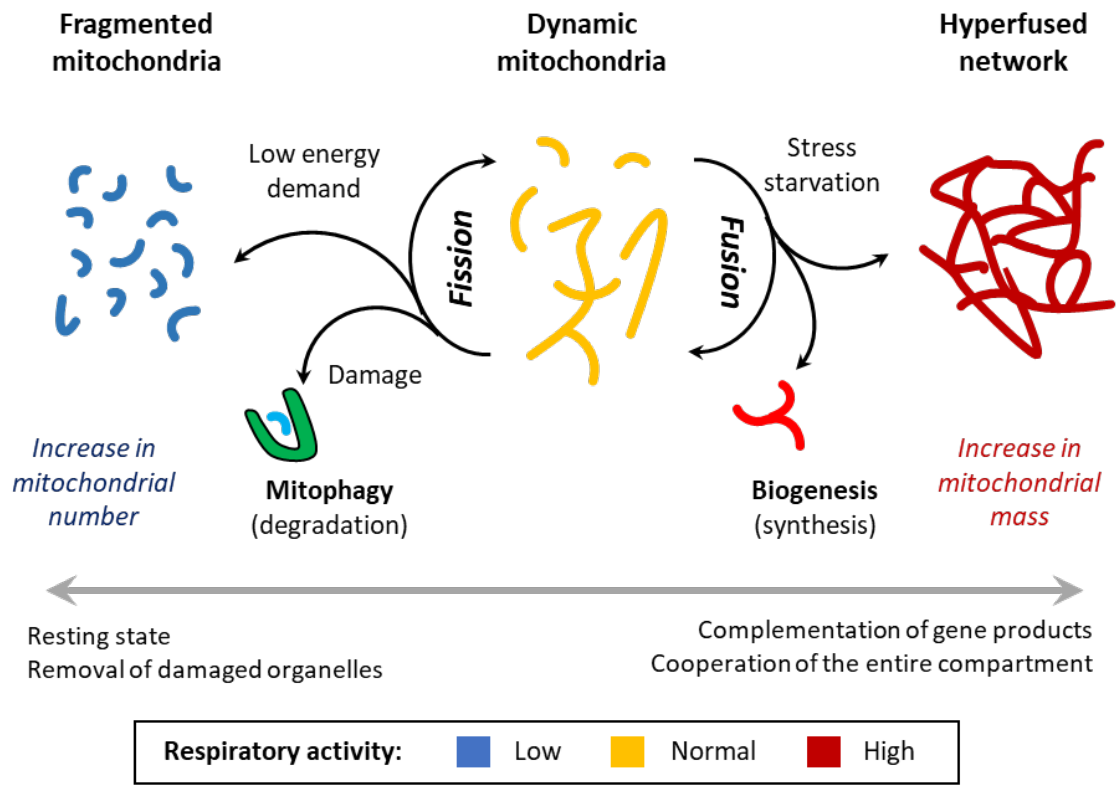

Figure 1-15: Mitochondrial dynamics. Mitochondria adapt to changing cellular requirements and functional status through dynamic processes including fusion, fission, mitophagy and biogenesis. Adapted from Yao *et al.* (2019).

1.7 Rationale

1.7.1 Mitochondrial free radical theory of ageing

Two key hallmarks of ageing are telomere attrition and accumulation of mtDNA mutations (Lopez-Otin *et al.*, 2013). According to the mitochondrial free radical theory of ageing, mitochondria produce free radicals as a by-product of normal metabolism, which cause oxidative damage, and this accumulation of oxidative damage is the main driving force in the aging process (Harman, 1972). This theory is supported by evidence from two mouse models. A transgenic model of catalase overexpression demonstrated reduced ROS production, reduced oxidative damage and a five-month increase in lifespan, in comparison to controls (Schriner *et al.*, 2005). In contrast, the *PolgA* mutator mouse model based on reduced mitochondrial DNA polymerase γ fidelity (described in further detail in section 1.6), accumulates mtDNA mutations with advancing chronological age, resulting in an accelerated ageing phenotype and reduced lifespan (Trifunovic *et al.*, 2004; Kujoth *et al.*, 2005). Age-associated increase in burden of mtDNA mutations and associated functional defects in oxidative phosphorylation have been reported in various human tissues including the prostate, brain, heart, skeletal muscle, intestine, and skin (Krishnan *et al.*, 2007; Blackwood *et al.*, 2011; Baines *et al.*, 2014; Hopkins *et al.*, 2017). Thus, mitochondrial OXPHOS defects accumulate as part of ageing.

1.7.2 Metabolic reprogramming in prostate tumourigenesis

Hanahan and Weinberg proposed deregulation of cellular energetics as a key hallmark of cancer. As described in section 1.5.4, reprogramming of the unique metabolism of prostate tissue during tumourigenesis, results in a mixed Warburg effect. Since the risk of prostate cancer is strongly associated with advancing age, and ageing results in accumulation of mtDNA mutations resulting in OXPHOS defects, age-related mitochondrial defects may be hypothesised to contribute to prostate tumourigenesis.

1.7.3 Transmitochondrial cybrids

Cybrid ("cytoplasmic hybrids") experiments have been extensively employed to study the functional consequences of pathogenic mtDNA mutations, and provide evidence supporting the emerging hypothesis that mitochondrial defects may accelerate prostate tumour progression. In these experiments, donor cells bearing mtDNA mutations of interest are enucleated (for example, by using actinomycin D) and then undergo fusion with cells depleted

of mtDNA (for example, by ethidium bromide), to form cybrids (Bayona-Bafaluy *et al.*, 2003). Using this method, Petros *et al.* (2005) generated mutant PC3 cybrid cells (**Figure 1-16**) using leucocytes from a patient with *ATP6* T8993G (Complex V) mutation. The T>G transversion at the 8993 base converts the highly conserved leucine to arginine in *ATP6* (subunit of Complex V), and is frequently observed in patients with Leigh Syndrome, a mitochondrial disease characterised by disabling neurological and neuro-ophthalmological syndromes (Trounce *et al.*, 1994). In this experiment, mutant T8993G mtDNA and wild-type PC3 cybrid cells were subcutaneously injected into nude mice and monitored for tumour formation. By day 110, average tumour volume was 7 times greater in mice injected with mutant PC3 cybrids, compared to wild type cybrid injected mice. Tumours from mutant cybrid injected mice also produced more ROS. Similarly, intra-tibial injection of mutant T8993G PC3 cybrids had a growth advantage in the bone stromal environment, thereby also implicating mtDNA mutations in development of bone metastases (Arnold *et al.*, 2009).

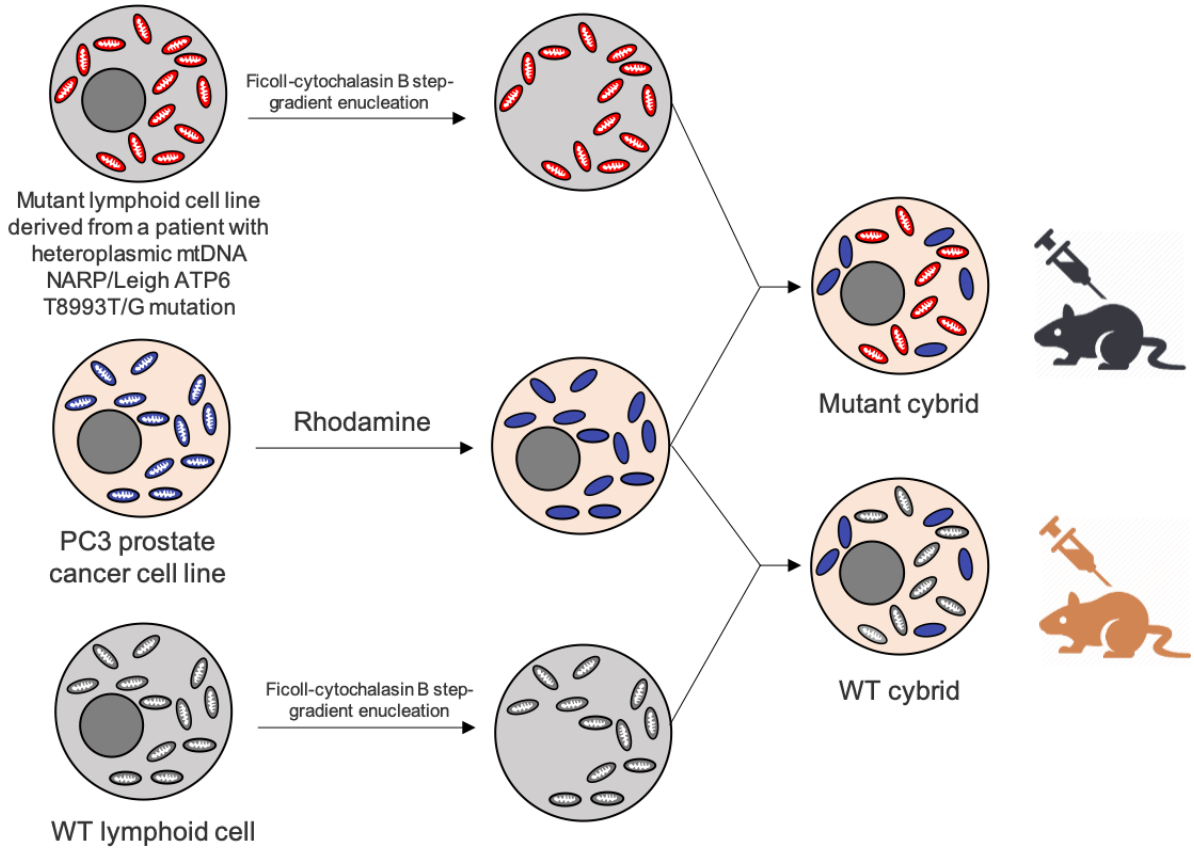

Figure 1-16: Cybrid experiments suggest tumourigenic potential of mtDNA mutations. Experimental evidence based on mutant cybrid PC3 cell lines suggest that mtDNA mutations may promote prostate tumourigenesis.

1.8 Aims and objectives

Given the above data linking ageing, accumulation of mitochondrial defects, metabolic reprogramming, and accelerated prostate cancer progression, I hypothesise that mitochondrial alterations accelerate prostate cancer progression. I aim to test this hypothesis by fulfilling the following objectives:

- Characterise the mitochondrial molecular landscape of prostate cancer and its association with markers of prostate cancer progression
- Develop an automated high-throughput quantitative method to assess oxidative phosphorylation (OXPHOS) protein abundance in formalin-fixed prostate tissue samples.
- Interrogate prostate tissue microarrays to test association between OXPHOS proteomic alterations, clinicopathological features of aggressive disease and overall survival
- Characterise prostate tissues from the *Polg* mutator mouse model to assess the impact of systemic age-related accumulation of mtDNA mutations on prostate cancer initiation
- Generate novel *Pten*-deficient prostate cancer mouse models with age-related accumulation of mtDNA mutations to test the impact of systemic OXPHOS defects on prostate cancer progression

Chapter 2 Materials and methods

2.1 Materials

2.1.1 Equipment

Item	Manufacturer
2100 antigen retriever	Aptum Biologics
Aperio CS2 whole slide scanner	Leica Biosystems
Axio Imager M1 fluorescence microscope	Zeiss
Axioskop 2 fluorescence microscope	Zeiss
Benchtop Centrifuge 5418	Eppendorf
Benchtop Centrifuge 5804	Eppendorf
Bioanalyser 2100	Agilent Technologies
Cellometer 1000 Bright Field Cell Counter	Nexcelom Bioscience
CoolSNAP HQ CCD camera	Photometrics
Cryostat	OFT 5000 Cryostat
Dissecting microscope, MZ75	Leica Biosystems
Ion Chef	Thermo Fisher
IonTorrent Personal Genome Machine	Thermo Fisher
Microplate reader, ELx800	BioTek
Microtome, HM325	Microm
Mini-PROTEAN® Tetra Cell, Mini Trans-Blot® Module, and PowerPac™ HC Power Supply	Biorad
Mr Frosty Freezing Container, 5100-0001	Thermo Fisher
NanoDrop ND-1000	Labtech International
Nikon A1R confocal laser microscope	Nikon Instruments
Odyssey Scanner	Li-Cor
Refrigerated centrifuge 5417R	Eppendorf
Seahorse XF96 analyzer	Seahorse Bioscience
Thermomixer C	Eppendorf
Verti 96-well thermal cycler	Applied Biosystems

2.1.2 Software

Software	Supplier
Aperio ImageScope 12.3.2	Leica Biosystems
AxioImager 2	Zeiss
Image Lab 6.0	BioRad
ImageJ 1.51w	National Institutes of Health
IncuCyte ZOOM 2016A	Sartorius
InForm 2.0.3 and 2.0.4	Perkin-Elmer
Integrative Genomics Viewer v2.3.75	Broad Institute
MATLAB v2018a	MathWorks Inc
MetaMorph	Molecular Devices, LLC
NIS Elements AR	Zeiss
Phenochart 1.0.7	Perkin-Elmer
QuPath v0.1.2	Queen's University Belfast
R v3.4.3	R Core Team
RStudio v1.1.423	RStudio Inc.
STATA 12	StataCorp

Torrent Suite software v5.4.0	Thermo Fisher
Wave 2.4	Agilent Technologies

2.1.3 Consumables

2.1.3.1 General consumables

Item	Cat. No.	Supplier
2.0ml TubeOne Microcentrifuge Tube	S1620-2700	Starlab
4',6-diamidino-2-phenyl indole dihydrochloride (DAPI)	D9542	Sigma-Aldrich
Avidin/biotin blocking kit	SP-2001	Vector Laboratories
Biopsy foam pad	720-2254	VWR International ltd.
Bovine serum albumin	A9418	Sigma-Aldrich
D-glucose	G7021	Sigma-Aldrich
Dako Envision Polymer	K4003	Agilent Technologies
DPX mountant	6522	BDH Laboratory Supplies
EDTA	15700	Affymetrix
Formalin solution, neutral buffered, 10%	HT501128	Sigma-Aldrich
Glycine	G8898	Sigma-Aldrich
Histoclear	HS-200	National Diagnostics, Atlanta, Georgia, USA
Hoechst 33342 trihydrochloride trihydrate	H3570	Life Technologies
Hydrogen peroxide	H1009	Sigma-Aldrich
Immun-Blot PVDF Membrane	1620177	Bio-Rad
Liquid DAB+ Substrate Chromogen System	K3467	Dako
Normal goat serum (NGS)	G9023	Sigma-Aldrich
OCT embedding matrix	KMA-0100-00A	Cell Path
Opal 4-Color Manual IHC Kit 50 slides	NEL800001KT	Perkin-Elmer
Opal 620 reagent pack	FP1495001KT	Perkin-Elmer
OXOID PBS tablets	BR0014G	Thermo Fisher
Peroxidase blocking solution	S2023	Dako
POLYSINE Microscope Slides	631-0107	VWR
Prolong Gold mountant	P10144	Thermo Fisher
Protein Assay Dye Reagent Concentrate (Bradford Reagent)	5000006	Bio-Rad
Restore Stripper Buffer	21059	Thermo Fisher
Sodium chloride	S7653	Sigma-Aldrich
Spectra Multicolor Broad Range Protein ladder	#26634	Thermo Fisher
Tris(hydroxymethyl)aminomethane (Trizma) base	T1503	Sigma-Aldrich
Tween-20	P1379	Sigma-Aldrich

2.1.3.2 Tissue culture consumables

Item	Cat. No.	Supplier
Blasticidin S HCl solution (10 mg/mL)	sc-495389	Santa Cruz
Cellometer Disposable Counting Chambers	SD100	Nexcelom Bioscience
CELLSTAR Tissue culture flasks (T75, T175)	658175, 661175	Greiner Bio-One
D-Glucose	G8270	Sigma Aldrich
Dimethyl Sulfoxide (DMSO)	276855	Sigma Aldrich
Dulbecco's Modified Eagle's Medium - high glucose (DMEM)	D6429	Gibco

Foetal bovine serum	10270-106	Gibco
Foetal bovine serum, charcoal stripped	S181F	VWR
Ham's F-12K (Kaighn's) Medium	21127022	Gibco
L-Glutamine (200mM)	25030-081	Gibco
RPMI 1640 Medium, HEPES, no glutamine	42401	Gibco
Sodium pyruvate (100mM)	11360-088	Gibco
Zeocin Selection Reagent (100mg/ml)	R25001	Thermo Fisher

2.1.3.3 Seahorse assay consumables

Item	Cat. No.	Supplier
37% paraformaldehyde	252549	Sigma-Aldrich
Antimycin-A	A8674	Sigma-Aldrich
Blasticidin S HCl solution	sc-495389	Santa Cruz
Dihydrotestosterone	A8380	Sigma-Aldrich
Draq-5	DR05500	Biostatus
FCCP	C2920	Sigma-Aldrich
Oligomycin	75351	Sigma-Aldrich
Rotenone	R8875	Sigma-Aldrich
Seahorse basal assay media	102353-100	Seahorse Biosciences
Seahorse calibrant	100840-000	Seahorse Biosciences
Seahorse FluxPak Cartridge	102416-100	Seahorse Biosciences
Seahorse XF96 Cell Culture Microplates	101085-04	Seahorse Biosciences
Zeocin(tm) Selection Reagent (100 mg/ml)	R25001	Invitrogen

2.1.3.4 Molecular biology kits

Item	Cat. No.	Supplier
1Kb DNA Ladder, 0.1µg/µl	G5711	Promega
2-mercaptoethanol	M3148	Sigma-Aldrich
AllPrep DNA/RNA/miRNA kit	80224	Qiagen
DNeasy Blood & Tissue DNA kit	69504	Qiagen
E-Gel Size Select 2% agarose gels	G661012	Thermo Fisher
High Sensitivity DNA Kit	5067-4626	Agilent Technologies
Hyperladder 100bp DNA ladder	BIO-33029	Bioline
Ion 316 chip v2	4488149	Thermo Fisher
Ion PGM Hi-Q View Chef Kit	A29902	Thermo Fisher
Ion Xpress Barcode Adapters	4471250	Thermo Fisher
Ion Xpress Plus Fragment Library Kit	4471269	Thermo Fisher
LA Taq DNA Polymerase	RR002A	Takara Bio Inc
QIAshredder	79654	Qiagen
RNA 6000 Nano chip	5067-1511	Qiagen
RNAase Zap	AM9780	Thermo Fisher
RNAlater storage solution	R0901	Sigma-Aldrich
Stainless steel beads (5 mm)	69989	Qiagen

2.1.4 Chemicals

Item	Supplier
Ethanol, 100%	Fisher Chemical
Methanol, 100%	Fisher Chemical

2.1.5 Solutions

Solution	Constituents
0.1M Glycine	11.1g Glycine 1L dH_20
10% Normal goat serum	1ml NGS 9ml TBST
20% RNAlater dissection media	8ml RNAlater 32ml PBS
Cryopreservative (freezing media)	9ml FBS 1ml DMSO
EDTA antigen retrieval buffer, pH 8.0, 1X	416mg EDTA 1L dH_20
Electrophoresis buffer, pH 8.3, 1X	100ml TAE buffer, 10X 900ml dH_20
Phosphate buffered saline (PBS), pH 7.4, 1X	10 OXOID TBS tablets 1L dH_20
Running buffer, 1X (western blot)	14.4g glycine 3g Trizma base 1g SDS 1L dH_20
Transfer buffer, 1X (western blot)	6.06g Trizma base 28.8g Glycine 150ml methanol 1.7L dH_20
Tris-Acetate-EDTA (TAE) Buffer, 10X	48.4g Trizma Base 11.42ml Glacial Acetic Acid 20ml 500mM EDTA pH 8.0 Make up to 1L with dH_2O
Tris-Buffered Saline and Tween-20 (TBST), pH 7.4, 1X	800ml TBS 2ml Tween-20 Make up to 1L with dH_20
Tris-Buffered Saline and Tween-20 (TBST), pH 7.4, 10X	121g Trizma Base 90g NaCl Make up to 800ml with ddH2O

2.2 Human prostate samples

2.2.1 Ethical approval

Human prostate samples were obtained from two sources: (a) the Manchester Cancer Research Centre Biobank (10_NOCL_02) from tissue collected following ethical approval by the Trent Multi-centre Research Ethics Committee (Ref. 01/4/061), and (b) the Newcastle Biobank from tissue collected following ethical approval by the Newcastle Research Ethics Committee (Ref. 2003/11).

2.2.2 Human prostate tissue samples

Formalin-fixed paraffin-embedded whole prostate blocks from patients undergoing cystoprostatectomy for bladder cancer were obtained from the Manchester Cancer Research Cancer Biobank. All samples were reviewed by a Consultant Histopathologist, and only those with normal prostate tissue were used. Five prostate blocks with high epithelial cell content were selected from three age-groups (30-45 years, 45-60 years, and above 60 years) to study age-related changes in normal prostate epithelium.

2.2.3 Human prostate cancer tissue micro-arrays

2.2.3.1 Overview

Tissue micro-arrays (TMAs) were sourced from two centres: Manchester (MCR) and Newcastle-upon-Tyne (NCL). In total, 3,709 donor cores from 698 patients were originally embedded in 39 recipient TMA blocks.

2.2.3.2 Manchester TMAs

TMA cohorts comprising samples from patients who underwent transurethral resection of the prostate (TURP) or transrectal ultrasound guided needle core biopsies (TRUSBx) between 1994 and 2004 were previously constructed by Miss Maya Harris, Clinical Fellow in Urology. Clinical follow-up data was censored at May 2017. Haematoxylin and eosin stained TMA tissue sections were reviewed by Dr Jonathan Shanks, Consultant Urological Histopathologist at The Christie Hospital. Each individual 1 mm core was categorised by histopathological type as either “normal-adjacent core” or “tumour core”.

In total, the Manchester TMAs comprised of 2,474 cores from 353 patients.

Tissue type	Number of TMA blocks	Total number of cores	
		Normal-adjacent cores	Tumour cores
TURP	25	979	1034
TRUSBx	8	10	451

Table 2-1: Description of the Manchester TMA cohort.

2.2.3.3 Newcastle TMAs

TMA cohorts comprising of samples from patients who underwent either channel TURP or radical prostatectomy between 1988 and 2003 were constructed by Mr Kanagasabai Sahadevan, Consultant Urologist, Sunderland Royal Hospital. Each 0.6 mm core was categorised as either BPH, normal-adjacent (NA), PIN or CaP, based upon regions of donor tissue annotated by Dr Marie Mathers, Consultant Pathologist, Newcastle-upon-Tyne NHS Foundation Trust. Clinical follow-up data was censored at March 2018.

In total, the Newcastle TMAs comprised of 1,235 cores from 345 unique patients, with some patients' tissue samples represented across multiple TMA blocks. Each patient was allocated a unique anonymised patient identifier, using which duplicate cores across all TMA blocks were identified.

TMA block	Tissue type	Number of patients by core type			
		BPH	NA	PIN	CaP
NCLPC1	TURP (2 cores/patient)	24	-	-	76
NCLPC2	RP (1 core/patient)	55	-	22	45
NCLCP3	RP (2 cores/patient)	45		-	45
NCLPC4	TURP (1 NA & CaP cores/patient)	-	38	-	81
NCLPC5	Sequential channel TURP*	10	-	-	69
NCLPC6	RP (1 NA & 1 CaP core/patient)	-	66	-	67

Table 2-2: Description of Newcastle TMA cohort. * Tissue samples from patients who underwent multiple TURPs, with reference to their hormone status (ie prior to starting ADT, during ADT, following development of castrate resistance) were included in NCLPC5.

2.2.3.4 Clinical annotation

The following clinical parameters were collated for patients included in the above TMAs:

- Anonymised patient ID
- Age at time of procedure (in years)
- Gleason group (GG 1-5)
- Clinical tumour stage at diagnosis (cT1-4)
- PSA at diagnosis (in ng/ml)
- Metastasis stage at diagnosis (M0, M1, Mx)
- Initial treatment (Conservative, hormone manipulation, or radical therapy)
- Vital status at last follow-up (alive or dead)
- Cause of death
- Time to last follow-up or death (in months)

Where available, electronic medical records were reviewed to update survival data.

Patients were categorised into Gleason Groups 1-5 as follows: Group 1 (GS ≤6), Group 2 (GS 3+4), Group 3 (GS 4+3), Group 4 (GS 8), and Group 5 (GS 9-10), based upon published criteria (Epstein *et al.*, 2016b). Patients were divided into risk groups based on criteria described in **Table 2-3**.

Risk group	Gleason group	PSA	T-stage	M-stage
Low risk*	GG 1	0-9.9	T1	M0
Intermediate risk	GG 2-3	10-19.9	T2	M0
High risk	GG 4-5	20-100	T3-T4	M0
Metastatic disease	Any	>100	Any	M1

Table 2-3: Criteria for prostate cancer risk stratification. * Patients were classified as low risk if all criteria were met, whereas remaining patients were classified into higher risk groups based upon any single highest risk feature.

2.2.3.5 Data linkage

Core co-ordinates for individual cores were extracted from all TMA maps and compiled into a core database which included the following data: patient ID, core region (a-c), core type, and Gleason score (GS) for the individual core as reported by a specialist Consultant Histopathologist. The core database was then linked to clinical database using the patient ID. The linked database was reviewed for inconsistencies which were addressed by reference to

original sources and medical records, where available. Linkage of clinical, imaging and TMA co-ordinate data was performed on RStudio.

For the Manchester cohort, TMA maps were used to generate a database of core coordinates associated with anonymised patient ID numbers and core type. This core database was linked to a clinical database using patient IDs. For the Newcastle cohort, the clinical databases associated with each of the six TMA blocks were collated, which contained core coordinates, linked with anonymised patient IDs and clinical data.

After batch cell segmentation, quality-checked epithelial single cell level cytoplasmic intensity data were linked to clinically annotated core databases based on block names and core co-co-ordinates, to associate unique patient IDs and core types with cell data from the associated cores. Tumour core data lacking associated patient data were excluded.

2.2.4 Removal of imaging and tissue artefacts

After batch image processing, each image was manually quality tested on InForm Tissue Studio software (**Figure 2-1**). Regions of disinterest were marked around small areas of artefact and subsequently excluded. Where tissue was folded, inadequate or the image had large areas of imaging artefacts, the whole core was excluded. Cell level data from epithelial cells were exported as a comma-separated file for further analysis.

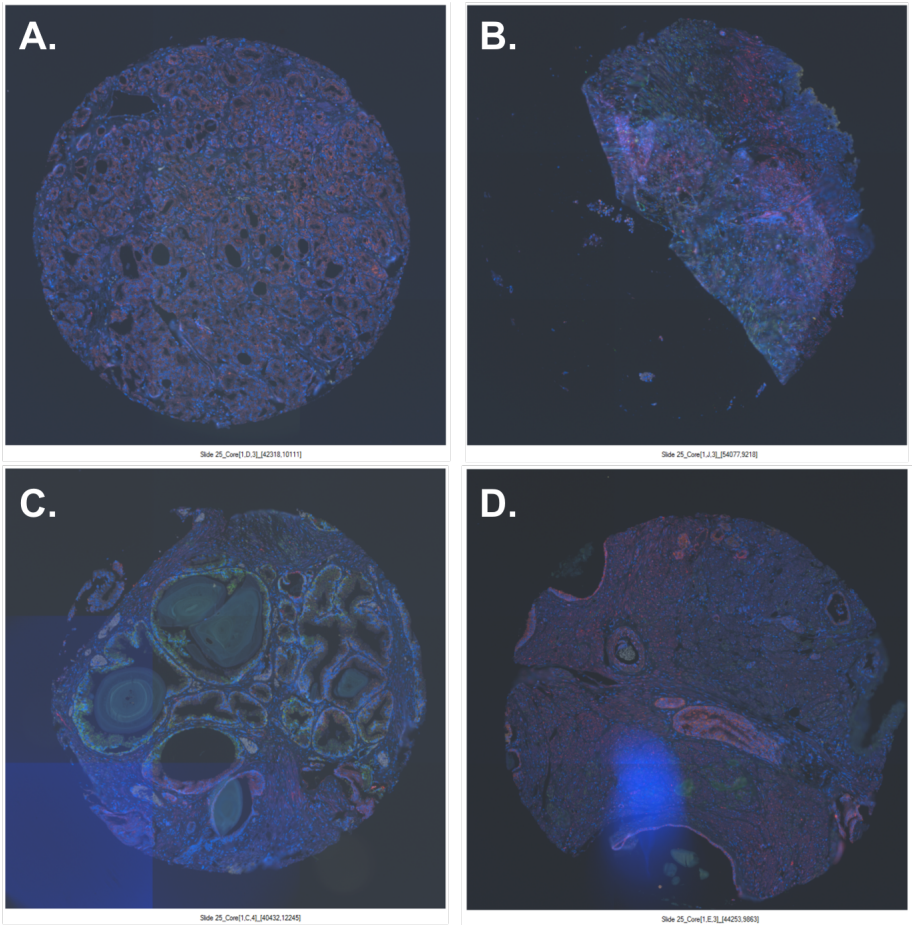

Figure 2-1: Quality checking of imaging data. Fluorescence images were collected from all TMA cores using the Vectra system. Each image was individually quality-checked for artefacts. RGB images are shown for **(A)** an ideal TMA core, **(B)** a TMA core with folded tissue, **(C)** an imaging artefact with tiled areas of high DAPI intensity, **(D)** artefact due to dirt on slide manifesting as an area of high DAPI intensity.

2.2.5 Statistical analysis

Survival analyses was performed using R packages "*survival*", with optimum thresholds determined using the "*survminer*" package, based upon log-rank tests and overall survival as the outcome measure. Kaplan-Meier survival curves were generated, and log-rank test was used to compare differences between patients in comparator groups. For evaluating correlations within non-gaussian data, Spearman rank correlation coefficients were calculated.

2.3 Experimental animals

2.3.1 Animal husbandry

All animal experiments were undertaken under valid personal, project and institutional licenses complying with UK Home Office regulations.

2.3.1.1 Newcastle colony

An animal colony was established at the Comparative Biology Centre at Newcastle University under project license PPL 60/4540. Mice were housed in groups of 4-6 in individually ventilated cages. All animals received RM3 expanded chow (Special Diet Services, UK) and water *ad libitum*. This breeding colony was maintained by Dr Laura Greaves and Miss Carla Bradshaw.

2.3.1.2 Cardiff colony

Similarly, animal colonies were established in collaboration with Dr Boris Shorning, Professor Matthew Smalley and Professor Alan Clarke at the European Cancer Stem Cell Institute, Cardiff University, under the project license PPL 30/3279. Mice were housed in groups of 4-6 in open Type II cages. All animals received Harland standard diet (Special Diet Services, UK) and water *ad libitum*. These colonies were maintained by Dr Boris Shorning.

2.3.2 Transgenic mouse models

2.3.2.1 Polg mutator mice

The Polg mutator (*Polg*$^{mut/mut}$) mouse has a knock-in missense mutation in the second proof-reading exonuclease domain of mitochondrial DNA polymerase-γ (D247A), which is encoded by exon 3 on Chromosome 7. Two strains of Polg mutator mouse models have been described, which differ in genetic backgrounds, targeting vectors and method of gene recombination technology employed. The *Polg*$^{mut/mut}$ strain described by (Trifunovic *et al.*, 2004) was generated by using mice with a C57Bl/6N background with a 11.5kb targeting vector spanning exons 1-10, resulting in a mutated exon 3 with two residual loxP sites upon *Flp*-recombinase mediated excision. In contrast, the *Polg*$^{mut/mut}$ described by (Kujoth *et al.*, 2005), and employed in this thesis, was generated by using mice with a C57Bl/6J background to introduce a targeting vector spanning exons 1-11 resulting in a single residual *loxP* site flanking a mutated exon 3 upon *Cre*-mediated excision. Both targeting vectors were designed to introduce an AC to either CT (Kujoth *et al.*, 2005) or CC (Trifunovic *et al.*, 2004) double base substitution at position 247 of exon 3, leading to a critical change in the amino acid from aspartic acid (GAC)

to alanine (GCT or GCC). Notably, C57Bl/6J have a mutation in the Nicotinamide nucleotide transhydrogenase (NNT) which increases NADH levels and dependence on ATP generation via oxidative phosphorylation (Ho *et al.*, 2017).

Polg$^{mut/mut}$ male mice (n=4) were kindly donated by Professor Thomas Prolla from University of Wisconsin, USA. Upon receipt, these were mated with female C57Bl/6J mice purchased from Charles Rivers Laboratories. The offspring male *Polg*$^{mut/+}$ mice and female *Polg*$^{mut/+}$ mice were crossbred to generate *Polg*$^{mut/mut}$ mice. A breeding colony was maintained by back-crossing male *Polg*$^{+/mut}$ with *Polg*$^{+/+}$ mice, which provided wild-type *Polg*$^{+/+}$ and heterozygous *Polg*$^{+/mut}$ controls. For simplicity, homozygous *Polg*$^{mut/mut}$, heterozygous *Polg*$^{+/mut}$ *and wild-type Polg*$^{+/+}$ mice are referred to as *Polg*-HOM, *Polg*-HET and *Polg*-WT, respectively.

2.3.2.2 Prostate-specific mutant mouse models

Prostate-specific mouse models were generated using Cre-lox technology, and were a gift of Professor Alan Clarke, Cardiff University. *B6.D2-Tg(Pbsn-Cre)4Prb* mice with a *PbCre* recombinase transgene comprising of a rat probasin promoter upstream of Cre recombinase (termed *PbCre4*$^{+}$) were originally supplied by the Mouse Models for Human Cancer Consortium repository (NCI, Frederick) to direct transgene expression to the prostate (Wu *et al.*, 2001). Probasin is an androgen regulated prostate-specific gene (Johnson *et al.*, 2000). Elevated androgen levels during prostate maturation activates the probasin promoter, leading to transcriptional activation of Cre recombinase from 2 weeks of age (Wu 2001), resulting in excision of loxP sites.

Since maternal inheritance of the *PbCre4*$^{+}$ allele has previously been found to produce mosaic phenotypes (Birbach, 2013), male *PbCre4*$^{+}$ mice were crossed with female mice with loxP targeted alleles, including *Pten*, *K-ras*, and *p53* (**Figure 2-2**). Mice with conditional deletion of a genomic fragment between exon 4 and 5 of the *Pten* allele (Suzuki *et al.*, 2001) were obtained (termed *Pten*$^{fl/fl}$). Mice with a conditional activating *K-ras* mutation in codon 12 of exon 1 encoding a valine residue upon Cre-mediated excision of the transcriptional STOP cassette (termed *K-ras*$^{+/V12fl}$) were originally derived by Mariano Barbacid (Guerra *et al.*, 2003). Mice with conditional p53 deletion upon Cre-mediated excision of exon 2-10 of the p53 allele, were originally derived by Anton Berns (Jonkers *et al.*, 2001).

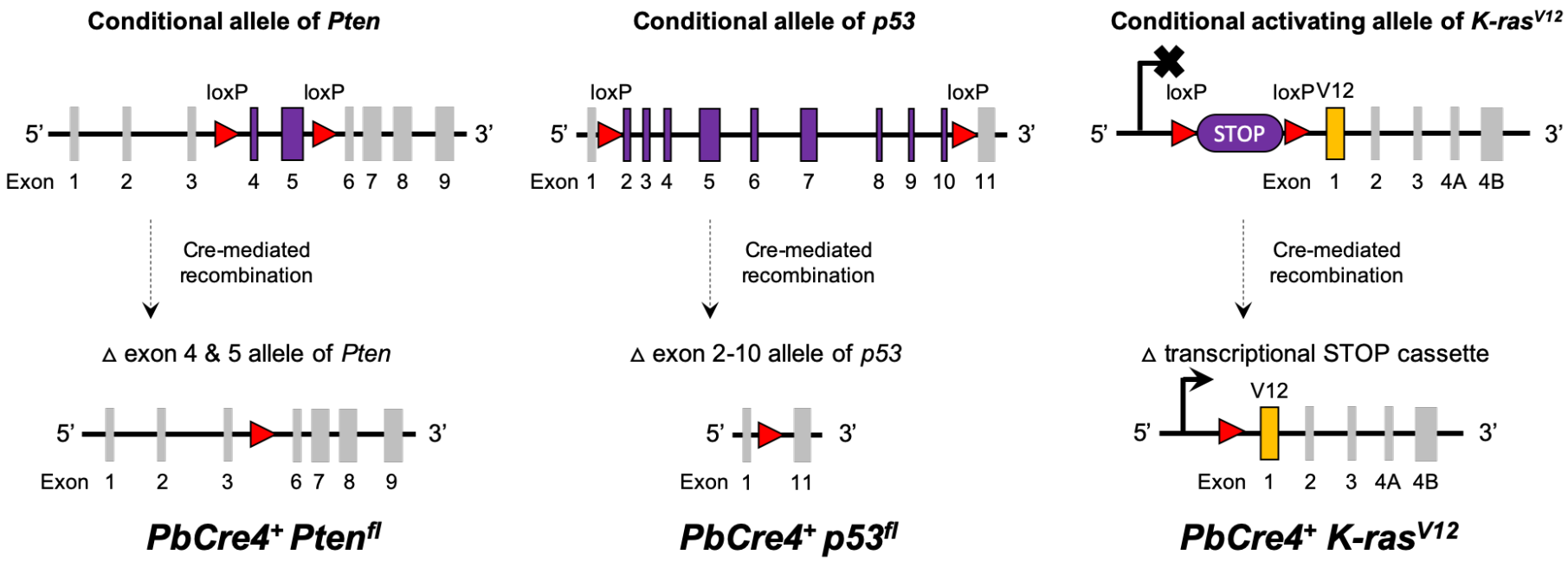

Figure 2-2: Cre-loxP technology for generating prostate-specific mouse models. Exons 4-5 of Pten gene, exon 2-10 of p53 gene, and a knocked-in stop codon adjacent to oncogenic mutant V12 at exon 1 of the K-ras gene are flanked by loxP sites (red triangles). Upon transcriptional activation by the probasin promoter, Cre-mediated recombinase excises gene fragments flanked by loxP sites. This leads to prostate-specific inactivation of Pten and p53, and transcriptional activation of the oncogenic K-ras (V12). loxP: locus of excision at P1 site.

2.3.3 Generation of mutant mouse colonies

Breeding colonies were set up to generate double mutant (*PbCre4^{+};Pten$^{fl/fl}$;Polg$^{mut/mut}$*) and triple mutant mice (*PbCre4^{+};Pten$^{fl/fl}$;p53$^{+/fl}$;Polg$^{mut/mut}$* and *PbCre4^{+};Pten$^{fl/fl}$;Kras$^{wt/V12fl}$;Polg$^{mut/mut}$*). Representative breeding schemes are outlined in **Figure 2-3**. The following guiding principles were used to mitigate for anticipated issues with breeding *PolgA$^{mut/mut}$* and *PbCre4^{+};Pten$^{fl/fl}$* mice, including:

(a) profoundly reduced fertility in *PolgA$^{mut/mut}$* mice (Trifunovic *et al.*, 2004) - mitigated by using the more fertile PolgA$^{+/mut}$ mice;

(b) maternal transmission of *PbCre4^{+}* allele leading to non-specific mosaic expression of the loxP-flanked allele (Birbach, 2013) - mitigated by ensuring paternal transmission of the *PbCre4^{+}* allele at each generation, by ensuring use of male breeders carrying this allele;

(c) maternal inheritance of mtDNA mutations leading to accumulation of pathogenic mutations and aggravation of the ageing phenotype (Trifunovic *et al.*, 2004; Stewart and Larsson, 2014) - mitigated by backcrossing with *Polg$^{+/mut}$* males at the F1 generation.

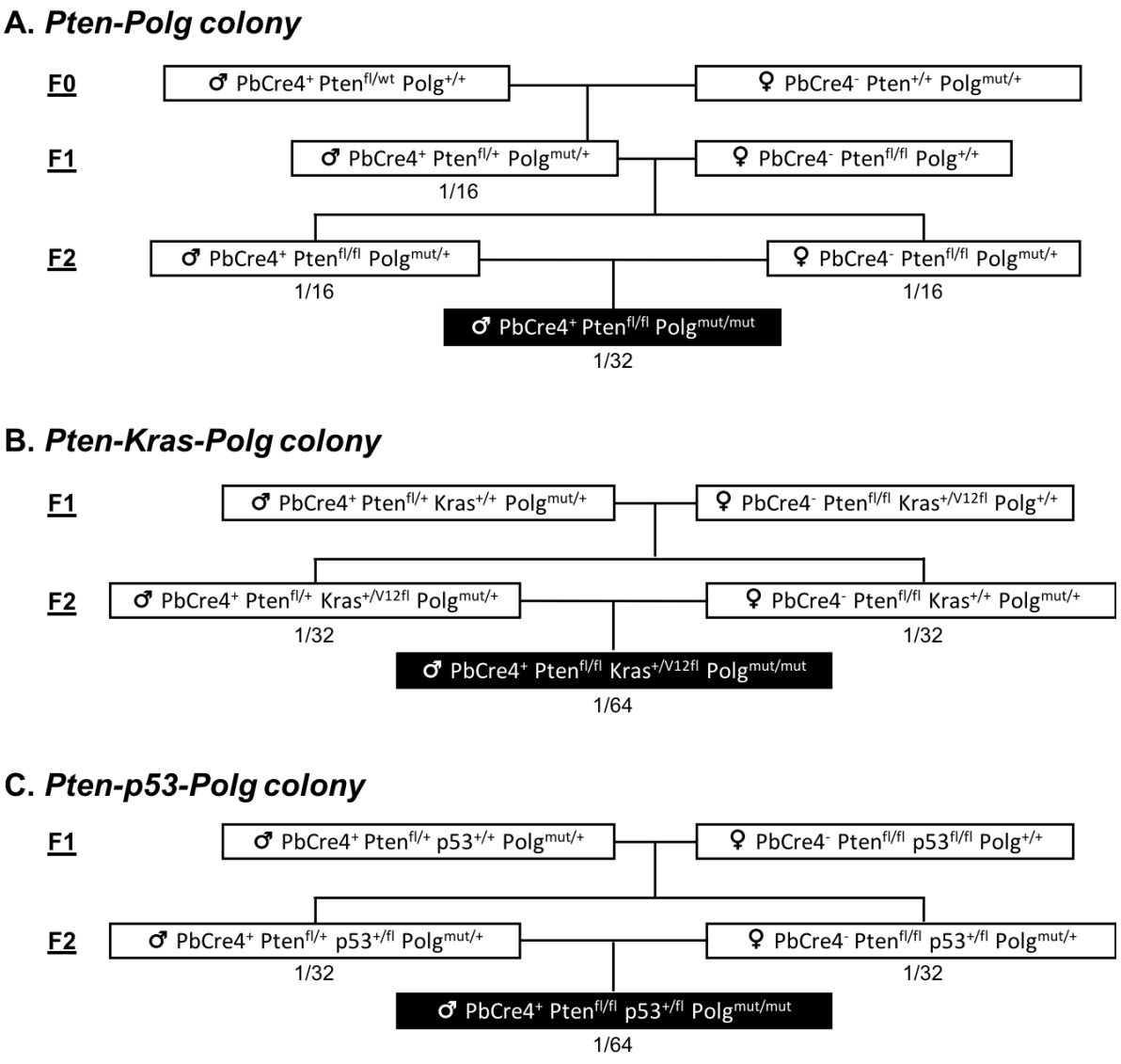

Figure 2-3: Example breeding schemes used to generate tumourigenic transgenic mouse models. Three breeding colonies were set up to generate **(A)** *PbCre4^{+}Pten$^{fl/fl}$;Polg$^{mut/mut}$*, **(B)** *PbCre4^{+}Pten$^{fl/fl}$;Kras$^{+/V12fl}$;Polg$^{mut/mut}$*, and **(C)** *PbCre4^{+}Pten$^{fl/fl}$;p53$^{+/fl}$;Polg$^{mut/mut}$* mutant mice (black boxes), and relevant controls. Male *PbCre4^{+}Pten$^{fl/+}$Polg$^{fl/+}$* mice generated at the F1 generation in the Pten-Polg colony were employed to set up breeding schemes for the Pten-Kras-Polg and Pten-p53-Polg mouse colonies. Expected mendellian frequency of required genotypes from indicated breeding pairs are reported.

2.3.4 Genotyping

Mice were weaned upon reaching a suitable size (usually by 3-5 weeks of age), and ear clippings were performed for identification and genotyping. Genotyping was performed by Dr Laura Greaves and Miss Carla Bradshaw for the mouse colony established at Newcastle, and by Dr Boris Shorning for the mouse colonies established at Cardiff.

2.3.4.1 PCR of ear notches

Ear notches were lysed overnight in a Thermocycler at 55°C at 1200 rpm in 47.5µl lysis buffer (1M Tris, 0.5 M EDTA, 10% SDS and dH_20), and 2.5µl Proteinase K.

For genotyping of the mouse colony at Newcastle, mastermix was prepared using 2.5µl ExTaq PCR Mg^{2+} buffer (Takara Bio Inc), 2.5µl dNTPs, 1µl forward and reverse primers, and 0.25µl LA Taq DNA Polymerase (Takara Bio Inc).

For genotyping of the mouse colony at Cardiff, mastermix was prepared using GOTaq 5X PCR buffer (Promega), 25mM dNTPs (Bioline), primers and either GOTaq (Promega) or Dream-Taq (Fermentas) DNA polymerase.

Genotyping primer sequences are listed in **Table 2-4**. Polymerase chain reactions (PCR) were implemented in a 96 well plate using 2µl of tissue lysate (1:10 dilution) and 23µl of mastermix in each well (**Table 2-5**).

2.3.4.2 Visualisation of PCR products by gel electrophoresis

Agarose gel electrophoresis of PCR products was carried out. A 1.5% agarose gel was prepared (1.5g agarose powder in 100ml TAE buffer) and heated to boil in a microwave. Once cooled under running tap water, 4µl SYBR Safe DNA gel stain (Life technologies) was added to the gel. SYBR Safe is a nucleic acid binding stain that fluoresces under ultraviolet light, allowing visualisation of nucleic acids. The gel was then poured into a mould and combs inserted to create wells. The combs were removed once the gel was set. The gels were then placed in a gel electrophoresis tank and covered with electrophoresis buffer. PCR product from each sample were mixed with loading buffer (0.25% (w/v) bromophenol blue, 30% (v/v) glycerol) in equal volumes (5µl) on parafilm and loaded into each well of the agarose gel. In the first well, 5µl 100bp DNA ladder (Hyperladder IV, Bioline) was added in order to assess PCR product size. The gel was run at 120 volts for 45 minutes. PCR products were visualised using BioRad GelDoc apparatus and interpreted with reference to the expected product size (**Table 2-4**).

Allele primer	Sequence (5'-3')	Product size (base pairs)
Polg	PolG58: GCCTCGCTTTCTCCGTGACT PolG59: GGATGTGGCCCAGGCTGTAACTCA	WT: 296 bp HOM: 468 bp
Cre	CreA: TGA CCG TAC ACC AAA ATT TG CreB: ATTGCCCCTGTTTCACTATC	Cre: 1000 bp
LacZ	LacZa: CTGGCGTTACCCAACTTAAT LacZb: ATAACTGCCGTCACTCCAAC	LacZ: 500 bp
Pten-loxP (Suzuki et al., 2001)	Pten1: CTCCTCTACTCCATTCTTCCC Pten2: ACTCCCACCAATGAACAAAC	WT: 228 bp HOM: 335 bp
K-ras^{V12}-loxP (Guerra et al., 2003)	510: AGGGTAGGTGTTGGGATAGC 3Ex1: CTCAGTCATTTTCAGCA 103rev-2: CTGTCCTTTACTGAAGGCTC	WT: 403 bp Floxed: 621 bp
p53-loxP	P53F-1F: CACAAAAACAGGTTAAACCCAG P53F 1R: AGCACATAGGAGGCAGAGAC	WT: 321 bp Floxed: 110 bp

Table 2-4: Primer sequences used for genotyping.

Cycles	Process	Temperature	Time
1	Initial denaturation	94°C	1 minute
35	Denaturation	94°C	20 seconds
	Primer annealing	64°C	20 seconds
	Extension	68°C	45 seconds
1	Final extension	72°C	5 minutes

Table 2-5: Cycling conditions used for genotyping PCR.

2.4 Tissue harvesting and processing

2.4.1 Tissue harvesting

Mice were sacrificed using a Schedule 1 method (cervical dislocation) and pinned on a dissecting board. After spraying the abdomen with 70% ethanol, a midline abdominal incision was made between the xiphisternum and pubic bone, through the skin and peritoneum to expose abdominal contents. The urogenitus, including the prostate, bladder, urethra and seminal vesicles, was dissected *en mass* (Valkenburg and Williams, 2011). The urogenitus was then placed in a petri dish containing 5mls phosphate buffered saline (PBS), and dissected using fine instruments under a dissecting microscope. Surrounding fatty tissue and remaining segments of vas deferens were carefully excised. The spleen, kidney, testes, intestines, liver, femurs, skin, skeletal muscle, and brain were also harvested.

Tissue samples were either placed in OCT embedding matrix and either snap frozen in liquid nitrogen or fixed in 10% normal buffered formalin for 24 hours. Fixed samples were then transferred to 70% ethanol for processing and paraffin embedding, which was undertaken by the Newcastle Biobank.

2.4.2 Prostate lobar dissection

Prostate lobar dissection was undertaken in a subset of Polg mutator mice at Newcastle. Following excision of the urogenitus, individual prostate lobes were dissected using a pair of fine forceps as follows. The ventral lobes were first identified and dissected from their proximal urethral attachment. Capillaries between the seminal vesicles and the anterior prostate were then cut. The seminal vesicles were then excised, taking utmost care to avoid spilling their contents. The anterior prostate was then excised. The remaining urogenitus was then placed on its dorsal surface, revealing the ampullary gland and the dorsolateral lobes. The ampullary gland was excised and disposed. The dorsolateral were then removed by gentle traction. Lobes were weighed on plastic weigh boats.

Where possible, one lobe was placed in an Eppendorf tube and snap frozen in liquid nitrogen, and the second lobe placed on a biopsy pad within a tissue cassette and fixed in 10% normal buffered formalin for 24 hours. Formalin fixed tissue samples were then transferred to 70% ethanol and embedded in paraffin blocks by Newcastle Biobank.

For prostate lobes subsequently used for RNA extraction, the PBS dissection medium was replaced with 20% RNAlater. This method was developed following a series of optimisation

experiments to maximise RNA integrity (Zingiryan *et al.*, 2016). Dissected lobes were individually placed in microcentrifuge tubes and snap frozen by immersion in liquid nitrogen. Snap frozen prostate lobes were held in long-term storage in a -80°C freezer.

2.5 Histopathological methods

2.5.1 Sequential cytochrome c-oxidase/succinate dehydrogenase enzyme histochemistry

2.5.1.1 Assay description

The cytochrome *c*-oxidase (COX) & succinate dehydrogenase (SDH) enzyme histochemical protocol has previously been used to assay burden of mitochondrial dysfunction (Old and Johnson, 1989). This method was employed to assess COX function in frozen prostate tissue as described in previous literature (Greaves *et al.*, 2010; Ross, 2011).

2.5.1.2 Preparation of assay media

COX and SDH media were prepared as described below:

COX medium: 200µl of cytochrome c stock solution (500µM cytochrome *c* in 0.2M phosphate buffer, pH 7.0) was added to 800µl of 3,3'diaminobenzidine tetrahydrochloride (DAB) stock solution (5mM DAB in 0.2M phosphate buffer, pH 7.0) with 20µg/ml catalase.

SDH medium: 800µl NitroBlue tetrazolium (NBT) stock solution (1.5mM NBT in 0.2M phosphate buffer, pH 7.0) was added to 100µl sodium succinate stock solution (1.3M sodium succinate in 0.2M phosphate buffer pH 7.0), 100µl phenazine methosulphate (PMS) stock solution (2mM PMS in 0.2M phosphate buffer pH 7.0) and 10µl sodium azide stock solution (100mM sodium azide in 0.2M phosphate buffer pH 7.0).

2.5.1.3 Assay protocol

Snap frozen mouse prostate tissue was embedded in OCT medium and 8µm thick sections were cut using a cryostat. Incubation times for the COX medium and SDH mediums were individually optimised. The ideal incubation times were found to be 15 minutes for both COX and SDH media. Therefore, tissue sections were incubated in 150µl of COX medium for 15 minutes, and then washed twice in PBS. Sections were then incubated in 150µl of SDH medium for 15 minutes, and washed twice in PBS, before dehydrating in increasing concentrations of ethanol, followed by two changes of Histoclear. Sections were then mounted with glass coverslips using DPX mountant and imaged using the Aperio CS2 whole slide scanner.

2.5.1.4 Quantification of COX deficiency

Prostate epithelial regions were marked freehand as regions of interest. The Genie Image Classifier Algorithm (Aperio ImageScope, Leica Biosystems) was used to calculate percentage of brown ("COX-positive") and blue ("COX-deficient") pixels. Percentage of COX-deficiency was calculated using ratio of number of blue pixels to total number of blue and brown pixels.

2.5.2 Preparation of formalin-fixed paraffin-embedded tissue

Tissue sections of 4-5μm thickness were cut on a microtome, floated on a heated water bath, and mounted on to glass slides. Paraffin embedded tissue sections were deparaffinised by placing glass slides in a 60°C oven for 45 minutes, followed by two washes of Histoclear, reducing concentrations of ethanol for 5 minutes at each concentration (100%, 95%, 90%, and 70% ethanol), and then finally placing them in distilled water for 10 minutes.

2.5.3 Haematoxylin & eosin staining

Deparaffinised slides were incubated in Meyer's haematoxylin solution for 10 minutes, and then washed in running water until the water ran clear. The slides were then incubated in Scott's tap water for 5 minutes, followed by a further wash in tap water and 1-minute incubation in Eosin solution. The slides were then placed in a running tap water and dehydrated by incubating in increasing concentrations of ethanol (70%, 95%, and 100%). After two cycles of 10-minute incubations in Histoclear, slides were mounted in DPX solution and left to dry at room temperature overnight.

2.5.4 Histopathological analysis of mouse prostate tissue

H&E stained formalin-fixed tissue sections were classified according to the consensus report of the mouse models of human cancers consortium prostate pathology committee (Shappell *et al.*, 2004; Ittmann *et al.*, 2013). Prostate tissue from each mouse was categorised into one of the following six categories, based upon the most advanced histological finding: normal, epithelial hyperplasia, prostate intra-epithelial neoplasia, micro-invasive adenocarcinoma, invasive adenocarcinoma, or sarcomatoid carcinoma. Histological changes associated with stages of murine PCa progression are described in detail in **7.2.6**.

2.5.5 Chromogenic immunohistochemistry

Antigen retrieval of deparaffinised slides was performed using 1mM ethylene diamine tetra-acetic acid medium (EDTA, Affymetrix) at pH 8.0 in an antigen retrieval unit, except when probing for CD8 and CD11b for which antigen retrieval was performed using citrate pH6 buffer

solution (x1) (Dako) in a Decloaking Chamber™ (Biocare). Slides were allowed to cool for 20 minutes, and then placed in tap water for 5 minutes. A hydrophobic border was drawn around tissue sections using a Dako pen.

Endogenous peroxidase was blocked by incubating tissue sections in peroxidase-blocking solution for 5 minutes, except when probing for CD8 and CD11b, where a 10-minute incubation in 3% H_20_2 (Sigma-Aldrich). In addition, endogenous biotin was quenched using the Vectastain Avidin-Biotin blocking kit, as per manufacturer's instructions (Vector Laboratories) when using primary antibodies raised in a mouse. Slides were then incubated in 10% normal goat serum (Sigma Aldrich) for 1 hour at room temperature to minimise non-specific binding of secondary antibodies raised in a goat. Slides were then washed in a solution containing Tris-Buffered Saline and Tween-20 (TBST) for 5 minutes.

Tissue sections were incubated in 80-100µl of primary antibody (diluted in 10% NGS) at 4°C overnight. For Ki-67 and cleaved-caspase-3 IHC, mouse spleen or intestine sections were used as positive controls (due to their high proliferative index), and one tissue section was incubated in antibody diluent (10% NGS) to act as a negative control.

The following morning slides underwent three 5-minute washes in TBST with gentle agitation. Detection of rabbit primary antibodies was achieved by incubating tissue sections in Dako Envision+ HRP polymer for 30 minutes at room temperature. In contrast, detection of mouse primary antibodies was achieved by incubating tissue sections in IgG-specific secondary antibodies (Jackson ImmunoResearch Laboratories) for 2 hours at 4°C, followed by three 5-minute washes in TBST, and then incubation in Vectastain ABC kit reagent for 30 minutes at room temperature. Detection of CD8 and CD11b was achieved by secondary antibody labelling with in immPRESS polymerised reporter enzyme solutions (Vector labs).

Slides were then washed in TBST (three 5-minute washes) and visualised using the liquid DAB+ chromogen substrate kit. After a further set of three 5-minute washes in TBST, tissue sections were counterstained by incubating in Mayer's haematoxylin for 10 minutes, and then gently washed in running tap water. Slides were then placed in Scott's tap water for 10 minutes, gently washed under running tap water, followed by serial 10-minute incubations in increasing concentrations of ethanol (70%, 95%, and 100%) to dehydrate the tissue sections. The slides were passed through two changes of Histoclear solution, and tissue sections then mounted with a glass coverslip using DPX.

Antibody (clone)	Host (isotype)	Dilution	Manufacturer (Cat No.)
Primary antibodies			
α-Pan-cytokeratin (polyclonal)	Rabbit	1:200	Abcam ab9377
α-Pan-cytokeratin (C-11)	Mouse (IgG1)	1:400	Sigma-Aldrich C-2931
α-B-catenin (polyclonal)	Rabbit	1:100	Abcam ab6302
α-PTEN (138G6)	Rabbit	1:200	CST #9559
α-pAkt^{S473} (D9E)	Rabbit	1:200	CST #4060
α-pS6RP$^{Ser235/236}$ (D57.2.2E)	Rabbit	1:200	CST #4858
α-Androgen receptor (N-20)	Rabbit	1:100	Sigma-Aldrich sc-816
α-Ki-67 (D3B5)	Rabbit	1:400	CST #12202
α-Cleaved caspase 3 (polyclonal)	Rabbit	1:40	Millipore AB3623
α-CD8 (4SM18)	Rat (IgG2a)	1:100	eBioscience #14-0808-82
α-CD11b (EPR1344)	Rabbit	1:8000	Abcam ab133357
Primary antibodies – mitochondrial markers			
α-NDUFB8 (20E9DH10C12)	Mouse (IgG1)	1:100	Abcam ab110242
α-MTCO1 (1D6E1A8)	Mouse (IgG2a)	1:100	Abcam ab14705
α-TOMM20 (EPR15581-39)	Rabbit	1:100	Abcam ab186734
α-VDAC1 (20B12AF2)	Mouse (IgG2b)	1:100	Abcam ab14734
Secondary antibodies			
α-mouse IgG1 biotin	Goat (IgG1)	1:200	Jackson IR Lab 115-065-205
α-mouse IgG2a biotin	Goat (IgG2a)	1:200	Jackson IR Lab 115-065-206
α-mouse IgG2b biotin	Goat (IgG2b)	1:200	Jackson IR Lab 115-065-207
α-rabbit IgG Alexa Fluor 405	Goat	1:200	Life Technologies A31556
α-mouse IgG2a Alexa Fluor 488	Goat	1:200	Life Technologies A21131
α-mouse IgG2b Alexa Fluor 546	Goat	1:200	Life Technologies A21143
α-rabbit IgG Alexa Fluor 546	Goat	1:200	Life Technologies A175732
Streptavidin conjugate, Alexa Fluor 647	Goat	1:200	Life Technologies S32357
α-mouse IgG Alexa Fluor 750	Goat	1:200	Life Technologies A175732

Table 2-6: Antibodies used in IHC and immunofluorescence experiments. CST: Cell Signalling Laboratories. Jackson IR: Jackson ImmunoResearch Laboratories.

2.5.6 Fluorescence immunohistochemistry

Deparaffinised tissue sections were subjected to antigen retrieval, and protein block using 10% NGS as outlined in section 2.5.5. Endogenous biotin was blocked using the Vectastain ABC blocking kit, as per manufacturer's instructions. Tissue sections were then incubated in 80-100 µl of primary antibody (diluted in 10% NGS) at 4°C overnight. One tissue section was included as a negative control, where the section was incubated in diluent (10% NGS) and primary antibody omitted.

Slides underwent three 5-minute washes in TBST, after which tissue sections were incubated in a secondary antibody in a dark humidified chamber at 4°C. Slides were washed in TBST, and then, if appropriate, incubated in a Streptavidin-conjugated tertiary antibody at 4°C for 2 hours. Slides were washed again in TBST, and then incubated in 1:1400 Hoechst 33342 for 10 minutes. Tissue sections were then mounted with a glass coverslip using ProLong Gold Antifade mountant and left to cure for 2 hours at room temperature. Stained slides were stored at 4°C long-term.

Slides were viewed using either an upright Nikon A1 confocal laser microscope (Nikon Instruments) or a Zeiss Axiovision fluoresence microscope (Zeiss Microscopy).

2.6 Functional characterisation

2.6.1 Cell line models

The following prostate cell lines were kindly provided by Dr Anastasia Hepburn, Northern Institute for Cancer Research, Newcastle University.

Cell line	Origin	Phenotype	Reference
PC3	Bone metastasis from 62-year-old Caucasian male with Grade IV PCa	Castrate resistant prostate cancer (AR^{wt}, $PTEN^{-/-}$)	Kaighn *et al.* (1979)
LNCaP	Left supraclavicular lymph node metastasis from 50-year-old male Caucasian	Androgen sensitive prostate cancer (AR^{T877A}, $PTEN^{-/mut}$)	Horoszewicz *et al.* (1983)
22Rv1	Patient-derived xenograft of parental androgen-dependent CWR22 cell line that was serially propagated in mice after castration-induced regression and eventual relapse of tumour.	Androgen sensitive prostate cancer (AR^{H874Y}, $PTEN^{+/+}$)	Sramkoski *et al.* (1999)
VCAP	Vertebral bone metastasis from 59yr Caucasian patient with CRPC - passaged as xenografts in mice then cultured in vitro.	Androgen sensitive prostate cancer (AR^{wt}, $PTEN^{+/+}$)	Korenchuk *et al.* (2001)
PNT1a	Normal post-mortem prostate from 35-year-old male immortalised with SV40 genome with a defective replicative origin	Non-tumorigenic in nude mice	Cussenot *et al.* (1991)
PNT2c2	Sub-clone of PNT2 cell line, which was originally generated from normal prostate tissue of a deceased 33-year-old male and immortalised with SV40 genome with a defective replicative origin	Non-tumorigenic in nude mice	Cussenot *et al.* (1991)

Table 2-7: Prostate epithelial cell lines used for in vitro experiments.

In addition, a doxycycline inducible PC3-PTEN cell line was kindly provided by Dr Ian Mills, Queens University Belfast (Maxwell *et al.*, 2013; McCabe *et al.*, 2015). This cell line was originally generated using the ViraPower T-REx Lentiviral Expression System (Life Technologies). Briefly, a PTEN-pLenti4.0/TO/V5-DEST viral vector was generated using the pLenti4.0/TO/V5-DEST vector and a PTEN expression construct acquired from Genart. PC3 cells were sequentially infected with the pLenti/tetracycline repressor and then the PTEN-

pLenti4.0/TO/V5-DEST vector. Clones were selected using Blasticidin 10µg/ml and Zeocin 300µg/ml for the PTEN-pLenti4.0/TO/V5-DEST vector and tetracycline repressor, respectively.

2.6.2 Cell culture

2.6.2.1 Maintenance of cells in culture

All cell lines were maintained in a CO_2 cell culture incubator at 37°C with 5% CO_2. Cells were grown in T75 tissue culture flasks, and aseptic or sterile techniques were used at all stages to minimise risk of contamination.

Unless specified, cells were maintained in DMEM media supplemented with 10mM L-glutamine and 10% fetal bovine serum. The PC3-PTEN cell line was maintained in Ham's F12 (Kaighn's modification) media, supplemented with 10mM L-glutamine, and 10% FBS. Blasticidin 10µg/ml and Zeocin 300µg/ml were used as selection antibiotics for PC3 cells with inducible PTEN vector. Doxycycline was titrated down to 10ng/ml as the minimum dose required to induce PTEN expression.

2.6.2.2 Sub-culturing of cell lines

Cells were passaged at 70-90% confluence by aspirating culture media, adding 2ml TrypLE Express Enzyme ensuring full coverage of the base of the flask, and incubating at 37°C for 5 minutes. Enzyme activity was quenched by adding a further 8ml fresh media to the flask, and transferring to a 50ml Falcon tube, and centrifuging at 185g for 4 minutes to obtain cell pellets. These were resuspended in fresh media and equally divided into four T75 flasks. Additional media was added to each flask to achieve a final volume of 10ml. Flasks were then left to incubate in the CO_2 incubator.

2.6.2.3 Harvesting cells

Cells were harvested using TrypLE Express Enzyme as outlined in section 2.6.2.2 until a cell pellet was obtained in a Falcon tube.

The cell pellet was resuspended in 1ml PBS, transferred to a microcentrifuge tube and centrifuged at 185g for a further 4 minutes. The supernatant was discarded. For subsequent experiments, the tube was snap frozen in liquid nitrogen, and finally stored in a -80°C freezer long-term. For cryopreservation, the cell pellet was resuspended in 1ml ice cold cryopreservative (90% FBS + 10% DMSO) and transferred to a cryovial. The cryovial was placed within a Mr Frosty Freezing Container for controlled-rate freezing and stored in -80°C freezer overnight. The cryovial was then moved into a liquid nitrogen tank for long-term storage.

2.6.2.4 Plating live cells

Cells were harvested using TrypLE Express Enzyme as outlined in section 2.6.2.2 until a cell pellet was obtained. The supernatant was discarded, and cells were resuspended in 1ml fresh media. Cell numbers were quantified using Trypan blue on a Cellometer 1000 Bright Field Cell Counter, as per manufacturer's instructions.

2.6.3 Western blotting

2.6.3.1 Cell lysis

Cells were suspended in 100µl cell lysis buffer (500µl 1M Tris/HCl pH 7.5, 100µl 5M NaCl, 100µl IGEPAL, 20µl 1M MgCl2, 3.5µl 14.25M B-ME, 1ml Glycerol, 1 EDTA-free protease inhibitor, 1x PhosSTOP phosphatase inhibitor tablet) and vortexed for 30 seconds and incubated on ice for 5 minutes. Samples were vortexed again and then centrifuged at 8000g for 5 minutes at 4°C to remove nuclei and unbroken cells. Supernatants were transferred to new lysate microcentrifuge tubes.

2.6.3.2 Bradford assay

Protein standards were prepared using 1µg/ml bovine serum albumin and 200µl Braford reagent made up 1000µl total volume with dH_20 at 0-20ng/ml concentrations. Similarly, 1µl and 2µl of each sample was made up to 1000µl volume with 200µl Bradford reagent and dH_20. Samples were incubated at room temperature for 5 minutes, before loading 200µl aliquots of each sample on to a 96 well plate. The plate was placed in a 595nm microplate reader to determine R^2 value using linear regression. Interpolated protein values were calculated for each sample.

2.6.3.3 Sample dissociation

50µg protein lysate was mixed with 4µl of 5x sample dissociation buffer (6.25mM Tris/HCl pH 6.8, 2% SDS, 10% glycerol, 0.01% bromophenol blue, 100mM DTT) and made up to 20µl/well with dH_20. Lysates were incubated at 37°C for 30 minutes in a thermocycler.

2.6.3.4 Gel electrophoresis

20µl dissociated lysates were loaded into wells of precast gels 12% 10-comb Mini-PROTEAN TGX gels, Biorad) secured in an assembly module placed within the Biorad tetracell tank. 7µl protein ladder was loaded into the first well. Running buffer was poured into the tetracell tank, and electrophoresis commenced at 100V for 1 hour.

2.6.3.5 Protein transfer

Once gel electrophoresis was completed, the precast gel was removed. A Polyvinylidene difluoride (PVDF) membrane was cut to size and activated by incubating in methanol for one minute. Transfer apparatus was prepared by placing sponge, two layers of filter paper, gel, activated PVDF membrane, two further layers of filter paper, and a sponge, ensuring that the PVDF membrane was between the gel and the positive electrode. The transfer apparatus was placed in a tetra-cell tank with a magnetic stirrer placed at its base. Cold transfer buffer was poured into the tank, which was placed on to a magnetic rotor and set to stir slowly. Protein transfer was undertaken at 100V, 350 amps for 1.5 hours at 4°C.

2.6.3.6 Western blot

The membrane was moved from the transfer apparatus and incubated in 5% powdered milk in TBST for 1 hour at room temperature under slight agitation. If probing for phosphorylated proteins, powdered milk was replaced with 5% bovine serum albumin. After washing 3 times in TBST for 5 minutes each, the membrane was incubated in primary antibody (diluted in 5% milk or BSA) overnight. The membrane was then washed in TBST five times for 5 minutes, and then incubated with an HRP-conjugated secondary antibody diluted in milk or BSA at room temperature for 1 hour.

Antibody (clone)	Host species	Dilution	Manufacturer, Cat No	Predicted size (kDa)
α-*PTEN* (138G6)	Rabbit	1:1,000	CST #9559	54
α-*pAkt*^{S473} (D9E)	Rabbit	1:1,000	CST #4060	60
α-*GAPDH* antibody	Mouse	1:10,000	Abcam ab8245	40
α-*NDUFB8* (20E9DH10C12)	Mouse	1:1,000	Abcam ab110242	22
α-*MTCO1* (1D6E1A8)	Mouse	1:2,000	Abcam ab14705	57
α-*SDHA* (2E3GC12FB2AE2)	Mouse	1:10,000	Abcam ab14715	70
α-*UQCRC2* (13G12AF12BB11)	Mouse	1:1,000	Abcam ab14745	48
α-*ATPB* (3D5)	Mouse	1:1,000	Abcam ab14730	52
α-alpha-tubulin (DM1A)	Mouse	1:10,000	Abcam ab7291	50
α-rabbit HRP-conjugated secondary	Swine	1:3,000	Dako P0399	-
α-mouse HRP-conjugated secondary	Rabbit	1:2,000	Dako P0260	-

Table 2-8: Antibodies used for western blotting.

2.6.3.7 Detection using chemiluminenscence

After secondary antibody incubation, the membrane was washed in TBST a further five times for 5 minutes. Detection of secondary antibodies was performed using the Clarity Western ECL substrate. The luminol-enhancer solution and stable peroxide solution were mixed in a 1:1 ratio. The mixture was poured over the membrane with the protein side up and incubated in the dark for 5 minutes at room temperature. The membrane was then visualised using the ChemiDoc MP imaging system and analysed using the Image Lab software.

2.6.3.8 Re-probing membrane

In order to probe for additional antigens, the membrane was washed in TBST and then stripped using Restore stripper buffer. The membrane was then incubated in 5% BSA or 5% milk for 1 hour, prior to incubation in primary antibodies as per section 2.6.3.6.

2.6.4 Seahorse metabolic flux analysis

Mitochondrial metabolism was tested in live cells using Seahorse metabolic flux analysis as described below.

2.6.4.1 Preparation of cell plate

For each experiment, 100ml of fresh growth media was prepared comprising of 2mM L-glutamine, 1mM sodium pyruvate, 10mM D-Glucose and 3% FBS. Media was filter sterilised using a 0.2µm filter and equilibrated to 37°C. For experiments evaluating influence of androgens, 3% FBS was replaced with 3% dextran-coated charcoal (DCC) stripped FBS.

Coating with 0.1% glycine was found to improve cell adherence. Therefore, the Seahorse XF96 cell culture plate was coated with 100µl/well 0.1% glycine and incubated for 15 minutes. The wells were then washed twice using 200µl PBS. On day 1 of the assay, cells were seeded on to the culture plate using optimised seeding densities outlined in **Table 2-9**. On day 2, media in the cell culture plate was replaced with 200µl/well Seahorse growth media and left to incubate for a total of 72 hours.

Cell line	Optimum seeding density
PC3	3000 cells/well
LNCaP	5000 cells/well
22Rv1	3000 cells/well
VCaP	10000 cells/well
PNT1a	5000 cells/well
PNT2c2	2000 cells/well
PC3-PTEN	4000 cells/well

Table 2-9: Optimised seeding densities for Seahorse Flux assays.

2.6.4.2 Preparation of sensor cartridge and mitochondrial inhibitors

On day 3, 200 µl/well calibrant was added to the Seahorse sensor cartridge and left to incubate in a non-CO_2 incubator at 37°C overnight. The following morning, growth media in the cell culture plate was replaced, ensuring a final volume of 180 µl/well. The cell plate was left to incubate in a non-CO_2 incubator at 37°C for one hour prior to running the Seahorse assay. Mitochondrial inhibitors were prepared as described in **Table 2-10**, 20 µl of each drug was injected into the appropriate port of the drug cartridge.

Order	Drug	Target	Final concentration
A	Oligomycin	Complex V inhibitor	1µM
B	FCCP	Mitochondrial uncoupler	2.5µM*
C	Rotenone	Complex I inhibitor	1µM
	Antimycin A	Complex III inhibitor	1µM

Table 2-10: Mitochondrial inhibitors used in Seahorse mitochondrial stress test. *The optimal final concentration for FCCP was determined as per manufacturer instructions.

2.6.4.3 Mitochondrial stress test

The utility plate was loaded on to the Seahorse metabolic flux analyser for calibration. The utility plate was discarded once calibration was completed. The sensor cartridge was placed over the cell culture plate and loaded on to the Seahorse system. Assay parameters were programmed to record three readings at 3-minute cycles, interspersed with a 3-minute wait cycle in between each read (**Figure 2-4**).

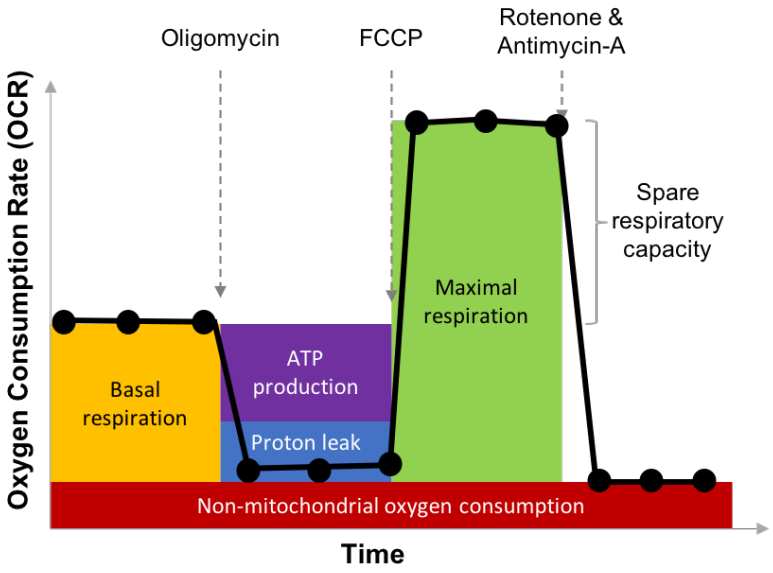

Figure 2-4: Interpretation of mitochondrial stress test using Seahorse metabolic flux analysis.

2.6.4.4 Data normalisation

Upon completion of the Seahorse assay, the sensor plate was discarded. Cells were fixed with a final concentration of 4% paraformaldehyde (PFA) and incubated at room temperature for 15 minutes. PFA was then aspirated and discarded. The wells were washed twice with 100µl PBS per well. Cells with stained with 0.5µM DRAQ5 nuclear stain diluted in 0.1% Triton-X100 and left to incubate at room temperature for 1 hour. Cells were washed with PBS twice (100µl/well). Finally, the cell plate was read on the Odyssey plate reader at 700nm. Signal intensity in each well was used as a surrogate of cell number. Data for oxygen consumption rate (OCR) and extra-cellular acidification rate (ECAR) from the mitochondrial stress test were normalised for cell number on Wave software (Seahorse Biosciences) and interpreted.

2.6.4.5 Glycolytic vs OXPHOS ATP production

ECAR is a composite measure of acidification of culture media, which is thought to primarily arise as a consequence of glycolytic lactate production. However, the contribution of CO_2 produced through oxidative phosphorylation to acidification of growth media may also bias assessment of glycolytic ATP production (Mookerjee *et al.*, 2015). The source of ATP production was therefore differentiated in data from the mitochondrial stress test, using methods recently reported by (Mookerjee *et al.*, 2015), aided by a Microsoft Excel template kindly provided by Dr Satomi Miwa, Centre for Ageing and Vitality, Newcastle University.

2.7 Molecular biology techniques

2.7.1 Nucleic acid extraction from mouse prostate tissue

2.7.1.1 Preparation of buffer solutions for RNA extraction

RNA extraction was performed using the Qiagen AllPrep DNA/RNA/miRNA kit as per manufacturer's instructions. Buffers were prepared by (1) adding 42ml isopropanol to 14ml Buffer FRN concentrate, (2) dissolving lypophilized DNase I in 550µl RNase-free water, (3) adding 44ml 100% ethanol to 11ml Buffer RPI concentrate, (4) adding 25ml 100% ethanol to 19ml Buffer AW1 concentrate, and (5) adding 30ml 100% ethanol to Buffer AW2 concentrate. 10µl ß-mercaptoethanol (ß-ME) was added per 1ml Buffer RLT Plus in a fume hood. All steps were carried out at room temperature, unless otherwise specified.

2.7.1.2 Cell lysis

Snap frozen mouse ventral prostate lobes dissected in 20% RNAlater diluted in PBS were used. One 5mm stainless-steel bead was placed in a 2ml TubeOne microcentrifuge tube containing up to 30mg of prostate tissue and 600µl Buffer RLT plus. Cell lysate was prepared by mechanical disruption using the TissueLyser II system for 4 minutes at 20Hz.

2.7.1.3 Homogenisation

Supernatant was transferred into a QiaShredder spin column placed over a fresh microcentrifuge tube. The sample was centrifuged for 2 minutes at 16,873g at room temperature. The QiaShredder spin column was then discarded and a fresh lid was placed over the microcentrifuge tube. The flow-through was again centrifuged for 3 minutes at 16,873g at room temperature. Supernatant was transferred on to an AllPrep DNA Mini spin column placed in a new 2ml microcentrifuge tube and centrifuged at 30s at 16,873g. The spin column was used for subsequent DNA extraction and the flow through used for RNA extraction.

2.7.1.4 RNA extraction

80µl Proteinase K was added to flow through and mixed by pipetting. Then, 350µl of 100% ethanol was added, mixed and left to incubate at room temperature for 10 minutes. A further 400µl 100% ethanol was then added to the sample and mixed. The sample was then transferred to a RNeasy spin column placed in a 2ml microcentrifuge tube and centrifuged for 15s at 16,873g. 500µl Buffer RPE was then added to the spin column, and the sample was centrifuged for a further 15s at 16,873g. Flow through was discarded, and the 10µl DNase I solution diluted in 70µl Buffer RDD was added to the spin column, which was incubated at

room temperature for 15 minutes. 500µl Buffer FRN was added to the spin column. The sample was centrifuged for 15s at 16,873g and the flow through transferred to a new microcentrifuge tube. The spin column was placed in a new microcentrifuge tube and the flow through from the previous step was added to the spin column and centrifuged for 15s at 16,873g. 500µl Buffer RPE was then added to the spin column and centrifuged for 15s at 16,873g. The flow through was discarded. 500µl 100% ethanol was added to the spin column, centrifuged for 2 minutes at 16,873g to wash the spin column membrane. The RNeasy mini spin column was then placed in a new microcentrifuge tube and 30µl RNase-free water was added directly to the spin column membrane. The tube was then centrifuged for 1 minute at 8000g to elute RNA.

2.7.1.5 DNA extraction

350µl Buffer AW1 was added to the AllPrep DNA spin column and centrifuged for 15s at 16,873g. After discarding the flow through, 20µl of Proteinase K was diluted in 60µl Buffer AW1 and the mixture added to the spin column. The sample was incubated for 5 minutes at room temperature. A further 350µl of Buffer AW1 was added to the spin column and centrifuged for 15s at 16,873g. After discarding the flow through, 500µl Buffer AW2 was added to the spin column and centrifuged for 2 minutes at 16,873g to wash the spin column. The spin column was then placed on a new 2ml microcentrifuge tube, and 100µl of Buffer EB was added directly over the spin column membrane. The sample was incubated at room temperature for 1 minute. The tube was then centrifuged for 1 minute at 8000g to elute DNA.

2.7.1.6 Quantification of RNA concentration and integrity

Initial quantification of eluted nucleic acids was performed using the NanoDrop ND-1000 spectrophotometer. The sample was diluted to a maximum concentration of 500ng/µl in RNase-free water. RNA concentrations and RNA integrity number (RIN) scores were obtained for each sample using the RNA Nano 6000 chip on the Agilent 2100 Bioanalyser, as per manufacturer's instructions.

2.7.1.7 RNA sequencing

RNA samples diluted to 22.9ng/µl concentration (total 800ng RNA) with RIN scores >7 from wild-type (n=4) and *Polg*$^{mut/mut}$ mouse ventral prostates (n=4) were transported to Eurofins Genomics (Ebersberg, Germany). Following a further quality check, cDNA libraries were prepared using the Illumina TruSeq Stranded mRNA kit. RNA sequencing was performed using the HiSeq 2500 with 2x100bp run mode, aiming for 30 million paired-end reads per sample.

2.7.1.8 Bioinformatics

Bioinformatic analyses were conducted by Dr Rebecca Steele, Queen's University Belfast. FASTQ reads were aligned to MM15 using STAR (Dobin *et al.*, 2013) and mapped to genes using HTSeq counts (Anders *et al.*, 2015). Differential expression analysis was performed on triplicate samples using DESeq2 (Love *et al.*, 2014). False discovery due to multiple testing was adjusted using Holm's method. Genes with an adjusted *p*-value ≤ 0.01 were taken forward for fold-change analysis.

2.7.2 Whole mitochondrial genome sequencing of prostate cell lines

2.7.2.1 Cell lysis

Cell lysis and DNA extraction was undertaken using Qiagen DNeasy Blood & Tissue DNA kit.

Prostate cancer cell lines were grown and $5x10^6$ cells from each cell line were snap frozen. Cell pellets were thawed and resuspended in 200µl PBS. Cells were lysed by adding 20µg Proteinase K and 200µl Buffer AL (without added ethanol) and mixed by vortexing. Samples were incubated at 56°C for 10 minutes.

2.7.2.2 DNA extraction

A homogenous solution was prepared by mixing a further 200µl 100% ethanol into each sample and vortexing. The solution was pipetted into the DNeasy Mini spin column placed in a 2ml collection tube and centrifuged at 6000g for 1 minute. The flow through and collection tube were discarded. The spin column was placed in a new 2ml collection tube, and 500µl Buffer AW1 was added. The sample was centrifuged at 6000g for 1 minute. The flow through and collection tube were discarded. The spin column was placed in a new 2ml collection tube, and 500µl Buffer AW2 was added. The sample was centrifuged at 20,000g for 3 minutes to dry the DNeasy membrane. Once again, the flow through and collection tube were discarded. Finally, the DNeasy Mini spin column was placed in a clean 1.5ml microcentrifuge tube and 200µl Buffer AE was pipetted directly on to the membrane. Samples were incubated at room temperature for 1 minute and then centrifuged at 6000g for 1 minute to elute DNA. DNA concentration was measured using the NanoDrop ND-1000 spectrophotometer.

2.7.2.3 Long-range PCR

DNA samples were diluted down to 50ng/µl. Long-range PCR was used to amplify the mitochondrial genome using overlapping primers (Primer 1A: forward m.550-569, reverse m.9839-9819; Primer 2A: forward m.9592-9611, reverse m.645-626). A mastermix was

prepared using 2.5µl 10x LA PCR (Mg^{2+} plus) Buffer II, 4µl dNTPs, 1µl forward and reverse primers, and 0.25µl LA Taq DNA Polymerase, and 15.25µl nuclease-free dH_20.

This provided two sets of samples for each cell line (one primer set in each sample). PCR tubes were prepared by adding 24µl mastermix with 1µl DNA. PCR was carried out in a Verti 96-well thermal cycler using cycling conditions in **Table 2-11**.

Cycles	Process	Temperature	Time
1	Initial denaturation	94°C	1 minute
35	Denaturation	98°C	10 seconds
	Primer annealing	60°C	30 seconds
	Extension	68°C	10 minutes
1	Final extension	72°C	10 minutes

Table 2-11: Cycling conditions used for long-range PCR.

2.7.2.4 Gel electrophoresis

A 0.7% agarose gel was prepared as described in section 2.3.4.2. Loading dye and loading buffer were mixed in equal proportion on parafilm to prepare a loading marker. For reference, 5µl 1kb DNA ladder was pipette into the first and last well. 5µl of each sample was mixed with the loading marker and pipetted into a separate well. Electrophoresis was undertaken at 50V for 4 hours. The gel was visualised using the Biorad GelDoc system to confirm presence of PCR products measuring approximately 10,000bp each.

2.7.2.5 Library preparation

PCR amplicons were quantified using the NanoDrop ND-1000 spectrophotometer. Overlapping 50ng amplicons from both primer sets were combined individually for each sample. Amplicons were then fragmented to 200bp fragments using the IonXPress Plus Fragment Library Kit, ligated to DNA barcodes using Ion Xpress Barcode Adapters 1-96, size-selected using E-Gel SizeSelect 2% agarose gels, and amplified as per manufacturer's instructions. DNA fragments were cleaned using Agencourt AMPure XP magnetic beads after each step of library preparation. Barcoded libraries were diluted 1:10 in molecular biology grade low TE buffer for quantification and quality checking on the Agilent 2100 Bioanalyser using the DNA High Sensitivity Chip.

2.7.2.6 Next generation whole mitochondrial genome sequencing

Equimolar libraries were pooled and diluted to 26pM. Dr Helen Tuppen, Wellcome Centre for Mitochondrial Research, performed subsequent steps, including bioinfomatic analyses. Clonal amplification on to Ion Sphere Particles using the Ion OneTouch 1 System and the Ion OneTouch 200 Template kit v2, was undertaken as per manufacturer's instructions. Coated spheres were enriched on the Ion Torrent ES and then loaded on to Ion 318 sequencing chips. Next generation sequencing was performed on the Ion Torrent Personal Genome Machine using the PGM Hi-Q View Chef Kit.

2.7.2.7 Bioinformatics

FASTQ files were aligned to the revised Cambridge mtDNA reference sequence (NC_012920.1) using Torrent Suite software v5.4.0. The variant caller plugin was used to identify significant nucleotide polymorphisms (SNPs). Aligned data were visualised and SNPs verified using Integrative Genomics Viewer v2.3.75 (Broad Institute).

2.8 Systematic review of mitochondrial molecular alterations

2.8.1 Data sources

Level 1 clinical data, level 4 GISTIC v2 copy number, and level 3 RSEM normalised gene expression data for patients in The Cancer Genome Atlas – Prostate Adenocarcinoma (TCGA-PRAD) cohort were obtained from the Broad Institute Firehose GDAC repository (gdac.broadinstitute.org). Quality-checked progression-free survival follow-up data were obtained (Liu *et al.*, 2018) and linked with genomic data. Remaining data sources are described in **Table 2-12**.

2.8.2 Data analysis

Data analyses were performed in the R environment using RStudio v 1.2.1335, using packages *survival*, *survminer*, *Hmisc* and *finalfit*. The *ggplot2* package was used for data visualisation.

2.8.3 Gene sets

2.8.3.1 OXPHOS gene sets

Two OXPHOS gene sets were curated (**Table 2-13**): a mitochondrial OXPHOS gene set comprising of 13 mtDNA-encoded OXPHOS genes, and a nuclear OXPHOS gene set comprising of 83 nuclear-encoded OXPHOS genes based upon HUGO Gene Nomenclature Committee (HGNC) gene lists (Yates *et al.*, 2017). Genomic loci of genes encoding nuclear-encoded

OXPHOS subuntis are reported in Appendix A (**Figure A-1**). The discrepancy between the number of nuclear-encoded genes and structural subunits may be due to multiple isoforms of complexes IV and V which may be encoded by different nuclear encoded genes.

2.8.3.2 Other gene sets and signature scores

The following gene sets were obstained: MSigDB Hallmarks (Subramanian *et al.*, 2005; Liberzon *et al.*, 2015), Cell cycle proliferation (Cuzick *et al.*, 2011), epithelial to mesenchymal (EMT) (Mak *et al.*, 2016; Gibbons and Creighton, 2017), Buffa hypoxia signature (Buffa *et al.*, 2010), Winter hypoxia signature (Winter *et al.*, 2007), and metabolic pathway signatures (Gaude and Frezza, 2016).

Pre-processed gene signature scores were also obtained from supplementary data using the following sources: pan-cancer hypoxia signatures (Bhandari *et al.*, 2019a), and KEGG signatures (Chen *et al.*, 2018).

Data type	**Data source**	**Reference**
Clinical data		
Level 1 TCGA-PRAD clinical data (n=499 patients)	Firehose, Broad Institute	Broad Institute TCGA Genome Data Analysis Center (2016)
TCGA - Clinical Data Resource (n=492 patients)	Progression-free survival	Liu *et al.* (2018)
CPCG – Clinical Data	Clinical Data	Chen *et al.* (2019)
EOPC – Clinical Data	Clinical Data	Gerhauser *et al.* (2018) Weischenfeldt *et al.* (2013)
ICGC – Clinical Data	ICGC Data Portal https://dcc.icgc.org	Zhang *et al.* (2011)
Molecular data		
mtDNA mutations	The Cancer Mitochondrial Atlas	Yuan *et al.* (2017)
Mitochondrial copy number	The Cancer Mitochondrial Atlas https://ibl.mdanderson.org/tcma/	Yuan *et al.* (2017)
Mitochondrial copy number (log10 corrected)	Supplementary table 1	Reznik *et al.* (2016)
Nuclear DNA mutations	cBioPortal http://bit.ly/2Kuo77o	Cerami *et al.* (2012)
Level 4 GISTIC2 nuclear copy number alterations	Broad Institute Firehose GDAC repository (gdac.broadinstitute.org)	Broad Institute TCGA Genome Data Analysis Center (2016)
Mitochondrial RNA (log2 normalised RSEM counts)	Supplementary table 2	Reznik *et al.* (2017)

Level 3 RSEM normalised nuclear gene expression data	Broad Institute Firehose GDAC repository (gdac.broadinstitute.org)	Broad Institute TCGA Genome Data Analysis Center (2016)
Mitochondrial genomic loci	MITOMAP	Lott *et al.* (2013)
OXPHOS gene lists	HUGO Gene Nomenclature Committee	Yates *et al.* (2017)

Table 2-12: Data sources used to study mitochondrial molecular alterations in prostate cancer.

Complex (HGNC group)	mtDNA-encoded genes		Nuclear genes	
Complex I (HGNC 1149 & HGNC 1150)	7	MT-ND1 MT-ND2 MT-ND3 MT-ND4 MT-ND4L MT-ND5 MT-ND6	37	***Core (7)*:** NDUFS1, NDUFS2, NDUFS3, NDUFS7, NDUFS8, NDUFV1, NDUFV2 ***Accessory (30)*:** NDUFA1, NDUFA2, NDUFA3, NDUFS4, NDUFA5, NDUFA6, NDUFA7, NDUFA8, NDUFA9, NDUFA10, NDUFA11, NDUFA12, NDUFA13, NDUFAB1, NDUFB1, NDUFB2, NDUFB3, NDUFB4, NDUFB5, NDUFB6, NDUFB7, NDUFB8, NDUFB9, NDUFB10, NDUFB11, NDUFC1, NDUFC2, NDUFS4, NDUFS5, NDUFS6, NDUFV3
Complex II (HGNC 641)	0	-	4	SDHA, SDHB, SDHC, SDHD
Complex III (HGNC 642)	1	MT-CYB	9	CYC1, UQCR10, UQCR11, UQCRB, UQCRC1, UQCRC2, UQCRFS1, UQCRH, UQCRQ
Complex IV (HGNC 643)	3	MT-CO1 MT-CO2 MT-CO3	16	***Essential (12):*** COX4I1, COX4I2, COX5A, COX5B, COX6C, COX7A1, COX7A2, COX7B, COX7B2, COX7C, COX8A, COX8C ***Non-essential (4):*** COX6A1, COX6A2, COX6B1, COX6B2
Complex V (HGNC 644)	2	MT-ATP6 MT-ATP8	18	ATP5F1A (ATP5A1), ATP5F1B (ATP5B), ATP5F1C (ATP5C1), ATP5F1D (ATP5D), ATP5F1E (APT5E), ATP5MC1 (ATP5G1), ATP5MC2 (ATP5G2), ATP5MC3 (ATP5G3), ATP5MD (DAPIT), ATP5ME (ATP5I), ATP5MF (ATP5J2), ATP5MG (ATL5L), ATP5MPL (C14orf2), ATP5PB (ATP5F1), ATP5PD (ATP5H), ATP5PF (ATP5J), ATP5PO (ATP5O), ATP5IF1 (ATPIF1)

Table 2-13: Mitochondrial and nuclear-encoded OXPHOS genes. Gene lists collated from HUGO Gene Nomenclature Committee (HGNC) are stratified by genomic origin and OXPHOS complex (I-V). HGNC gene group is reported in brackets. Total number of genes encoded by each genome for each complex are annotated. Old gene nomenclature for complex V genes are included in brackets.

2.8.4 Analysis of DNA mutation data

Mutation data from The Cancer Mitochondrial Atlas (TCMA) (Yuan *et al.*, 2017) were collated and linked to clinical data, where available, and annotated to genome regions as per reported in the MITOMAP database (Lott *et al.*, 2013). PolyPhen annotation of mtDNA variants was

performed using the mvTool on MSeqDR (Shen *et al.*, 2018). In order to explore clonal dynamics, frequency of mtDNA mutations in genomic regions were normalised to gene lengths encompassed within each region. Expected and actual normalised frequencies were compared using the binomial test.

2.8.5 Analysis of copy number data

Mitochondrial copy number (MCN) data were available for the TCGA-PRAD cohort (Reznik *et al.*, 2016) and the TCMA-PRAD cohort (Yuan *et al.*, 2017). Nuclear copy number data (n=492 patients) was obtained from the Firehose repository in GISTIC 2.0 format (Mermel *et al.*, 2011). Nuclear OXPHOS copy number burden (CNB) was calculated as the sum of all deletions and all amplifications observed in each individual patient, based upon previously reported methods (Hieronymus *et al.*, 2014).

2.8.6 Analysis of mRNA data

Level 3 processed RNA-Seq by Expectation-Maximization (RSEM) normalized expression values from the Illumina RNASeqV2 (genes) datasets for nuclear-encoded OXPHOS genes in the TCGA-PRAD cohort were obtained from the Firehose repository (Broad Institute). Processed quality-checked mtRNA data for mitochondrial-encoded OXPHOS genes were obtained from supplementary data from Reznik *et al.* (2017). Processed RNA sequencing data for mitochondrial-encoded tRNA and rRNA were unavailable, and thus analysis was focussed on OXPHOS gene expression. In total, both mitochondrial and nuclear mRNA data were available for 426 tumour samples, including 47 samples with paired normal-adjacent samples.

2.8.7 Calculating gene expression scores

Gene expression scores were estimated as the average median-centred expression of all genes included in a gene set, normalised to the number of genes included in the gene set. Using this method, nuclear and mitochondrial OXPHOS scores were calculated using the associated gene sets (**Table 2-13**). An OXPHOS defect score was devised, which was calculated as the difference between nuclear OXPHOS gene expression score and the mitochondrial OXPHOS gene expression score. This score, therefore, represents discordance in nuclear and mitochondrial

gene expression, which is hypothesised to occur in the context of mitochondrial dysfunction. Similarly, EMT signatures were calculated as previously described (Mak *et al.*, 2016; Gibbons and Creighton, 2017). Where available, gene expression scores for TCGA-PRAD patients were also sourced from external data sources for validation, as described in section 2.8.3.

2.8.8 Survival analyses

TCGA-PRAD follow-up data were last updated on 31st May 2016. Progression-free survival data were available for 492 patients. This endpoint was defined as two or more consecutively elevated PSA results greater than 0.2ng/ml. Since positive tumour margins are an independent predictor of biochemical recurrence (Yossepowitch *et al.*, 2014; Preisser *et al.*, 2019b), patients with positive surgical margins (defined as either R1 or R2; n=151/492, 30.7%) were excluded from survival analyses.

Patients were classified into low and high expression groups using maximally selected rank statistics (Hothorn and Lausen, 2003) using the *survival* and *survminer* packages. This method evaluates all data points from continuous gene expression score data and establishes a cut-off point where the standardised statistics achieve maximum significance to separate patients into 'high' and 'low' expression groups, using disease free survival as outcome. Log rank test was used to estimate univariate hazard ratios. Cox proportional hazards estimation was performed for multivariate analyses using marker categorical data (ie high vs low expression), adjusting for age at diagnosis, log10-transformed PSA at diagnosis, ISUP Gleason group, pathological tumour stage, lymph node involvement, and presence of distant metastases.

2.8.9 Statistical analyses

Correlation analyses were performed on RStudio using the *Hmisc* package. Pearson's correlation coefficients are reported for normally distributed variables, whereas Spearman's correlation coefficients are reported for non-gaussian variables. The relationship between individual markers as continuous data and categorical clinical variables were tested using Wilcoxon rank test.

Chapter 3 The mitochondrial molecular landscape of prostate cancer

3.1 Introduction

3.1.1 Background

Over the past two decades, a plethora of large-scale sequencing studies has vastly improved our understanding of molecular alterations in various stages of prostate cancer. These efforts have identified a number of somatic and germline mutations, and downstream transcriptomic alterations, which have subsequently led to the development of novel drug targets for a subset of patients (Wedge *et al.*, 2018). However, the vast majority of these molecular alterations in localised prostate cancer occur at low frequency (pprox.. 5-15%, (Armenia *et al.*, 2018)) with subsequent expansion of sub-clones as part of progression to metastatic disease (Hong *et al.*, 2015).

The contribution of mitochondrial genomic alterations to prostate cancer progression is relatively poorly understood. Early studies evaluating mtDNA mutations were limited by small sample size. A number of recent pan-cancer studies have proposed diverse mitochondrial genomic alterations, which vary by tissue type. More recent data propose varied influence of specific low frequency mtDNA mutations on features of aggressive PCa and progression-free survival (Hopkins *et al.*, 2017).

Mutations in nuclear-encoded subunits of the electron transport chain (ETC) have also been implicated in carcinogenesis. Mutations in nuclear genes encoding Complex II (SDH) have been associated with paraganglionomas, phaeochromocytomas, breast cancer, gastrointestinal stromal tumours and renal carcinomas. Similarly, nuclear genes encoding essential enzymes of the tricarboxylic acid cycle have been implicated in various cancers. These involve mutations in genes encoding fumarate dehydrogenase leading to leiomyomata (affecting the uterus and skin) and papillary renal cell carcinomas (Kirches, 2009; Gaude and Frezza, 2014). In addition, mutations in genes encoding isocitrate dehydrogenase 1 (*IDH1*) & *IDH2* of the TCA cycle have been observed in gliomas, astrocytomas, chondromas and acute myeloid leukaemia (Wallace, 2012). Mutations affecting nuclear-encoded subunits of the ETC have not previously been reported in prostate cancer.

Gene expression studies have thus far largely relied on mRNA abundance of nuclear-encoded OXPHOS genes as a surrogate of mitochondrial function (Gaude and Frezza, 2016). Furthermore, due to low early mortality in localised and locally advanced prostate cancer, the impact of mitochondrial genomic alterations on PCa outcome is often not reported in pan-cancer studies, which primarily use overall survival as their primary endpoint.

3.1.2 Chapter aims

In this chapter, I aim to characterise the mitochondrial molecular landscape of prostate cancer by summarising associated prior literature and interrogating relevant publicly available molecular datasets. The key objectives are thus to:

1. Undertake a review of mutations and copy number alterations in mitochondrial and nuclear-encoded OXPHOS genes in prostate cancer.
2. Assess the impact of copy number and transcriptomic alterations on clinicopathological features of prostate cancer and progression-free survival.

3.2 Results – DNA mutations

3.2.1 Inherited mtDNA mutations

Family history and Afro-Caribbean ancestry are associated with increased PCa risk. Marginally greater familial risk of PCa is conferred by an affected brother (x3.14), as compared to an affected father (x2.35) (Kicinski *et al.*, 2011; Bratt *et al.*, 2016). Together, these epidemiological data raise the possibility of a potential contribution of maternally inherited risk features, such as germline mtDNA mutations, impacting risk of developing PCa.

Mitochondrial haplogroups are groups of populations that share a similar mtDNA sequence, with associated single nucleotide polymorphisms (SNPs) or haplotypes. The most common haplogroup in Europeans is H, whereas the most common African haplogroup is L. Haplogroups may confer varying metabolic profiles across different races (Kenney *et al.*, 2014), which has been hypothesised to influence population-level susceptibility to common diseases. Numerous studies have tested this hypothesis with a wide variation in results suggesting increased risk of PCa in both European-derived U-haplogroup (Booker *et al.*, 2006; Canter *et al.*, 2006) and the earliest diverging L0 haplogroup from southern Africa (McCrow *et al.*, 2016). Similarly, population-based studies have noted an association between missense *MT-CO1* mutations in European, but not African American men (Ray *et al.*, 2009; Scott *et al.*, 2012). However, studies evaluating the associations between mitochondrial haplogroups, ethnicity related variations in mtDNA SNPs and PCa diagnosis or risk have tended to be largely underpowered (Kalsbeek *et al.*, 2017). Indeed, a large multi-ethnic cohort study comprising 4,086 PCa patients and 3,698 controls across five racial/ethnic groups found no significant impact of mitochondrial haplogroup or individual SNPs with PCa risk features, upon adjustment for multiple testing (Giorgi *et al.*, 2016). Robust evaluation of the true impact of germline mtDNA mutations on PCa risk is therefore likely to require much larger studies. Thus, the role of inherited mtDNA mutations on PCa progression has not been evaluated further in this thesis.

3.2.2 Somatic mtDNA mutations in prostate cancer

Early studies evaluating somatic mtDNA mutations in prostate cancer used Sanger sequencing targeting D-loop (Jeronimo *et al.*, 2000; Chen *et al.*, 2002b; Chen *et al.*, 2003; Ashtiani *et al.*, 2012), 16S rRNA (Jeronimo *et al.*, 2000), *MT-CO1* (Petros *et al.*, 2005; Ray *et al.*, 2009) and Complex I subunits (Jeronimo *et al.*, 2000). These studies noted an increased frequency of mtDNA mutations in tumour foci, as compared to PIN lesions and BPH tissue. However, they were limited by small sample sizes, poor study design, low read depth and incomplete mitochondrial genome coverage.

Next generation sequencing technology combined with advancements in computational capabilities have revolutionised the assessment of DNA mutations in prostate cancer. Though both whole genome and whole exome sequencing strategies generate mitochondrial genomic data, these data are often excluded from subsequent analysis, as part of standard bioinformatic approaches, which primarily focus on autosomal alterations. With greater appreciation for the role metabolic aberrations in driving PCa progression, there has been a recent resurgence of interest in evaluating mitochondrial genomic alterations in prostate cancer (**Table 3-1**).

Yuan *et al.* (2017) curated The Cancer Mitochondrial Atlas (TCMA), using 2,658 cancer and normal-matched samples from ICGC whole-genome sequencing (WGS) data, covering 37 cancer types. WGS data achieved higher sequencing depth (mean depth 14,533x) as compared to prior whole exome sequencing data, which improved the ability to call somatic mutations at very low variant allele frequency (VAF>1%) more confidently. This was coupled with a well-designed computational pipeline to overcome known challenges in evaluating mtDNA mutations, such as tumour purity, ploidy, and false positive calls of mitochondrial pseudogenes in the nuclear genome, also referred to as nuclear integrations of mitochondrial genes (NUMTs).

Since this study primarily focussed on pan-cancer analyses, data pertaining to prostate cancer samples were extracted from the TCMA database and linked associated clinical data for prostate-specific in-depth analyses. Clinical characteristics of the included patient cohorts explored in this chapter are outlined in **Table 3-2**.

In total, 831 mutations were reported amongst 194 of 210 patients (92.4%) with PCa in the TCMA cohort, including 739 substitutions (89.1%) and 92 indels occurring at 703 unique loci

(**Figure 3-1**). Mutations were observed throughout the mitochondrial genome, with the vast majority (508/831, 61.1%) occurring in the protein coding region. The median number of protein-coding and rRNA SNPs per patient were 2 and 1, respectively. Of the 508 mutations occurring in genes encoding OXHOS subunits, 59 were indels (11.6%), 377 non-synonymous (74.2%) and 72 synonymous substitutions (14.1%, **Figure 3-2**), comparable to findings from prior studies (Lindberg *et al.*, 2013; Hopkins *et al.*, 2017). The vast majority of non-synonymous mutations were missense mutations (91.5%), which were functionally predicted to be "probably damaging" using the PolyPhen tool in 58-74% cases in Complex I, III and IV, and only 33% of Complex V missense mutations.

Study	Number of samples	Key findings
Lindberg *et al.* (2013)	64 PCa tumours (55 patients) 55 SNVs in 33 patients *Read depth:* 279x Median mutations/pt: 1	Non-synonymous mtDNA mutations observed in 40% cases. mtDNA mutational rate 55x that of nuclear DNA, and correlated with ROS exposure, chromosomal damage, increased cell proliferation, and aggressive PCa features.
Ju *et al.* (2014) (31 cancer types)	1675 tumours (80 PCa tumours) *Read depth:* 17,811x *Median mutations/pt:* 2	Number of mtDNA mutations associated with age but varies by tumour type. Neutral drift of missense mutations leading to homoplasmy, negative selection of protein truncating and mt-tRNA mutations which remain heteroplasmic.
McCrow *et al.* (2016)	87 PCa patients 144 SNVs *Read depth:* 3,000x *Median mutations/pt:* n/a	Primarily focussed on men with African ancestry. Number and frequency of mtDNA mutations associated with higher pathological stage and Gleason scores. VAF associated with higher Gleason scores. Enrichment of D-loop and rRNA mutations consistent with positive selection. Negative selection of complex I and tRNA mutations.
Stewart *et al.* (2015) (14 cancer types)	527 tumours (19 PCa tumours) *Read depth (mean):* 5,000x *Mean mutations/pt: 0.32*	Non-synonymous mtDNA mutations observed in 64% cases. Nonsense and frameshift indels predominantly heteroplasmic, suggestive of negative selection. High DNA:RNA allelic ratios despite coding mtDNA mutations, except for tRNA mutations.
Kalsbeek *et al.* (2016)	115 patients, 76 SNVs in 50 patients *Read depth:* 2,000x *Mean mutations/pt: 0.66*	Haplogroups not associated with Gleason scores. Positive selection of mtDNA mutations in D-loop and tRNA mutations. Total mtDNA mutational burden (VAF>0.1) correlated with Gleason score and risk of biochemical recurrence on univariate analysis.
Grandhi *et al.* (2017) (24 cancer types)	1,916 patients (121 PCa) (150 SNVs in 81 pts) *Read depth: n/a* *Median mutations/pt:* 1	Tumours had lower proportion of D-loop mutations than normal tissues. Positive selection of rRNA, tRNA and coding mRNA aberations, and nonsynonymous mutations increased with progression to metastasis. These findings driven by KICH and TCHA tumours. mtDNA mutations observed in ≈60% PCa tumours with dN:dS ratio ≈1.
Hopkins *et al.* (2017)	384 PCa patients 293 SNVs in 183 patients *Read depth:* 13,577x *Median mutations/pt:* 1	mtDNA mutational burden (VAF>0.2) associated with age and tumour stage. Mutations in CO2, CO3, and HV1 associated with reduced BCR risk, whereas ATP8, ND4L, OHR and CSB1 associated with increased BCR risk on univariate analysis. HV1 and OHR predictive of increased BCR risk on multivariate analysis.
Yuan *et al.* (2017) (37 cancer types)	2,700 patients (210 PCa patients with 831 mutations) *Read depth:* 14,533x *Median mutations/pt:* 4	Neutral drift of missense mutations. Frameshift mutations are negatively selected in PCa and positively selected in KICH, COAD and TCHA, where they are associated with upregulation of cell cycle, mTOR and TNFα signalling pathways.

Table 3-1: Mitochondrial genome sequencing studies in prostate cancer employing next generation sequencing technologies. Studies with fewer than 50 samples have been excluded.

		TCGA-PRAD	TCMA-PRAD	*p* value
Total patients		499	220	-
Patient age	Median (IQR)	61.0 (10.0)	59.8 (14.7)	0.017
PSA (ng/ml)	Median (IQR)	7.5 (6.3)	7.0 (6.1)	0.949
Gleason group	GG1-GG2	187 (37.5)	101 (73.2)	<0.001
	GG3	69 (13.8)	27 (19.6)	
	GG4-GG4	243 (48.7)	10 (7.2)	
	Missing	0	82	
Clinical tumour stage	T1	178 (43.8)	66 (32.8)	0.028
	T2	173 (42.6)	106 (52.7)	
	T3-T4	55 (13.5)	29 (14.4)	
	Missing	93	19	
BCR event	No	406 (81.4)	112 (70.9)	0.005
	Yes	93 (18.6)	46 (29.1)	
	Missing	0	62	
mtDNA data	Available	0	220 (100.0)	<0.001
	Unavailable	499 (100.0)	0	
CNA data	Available	306 (61.3)	146 (66.4)	0.197
	Unavailable	193 (38.7)	74 (33.6)	
mRNA data	Available	427 (85.6)	0	<0.001
	Unavailable	72 (14.4)	220 (100.0)	

Table 3-2: Patient characteristics of TCGA-PRAD and TCMA-PRAD cohorts. Clinical variables were compared between cohorts using generalised linear models, with p values reported. Percentage of patients in each subgroup are reported in brackets. Note: 18 patients overlapped across the two cohorts and have not been de-duplicated. TCGA: The Cancer Genome Atlas; TCMA: The Cancer Mitochondrial Atlas; PRAD: Prostate adenocarcinoma.

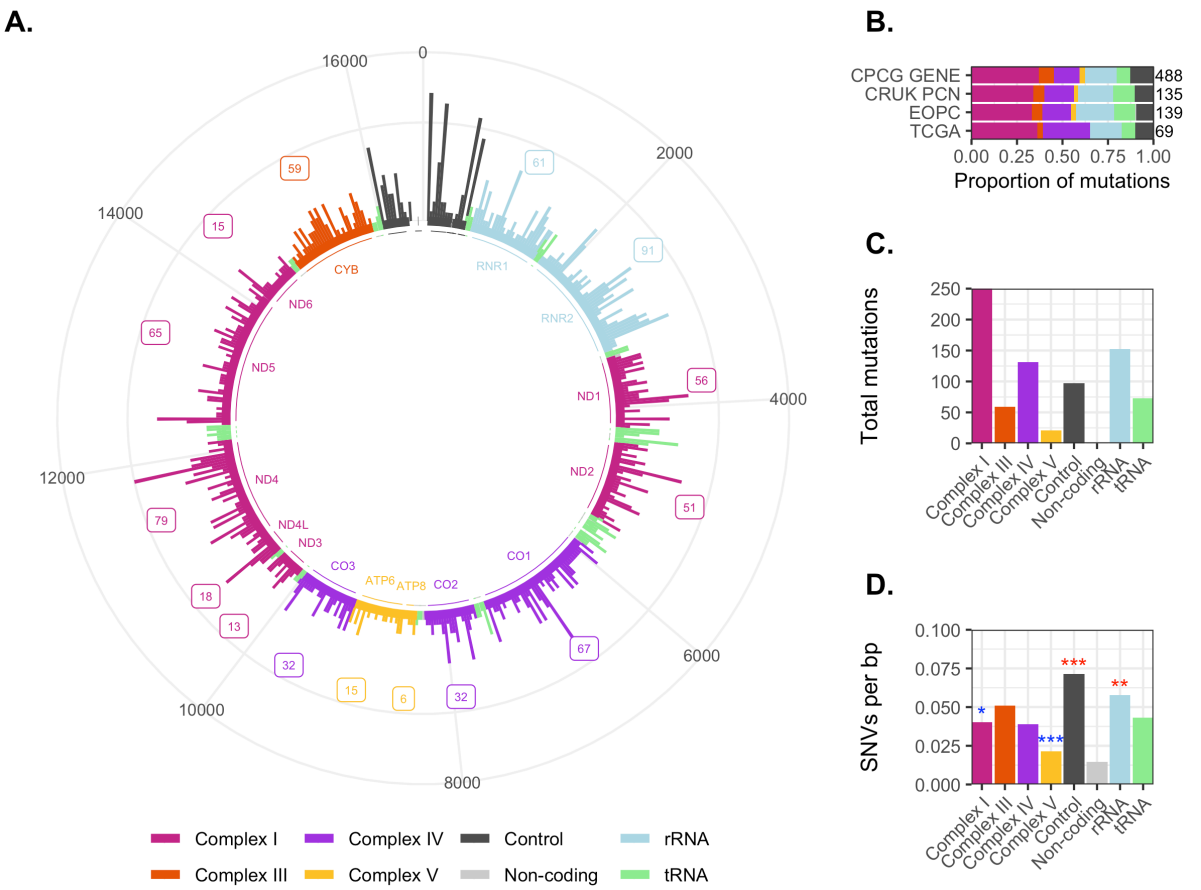

Figure 3-1: Somatic mtDNA mutations in human prostate cancer. **(A)** Amongst 210 patients in the TCMA-PRAD cohort, 831 mutations were observed in 194 patients. Frequency of mutations at 30bp intervals are represented across the mitochondrial genome and stratified by corresponding genes. Number of mutations in each gene are annotated. **(B)** Proportion of mutations in components of the mitochondrial genome were comparable across the three included cohorts, including CPC GENE (106 patients), CRUK PCN (31 patients), EOPC (39 patients), TCGA (18 patients). Total number of mutations from each cohort are reported on the right. Mutations in each component of the mitochondrial genome represented as **(C)** absolute numbers and **(D)** normalised to sum of gene lengths for all genes associated with each genomic region. Results of binomial test for stochasticity are reported as *, **, and *** represent $p<0.05$, $p<0.01$, and $p<0.001$, respectively. Red and blue asterisk colours denote components with more than expected and fewer than expected mutations by chance, respectively.

In keeping with prior studies (Lindberg *et al.*, 2013; Ju *et al.*, 2014);(Stewart *et al.*, 2015), mtDNA mutations were dominated by C>T/G>A substitutions (54.3%, **Figure 3-2C**), consistent with mutational signatures 1A/B, 6, 7, 11, 15 and 19 (Alexandrov *et al.*, 2013). Notably, of these mutational signatures 1A/B are associated with ageing, whereas signature 6 is associated with DNA mismatch repair defects. Furthermore, a replicative strand bias for G>A substitutions in the H strand, followed by a relatively lower proportion of T>C substitutions in the L strand has previously been reported (Ju *et al.*, 2014; Stewart *et al.*, 2015; Grandhi *et al.*, 2017). Consistent with these prior data (and Lindberg *et al.* (2013)), T>C transitions were the second major source of point mutations (27.1%), which are thought to arise from mtDNA polymerase gamma fidelity (Song *et al.*, 2005). This contrasts with G>T/C>A transversions, a hallmark of guanine modifications induced by oxidative stress (Waris and Ahsan, 2006), which only accounted for 1.1% of all mutations. Thus, somatic mtDNA mutations in PCa are unlikely to be solely a consequence of exposure to reactive oxygen species, and more likely emerge from proof-reading errors during mtDNA replication.

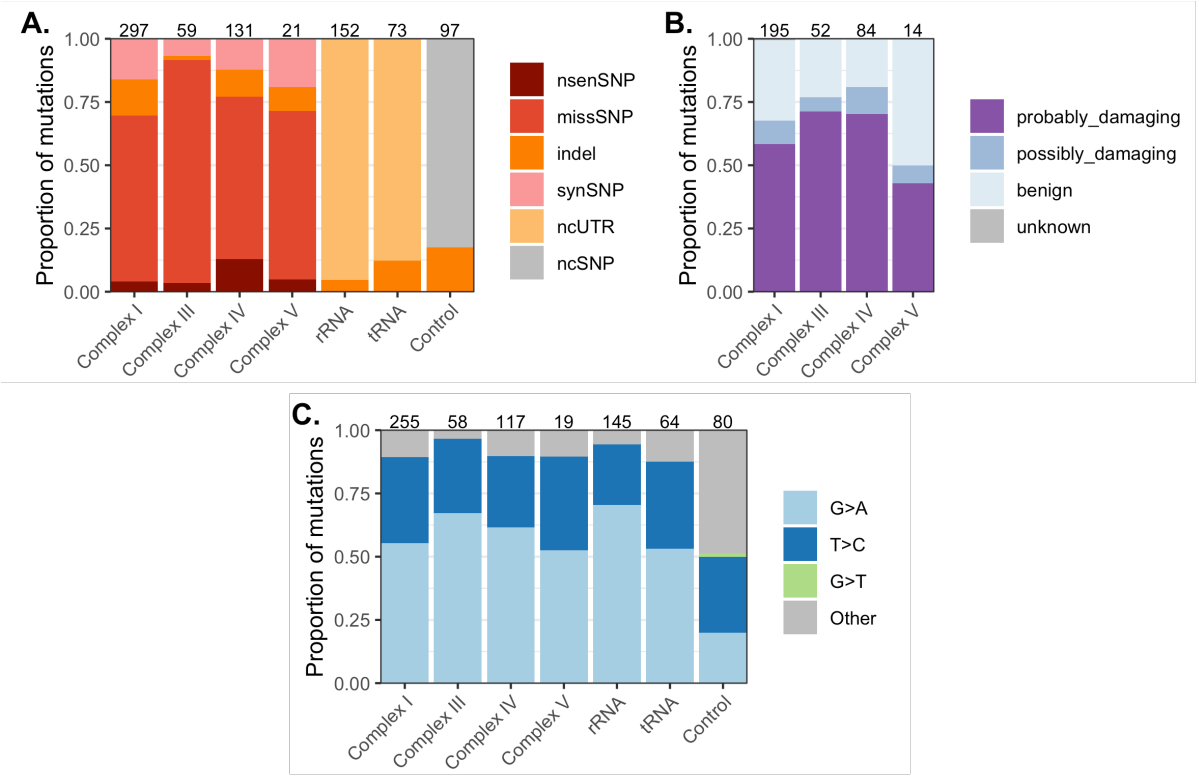

Figure 3-2: Mitochondrial mutational spectrum in human prostate cancer. The 831 mutations observed in 155 of 210 PCa patients in the TCMA cohort are classified by **(A)** type of mutation (nsenSNP: nonsense single nucleotide polymorphism (SNP), missSNP: missense SNP, synSNP: synonymous SNP, ncUTR: non-coding untranslated region, ncSNP: non-coding SNP, indel: insertion or deletion); **(B)** PolyPhen predictions of 345 missense SNPs from panel A; and **(C)** Substitutions (n=617) stratified by nucleotide change. Total number of mutations are annotated above each bar plot. A single mutation in the non-coding region, MT-NC1, was excluded.

3.2.2.1 Clonal selection pressures

The top three most frequently mutated genes were *MT-ND4*, *MT-CO1*, and *MT-ND5*, which accounted for 79 (17.6%), 67 (14.9%) and 65 (14.5%) of 449 SNVs in the protein coding region. Complexes I, IV, III, and V genes accounted for 56.8%, 26.1%, 12.9% and 4.2% of SNPs in protein-coding regions respectively. Though complex I and IV mutations accounted for the vast majority of mutations, upon adjustment for functional gene lengths (based upon Iommarini *et al.* (2013)), the control region and rRNA genes were more enriched for mtDNA mutations than expected, whereas Complex V genes had fewer mutations than expected (**Table 3-3**). The observed normalised frequency of mtDNA mutations in genes *MT-ND5*, *MT-ND6*, and *MT-ATP6* were lower, whereas *MT-TM* ($tRNA^{Met}$), *MT-TI* ($tRNA^{Ile}$), *MT-RNR1*, *MT-RNR2*, *MT-NC1*, and *MT-HV1* were higher as compared to expected frequencies under a purely stochastic process (**Figure 3-3**). These data thus suggest a possible role of purifying selection, positively enriching for rRNA, tRNA, and control region mutations, and depletion of complex I (*MT-ND5*, *MT-ND6*) and complex V (*MT-ATP6*) mutations in prostate tumourigenesis. However, these analyses do not take mtDNA heteroplasmy into account, as such data were not publicly available for the TCMA cohort.

	Number of mutations		Probability			Binomial test
Region	**Actual**	**Expected**	**Actual**	**Expected**	**Difference**	***p* value**
Complex I	255	284	0.345	0.385	-0.040	0.028
Complex III	58	51	0.078	0.069	+0.009	0.3
Complex IV	117	134	0.158	0.182	-0.024	0.095
Complex V	19	39	0.026	0.054	-0.028	3.0×10^{-4}
Control	80	50	0.108	0.068	+0.040	5.2×10^{-5}
Non-coding	1	3	0.001	0.004	-0.003	0.4
rRNA	145	112	0.196	0.152	+0.044	1.2×10^{-3}
tRNA	64	66	0.087	0.090	-0.004	0.8

Table 3-3: Expected and actual frequency of 739 somatic SNVs in the TCMA-PRAD cohort, stratified by regions of the mitochondrial genome. Binomal test was used to assess stochasticity of somatic SNVs in various regions of the mitochondrial genome in the TCMA-PRAD patient cohort. The actual and expected frequency of mutations, probability of mutations per base pair, and p value are reported.

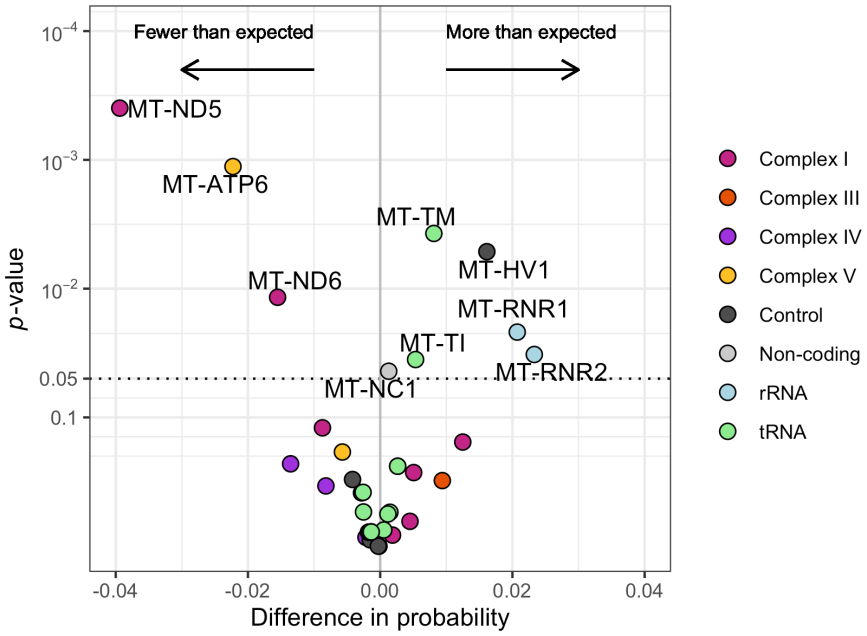

Figure 3-3: Expected and actual frequency of somatic SNVs in prostate cancer, stratified by individual genes. Binomal test was used to assess stochasticity of somatic SNVs in various regions of the mitochondrial genome in the TCMA-PRAD patient cohort reported. The actual and expected frequency of mutations, probability of mutations per base pair, and p values are reported. Dotted horizontal line represents *p*=0.05.

Early pan-cancer studies, including Stewart 2015, noted a reduced distribution of frameshift mutations and increased frequency of mutations in the control region than expected by chance. This conflicted with tissue-specific variation in VAF reported by Ju *et al.* (2014), who found 20% of protein-truncating mutations occurring at 0.4-0.8 VAF amongst 80 PCa patients, and none occurring at homoplasmic levels. The authors hypothesised that missense mutations at or near homoplasmic VAF may therefore confer a selective disadvantage to the cell. Grandhi *et al.* (2017), subsequently further dissected variation in clonal selection based upon tumour tissue type, finding evidence of relaxed negative selection in cancer as compared to strong negative selection in normal cells, with a subset of tumours demonstrating positive selection (thyroid and kidney). In keeping with these findings, Yuan *et al.* (2017) report low VAF amongst most tumour types, including prostate, in contrast to increased VAF in truncating mutations in kidney, colorectal and thyroid tumours. Truncating mutations in PCa accounted for 25% of all mutations, with only a small minority with VAF>60%, as compared to over 10% of kidney and colorectal tumours with VAF>60%. As demonstrated by Grandhi *et al.* (2017), PCa tumours had a dN/dS ratio of 1.0 in PCa, suggesting neutral evolution of mtDNA mutations in prostate tumourigenesis. Interestingly, the authors also noted a trend of increasing proportion of

mtDNA mutations in the coding region with disease progression from normal cells (69%), primary tumours (87%), metastatic tumours (91%) through to recurrent tumours (96%), suggesting that tumours gradually develop greater tolerance to disruptive mtDNA variants.

Nevertheless, mutations in non-coding regions, such as tRNA and rRNA genes, may also impact mitochondrial function by affecting transcription and translational processes. In a pan-cancer study of 1,916 patients across 24 cancer types, Stewart *et al.* (2015) reported high concordance in allelic DNA:RNA ratios, however a discordant increase in RNA levels associated with mutant tRNA molecules were noted. This phenomenon was thought to arise from a failure to process and clear mutant tRNA molecules. It is therefore anticipated that mutant tRNAs result in altered protein transcription and consequent mitochondrial dysfunction. In keeping with this finding, 64 mutations in tRNA genes were observed in 43 patients (19.5% of all PCa patients) in the TCMA cohort (**Table 3-3**). This is also consistent with a prior smaller study of 30 PCa patients (Kloss-Brandstätter *et al.*, 2010), which noted a comparable frequency of tRNA alterations and additionally reported an association between presence of tRNA mutations and increasing PSA levels. Further study of tRNA alterations in larger PCa cohorts, their impact on mitochondrial function, and association with clinicopathological markers of PCa progression is therefore warranted.

Since nuclear DNA mutations are often observed in morphologically normal prostate tissue and provide a background against which PCa develops (Cooper *et al.*, 2015), it is feasible that similar phenomena may also be at play in mtDNA and influence subsequent tumourigenesis. However, mtDNA heteroplasmy or mtDNA mutational data in adjacent normal tissue were not publicly available for the TCMA cohort but may be obtained from analysis of the original genomic data sources. Thus, future work evaluating mtDNA mutations in normal tissue may help evaluate whether specific mtDNA mutational backgrounds may provide a suitable niche supportive of subsequent PCa development.

3.2.3 mtDNA deletions in prostate cancer

Using long-range PCR, several prior studies have reported frequent occurrence of the large-scale deletions in PCa (**Figure 3-4**) and proposed their use as prognostic and diagnostic biomarkers. Amongst 210 patients in the TCMA-PRAD cohort, 41 (19.5%) had at least one short range mtDNA deletion (<30bp), five had more than one mtDNA deletion (2.4%), and

none had large-scale mtDNA deletions. This may be explained by known challenges in accurately detecting large-scale mtDNA deletions using next generation sequencing methods, due to the occurrence of deletions at multiple break points, very low heteroplasmy, and difficulty in amplifying the genome in an unbiased manner. Notably, more recent developments in bioinformatics provide a novel opportunity to investigate mtDNA deletions in curated pan-cancer datasets.

Jessie *et al.* (2001) provided the earliest report of mtDNA deletions amongst a cohort of 37 PCa patients, with a 14.8kbp deletion occurring in 91% of patients. Multiple additional smaller deletions were observed to be increasing in frequency with advancing age, and ranging from an average of 1.25 deletions amongst men in their 40s, as compared to 5.9 deletions amongst men in their 70s. However, DNA sequencing was not performed in these patients to identify the associated breakpoints.

Over one-third of all mtDNA deletions, referred to as the 'common deletion', occur between two 13bp direct repeats at position 13447-13459 and 8470-8482 and remove the 4,977bp region between *MT-ND5* and *MT-ATP8* genes. This removes all, or parts of genes encoding four complex I (*MT-ND5*, *MT-ND4*, *MT-ND4L*, *MT-ND3*), one complex IV (*MT-CO3*) and both complex V subunits (*MT-ATP6*, *MT-ATP8*), in addition to five tRNA genes ($tRNA^{Leu}$, $tRNA^{Ser}$, $tRNA^{His}$, $tRNA^{Arg}$, $tRNA^{Gly}$), resulting in OXPHOS dysfunction. This deletion has been observed as part of normal ageing (Cortopassi and Arnheim, 1990), but also a variety of pathological conditions (Tanaka *et al.*, 1996), including multiple cancers (Yusoff *et al.*, 2019). Nie *et al.* (2013) performed a meta-analysis of 33 studies, encompassing 1,613 cancer cases, 1,516 normal-adjacent and 683 healthy controls. The authors noted increased frequency of the common deletion in cancer tissues, as compared to healthy controls. Interestingly, adjacent normal tissue had an even higher deletion frequency, as compared to cancer foci. Notably, only a single study (Yu and Yan, 2010) has evaluated the common deletion in prostate tissue (130 PCa patients and 61 patients with BPH) and noted higher prevalence in laser capture micro-dissected PCa cancer cells (75.4%), compared to adjacent normal (10.8%) or benign controls (14.7%). Patients with the common deletion tended to be older with higher Gleason scores. The authors proposed that the common deletion may be a diagnostic marker of prostate cancer, with sensitivity 75.4%, specificity 85.2%, and AUC of 0.82. However, these results have not been subsequently validated in independent cohorts.

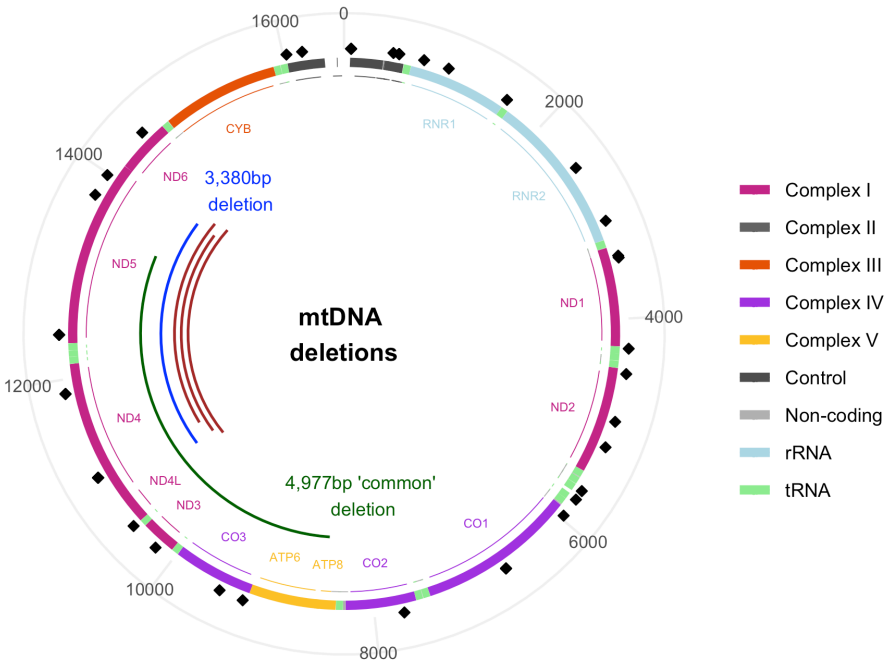

Figure 3-4: mtDNA deletions in prostate cancer. Short-range deletions in the TCMA-PRAD cohort (n=47, <30bp in length) are denoted as black points. Long-range deletions reported by McCrow *et al.* (2016) (red lines), the 'common' 4,977bp region (green line), and the 3,380bp deletion used in the Prostate Core Mitomic Test (PCMT, blue line), are annotated on the corresponding region of the mitochondrial genome.

A series of studies have also described a 3,380bp deletion between 10744:14124 of the mitochondrial genome, removing parts of *MT-ND4L* and *MT-ND5*, all of *MT-ND4*, and three tRNAs ($tRNA^{his}$, $tRNA^{ser2}$, $tRNA^{leu2}$) in prostate cancer samples (Maki *et al.*, 2008). This deletion was observed at high frequency across cancer foci (91%) and normal-adjacent tissue. High concordance between normal-adjacent and cancer foci suggested a field effect and the authors therefore proposed its value as a biomarker amongst patients with risk features of PCa despite prior negative prostate biopsy. These results were validated in an independent externally evaluated cohort, which confirmed sensitivity and specificity of 80-83% and 71-70%, respectively, with AUC 0.83-0.87 and a negative predictive value up to 91%. Subsequent further validation studies (Robinson *et al.*, 2010) led to commercialisation of this deletion as the Prostate Core Mitomic Test (PCMT), which has reportedly reduced repeat biopsy rates and increased PCa detection rates as part of clinical practice (Legisi *et al.*, 2016). Two recent studies have also proposed the use of this deletion as a diagnostic marker for clinically significant PCa, using cell free DNA in urine (Maragh *et al.*, 2015) and plasma (Creed *et al.*, 2018). Notably, studies focussing on the 3,380bp mtDNA deletion were largely performed on men of European

descent. This deletion was absent in a study of 77 men of African descent by (McCrow *et al.*, 2016), who performed both targeted long-range PCR and next generation sequencing (as described in section 3.2.1). However, three deletions varying in length (2,879 bp to 3,769 bp) were identified in a similar region, amongst two PCa and two non-PCa patients in this study, suggesting patient specific genomic instability in this region.

3.2.4 Clinicopathological features of prostate cancer progression

A weak association between advancing age and increasing frequency of mtDNA mutations was observed in the TCMA-PRAD cohort (n=193 patients, Pearson's R 0.15, p=0.038). This was consistent with findings from Hopkins *et al.* (2017), where frequency of mtDNA mutations was observed to increase with advancing age, and early onset PCa were found to be more likely to have no mtDNA mutations, as compared to late onset PCa.

Increasing Gleason score has previously been associated with both mtDNA mutational burden (Kalsbeek *et al.*, 2016; McCrow *et al.*, 2016) and increasing VAF (Kalsbeek *et al.*, 2016). In contrast to these reports, but consistent with Hopkins *et al.* (2017), histopathological grade was not associated with frequency of mtDNA mutations in the TCMA-PRAD cohort (GG1-2 vs GG3: p=0.2). Furthermore, also in keeping with Hopkins *et al.* (2017), patients with increased frequency of mtDNA mutations tended to have lower stage disease (T1 vs T3-4: Δ 1.0, p=0.016; **Figure 3-5**). Consistent with this finding, an inverse association between mtDNA mutational burden and PSA was also observed (Pearson's R=-0.19, p=-0.017). Though VAF data were unavailable, it may be that either (a) fewer mutations with higher VAF are selected; or (b) an increased burden of mtDNA mutations confer a survival disadvantage during disease progression and are therefore negatively selected; or (c) a survival disadvantage due to high mtDNA mutational burden suppresses PCa progression.

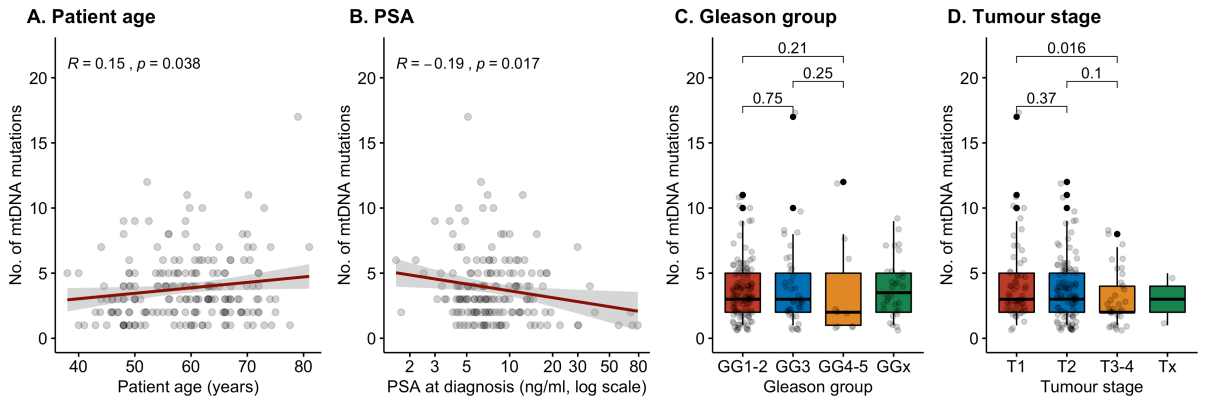

Figure 3-5: Mitochondrial mutational burden by clinical characteristics. Association between number of mtDNA mutations (SNVs and small indels) and **(A)** patient age and **(B)** PSA at diagnosis (n=163 patients), **(C)** Gleason group, and **(D)** clinical tumour stage in 193 patients with at least one mtDNA mutation in the TCMA-PRAD cohort (Yuan *et al.*, 2017). In panels A-B, red line denotes linear regression model with 95% confidence interval. Pearson's correlation co-efficient reported above. In panels C-D, groups were compared using Wilcoxon rank test with p values reported. TCMA: The Cancer Mitochondrial Atlas; PRAD: Prostate adenocarcinoma.

Through integrated analyses of multi-genome data, Lindberg *et al.* (2013) found that cell cycle proliferation scores were higher amongst PCa samples with an increased fraction of cells with a mtDNA variant. Similarly, a variety of mito-nuclear interactions were reported by (Hopkins *et al.*, 2017), including copy number alterations (CNA) in *PTEN*, *TP53*, *CHD1*, *RB1*, *MYC*, *CDKN1B*, *NKX3.1*; mutations in *MED12*, *FOXA1*, *SPOP*, *ATM* and *TP53*; and nuclear genomic features including percentage genome altered, kataegis, number of genomic arrangements, chromotripsis and number of autosomal SNVs. A strong association between mitochondrial and autosomal mutational frequency was reported across both studies (Lindberg *et al.*, 2013; Hopkins *et al.*, 2017), reflecting either a global increase in mutagenesis in cancer, or a reduction of DNA repair, as suggested by McCrow *et al.* (2016).

3.2.5 Impact on outcome

The impact of mtDNA mutations on biochemical recurrence free survival has previously been evaluated by Kalsbeek *et al.* (2016) and Hopkins *et al.* (2017). Kalsbeek *et al.* (2016) noted increased risk of BCR amongst patients with 0 vs ≥1 mtSNVs and ≤1 vs ≥2 mtSNVs on univariate analysis, amongst a cohort of 115 men who underwent radical prostatectomy for PCa. This work was further refined by Hopkins *et al.* (2017) in a larger cohort of 165 men undergoing radical therapy, which noted increased risk of BCR amongst patients with mutations in *MT-ATP8*, *MT-CSB1* and *MT-OHR* genes, and reduced BCR risk amongst patients with HV1 mutations, upon univariate Cox proportional hazards modelling. Using a leave one out cross-validation approach, the authors proposed a prognostic gene signature comprising mutations in *MT-CO2*, *MT-CO3* and *MT-HV1* to be predictive of low risk, and mutations in *MT-ATP8*, *MT-OHR*, *MT-ND4L*, and *MT-CSB1* to be predictive of high risk of biochemical recurrence. Total number of SNVs did not impact outcome. Upon multivariate analysis, control regions HV1 and OHR remained independently prognostic of low and high risk of BCR, respectively. Co-occurrence of autosomal *MYC* amplification with *OHR* mutations was also associated with increased BCR risk.

A key limitation of these data is the relatively low number of patients with mtDNA mutations with modest heteroplasmy (VAF≥0.2) in each genomic locus (eg 12 and 18 of 165 patients had mutations in OHR and HV1 regions, respectively). Furthermore, the current lack of a biologically plausible hypothesis accounting for the variation in impact of two different non-coding regions of the genome on PCa outcome also merits further investigation. Since frequency of mtDNA mutations is correlated with the burden of autosomal mutations and high-risk clinical features, it is possible that mtDNA mutational burden may be a surrogate, rather than a driver of high risk PCa. In addition, these studies reported BCR rate rather than overall survival. This is due to the relatively low mortality rate in patients receiving radical therapy for PCa in the included cohorts. Therefore, validation of these findings in larger cohorts using overall survival as an endpoint would be of valuable.

3.2.6 mtDNA mutations in metastatic prostate cancer

The above studies largely focussed on patients with either localised or locally advanced primary PCa. Only two small studies have assessed the mtDNA mutational landscape in metastatic PCa, focussing primarily on bone metastases (Arnold *et al.*, 2015; Kalsbeek *et al.*, 2017).

Arnold *et al.* (2015) evaluated mtDNA mutations in 10 PCa patients with bone metastases in a rapid autopsy programme, including sequencing of the primary tumour, adjacent normal tissue, soft tissue metastases, and bone metastases. As compared to the primary tumour, mtDNA mutations were encountered more frequently in soft tissue (2.13x) and bone metastases (6.78x). Upon adjustment for gene lengths, bone metastases demonstrated a higher than expected frequency of Complex I and tRNA mutations, suggesting a non-random process. The Complex I gene *MT-ND3* was exclusively recurrently mutated (m.10398A>G, resulting in AA change Thr114Ala) in 7/10 bone metastases, which the authors postulated as a consequence of pervasive selective pressures. Mutations in tRNA genes *MT-tRNA*^{Arg} and *MT-tRNA*^{Thr} were also observed. The authors also hypothesised that the mtDNA mutations may result in ROS-mediated activation of signalling pathways supportive of tumour growth and metastases.

Kalsbeek *et al.* (2017) analysed data from Hong *et al.* (2015) including 27 samples from 9 patients with PCa metastases, and again noted an increased mtDNA mutational rate in bone metastases with two Complex I mutations approaching homoplasmic levels (m.13019G>A, *MT-ND5* gene; m.10170G>C, *MT-ND3* gene). Mutations observed in available primary tumour from two patients were, however, absent in the matched bone metastases. The scarcity of sequencing data from matched primary and tumour samples therefore limits any clear assessment of the underlying processes, which warrants further research.

3.2.7 Nuclear OXPHOS gene mutations in prostate cancer

Since all OXPHOS complexes are composed of nuclear encoded OXPHOS subunits, autosomal mutations may also influence mitochondrial function. Grandhi *et al.* (2017) noted high mtDNA:nDNA mutational discordance, suggesting that tumours lacking protein truncating mtDNA mutations were more likely to bear nuclear OXPHOS mutations. However, recurrent autosomal OXPHOS mutations have not been specifically evaluated in PCa.

Publicly available data from five large cohorts were therefore interrogated for mutations in nuclear-encoded OXPHOS genes using cBioPortal (Cancer Genome Atlas Research, 2015; Beltran *et al.*, 2016; Fraser *et al.*, 2017; Armenia *et al.*, 2018; Abida *et al.*, 2019), and divided into seven cohorts based on disease stage, tissue source, and sub-type. In total, the 300 mutations were observed amongst 153 of 2,495 patients (6.1%) and 243 of 2542 samples (9.6%). Eighty-six patients (0.57%) and 21 samples (0.83%) had more than one mutation. Each patient had an average of 0.12 mutations, which represented a mutational frequency of 7.0 x 10^{-5} mutations/kbp/patient. This was approx. 3000-fold lower than the 0.2 mutations/kbp/patient noted in mtDNA encoded OXPHOS genes (t-test, p<0.0001) in the TCMA-PRAD cohort in section 3.2.1.

Study	Cohort	Number of mutations	Samples with at least 1 mutation	Patients with at least 1 mutation
CPC-GENE 2017	Primary	35	7.7%	3.1%
TCGA-PRAD 2018	Primary	73	7.3%	5.1%
MSKCC/DFCI 2018	Primary	87	11.7%	5.1%
MSKCC/DFCI 2018	Metastases	46	10%	10.2%
SU2C/PCF 2019	Metastases	41	11.5%	7.8%
NEPC 2016	CRPC	10	8.6%	11.5%
NEPC 2016	NEPC	8	9.1%	13.3%

Table 3-4: Nuclear-encoded OXPHOS mutations in five publicly-available PCa studies, comprising 2,542 samples from 2,495 patients. Studies have been subdivided into cohorts by disease type. Note: overlapping samples included in multiple studies were not de-duplicated.

Mutations were observed most frequently in Complex I genes (3.1% patients across all studies). Notably, cohorts comprising predominantly metastatic PCa and neuroendocrine prostate cancer (NEPC) patients had a higher frequency of mutations (**Table 3-4**), which may be in keeping with known increased global mutational frequency in advanced disease, where mismatch repair defects are more frequently observed (Chung *et al.*, 2019). Complex I and V mutations were enriched in patients with NEPC and CRPC whereas Complex I mutations were also enriched in patients with metastatic disease. Missense (passenger), truncating (driver), truncating (passenger), missense (driver) and in-frame mutations accounted for 80.0%, 15.3%, 3.0%, 1.3%, and 0.8% of all 300 mutations, respectively. Only 13 mutations (4.3%) were putative driver mutations, affecting complex II genes *SDHA*, *SDHB* and *SDHC* in 7 (2.8%) of 2,495 patients. SDH mutations have previously been implicated in approximately 30% of phaeochromocytomas and paragangliomas, and also observed less frequently in other cancer types, including renal cell carcinoma, gastro-intestinal stromal tumours, testicular seminoma and neuroblastomas (Bardella *et al.*, 2011). However, due to the low frequency of driver nuclear-encoded OXPHOS mutations in PCa, these were not further evaluated in this chapter.

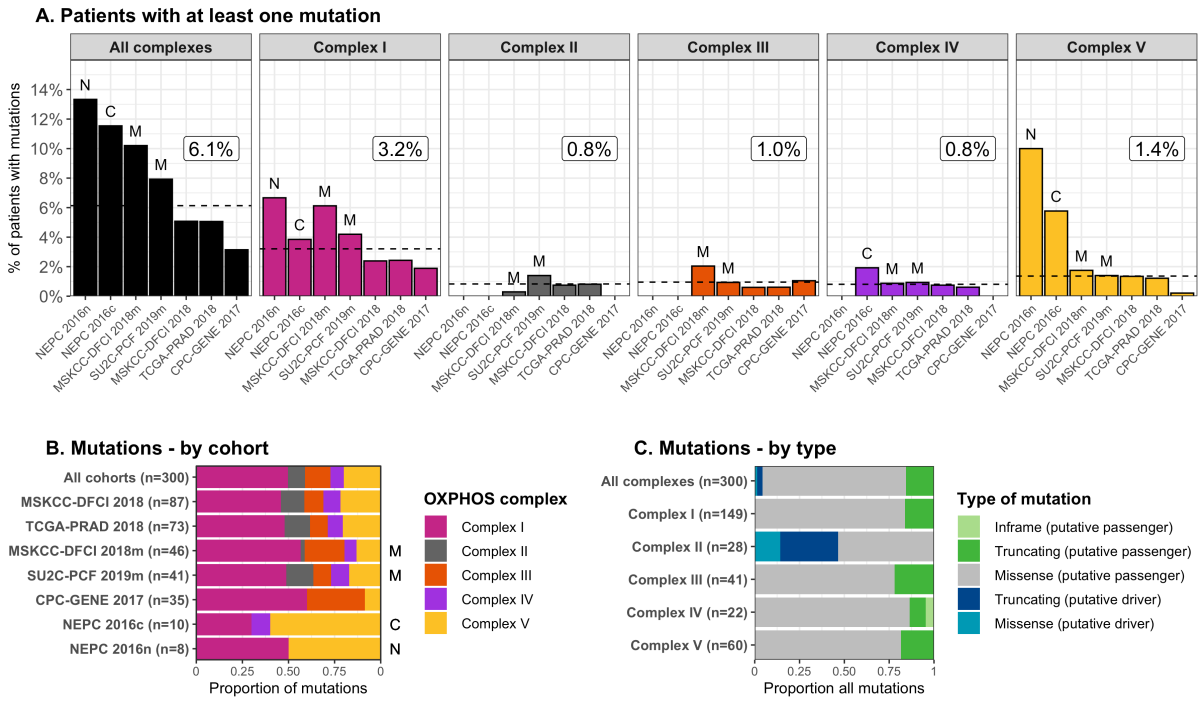

Figure 3-6: Frequency of mutations in nuclear-encoded OXPHOS genes in prostate cancer. Data acquired from cBioPortal for 2,542 patients across five large PCa studies divided into seven cohorts. **(A)** Percentage of patients with mutations with at least one mutation stratified by study and OXPHOS complex. Mean percentage for mutations in each complex across all five studies is annotated and represented by a dashed horizontal line. Studies predominantly comprising of patients with neuroendocrine prostate cancer ('N'), metastatic disease ('M') or castrate resistant prostate cancer ('C') are annotated above each bar plot. **(B)** Proportion of mutations in each OXPHOS complex, stratified by patient cohort patient cohort. **(C)** Type of mutation stratified by complex. Total number of mutations observed in each study is annotated in brackets.

3.2.8 Concluding remarks

Somatic mtDNA mutations are frequently observed in prostate cancer. Non-coding mutations in the control region and rRNA genes appear to be under either positive selection or neutral drift, whereas mutations in *MT-ND5*, *MT-ND6* and *MT-ATP6* genes appear to be under negative selection. Missense mutations at or near homoplasmic levels may confer a selective disadvantage to the PCa cells, as opposed to kidney, colorectal and thyroid tumours. Moreover, mutations in non-coding mutations may impact transcription and translational processes contributing to mitochondrial dysfunction. Nevertheless, tumours may develop tolerance to disruptive mtDNA alterations during progression to metastatic disease. Mutational events as individual genomic loci have been hypothesised to impact PCa outcomes, however further validation studies in larger cohorts are required. The polyploid nature of the mitochondrial genome and potential contributions from nuclear genomic alterations, however, further adds to the complexity in inferring the potential phenotypes associated with individual mutations. Thus, the assessment of associated copy number alterations or downstream consequences at the transcriptomic or proteomic level may provide more robust surrogates of altered mitochondrial function.

3.3 Results - Copy number alterations

3.3.1 Background/rationale

Mitochondrial copy number (MCN) remains relatively stable under physiological conditions and is thought to be regulated by a fine balance between mtDNA degradation and replication (Clay Montier *et al.*, 2009). The loss of regulation through increased mitophagy or reduced mitochondrial biogenesis has been implicated in multiple conditions, including cancer. Though exact mechanisms regulating MCN are not fully understood, ATP demand and hypoxia are thought to play a key role. MCN alterations have thus been hypothesised to contribute to cancer risk.

Along with colorectal, biliary, liver and ovarian cancers, PCa has higher mtDNA copy number compared to other tissue types (Yuan *et al.*, 2017). Indeed, tumour mtDNA copy number has been proposed as a potential diagnostic and prognostic biomarker in PCa (Ellinger *et al.*, 2012; Maragh *et al.*, 2015; Moore *et al.*, 2017; Xu *et al.*, 2019). However, these data have been questioned by a recent meta-analysis (Hu *et al.*, 2016), where no overall change in cancer risk was noted. Elevated mtDNA content was found to be associated with increased risk of lymphoma and breast cancer, reduced risk of hepatic carcinoma, and not associated with PCa risk upon sub-group analysis.

Key findings from studies evaluating MCN in PCa tissue are outlined in **Table 3-5**. This demonstrates highly variable results with conflicting reports of relative CN change in tumour versus adjacent benign tissue, and reports of direct (Kalsbeek *et al.*, 2018), inverse (Hopkins *et al.*, 2017) and absence (Koochekpour *et al.*, 2013) of associations with PCa risk features. Similarly, MCN was not prognostic of either BCR in an Australian cohort (Kalsbeek *et al.*, 2018) or overall survival in the TCGA-PRAD cohort (Reznik *et al.*, 2016).

Study	Number of samples	Findings
Koochekpour *et al.* (2013)	38 tumours 20 BPH 30 NA prostates	Lower mtDNA content in tumour and BPH tissue in AA men vs Caucasian men. Both decreases with age. NA MCN is lower than tumour MCN. NA MCN associated with increased Gleason score and tumour stage.
Reznik *et al.* (2016)	306 PCa 59 matched NA pairs	NA MCN lower than tumour MCN, and anti-correlated with mitochondrial gene expression. Tumour MCN strongly correlated with metabolic gene signatures but weak negative association with immune infiltration scores. No association with overall survival in PCa. (Adjusted for tumour purity and ploidy; Corrected for batch effects across sequencing centres).
Kalsbeek *et al.* (2018)	115 PCa 46 NA samples	NA MCN greater than tumour MCN. Tumour MCN, but not NA MCN, associated with Gleason score and pathological tumour stage. BCR risk: No association.
Hopkins *et al.* (2017)	384 PCa 381 blood 3 paired NA	Direct associations: age, SPOP mutation, PGA, Kataegis, PTEN & CN, GR, chromothripsis. Inverse associations: clinical tumour stage, Gleason score, CDKN1B mutations, NKX3-1 CN, CHD1 CN, ATL7B methylation.
Yuan *et al.* (2017)	210 patients	Tumour MCN decreases with age and is poorly correlated with mitochondrial gene expression. (Adjusted for tumour purity and ploidy). Increased MCN with high VAF truncating mutations.

Table 3-5: Key studies evaluating mitochondrial copy number (MCN) in prostate cancer. NA: Normal-adjacent tissue. BCR: Biochemical recurrence. VAF: Variant allele frequency.

3.3.2 Clinicopathological features of PCa progression

Reznik *et al.* (2016) reported increased MCN across the vast majority of cancer types in the TCGA dataset. Intriguingly, an anti-correlation between MCN and OXPHOS gene expression in normal-adjacent prostate tissue samples was observed. The authors postulated that this may be due to the uniquely increased citrate secretion in normal prostate epithelia, which would otherwise have been oxidised with the resulting NADH accumulation subsequently utilised in OXPHOS. Mitochondrial copy number data for 306 TCGA-PRAD patients were sourced from this study and linked with associated clinical data in order to evaluate association between MCN and PCa risk features. Similarly, MCN data for 137 patients were available from the TCMA-PRAD cohort (Yuan *et al.*, 2017) and linked to clinical data.

In keeping with findings from Reznik *et al.* (2016), paired analysis of tumour and normal-adjacent tissue amongst 77 TCGA-PRAD patients with matched data noted comparable MCN across both tissue types (paired Wilcox test, p=0.21, **Figure 3-7**). Previous data reports conflicting findings, with increased MCN reported in both tumour tissue (Mizumachi *et al.*, 2008; Hopkins *et al.*, 2017) and normal-adjacent tissue (Koochekpour *et al.*, 2013; Kalsbeek *et al.*, 2018). Matched MCN data from normal-adjacent tissue in the TCMA-PRAD cohort were not available for comparison.

MCN declines with age and declining health status in a tissue-specific manner (Laderman *et al.*, 1996; Mengel-From *et al.*, 2014). In keeping with this observation in other tissues, Hopkins *et al.* (2017) noted decreasing MCN with advancing age in normal-adjacent prostate tissue. Notably, both Yuan *et al.* (2017) and Hopkins *et al.* (2017) reported a converse increase in tumour MCN with advancing age. Indeed, a strong correlation between advancing age and tumour MCN was also noted in the TCMA-PRAD cohort (Pearson's r=0.29, p=0.00034). This phenomenon was not recapitulated in the TCGA-PRAD cohort (Reznik *et al.* (2016) dataset, >60 years vs <60 years, p=0.83), likely due to the lower number of cases with EOPC in this cohort. These data suggest that diverse factors may influence MCN in normal and malignant prostate tissue. Variation in ATP requirements and hypoxic conditions across tissue types may plausibly explain this finding.

Notably, tumour MCN was inversely correlated with PSA in the TCMA-PRAD cohort (Pearson's R -0.22, p=0.017), but this association was not observed in the TCGA-PRAD cohort (Pearson's r=-0.018, p=0.76, **Figure 3-7A**). Both Kalsbeek *et al.* (2018) and Hopkins *et al.* (2017) reported an association between tumour MCN and tumour stage and Gleason score. Tumour stage was inversely associated with tumour MCN in the TCMA-PRAD cohort (T1 vs T3-4, p=0.0037). However, consistent with findings from Koochekpour *et al.* (2013), association with Gleason group was not observed in either TCGA-PRAD and TCMA-PRAD cohorts (**Figure 3-7**, **Figure 3-8**).

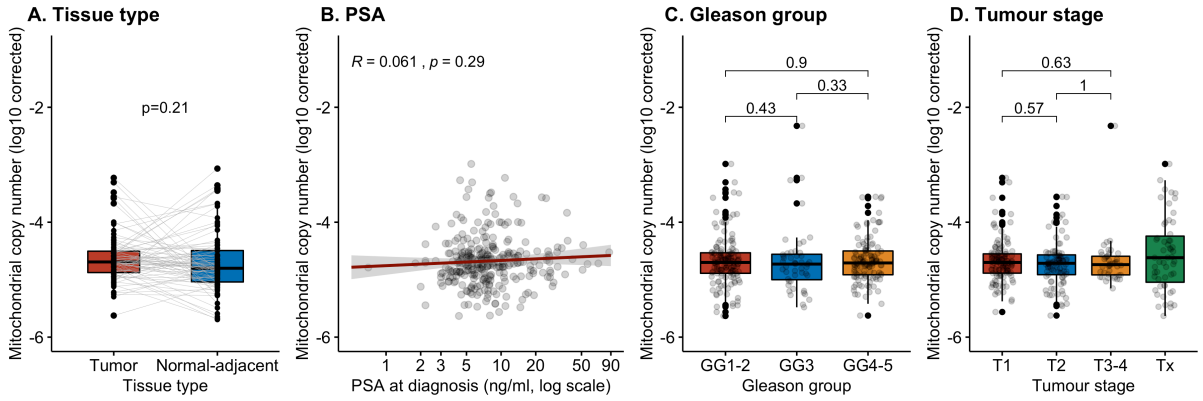

Figure 3-7: Mitochondrial copy number by clinical characteristics – TCGA-PRAD cohort. Log10 corrected mitochondrial copy number stratified by **(A)** tissue type (n=77 paired patients). Tumour MCN sub-stratified by **(B)** PSA group, **(C)** Gleason group at radical prostatectomy, and **(D)** clinical tumour stage in 306 patients in the TCGA-PRAD cohort. Based upon data from Reznik *et al.* (2016). Groups were compared using Wilcoxon rank test with *p*-values reported.

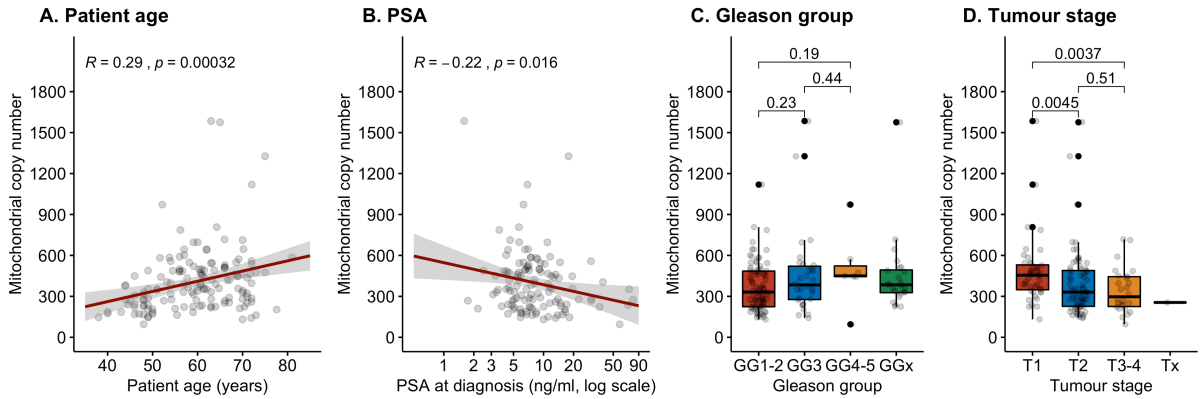

Figure 3-8: Mitochondrial copy number by clinical characteristics – TCMA-PRAD cohort. Tumour mitochondrial copy number stratified by **(A)** patient age, **(B)** log10-transformed PSA at diagnosis (n=122 patients), **(C)** Gleason group at radical prostatectomy, and **(D)** clinical tumour stage. Based on data from 146 patients in the Yuan *et al.* (2017) cohort. Correlations evaluated using Pearson's correlation coefficient. Groups were compared using Wilcoxon rank test with *p*-values reported.

3.3.3 Impact on outcome

A meta-analysis of 18 studies comprising 3,961 cancer patients across multiple cancer types concluded that high tumour MCN predicted better survival, whereas high MCN in peripheral blood was predictive of poor survival (Chen *et al.*, 2016). Reznik *et al.* (2016) reported worse survival in patients with renal clear cell carcinoma and melanoma and better overall survival outcome in adrenocortical and kidney chromophobe carcinoma with high tumour MCN in TCGA cohorts. Since association of MCN with risk of BCR has previously not been evaluated in the TCGA-PRAD cohort by either Reznik *et al.* (2016) or Yuan *et al.* (2017), MCN data for 342 patients from Reznik *et al.* (2016) were matched with clinical characteristics. After excluding 67 patients with positive surgical margins, data for 239 patients were available for outcome assessment. Low MCN from both tumour and normal-adjacent tissue were associated with increased BCR risk (**Figure 3-9**, log-rank test, p=0.019 and 0.029, respectively). Consistent results were obtained in the TCMA-PRAD cohort, where survival data were available for 103 patients (**Figure 3-10**, log-rank test, p=0.042).

These findings are in consistent with the pan-cancer meta-analysis by Chen *et al.* (2016), but contrast findings by Kalsbeek *et al.* (2018), who reported low MCN from normal-adjacent tissue (n=46), but not PCa tumour tissue (n=115), was associated with reduced BCR risk on univariate analysis. Similarly, these findings are also in contrast to Hopkins *et al.* (2017)(n=384), where tumour MCN was not associated with risk of BCR on univariate analysis. However, multivariable analyses were not performed in either of these reports.

Therefore, in order to adjust for potential clinical covariates, Cox regression analysis were performed in the TCGA-PRAD cohort. Reduced tumour MCN, but not normal-adjacent MCN, was found to be independently associated with increased BCR risk (HR 2.30, 95% CI 1.04-5.11, p=0.041). This finding was reproduced in the TCMA-PRAD cohort (HR 2.97, 1.02-8.66, p=0.046). However, wide confidence intervals in these results necessitate evaluation in larger cohorts.

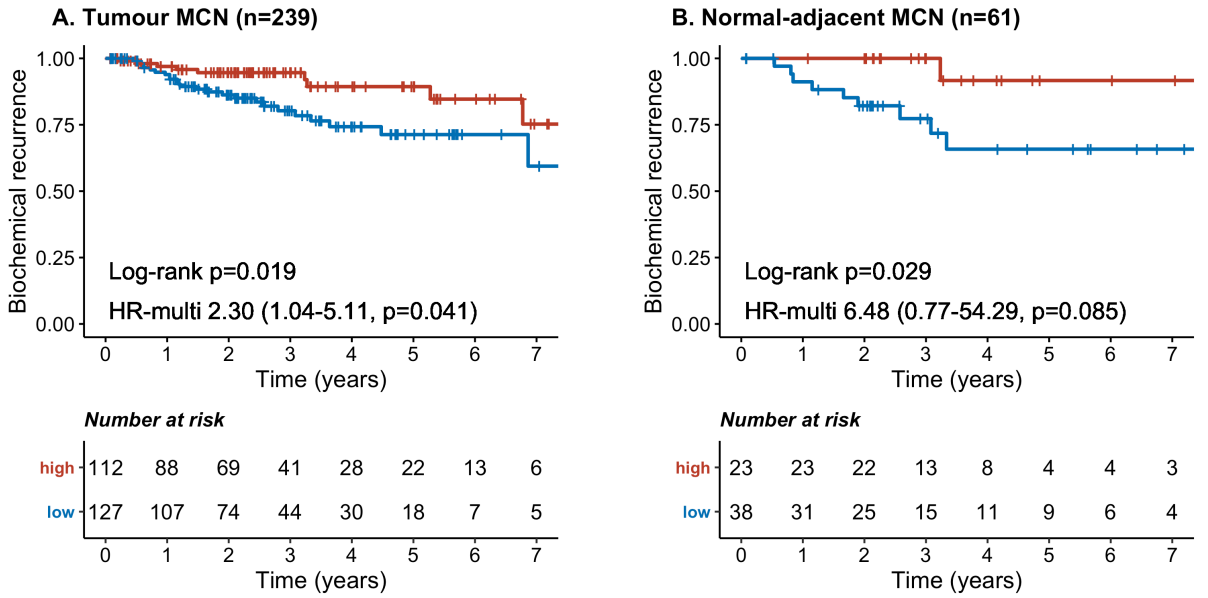

Figure 3-9: Impact of mitochondrial copy number on biochemical recurrence – TCGA-PRAD cohort. Mitochondrial copy number (MCN) data from **(A)** tumour tissue, and **(B)** normal-adjacent were obtained from 239 TCGA-PRAD patients without residual disease in the Reznik *et al.* (2016) dataset. Log rank test was used to determine *p*-values for unadjusted hazards estimation. Hazard ratios were estimated using a multivariate Cox regression model, adjusting for the following covariates: age, log-10 PSA at diagnosis, Gleason group, pathological tumour stage, metastasis stage and lymph node involvement.

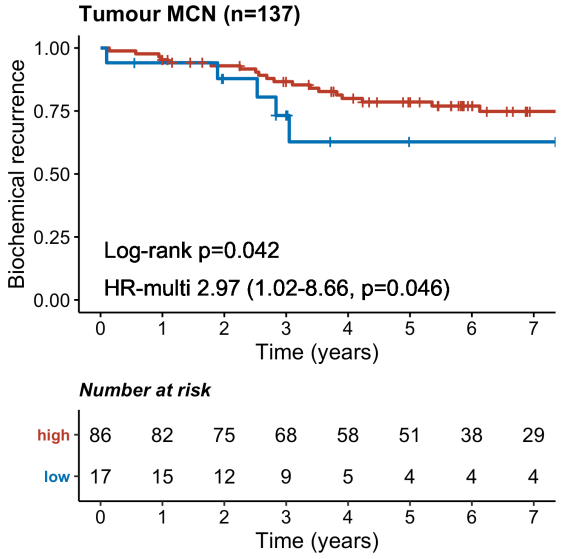

Figure 3-10: Impact of mitochondrial copy number on biochemical recurrence – TCMA-PRAD cohort. Mitochondrial copy number (MCN) data from tumour tissue obtained from 103 TMCA-PRAD patients in the Yuan *et al.* (2017) dataset (cut-off of 211.5). Log rank test was used to determine p-values for unadjusted hazards estimation. Hazard ratios were estimated using a multivariate Cox regression model, adjusting for the age, log-10 PSA at diagnosis, Gleason group, and clinical tumour stage. Note: Unlike **Figure 3-9**, data regarding lymph node involvement and metastasis stage were unavailable for the TCMA-PRAD cohort and were therefore not included in multivariate analyses.

3.3.4 CNA in nuclear-encoded OXPHOS genes

Tumour nuclear copy number burden is an independent prognostic factor in a number of cancers, including PCa (Hieronymus *et al.*, 2018). Since interactions between alterations in both mitochondrial and nuclear-encoded genes are likely to impact downstream mitochondrial function, copy number alterations (CNA) in nuclear-encoded OXPHOS genes was evaluated in the TCGA-PRAD cohort. Nuclear CNAs were determined using the Genomic Identification of Significant Targets in Cancer (GISTIC 2.0) segmentation algorithm (Mermel *et al.*, 2011). Copy number gain was defined as either +1 gain, or +2 amplification, whereas copy number loss was defined as either a homozygous (-2) or heterozygous (-1) loss. Nuclear copy number data were only available for tumour samples.

3.3.4.1 Frequency of CNA in OXPHOS genes

Amongst 492 patients with available data, 358 patients had at least one CNA (72.8%). In total, 5424 CNAs were identified, of which 2777 (52.2%) were deletions. CN gains were most frequently observed in *COX6C*, *UQCRB* and *NDUFB9* genes, in 32.1%, 31.9% and 30.5% of patients, respectively. CN loss was most frequently observed in *COX4I1*, *ATP5A1*, and *COX7A2* in 42.7%, 22.2% and 20.5% patients, respectively (**Figure 3-11A**). OXPHOS genes alterations were observed in known CNA hotspots in PCa (Hieronymus *et al.*, 2018), including 8q gain (*UQCRB*, *COX6C*, *NDUFB9*, *CYC1*) and 16p loss (*NDUFB10*, *UQCRC2*, *NDUFAB1*, *COX6A2*).

3.3.4.2 Association with clinical features of aggressive prostate cancer

OXPHOS copy number burden (CNB) was calculated for each patient as the absolute sum of all copy number alterations in nuclear-encoded OXPHOS genes. Median OXPHOS CNB across the cohort was 8.3%, which is greater than 6.2% global CNB previously reported in the TCG-PRAD cohort(Cancer Genome Atlas Research, 2015). OXPHOS CNB was directly correlated with patient age (Pearson's R 0.19, $p=3.4x10^{-5}$), PSA (Pearson's R 0.13, $p=3.4x10^{-3}$), Gleason group (2.4% in GG1-2 vs 15.5% in GG3-4, $p<2.2x10^{-16}$) and clinical tumour stage (6.0% in T1 vs 11.9% in T3-4, p=0.02; **Figure 3-11B**).

3.3.4.3 Impact of nuclear encoded OXPHOS genes on outcome

Though global CNB is an independent prognostic marker of poor PCa outcome (Hieronymus *et al.*, 2018), the impact of OXPHOS CNB or individual CNAs in nuclear-encoded OXPHOS subunits has previously not been specifically evaluated. Positive tumour margins were reported in 149 of 426 patients (35.0%), which were excluded due to the established associated increased risk of biochemical recurrence (Yossepowitch *et al.*, 2014; Preisser *et al.*,

2019b). Thus, 343 patients with nuclear CNA data and 239 patients with MCN data were suitable for survival analysis.

Copy number alterations (either as deletions or amplifications) in nuclear-encoded OXPHOS subunits were associated with increased risk of biochemical recurrence (**Figure 3-11C**). Upon adjustment for clinical covariates using Cox proportional hazards models, only *ATP5D* copy number gain (n=7 vs 448 patients, HR 37.7, 95% CI 6.2-172.8, $p=4 \times 10^{-5}$) and reduced mtDNA copy number (HR 2.4, 95% CI 1.2-5.3, p=0.034) were associated with increased risk of BCR. However, low frequency of ATP5D gain resulted in a wide confidence interval and would therefore require validation in external cohorts.

High CN burden, using a cut-off of 9.5%, was associated with increased risk of BCR on univariate analysis (log rank test, p=0.0028; Cox regression HR 2.37, 95% CI 1.32-4.24, p 0.0037). However, this was not significant once adjusted for clinical co-variates (Cox regression, HR 1.29, 95% CI 0.67-2.53, p=0.4).

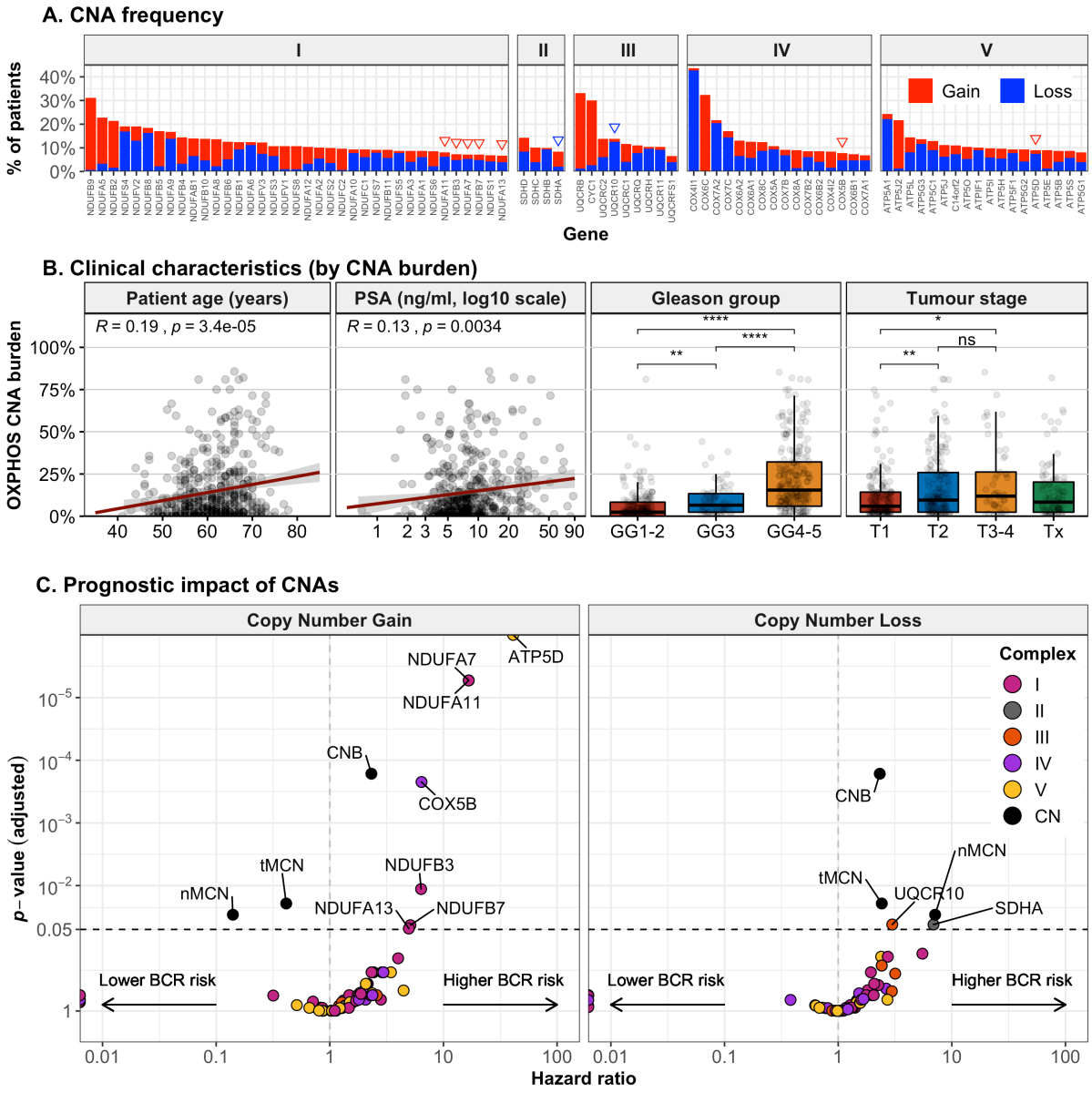

Figure 3-11: Copy number alterations (CNA) in nuclear-encoded OXPHOS genes in the TCGA-PRAD cohort. (A) Frequency of CNAs amongst nuclear-encoded genes, stratified by OXPHOS complex (n=492). Inverted triangles denote genes with copy number gain (red) or copy number loss (blue), which impact risk of biochemical recurrence (see panel C). **(B)** Association between tumour OXPHOS CNA burden (CNB) and clinical characteristics, including patient age at diagnosis, PSA group, Gleason group, and tumour stage (N=492 patients). Groups were compared using Wilcoxon rank test with p values denoted as *, **, ***, ****, representing p<0.05, p<0.01, p<0.001, p<0.0001, respectively. **(C)** Impact of copy number gain (left panel) and copy number loss (right panel) on risk of biochemical recurrence (BCR) was tested using log rank test (N=347 patients without positive tumour margins). Univariate hazard ratios and false discovery rate adjusted p-values are reported. Tumour MCN (tMCN) and normal-adjacent MCN (nMCN) from **Figure 3-9** (n= 239) and OXPHOS CNB results are included for comparison (black circles). Horizonal line denotes p=0.05.

3.3.5 Concluding remarks

Copy number burden in nuclear-encoded OXPHOS genes was associated with increased PCa risk features consistent with prior reports of global nuclear CNB in the TCGA-PRAD cohort. However, OXPHOS CNB was not associated with BCR risk. The above data also suggest that depletion of tumour MCN may correlate with aggressive PCa features and increased risk of BCR in the TCMA-PRAD cohort. However, these results could not be replicated in the TCGA-PRAD cohort.

The mechanisms underlying maintenance of mtDNA copy number and its criticality in cell survival remains poorly understood. Though discrepancies across datasets may be due to variations in bioinformatic pipelines, altered MCN is not sufficient evidence to conclude that mitochondrial respiration is downregulated in a tumour (Reznik *et al.*, 2016). Similarly, only modest correlation between MCN and mtDNA gene expression was observed in the TCMA-PRAD cohort and an anti-correlation in the TCGA-PRAD cohort, suggesting potential impact of other regulatory mechanisms, such as altered mtDNA transcription.

Furthermore, mtDNA depletion does not reliably result in alteration in mitochondrial protein abundance, suggestive of other mechanisms compensating for mtDNA depletion. Experimental methodologies modelling total or near total depletion of mtDNA copy number have demonstrated subtle or temporally delayed effect on mitochondrial function (Gammage and Frezza, 2019). This has been elucidated *in vivo* by unchanged protein expression in mtDNA-depleted urothelial bladder tumours (Reznik *et al.*, 2016), and *in vitro* in HeLa cells, which maintained mitochondrial transcription despite mtDNA depletion by ethidium bromide (Seidel-Rogol and Shadel, 2002).

These data underscore the complex interaction between MCN and downstream mRNA and protein level changes. Therefore, MCN cannot be reliable used as a proxy for respiratory activity in tumour tissue, and valuation of downstream alterations in mRNA or protein abundance may, instead, provide a more reliable method to infer mitochondrial function.

3.4 Results – Transcriptomic alterations

In light of the low frequency of mtDNA at high VAF and driver nucDNA OXPHOS mutations and inconsistent findings in MCN, the likely downstream transcriptomic mitochondrial alterations were next evaluated. Using an integrative pan-cancer DNA/RNA study design of 527 tumours, Stewart *et al.* (2015) reported high consistency in allelic ratios (R=0.91) across genes encoding OXPHOS subunits, despite the presence of frameshift and nonsense mutations. However, dramatically discordant allelic ratios were observed in the presence of tRNA gene mutations suggesting that tRNA mutations may have a functional impact on neighbouring coding genes. Together with similar findings from Yuan *et al.* (2017), these data suggest that even in the presence of mutations affecting mitochondrial-encoded OXPHOS subunits, there is no evidence for increased mRNA transcripts or mRNA surveillance mechanisms, such as nonsense mediated decay observed in the context of nuclear DNA mutations (Kurosaki and Maquat, 2016). However, nuclear genomic alterations may impact mitochondrial gene expression with potential downstream functional consequences (Ali *et al.*, 2019). Thus, as compared to MCN, mRNA abundance of mitochondrial encoded OXPHOS genes may more reliably reflect altered mitochondrial function.

3.4.1 Literature review

Large scale pan-cancer transcriptomic studies have suggested an association between OXPHOS gene expression and poor outcome. Using this approach on pan-cancer TCGA data, (Gaude and Frezza, 2016) evaluated nuclear-encoded OXHPOS gene expression, noting downregulation in 25% and upregulation in 35% of cancers across 20 tissue types. Low nuclear OXPHOS gene expression was found to be associated with enrichment of genes implicated in epithelial to mesenchymal (EMT) transition. The authors hypothesised that partial mitochondrial dysfunction may therefore be associated with increased metastatic potential of cancer cells. Notably, nuclear OXPHOS gene expression was upregulated in PCa tissue. However, prostate cancer cases excluded from survival analyses due to the low mortality rate in this cohort. A subsequent study focussing on TCGA-PRAD cases developed a classifier RNAseq data to divide patients into six metabolic groups with distinct biochemical relapse-free survival outcomes (Srihari *et al.*, 2018), which were reproduced in an independent dataset (Taylor *et al.*, 2010). The authors found patients with altered nuclear OXPHOS gene expression to be associated with poor outcome, and enriched for molecular alterations in *RB1*, *SPOP*, *STK11*, and *HOXB13* genes. However, most studies have relied on curated gene signatures

based on alterations in nuclear-encoded OXPHOS gene expression to evaluate mitochondrial function. Thus, the key contribution of mtDNA gene expression has been largely ignored.

Mitochondrial gene expression has recently been evaluated in TCGA cohorts (Reznik *et al.*, 2017; Yuan *et al.*, 2017). Yuan *et al.* (2017) found reduced mitochondrial gene expression to be associated with upregulation of DNA repair, *MYC* and cell cycle pathway scores. Reznik *et al.* (2017) reported a trend towards increased mitochondrial gene expression in PCa tumours, as compared to normal-adjacent controls, suggesting increased reliance on OXPHOS in cancerous prostate tissue. Five cancer types demonstrated an association between high mitochondrial gene expression and improved outcome. However, likely due to the low mortality rate in radically treated non-metastatic PCa, no association between mitochondrial gene expression and overall survival was observed.

3.4.2 Tumour vs normal

Gene expression data from TCGA-PRAD cases in Reznik *et al.* (2017) were linked with normalised nuclear-encoded OXPHOS gene expression data, MCN data from section 3.3.2 and associated clinical data to evaluate the association between transcriptomic OXPHOS alterations with aggressive PCa features and risk of biochemical recurrence. Amongst the 499 TCGA-PRAD patients, both nuclear and mitochondrial gene expression data were available for 426 patients. Correlation between mRNA and tumour mitochondrial copy number was only observed for *MT-CO2* (Spearman's ρ 0.19, FDR-adjusted p=0.029) and *MT-CO3* genes (Spearman's ρ 0.19, FDR-adjusted p=0.029), amongst 250 patients with available MCN data. Notably, *MT-CO2* gene expression has previously also been shown to also correlate with protein level expression in renal clear cell carcinoma (Reznik *et al.*, 2017).

RNA data were available for matched tumour and normal-adjacent samples from 47 patients. In total, 8 nuclear-encoded (*NDUFB4*, *NDUFS2*, *NDUFV2*, *SDHD*, *UQCRC2*, *COX4I1*, *ATP50*, *ATP5G2*) and 2 mitochondrial encoded genes (*MT-ND4L*, *MT-CO2*) were found to be altered between these tissue types (**Figure 3-12**). Mitochondrial genes more often tended to be upregulated in tumour tissue, as compared to nuclear-encoded genes (Kolmogorov-Smirnov test, p=1.2x10^{-5}). This may represent an upregulation of mitochondrial metabolism during carcinogenesis, or a compensation for reduced copy number, as observed in section 3.3.2.

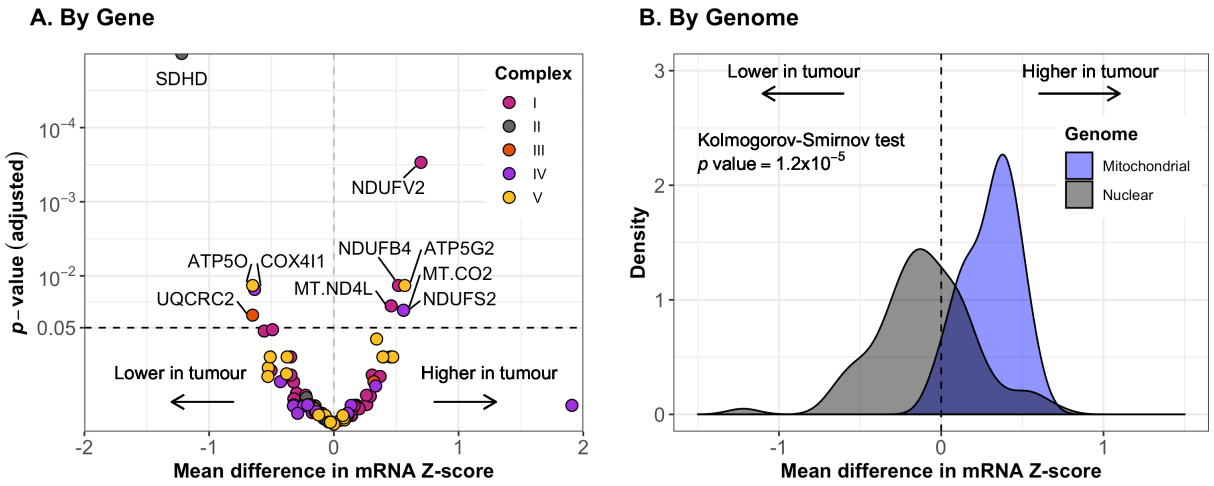

Figure 3-12: Transcriptomic alterations between tumour and normal-adjacent tissue samples. Abundance of nuclear and mitochondrial encoded OXPHOS mRNA transcripts across 47 paired tissue samples in the TCGA-PRAD cohort is reported. Mitochondrial OXPHOS data were obtained from Reznik *et al.* (2017). **(A)** Mean difference in mRNA abundance between tumour and normal-adjacent tissues stratified by OXPHOS complex is reported. The results of paired Wilcoxon rank test, with false discovery rate adjusted *p*-values reported on a logarithmic scale. **(B)** Mean difference in mRNA abundance between tumour and normal-adjacent tissues by genome. The result of Kolmogorov-Smirnov test used to compare variance between mitochondrial and nuclear genes is reported.

3.4.3 Clinicopathological features of PCa progression

Mitochondrial and nuclear gene expression were not correlated with either age or PSA.

MT-ND5 and *MT-ND6* abundance was significantly lower amongst patients with advanced Gleason group (GG1-2 vs GG3-4 - *MT-ND5*: Δ 0.331, p=9.7x10^{-4}; *MT-ND6*: Δ -0.294, p=1.9x10^{-3}) or pathological tumour stage disease (T2 vs T3-4 - *MT-ND5*: Δ 0.325, p=6.8x10^{-4}; *MT-ND6*: Δ -0.331, p=7.3x10^{-4}), in keeping with similar findings previously reported in TCGA lung cancer patients (Li *et al.*, 2018). The remaining 11 mitochondrial-encoded genes were not associated with either clinical feature.

Amongst nuclear genes, only *UQCRH* expression was associated with both higher tumour stage (T2 vs T3-4: Δ 0.359, p=1.4x10^{-4}) and higher Gleason group (GG1-2 vs GG3-4: Δ 0.402, p=3.4x10^{-5}). The following nuclear genes were also associated with higher tumour stage but not Gleason group: *COX6B2*, *COX6C*, *NDUFB4*, and *NDUFV1*. Notably, mitochondrial and nuclear genes had opposite associations with increased mitochondrial and decreased nuclear gene expression being more frequently associated with increased risk features (Kolmogorov-Smirnov test, tumour stage: p=3.6x10^{-8}; Gleason group: p=2.0x10^{-4}).

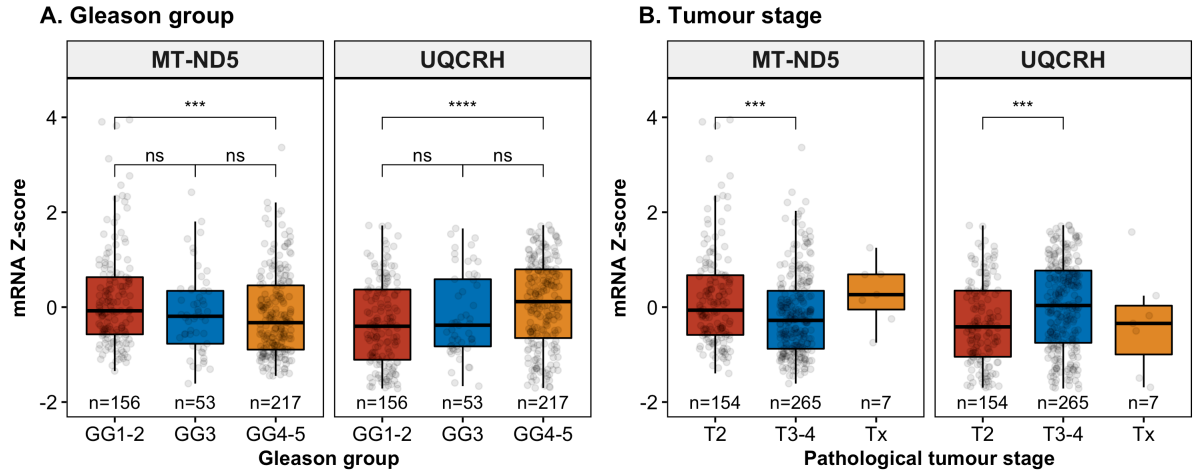

Figure 3-13: Mitochondrial and nuclear gene expression have opposite associations with features of aggressive prostate cancer. Representative examples of mitochondrial-encoded *MT-ND5* and nuclear-encoded *UQCRH* gene expression in TCGA-PRAD data for 426 patients stratified by **(A)** Gleason group, and **(B)** pathological tumour stage. mRNA abundance in each subgroup compared using the Wilcoxon rank sum test, with p values reported as ns, **, and ***, representing p>0.05, p<0.001, and p<0.0001 respectively.

3.4.4 Diverse patterns of mito-nuclear gene expression determine patient clusters

OXPHOS gene expression from PCa tumour tissue from the TCGA-PRAD cohort are shown in **Figure 3-14**, with associated clinical features. Four patient clusters (PC) were identified using unsupervised k-means clustering. These clusters were broadly based upon variations in abundance of mRNA abundance of mitochondrial genes (gene cluster 3, GC3, n=13 genes) and a subset of nuclear genes (GC2, n=55 genes). Mean mitochondrial gene expression was highest in PC1 and lowest in PC2, whereas mean nuclear gene expression was highest in PC3 and lowest in PC4.

Gene expression was tightly correlated amongst mtDNA genes, however poorly correlated with nuclear gene expression in both tumour tissue (**Figure 3-15**) and normal-adjacent prostate tissue (see Appendix A, **Figure A-2**). This is consistent with previous reports in benign prostate tissue using the Genotype-Tissue Expression (GTEx) cohort (Barshad *et al.*, 2018). Mitochondrial complex IV genes *MT-CO2* and *MT-CO3* were directly correlated with GC2 genes, whereas complex I genes *MT-ND5* and *MT-ND6* were inversely correlated. Genes in GC1 accounted for 29 of 84 (34.5%) nuclear genes and were poorly correlated with both mitochondrial (GC3) and nuclear (GC1) genes.

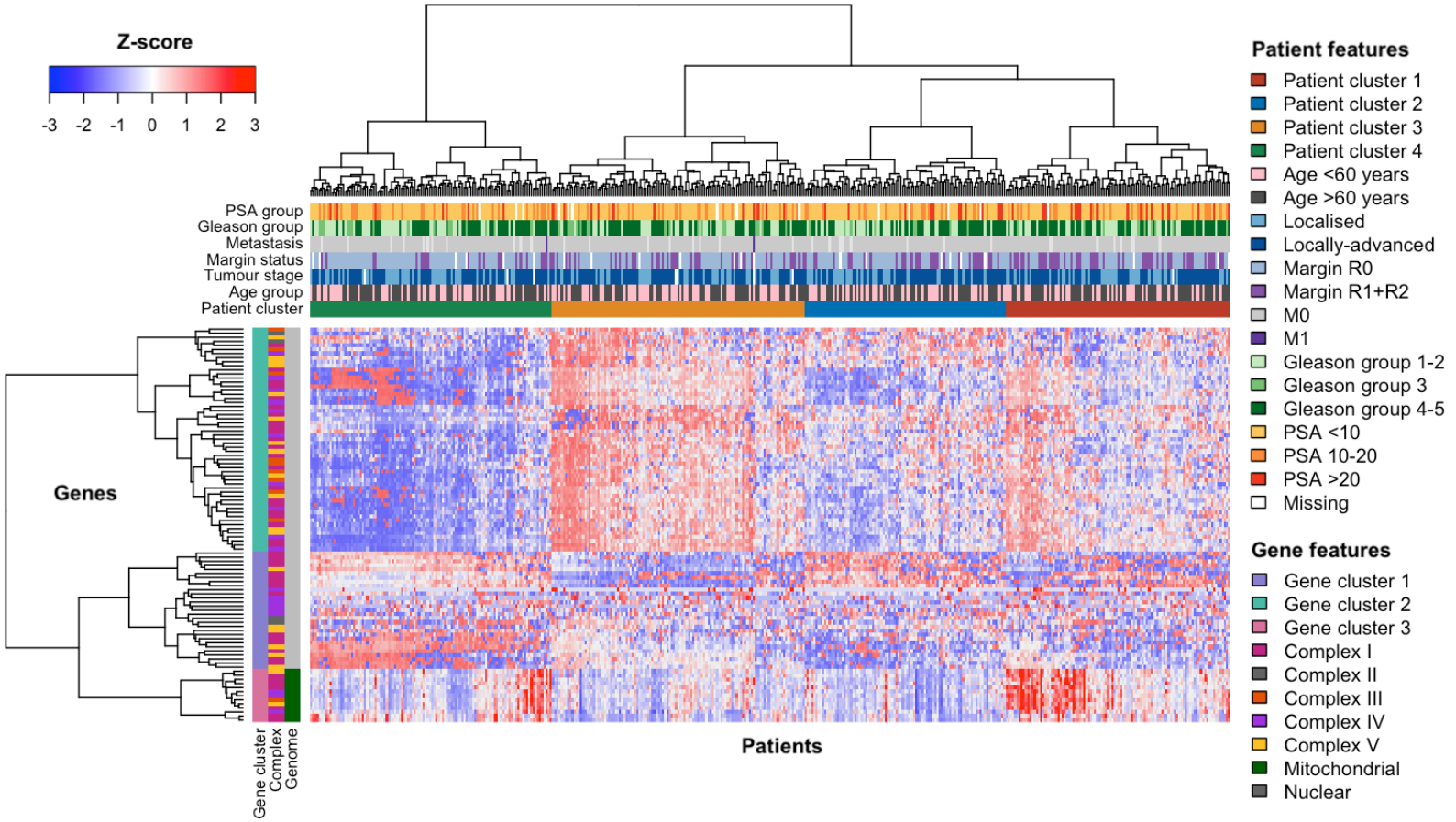

Figure 3-14: Transcriptomic OXPHOS gene alterations in the TCGA-PRAD cohort. The heatmap represents OXPHOS gene expression Z-scores for 426 patients in the TCGA-PRAD cohort, with individual patients along the x-axis (4 clusters) and genes along the y-axis (3 clusters). The heatmap represents OXPHOS gene expression data for 426 patients, with individual patients along the x-axis and genes along the y-axis. Clinical characteristics of patients are annotated. Localised and locally advanced tumour stage are defined as T1-T2, and T3-4, respectively. Dendrograms were generated by k-means clustering using the Ward.D2 method to calculate distances.

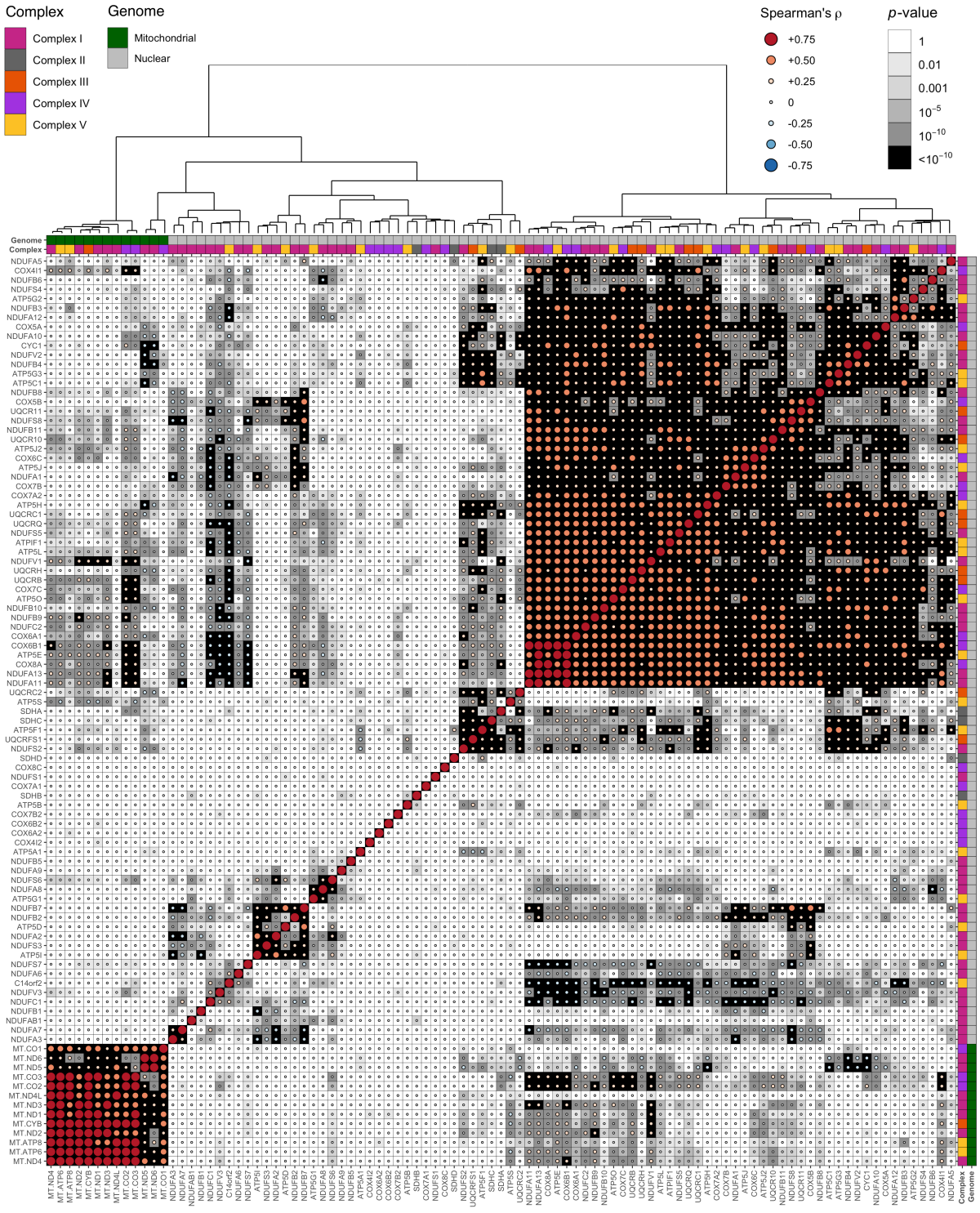

Figure 3-15: Relationship between gene expression of nuclear-encoded and mitochondrial-encoded OXPHOS subunits in TCGA-PRAD tumour samples. RNA data available for 474 samples – 426 tumours and 48 normal-adjacent samples from the TCGA-PRAD cohort. Spearman correlation were calculated between mRNA z-scores, with genes clustered using Euclidean distances calculated by the Ward.D2 method. FDR adjusted *p*-values are reported.

3.4.5 Impact of OXPHOS gene expression on progression free survival

Since positive tumour margins are an independent predictor of biochemical recurrence (Yossepowitch *et al.*, 2014; Preisser *et al.*, 2019b), 134 of 426 patients (30.5%) with positive tumour margins were excluded, resulting in data for 292 patients available for subsequent survival analysis.

Sixteen genes were found to impact risk of BCR using the univariate log rank test. This included 13 nuclear and three mitochondrial-encoded genes (*MT-ND5*, *MT-ND6*, *MT-CO1*). In comparison to nuclear genes, increased expression of mitochondrial genes tended to be associated with lower risk of BCR (Kolmogorov-Smimov test, p=0.002).

Upon multivariate Cox regression analysis, adjusting for age, PSA at diagnosis, Gleason group, pathological tumour stage, metastasis stage and lymph node involvement, only two genes (*NDUFA10* and *COX8C*) appeared to impact BCR-free survival, of which *COX8C* was an extreme outlier (**Figure 3-4**). Mitochondrial gene expression again tended to be associated with reduced risk of BCR, as compared to nuclear encoded genes (Kolmogorov-Smimov test, p=0.018). Meta-analysis of individual genes revealed that increased expression of nuclear genes (mean HR 1.59, $p=3.49\text{x}10^{-40}$) overall, and nuclear complex I (mean HR 1.44, $p=1.97\text{x}10^{-12}$) and IV (mean HR 1.50, $p=1.72\text{x}10^{-12}$) genes in particular, had the highest probability to adversely impact prognosis, whereas increased mitochondrial gene expression was more likely to be associated with lower BCR risk (mean HR 0.77, $p=2.47\text{x}10^{-4}$).

Gene	Complex	Log rank test			Multivariate Cox regression		
		HR (95% CI)	p	FDR	HR (95% CI)	p	FDR
MT-ND5	**I**	0.42 (0.20-0.91)	0.006	0.049	0.56 (0.29-1.09)	0.090	0.210
MT-ND6	I	0.44 (0.22-0.87)	0.006	0.049	0.54 (0.28-1.03)	0.060	0.180
MT-CO1	IV	0.37 (0.15-0.90)	0.002	0.023	0.42 (0.21-0.86)	0.018	0.114
NDUFA10	I	4.10 (1.83-9.20)	$9\text{x}10^{-7}$	$9\text{x}10^{-5}$	3.04 (1.60-5.77)	0.001	0.033
COX8C	IV	0.16 (0.07-0.40)	0.04	0.091	$1.5\text{x}10^{-6}$ ($1.6\text{x}10^{-7}$-$1.3\text{x}10^{-5}$)	$3\text{x}10^{-33}$	$3\text{x}10^{-31}$

Table 3-6: Impact of mRNA abundance of individual OXPHOS genes on BCR-risk. Z-scores for individual genes were categorised into low and high, using maximal rank statistics, amongst 292 TCGA-PRAD patients with available mRNA data and no residual disease. subjected to univariate analysis using log rank test, and multivariate Cox regression adjusting for patient age at diagnosis, log-10 transformed PSA at diagnosis, pathological Gleason group, pathological tumour stage and lymph node involvement. FDR adjusted p-values are reported.

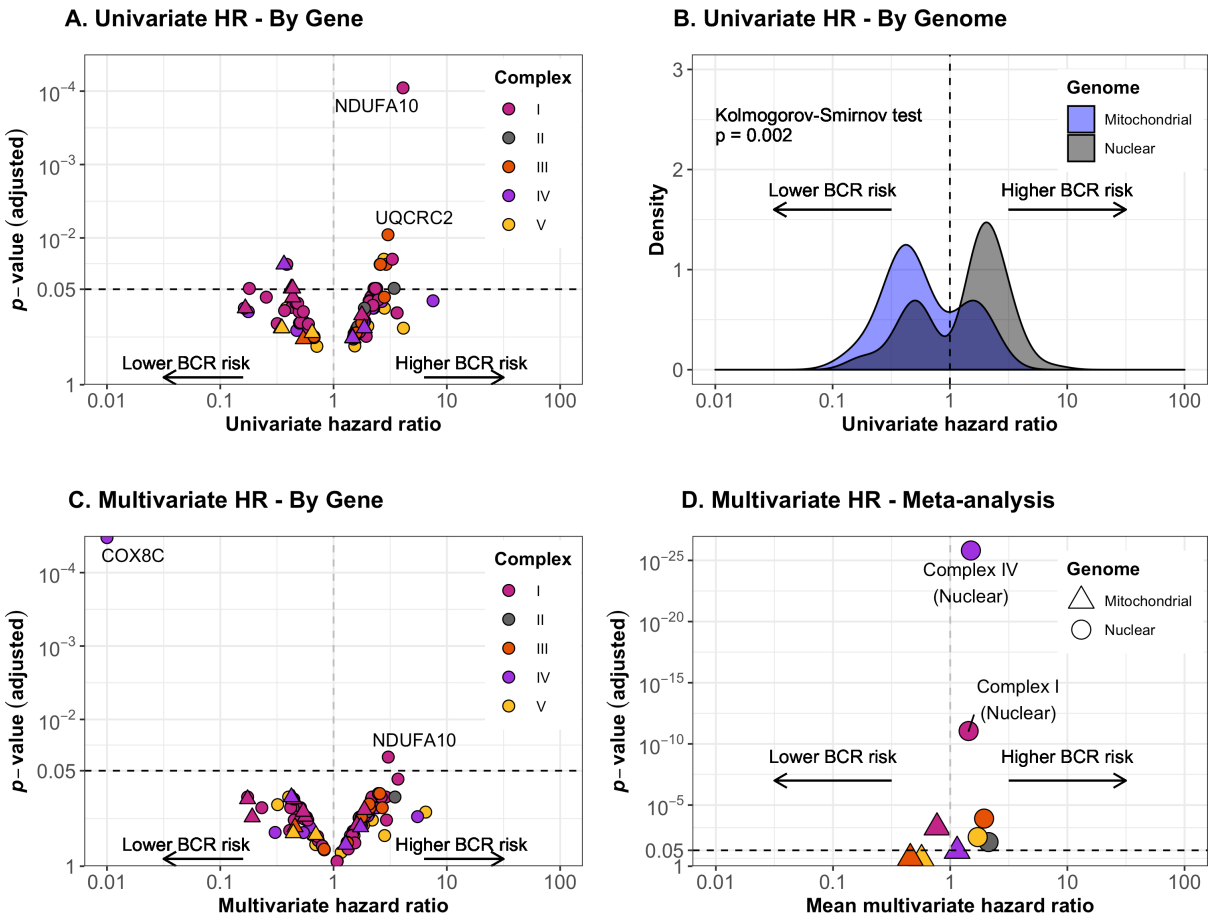

Figure 3-16: Prognostic potential of transcriptomic alterations in nuclear and mitochondrial-encoded OXPHOS genes. Z-scores for individual genes were categorised into low and high, using maximal rank statistics, amongst 292 TCGA-PRAD patients with available mRNA data and no residual disease. Time to biochemical recurrence was used as the outcome measure. Hazard ratios (HR) and associated false-discovery adjusted p-values are reported. **(A)** Volcano plot of univariate HRs of individual OXPHOS genes estimated using log rank test. **(B)** Distribution of HRs for mitochondrial and nuclear genes from panel A, compared using the Kolmogorov-Smirnov test. **(C)** Volcano plot of multivariate HRs estimated for categorised z-scores for individual genes using a Cox regression model, adjusting for patient age at diagnosis, log-10 transformed PSA at diagnosis, pathological Gleason group, pathological tumour stage and lymph node involvement. **(D)** Meta-analysis of prognostic potential of constituent genes stratified by complex and genome, using Fisher's method.

3.4.6 OXPHOS gene signatures predict risk of biochemical recurrence

Based upon the above data evaluating the prognostic potential of individual genes, I posited that upregulation of nuclear-encoded OXPHOS genes may be associated with poor outcome, whereas upregulation of mitochondrial-encoded OXPHOS genes may ameliorate risk of BCR. In order to simplify these results for ease of interpretation and clinical translation, OXPHOS gene expression scores were generated as the mean expression of nuclear genes ('*Nuclear OXPHOS score*') or mitochondrial genes ('*Mitochondrial OXPHOS score*'). OXPHOS scores were not correlated with MCN (for example, OXPHOS defect score: Spearman's ρ -0.03, FDR-adjusted *p*=0.7).

Gene signatures were dichotomised using maximal rank statistics into '*low*' and '*high*' score groups. At 5-year follow-up, the BCR-free rate in the included TCGA-PRAD cohort was 79.1% (95% CI 72.7-86.1%). Upon stratification by mitochondrial OXPHOS score, BCR-free survival rate was 100% and 77.1% in patients with low and high scores, respectively (**Figure 3-17**). However, these data did not reach statistical significance (log rank test, *p*=0.081). In contrast, patients with high nuclear OXPHOS scores were at increased risk of BCR (90% vs 76.3%, log rank test, *p*=0.036). Multivariate analysis suggested a non-significant trend towards increased risk of BCR in nuclear OXPHOS 'high' patients (HR 2.38, 95% CI 0.73-7.75, *p*=0.151).

Thus, neither nuclear nor mitochondrial OXPHOS scores alone were predictive of BCR upon multivariate analysis. Give than mitochondrial function depends on an interplay between both mitochondrial and nuclear-encoded OXPHOS genes (Couvillion *et al.*, 2016) and co-existing mito-nuclear molecular alterations have previously been identified in PCa (Hopkins *et al.*, 2017), categorical data from nuclear and mitochondrial OXPHOS scores were combined (referred to as '*OXPHOS status*'). In comparison to patients with high mitochondrial scores irrespective of nuclear OXPHOS status ('*mito-high'*), patients with high nuclear score and low mitochondrial score ('*nuc-high, mito-low'*) were found to be an increased risk of BCR (5-year BCR: 100% vs 74.2%, HR 4.82, 95% CI 0.03-1.65, p=0.0143).

Similarly, mito-nuclear OXPHOS scores were also combined as a continuous variable, by calculating the difference between the nuclear and mitochondrial OXPHOS scores (referred to as *'OXPHOS defect score*'), whereby discordance in scores would infer a defect in OXPHOS. Thus, high nuclear and low mitochondrial OXPHOS gene expression would contribute to a high OXPHOS defect score, which is hypothesised to be a surrogate marker for mitochondrial dysfunction and aggressive PCa features. In comparison to patients with low OXPHOS defect

scores, patients with high OXPHOS defect scores tended to have higher PSA, higher ISUP Gleason scores, higher pathological tumour stage (**Table 3-7**) and at increased risk of BCR, (5-year BCR: 82.7% vs 61.8%, HR 2.20, 95% CI 1.11-4.36, p=0.025).

These data support the hypothesis that the interplay between transcriptomic alterations in nuclear and mitochondrial OXPHOS genes may be predictive of BCR-free survival amongst PCa patients, rather than isolated alterations in either mitochondrial or nuclear gene expression.

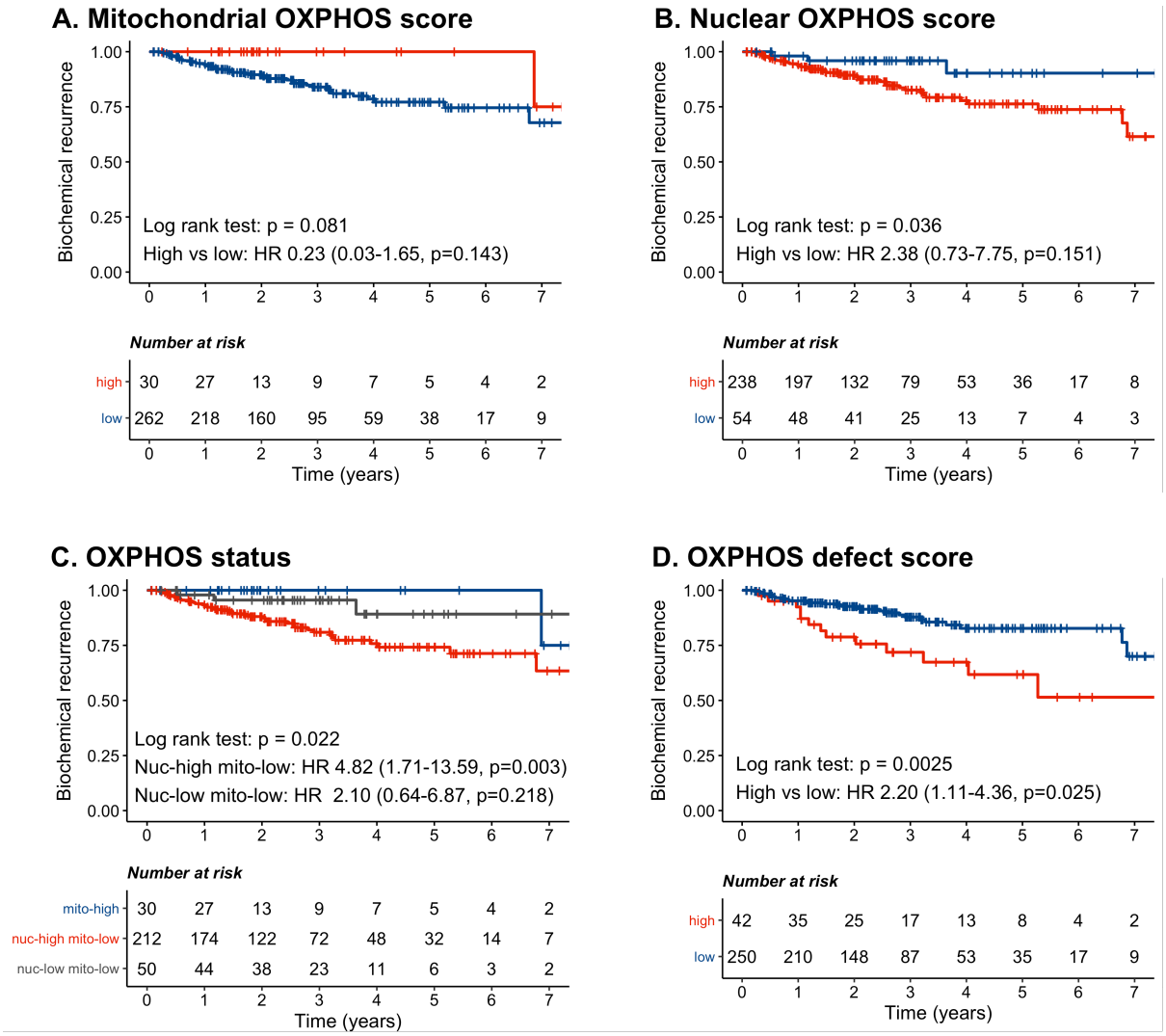

Figure 3-17: OXPHOS gene expression signatures predict risk of biochemical recurrence. TCGA-PRAD patients (n=292) were stratified into 'low' (blue) and 'high' (red) gene expression groups using **(A)** mitochondrial OXPHOS score, and **(B)** nuclear OXPHOS score. **(C)** OXPHOS status was determined by sub-stratifying patients with low mitochondrial OXPHOS scores by nuclear OXPHOS group. **(D)** OXPHOS defect score was calculated as the difference between nuclear and mitochondrial OXPHOS scores. Time to biochemical recurrence was used as the outcome measure. Log rank test was used to determine p values for unadjusted hazards estimation. Multivariate hazard ratios were estimated using Cox regression models, adjusting for the following covariates: age, log-10 PSA at diagnosis, pathological Gleason group, pathological tumour stage, metastasis stage and lymph node involvement.

By OXPHOS defect		High	Low	Overall	*p* value
Total patients		68 (16.0)	358 (84.0)	426	-
Patient age	Median (IQR)	59.5 (8.2)	62.0 (9.0)	62.0 (10.0)	0.12
Age group	≤ 50 years	5 (7.4)	28 (7.8)	33 (7.7)	0.232
	50-69 years	31 (45.6)	128 (35.8)	159 (37.3)	
	70-79	28 (41.2)	174 (48.6)	202 (47.4)	
	≥ 79 years	4 (5.9)	28 (7.8)	32 (7.5)	
PSA (ng/ml)	Median (IQR)	8.1 (8.8)	7.5 (6.4)	7.5 (6.6)	0.184
PSA group	0-9.9 ng/ml	39 (57.4)	237 (66.2)	276 (64.8)	0.036 *
	10-19.9 ng/ml	14 (20.6)	74 (20.7)	88 (20.7)	
	≥ 20 ng/ml	9 (13.2)	39 (10.9)	48 (11.3)	
	Missing	6 (8.8)	8 (2.2)	14 (3.3)	
ISUP Gleason group	GG1-GG2	15 (22.1)	141 (39.4)	156 (36.6)	0.021 *
	GG3	9 (13.2)	44 (12.3)	53 (12.4)	
	GG4-GG4	44 (64.7)	173 (48.3)	217 (50.9)	
Pathological tumour stage	T1-T2	13 (19.1)	141 (39.4)	154 (36.2)	0.006 *
	T3-T4	54 (79.4)	211 (58.9)	265 (62.2)	
	Missing	1 (1.5)	6 (1.7)	7 (1.6)	
Metastasis stage	M0	62 (100.0)	327 (99.4)	389 (99.5)	0.538
	M1	0 (0.0)	2 (0.6)	2 (0.5)	
Lymph node involvement (%)	N0	44 (64.7)	252 (70.4)	296 (69.5)	0.112
	N1	17 (25.0)	54 (15.1)	71 (16.7)	
	Nx	7 (10.3)	52 (14.5)	59 (13.8)	
Margin status (%)	R0	36 (52.9)	234 (65.4)	270 (63.4)	0.097
	R1+R2	26 (38.2)	108 (30.2)	134 (31.5)	
	Missing	6 (8.8)	16 (4.5)	22 (5.2)	

Table 3-7: Clinical characteristics of TCGA-PRAD cohort stratified by OXPHOS defect category. Patients categorised as 'high' and 'low' OXPHOS defects were compared using generalised linear models with univariate p-values reported. Asterisk denotes variables with $p<0.05$.

These data are consistent with findings by Reznik *et al.* (2017), who reported poorer overall survival with reduced mtRNA expression in several cancers, including adrenocortical carcinomas, low grade gliomas, and chromophobe renal cell carcinomas. Similarly, upregulation of nuclear-encoded OXPHOS genes has previously been associated with high Gleason grade PCa tumours in a nested control study amongst men enrolled on the US Health Professionals Follow-up Study (HPFS) or Physicians' Health Study (Kelly *et al.*, 2016). However, results should be interpreted with caution due to (a) risk of over-fitting due to the use of six co-variates; (b) risk of false discovery associated with multiple testing; and (c) the lack of an independent validation set. Furthermore, results may be adversely affected by the low proportion of patients with metastatic disease in the TCGA-PRAD cohort. If relevant clinical data were available for a future validation set, multivariate analyses across validation cohorts should include potential covariates including age, PSA at diagnosis, Gleason grade group, tumour stage and lymph node involvement.

3.4.7 OXPHOS defect scores correlate with molecular features of PCa

As observed in other cancers (Haider *et al.*, 2016), the pathophysiological impact of transcriptomic OXPHOS alterations is likely to vary by other established molecular features of PCa. Thus, OXPHOS defect scores were evaluated in frequently altered molecular subgroups of PCa, using the Wilcoxon rank test, and adjusted for multiple testing (**Figure 3-18**).

Increased OXPHOS defects scores were associated with *TMPRSS2:ERG* fusion status (Δ 0.249, p=9.0x10^{-4}), copy number loss in *PTEN* (Δ 0.346, p=1.6x10^{-3}), *ERG* (Δ -0.339, p=7.6x10^{-3}) and *KLLN* (Δ 0.316, p=9.9x10^{-3}), and reduced androgen receptor mRNA abundance (Spearman's ρ -0.13, p=0.027). OXPHOS defects enriched for *PTEN* mutation, however this did not reach statistical significance upon adjustment for multiple testing (p=0.0233, FDR-adjusted p=0.187). Notably, patients with *PTEN*-loss and *TMPRSS2:ERG* fusion (n=54) had higher OXPHOS defect scores (Δ 0.474, p=4.3x10^{-5}), compared to patients with *PTEN*-proficient *ERG*-negative disease (n=227). A consistent trend of reduced mRNA abundance was observed in *PTEN*-loss and *TMPRSS2:ERG* fusion PCa across individual mitochondrial OXPHOS genes, except *MT-CO1* (p=0.2).

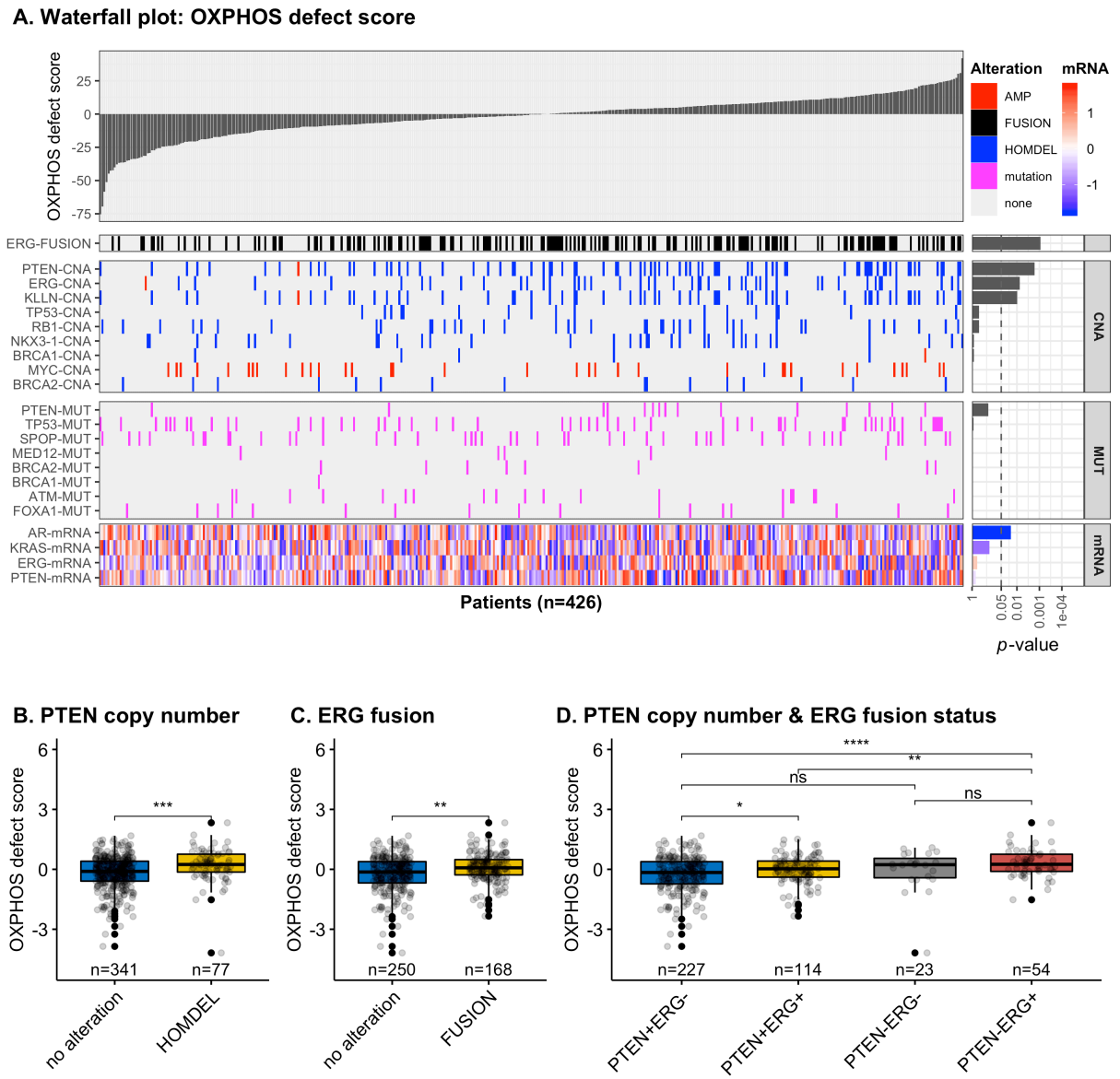

Figure 3-18: Association between OXPHOS defect score and molecular alterations in the TCGA-PRAD cohort. (A) Patients from the TCGA-PRAD cohort (n=426) are arranged in order of increasing OXPHOS defect score from left to right (top panel). *TMPRSS2:ERG*-fusion status, copy number alterations, mutation status and mRNA abundance of frequently altered genes in PCa is reported (bottom panel), with false-discovery rate adjusted *p*-values (right panel). **(B-D)** Association between OXPHOS defect score and *PTEN-ERG* status (n=418 patients). OXPHOS defect scores in each subgroup compared using the Wilcoxon rank sum test, with unadjusted *p*-values reported as ns, **, and ***, representing p>0.05, p<0.001, and p<0.0001 respectively.

3.4.8 OXPHOS defect scores correlate with pathways implicated in PCa progression

Similarly, the association between OXPHOS defects scores and a variant of gene expression signatures were calculated using Pearson's correlation coefficient and adjusting for multiple testing (**Figure 3-19**). The topmost upregulated scores included the *MYC* signature (Pearson's r=0.38, p=3.87x10^{-14}) and hypoxia signatures (for example, Buffa *et al.* (2010) signature: Pearson's r=0.32, p=9.82x10^{-10}). These data are consistent with previous reports from the Toronto group, who recently described an association between *MYC* (Hopkins *et al.*, 2017) and hypoxia signatures (Bhandari *et al.*, 2019a) with mtDNA mutations in PCa. Similarly, upregulated cell cycle proliferation scores (including Ki67 and CCP scores) and DNA repair signature are in keeping with previous reports by Lindberg *et al.* (2013). Similarly, other upregulated tumourigenic signatures included *Yap1* (Kuser-Abali *et al.*, 2015) and *Ras* signatures, which have also been implicated in PCa progression. As expected, multiple metabolic signatures were upregulated, including TCA cycle, pentose phosphate pathway, fatty acid, amino acid, and nucleotide metabolism. Notably, the KEGG glycolysis signature was also directly correlated with OXPHOS defect scores (Pearson's r=0.25, p=1.91x10^{-7}), in keeping with the Warburg effect (Warburg, 1956).

Downregulated signatures were primarily enriched in immune cell signatures, consistent with emerging data implicating mitochondrial dysfunction with altered immune cell function (Angajala *et al.*, 2018), suggesting that mitochondrial dysfunction may contribute to a pro-tumourigenic microenvironment. An inverse relationship with *Wnt* signatures was also observed (Pearson's r=-0.23, p=1.02x10^{-5}), supporting a recent hypothesis whereby mitochondrial dysfunction may impair *Wnt* activity, mediated by reduced mitochondrial calcium uptake and consequent endoplasmic reticulum stress (Costa *et al.*, 2019). However, in contrast to a previous pan-cancer study by Gaude and Frezza (2016), OXPHOS defect scores were anti-correlated with EMT signatures (Pearson's r=0.22, p=9.73x10^{-5}) and EMT genes including *ZEB1* and vimentin. Two potential reasons could account for this finding. Firstly, Gaude and Frezza (2016) calculated their OXPHOS signature exclusively using nuclear-encoded OXPHOS genes, whereas the OXPHOS defect scores is calculated as the difference between nuclear and mitochondrial OXPHOS gene expression scores. Secondly, since expression of EMT genes varies by age (Jedroszka *et al.*, 2017), the interaction between age and altered mitochondrial gene expression may also impact an association with OXPHOS defect scores.

Thus, OXPHOS defects may be associated with a diverse range of metabolic, immunological, and pathway alterations, which may potentially impact PCa progression. Validation of these findings in an independent dataset and use of more sophisticated bioinformatics methodology would be beneficial to minimise the risk of false positives.

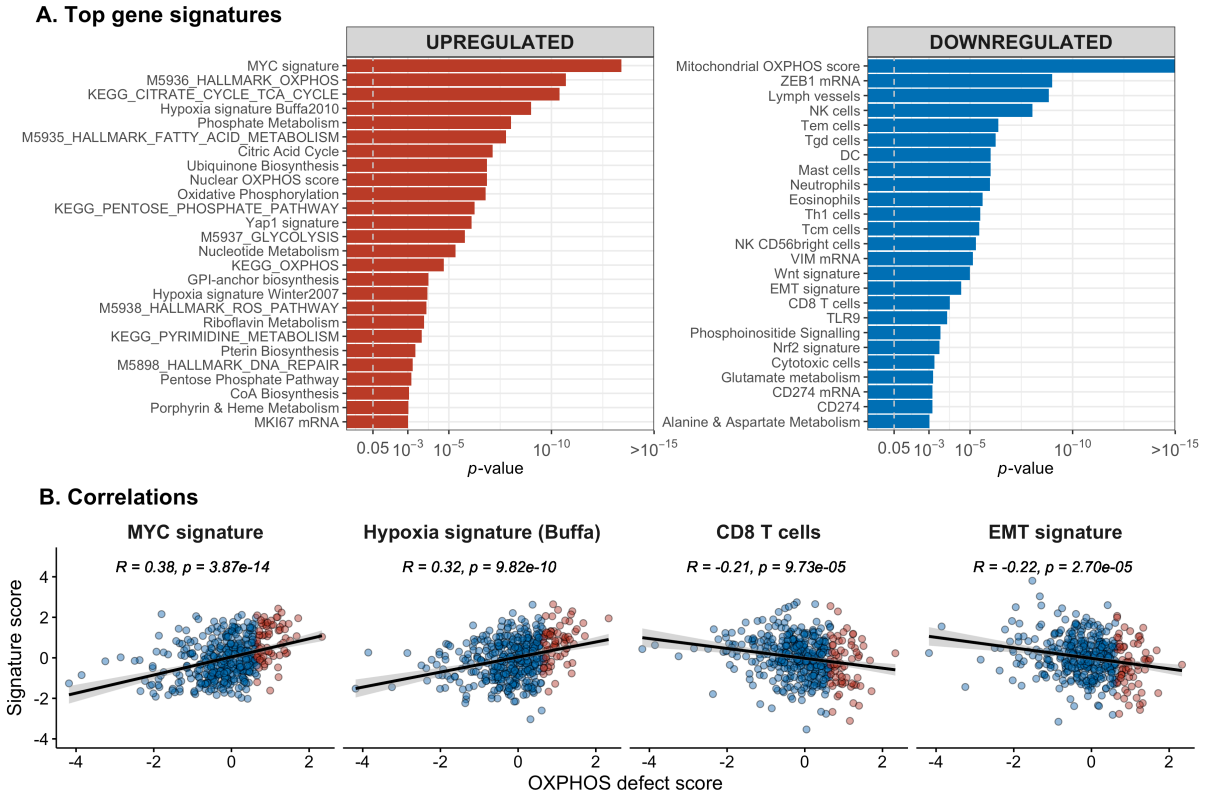

Figure 3-19: Correlation between OXPHOS defect score and gene expression signatures in the TCGA-PRAD cohort. Signatures from the MSigDB database, Chen *et al.* (2018) and Bhandari *et al.* (2019a) were tested using Pearson's product moment correlation coefficient. Signatures with false discovery rate adjusted *p*-values greater than 0.0001 are reported. Buffa signature calculated using gene set from Buffa *et al.* (2010). *MYC*, CD8 T cells and EMT signature data extracted from Chen *et al.* (2018).

3.4.9 Concluding remarks

Upregulation of mitochondrial encoded OXPHOS genes in PCa tumours suggests dependence on oxidative metabolism, consistent with the bioenergetic theory and resultant mixed Warburg effect unique to early prostate cancer (Costello and Franklin, 2006). In keeping with this finding and the observed discordant mito-nuclear gene expression, reduced mitochondrial and increased nuclear gene expression were associated with unfavourable clinicopathological features and progression to aggressive PCa. Leveraging this finding, an OXPHOS defect score was generated as the difference between mean expression of nuclear and mitochondrial genes. High OXPHOS defect score was associated with clinical PCa risk features, and molecular features including *PTEN* loss, *TMPRSS2:ERG* fusion, *MYC* signalling, and hypoxia signatures. Despite adjusting for clinical risk features using multivariate analysis, OXPHOS defect scores predicted increased risk of biochemical recurrence.

3.5 Conclusion

3.5.1 Summary of findings

mtDNA mutations across the mitochondrial genome and appear to be regulated by clonal selection pressures. Large scale sequencing studies have identified an association between patterns of mtDNA mutations with nuclear genomic alterations and risk of biochemical recurrence. However, these data are limited by the low mutational frequency and additional downstream alterations in transcription, translation and epigenetic modifications, which may impact eventual mitochondrial function. Together with the reported widespread transcriptomic alterations observed in the presence of MT-tRNA mutations, it is estimated that the true burden of mitochondrial dysfunction may be greater than that predicted by mtDNA mutations alone.

Furthermore, interpretation of mtDNA mutational data is complicated by the polyploid nature of the mitochondrial genome. However, mitochondrial copy number (MCN) does not reliably correlate with either mutational burden or mitochondrial gene expression, with mechanisms regulating MCN still poorly understood. Despite inconsistent association with clinicopathological risk features, reduced MCN appears to be associated with increased BCR risk across two cohorts.

Given that complexes of the electron transport chain are formed of subunits encoded by both nuclear and mitochondrial-encoded genes, the interplay between the two genomes is likely to have a greater impact on disease progression. Indeed, discordance in mito-nuclear gene expression, determined using a curated OXPHOS defect signature, was found to be associated with PCa risk features and independently predicted risk of biochemical recurrence. This signature also enriched for molecular subgroups of prostate cancer and highlights associated tumourigenic features such as ROS signalling, DNA repair pathways and hypoxia, which may help elucidate the nature of a hypothesised link between mitochondrial dysfunction and poor PCa outcome.

3.5.2 Next steps

Genes encoding core subunits of OXPHOS complex I and IV were frequently encountered as either sites of recurrent mutations, or altered expression in PCa tumours, associated with clinicopathological features and outcome. It would thus be beneficial to assay alterations in OXPHOS complexes in independent cohorts to validate these findings.

However, studies thus far have employed bulk nucleic acid sequencing approaches to a single tumour focus from each with and have thus not been able to capture intra-patient tumour heterogeneity in mitochondrial molecular alterations. Though the increasing use of innovative single cell sequencing approaches has helped unpick the mutational and transcriptional heterogeneity in prostate cancer (Horning *et al.*, 2018), the reliance on historically archived tissue samples and associated limitations in extracting high quality nucleic acids have limited the application of this technology in evaluating impact on long-term survival outcomes. Current prohibitive costs of such approaches also limit feasible samples sizes for single cell level experimental designs.

The curated mRNA OXPHOS defect signature devised in this chapter was associated with clinicopathological features of aggressive disease and increased BCR risk. It is important to note that most studies in this area have similarly exclusively used biochemical recurrence as their primary survival endpoint, amongst a cohort of primarily radically treated patients with PCa (Cancer Genome Atlas Research, 2015; Hopkins *et al.*, 2017; Yuan *et al.*, 2017). These findings thus require validation in independent cohorts with adequately long follow-up for all-cause mortality. However, due to the latency of prostate cancer mortality in low/intermediate risk PCa, retrospective biomarker studies require adequate preservation of RNA from archived tissue biobanks. Routine clinical protocols involving formalin-fixation and embedding in paraffin (FFPE) for preservation of tissue architecture are associated with harsh conditions which cause nucleic acid degradation (Groelz *et al.*, 2018), resulting in significant challenges in extracting high quality RNA for next generation sequencing studies. Furthermore, post-transcriptional modification resulting in uneven steady-state mRNA abundance (Rorbach and Minczuk, 2012) may also pose considerable challenges in accurately inferring protein level defects associated with mitochondrial dysfunction (Latonen *et al.*, 2018). Since mitochondrial epitopes are well preserved in FFPE tissue, validation of the pathogenicity of these molecular alterations at the protein amongst treatment naïve patients with long follow-up using cost-effective high throughput assays may therefore help dissect the link between the observed molecular alterations in tumour evolution and overall survival more precisely.

Chapter 4 Development of an automated high-throughput quantitative immunofluorescence assay to evaluate OXPHOS protein defects in human prostate tissue

4.1 Introduction

4.1.1 Current methods for quantifying OXPHOS defects in human tissue samples

Age-related mitochondrial DNA (mtDNA) mutations lead to defects in the electron transport chain, which is the site of oxidative phosphorylation (OXPHOS). Consequently, activity of complex I and IV decreases with advancing age in mammalian heart, brain, liver and kidney tissue (Lenaz *et al.*, 1997; Müller-Höcker *et al.*, 1997), however, intriguingly, activity of complexes II, III, and V remain largely unchanged (Navarro and Boveris, 2007; Bratic and Larsson, 2013).

Until recently, *in situ* assessment of mitochondrial OXPHOS defects in intact tissue sections was limited to the use of sequential cytochrome c-oxidase and succinate dehydrogenase (COX/SDH) enzyme histochemistry (reviewed further in section 6.2.5). This method measures the activity of cytochrome c oxidase (COX), which forms complex IV of the electron transport chain. COX catalyses the oxidation of 3,3'-diaminobenzidine (DAB). MtDNA mutations may lead to defects in core subunits of Complex IV (*COX1*, *COX2*, and *COX3*) which form its catalytic site, leading to defects in assembly, stability and loss of enzymatic function of Complex IV. Consequently, COX deficient cells appear DAB negative on COX histochemistry (ie loss of brown colour). These cells are counterstained by the activity of succinate dehydrogenase (SDH), nuclear-encoded complex II, in blue. Cells with complex IV loss are therefore stained blue.

Interpretation of tissue sections using the sequential COX-SDH assay remains subjective (Rocha *et al.*, 2015), specific cell types cannot be reliably identified based on cell morphology alone, and the requirement of frozen samples precludes the assessment of archival clinical samples. Age-related mtDNA mutations and associated complex I defects are also reported in intestinal tissue (Taylor *et al.*, 2003; Greaves *et al.*, 2010). However, there remains a paucity of reliable *in situ* assays for the detection of Complex I defects.

4.1.2 Quadruple immunofluorescence assay for quantification of OXPHOS defects

Rocha *et al.* (2015) recently described a quantitative immunofluorescence-based method for the simultaneous quantification of frequency and degree of defects in Complex I and Complex IV in frozen muscle biopsies. This method was validated in a cohort of patients with well characterised mitochondrial disorders and has since been successfully employed to diagnose mitochondrial disorders (Ahmed *et al.*, 2017b).

Since this assay was primarily designed for the study of large muscle fibres, its use in the study of cells with high nuclear-cytoplasmic ratio is complicated by autofluorescence and reliance on confocal microscopy (Dobson *et al.*, 2016). The absence of a nuclear marker also precludes the ability to employ automated cell segmentation algorithms. These issues contribute to high cost and low throughput of this assay.

4.1.3 Automated staining platforms

Improved throughput of clinical samples may be achieved through automation. Automated staining platforms are routinely used in clinical histopathology laboratories as they offer good reproducibility through standardisation of immunohistochemical assays with minimal human input (Biesterfeld *et al.*, 2003). A comparison of manual and automated staining methods in described in **Table 4-1**.

	Manual staining	Automated staining
Time and labour	Intensive	Minimal
Flexibility	Infinite, with option to combine reagents from multiple vendors	Limited by “closed” platforms, restricted to use of reagents manufactured by vendor
Alert systems	Minimal	Reagent stocks, temperature errors, barcode tracking
Training	Knowledge of science and theory of IHC required	Minimal running knowledge and skill required, except for troubleshooting
Maintenance	Minimal	Regular vendor maintenance and service required
Reagent costs	Variable	Often restricted to reagents manufactured by vendor, leading to high running costs

Table 4-1: Comparison of manual and automated staining methods. Adapted from Prichard (2014).

4.1.4 Quantitative Immunofluorescence

Immunofluorescence enables the relative quantification of targets in accordance with the Beer-Lambert law which states that the absorption spectrum of a synthetic dye is linearly dependant on the concentration of the target. This may be represented using the following equation:

$$A(\lambda) = \sum_i \varepsilon_i(\lambda) \bullet C_i \bullet L_i$$

where, '*A*' is the absorbance, ε is the molar absorption coefficient, and '*C*' is concentration of the dye species *i*. '*L*' is optical path length of the specimen (in μm). Since the optical path length and molar absorption coefficient are kept constant, the absorbance of the dye provides a relative measure of the concentration of the target.

4.1.5 Multiplex immunofluorescence

Multiple targets can be simultaneously probed using either 'simultaneous' or 'sequential' methods, with regards to the application of antibodies, or the assessment of fluorescence intensity (Dixon *et al.*, 2015).

4.1.5.1 Simultaneous multiplex immunofluorescence

Using a simultaneous approach, a combination of antibodies can be applied to the tissue section at the same time. This can be done using either fluorophore conjugated primary antibodies (direct immunofluorescence) or primary antibodies differing in isotypes or raised in different animals, with subsequent application of isotype-specific or host-specific fluorophore-conjugated secondary antibodies (indirect immunofluorescence). For low-abundance targets, fluorescence signal can be enhanced by leveraging the avidin-biotin system in an indirect immunofluorescence approach, whereby a streptavidin-conjugated secondary antibody binds to a tertiary linker conjugated to both streptavidin and a fluorophore. The use of these methods for multiplexing is, however, limited by (a) availability of antibodies with unique isotypes or raised in different animal species, (b) cross-reactivity between multiple antibodies, and (c) spectral overlap when using multiple fluorophores (**Figure 4-1**).

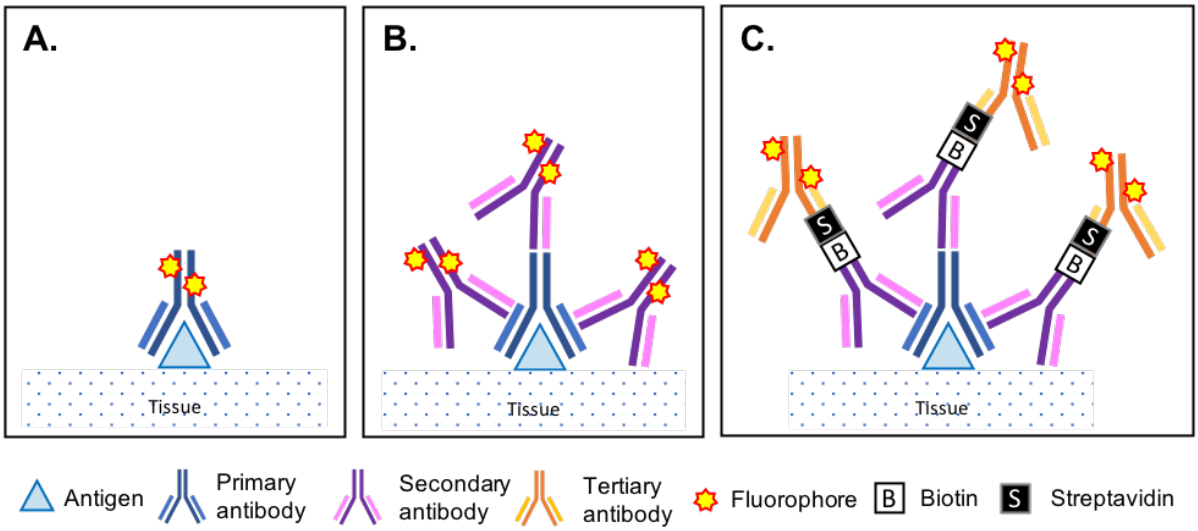

Figure 4-1: Direct and indirect immunofluorescence. **(A)** Direct immunofluorescence: fluorophore-conjugated primary antibody binds to the target antigen epitope. **(B)** Indirect immunofluorescence: an unconjugated primary antibody binds to the target antigen epitope, and a fluorophore-conjugated secondary antibody linked with a reporter directed against the host animal in which the primary antibody was raised. **(C)** Biotin-conjugated secondary antibodies are bound to a streptavidin conjugated tertiary linker conjugated to a fluorophore.

4.1.5.2 Sequential multiplex immunofluorescence

Sequential multiplexing involves multiple cycles of antibody staining, interspersed by a heat-mediated denaturation step to remove residual antibody-HRP complexes, which avoids cross-reaction with HRP-conjugated secondary antibodies in subsequent staining cycles. However, fluorescent signal intensity from conventional Alexa Fluor secondary fluorophores is diminished upon heat treatment, limiting their use in sequential multiplexing protocols (Toth and Mezey, 2007).

This limitation may be overcome by the use of tyramide signal amplification (TSA). The TSA method is based upon Catalysed Reporter Deposition (CARD) where, in the presence of hydrogen peroxide, oxidation of a fluorophore-labelled or chromogen-labelled tyramide substrate by horse-radish peroxidase leads to deposition of the label (**Figure 4-2**). The TSA-fluorophore complex is highly stable and insoluble in water, due to which fluorescence binding, and thereby signal intensity, is not influenced by heat-mediated denaturation (Toth and Mezey, 2007). Furthermore, TSA is particularly well suited to sequential multiplexing since it (a) offers increased signal to noise ratio compared to Alexa Fluor fluorophores, significantly improving sensitivity for targets at low abundance (Van Heusden *et al.*, 1997; Clutter *et al.*, 2010), (b) often requires lower primary antibody concentration (Hunyady *et al.*, 1996), thereby reducing cost, and also (c) helps overcome the requirement for use of combinations of antibodies raised in different species or unique isotypes (Toth and Mezey, 2007).

Detection of targets with very low abundance can be further enhanced by including an additional hapten-based amplification step (Nitta *et al.*, 2013). Binding of multiple moieties of HRP-conjugated polymer with each species-specific hapten 3-hydroxy-2-quinoxaline (HQ)-conjugated polymer moiety bound to the primary antibody provides an additional level of signal amplification (**Figure 4-3**).

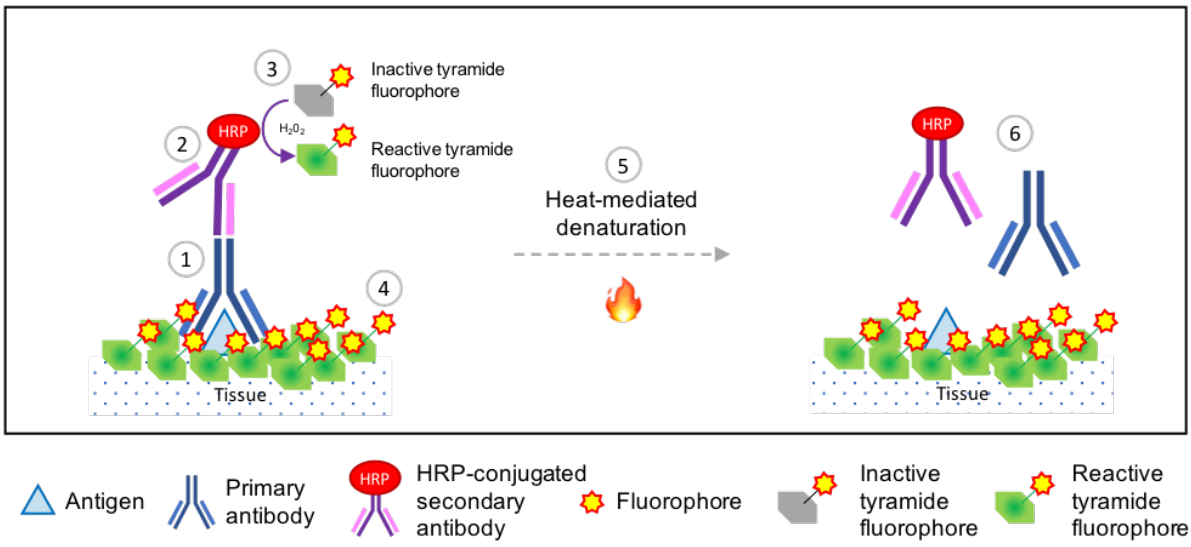

Figure 4-2: Tyramide signal amplification. **(1)** Primary antibody binds to the target antigen epitope. **(2)** A species-specific HRP polymer is then bound to the primary antibody. **(3)** In the presence of hydrogen peroxide, HRP catalyses the activation of the tyramide fluorophore, which is **(4)** deposited at the site of antigen detection. **(5)** Heat-mediated denaturation leads to the degradation of the antibody-HRP complex without affecting fluorophore signal intensity.

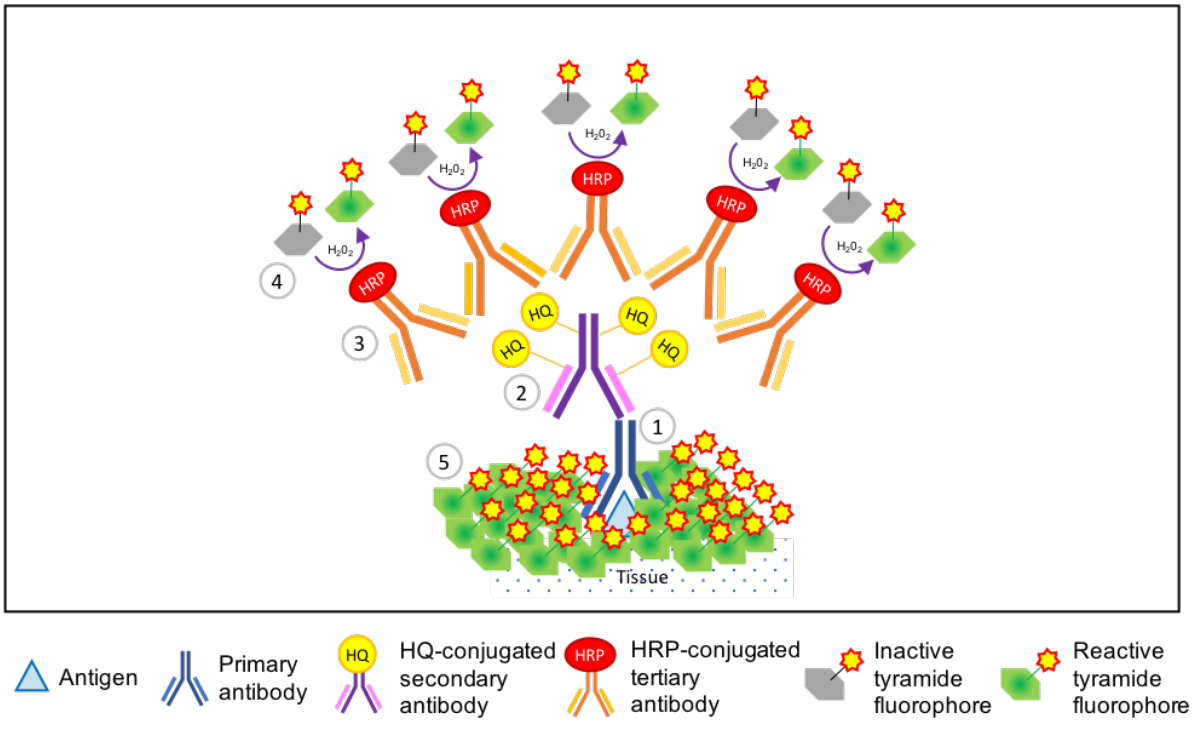

Figure 4-3: Hapten-based tyramide signal amplification. **(1)** Primary antibody binds to the target antigen epitope. **(2)** A species-specific Hapten 3-hydroxy-2-quinoxaline (HQ)-conjugated polymer is then bound to the primary antibody. **(3)** The HQ polymer is bound to anti-HQ HRP polymer. **(4)** HRP catalyses the activation of the tyramide fluorophore, which is **(5)** deposited at the site of antigen detection. **(6)** Heat-mediated denaturation leads to the degradation of the antibody-HQ-HRP complex without affecting fluorophore signal intensity.

4.1.6 Multispectral imaging

A potential hurdle in multiplexing fluorophores is the risk of signal crossover across multiple detection channels, due to spectral overlap between fluorophores. The following approaches may help minimise spectral overlap: (1) use of narrow-range detection filters which may consequently also lower the signal to noise ratio, (2) limit markers in each multiplex to the number of detection filters, thereby requiring multiple tissue sections and limiting ability to assess co-expression of multiple target proteins, (3) use fluorophores with narrow emission range (eg quantum dots), which currently provide low long-term stability, (4) use a laser light source with narrow excitation wavelengths, or (5) perform spectral imaging and linear unmixing to estimate the contribution of overlapping fluorophores to the cumulative signal intensity at each pixel.

Multi-spectral imaging (MSI) is a molecular spectroscopy-based approach, whereby target tissue is imaged at low spectral resolution, of the order of 10-20 nm grating, across a wide spectral range (Mansfield, 2014). MSI of individually stained tissue sections is undertaken to measure the fluorescence emission spectrum of individual fluorophores, which are then compiled into a spectral library. The following linear unmixing algorithm is then applied to ascertain the contribution of overlapping fluorophores:

$$I(\lambda) = \sum_i C_i \bullet R_i(\lambda)$$

where, '*I*' is the signal intensity for each pixel across the spectral range, '*λ*', and is the sum of the concentration, '*C*', of each individual fluorophore reference spectra, '*R*'.

The concentration of each fluorophore can therefore be ascertained from the above equation and is proportional to the relative abundance of the target protein as per the Beer Lambert law (see section 4.1.4).

4.1.7 Chapter aims

In this chapter, I describe the development of a fully automated high-throughput quantitative method to assess OXPHOS protein abundance in formalin-fixed prostate tissue samples. This multiplex assay measures the abundance of Complex I, Complex IV and mitochondrial mass as surrogate measures of mitochondrial function.

4.2 Methods

4.2.1 Overview

The optimised workflow leverages the benefits of tyramide signal amplification (TSA) with the Ventana Discovery Ultra automated staining platform and multispectral imaging using Vectra 3 system as part of a 5-plex assay (**Figure 4-4**).

4.2.2 Patient samples

Prostate tissue samples were acquired from the Manchester Cancer Research Centre Biobank following ethical approval (10_NOCL_02) and informed consent from patients undergoing either radical prostatectomy (prostate cancer samples) or radical cystoprostatectomy (patients with bladder cancer but no histopathological evidence of prostate cancer).

Samples were processed as per routine clinical protocols, which included formalin fixation and embedding into paraffin blocks. Microtomy of tissue blocks provided 4μm thick sections on glass slides for subsequent study. Prostate tissue blocks from patients undergoing cytoprostatectomy for bladder cancer were reviewed by a specialist consultant histopathologist, and only blocks with benign prostate tissue were used as controls.

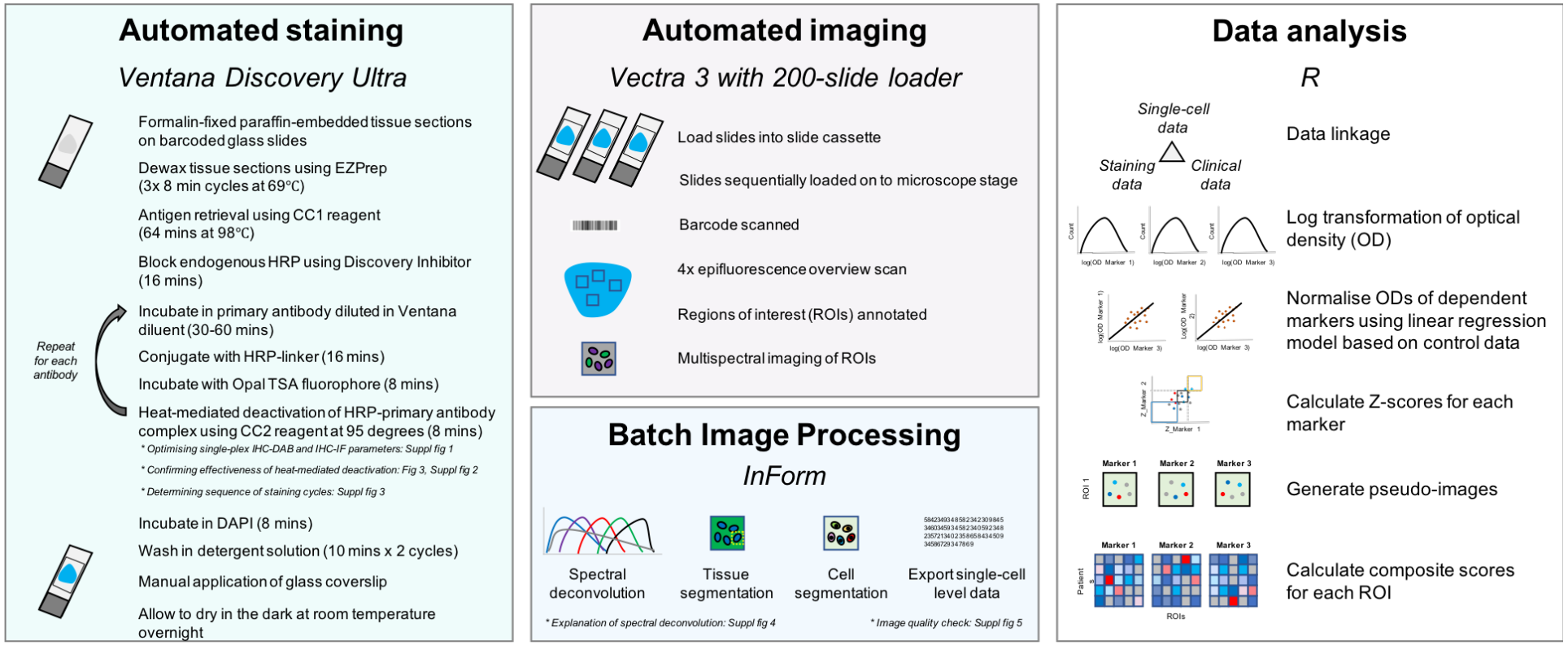

Figure 4-4: Overview of automated workflow. The automated workflow comprises of four stages. Formalin-fixed tissue sections undergo automated staining on the Ventana Discovery Ultra platform followed by automated imaging on the Vectra 3 system. Multispectral images were unmixed, segmented and single cell data generated using InForm Tissue Finder software. Data linkage and analysis was undertaken on RSudio.

Patient	Age	Procedure	Comments	Category
1	69 years	Cystoprostatectomy	Benign prostate histology	Benign
2	64 years	Cystoprostatectomy	Benign prostate histology	Benign
3	54 years	Cystoprostatectomy	Benign prostate histology	Benign
4	69 years	Cystoprostatectomy	Benign prostate histology	Benign
5	66 years	Cystoprostatectomy	Benign prostate histology	Benign
6	58 years	Radical prostatectomy	GS 3+4=7 pT3a N0 NSM BCR free at 9.8 years	Cancer
7	62 years	Radical prostatectomy	GS 3+3=6 pT3a N0 PSM	Cancer
8	59 years	Radical prostatectomy	GS 3+3=6 pT2 N0 PSM BCR at 12.3 years	Cancer
9	65 years	Radical prostatectomy	GS 3+3=6 pT3a N0 PSM BCR free at 12.2 years	Cancer
10	66 years	Radical prostatectomy	GS 3+4=7 pT2 N0 PSM BCR at 5.3 years	Cancer
11	37 years	Cystoprostatectomy	Benign prostate histology	Control
12	37 years	Cystoprostatectomy	Benign prostate histology	Control
13	32 years	Cystoprostatectomy	Benign prostate histology	Control
14	41 years	Cystoprostatectomy	Benign prostate histology	Control
15	34 years	Cystoprostatectomy	Benign prostate histology	Control

Table 4-2: Whole prostate blocks used in exemplar experiment. BCR: biochemical recurrence. PSM: Positive surgical margin.

4.2.3 Antibodies used

Antibodies used in this study are outlined in **Table 4-3**. In keeping with Rocha et al, antibodies against NADH:Ubiquinone Oxidoreductase Subunit B8 (*NDUFB8*) and mitochondrial cytochrome c oxidase subunit 1 (*MTCO1*), were used as markers of Complex I and Complex IV, respectively. These markers have also been employed in previous studies evaluating mitochondrial dysfunction in various cancers (Lang *et al.*, 2015; Iglesias-Gato *et al.*, 2016; Gopal *et al.*, 2018).

NDUFB8 is a nuclear-encoded accessory subunit of Complex I. Reduced abundance of *NDUFB8* has been found to be strongly correlated with defects in mitochondrial complex assembly, and subsequent loss of function (Stroud *et al.*, 2016). In line with these reports, *NDUFB8* has previously been used as a marker of assembled Complex I (Perales-Clemente *et al.*, 2010; Murphy *et al.*, 2012).

MTCO1 is a mtDNA-encoded core subunit of Complex IV. *MTCO1* abundance correlates with COX defects upon COX/SDH enzyme histochemistry, consistent with previous reports demonstrating reduced *MTCO1* abundance in COX-deficient muscle fibres (Oldfors *et al.*, 1992; Rahman *et al.*, 2000; Mahad *et al.*, 2009).

These antibodies have been previously validated in a cohort of patients with well characterised genetically-confirmed mitochondrial disorders (Rocha *et al.*, 2015; Fraser *et al.*, 2017) and are currently used in diagnostic evaluation of muscle biopsy samples from patients with suspected mitochondrial diseases at the National Highly Specialised Commissioned Diagnostic Laboratory at the Wellcome Centre for Mitochondrial Research, Newcastle upon Tyne.

Translocase of outer mitochondrial membrane 20 (*TOMM20*), a well-established marker of mitochondrial mass (Johnson *et al.*, 2015), was included in the multiplex assay to normalise *NDUFB8* and *MTCO1* abundance for mitochondrial mass.

α-pan-cytokeratin antibody was used to target cytokeratins 4, 5, 6, 8, 10, 13, and 18 in prostate tissue for identification of a broad spectrum of epithelial cells, including both luminal and basal cell types.

4.2.4 Automated staining

Automated multiplex staining was performed on a Ventana Discovery Ultra platform (Roche Inc). The Ventana platform was chosen as it offered the ability to programme up to 30 protocols for optimisation in parallel, and also wide selection of polymer systems for signal amplification. Opal TSA fluorophores were used since they provided a well-established set-up for multiplexing and multispectral imaging.

The Ventana system was programmed to perform the following steps

(1) dewaxing using EZPrep reagent (Roche Inc, Cat No 950-102),
(2) heat-mediated antigen retrieval using CC1 reagent (Roche Inc, Cat No 950-124),
(3) incubation in 3% hydrogen peroxide-based Discovery Inhibitor (Roche Inc, Cat No 760-4840),
(4) followed by five sequential staining cycles.

Each staining cycle included incubation in the primary antibody, followed by an HRP-linker (Roche) and an Opal TSA fluorophore (Perkin-Elmer). Heat-mediated antibody denaturation was performed using CC2 reagent (Roche Inc, Cat No. 950-123) prior to each cycle of sequential staining to denature the primary antibody-HRP complex, and deposit secondary TSA fluorophore. This avoids the binding of subsequent fluorophores to any residual unbound HRP-conjugated primary antibody. Targets were probed using the following optimised sequence: *NDUFB8*, *TOMM20*, *MTCO1*, pan-cytokeratin, and then DAPI. Details are provided in **Table 4-4**.

4.2.5 Manual staining and imaging

Paraffin-embedded tissue sections were dewaxed in histoclear and immersed in graded ethanol solutions. Antigen retrieval was performed in a pressurised antigen retrieval unit using EDTA pH 8.0 buffer. Tissue sections were then incubated in 10% normal goat serum for one hour, following which endogenous biotin was blocked (Vectastain ABC kit, Vector laboratories). Tissue sections were then incubated in a combination of primary antibodies, which included α-*NDUFB8*, α-*MTCO1*, and α-*TOMM20* at 4°C for 16 hours. After washing in TBST, the sections were incubated in a combination of secondary antibodies conjugated to AlexaFluor fluorophores and biotinylated IgG1 antibody at 4°C for 2 hours. Slides were then incubated in AlexaFluor 647 streptavidin-conjugated secondary antibody at 4°C for 2 hours. Subsequently, tissue sections were incubated in pan-cytokeratin antibody, conjugated to

AlexaFluor 750, and then incubated in DAPI for 15 minutes. Cover slips were mounted on to slides using Prolong Gold. Finally, slides were visualised at 20x magnification using a Zeiss Axioimager M1 epifluorescence microscope, and images analysed using FIJI software.

4.2.6 Multispectral imaging

The Vectra 3 equipped with a 200-slide system (Perkin-Elmer), comprising of a multi-spectral imaging microscope (DAPI, FITC, Cy3, Texas Red and Cy5 filter cubes) coupled to an automated slide stage and slide loader, was used for image acquisition. Overview images were taken using a 4x objective, and regions of interest were imaged using a 20x objective. Exposure times were optimised for all filter cubes using a range of multiplex stained slides. Following whole-slide epifluorescence imaging, at least 10 regions of interest were selected per sample to collect multispectral images across the 440 nm – 720 nm spectral range at 20 nm intervals.

For manually stained slides, an Axioskop 2 epifluorescence microscope with a 40x objective and a CoolSNAP HQ CCD camera (Photometrics) was used. Images were viewed on Metamorph and FIJI software.

Type	Antibody	Target	Species	Cat No.	Manufacturer	Dilution
Primary	α-*NDUFB8*	Complex I subunit	Mouse IgG1	ab10242	Abcam	1:100 [a,m]
Primary	α-*MTCO1*	Complex IV subunit	Mouse IgG2a	ab14705	Abcam	1:500 [a] 1:100 [m]
Primary	α-*TOMM20*	Mitochondrial mass marker	Rabbit IgG	ab186734	Abcam	1:500 [a] 1:100 [m]
Primary	α-Pan-cytokeratin	Epithelial cell marker	Mouse IgG1	C-2931	Sigma Aldrich	1:10,000 [a] 1:400 [m]
Secondary	AlexaFluor 488	Mouse IgG2a	Goat	A21131	Life Technologies	1:200 [m]
Secondary	AlexaFluor 546	Rabbit IgG	Goat	A175732	Life Technologies	1:200 [m]
Secondary	Biotin-conjugate	Mouse IgG1	Goat	115-065-205	Jackson IR lab	1:200 [m]
Tertiary	AlexaFluor 647	Streptavidin	Goat	S1125	Life Technologies	1:200 [m]
Secondary	AlexaFluor 750	Mouse IgG H+L	Goat	A175732	Life Technologies	1:200 [m]
Secondary	Hoechst 33342	DNA	-	H3570	Life Technologies	1:1400 [m]
Secondary	Spectral DAPI	HRP	Synthetic	FP1490A	Perkin-Elmer	1 drop in 500ul [a]
Secondary	Opal 520	HRP	Synthetic	FP1487A	Perkin-Elmer	1:100 [a]
Secondary	Opal 570	HRP	Synthetic	FP1488A	Perkin-Elmer	1:500 [a]
Secondary	Opal 620	HRP	Synthetic	FP1495A	Perkin-Elmer	1:150 [a]
Secondary	Opal 650	HRP	Synthetic	FP1496A	Perkin-Elmer	1:150 [a]
Secondary	Opal 690	HRP	Synthetic	FP1497A	Perkin-Elmer	1:150 [a]

Table 4-3: Antibodies used in automated and manual multiplex immunofluorescence. [a] Antibody dilution used in automated workflow. [m] Antibody dilution used in manual workflow. Jackson IR lab = Jackson ImmunoResearch Laboratories.

4.2.7 Spectral unmixing

Image processing was performed on InForm Tissue Finder 2.3 software (Perkin-Elmer). Representative images from single-stained slides and the autofluorescence slide were used to generate a spectral library, describing spectral profiles of each fluorophore and contribution of autofluorescence. All multispectral images were then spectrally unmixed, including the removal of autofluorescence artefact (**Figure 4-5**), which may have otherwise adversely influenced accuracy of true fluorophore signal intensity and estimation of the associated target abundance.

4.2.8 Image segmentation

A tissue segmentation algorithm was trained to determine epithelial and stromal regions using the DAPI and pan-cytokeratin channels. The algorithm classified areas containing pan-cytokeratin as epithelial in origin, whereas the remaining tissue areas were classified as stroma. A third category of non-tissue areas was also included, in order to improve classification accuracy.

Epithelial cell segmentation was performed using DAPI counterstain for nuclear identification, and pan-cytokeratin staining to determine cytoplasmic area. The mean optical density (OD) of each of the fluorophores was measured at an individual cell level, providing OD-*NDUFB8*, OD-*MTCO1*, and OD-*TOMM20* values. Due to the highly heterogenous composition of the tumour micro-environment and the absence of cell-type specific stromal markers, only data from epithelial cells were used for subsequent analysis.

4.2.9 Single cell data analysis

Measurement of protein abundance relative to a control cohort was performed by calculating Z-scores. Single-cell level OD data were used to generate Z-scores on R 3.4.3, as previously described by Rocha *et al.* (2015). Briefly, log transformation of OD data was first performed to achieve normality, which was confirmed by visual inspection, assessment of quantile-quantile plots, and the Shapiro-Wilk test. Data from young patients (under 45 years of age) were used as controls. Linear regression of OD-*MTCO1* and OD-*NDUFB8* (dependent variables) against OD-*TOMM20* (independent variable) was performed using data from control patient tissue. Parameters describing the distribution of OD-*TOMM20* (mean and standard deviation, SD), as well as parameters describing the linear relationship between OD-*NDUFB8* versus OD-*TOMM20* and OD-*MTCO1* versus OD-*TOMM20*, were calculated. The deviation of OD-*MTCO1*

and OD-*NDUFB8* of each cell from the expected OD values was used to calculate Z-scores. Z-scores for *NDUFB8* and *MTCO1* were categorised as follows: “very low” (Z-score < -6SD), “low” (Z-score < -3SD), “normal” (Z-score between -3SD to +3SD), and “high” (Z-score > +3SD). Z-scores for *TOMM20* were categorised as follows: “low” (Z-score < -2SD), “normal” (Z-score -2SD to +2SD), and “high” (Z-score > +2SD). Z-score thresholds for OD-*TOMM20* data were narrower (+/- 2SD) since these data are based on true values, rather than expected values of OD-*TOMM20*, in contrast to OD-*MTCO1* and OD-*NDUFB8* (+/- 3SD) where data had been transformed using a linear regression model.

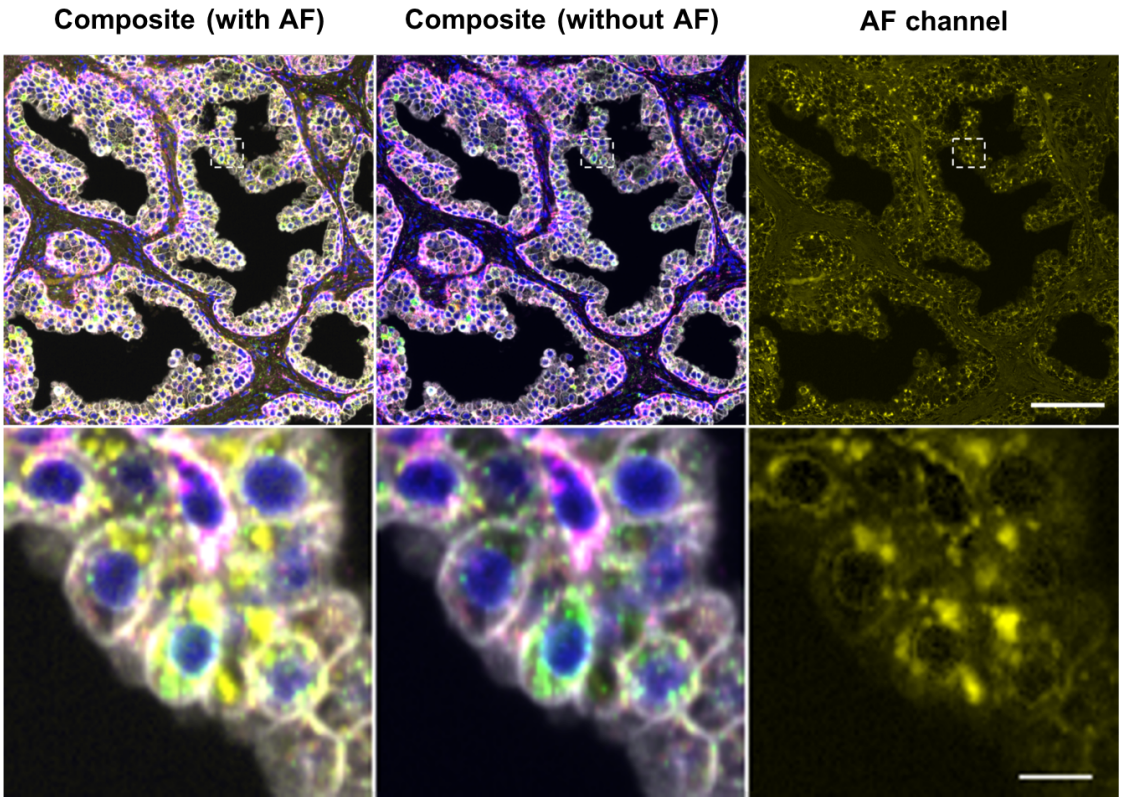

Figure 4-5: Removal of autofluorescence (AF). Representative unmixed composite images before (*left panels*) and after removal of AF signal (*middle panels*), where scale bar represents 100 µm. High magnification images of a representative region are shown in the bottom panels, with the size of the scale bar indicating 10 µm. Composite image following removal of autofluorescence (*middle panels*) demonstrate relatively homogenous distribution of mitochondrial proteins in the peri-nuclear region, in this case highlighting adjacent cells with varying levels of Complex I (*NDUFB8*, pink) and Complex IV (*MTCO1*, green) abundance.

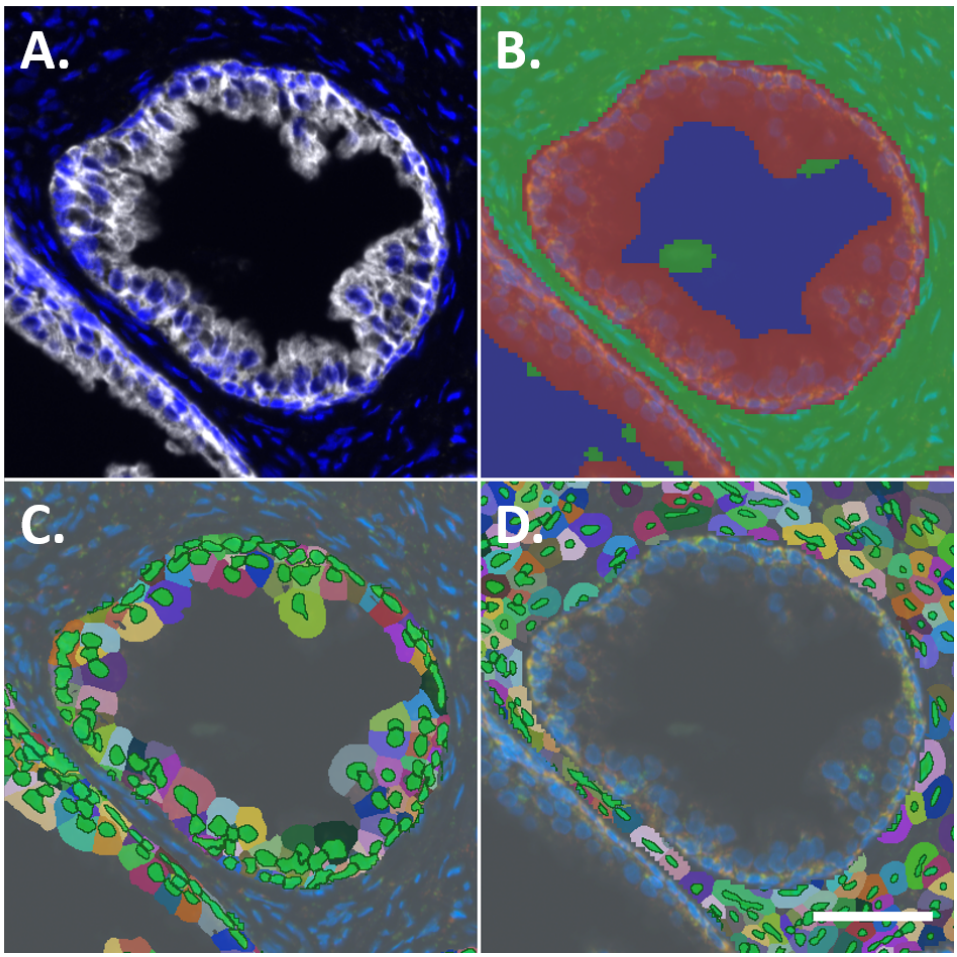

Figure 4-6: Automated cell and tissue segmentation. Representative images of human prostate tissue sections following automated staining and multispectral imaging, analysed on InForm software. **(A)** Composite image of DAPI and pan-cytokeratin channels. **(B)** Trained tissue segmentation with epithelial (red), stromal (green), and empty tissue regions (blue). **(C)** Epithelial nuclear and cell segmentation based on nuclear detection using DAPI counterstaining (green), followed by outward cell growth into surrounding cytoplasm (various colours) based on extent of pan-cytokeratin-positive epithelial regions. **(D)** Stroma nuclear and cell segmentation, based on nuclear detection using DAPI counterstaining (green), followed by outward cell growth into surrounding cytoplasm (various colours) based on empirical cell size. Scale bar 50 µm.

4.3 Results

4.3.1 Optimisation of primary antibodies for single-plex automated chromogenic IHC and fluorescence IHC

In the first instance, primary antibody dilutions were optimized using IHC-DAB immunohistochemistry, using the OmniMap HRP system and the Chromogenic IHC kit on the Ventana Discovery Ultra platform (Roche Inc). Adjacent sections were labelled with IgG control antibodies to assess for non-specific binding. Subsequently, optimised antibody concentrations from IHC-DAB were used for automated IHC-IF staining using the Opal 520 fluorophore with OmniMap HRP for immunofluorescence microscopy.

Due to low abundance of *NDUFB8* antigens, OmniMap HRP amplification was found to be inadequate. Therefore, a secondary antibody conjugated to hapten-based anti-mouse HQ polymer followed by an HRP-conjugated Anti-HQ tertiary antibody were employed. This resulted in improved *NDUFB8* signal intensity. Representative images are presented in **Figure 4-7**.

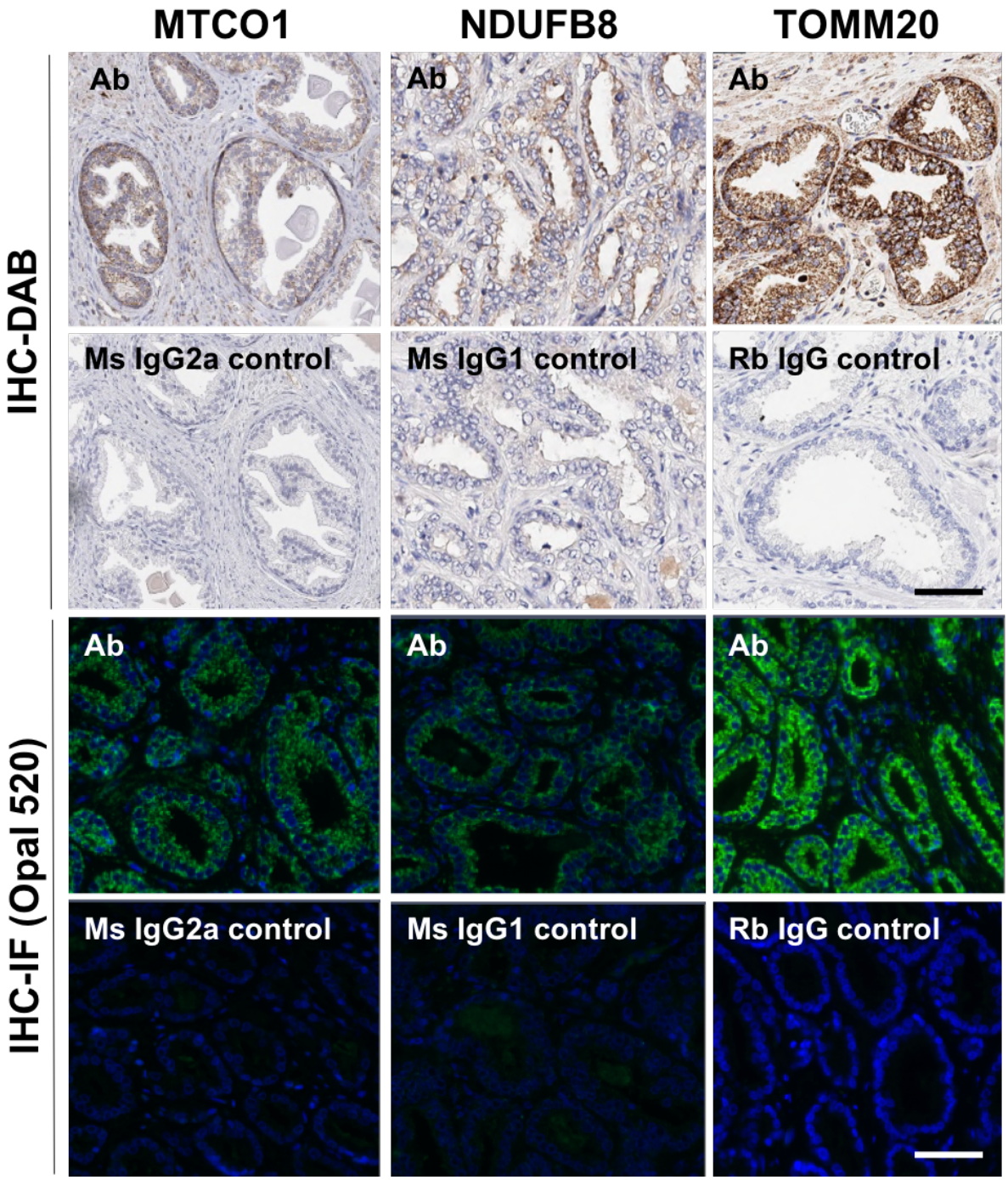

Figure 4-7: Optimised single-plex automated IHC-DAB and IHC-fluorescence assays. Prostate tissue sections on the Ventana Discovery Ultra platform for IHC-DAB using the Chromogenic IHC kit, and the IHC-IF using Opal 520. Representative images of optimised antibody dilutions for *NDUFB8* (1:100, anti-Ms HQ system), *MTCO1* (1:500, anti-Ms OmniMap) and *TOMM20* (1:500, Anti-Rb OmniMap), and appropriate isotype controls are shown. IHC-DAB sections were imaged using the Aperio CS2 whole slide brightfield scanner, whereas the IHC-IF sections were imaged using the Axioskop 2 epifluorescence microscope with a 10x objective and DAPI and FITC filters at 200ms exposure. Scale bars 50 µm.

4.3.2 Effectiveness of heat-mediated denaturation

Each cycle consists of a consecutive staining with an antibody, HRP polymer and TSA fluorophore. Heat-mediated denaturation of antibody-HRP conjugate was undertaken prior to subsequent staining cycles. Sequential staining cycles may therefore introduce artefacts due to inadequate heat-mediated denaturation of antibody-HRP conjugates earlier in the sequence. The use of three antibodies (α-*NDUFB8*, α-*MTCO1* and α-pan-cytokeratin) raised in the same species (mouse) further increases the likelihood of such artefacts.

In order to test effectiveness of heat-mediated denaturation, tissue sections were subjected to staining cycles for each of the four primary antibodies individually using the Opal 520 fluorophore followed by heat mediated denaturation. This was followed by a further staining cycle with the Opal 650 fluorophore, with the second primary antibody omitted. It was hypothesised that the presence of unbound residual primary antibody or inadequately denatured antibody-HRP conjugate from the first staining cycle would be revealed by the deposition of the second TSA fluorophore.

Tissue sections were imaged using an epifluorescence microscope equipped with DAPI, FITC and Cy3 filter cubes. Profound Opal 650 fluorescence was noted in the Cy3 channel for tissue sections stained with α-pan-cytokeratin antibody, with a faint fluorescent Opal 650 signal also noted in tissue sections stained with α-*MTCO1* antibody, suggesting inadequate heat-mediated denaturation of antibody-HRP complexes. No detectable signal was observed in tissue sections stained with α-*NDUFB8* and α-*TOMM20* antibodies (**Figure 4-8**).

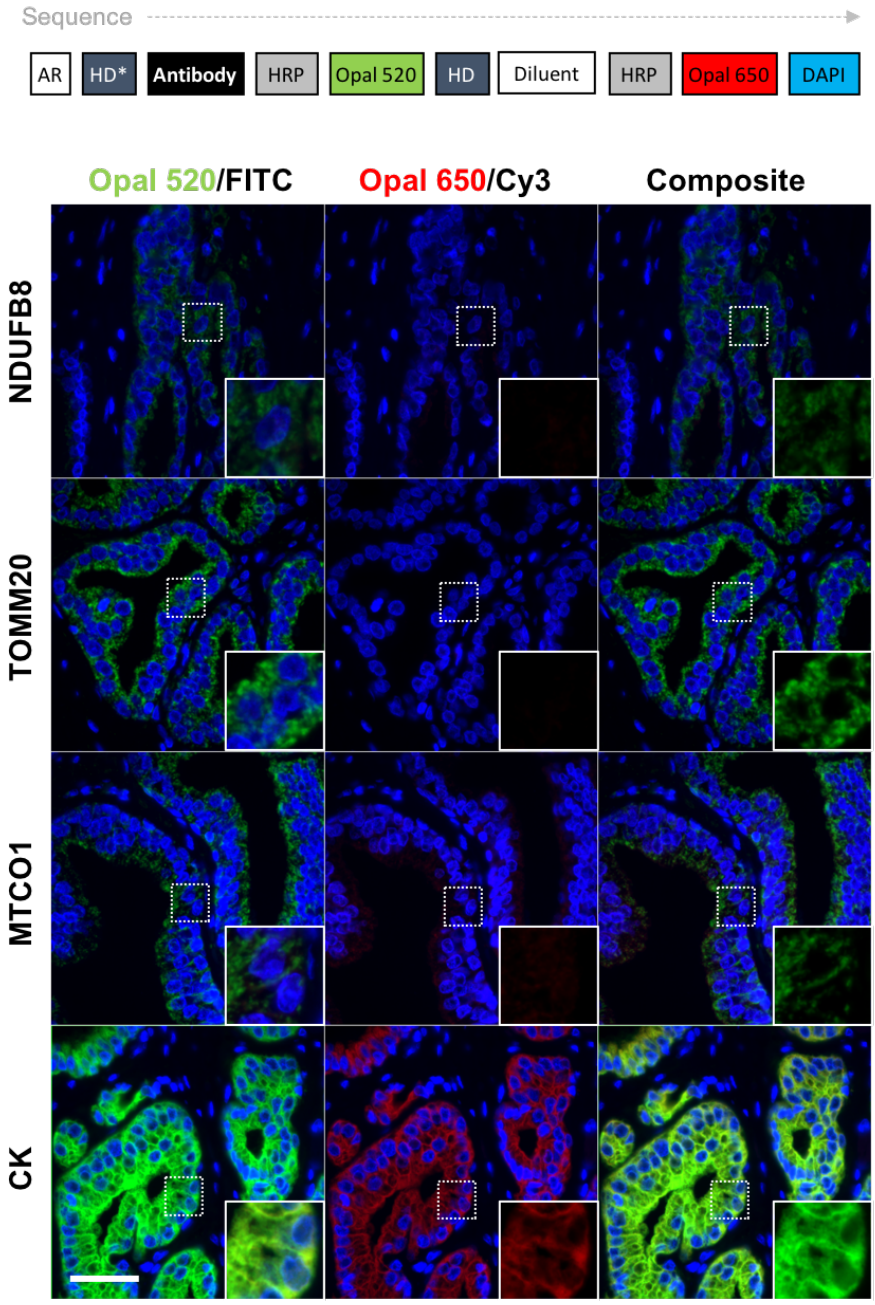

Figure 4-8: Effectiveness of heat-mediated denaturation. Each antibody-HRP complex was separately evaluated using the staining sequence highlighted in the top panel. After antigen retrieval, tissue sections underwent expected heat steps for the following empirically determined staining sequence: pan-cytokeratin (*CK*), *TOMM20*, *MTCO1*, and *NDUFB8*. Tissue sections were then incubated in primary antibody at optimised concentrations. The tissue sections were washed and then incubated in species-specific HRP-conjugated polymer, followed by Opal 520 TSA substrate. To test the adequate removal of antibody-HRP complex, the sections were then incubated in antibody diluent, followed by HRP-conjugated polymer specific to the species of the subsequent staining cycle for the empirically determined staining sequence. This was followed by incubation in Opal 650 TSA substrate and DAPI. The presence of signal in the Cy3 channel confirmed inadequate denaturation of the primary antibody-HRP complex, as observed for cytokeratin (strong Cy3 signal) and *MTCO1* (faint Cy3 signal) antibodies. Images were acquired using an Axioskop 2 epifluorescence microscope with a 40x objective and DAPI, FITC and Cy3 filters. High magnification insets are included. Scale 100 µm.

4.3.3 Determining optimal sequence of staining cycles

Given the inadequate denaturation of α-pan-cytokeratin antibody-HRP complex, the pan-cytokeratin staining cycle was placed at the end of the staining sequence. Since pan-cytokeratin is used as an epithelial cell marker and not for quantification purposes, any artefactual signal from prior staining cycles probing less abundant mitochondrial targets is unlikely to influence planned downstream image analysis for cell phenotyping.

In light of concern regarding inadequate denaturation of α-*MTCO1* antibody-HRP conjugates using standard heat-mediated denaturation conditions and the need for accurate quantification of both α-*MTCO1* and α-*NDUFB8* targets, the sequence of *NDUFB8* and *MTCO1* staining cycles and various denaturation conditions were evaluated (**Figure 4-9**). This included a variety of temperatures and incubation periods in CC2 reagent. When the *MTCO1* cycle was placed prior to *NDUFB8* (**Figure 4-9**, *Sequence A*), inadequate denaturation was observed in all conditions. However, adequate denaturation of α-*NDUFB8* was noted when the *NDUFB8* cycle was placed prior to the *MTCO1* cycle (**Figure 4-9**, *Sequence B*).

Given robust heat-mediated denaturation of the α-*NDUFB8* antibody-HRP conjugate in Sequence A, and the low abundance of the *NDUFB8* target antigen, the *NDUFB8* cycle was placed at the start of staining sequence. This also helped minimise potential degradation of the target antigen during subsequent heat-mediated denaturation steps.

Finally, the α-*TOMM20* antibody, raised in rabbit, was placed between *NDUFB8* and *MTCO1* cycles to provide an additional subsequent heat-mediated denaturation step, prior to probing with the anti-mouse OmniMap HRP conjugated polymer in the *MTCO1* cycle.

Once the optimum staining sequence was determined, primary antibodies were paired with fluorophores based upon relative target abundance of each primary antibody estimated by signal intensities at single-plex IF staining with Opal 520, and relative quantum efficiency of spectrally separated fluorophores.

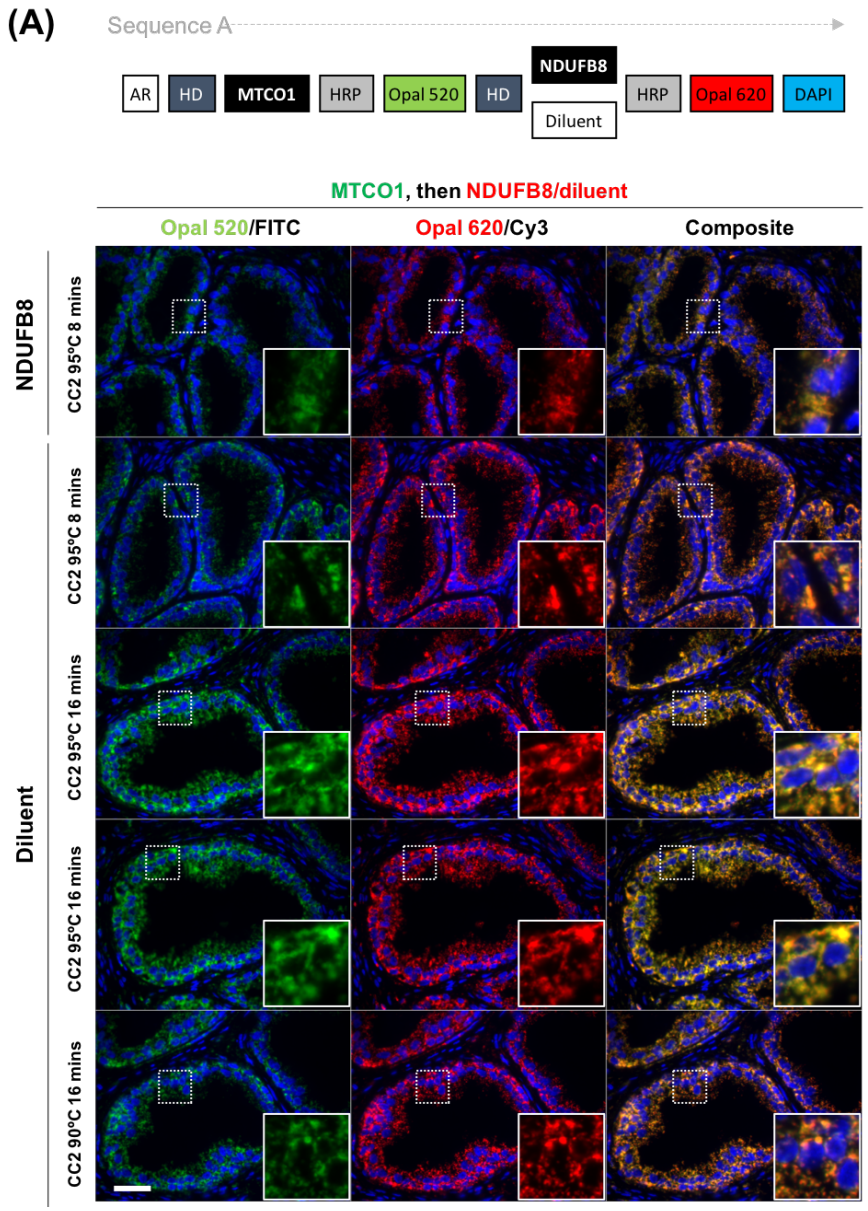
(A)
Sequence A
AR
HD
MTCO1
HRP
Opal 520
HD
NDUFB8
Diluent
HRP
Opal 620
DAPI
MTCO1, then NDUFB8/diluent
Opal 520/FITC
Opal 620/Cy3
Composite
NDUFB8
Diluent
CC2 95°C 8 mins
CC2 95°C 8 mins
CC2 95°C 16 mins
CC2 95°C 16 mins
CC2 90°C 16 mins

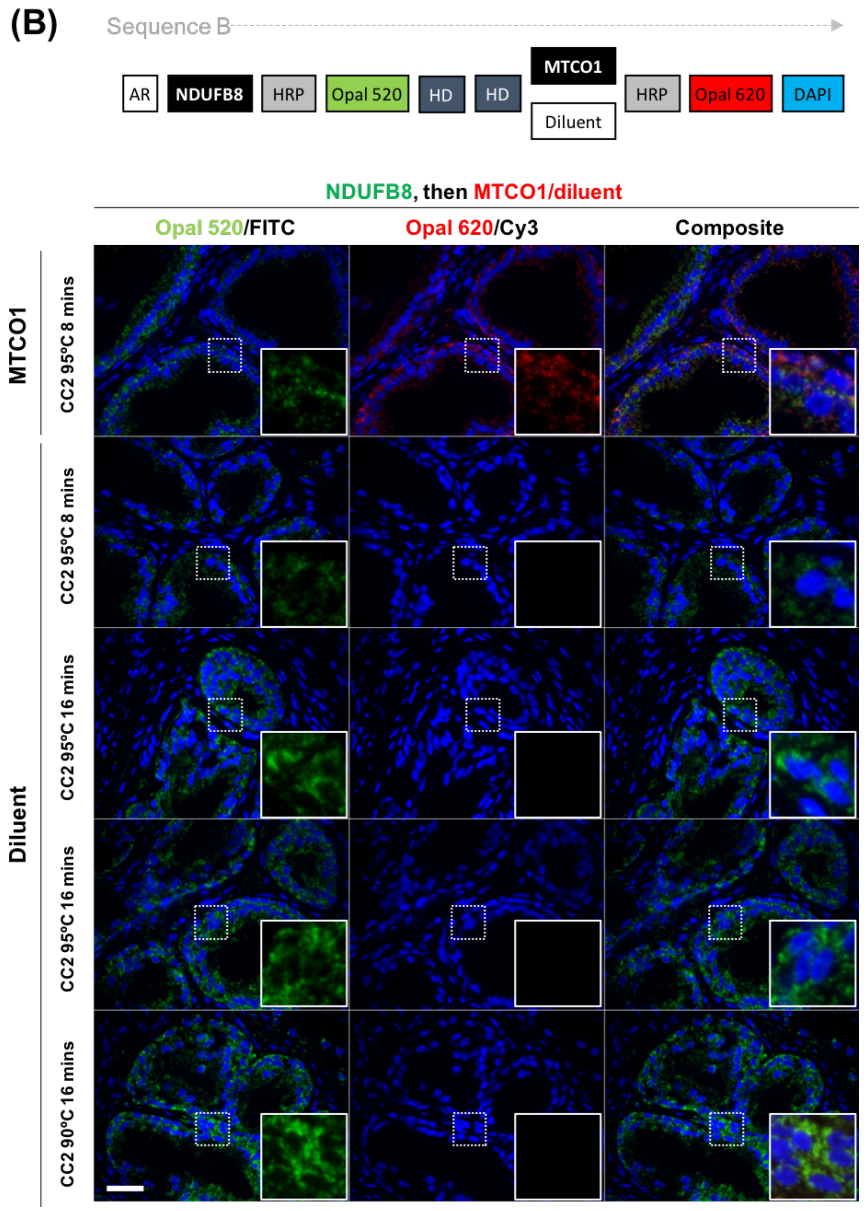
(B)
Sequence B
AR
NDUFB8
HRP
Opal 520
HD
HD
MTCO1
Diluent
HRP
Opal 620
DAPI
NDUFB8, then MTCO1/diluent
Opal 520/FITC
Opal 620/Cy3
Composite
MTCO1
Diluent
CC2 95°C 8 mins
CC2 95°C 8 mins
CC2 95°C 16 mins
CC2 95°C 16 mins
CC2 90°C 16 mins

Figure 4-9: Influence of effective heat-mediated antibody denaturation on selection of sequence of primary antibodies raised in mouse. The optimum sequence of the two mitochondrial antibodies raised in mouse, *NDUFB8* and *MTCO1*, was determined by evaluating two staining sequences, with a variety of heat denaturation conditions. **(A)** In sequence A, the *MTCO1* staining cycle was followed by a single heat denaturation step and the *NDUFB8* cycle. To test the effectiveness of heat denaturation α-*MTCO1*-HRP complex, the second antibody, α-*NDUFB8*, was replaced by incubation in the diluent. Comparable signal intensity was noted both with and without the inclusion of α-NDUFB8 antibody in the second staining cycle, highlighting inadequate heat denaturation of the α-*MTCO1*-HRP complex at all heat denaturation conditions. **(B)** In sequence B, the *NDUFB8* staining cycle was followed by two heat denaturation steps and the *MTCO1* cycle. It was envisaged that the rabbit α-*TOMM20* cycle would later be placed between the two heat denaturation steps in the multiplex staining protocol. Conditions used in the first heat denaturation step are reported in the figure above, and the second heat step comprised of incubation in CC2 reagent at 95°C for 8 minutes as per standard protocol. To test effectiveness of heat denaturation of α-*NDUFB8*-HRP complex, the second antibody, α-*MTCO1*, was replaced by incubation in the diluent. Adequate heat denaturation was confirmed by the absence of signal in the Cy3 channel using all heat denaturation conditions. Images were acquired using an Axioskop 2 epifluorescence microscope with a 40x objective and DAPI, FITC and Cy3 filters. High magnification insets are included. Scale bar 100 µm. AR: Antigen retrieval; HD: Heat-mediated denaturation.

Cycle	Primary antibody	Amplification system	Fluorophore
1	Mouse α-*NDUFB8* (60 mins)	Anti-mouse HQ (16 mins), followed by anti-HQ HRP (16 mins)	Opal 520 (8 mins)
2	Rabbit α-*TOMM20* (30 mins)	OmniMap anti-rabbit HRP (16 mins)	Opal 570 (8 mins)
3	Mouse α-*MTCO1* (60 mins)	OmniMap anti-mouse HRP (16 mins)	Opal 620 (8 mins)
4	Mouse α-Pan-cytokeratin (30 mins)	OmniMap anti-mouse HRP (16 mins)	Opal 690 (8 mins)
5	Spectral DAPI (8 mins)	-	-

Table 4-4: Optimised automated multiplex staining sequence. Incubation times in brackets.

4.3.4 Comparison of automated and manual protocols

Adjacent tissue sections were stained using the optimised automated protocol (**Table 4-4**) and the conventional manual multiplex staining protocol (section 4.2.5). The Vectra system was used for spectral imaging of tissue sections at 20 nm wavelength intervals using DAPI, FITC, Cy3, Texas Red, and Cy5 filter cubes. Multispectral images were spectrally unmixed, providing signal intensities of each of the five fluorophores while also removing artefactual autofluorescence signal. The absence of a Cy7 channel in the Vectra multispectral microscope precluded the ability to capture Opal 690 labelled pan-cytokeratin in the manually stained tissue section. The adjacent manually stained section was therefore imaged using the Axio Imager M1 fluorescence microscope equipped with DAPI, FITC, Cy3, Cy5, and Cy7 filter cubes. Composite images from contiguous regions were subjectively comparable (**Figure 4-10**).

The automated staining approach reduced hands-on time for manual staining from 2 days down to a fully automated 14-hour protocol, including a conservative 1-hour set-up period, which could be run overnight. Once stained, tissue sections were scanned using the robotic slide loader coupled with the Vectra system, which can be programmed to process up to 200 slides in an automated manner with minimal human input.

For comparison, a serial section was stained with cell marker (pan-cytokeratin) and all fluorophores, with the exception of all mitochondrial primary antibodies, to ascertain background signal intensity using automated and manual approaches (**Figure 4-11**).

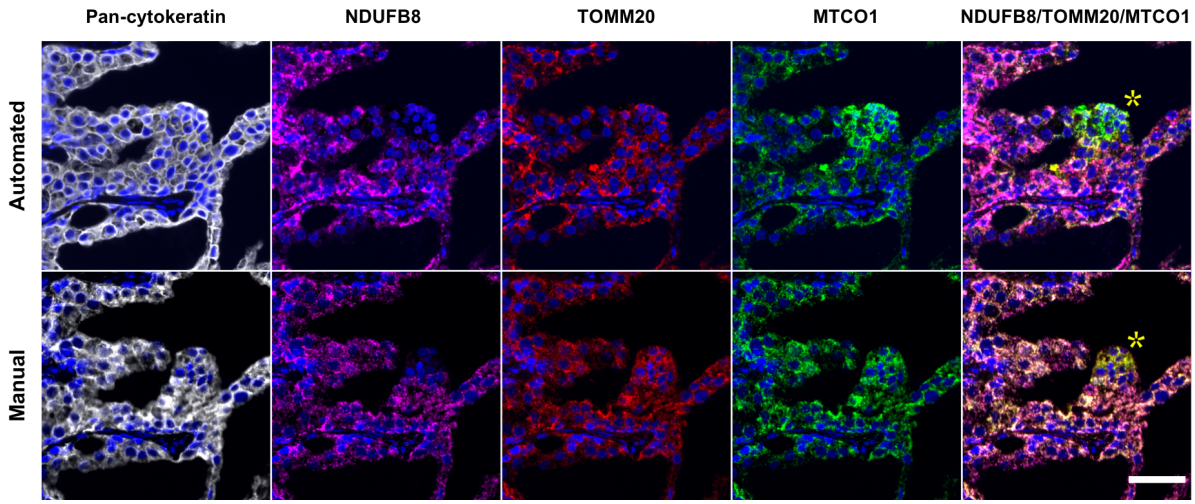

Figure 4-10: Comparison of automated and manual multiplex assays. Adjacent tissue sections were subjected to automated and manual staining protocols. Asterix denotes a cluster of epithelial cells deficient in *NDUBF8* evident in both sections. Scale bar 50 µm.

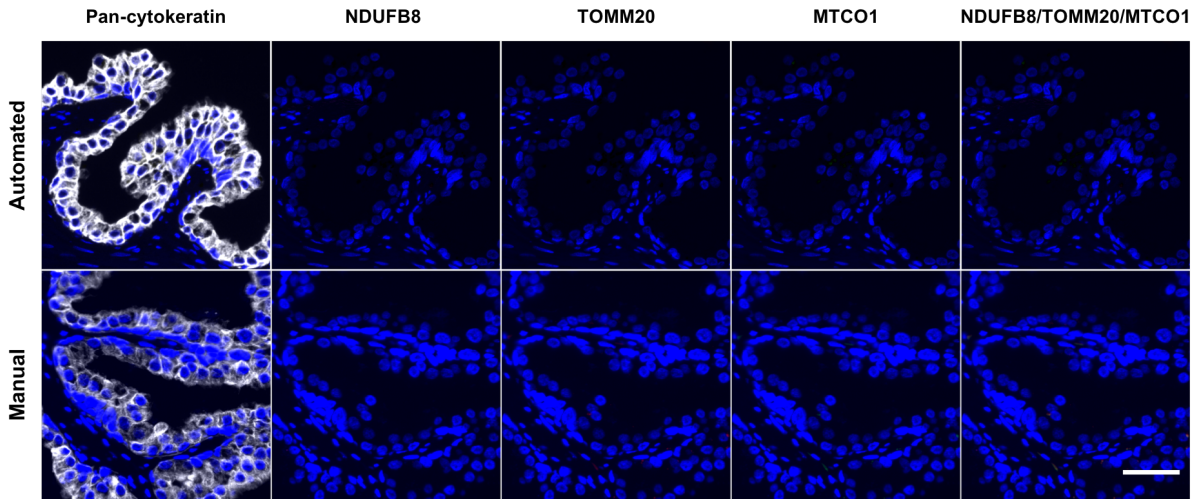

Figure 4-11: Comparison of background fluorescence in automated and manual assays. Serial tissue sections were subjected to standard automated and manual protocols, with the exception of incubation in mitochondrial antibodies, which were replaced with incubation in diluent. No gross background signal was evident in fluorescence images acquired from tissue slides subjected to automated or manual staining protocols. Scale bar 50µm.

4.3.5 Quality testing

The effectiveness of heat-mediated denaturation was once again tested in a multiplex setting by sequentially omitting individual primary antibodies and assessing any residual signal from the previous antibody cycle (**Figure 4-12A**), in comparison to background signal. The absence of residual signal from the previous antibody cycle confirms effective denaturation.

For example, upon omission of the α-*TOMM20* antibody (second staining cycle), any residual α-*NDUFB8* antibody-HRP complex from the first staining cycle would catalyse the deposition of Opal 570 TSA substrate. However, Opal 570 signal intensity in this experiment was comparable to the background signal intensity, where all mitochondrial antibodies had been omitted (**Figure 4-12B**). This represented a reduction of signal by two orders of magnitude.

Similarly, omission of the α-*MTCO1* antibody (third staining cycle) abolished fluorophore signal in the Opal 620 channel to background levels, suggesting absence of residual α-*TOMM20* antibody-HRP complex from the second staining cycle after denaturation. Thus, quantitative single cell analysis confirmed effective denaturation of α-*NDUFB8* and α-*TOMM20* antibody-HRP complexes, supporting reliable quantification using this multiplex assay.

In order to test assay reproducibility across staining batches, serial tissue sections from two patient samples were stained on separate runs using the same batch of antibodies, HRP-conjugated polymers and fluorophores to test assay reproducibility. Quantitative single cell analysis again noted high consistency in signal intensity across both batches (**Figure 4-12C**).

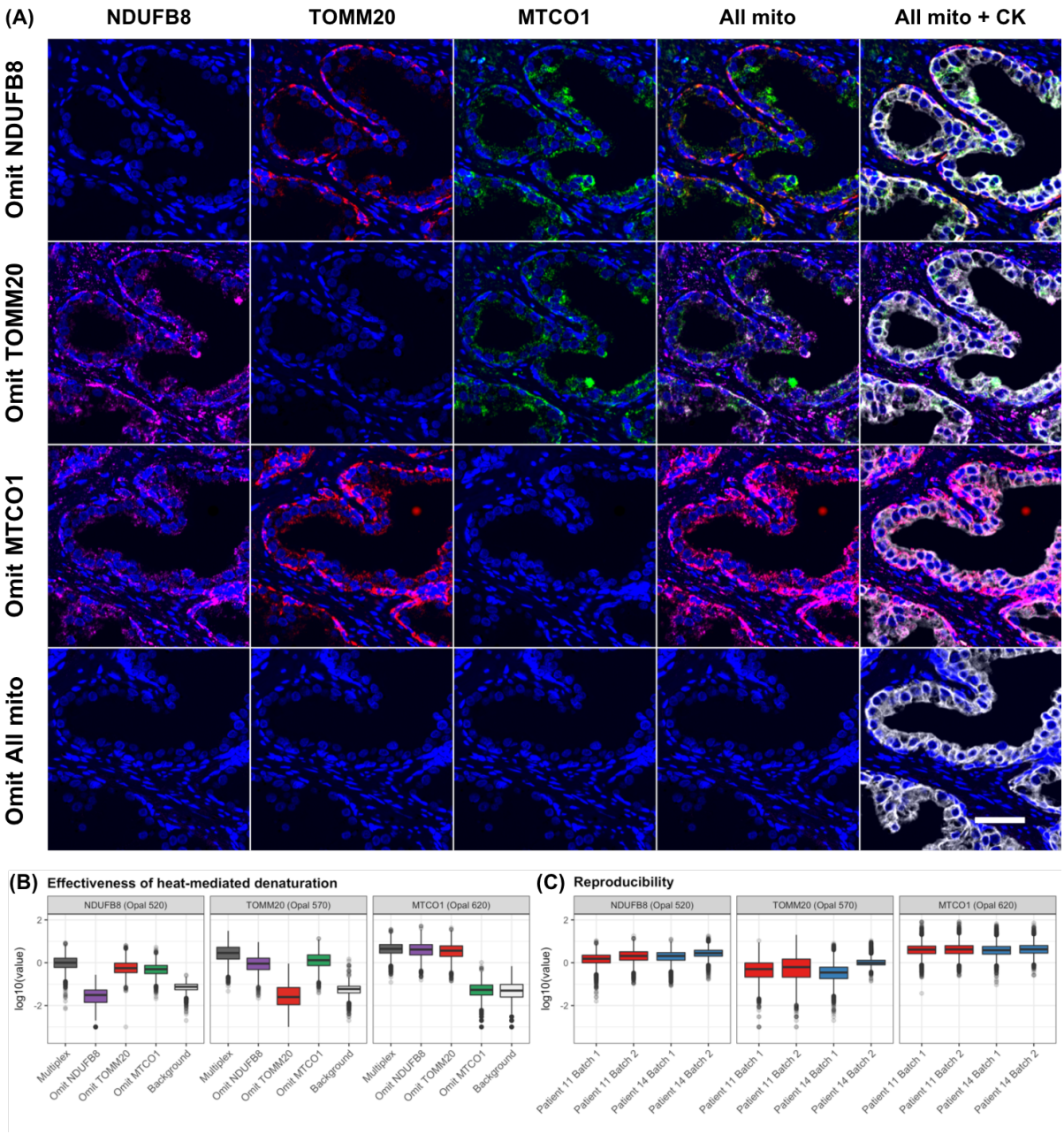

Figure 4-12: Validation of heat-mediated denaturation and reproducibility of automated multiplex OXPHOS assay. (A) Individual primary antibodies were sequentially omitted and replaced with incubations in diluent to evaluate effectiveness of heat-mediated denaturation of the antibody-HRP from the previous staining cycle. Residual signal from the previous staining cycle in the subsequent fluorophore channel would represent inadequate denaturation. Representative images are shown. Scale bar 50µm. **(B)** Quantitative single cell analysis of epithelial cells from 10 randomly selected regions confirmed adequate heat-mediated denaturation of *NDUFB8* and *TOMM20* antibody-HRP complexes. **(C)** Consistent signal intensity of mitochondrial markers noted across adjacent tissue sections from two patient samples (patients 11 and 14) stained in two separate batches, confirming good reproducibility of the assay. Multispectral images acquired from 10 regions per condition, 6000-8000 cells per image, using the Vectra system.

4.3.6 Spatial heterogeneity in OXPHOS protein abundance

Z-scores were calculated from single cell optical density data, using control data from a cohort of patients aged 45 years or younger. Pseudo-images demonstrate spatial heterogeneity in OXPHOS protein expression (**Figure 4-13**), predominantly comprising of three mitochondrial phenotypes: (a) normal OXPHOS abundance (ROI1), (b) low *NDUFB8* with normal or high *MTCO1*, and (c) low *NDUFB8* and low *MTCO1*, with increased *TOMM20*.

Significant heterogeneity in OXPHOS protein abundance was noted at both cellular level within individual regions of interest, and also at regional and patient level. This poses a significant challenge in data analysis approaches to capture heterogeneity while simultaneously generating a metric to summarise OXPHOS status at a patient level. Historically, this has been achieved using weighted scores, such as the histological or H-score, and the Allred Scores, which generally involve a semi-quantitative composite assessment of estimated cellular frequency and intensity of marker expression (Fedchenko and Reifenrath, 2014). These weighted scoring systems were developed and validated for specific applications, though have since been applied more generally in biomarker discovery. In keeping with previous criticism of H-scores in digital image analysis (Camp *et al.*, 2002), this metric was noted to be inferior to mean Z-scores in the assessment of OXPHOS protein abundance in prostate tissue (see Appendix B, Figure B-2),

Such summary metrics can be generated using single-cell level protein abundance from immunofluorescence experiments. However, the use of such metrics for quantitative single cell data results in loss of dynamic range of the available data, which may have downstream implications in assessment of biomarker performance. In contrast, mean signal intensity or mean Z-scores from single cell data from either individual regions of interest or across multiple regions from individual patients may help maintain the dynamic range of the available data, and therefore thought to be best suited for normally distributed data. Clustering and dimensionality reduction approaches were also employed for multiplex single-cell datasets, though the results are less intuitive to interpret (see Appendix B, Figure B-3). Mean Z-score data are therefore presented.

(A) Whole-tissue pan-cytokeratin map

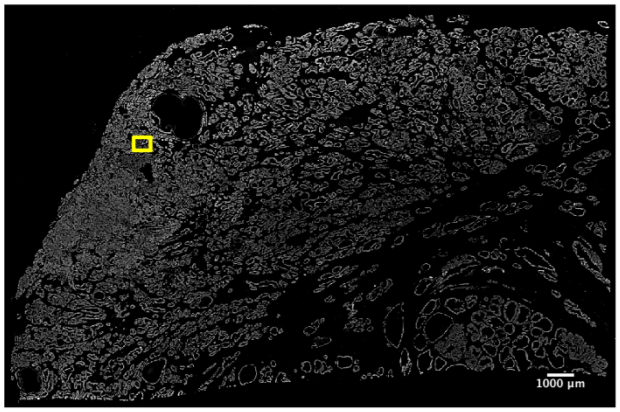

(B) Multiplex composite image

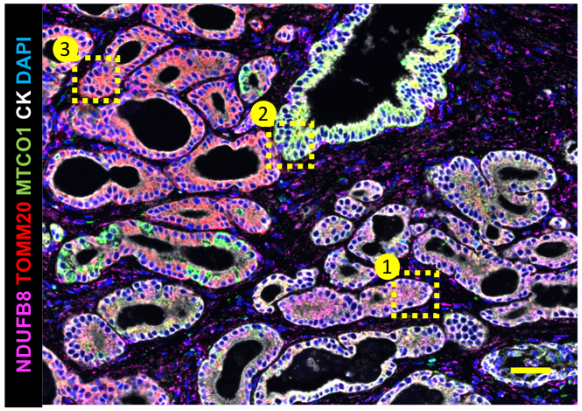

(C) Mitochondrial respiratory chain graph

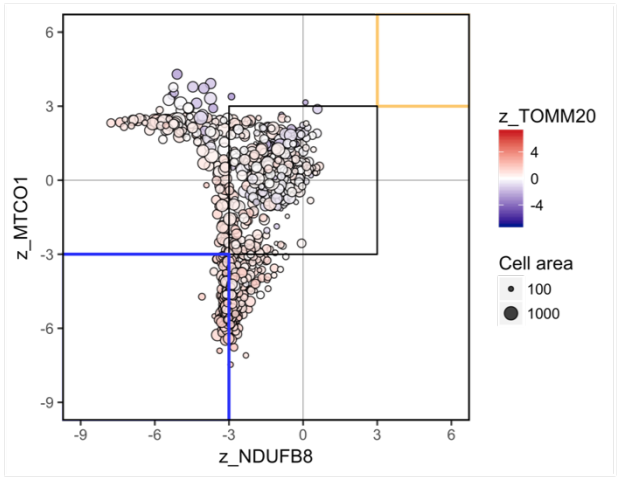

(D) Individual markers of interest

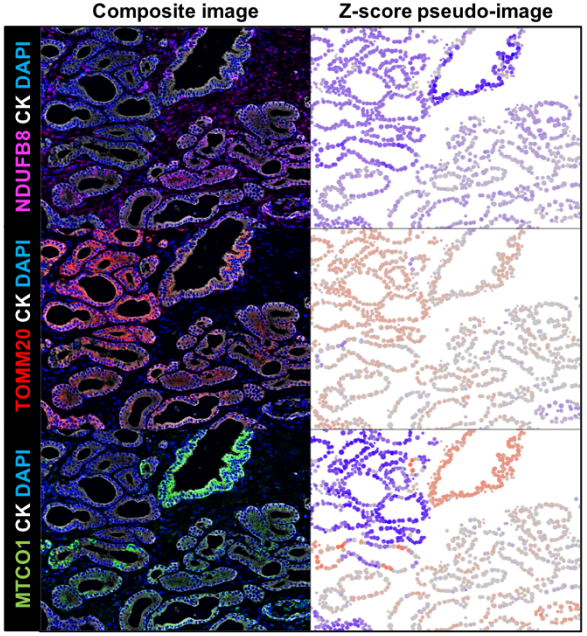

(E) Cropped regions of interest

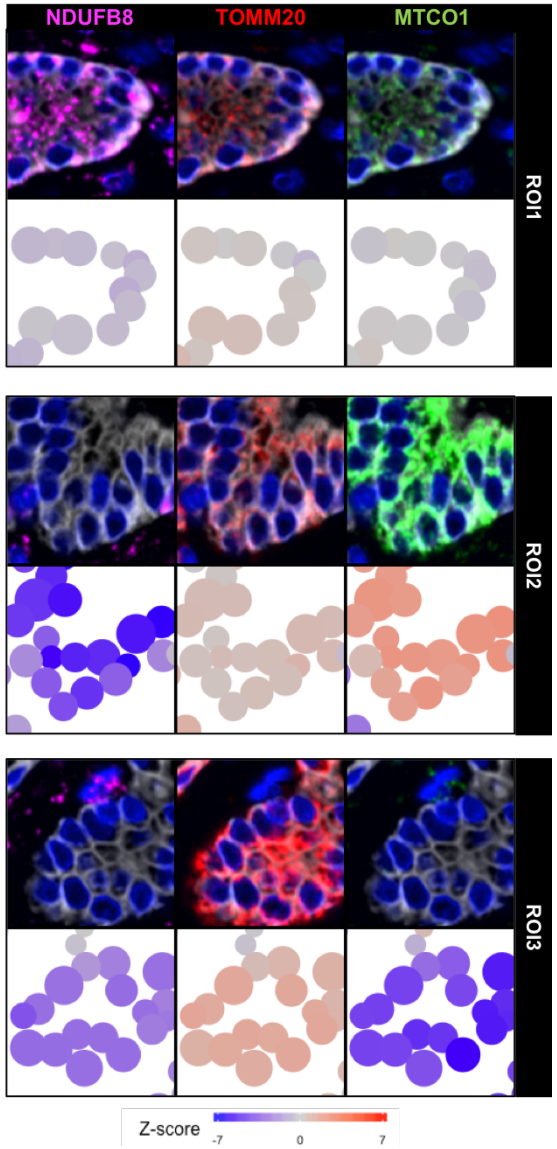

Figure 4-13: Spatial heterogeneity in OXPHOS protein abundance in prostate cancer tissue. **(A)** A region of interest was selected from an overview pan-cytokeratin map of a prostate cancer tissue section from patient 8 stained on the Ventana Discovery Ultra using the automated staining protocol and imaged using the Vectra system. **(B)** Composite image generated from multispectral imaging and spectral deconvolution noted spatial variations in raw *NDUFB8* and *MTCO1* abundance. Single cell level OD-*NDUFB8* and OD-*MTCO1* were obtained following automated tissue and cell segmentation. **(C)** Mitochondrial raspatory chain graph. Single cell level OD-*NDUFB8* and OD-*MTCO1* data were log-transformed and normalised for variable mitochondrial mass using OD-*TOMM20*. Z-scores were calculated for each of the mitochondrial markers, using data from benign prostate tissue from patients aged ≤ 45 years as controls. Each spot represents an individual epithelial cell from the region of interest in panel B. The size of each spot correlates with cell area (in pixels) **(D)** Pseudo-colour images were generated for each mitochondrial marker, demonstrating spatial heterogeneity in protein abundance. **(E)** Cropped regions of interest from panel B represent three cell phenotypes: normal mitochondrial protein abundance (ROI1), isolated *NDUFB8* defects (ROI2), and combined *NDUFB8* and *MTCO1* defects (ROI3).

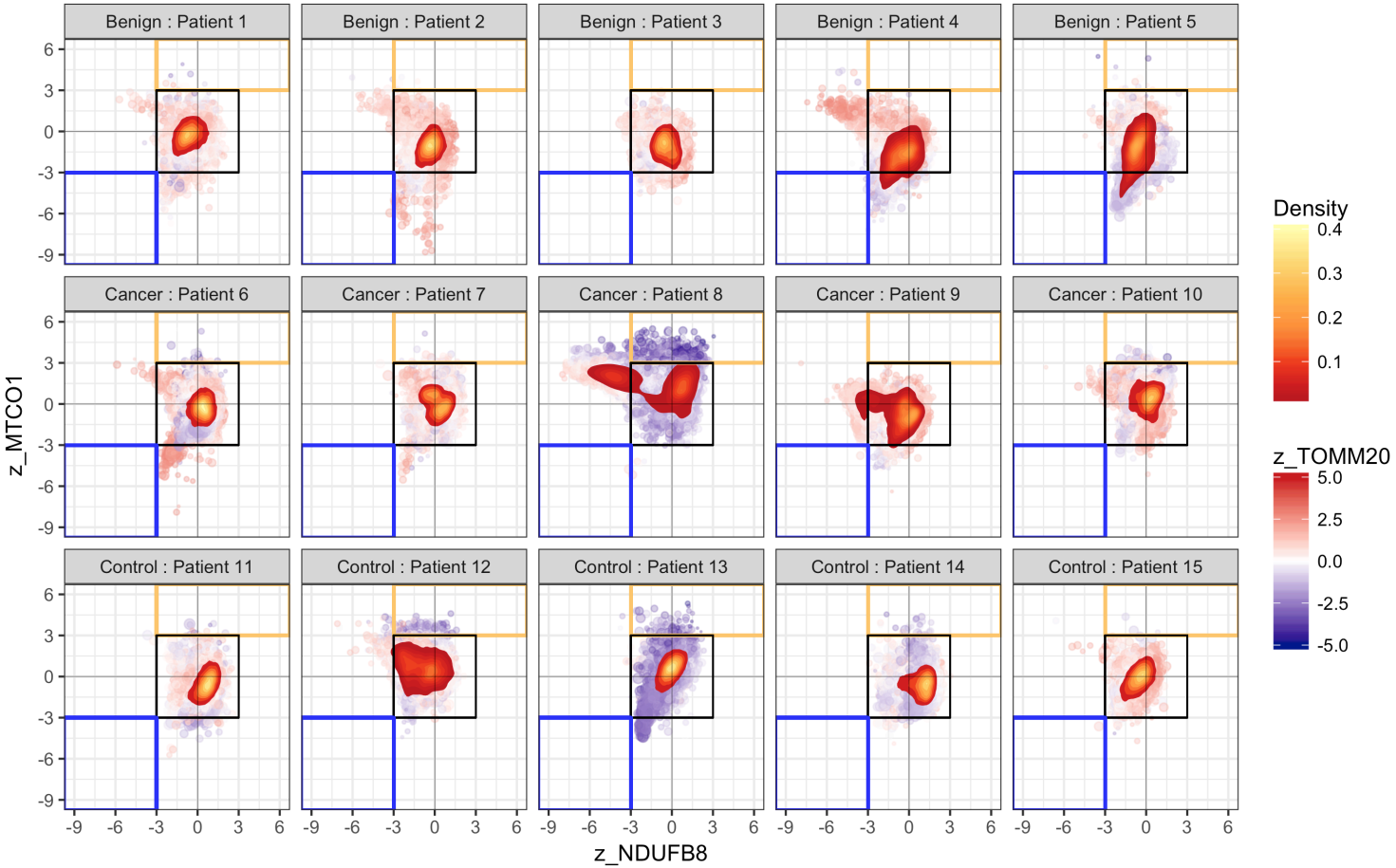

Figure 4-14: Cellular heterogeneity in OXPHOS protein abundance. Mitochondrial respiratory chain graphs were generated from data from patients with either benign prostate tissue and prostate cancer. Data from patients aged ≤45 years were included as a control cohort. Data for 216,731 cells represented (median 14,670 cells per patient). Widespread intra-patient and inter-patient cellular heterogeneity in OXPHOS protein abundance was observed. For example, two distinct cell populations were noted in patient 8.

4.3.7 Inter-patient and intra-patient heterogeneity in OXPHOS protein abundance

Widespread heterogeneity was also noted in mean OXPHOS Z-scores across spatially disparate regions of benign and malignant tissue samples (**Figure 4-15**). Cells were classified to have either low, normal, or high protein abundance, as described previously (section 4.2.9). Benign prostate tissue from older patients more frequently had regions of *MTCO1* deficiency, as compared to tissue from younger control patients and prostate cancer tissue. Regions with low mean *NDUFB8* Z-scores were observed more frequently in two included patients with prostate cancer (patients 8 & 9, **Figure 4-15**).

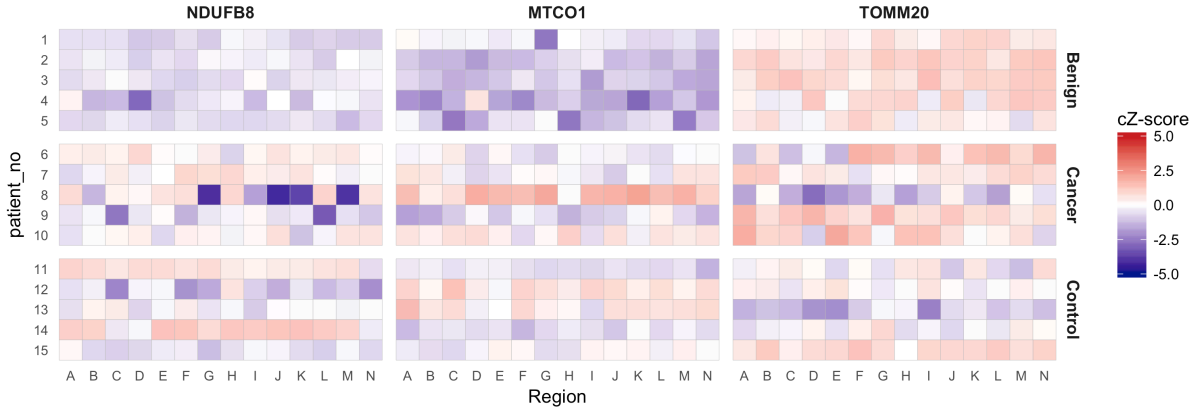

Figure 4-15: Intra-patient and inter-patient heterogeneity in OXPHOS protein expression. Mean single cell expression of *NDUFB8*, *MTCO1* and *TOMM20* across spatially disparate ranges of benign, cancerous and control prostate tissue (n=5 patients in each group). Tissue samples from patients with no histological evidence of prostate cancer, under 45 years of age, were used as controls. Widespread heterogeneity both within and between patient cohorts was noted, with regions of complex IV loss (low *MTCO1*) noted more frequently in older benign prostate tissue.

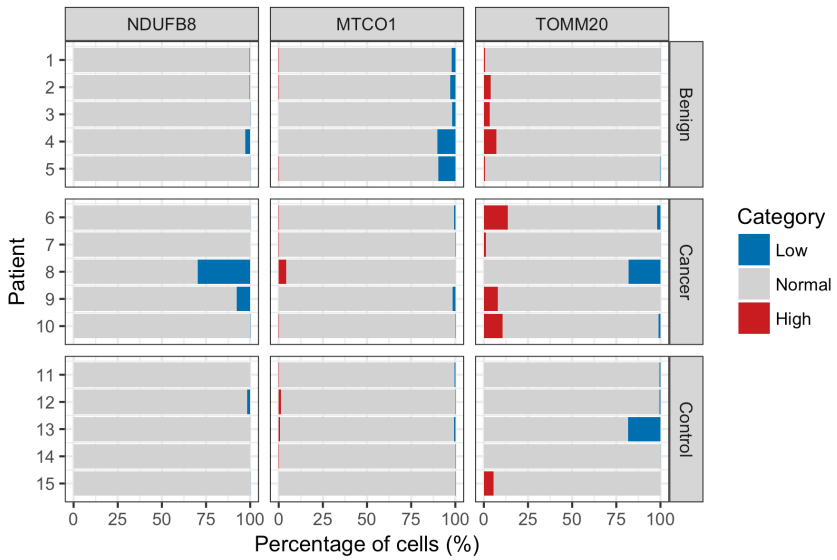

Figure 4-16: Frequency of OXPHOS defects in human prostate tissue. Cells from each patient were classified based on mitochondrial protein abundance (median 14,670 cells per patient, 216,731 cells in total). *MTCO1*-deficient cells were observed more frequently in the benign cohort, whereas *NDUFB8*-deficient cells were observed most frequently in a subset of patients from the cancer cohort.

4.4 Discussion

In this chapter, a novel workflow has been described for automated quantitative assessment of OXPHOS protein abundance in formalin-fixed human prostate tissue. Together with an image processing and data analysis pipeline, this workflow enables high-throughput assessment of tissue samples, with minimal human input.

4.4.1 Effectiveness of heat-mediated denaturation

The optimum staining sequence for the assay developed in this chapter was determined to be *NDUFB8*, *TOMM20*, *MTCO1*, and lastly pan-cytokeratin. A key technical challenge using the sequential staining approach is effective heat-mediated denaturation of antibody-HRP complex from earlier staining cycles in the sequence, which may artefactually increase signal intensity of targets later in the staining sequence. Thus, the assay was rigorously evaluated for adequate heat-mediated denaturation and subsequently validated as part of a multiplex protocol. Similar approaches for testing efficacy of multiplex sequential immunofluorescence have been previously employed in assay development (Zhang *et al.*, 2017; Lin *et al.*, 2018), though some reports (Parra *et al.*, 2017) have lacked thorough assessment evaluation of heat-mediated denaturation, thereby limiting the reliability of such assays.

The use of multispectral imaging provided assessment of multiple markers previously on the same tissue section in a single imaging step, in contrast to challenges associated with co-registration of low-plex images in approaches involving iterative cycles of staining and imaging.

Once tissue classification and cell segmentation had been optimised, all multispectral images were batch processed to generate a wealth of single cell data for downstream analyses. Widespread spatial, cellular and inter-patient heterogeneity in OXPHOS protein abundance was observed. Intra-patient heterogeneity, however, poses a significant challenge in the analysis of single cell data. Potential approaches to distil such results at the patient level include (a) simple statistical measures such as measurement of mean intensities, which diminish the effect of outliers; (b) measurement of proportion of cells within empirically determined ranges, (c) calculation of H-scores to summarise intensity and proportion data, which were initially designed for semi-quantitative assessment of IHC-DAB images and resulted in loss of dynamic range of markers of interest as previously reported (Camp *et al.*, 2002), and (d) dimensionality reduction methods such as K-means clustering, principal component analyses, t-Distributed Stochastic Neighbour Embedding, the results of which are difficult to interpret intuitively.

This method has potential to greatly reduce costs associated with labour and consumables for the assessment of large numbers of samples. In comparison to the manual method developed by Rocha *et al.* (2015), the automated workflow reduces staining time from a 2-day protocol to a 13-hour protocol that can be run overnight with about 1 hour of hands-on setup time. The concentration of *MTCO1* and *TOMM20* antibodies is already greatly reduced using TSA chemistry, from 1:100 to 1:500 dilution, leading to substantial cost savings. Image acquisition is reduced from approximately 7.5 hours (30 minutes per sample) of hands-on time to 1 hour of set-up time, followed automated image acquisition using the motorised stage and robotic slide handler. Previously the most time-consuming step in applying the conventional assay to prostate tissue sections was manual cell segmentation. The semi-automated segmentation described by Rocha et al was developed primarily for evaluation of muscle biopsy samples with an average diameter of approximately 80-100µm. This method could not be readily translated to the much smaller prostate epithelial cells, with a high nuclear:cytoplasmic ratio. Manual annotation of individual cells was therefore initially undertaken, which was laborious, often requiring many days for each experiment. Batch image processing using trained tissue

and cell segmentation algorithms drastically accelerated the workflow. Previous studies have reported high consistency between results of digital image analysis and experimenter or pathologist assessment. Importantly, prognostic power of biomarkers is also comparable across both approaches (Camp *et al.*, 2002; Rocha *et al.*, 2015; Zarrella *et al.*, 2016).

Taken together, the automated workflow described in this chapter can now be completed in 2 days, from tissue staining to data analysis, as compared to many weeks previously required for evaluating prostate tissue using the conventional manual workflow.

Another emerging concern is the assay reproducibility in biomarker studies. This was evaluated using consecutive patient sections on two separate batches of staining on two separate days. Consistent results were obtained. Though batch effects were minimal, the influence of additional factors such as ambient temperature, antigen preservation after microtomy, and possibility of inter-operator variability, were not comprehensively examined.

4.4.2 Comparison with other multiplex approaches

The vast majority of conventional sequential multiplex IF assay have been developed for immune cell phenotyping (Gerner *et al.*, 2012; Carstens *et al.*, 2017; Feng *et al.*, 2017; Gorris *et al.*, 2018). An iterative improvement in the assay described in this chapter over conventional applications has been the quantitative assessment of protein abundance localised to a sub-cellular organelle, as opposed to the broadly binary assessment of cell phenotypes using nuclear or cytoplasmic markers in previous reports. Assessment of sub-cellular protein abundance has, however, previously been studied using simultaneous multiplexing approaches (Camp *et al.*, 2002) based on deconvolution of Z-stack images.

The extension of this 5-plex assay to additional markers is limited by the maximum number of fluorophores with distinct spectral profiles (estimated at 7 fluorophores), and the requirement of heat-denaturation at each step, which may eventually lead to antigen degradation. Sequential staining approaches have been described recently which may allow detection of up to 60 markers by employing multiple simultaneous multiplexing with batches of 3 fluorescence-labelled markers in each cycle, interspersed by sequential imaging and heat-denaturation steps (Gerdes *et al.*, 2013; Remark *et al.*, 2016; Lin *et al.*, 2018). Similarly, sequential IHC-DAB based multiplex assays have also been described (Tsujikawa *et al.*, 2017; Harder *et al.*, 2018), which include cyclically labelling and imaging the same tissue sections using individual markers, followed by co-registration of all resulting single-plex brightfield

images using fiducial or reference markers. Both such approaches rely heavily on multiple rounds of heat-denaturation, leading to tissue degradation. For instance, 48% of prostate epithelial cells were lost by 10 cycles of staining using the approach outlined by Lin *et al.* (2018), which disproportionally resulted in the loss of luminal cells, thereby potentially biasing subsequent analyses. This cyclical approach is currently carried out manually, making the use of multiple cycles very time consuming and laborious.

Two relatively recent developments may provide alternative methods for the development of highly multiplex assays, including imaging mass cytometry (IMC) and multiplex ion beam imaging (MIBI). These approaches are based on the use of antibodies conjugated to heavy metals isotopes, each of which have a distinct spectral peak on mass spectrometry. In IMC, an inductively coupled time of flight mass spectrometer (CyTOF) is coupled to a laser ablation system (Giesen *et al.*, 2014; Bodenmiller, 2016). The laser ablates tissue spots and resulting particles are transported to the CyTOF instrument for mass spectrometry. In contrast, MIBI uses a secondary ion mass spectrometer where an oxygen ion beam is rastered over tissue at 5-10 nm depth to remove antibody-bound metal isotopes as ions, which then undergo mass spectrometry (Angelo *et al.*, 2014).

The key advantages of these mass spectrometry-based approaches include (a) the ability to target up to 32 markers (using IMC), (b) increased dynamic range, and (c) the absence of tissue background signal, owing to the use of non-biological metals and high signal to noise ratio. Higher order multiplex using IMC and MIBI has been used to improve cell phenotyping and simultaneously probing putative downstream signalling pathways and associated transcripts (Gerner *et al.*, 2012; Giesen *et al.*, 2014; Schulz *et al.*, 2018). The dynamic range of IHC-DAB is 1-1.5, IHC-IF is 1.5-2.5, and of IMC and MIIBI are 5 orders of magnitude (McCabe *et al.*, 2005; Levenson *et al.*, 2015). Increased dynamic range minimises artefacts associated with tissue autofluorescence. In contrast, the autofluorescence spectrum is spectrally unmixed and removed using MSI, which may also, theoretically, diminish true fluorophore signal.

Nevertheless, both IMC and MIBI are relatively low throughput at present. Acquisition of a $1mm^2$ area of tissue, stained for 7 markers, at 200-300 nm lateral resolution for MIBI or 1000 nm lateral resolution for IMC currently takes 6-8 hours (Levenson *et al.*, 2015; Bodenmiller, 2016). This compares to the substantially lower acquisition time of 2-5 minutes for scanning a similar area of tissue at 500 nm lateral resolution for 5 markers using MSI. Thus, MSI allows

greater throughput at higher spatial resolution in comparison to IMC. Following MSI and MIBI, the tissue section can be stained using standard histochemical techniques such as H&E to obtain morphological information since, unlike IMC, tissue degradation using these approaches is minimal.

4.4.3 Future directions

In its current form, the assay can also be used to study other human epithelial tissue. Though the use of a pan-cytokeratin antibody allows the identification of most epithelial cell types, it limits the ability to study differences between different epithelial cell sub-types, such as comparing $CK5^{+}CK14^{+}$ basal cells with $CK8^{+}CK18^{+}$ luminal cells. Since the pan-cytokeratin cycle is at the end of the staining sequence, the current assay can, however, be easily adapted to study individual cell types by replacing pan-cytokeratin with other cell type markers.

The sensitivity and specificity of this can be formally tested using tissue samples from patients with genetically confirmed mitochondrial disorders, or by undertaking laser-capture microdissection and next generation sequencing of regions of OXPHOS defects highlighted by the assay.

In summary, the automated workflow described in this assay provides a high-throughput method for reproducibly evaluating OXPHOS defects in large numbers of archived formalin-fixed human prostate tissue samples.

Chapter 5 OXPHOS alterations in human prostate cancer

5.1 Introduction

5.1.1 Mitochondrial proteomics

Steady state transcriptomic alterations only partially predict target protein abundance, which may also be affected by downstream post-translational alterations or protein degradation (Vogel and Marcotte, 2012; Liu *et al.*, 2016). Two proteomic studies have demonstrated poor or inverse mRNA-protein correlations in prostate cancer (PCa), as previously reported in colorectal (Zhang *et al.*, 2014) and lung cancers (Chen *et al.*, 2002a). These studies further question the reliability of inferring mitochondrial function using transcriptomic data.

Latonen *et al.* (2018) undertook high-throughput mass spectrometry on 10-17 prostate tissue samples with BPH, untreated PCa and castrate-resistant prostate cancer (CRPC). The authors found that proteomic markers of mitochondrial dysfunction were significantly altered in both PCa vs BPH and CRPC vs PCa comparisons. Proteomic data were integrated with previous molecular data including copy number alterations, bisulphite sequencing, RNA sequencing and DNA sequencing. Integrative analyses revealed that mitochondria-related and TCA-related metabolic pathway proteins were found to be differentially altered only using proteomics, and not in transcriptomic data. In contrast, glycolysis related pathways were identified by both transcriptomics and proteomics. Interestingly, with the exception of malate dehydrogenase 2 (*MDH2*) which increased with prostate cancer progression, TCA related pathway proteins were upregulated in PCa vs BPH but downregulated in CRPC vs PCa comparisons.

Iglesias-Gato *et al.* (2018) compared mRNA levels against protein expression from bone metastases from 20 patients undergoing surgery for cord compression and noted poor or even inverse mRNA-protein correlations in a number of biological processes including mitochondrial complex I (Spearman's correlation coefficient -0.48, p=0.003) and oxidative phosphorylation (Spearman's correlation coefficient -0.26, p=0.004).

However, high throughput proteomic studies are currently restricted to a small number of samples, with limited availability of long-term follow-up data. Immunohistochemical validation of potential protein markers in clinically annotated archived tissue samples with

long-term follow-up data would therefore help validate these findings and evaluate the prognostic impact of proteomic alterations.

The results of previous proteomic studies of OXPHOS markers in prostate cancer are summarised in **Table 5-1**. All samples were obtained from patients undergoing radical prostatectomy.

Complex I protein abundance has not been previously evaluated in PCa, except for a single case of complex I loss in a patient with a confirmed ND4 gene mutation (Philley *et al.*, 2016). In contrast, two studies have evaluated subunits of Complex IV in separate PCa tissue micro-array (TMA) cohorts. Moro *et al.* (2009) studied 315 cores from 80 patients and noted reduction of *MT-CO1* expression in 25% tumour cores, as compared to only 1.5% benign cores. The authors found heterogeneous *MT-CO1* expression in 13% of tumour cores. In contrast, Grupp *et al.* (2013) reported homogenously increased *MT-CO2* expression in PCa, with high expression found to be associated with increased risk of biochemical recurrence in *ERG*-negative PCa. Since both *MT-CO1* and *MT-CO2* are mitochondrial-encoded subunits, it is plausible that mtDNA mutations affecting complex IV integrity may bias the use of these subunits as markers of global mitochondrial OXPOS protein abundance.

Electron microscopy studies have noted increased mitochondrial number and volume in tumour regions (Mao *et al.*, 1966; Philley *et al.*, 2016), supported by data linking mitochondrial morphology and increasing Gleason scores (Sun *et al.*, 2012). Using mass spectrometry, Iglesias-Gato *et al.* (2016) noted elevated mitochondrial protein content (*ACAD9* & *NDUFAF1*) in tumour versus patient-matched control tissue (n=9). *ACAD9* is involved in fatty acid B-oxidation, which is known to be upregulated in cancer (Liu, 2006), whereas *NDUFAF1* is a nuclear-encoded assembly factor, the loss of which leads to reduction or loss of Complex I assembly (Vogel *et al.*, 2005; Stroud *et al.*, 2016). However, increased *NDUFAF1* levels may reflect mitochondrial content rather than mitochondrial function. Of note, the authors noted reduced *MAP1BLC3* abundance in tumours, suggesting impaired autophagosome formation, which may lead to reduced mitophagy and increased accumulation of dysfunctional mitochondria.

This demonstrates sparse evidence quantifying Complex I abundance, and conflicting reports regarding markers of complex IV abundance in PCa. None of these reports adjusted complex I or IV abundance for intra-tumoural variation in mitochondrial mass at the single cell level.

Since mitochondrial mass is often increased in most cancers, it is likely that adjustment for mitochondrial mass may result in a further reduction in relative Complex I & IV abundance. The prognostic impact of OXPHOS protein alterations therefore remains unclear.

Study & sample size	Marker	Method	Findings
Subunits of Complex I			
Philley *et al.* (2016)(n=1)	*NDUFB8*	IHC	Loss of NDUFB8 expression in a single patient harbouring the frameshift 11038delA mutation affecting ND4 gene of Complex I.
Subunits of Complex IV			
Herrmann *et al.* (2003) (n=26 IHC, 4 WB, 4 RPPA)	*MT-CO1* *MT-CO2* *COX-IV* *COX-Vb* *COX-Vic*	IHC, RPPA, WB	As compared to normal prostate tissue, PCa had increased expression of nuclear-encoded markers (COX-IV, COX-Vb, COX-Vic), but no change in mitochondrial encoded markers (MT-CO1, MT-CO2).
(Petros *et al.*, 2005) (n=1)	*MT-CO1*	IHC	Loss of MT-CO1 expression in PCa gland relative to adjacent benign gland from a single sample with m.5949G>A mutation.
Moro *et al.* (2009) (n=315 cores from 80 patients, 4-6x 0.6mm cores/case)	*MT-CO1*	IHC	PIN & benign glands had high MTCO1 expression. Low MT-CO1 expression in 25.5% PCa. Higher Gleason score associated with lower MT-CO1 expression.
Grupp *et al.* (2013) (n=8412 cases, 1x 0.6mm core/case)	*MT-CO2*	IHC	Increased MT-CO2 in tumour cores, with higher expression associated with increasing PCa risk features and biochemical recurrence.
Iglesias-Gato *et al.* (2016) (n=28)	n/a	Mass spectrometry	Increased NDUFAF1 (subunit of Complex I) and increased COX activity (n=11) on enzyme histochemistry. Decreased glycolytic markers & markers of autophagosome formation.

Table 5-1: Proteomic studies of mitochondrial OXPHPOS expression. Key studies evaluating complex I and complex IV proteomic alterations in human prostate cancer are reported. Details regarding marker used, method employed, and key findings are listed below. IHC: Immunohistochemistry; RPPA: Reverse phase protein assay; WB: Western blotting.

5.1.2 Tumour heterogeneity impacts biomarker performance

Prostate cancer is frequently multi-focal (Villers *et al.*, 1992) with significant genomic (Boutros *et al.*, 2015), transcriptomic (Salami *et al.*, 2018), and proteomic heterogeneity (Guo *et al.*, 2018). Indeed, recent work on tissue from patients with localised PCa noted multiple sub-clones in 59% of patients, with increasing multi-focality being associated with higher risk of relapse (Espiritu *et al.*, 2018). In this context, making treatment decisions or evaluating biomarkers based on a single low-grade tumour focus may under-estimate the risk determined by a disparate tumour focus that was not adequately sampled at biopsy.

Cyll *et al.* (2017) have previously evaluated the impact of tumour heterogeneity on prognostic performance of DNA ploidy status in PCa patients. The authors noted that determination of DNA ploidy status based upon a single randomly selected core resulted in poor prognostic power. In light of established heterogeneity in Gleason grade across tumour tissue, the researchers evaluated the influence of selecting the patient tissue block with most advanced Gleason grade for prognostication, which improved biomarker performance. In keeping with this finding, categorising patients based upon a single core with lowest DNA ploidy resulted in the most significant improvement in prognostic power. Given the significant impact of heterogeneity on prognostic ability of established biomarkers, and emerging data using gene signature-based risk stratification tools such as Decipher and Polaris, various groups (Cyll *et al.*, 2017; Guo *et al.*, 2018; Salami *et al.*, 2018) therefore recommend multi-region sampling for more accurate evaluation of biomarkers. The minimum number of regions required for adequate sampling is, however, biomarker dependent (Eckel-Passow *et al.*, 2010).

5.1.3 Evaluating biomarker performance in molecular subgroups of PCa

Dependence upon OXPHOS for cancer cell metabolism may also vary by molecular subgroup, including *PTEN* and *TMPRSS2:ERG* status.

5.1.3.1 PTEN status

The *Pi3k/Akt* signalling pathway, regulated by the Phosphatase and tensin homolog (*PTEN*) gene, is upregulated in 42% of localised PCa and all metastatic PCa cases (Taylor *et al.*, 2010). *PTEN* is a dual phosphatase of proteins and lipids, which acts as a tumour suppressor by regulating growth and survival by suppressing the *Pi3k/Akt* signalling pathway. *PTEN* also acts as a metabolic regulator, by negatively regulating glycolysis and glutaminolysis and increasing mitochondrial OXPHOS by upregulating mitochondrial biogenesis (Garcia-Cao *et al.*, 2012).

PTEN loss results in the activation of *Akt* signalling, coupling glucose metabolism to mitochondrial OXPHOS (Gottlob *et al.*, 2001), and increased expression and activity of mitochondrial complex I (Li *et al.*, 2013a). This would suggest that *PTEN*-deficient prostate cancers may be vulnerable to targeted mitochondrial complex I loss. Indeed, this hypothesis has borne out in transgenic studies (Naguib *et al.*, 2018), though the impact of Complex I expression on progression of *PTEN*-deficient human PCa is currently unknown.

5.1.3.2 *TMPRSS2:ERG* fusion status

PCa patients may also be molecularly sub-stratified based upon the erythroblast transformation-specific (*ETS*) rearrangement status. *ETS* are a family of transcription factors, amongst which the *ETS*-related transcription gene (*ERG*) is most frequently dysregulated (Tomlins *et al.*, 2005). The genetic fusion between the *ETS* transcriptional factor related gene (*ERG*) and the androgen-responsive promotor transmembrane protease, serine 2 (*TMPRSS2*) gene, termed *TMPRSS2:ERG* fusion, is the most common gene arrangement in PCa, occurring in approximately half of all PCa patients (Esgueva *et al.*, 2010). Immunohistochemically-detected *ERG* protein expression is highly sensitive for FISH-detected *TMPRSS2:ERG* fusion (Park *et al.*, 2010; Minner *et al.*, 2011). The prognostic value of *ERG*-fusion status varies from none in post-prostatectomy cohorts (Minner *et al.*, 2011; Lippolis *et al.*, 2013), increased risk of progression in active surveillance cohorts (Berg *et al.*, 2014), and predicting good response to androgen deprivation therapy and abiraterone acetate in CRPC cohorts (Attard *et al.*, 2009).

Though the *TMPRSS2:ERG* fusion alone is unable to initiate invasive prostate adenocarcinoma, *TMPRSS2:ERG*-positive cells have greater potential for epithelial-to-mesenchymal transition (EMT), cell invasion and proliferation (Tomlins *et al.*, 2008). They are thought to be more metabolically active as they take up more glucose and have increased fatty acid metabolism (Hansen *et al.*, 2016; Meller *et al.*, 2016).

ERG-positive cells may progress to hyperplastic or PIN lesions, though not invasive carcinoma (Klezovitch *et al.*, 2008; Tomlins *et al.*, 2008; Zong *et al.*, 2009). However, ERG overexpression may synergise with alternative oncogenic signalling pathways, including the *Pi3k/Akt* signalling, to progress to invasive adenocarcinoma. ERG overexpression enriches for *PTEN*-loss (Carver *et al.*, 2009; King *et al.*, 2009), restores transcriptional activity of the androgen receptor in *Pten*-deficient mice (Chen *et al.*, 2013b) and promotes progression of HGPIN lesions to adenocarcinoma in mice with *Pten* haploinsufficiency (Carver *et al.*, 2009). Co-occurrence of *PTEN* loss with *ERG*-fusion is an independent predictor of biochemical

recurrence (Yoshimoto *et al.*, 2008). Therefore, *ERG*-positive *PTEN*-deficient PCa defines a poor prognostic sub-group of patients with PCa.

Interestingly, in the Grupp *et al.* (2013) study discussed in section 5.1.1, increased mitochondrial mass was associated with an increased risk of biochemical recurrence amongst *ERG*-negative PCa patients with proficient *PTEN*, but not *PTEN*-loss, further emphasising the importance of evaluating the impact of mitochondrial function amongst distinct molecular subgroups of PCa.

5.1.4 Chapter aims

In this chapter, archived prostate tissue samples are interrogated for proteomic alterations in oxidative phosphorylation (OXPHOS) which are then correlated with long-term overall survival. Specifically, as outlined in Chapter 4, *NDUFB8* and *MT-CO1* are used as surrogate markers of mitochondrial complex I integrity and complex IV integrity, since these components of mitochondrial OXPHOS are most often affected in prostate cancer. *VDAC1* and *TOMM20* are used as markers of mitochondrial mass.

The key objectives of this chapter are to:

1. Assess pattern and frequency of OXPHOS protein alterations in benign and malignant human prostate tissue.
2. Evaluate association between OXPHOS protein abundance, advancing age and established clinical risk features of high-risk prostate cancer.
3. Assess association between OXPHOS protein abundance and long-term survival in patients in defined molecular sub-groups of prostate cancer, including *PTEN* and *TMPRSS2:ERG* status.

5.2 Results

5.2.1 OXPHOS protein abundance in human prostate tissue

As observed in other mitotic tissues, OXPHOS defects are hypothesised to accumulate with advancing age. The pattern of OXPHOS defects was therefore initially evaluated in benign prostate tissue from a 57-year old patient undergoing a transurethral resection of the prostate (TURP) and labelled with mitochondrial markers, using a manual protocol described in section 4.2.5. Scattered epithelial cells subjectively deficient in *NDUFB8*, a core subunit of complex I subunit, were observed within individual glands, with otherwise low regional heterogeneity (**Figure 5-1**). Notably, tissue edges demonstrated artefacts likely associated with the use of diathermy during TURP.

In contrast, distinct regions of variable OXPHOS protein abundance were noted in channel TURP prostate tissue from an 88-year old patient with advanced castrate-resistant prostate cancer, characterised by Gleason 4+5=9, clinical tumour stage 3, diagnostic PSA 58.7, and bone metastases (**Figure 5-2**). Notably, variation in mitochondrial mass were observed across adjacent regions, including highly variable expression of mitochondrial targets *NDUFB8*, and *MT-CO1*, a mitochondrial-encoded subunit of Complex IV. Mitochondrial mass marker, *VDAC1*, was also grossly increased in this PCa sample, in comparison to benign prostate tissue discussed above.

These findings suggested gross variations in OXPHOS protein abundance characterised by marked upregulation in mitochondrial mass in malignant tissue, associated with highly heterogeneous expression of Complex I and Complex IV markers, in comparison to benign prostate tissue. However, the use of this methodology was limited by autofluorescence, absence of a nuclear marker, poor signal to noise, and long scanning times required for whole slide imaging. These limitations precluded more detailed quantiative evaluation of OXPHOS defects using manual labelling and imaging approaches with individual patient samples at acceptable throughput.

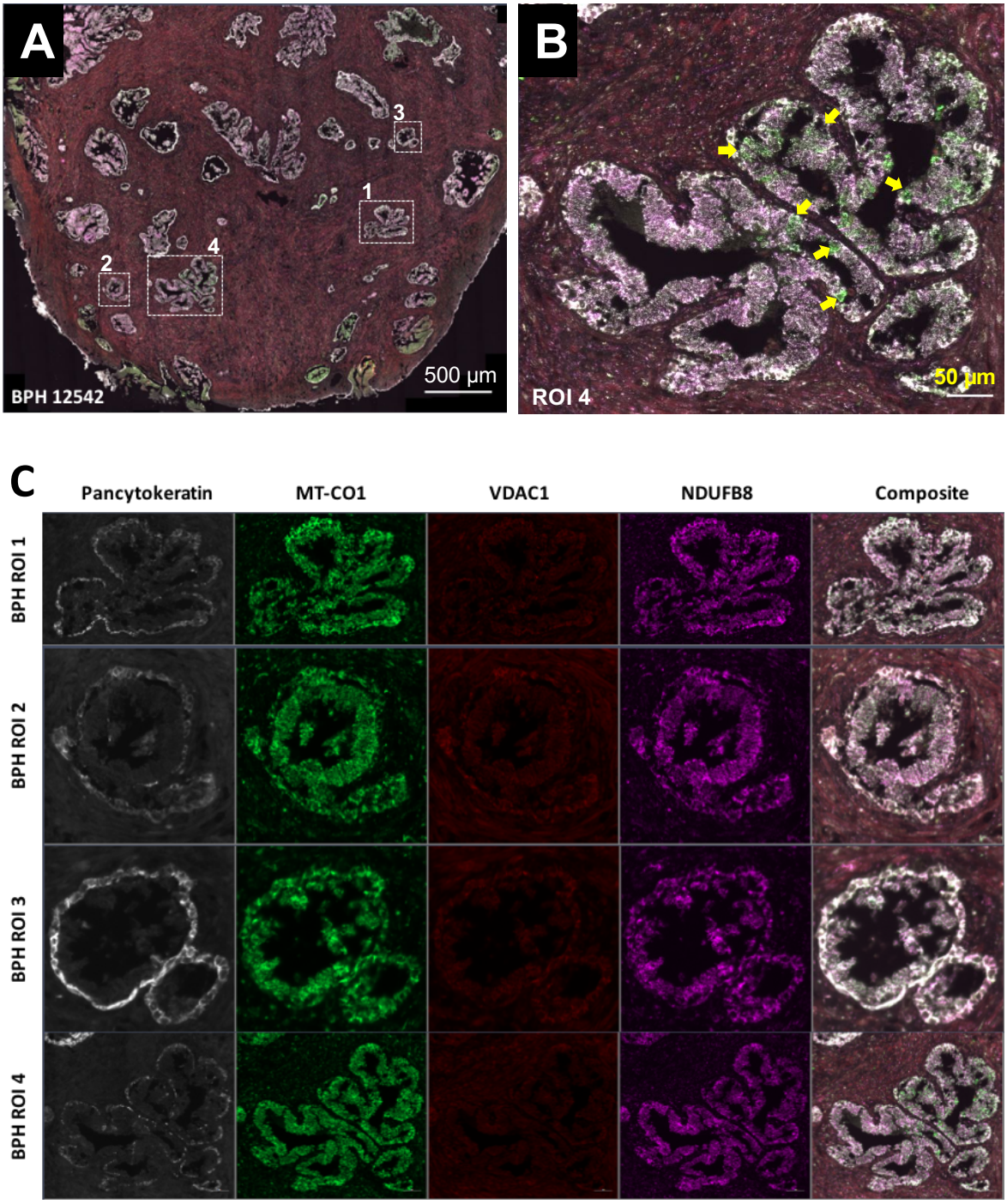

Figure 5-1: Immunofluorescence imaging of TURP tissue from a 57 year-old patient with benign prostatic hyperplasia (BPH). Fluorescence detection using pan-cytokeratin (white, 405 nm), *MTCO1* (green, 488 nm), *VDAC1* (red, 546 nm), and *NDUFB8* (purple, 647 nm). **(A)** Tiled representative region of BPH tissue. Scale bar represents 500µm. **(B)** Composite image of a region of interest demonstrating individual cells with *NDUFB8* deficiency (yellow arrows) within a single gland. Scale bar represents 50µm. **(C)** Separated channels of four regions of interest demonstrate comparable global mitochondrial protein abundance across tissue.

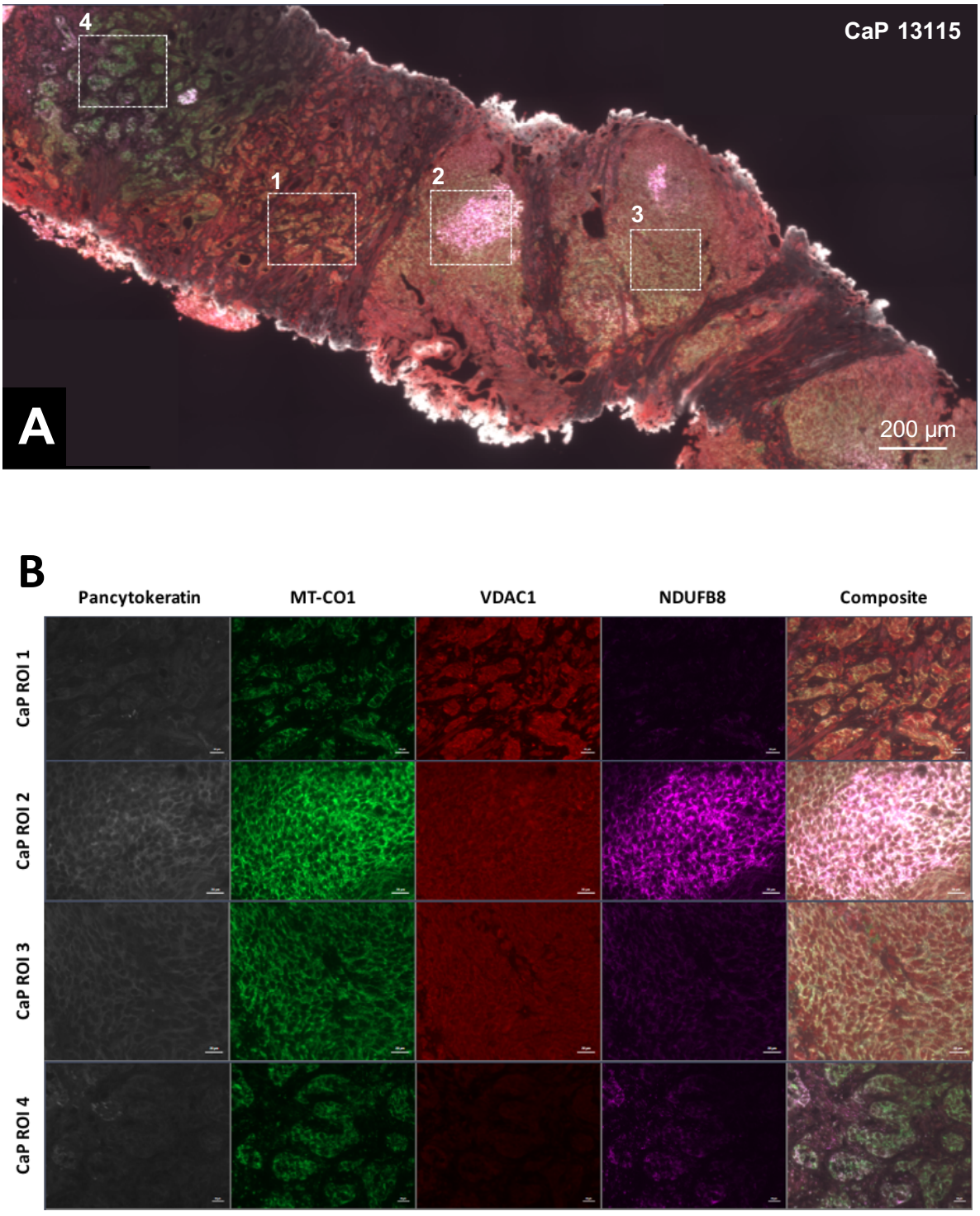

Figure 5-2: Immunofluorescence imaging of TURP tissue from an 88 year old male with a background of advanced castrate-resistant prostate cancer. Fluorescence detection was performed as in figure 3. **(A)** Tiled representative region of PCa tissue noting widespread variation in mitochondrial protein abundance. Scale bar represents 200µm. **(B)** Separated channels of four regions of interest highlighting relative reduction in *NDUFB8* abundance in ROIs 1, 3 and 4, and high abundance of *MTCO1* and *NDUFB8* in ROI 2, in comparison in BPH tissue (**Figure 5-1**). Increased mitochondrial mass noted in ROIs 1-3. Scale bar represents 20µm.

5.2.2 OXPHOS alteration in human PCa tissue micro-arrays

In order to evaluate OXPHOS alterations in a larger cohort of patients, and address limitations of the approach outlined in section 5.2.1, tissue micro-arrays (TMAs) comprising prostate tissue samples from four patient cohorts were sourced from centres at Manchester (MCR) and Newcastle-upon-Tyne (NCL). The TMAs are henceforth referred to by the originating centre (MCR or NCL) and tissue type (RP, TURP, and biopsy). Details of TMA construction are outlined in section 2.2.3.

5.2.2.1 Characteristics of TMA cohorts

Altogether, the TMAs consisted of 3709 cores from 575 patients, spread over 39 TMA blocks. Clinical characteristics of patients with tumour cores available for analysis are presented in **Table 5-2**. Prostate tissue samples from 10 patients at a variety of ages without histopathological evidence of prostate cancer were included as controls (referred to as '*MCR benign*', see section 2.2.3.2 for details).

Based on criteria outline in section 2.2.3.4, TURP and biopsy cohorts comprised of patients with primarily high-risk and metastatic disease at presentation. Consistent with contemporary clinical practice, the radical prostatectomy (RP) cohort comprised of patients with low or intermediate risk disease (**Figure 5-3**).

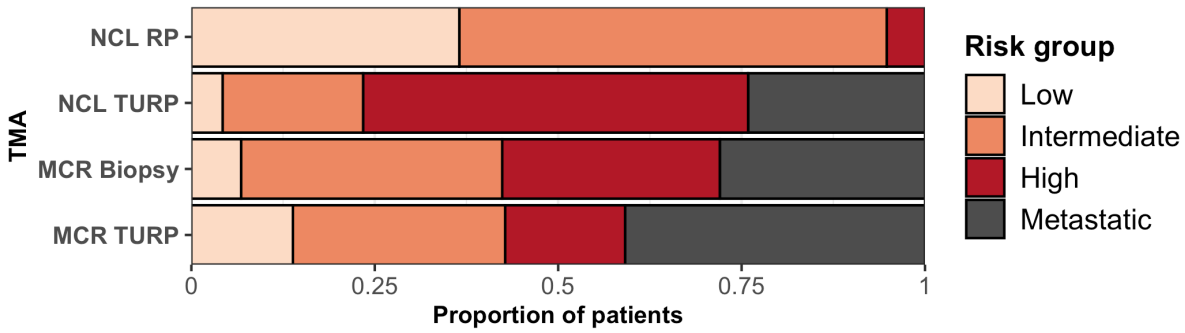

Figure 5-3: Prostate cancer risk groups of patients included in TMAs. Risk groups were defined as follows: low (T1, Gleason group 1-2, and PSA <10); intermediate (T2, or Gleason group 3, or PSA10-20); high (T3-T4, or Gleason group 4-5, or PSA>20); and metastatic (any tumour stage, any Gleason score, PSA > 100 or presence of distant metastases).

		Manchester (MCR)		Newcastle (NCL)		
		TURP	Biopsy	TURP	RP	Total
Total patients		145	134	123	104	506
Age	Median (IQR)	74 (10)	71 (11)	73 (11)	62 (7.25)	70 (14)
Age group	<65 years	23 (15.9)	25 (18.7)	15 (12.2)	76 (73.1)	139 (27.5)
	65-74 years	44 (30.3)	51 (38.1)	44 (35.8)	28 (26.9)	167 (33.0)
	>74 years	65 (44.8)	43 (32.1)	50 (40.7)	0 (0.0)	158 (31.2)
	Missing	13 (9.0)	15 (11.2)	14 (11.4)	0 (0.0)	42 (8.3)
PSA	Median (IQR)	39.5 (102)	32 (76)	43 (91.5)	7.85 (6.8)	26 (66)
PSA group	0-9.9	26 (17.9)	15 (11.2)	4 (3.3)	36 (34.6)	81 (16.0)
	10-19.9	16 (11.0)	26 (19.4)	7 (5.7)	14 (13.5)	63 (12.5)
	20-99.9	54 (37.2)	53 (39.6)	22 (17.9)	4 (3.8)	133 (26.3)
	>=100	35 (24.1)	24 (17.9)	13 (10.6)	0 (0.0)	72 (14.2)
	Missing	14 (9.7)	16 (11.9)	77 (62.6)	50 (48.1)	157 (31.0)
Gleason group	GG1	23 (15.9)	21 (15.7)	27 (22.0)	43 (41.3)	114 (22.5)
	GG2	10 (6.9)	24 (17.9)	6 (4.9)	47 (45.2)	87 (17.2)
	GG3	7 (4.8)	15 (11.2)	10 (8.1)	6 (5.8)	38 (7.5)
	GG4	38 (26.2)	15 (11.2)	34 (27.6)	6 (5.8)	93 (18.4)
	GG5	56 (38.6)	21 (15.7)	27 (22.0)	1 (1.0)	105 (20.8)
	Missing	11 (7.6)	38 (28.4)	19 (15.4)	1 (1.0)	69 (13.6)
Clinical tumour stage	T1-T2	49 (33.8)	43 (32.1)	30 (24.4)	46 (44.2)	168 (33.2)
	T3	48 (33.1)	49 (36.6)	18 (14.6)	1 (1.0)	116 (22.9)
	T4	31 (21.4)	20 (14.9)	11 (8.9)	0 (0.0)	62 (12.3)
	Missing	17 (11.7)	22 (16.4)	64 (52.0)	57 (54.8)	160 (31.6)
Metastasis stage at diagnosis	M0	55 (37.9)	53 (39.6)	65 (52.8)	104 (100.0)	277 (54.7)
	M1	41 (28.3)	27 (20.1)	18 (14.6)	0 (0.0)	86 (17.0)
	Mx	49 (33.8)	54 (40.3)	40 (32.5)	0 (0.0)	143 (28.3)
Initial treatment received	Conservative	11 (13.3)	6 (7.2)	6 (7.6)	0 (0.0)	23 (6.6)
	Hormonal	29 (34.9)	28 (33.7)	57 (72.2)	0 (0.0)	114 (32.7)
	Radical	13 (15.7)	15 (18.1)	0 (0.0)	104 (100.0)	132 (37.8)
	Unknown	30 (36.1)	34 (41.0)	16 (20.3)	0 (0.0)	80 (22.9)
Cause of death	Alive at last FU	25 (17.2)	28 (20.9)	20 (18.5)	69 (74.2)	142 (29.6)
	Prostate cancer	41 (28.3)	30 (22.4)	40 (37.0)	0 (0.0)	111 (23.1)
	Other cause	74 (51.0)	63 (47.0)	30 (27.8)	5 (5.4)	172 (35.8)
	Missing	5 (3.4)	13 (9.7)	18 (16.7)	19 (20.4)	55 (11.5)

Table 5-2: Clinical characteristics of patients with tumour cores included in TMA analysis. Percentages reported in brackets, unless otherwise stated. Group-wise proportions were compared using generalised linear models, with $p<0.001$ confirming variation between the four included TMA cohorts. IQR: Inter-quartile range. FU: Follow-up.

5.2.2.2 OXPHOS protein abundance in PCa TMA

A 4µm tissue section from each TMA and control tissue block was subjected to the automated quantitative OXPHOS staining workflow described in Chapter 4. Briefly, this comprised of automated staining on the Ventana Discovery Ultra platform with the following markers: *NDUFB8* (Complex I sub-unit), *MT-CO1* (Complex IV sub-unit), *TOMM20* (mitochondrial mass marker) and pan-cytokeratin (epithelial cell marker). Labelled tissue sections were imaged on a Vectra 3 multi-spectral microscope with an automated stage controller and robotic slide loader. All tissue sections were stained using the same batch of reagents and imaged in the same experiment to minimise technical artefacts.

Multispectral images were linearly unmixed, and batch processed on InForm Tissue Studio software. Each image was then manually quality checked for technical and tissue artefacts individually. Z-scores for mitochondrial markers were calculated with reference to a control cohort comprising of patients without histopathological evidence of prostate cancer, aged 45 years or below. Z-scores are therefore used as a measure of relative OXPHOS protein abundance. Since deficiency in *NDUFB8* and *MTCO1* is associated with loss of complex I and complex IV respectively (Rocha *et al.*, 2015), these terms have been used interchangeably.

Data were available for a total of 3,374,343 epithelial cells from 2,094 tissue cores (approx. 1600 cells per core) from 578 patients (approx. 5800 cells per patient). Of these, data from suitable tumour cores were available for 506 patients, following quality control checks. Mean z-scores were calculated for each of the three markers at core-level and patient-level, stratified by core type (normal-adjacent, PIN, or tumour core).

Representative spectrally unmixed immunofluorescence images, corresponding pseudo-images and associated mitochondrial respiratory chain (MRC) graphs for TOMM20 (**Figure 5-4**), *NDUFB8* (**Figure 5-5**), and *MTCO1* (**Figure 5-6**) are shown.

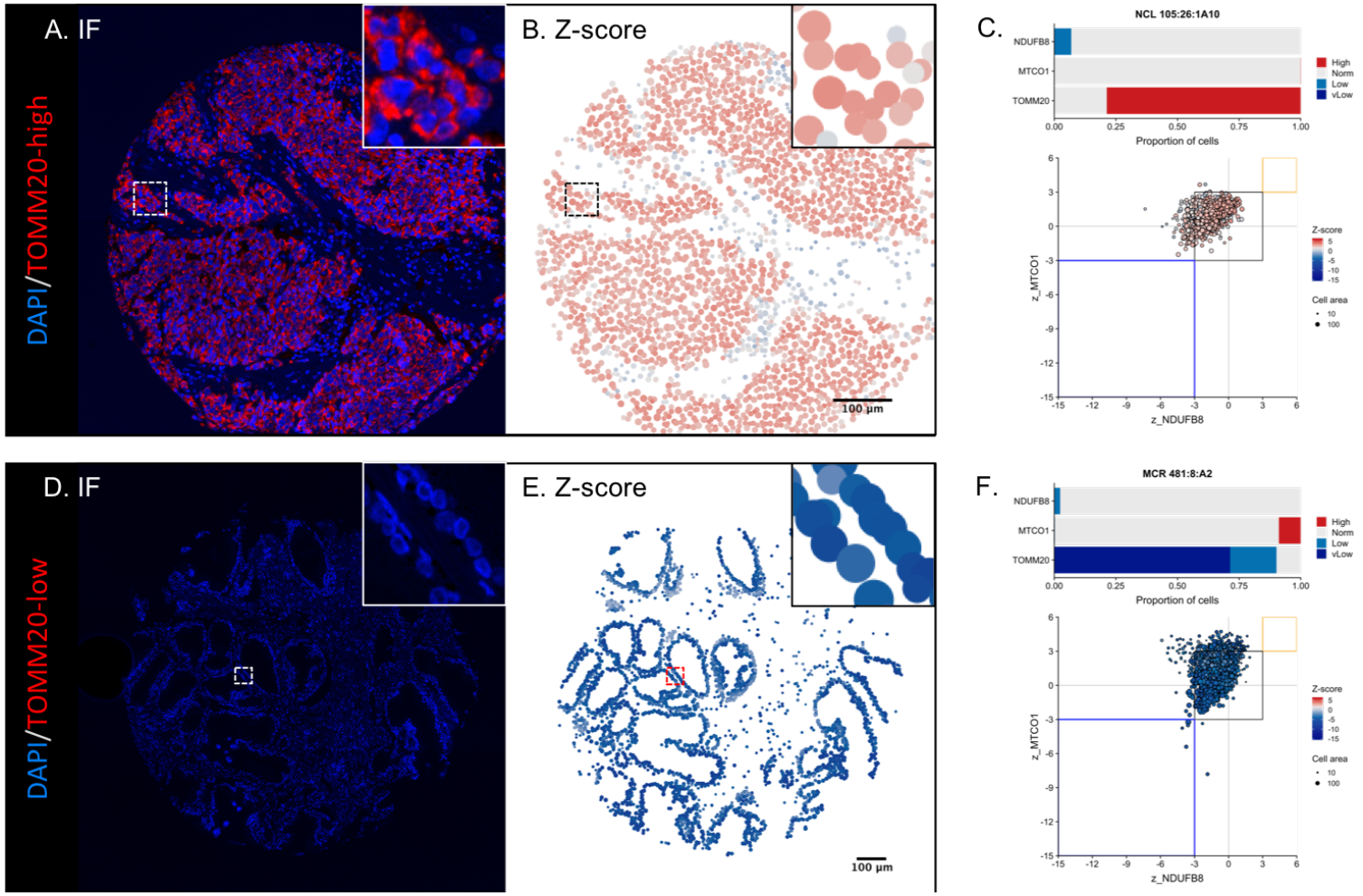

Figure 5-4: Representative images of *TOMM20* protein abundance. (A, D) *TOMM20* immunofluorescence with DAPI counterstaining, **(B, E)** *TOMM20* Z-score pseudo-images and **(C, F)** associated MRC graphs represent cores with either (A-C) high or (D-F) low *TOMM20* expression. Each point in the MRC graph represents an individual cell, with colour denoting *TOMM20* Z-score (*blue*: low; *red*:high) and size denoting cell area. Scale bar represents 100µm.

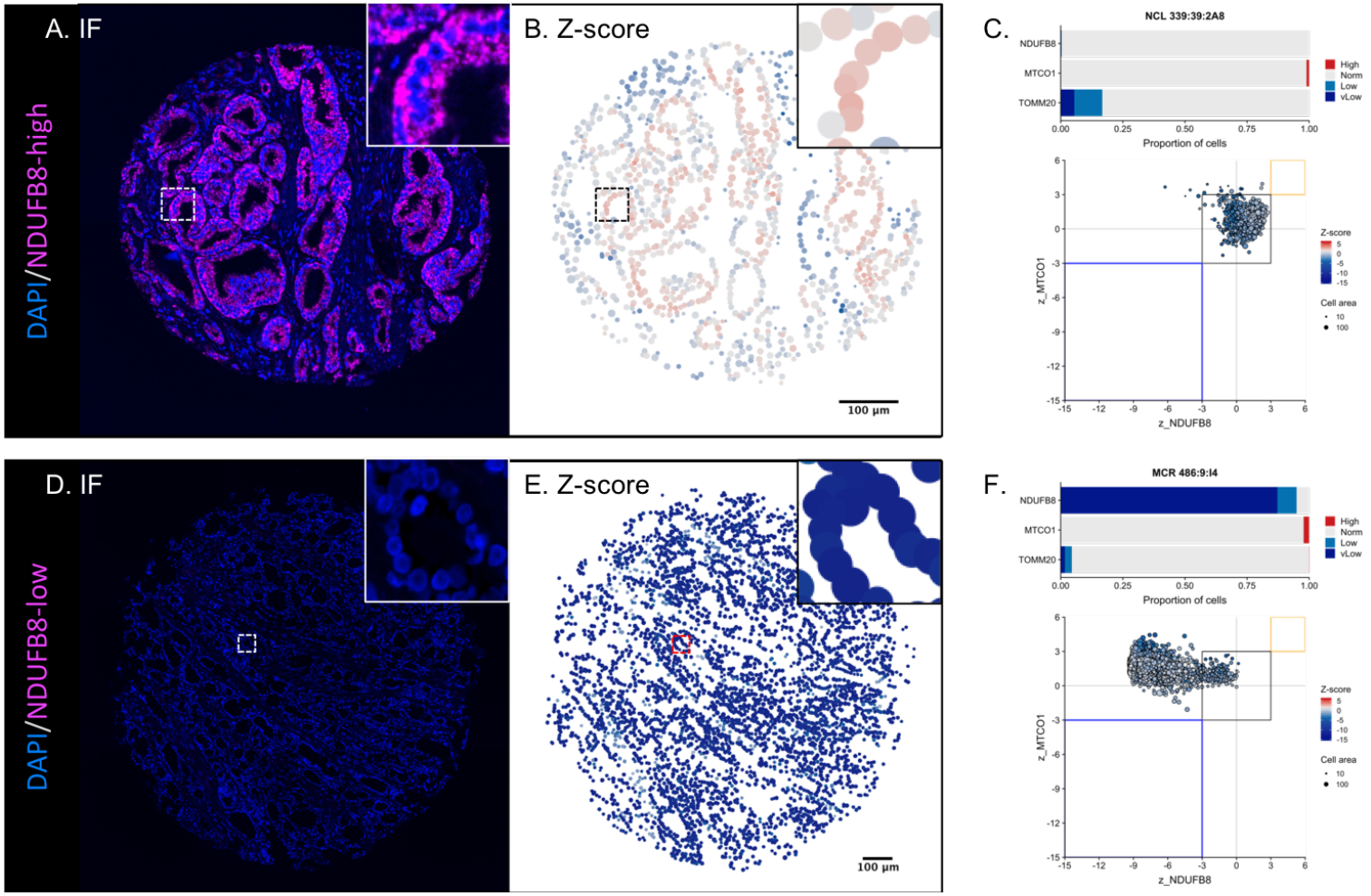

Figure 5-5: Representative images of *NDUFB8* protein abundance. **(A, D)** *NDUFB8* immunofluorescence with DAPI counterstaining, **(B, E)** *NDUFB8* Z-score pseudo-images and **(C, F)** associated MRC graphs represent cores with either (A-C) high or (D-F) low *NDUFB8* expression. Each point in the MRC graph represents an individual cell, with colour denoting *NDUFB8* Z-score (*blue*: low, *red*: high) and size denoting cell area. Scale bar represents 100µm.

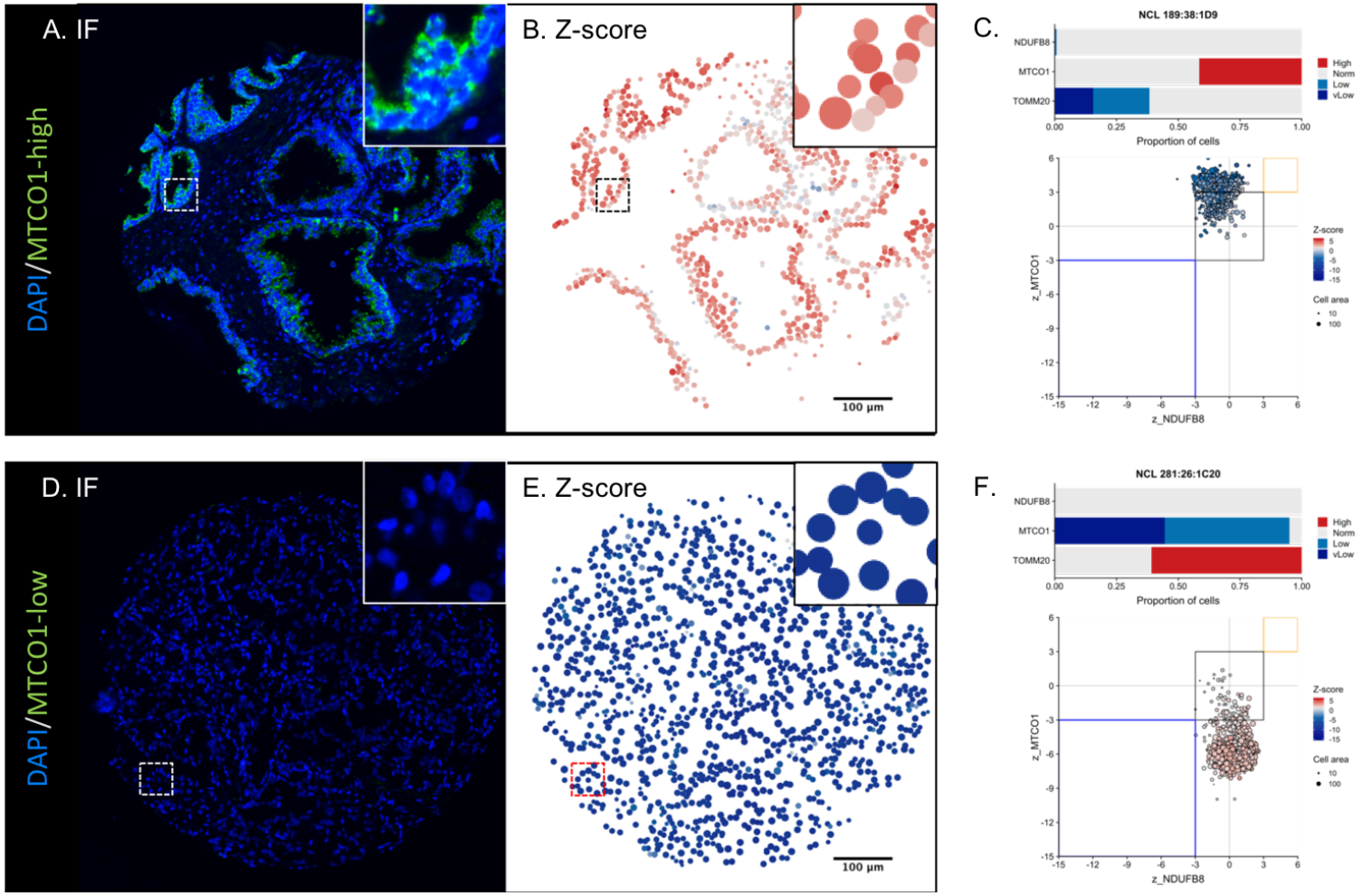

Figure 5-6: Representative images of *MTCO1* protein abundance. (A, D) *MTCO1* immunofluorescence with DAPI counterstaining, **(B, E)** *MTCO1* Z-score pseudo-images and **(C, F)** associated MRC graphs represent cores with either (A-C) high or (D-F) low *MTCO1* expression. Each point in the MRC graph represents an individual cell, with colour denoting *MTCO1* Z-score (*blue*: low; *red*: high) and size denoting cell area. Scale bar represents 100µm.

5.2.2.3 Mitochondrial mass in tumour cores is greater than normal-adjacent cores

OXPHOS protein abundance was evaluated in 152 patients with paired tumour and non-tumour cores to assess potential changes during carcinogenesis, using mean z-scores across all cells within all cores of each core type for each patient (**Figure 5-7**).

As noted in section 5.2.1, mitochondrial mass was again higher in tumour cores, as compared to normal-adjacent cores in both MCR TURP (T 0.16 vs NA -0.4, Δ 0.56, p<0.001), and NCL RP cohorts (T -0.58 vs NA -0.98, Δ 0.40, p=0.029). PIN cores had higher mitochondrial mass compared to tumour cores in the Newcastle RP cohort (PIN: 0.01 vs T 0.58, Δ 0.59, p=0.014). This raises the possibility that mitochondrial mass may change dynamically during stages of cancer initiation, potentially reflecting changing metabolic requirements. These findings are corroborated by previous data using *MT-CO2* as a marker of mitochondrial mass by Grupp *et al.* (2013).

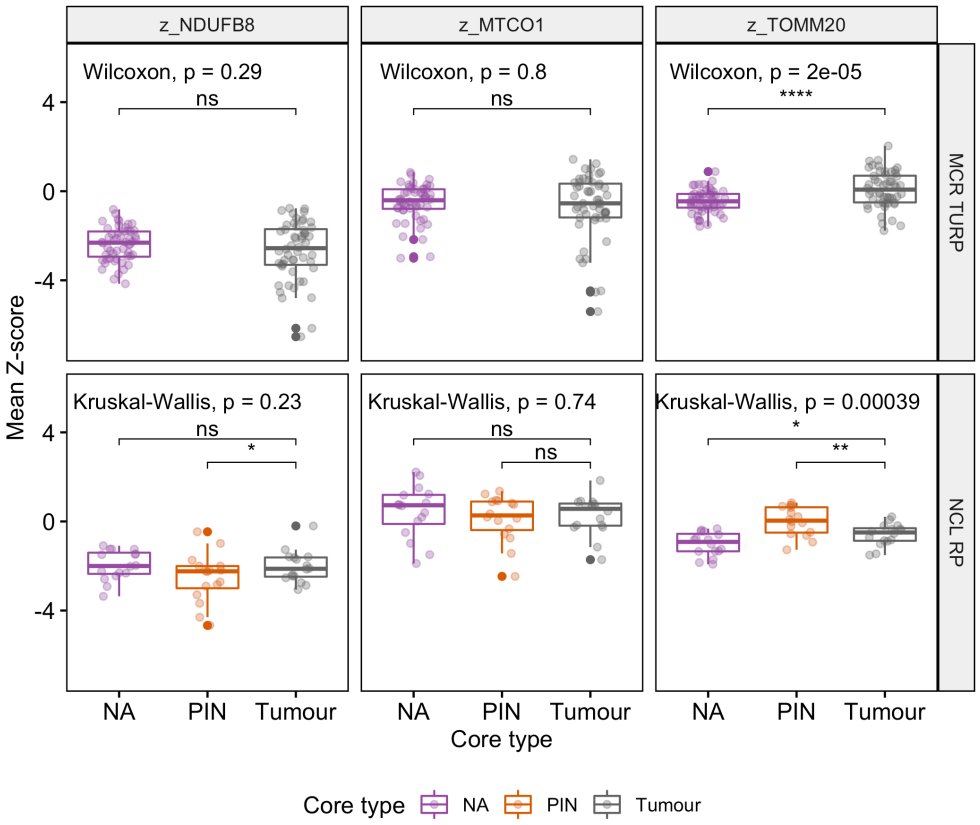

Figure 5-7: OXPHOS protein abundance by core type. Mean patient-level OXPHOS protein abundance measured amongst 152 patients with paired tumour and non-tumour cores were evaluated (n=104 patients from MCR TURP cohort and 48 patients from NCL RP cohort). The Wilcoxon rank test (non-parametric comparison of 2 groups) and Kruskal-Wallis test (non-parametric comparison of 3 groups) were used to calculate p-values, which are denoted as '*', '**', '***', and '****' for p<0.05, p<0.01, p < 0.001, and p<0.0001, respectively.

In contrast, tumour and normal-adjacent cores had comparable complex I z-scores (p>0.2 in both cohorts), and complex IV abundance between core types was observed in either cohort (p>0.7 in both cohorts).

5.2.2.4 OXPHOS protein abundance does not alter with advancing age in human prostate tissue

OXPHOS defects accumulate with advancing age in a number of mitotic tissues, including intestine (Taylor *et al.*, 2003), liver (Stocco *et al.*, 1977), and testes (Jiang *et al.*, 2017), and post-mitotic tissues including heart (Gomez *et al.*, 2009) brain (Frenzel *et al.*, 2010) and skeletal muscles (Lombardi *et al.*, 2009). Therefore, this phenomenon was first evaluated in non-malignant prostate tissue from 12 patients undergoing radical cystoprostatectomy for bladder cancer with benign prostate histology, and amongst cohorts of normal-adjacent TURP and radical prostatectomy cores. Patient-level mean z-scores for *NDUFB8*, *MTCO1* and *TOMM20* were not found to be correlated with advancing age in both benign and normal-adjacent prostate tissue (p-values > 0.1 in all cohorts amongst all three markers, see **Figure 5-8**). Tumour cores from prostate biopsy, TURP and RP tissue also lacked association between age and OXPHOS z-scores (p-values > 0.1 all cohorts amongst the three markers, see **Figure 5-9**), likely due to the small number of patients aged <55 years and >80 years.

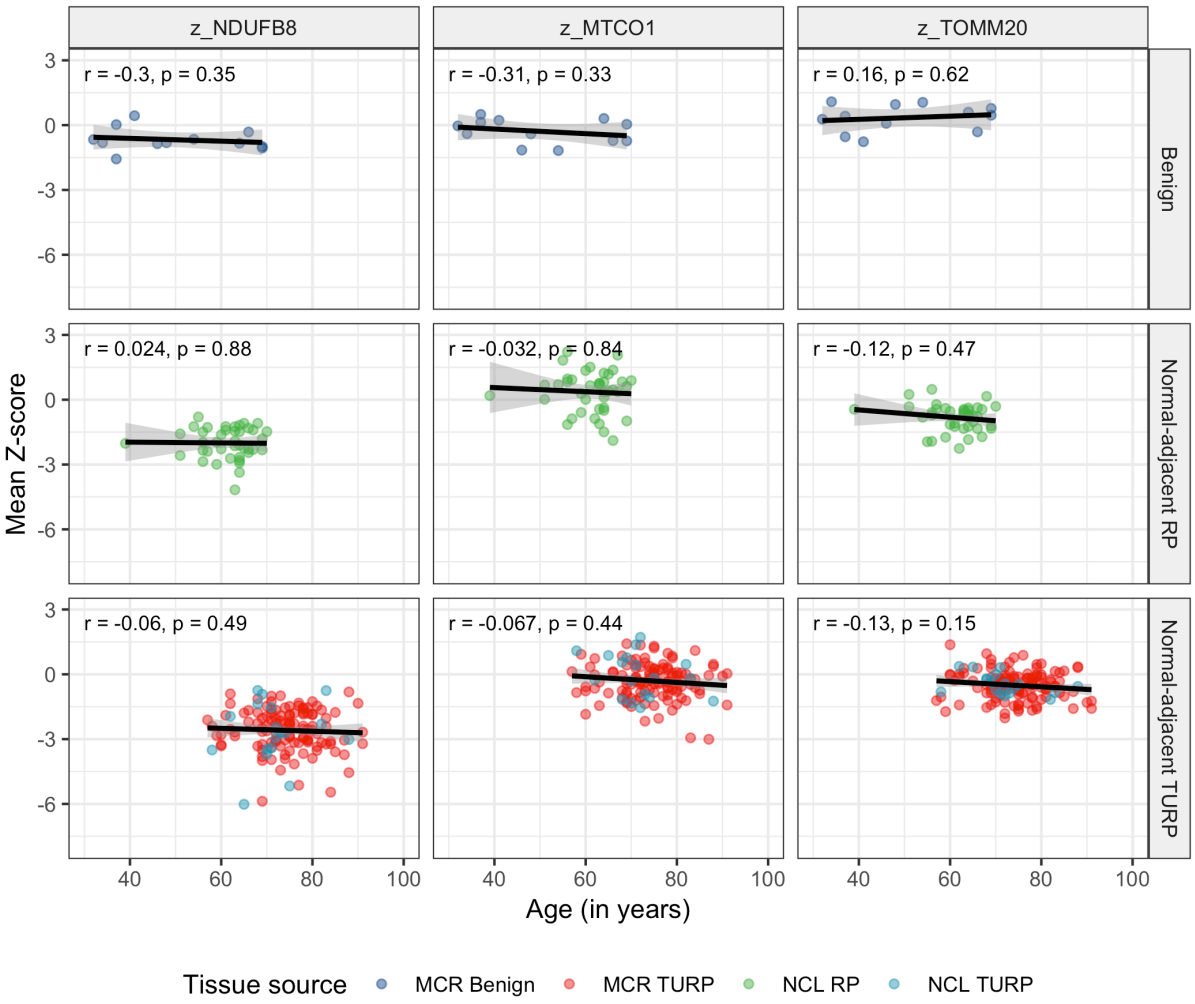

Figure 5-8: Association between age and OXPHOS protein abundance in non-malignant human prostate tissue. Patient-level mean OXPHOS protein abundance measured in 12 patients with benign prostate histology, 136 normal-adjacent tissue samples from patients undergoing TURP and 41 patients who underwent RP, following a diagnosis of prostate cancer. No correlation between advancing age and OXPHOS protein abundance were observed. Spearman's rank correlation coefficients and *p*-values reported.

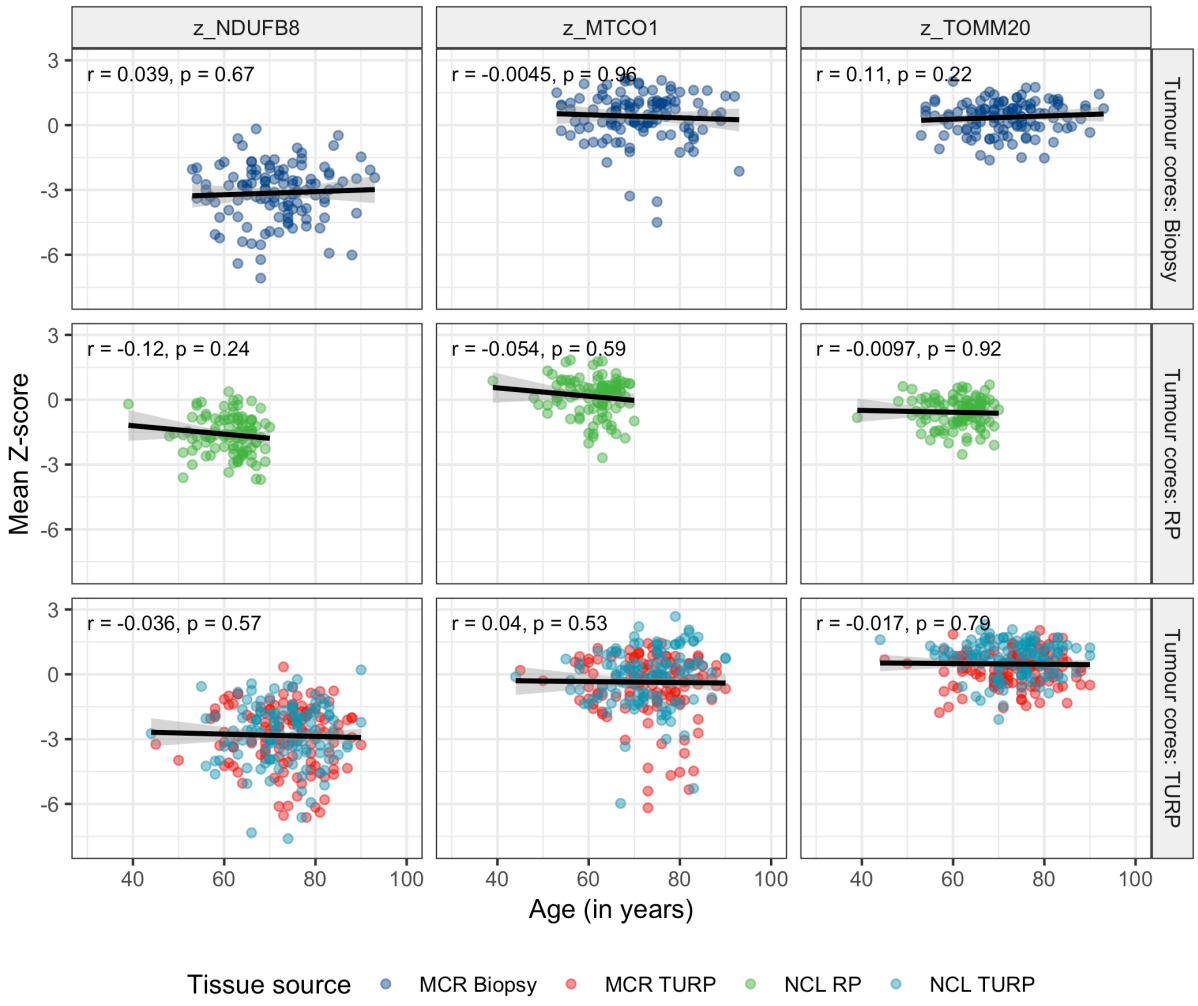

Figure 5-9: Association between age and OXPHOS protein abundance in malignant human prostate tissue. Patient-level mean OXPHOS protein abundance measured in tumor cores from 119 patients undergoing prostate biopsy (MCR Biopsy cohort), 249 patients undergoing TURP (129 from MCR TURP and 120 from NCL TURP cohort), and 104 patients undergoing RP (NCL RP cohort). No correlation between advancing age and OXPHOS protein abundance were observed. Spearman's rank correlation coefficients and *p*-values reported.

5.2.2.5 OXPHOS protein abundance varies by TMA cohorts and prostate cancer risk group

Substantial variation in z-scores amongst the four TMA cohorts was noted for all markers (**Figure 5-10A**). The NCL RP cohort had notably higher complex I (NCL RP: -1.61 in 104 patients vs rest: -2.93 in 357 patients, Δ 1.32, p<0.0001) and lower mitochondrial mass (NCL RP: -0.58 in 104 patients vs rest: 0.42 in 357 patients, Δ -1.0, p=0.03), whereas the MCR TURP cohort had lower Complex IV abundance (MCR TURP: -0.58 in 129 patients vs rest: 0.19 in 332 patients, Δ -0.77, p<0.0001).

Therefore, potential sources of this observed variation between TMA cohorts were considered, and broadly divided into technical and clinical features. Technical features included variation in antigen preservation, formalin fixation, and diathermy artefacts in TURP samples. It was estimated that technical features of TURP and biopsy cohorts were more similar, as compared to RP tissue. TURP cores were likely to have more frequent areas of diathermy artefacts, whereas edge effects and tissue loss may be more frequent in biopsy cores. In contrast, RP tissue was likely to have greater tissue integrity due to the larger specimen size and rapid fixation in formalin following surgical resection.

Variation in clinical features may be due to random selection of tumour regions at initial TMA construction, and variable distribution of PCa risk factors, such as age, ethnicity, Gleason group, tumour stage, diagnostic PSA, and presence of metastases. Ethnicity data were unavailable though the vast majority of patients across all cohorts are likely to be Caucasian, in keeping with contemporaneous local population statistics. Of note, younger patients with early stage and lower grade PCa were more frequently offered radical prostatectomy, which biased the NCL RP cohort towards a predominantly lower risk group.

Patients with high risk features had significantly lower complex I (very high risk: -3.0, vs low risk: -1.99, Δ -1.01, p<0.001), and higher mitochondrial mass (very high risk: 0.54, vs low risk: -0.41, Δ -0.95, p<0.0001, **Figure 5-10B**). No association between complex IV and risk group was observed (p=0.23).

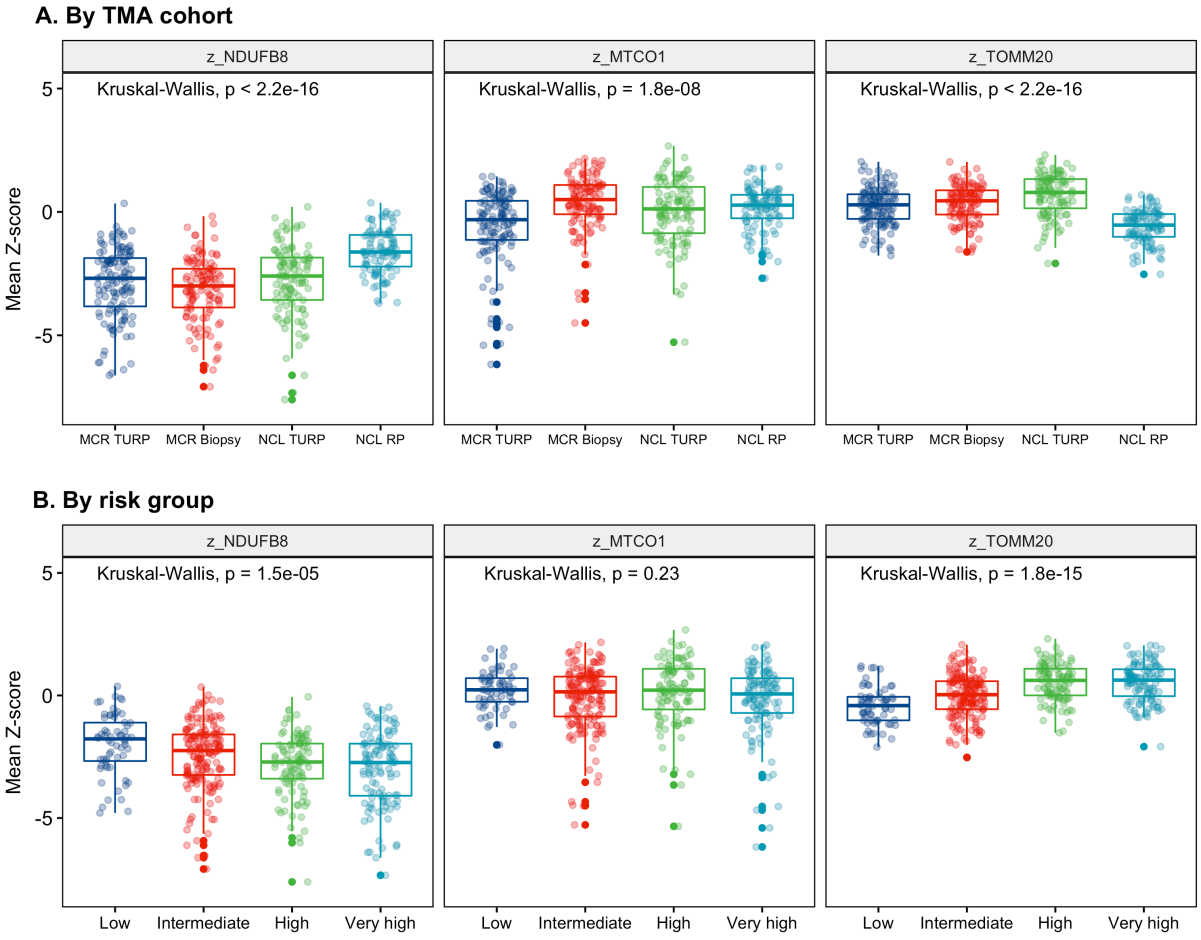

Figure 5-10: Global variation in OXPHOS protein abundance amongst PCa tumour cores. Mean patient-level OXPHOS protein abundance was evaluated from tumour cores from 506 patients, stratified by **(A)** TMA cohort, and **(B)** risk group. *P* value from Kruskall Wallis one-way ANOVA test reported.

5.2.2.6 Low Complex I and high mitochondrial mass in tumour cores are associated with high risk clinical features

The association between OXPHOS protein abundance and established prostate cancer risk features were evaluated individually, and tested using one-way ANOVA, except presence of metastases which was tested using the Wilcoxon rank test.

Amongst tumour cores (**Figure 5-11**), consistent with risk stratification in section 5.2.2.5, low *NDUFB8* and high *TOMM20* mean z-scores were observed with increasing PSA (*NDUFB8*: p=0.024, *TOMM20*: p=2.8x10^{-7}), Gleason group (*NDUFB8*: p=6.8x10^{-5}, *TOMM20*: p=8x10^{-12}), tumour stage (*NDUFB8*: p=1.4x10^{-5}, *TOMM20*: p=3.9x10^{-5}) and in the presence of metastases (*NDUFB8*: p=3.4x10^{-4}, *TOMM20*: p=6.8x10^{-9}). *MTCO1* z-score did not vary significantly with increasing risk features (PSA group: p=0.071; Gleason group: p=0.23; tumour stage: p=0.2; presence of metastasis: p=0.94).

OXPHOS protein abundance in normal-adjacent cores was not associated with clinical risk features either individually (p>0.05 across all comparisons, except *NDUFB8* vs Gleason group where p=0.031, **Figure 5-12**), or upon composite risk stratification (p>0.1 across all comparisons, **Figure 5-13**).

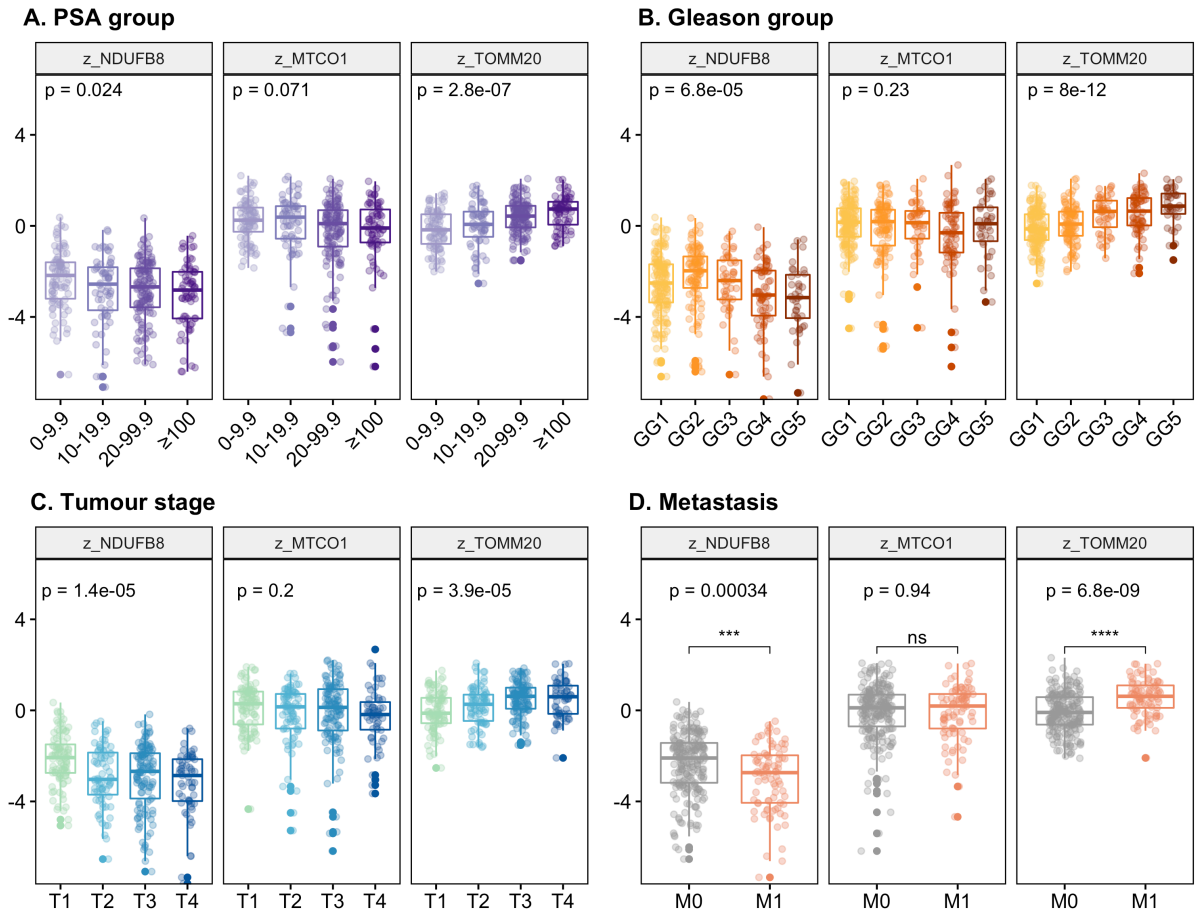

Figure 5-11: OXPHOS protein abundance and clinical risk features: tumour cores. Patient-level tumour core mean epithelial Z-scores were stratified by **(A)** PSA group, **(B)** Gleason group, **(C)** clinical tumour stage, and **(D)** presence of metastasis. *P* value from Kruskall Wallis test one-way ANOVA reported for PSA group, Gleason group, and tumour stage. *P* value from Wilcoxon rank test for presence of metastasis reported. *** denotes p<0.001 and **** denotes p<0.0001.

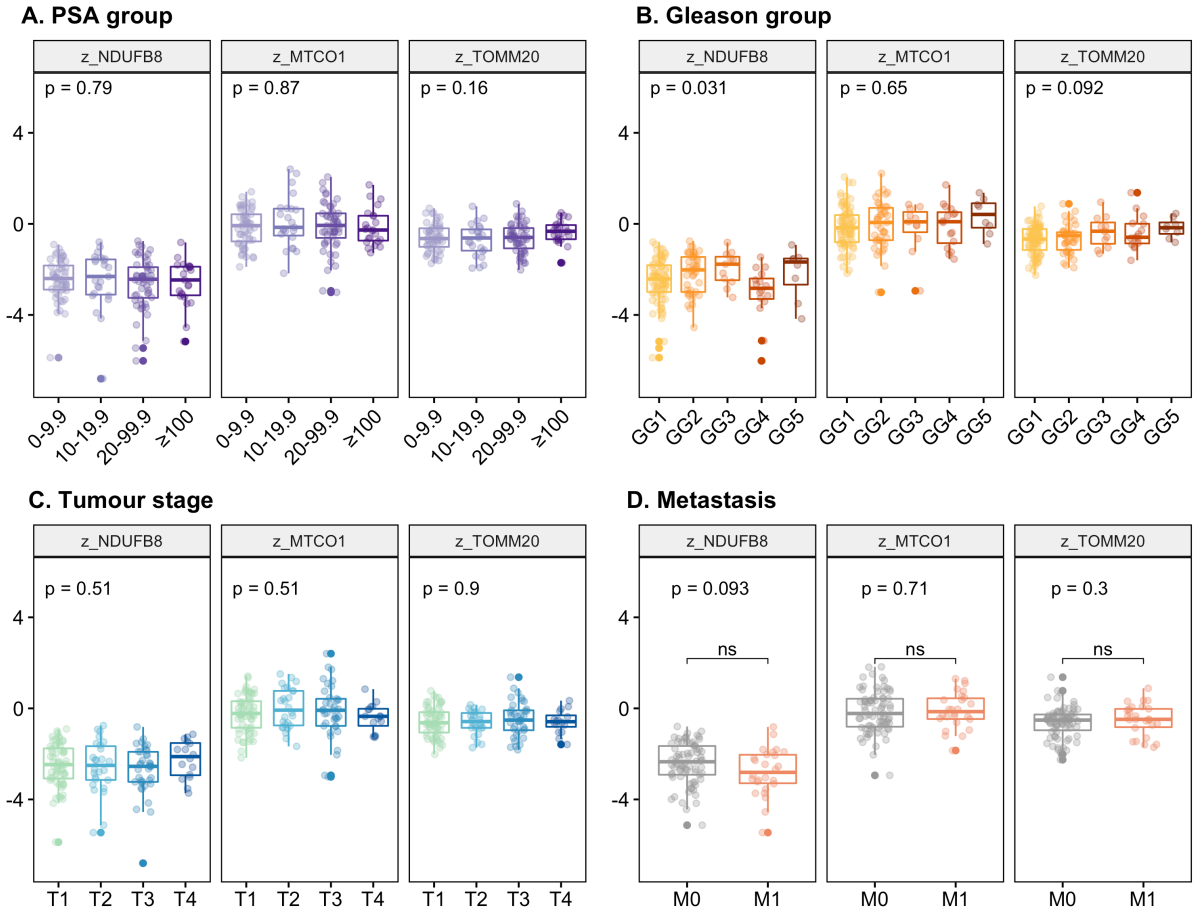

Figure 5-12: OXPHOS protein abundance and clinical risk features: normal-adjacent cores. Patient-level mean epithelial Z-scores in normal-adjacent cores were stratified by **(A)** PSA group, **(B)** Gleason group, **(C)** clinical tumour stage, and **(D)** presence of metastasis. *P* value from Kruskall Wallis test one-way ANOVA reported for PSA group, Gleason group, and tumour stage. *P* value from Wilcoxon rank test for presence of metastasis reported, with 'n.s.' denoting no statistical significance.

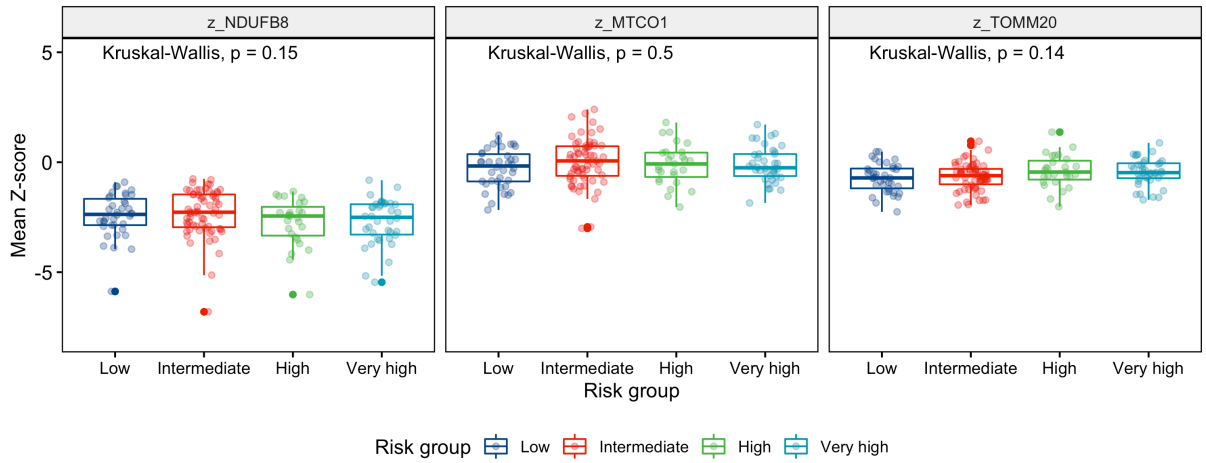

Figure 5-13: OXPHOS protein abundance and clinical risk features: normal-adjacent cores. Patient-level mean epithelial Z-scores in normal-adjacent cores were stratified by risk group. *P* value from Kruskall Wallis one-way ANOVA test reported.

5.2.2.7 Widespread intra-patient heterogeneity in OXPHOS protein abundance

It is also plausible that OXPHOS protein abundance may vary between different tumour foci, as observed in the preliminary evaluation across a PCa tissue sample in section 5.2.1. Therefore, the degree of heterogeneity in OXPHOS abundance was studied using z-scores from tumour and non-tumour cores across 66 MCR TURP and 17 NCL RP cases, where more than 3 tumour cores and 2 normal-adjacent cores from each patient were available. Heterogeneity was quantified by calculating coefficients of variation (**Figure 5-14**) and visual assessment of a mean z-score heat map (**Figure 5-15**). Coefficients of variation (CV) is a measure of variability relative to the mean. It is calculated as the ratio of standard deviation to the mean value of a population, which helps improve comparability across different TMA cohorts and different markers.

As compared to normal-adjacent cores, complex I abundance in tumour cores had higher intra-patient (T 14.6% vs NA 13.0%, Δ 1.6%, p=0.011, n=83) but comparable intra-core heterogeneity (T 6.3% with n=406 vs NA 6.0% with n=340, Δ 0.3%, p=0.2). In contrast, mitochondrial mass in tumour cores demonstrated lower intra-core (T 3.9% with n=406 vs NA 4.3% with n=340, Δ -0.4%, p<0.001) and intra-patient (T 7.9% vs NA 8.9% Δ -1.0%, p=0.0037, n=83) heterogeneity. Notably, intra-patient heterogeneity was greater than intra-core heterogeneity across all three markers (for example, *NDUFB8* in tumour cores: 19.6% within n=83 patients vs 6.3% within n=406 cores, Δ 12.6%, p<0.001), suggesting clonal variation in

OXPHOS abundance in different tumour foci from each patient. Inter-patient heterogeneity was low across both tumour and normal-adjacent cores across all three markers (p>0.3, n=83 patients). Upon sub-group analysis by TMA cohort, inter-patient heterogeneity was comparable across both TURP and RP cohorts (p>0.4 across all markers).

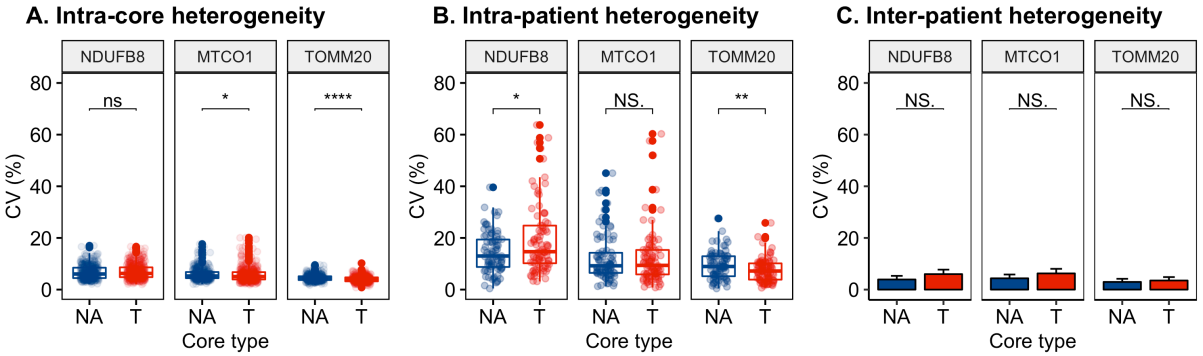

Figure 5-14: Heterogeneity in OXPHOS abundance. Heterogeneity was estimated using co-efficient of variance (CV) amongst 83 patients with paired tumour (denoted as T) and normal-adjacent (denoted as NA) cores from TURP or radical prostatectomy samples. **(A)** Intra-core heterogeneity in patients. Each point represents an individual core. **(B)** Heterogeneity between cores within individual patients. Each point represents data for an individual patient. **(C)** Inter-patient heterogeneity stratified by tumour and normal-adjacent cores across the four patient cohorts. Horizontal bar represents median CV values. *P* values reported using Wilcoxon rank test and represented as * <0.05, ** < 0.01, **** < 0.0001.

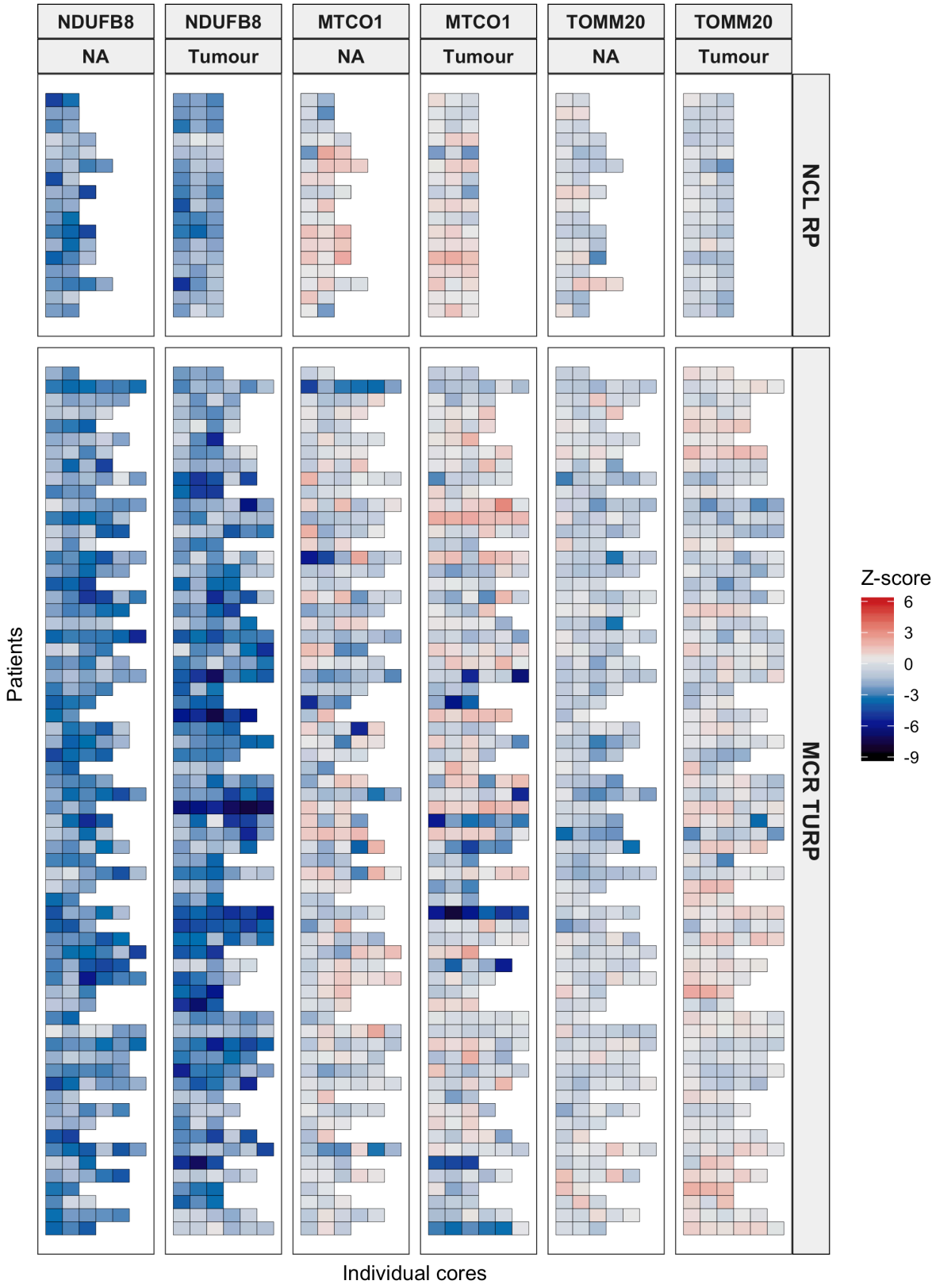

Figure 5-15: Inter- and intra-patient heterogeneity in OXPHOS protein abundance. Mean Z-scores were calculated from individual cores from patients with at least 3 tumour and 2 non-tumour (NA) cores. Each box represents mean Z-score for an individual TMA core. Widespread variation in OXPHOS protein abundance both within prostates from individual patients, and also between different patients was noted.

5.2.3 Impact of OXPHOS alterations on overall survival

High intra-patient tumoural heterogeneity in protein expression noted in section 5.2.2.7 above can significantly impact biomarker performance (Allott *et al.*, 2016). Of note, the magnitude of intra-patient heterogeneity was greater than both intra-core and inter-patient heterogeneity across all markers. Since the true direction of effect of OXPHOS protein abundance on overall survival is currently unclear, an unbiased approach was taken to generate three patient classifiers for each marker based on (a) tumour core with lowest mean z-score (referred to as '*min*'), (b) tumour core with highest mean z-score (referred to as '*max*'), and (c) mean z-score across cells from all tumour cores (referred to as '*mean*').

Technical variation between the four cohorts cannot be adequately modelled in regression analyses, since the true magnitude of effect associated with each technical factor is unknown. Patients in each cohort were therefore classified into low and high expression groups for each marker individually, using cohort-specific thresholds and maximally selected rank statistics (Hothorn and Lausen, 2003) using the *survival* and *surminer* packages. This method evaluates all data points from continuous z-score data and establishes a cut-off point where the standardised statistics achieve maximum significance to separate patients into 'high' and 'low' marker expression groups. Z-score thresholds determined for each TMA cohort are described in **Table 5-3**. By employing this method in a cohort-specific manner, categorical data from the four cohorts can be pooled for improved statistical power.

Marker	Metric	MCR Biopsy	MCR TURP	NCL TURP
Complex I	*NDUFB8*-mean	-2.07	-1.59	-4.42
	NDUFB8-min	-4.29	-6.61	-4.42
	NDUFB8-max	-3.23	-1.62	-0.82
Complex IV	*MTCO1*-mean	1.24	0.54	0.48
	MTCO1-min	1.11	-0.36	0.48
	MTCO1-max	1.14	-0.30	0.55
Mitochondrial mass	*TOMM20*-mean	0.63	-0.58	1.03
	TOMM20-min	0.50	-1.95	0.94
	TOMM20-max	0.53	-0.57	0.40

Table 5-3: Cohort-specific thresholds determined for each metric. Z-score thresholds were determined for each metric in each TMA cohort individually to classify patients into 'high' and 'low' abundance groups.

Patients from the NCL RP cohort were excluded from outcome analyses due to the low event rate in this group (4.8% mortality with all 5 of 104 patients dying of causes other than prostate cancer), in keeping with largely low risk disease characteristics and management with curative intent. After excluding radical prostatectomy patients, outcome data were available for 360 patients (MCR TURP n=135, MCR biopsy n=120; NCL TURP n=105).

Results using both univariable and multivariable Cox regression are reported, with 95% confidence interval and p values. Since inclusion of co-variates available at the time of initial diagnosis may help improve translational application of biomarkers (Director's Challenge Consortium for the Molecular Classification of Lung *et al.*, 2008), established clinical variables routinely used in evaluating prostate cancer risk were included in all multivariable models, including age, log10-transformed PSA at diagnosis, Gleason group, clinical tumour stage, and presence of metastasis. As expected, good prognostic performance of established clinical variables was confirmed, with increasing age, increasing PSA, Gleason grade 5, and presence of metastasis independently associated with poor overall survival upon multivariate analysis (**Table 5-4**).

Variable		HR (univariable)	HR (multivariable)
Age (years)	Mean (SD)	1.04 (1.03-1.05, *p*<0.001)	1.04 (1.02-1.06, *p*<0.001) ***
PSA at diagnosis (log10)	Mean (SD)	2.00 (1.67-2.40, *p*<0.001)	1.67 (1.31-2.14, *p*<0.001) ***
Gleason group (GG)	GG1	-	-
	GG2	0.98 (0.63-1.52, *p*=0.921)	0.78 (0.47-1.29, *p*=0.335)
	GG3	1.33 (0.84-2.11, *p*=0.222)	1.05 (0.62-1.79, *p*=0.848)
	GG4	1.72 (1.22-2.42, *p*=0.002)	1.14 (0.73-1.77, *p*=0.571)
	GG5	2.54 (1.82-3.55, *p*<0.001)	1.90 (1.24-2.92, *p*=0.003) **
	GGx	1.62 (1.12-2.35, *p*=0.011)	1.37 (0.87-2.15, *p*=0.169)
Clinical tumour (T) stage	T1-T2	-	-
	T3	1.67 (1.28-2.20, *p*<0.001)	1.09 (0.80-1.50, *p*=0.588)
	T4	2.24 (1.62-3.09, *p*<0.001)	1.05 (0.69-1.59, *p*=0.825)
	Tx	1.90 (1.38-2.62, *p*<0.001)	1.48 (0.92-2.37, *p*=0.106)
Metastasis (M) stage at diagnosis	M0	-	-
	M1	2.23 (1.69-2.93, *p*<0.001)	1.96 (1.41-2.74, *p*<0.001) ***
	Mx	1.01 (0.78-1.31, *p*=0.944)	1.16 (0.85-1.58, *p*=0.359)

Table 5-4: Univariable and multivariable Cox regression analysis of clinical markers. Hazard ratios (HR) reported with 95% confidence interval (CI), using the high-expression group as reference. Multivariable Cox regression model adjusted for age, PSA at diagnosis, Gleason group, clinical tumour stage, and presence of metastasis. *P* values are represented as * <0.05, ** < 0.01, *** < 0.001. GGx: Missing Gleason group; Tx: Missing tumour stage; Mx: Missing metastasis stage.

5.2.3.1 Low Complex I and high mitochondrial mass are independent prognostic markers of poorer overall survival

Patient stratification based upon cores with the lowest *NDUFB8* z-score (*NDUFB8-min*), and highest *TOMM20* z-score (*TOMM20-max*) were noted to be most prognostic (**Figure 5-16**). None of the *MTCO1* metrics evaluated were found to be prognostic in the overall cohort (**Figure 5-17**). For all subsequent analyses, *NDUFB8*-min, *TOMM20*-max, and *MTCO1*-max z-scores are used as patient-level markers for complex I, mitochondrial mass and complex IV, respectively.

Low *NDUFB8*-min and high *TOMM20*-max levels were associated with worse overall survival on multivariate analysis (**Table 5-5**), and a reduction in median survival of 30.9 (95% CI 10.2-51.6, p=0.0032) and 34.7 (95% CI 18.4-50.9, p=0.0007) months, respectively (**Table 5-6**). *NDUFB8*-min was independent of *TOMM20*-max and all included clinical features (HR 1.64, 95% CI 1.17-2.30, p=0.004). Similarly, *TOMM20*-max was also independent of *NDUFB8*-min and all included clinical markers (HR 0.66, 95% CI 0.49-0.88, p=0.005).

Variable		HR (univariable, 95% CI)	HR (multivariable, 95% CI)	FDR
Complex I metrics				
***NDUFB8*-max**	high	-	-	
	low	0.98 (0.77-1.23, *p*=0.850)	1.10 (0.83-1.46, *p*=0.513)	0.695
***NDUFB8*-mean**	high	-	-	
	low	0.87 (0.69-1.11, *p*=0.272)	0.92 (0.69-1.24, *p*=0.599)	0.695
***NDUFB8*-min**	high	-	-	
	low	1.53 (1.15-2.02, *p*=0.003)	1.68 (1.20-2.36, *p*=0.003)	0.014*
Complex IV metrics				
***MTCO1*-max**	high	-	-	
	low	0.95 (0.75-1.19, *p*=0.639)	0.95 (0.72-1.24, *p*=0.695)	0.695
***MTCO1*-mean**	high	-	-	
	low	0.94 (0.75-1.18, *p*=0.583)	0.87 (0.67-1.14, *p*=0.322)	0.695
***MTCO1*-min**	high	-	-	
	low	1.05 (0.81-1.36, *p*=0.691)	0.85 (0.62-1.15, *p*=0.286)	0.695
Mitochondrial mass metrics				
***TOMM20*-max**	high	-	-	
	low	0.67 (0.53-0.84, *p*=0.001)	0.64 (0.48-0.86, *p*=0.003)	0.014*
***TOMM20*-mean**	high	-	-	
	low	0.75 (0.59-0.95, *p*=0.018)	0.89 (0.67-1.20, *p*=0.459)	0.695
***TOMM20*-min**	high	-	-	
	low	0.77 (0.61-0.97, *p*=0.026)	0.91 (0.68-1.21, *p*=0.514)	0.695

Table 5-5: Cox regression models of OXPHOS marker metrics for overall survival (n=360). Three metrics were calculated for each marker based upon mean z-scores across all tumour cores (mean), a single core with the lowest mean marker z-score (min), and a single core with the highest mean marker z-score (max). Hazard ratios (HR) reported with 95% confidence interval (CI), using the high-expression group as reference. Multivariable Cox regression model adjusted for age at diagnosis, log-10 PSA at diagnosis, Gleason group, clinical tumour stage, and presence of metastasis. False-discovery rate (FDR) adjusted *p*-values calculated using multivariable Cox regression are represented as * <0.05, ** < 0.01, and *** < 0.001.

Marker	Status	Events/Total	Median survival (95% CI)	*p* value
Overall cohort	-	292/360	61.9 (50.9-73.7)	-
***NDUFB8*-min**	low	62/71	38.3 (32.3-53.9)	-
	high	230/289	69.2 (58.2-78.1)	-
		Difference	***30.9 (10.2-51.6) months***	0.0032 **
***TOMM20*-max**	low	121/155	79.6 (69.4-107.9)	-
	high	171/205	44.9 (38.7-59.6)	-
		Difference	***34.6 (18.4-50.9) months***	0.0007 ***

Table 5-6: Median survival stratified by OXPHOS marker status. Median survival reported in months with 95% confidence interval (CI) amongst all patients, and patients stratified by NDUFB8-min and TOMM20-max status. *P* values calculated using unpaired two-tailed t test are represented as * <0.05, ** < 0.01, *** < 0.001.

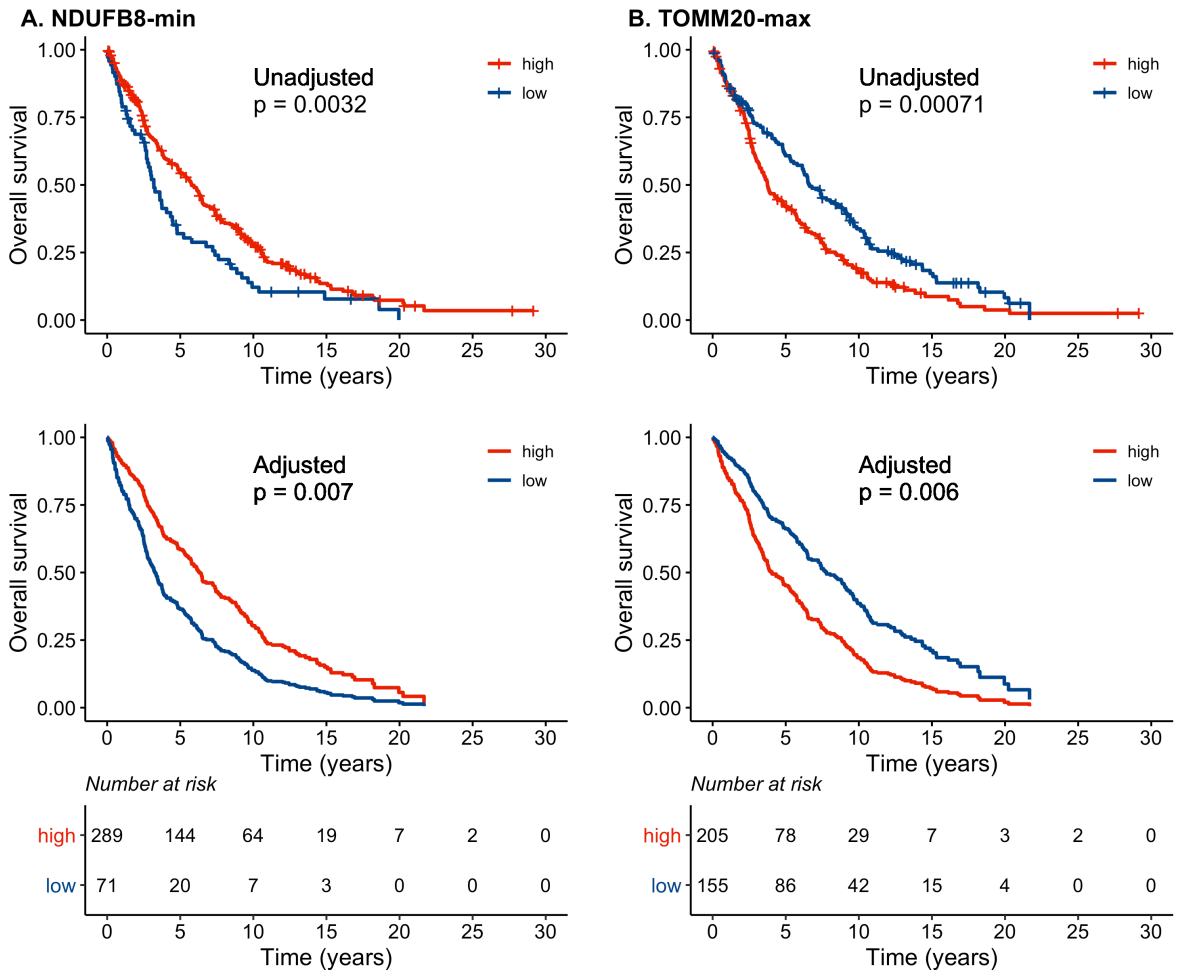

Figure 5-16: Low complex I and high mitochondrial mass are associated with poor long-term survival. Kaplan-Meier survival plot for 360 patients with prostate cancer evaluated using the log-rank statistic, based upon **(A)** complex I abundance (a single tumour core with the lowest *NDUFB8* z-score for each patient), and **(B)** mitochondrial mass (a single tumour core with the highest *TOMM20* z-score for each patient). Unadjusted (*top panel*) and Cox-proportional hazards adjusted Kaplan Meier curves (*bottom panel*) are presented. Log rank test was used to determine *p*-values for unadjusted hazards estimation. The following co-variates were included in the Cox regression model: age at diagnosis, log-10 PSA at diagnosis, Gleason group, clinical tumour stage, and metastasis stage at time of diagnosis.

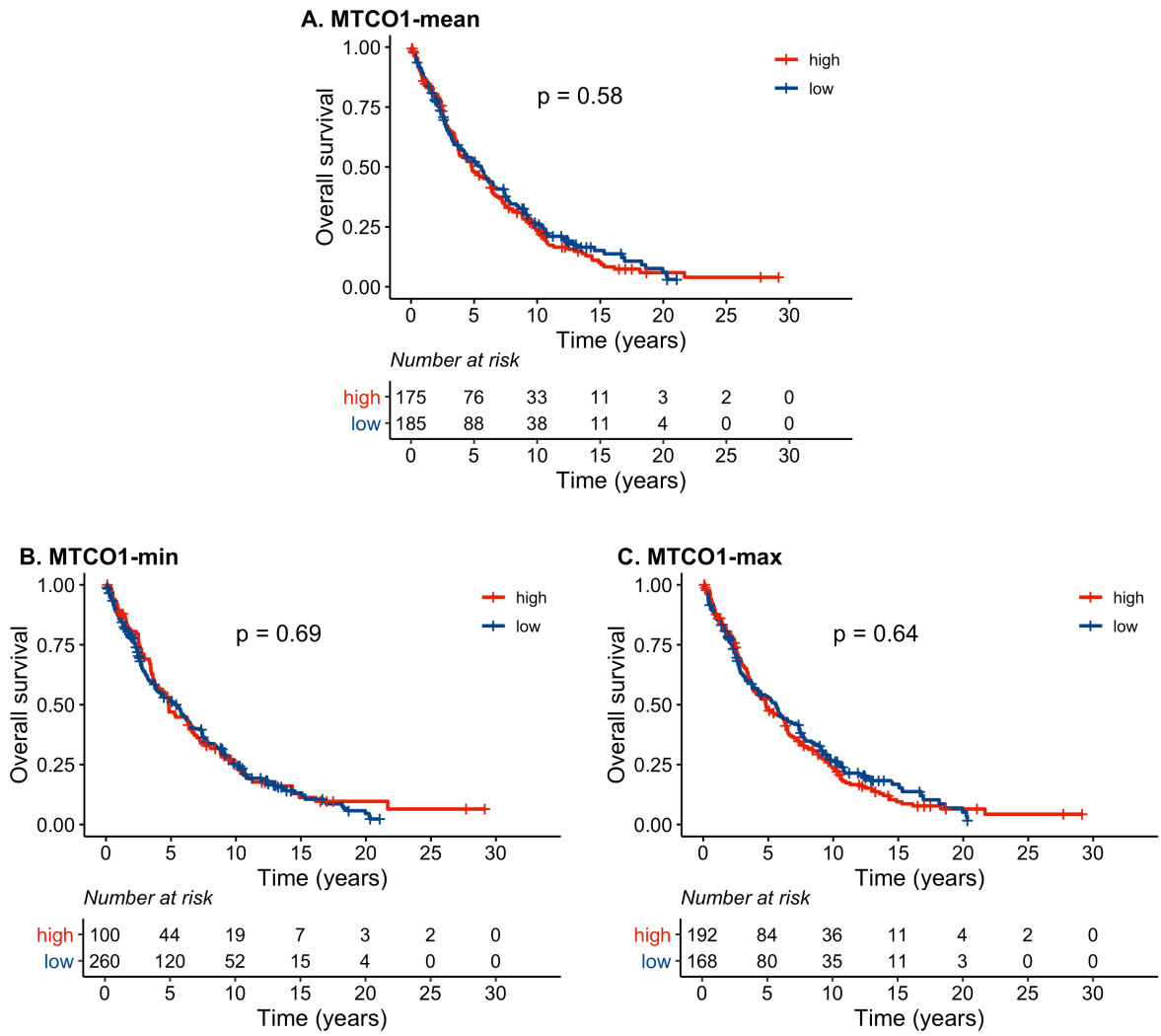

Figure 5-17: Complex IV abundance does not influence long-term survival. Survival outcomes stratified by *MTCO1* (complex IV) abundance amongst 360 PCa patients evaluated using three summary metrics **(A)** *MTCO1*-mean: mean patient *MTCO1* z-score across all tumour cores, **(B)** *MTCO1*-min: mean *MTCO1* z-score in core with lowest *MTCO1* abundance, **(C)** *MTCO1*-max: mean *MTCO1* z-score in core with highest *MTCO1* abundance. Log rank test was used to determine *p*-values.

5.2.4 Impact of OXPHOS alterations in molecular subgroups of prostate cancer

Since *TMPRSS2:ERG* gene fusion and alterations in *Pi3k/Akt* signalling (driven by *PTEN* loss) are observed in up to 50% (Esgueva *et al.*, 2010) and 75% (Taylor *et al.*, 2010) of patients with PCa respectively, the impact of OXPHOS alterations in these subgroups was evaluated.

Epithelial *PTEN* and *ERG* data were available from studies previously undertaken on the Manchester TMA by Claire Hart and Ahmad Al-Sukaini (Genito-urinary Cancer Research Group, University of Manchester), where sections were labelled with α-*PTEN* (D4.3) (#9188, Cell Signalling Technology) and α-*ERG* (ab92513, Abcam) antibodies.

IHC for *ERG* expression has been shown previously to be highly sensitive and specific for *TMPRSS2:ERG* fusion (Chaux *et al.*, 2011). Epithelial *ERG* H-scores calculated amongst tumour cores by digital image analysis using Definiens and Image Miner. Similarly, mean epithelial *PTEN* intensity across all epithelial cells from tumour cores were calculated for each patient using InForm Tissue Studio software and RStudio. Optimum cut-off thresholds were determined using maximally selected rank statistics. Representative images from patients with *PTEN-high* and *PTEN-low* status are shown in **Figure 5-18**.

Complete data were available for *PTEN* status for 272 patients, and *ERG* status for 226 patients, and both markers for 222 patients. Survival data were available for 248, 209, and 205 patients respectively.

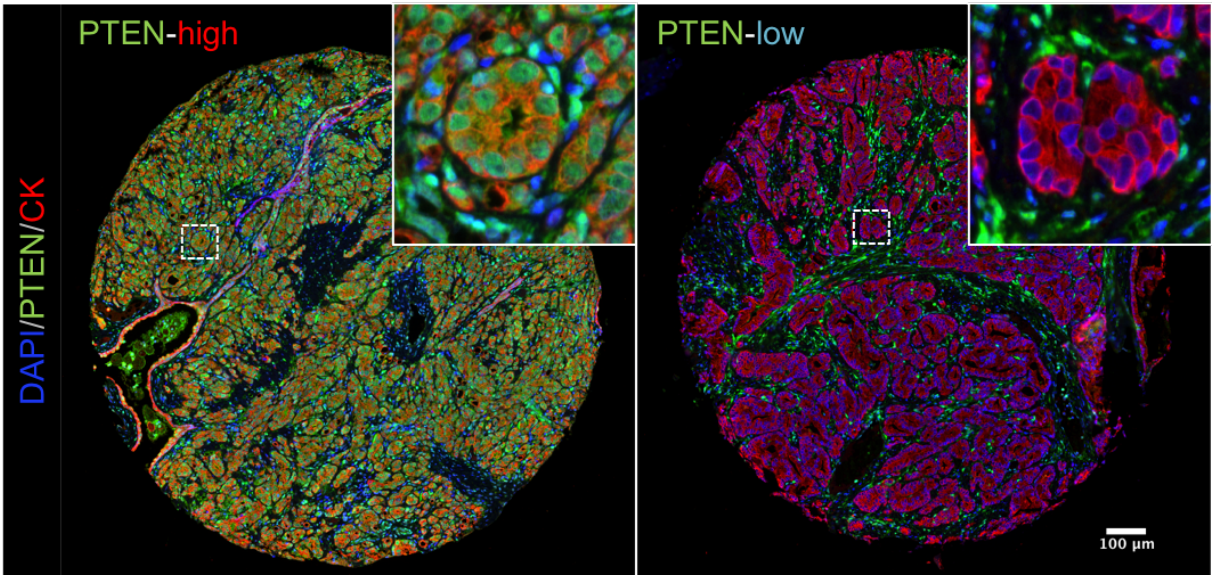

Figure 5-18: *PTEN* abundance in prostate tumour cores. Representative prostate cores from patients with *PTEN*-high (*left panel*) and *PTEN*-low (*right panel*) tumour tissue. *PTEN* expression is apparent in both nuclear and cytoplasmic regions. Epithelial cells marked with pan-cytokeratin (CK, red). *PTEN*-positive cells appear orange, whereas *PTEN*-deficient epithelial cells appear red. High magnification image of a representative regions highlighted in insets. Scale bar represents 100µm.

5.2.4.1 Stratification by *PTEN* status

PTEN data were available for 272 patients, of which survival data were available for 248 patients. Upon stratification by PTEN status, complex I (*NDUFB8*, *p*=0.15) and complex IV (*MTCO1*, *p*=0.17) z-scores were comparable, however mitochondrial mass was higher amongst patients with *PTEN-high* PCa (TOMM20, 0.47 in n=115 vs 0.71 in n=157, Δ 0.24, *p*=0.0043, **Figure 5-19**). The lower mitochondrial mass in the *PTEN-low* cohort may reflect the predominantly glycolytic state observed in *PTEN*-deficient PCa (Pertega-Gomes *et al.*, 2015).

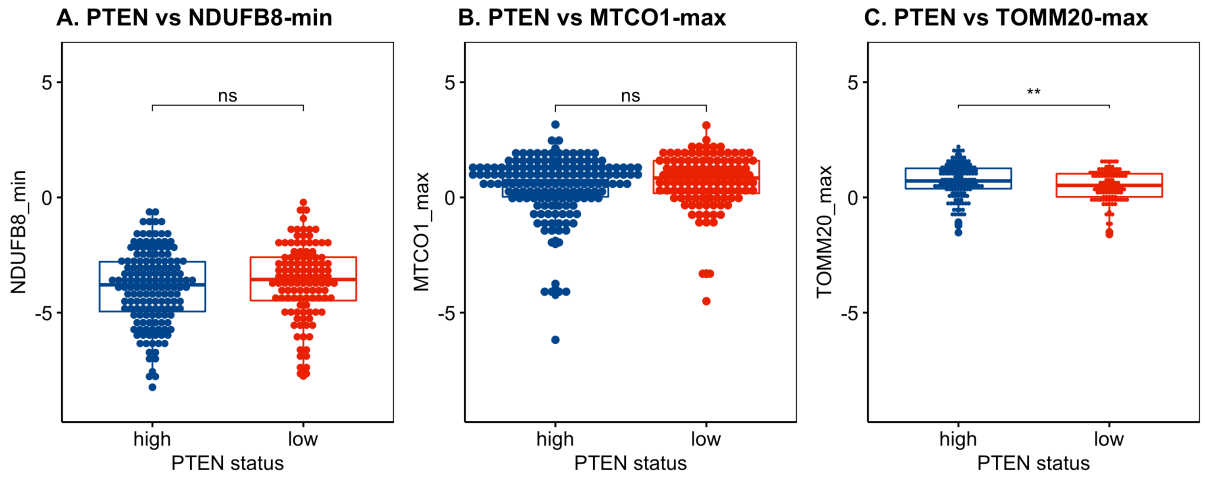

Figure 5-19: OXPHOS protein abundance stratified by *PTEN* status. Mean z-scores for **(A)** complex I (single tumour core with lowest z-score per patient, *NDUFB8*-min), **(B)** complex IV/*MTCO1* (single tumour core with lowest z-score per patient, *MTCO1*-max) and **(C)** mitochondrial mass (single tumour core with highest z-score per patient, *TOMM20*-max). P value calculated using the Wilcoxon rank test are represented as ns=not significant, * <0.05, ** < 0.01, *** < 0.001.

PTEN status was not associated with outcome in this cohort (**Figure 5-20*A***, *p*=0.65, log rank statistic), despite multivariate adjustment for clinical covariates (**Table 5-7**, *p*=0.613, Cox regression). Amongst patients with available *PTEN* data, high mitochondrial mass (*TOMM20*, HR 0.62, 95% CI 0.45-0.87, *p*=0.006) and low complex I abundance (*NDUFB8*, HR 1.79, 95% CI 1.20-2.65, *p*=0.004) were found to be independently prognostic of poor outcome, independent of PTEN status. Upon sub-group analysis based on *PTEN* status (**Table 5-8**), high mitochondrial mass was independently associated with worse overall survival amongst *PTEN-high* patients (*TOMM20*, HR 0.55, 95% CI 0.34-0.90, *p*=0.017), whereas low Complex I was associated with poor outcome amongst *PTEN-low* patients (*NDUFB8*, HR 2.97, 95% CI 1.69-

5.24, $p<0.001$). Complex IV did not provide sufficient prognostic power in either sub-group (*MTCO1*, $p=0.556$ and $p=0.058$, respectively).

These results suggest that complex I loss may be relevant in *PTEN*-deficient PCa, whereas increased mitochondrial mass may be implicated in *PTEN*-proficient PCa.

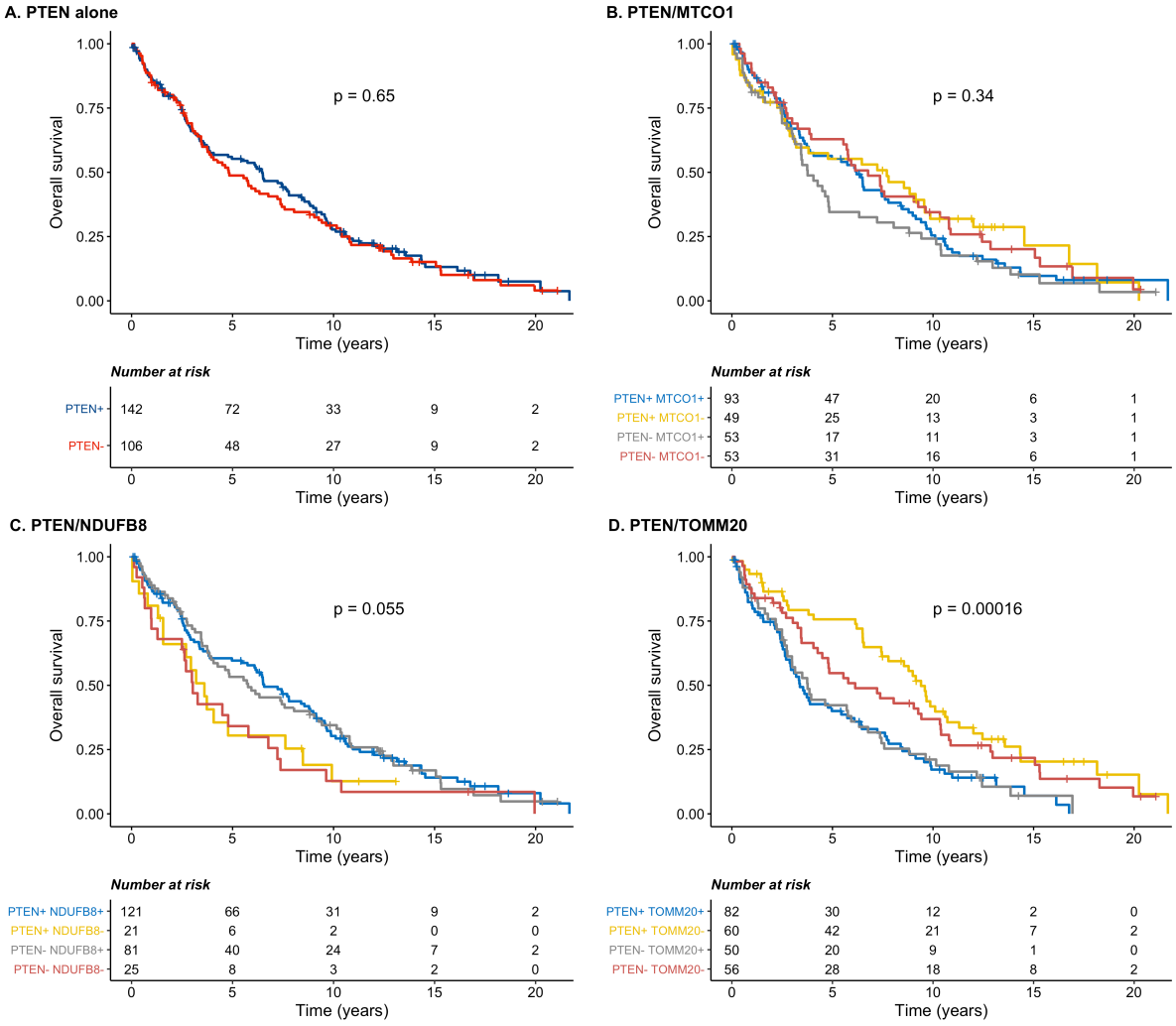

Figure 5-20: Survival outcome stratified by *PTEN*, *NDUFB8* and *TOMM20* status. Outcome data from the Manchester TMA cohort were linked to *PTEN* status data for 234 patients from previous work. Kaplan-Meier curves for overall survival stratified by **(A)** *PTEN* status, and sub-stratification based upon **(B)** complex IV/*MTCO1* status; **(C)** complex I/*NDUFB8* status; and **(D)** mitochondrial mass/*TOMM20* status. *P* value using log rank test reported.

Marker		HR (univariable, 95% CI)	HR (multivariable, 95% CI)
***PTEN* status**	high	-	-
	low	1.07 (0.81-1.41, *p*=0.645)	A: 1.08 (0.79-1.48, *p*=0.613) B: 1.14 (0.80-1.61, *p*=0.465)
Complex I	high	-	-
(NDUFB8-min*)*	low	1.63 (1.15-2.31, *p*=0.006)	B: 1.79 (1.20-2.65, *p*=0.004) **
Complex IV	high	-	-
(MTCO1-max*)*	low	0.80 (0.60-1.07, *p*=0.130)	B: 0.75 (0.54-1.03, *p*=0.079)
Mitochondrial mass	high	-	-
(TOMM20-max*)*	low	0.53 (0.40-0.71, *p*<0.001)	B: 0.62 (0.45-0.87, *p*=0.006) **

Table 5-7: Univariable and multivariable Cox regression models including PTEN status. Hazard ratios (HR) reported with 95% confidence interval (CI), using the high-expression group as reference. Results are reported for two Cox regression models: Model A is adjusted for age at diagnosis, log10-PSA at diagnosis, Gleason group, clinical tumour stage, and presence of metastasis; Model B is adjusted for co-variates in Model A, and *PTEN*, *NDUFB8*-min, *MTCO1*-max and *TOMM20*-max status. *P* values calculated using Cox regression are represented as * *p*<0.05, ** *p*<0.01, and *** *p*<0.001.

		HR (univariable, 95% CI)	HR (multivariable, 95% CI)
PTEN-high	***n=142***		
Complex I	high	-	-
(NDUFB8-min*)*	low	1.62 (0.96-2.73, *p*=0.074)	1.17 (0.63-2.17, *p*=0.619)
Complex IV	high	-	-
(MTCO1-max*)*	low	0.84 (0.56-1.25, *p*=0.389)	0.87 (0.56-1.37, *p*=0.556)
Mitochondrial mass	high	-	-
(TOMM20-max*)*	low	0.46 (0.31-0.68, *p*<0.001)	0.55 (0.34-0.90, *p*=0.017) *
PTEN-low	***n=106***		
Complex I	high	-	-
(NDUFB8-min*)*	low	1.60 (0.99-2.59, *p*=0.054)	2.97 (1.69-5.24, *p*<0.001) ***
Complex IV	high	-	-
(MTCO1-max*)*	low	0.71 (0.47-1.08, *p*=0.114)	0.61 (0.36-1.02, *p*=0.058)
Mitochondrial mass	high	-	-
(TOMM20-max*)*	low	0.63 (0.41-0.96, *p*=0.032)	0.74 (0.45-1.21, *p*=0.230)

Table 5-8: Univariable and multivariable Cox regression models amongst 234 patients stratified by *PTEN* status. Hazard ratios (HR) reported with 95% confidence interval (CI), using the high-expression group as reference. Multivariable Cox regression models are adjusted for age at diagnosis, log-10 PSA at diagnosis, Gleason group, clinical tumour stage, and presence of metastasis. P values calculated using Cox regression are represented as * $p<0.05$, ** $p<0.01$, and *** $p<0.001$.

5.2.4.2 Stratification by *TMPRSS2:ERG* fusion status

In light of established metabolic derangements in *TMPRSS2:ERG* fusion prostate cancer, patients were stratified by *ERG* status. *ERG* status (*high* or *low*) was available for 226 patients in the MCR TMA cohorts, of which survival data were available for 209 patients. No difference in expression of any of the three mitochondrial markers were noted upon stratification by *ERG* status (p>0.1 for all markers, **Figure 5-21**).

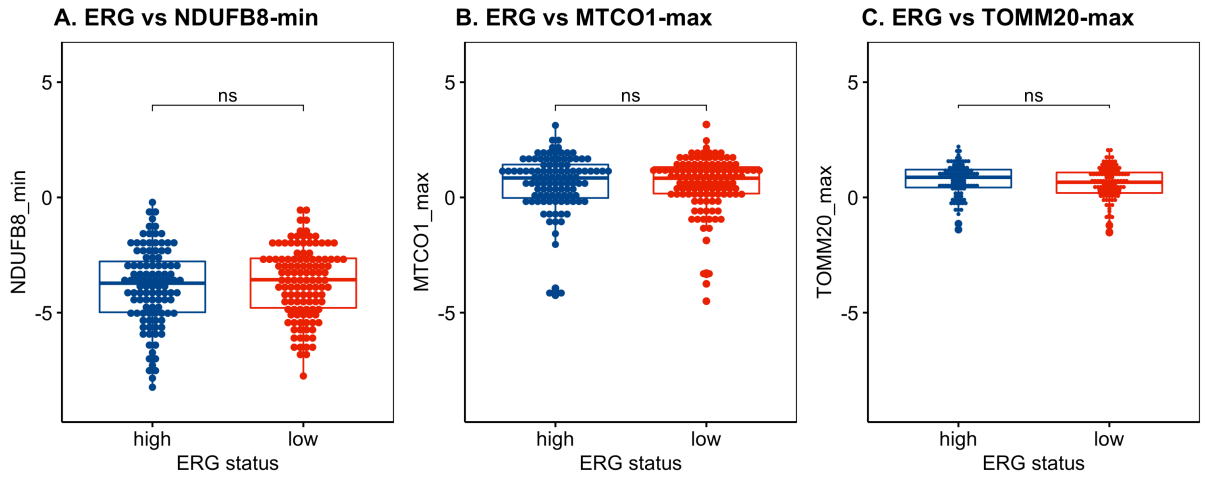

Figure 5-21: OXPHOS protein abundance stratified by *ERG* status. Mean z-scores for **(A)** complex I (single tumour core with lowest z-score per patient, *NDUFB8*-min), **(B)** complex IV/*MTCO1* (single tumour core with lowest z-score per patient, *MTCO1*-max) and **(C)** mitochondrial mass (single tumour core with highest z-score per patient, *TOMM20*-max). Wilcoxon rank test used to calculate p-values, with p>0.1 denoted as 'ns' (not significant).

Upon adjustment for clinical covariates (age at diagnosis, log-10 PSA at diagnosis, Gleason group, clinical tumour stage, and presence of metastasis), *ERG* status, and OXPHOS marker status, low complex I expression (*NDUFB8*, HR 1.66, 95% CI 1.07-2.55, p=0.023) and high mitochondrial mass (*TOMM20*, HR 0.52, 95% CI 0.36-0.76, p=0.001) were associated with poorer overall survival.

These trends were evaluated further by sub-stratifying patients based on *ERG* status (**Table 5-10**). Amongst 101 *ERG-high* cases, low complex I was independently associated with poor overall survival (*NDUFB8*, HR 3.31, 95% CI 1.44-7.62, p=0.005), whereas complex IV abundance (*MTCO1*, p=0.709) and mitochondrial mass (*TOMM20*, p=0.095) did not influence overall survival. In contrast, amongst 108 *ERG-low* cases, high mitochondrial mass (*TOMM20*, HR

0.39, 95% CI 0.23-0.67, *p*=0.001) and high complex IV abundance (*MTCO1*, HR 0.54, 95% CI 0.33-0.89, *p*=0.016) were independently prognostic of poor overall survival.

These results suggest that complex I loss may be relevant in *ERG*-positive PCa, whereas mitochondrial mass and complex IV may be implicated in *ERG*-negative PCa.

		HR (univariable, 95% CI)	HR (multivariable, 95% CI)
ERG status	high	-	-
	low	0.96 (0.71-1.30, *p*=0.803)	A: 1.34 (0.94-1.90, *p*=0.104) B: 1.45 (1.01-2.09, *p*=0.047) *
Complex I	high		
(NDUFB8-min*)*	low	1.60 (1.08-2.35, *p*=0.018)	B: 1.66 (1.07-2.55, *p*=0.023) *
Complex IV	high		
(MTCO1-max*)*	low	0.77 (0.56-1.05, *p*=0.102)	B: 0.71 (0.50-1.02, *p*=0.061)
Mitochondrial mass	high		
(TOMM20-max*)*	low	0.44 (0.32-0.61, *p*<0.001)	B: 0.52 (0.36-0.76, *p*=0.001) ***

Table 5-9: Univariate and multivariable Cox regression analysis amongst 209 patients with *ERG* status. Hazard ratios (HR) reported with 95% confidence interval (CI), using the high-expression group as reference. Results are reported for two Cox regression models: Model A is adjusted for age at diagnosis, log-10 PSA at diagnosis, Gleason group, clinical tumour stage, and presence of metastasis; Model B is adjusted for co-variates in Model A, and *ERG*, *NDUFB8*-min, *MTCO1*-max and *TOMM20*-max status. *P* values calculated using Cox regression are represented as * <0.05, ** < 0.01, and *** < 0.001.

		HR (univariable, 95% CI)	HR (multivariable, 95% CI)
ERG high	***n=101***		
Complex I	high	-	-
(NDUFB8-min*)*	low	4.36 (2.27-8.34, *p*<0.001)	3.31 (1.44-7.62, *p*=0.005) **
Complex IV	high	-	-
(MTCO1-max*)*	low	0.55 (0.34-0.86, *p*=0.010)	1.11 (0.64-1.93, *p*=0.709)
Mitochondrial mass	high	-	-
(TOMM20-max*)*	low	0.79 (0.50-1.27, *p*=0.337)	0.61 (0.34-1.09, *p*=0.095)
ERG low	***n=108***		
Complex I	high	-	-
(NDUFB8-min*)*	low	1.12 (0.67-1.87, *p*=0.662)	1.44 (0.82-2.52, *p*=0.205)
Complex IV	high	-	-
(MTCO1-max*)*	low	0.75 (0.49-1.15, *p*=0.187)	0.54 (0.33-0.89, *p*=0.016) *
Mitochondrial mass	high	-	-
(TOMM20-max*)*	low	0.36 (0.23-0.56, *p*<0.001)	0.39 (0.23-0.67, *p*=0.001) ***

Table 5-10: Univariable and multivariable Cox regression analysis of OXPHOS markers amongst patients stratified by *ERG* status. Hazard ratios (HR) reported with 95% confidence interval (CI), using the high-expression group as reference. Multivariable Cox regression models are adjusted for age at diagnosis, log-10 PSA at diagnosis, Gleason group, clinical tumour stage, and presence of metastasis. *P* values calculated using Cox regression are represented as * *p*<0.05, ** *p*<0.01, and *** *p*<0.001.

5.2.4.3 Stratification by *TMPRSS2:ERG* fusion & *PTEN* status

Patients were then stratified by both *PTEN* and *ERG* status, with survival data available for 205 patients (**Table 5-11**). Complex I was a strong independent prognostic marker for poor outcome amongst *PTEN-low ERG-high* patients (*NDUFB8*, HR 90.1, 95% CI 6.23-1303.3, *p*=0.001). High mitochondrial mass was associated with worse outcome in *ERG-low* patients from both *PTEN-high* (*TOMM20*, HR 0.30, 95% CI 0.14-0.67, *p*=0.003) and *PTEN-low* cohorts (*TOMM20*, HR 0.34, 95% CI 0.14-0.85, *p*=0.020). Sub-stratification of *ERG-low* cases by *PTEN* status suggested that the prognostic performance of complex IV was largely driven by *PTEN-high* cases on multivariate analysis (*MTCO1*, HR 0.36, 95% CI 0.15-0.86, *p*=0.022), whereas low complex IV abundance was associated with better long-term survival.

		HR (univariable, 95% CI)	HR (multivariable, 95% CI)
PTEN-high ERG-high (n=64)			
Complex I	high	-	-
(NDUFB8-min*)*	low	3.48 (1.57-7.69, *p*=0.002)	2.11 (0.77-5.79, *p*=0.145)
Complex IV	high	-	-
(MTCO1-max*)*	low	1.19 (0.65-2.17, *p*=0.572)	1.97 (0.87-4.43, *p*=0.103)
Mitochondrial mass	high	-	-
(TOMM20-max*)*	low	0.49 (0.28-0.87, *p*=0.014)	0.43 (0.17-1.06, *p*=0.067)
PTEN-high ERG-low (n=62)			
Complex I	high	-	-
(NDUFB8-min*)*	low	0.99 (0.42-2.35, *p*=0.979)	0.84 (0.30-2.36, *p*=0.737)
Complex IV	high	-	-
(MTCO1-max*)*	low	0.72 (0.39-1.33, *p*=0.291)	0.36 (0.15-0.86, *p*=0.022) *
Mitochondrial mass	high	-	-
(TOMM20-max*)*	low	0.34 (0.18-0.63, *p*=0.001)	0.30 (0.14-0.67, *p*=0.003) ****
PTEN-low ERG-high (n= 37)			
Complex I	high	-	-
(NDUFB8-min*)*	low	8.51 (2.49-29.04, *p*=0.001)	90.1 (6.23-1303.3, *p*=0.001) ***
Complex IV	high	-	-
(MTCO1-max*)*	low	0.51 (0.24-1.12, *p*=0.092)	0.35 (0.11-1.15, *p*=0.084)
Mitochondrial mass	high	-	-
(TOMM20-max*)*	low	0.64 (0.28-1.45, *p*=0.282)	0.43 (0.12-1.55, *p*=0.196)
PTEN-low ERG-low (n=42)			
Complex I	high	-	-
(NDUFB8-min*)*	low	1.05 (0.52-2.13, *p*=0.886)	2.12 (0.84-5.33, *p*=0.110)
Complex IV	high	-	-
(MTCO1-max*)*	low	0.78 (0.39-1.54, *p*=0.471)	0.45 (0.17-1.18, *p*=0.105)
Mitochondrial mass	high	-	-
(TOMM20-max*)*	low	0.37 (0.18-0.76, *p*=0.006)	0.34 (0.14-0.85, *p*=0.020) *

Table 5-11: Cox regression models based *PTEN* and *ERG* status amongst 190 patients. Hazard ratios (HR) reported with 95% confidence interval (CI), using the high-expression group as reference. Multivariable Cox regression model adjusted for age, PSA at diagnosis, Gleason group, clinical tumour stage, and presence of metastasis. *PTEN* status unavailable for 4 *ERG*-low cases. ERG status unavailable for 16 *PTEN*-high and 27 *PTEN*-low cases. *P* values calculated using Cox regression are represented as * $p<0.05$, ** $p<0.01$, and *** $p<0.001$.

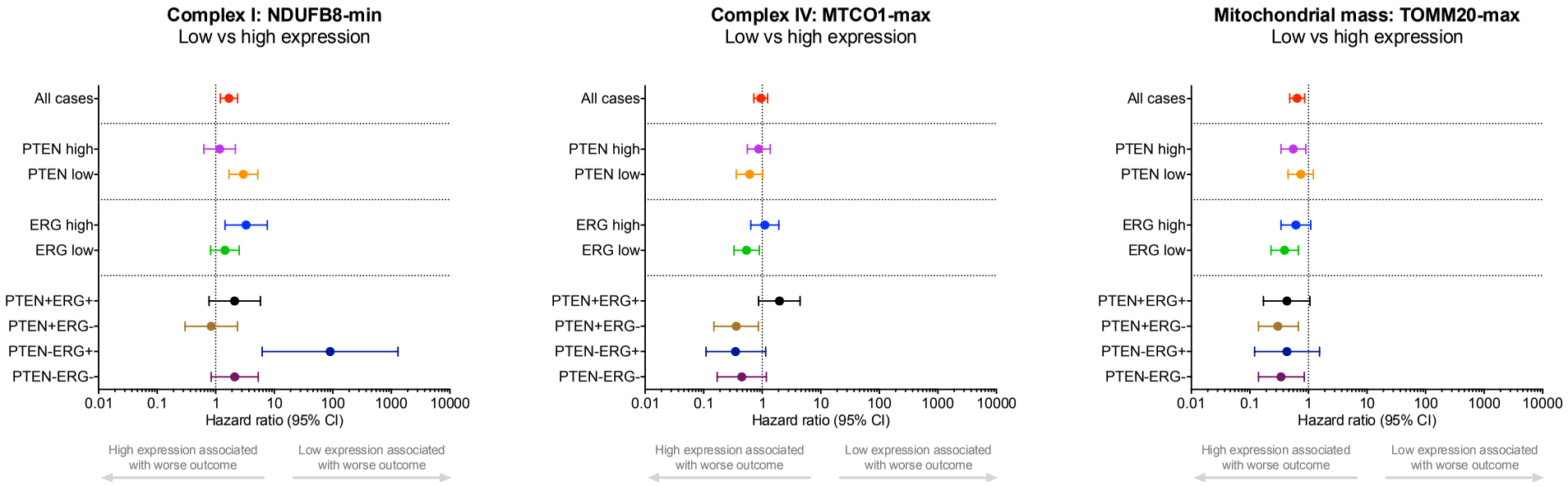

Figure 5-22: Molecularly stratified impact of OXPHOS alterations on overall survival. Patients were classified into high and low expression groups for each marker. The high-expression group was used as reference. Hazard ratios reported for complex I (*NDUFB8*-min), complex IV (*MTCO1*-max), and mitochondrial mass (*TOMM20*-max). Cox proportional hazards estimated with adjustment for the following confounders: age at diagnosis, log-10 PSA at diagnosis, Gleason group, clinical tumour stage, and presence of metastasis. The high expression group was used as the reference. Patients were sub-stratified based upon *ERG* status (high+, or low-) and *PTEN* status (high+, or low-). Error bars denote 95% confidence interval.

5.3 Discussion

According to the Warburg effect, tumour cells switch their metabolism from mitochondrial OXPHOS to aerobic glycolysis. Consistent with this phenomenon, overexpression of glycolytic markers has been demonstrated previously in a number of human cancer types, including prostate cancer (Pertega-Gomes *et al.*, 2015). A potential hypothesis for this switch from OXPHOS to glycolysis has been the age-related accumulation of mitochondrial OXPHOS defects.

5.3.1 OXPHOS abundance does not alter with advancing age in benign human prostate tissue

Contrary to this hypothesis and observations in other ageing mitotic tissues (Gomez and Hagen, 2012), the data presented herein suggests that advancing age was not correlated with OXPHOS protein abundance in either benign tissue from patients without prostate cancer, normal-adjacent prostate tissue from patients with PCa, or PCa tumour tissue. Similarly, no association between age and OXPHOS supercomplex abundance was noted in ageing rat kidney tissue (O'Toole *et al.*, 2010).

Potential explanations for this phenomenon include (a) reduced mtDNA copy number in normal-adjacent prostate epithelial tissue (as observed by Hopkins *et al.* (2017)) resulting in low mtDNA replication and fewer proof-reading related errors, (b) accumulation of mtDNA mutations at low heteroplasmy leading to no change in steady-state OXPHOS protein levels, and (c) clonal advantage offered by cells with functioning OXPHOS, which supersede cells with OXPHOS alterations. It is also plausible that, in the data presented herein, low frequency phenomena may be missed in bulk data analysis using mean z-scores, rather than assessment of OXPHOS abundance in distinct cell types (for example, using basal and luminal cell markers to analyse epithelial cell types separately). Furthermore, the small number of patients at extremes of age (<55 years or >80 years) of age may bias linear models used to determine trends in these data, and thereby true effects.

5.3.2 Tumour cores have high mitochondrial mass and low complex I, in comparison to normal-adjacent benign tissue

Amongst the TMA cores evaluated in this chapter, tumour regions were noted to have higher mitochondrial mass, as compared to normal-adjacent regions, which validated findings from a previous large TMA study of prostate cancer samples (Grupp *et al.*, 2013). Furthermore, increased mitochondrial mass and reduced complex I expression in tumour cores, but not normal-adjacent cores, were associated with established clinical features of aggressive

prostate cancer. These observations may reflect either (a) increased mitochondrial biogenesis leading to increased mitochondrial mass, or (b) reduced mitophagy resulting in increased mitochondrial mass with accumulation of dysfunctional complex I.

These opposing hypotheses have been previously explored by Torrano *et al.* (2016) who evaluated the role of *PGC1α*, a master transcriptional regulator playing a key role in mitochondrial biogenesis, in PCa progression. The authors noted suppressed tumour progression and metastatic dissemination in *Pten*-deficient mice with transgenic overexpression of *PGC1α*. Therefore, these data suggest that the observed increase in mitochondrial mass and loss of complex I are more likely associated with reduced mitophagy, which may result in accumulation of dysfunctional mitochondria with low complex I and support tumour progression (Chang *et al.*, 2017). Further work evaluating mitophagy markers in PCa may help evaluate the role of underlying mechanisms responsible for increased mitochondrial mass observed in PCa tumour cores in this chapter. Consistent with this hypothesis, therapeutic induction of mitophagy has shown promise in suppressing colorectal cancer cell proliferation (Boyle *et al.*, 2018).

A number of potential hypotheses may help explain the observed increased frequency of complex I defects in PCa tumour cores in this work: (a) clonal expansion of cells preferentially reliant on glycolysis, rather than OXPHOS metabolism (in keeping with the Warburg hypothesis), (b) a bystander effect, whereby complex I loss is mitigated by electrons instead entering the electron transport chain via Complex II and therefore not resulting in change in overall cell metabolism (Weber *et al.*, 2018), (c) maintenance of oncogenic signalling through consequent accumulation of NADH and lactate, (d) increased production of ROS leading to further genomic damage and propagation of OXPHOS defects, and (f) apoptosis resistance through mitochondrial dysfunction (Chaudhary *et al.*, 2016).

A similar pattern of low complex-I, with increased mitochondrial mass (citrate synthase activity) and variable complex-IV activity has been observed in renal oncocytomas (Gasparre *et al.*, 2008). The authors noted discordance in mtDNA mutation levels and mRNA levels of OXPHOS subunits. Complex I loss due to mtDNA mutations in oncocytoma is also supported by Mayr *et al.* (2008) and loss of complex I enzyme function as observed by Simonnet *et al.* (2003). However, importantly, oncocytomas are benign tumours with an indolent slow-growing phenotype, with no impact on patient survival. In addition, they are characterised by

homoplasmic mtDNA mutations resulting in low complex I activity and increased mitochondrial mass, making them a suitable model to study the relationship between mtDNA mutations and an indolent cancer phenotype. However, in contrast to the indolent nature of oncocytomas, similar to the results reported in this chapter, reduced complex I expression has also been found to be an independent marker of poor prognosis in non-small cell lung cancer and renal clear cell carcinoma (Su *et al.*, 2016; Ellinger *et al.*, 2017).

5.3.3 Heterogeneity in OXPHOS protein expression

Significant intra-patient and inter-patient heterogeneity was observed in complex I abundance amongst tissue samples evaluated in this chapter. In contrast, mitochondrial mass appeared more homogenous within and between tumour cores, as compared to normal adjacent cores. Together with the finding of increased mitochondrial mass in tumour cores, these data suggest a trend towards clonal selection for maintaining high mitochondrial mass in tumour cells.

Intra-patient heterogeneity could be associated with areas of hypoxia in PCa tumours, leading to downregulation of OXPHOS in these regions. In keeping with this hypothesis and the poor prognostic potential of patients with OXPHOS defects, PCa patients with upregulated hypoxia-induced signalling tend to develop more aggressive tumours (Yang *et al.*, 2018), with hypoxia-modifying therapy (such as Carbogen and Nicotinamide) currently in clinical trials to improve response to radical radiotherapy (ISRCTN08912168). Also, consistent with the finding that low complex I abundance is an independent prognostic marker of poor outcome in *PTEN*-deficient PCa, Bhandari *et al.* (2019a) noted (a) elevated hypoxia signatures in tumours with mtDNA mutations; an increased risk of biochemical recurrence in (b) *PTEN*-deficient hypoxic PCa cases, and as well as (c) *PTEN*-deficient hypoxic intraductal adenocarcinoma. More recently, Bhandari *et al.* (2019b) reported that *PTEN*-deficient hypoxic PCa also enriches for polyclonal tumour architecture. Therefore, assessment of hypoxia markers, IDC-CA histology, clonality, and in PCa samples, with linkage to OXPHOS protein data is warranted to assess whether these phenomena co-occur with OXPHOS alterations.

5.3.4 OXPHOS alterations impact overall survival

In order to account of intra-patient heterogeneity, three metrics were determined for each patient, based upon cores with lowest and highest Z-scores, and a mean Z-score calculated across all tumour cores from each patient. Patients were eventually divided into high and low abundance groups based on a single core with lowest complex I abundance, highest complex

IV abundance and highest mitochondrial mass. Of these markers, low complex I and high mitochondrial mass were found to be independent prognostic markers of overall survival across the whole cohort.

Cumulatively, high complex I heterogeneity, low complex I abundance and prognostic significance of tumour cores with the lowest complex I levels, raises the possibility that complex I deficient tumours may be an index lesion accounting for long-term patient outcomes. Of note, TURP samples are likely to be obtained from the transitional zone of the prostate, whereas biopsy samples are more likely to be obtained from peripheral zone. Thus, it is important to note that these data suffer from significant sampling bias, which limits over-interpretation of these findings, without designing an appropriately targeted experiment for this purpose. The ISUP guidelines recommend that index lesions be determined based on clinical context in the following order of priority: extra-prostatic extension, Gleason score and then tumour volume (van der Kwast *et al.*, 2011). Since these data, with the exception of Gleason score, are unavailable for tumour cores included in this experiment, it remains challenging to reliably determine whether tumour cores with the lowest complex I abundance were truly index lesions.

5.3.5 Reduced complex I abundance is an independent prognostic marker in *PTEN*-low PCa

Few previous studies have evaluated the prognostic value of *PTEN* using overall survival as the endpoint (Ahearn *et al.*, 2016). Coherent with findings reported in this chapter, Chen et al also noted that upon adjustment for clinical co-variates, the association between *PTEN* status and overall survival was not significant (Chen *et al.*, 2013b). In the presented data, patients were classified into low and high expression groups for *PTEN* and *ERG*-status as determined by IHC protein expression, rather than the gold-standard FISH assays. Though both FISH and IHC are complementary methods to assess *PTEN*-status (Lotan *et al.*, 2017) and *ERG* (Chaux *et al.*, 2011) with relatively straightforward interpretation, FISH-based assessment of a subset of patients would help improve accuracy and external validity of the reported findings. Furthermore, patient-level expression status was determined for both markers, not accounting for heterogeneity in marker expression across disparate tumour foci, which may influence patient classification and eventual outcome (Shah *et al.*, 2015).

In MCR TMA cohorts, *PTEN-low* tumour cores had lower mitochondrial mass, in comparison to *PTEN-high* cores. These findings were corroborated with an independent *ERG-positive*

radical prostatectomy cohort by Grupp *et al.* (2013), who also noted a reciprocal trend in *ERG-negative* PCa. Contrary to these observations, upregulation of the *Pi3k/Akt* signalling has been previously noted to increase mitochondrial mass, using *in vitro* hepatocyte and mouse embryonic fibroblast models (Li *et al.*, 2013b), where frequency of *TMPRSS2:ERG* fusions events are undocumented. It is also plausible that OXPHOS alterations may synergistically interact with other molecular subgroups of PCa, including *p53*-mutant, *c-MYC* over-expressing and *KRAS*-overexpressing PCa. Alterations in other established PCa signalling pathways such as *c-MYC* (Fan *et al.*, 2010) and *MAPK/KRAS* (Weinberg PNAS 2010) have been shown previously to be linked to mitochondrial abundance and function. Therefore, these reports highlight the importance of evaluating the impact of OXPHOS alterations in distinct molecular subgroups of PCa, and the need for caution in evaluating data from different tissue types.

Amongst patients with *PTEN-low* PCa, only low complex I expression was found to be prognostic of poor outcome. Consistent with this observation, Weber *et al.* (2018) previously reported a metabolic switch from NADH-driven entry of protons into complex I to succinate driven entry into complex II in *PTEN*-deficient PCa cells, enabling their growth and differentiation despite loss of complex I function. The authors further reported that succinate accumulation following *PTEN* loss led to the stabilisation of *HIF1α* and elevated lactate production, resulting in a hypoxia response and tumour growth. This may help explain the aggressive nature of *PTEN*-low cases with low complex I expression.

Amongst patients with *PTEN-low ERG-high* PCa in the MCR TMA cohorts, complex I loss was found to be a strong independent prognostic marker of poor outcome. In contrast, prognostic power of complex I was lost in *PTEN-low ERG-low* cases. The interplay between *ERG* status, *PTEN* status and disease progression has been studied previously using transgenic experiments, where *ERG*-overexpression in a prostate-specific *Pten*-deficient PCa mouse model restored androgen receptor signalling and led to the development of invasive adenocarcinoma (Chen *et al.*, 2013b). Together, these data suggest that *ERG*-mediated alterations, including the restoration of androgen receptor mediated signalling, may play a key role in determining response to complex I loss.

5.3.6 Low complex IV abundance is prognostic for better outcome in ERG-low PCa

Upon adjusting for clinical co-variates (age at diagnosis, log-10 PSA at diagnosis, Gleason group, clinical tumour stage, and presence of metastasis), complex IV abundance was only prognostic in *ERG-low* prostate cancers, with greatest effect size in *ERG-low PTEN-high* PCa, where low complex IV abundance was associated with improved long-term survival. For direct comparison with the study by Grupp *et al.* (2013), unadjusted *MTCO1* z-scores were evaluated in this patient cohort (see Appendix C (i)), and again found to be associated with adverse outcome (HR 0.33, 95% CI 0.15-0.74, p=0.007).

A potential explanation for this may be that functioning complex IV is a critical step in the transfer of electrons to complex V/ATPase, without which tumour cells lose metabolic flexibility in high oxygen environments. Furthermore, loss of complex IV may also result in a secondary loss of other OXPHOS complexes (Hargreaves *et al.*, 2007) and thereby reduced ATP production. Furthermore, pharmacological inhibition of complex IV using tetrathiomolybdate attenuated *HIF1α* signalling (Kim *et al.*, 2015), which would theoretically suppress tumour progression. Therefore, further evaluation of complex IV inhibitors in *ERG-negative* PCa models is required to test this hypothesis further.

5.3.7 Critical appraisal

The key strengths of this study include (a) a large sample size, (b) use of an automated quantitative assay, (c) measurement of protein level alterations using validated antibodies, (d) use of multiple tumour cores to capture heterogeneity, (e) normalisation of mitochondrial mass at the single cell level, (e) patient stratification by *PTEN* and *ERG* status, and (f) availability of long-term overall survival data.

“Normal” OXPHOS protein abundance was defined with reference to benign prostate tissue samples from young patients undergoing cystoprostatectomy. Though this provides a rich resource for such valuable tissue, it is unclear whether concomitant bladder cancer may influence OXPHOS protein abundance in adjacent prostate tissue. Nevertheless, all control prostate blocks were carefully reviewed to ensure that only histologically benign prostate tissue was included. Assessment of thresholds for loss of OXPHOS protein using suitable negative controls (eg tissue samples with established pathogenic homoplasmic mtDNA mutations in core OXPHOS subunits) would help further establish a reproducible scale for

OXPHOS marker abundance. Similarly, validation of *ERG* and *PTEN* status using a sub-set of samples with FISH-assessed genomic alterations would also help improve molecular stratification.

However, since archival tissue samples were used, variable tissue fixation protocols may bias results (Permuth-Wey *et al.*, 2009). Furthermore, it is difficult to establish whether patients included in TMA cohorts were truly disease-free following any primary curative treatment, though the vast majority of patients were treated with androgen deprivation therapy alone. Heterogeneity in subsequent treatment received may bias results for a subset of patients as well. Radical prostatectomy patients were not included in survival analyses due to the very low event rate in this population. Additional patients were excluded from survival analyses or multivariate Cox regression models due to missing data.

5.4 Conclusion

In this chapter, I have described OXPHOS protein abundance in a large cohort of patients with prostate cancer and evaluated the impact of OXPHOS alterations on long-term overall survival.

Though OXPHOS abundance in prostate tissue did not alter in an age-dependent manner, OXPHOS alterations frequently occurred in PCa tumour foci and impacted long-term overall survival (summarised in **Table 5-12**). Upon patient stratification by *PTEN* and *ERG* status and adjustment for clinical co-variates (age at diagnosis, log-10 PSA at diagnosis, Gleason group, clinical tumour stage, and presence of metastasis), complex I was implicated in *PTEN-low ERG-high* PCa, whereas complex IV and mitochondrial mass were implicated in *PTEN-high ERG-low* PCa.

Further work is required to (a) validate these findings in independent patient cohorts, (b) study the impact of OXPHOS alterations in other molecular subgroups of prostate cancer, and (c) test potential underlying mechanisms for these observations in transgenic models of PCa.

Notably, complex I deficiency was found to be associated with worse outcome in *PTEN-low* prostate cancers. This phenomenon will be explored further using transgenic mouse models.

OXPHOS component (*marker*)	Expression	Intra-patient tumoural heterogeneity	Impact on overall survival
Complex I (*NDUFB8*)	CaP vs BPH: No difference *PTEN-low vs PTEN-high*: No difference	High	Overall: Low CI associated with worse prognosis Sub-group analysis: Greatest effect in *PTEN-low ERG-high* PCa
Complex IV (*MTCO1*)	CaP vs BPH: No difference *PTEN-low* vs *PTEN-high*: No difference	Low	Overall: No impact Sub-group analysis: High CIV associated with worse prognosis in *PTEN-high ERG-low* PCa
Mitochondrial mass (*TOMM20*)	CaP vs BPH: Higher in PCa *PTEN-low* vs *PTEN-high*: Higher in PTEN-high	Low	Overall: High mitochondrial mass associated with worse prognosis Sub-group analysis: Greatest effect in *PTEN-high ERG-low* PCa

Table 5-12: OXPHOS protein abundance in human prostate cancer and its impact on overall survival.

Chapter 6 Modelling mitochondrial dysfunction *in vivo*

6.1 Introduction

6.1.1 Background

Metabolic alterations are frequently observed in both normal ageing (Kadenbach *et al.*, 1995) and prostate cancer (Kelly *et al.*, 2016; Giunchi *et al.*, 2019), and impact long term cancer outcomes (Hopkins *et al.*, 2017). As described in chapters 3 and 5, these alterations may be associated with defects in proteins involved in oxidative phosphorylation (OXPHOS), which may be explained by a number of phenomena including accumulation of mtDNA mutations, downstream transcriptomic or epigenetic alterations, or a consequence of clonal selection.

The impact of mtDNA polymorphisms and downstream OXPHOS alterations on initiation and progression of prostate cancer, at both local and systemic level, is currently poorly understood.

6.1.2 Mouse models of mitochondrial dysfunction

Mice have been extensively employed in the study of mitochondrial diseases, ageing and carcinogenesis, given their genetic (Mouse Genome Sequencing *et al.*, 2002), physiological and cellular similarity to humans (Shappell *et al.*, 2004), ease of maintenance, small body size, relatively short reproductive cycle (approx. 12 weeks) and large litter sizes. Comparative human and mouse prostate anatomy is discussed in section 1.1.7.

Mouse models of mitochondrial dysfunction may be generated by genetic manipulation of nuclear-encoded OXPHOS genes, introduction of mutant mtDNA into mice, or through dysregulation of mtDNA stability or replication. Frequently used mouse models of mitochondrial dysfunction are described in **Table 6-1**, However, models harbouring a stable mutation in any of the seven mtDNA encoded complex I subunit genes are currently unavailable (Irwin *et al.*, 2013). The only nuclear-encoded complex I gene that has been successfully targeted in mice is *Ndufs4* (Kruse *et al.*, 2008). Homozygous knock-out of *Ndufs4* is associated with severe neuro-muscular phenotypes and death by 7 weeks of age, whereas homozygous *Ndufs4* knock-in mice with constitutive insertional mutagenesis at exon 2 demonstrated embryonic lethality. Tissue specific *Ndufs4* knock-out has been used in the study of neurodegeneration (Quintana *et al.*, 2010; Choi *et al.*, 2017), but not carcinogenesis. In contrast, two knock-out mutants leading to the loss of *COXIV* and *COX10*, and thereby

complex IV dysfunction have been reported. These are associated with normal lifespan in both tissue-specific and constitutive knock-out models. However, alterations in complex IV were only found to be implicated in *PTEN*+ *ERG*- prostate cancers and were therefore felt unlikely to impact PTEN-deficient PCa progression. Furthermore, gene-specific mitochondrial mouse models may not be ideal for the study of features associated with normal human ageing, since they do no not fully recapitulate the heterogenous age-related spectrum of mtDNA mutations, as observed in human PCa.

Model	Reference	Gene, Mutation	Phenotype
Nuclear-encoded components of OXPHOS			
COXIVa KO	Radford *et al.* (2002)	CIV only	Normal life span, left diastolyic dysfunction.
COX10 cd-KO	Diaz *et al.* (2005) Diaz *et al.* (2008) Zahalka *et al.* (2017)	CIV only	Tissue-specific to muscle (MLC1f promoter), liver, brain, endothelial cells
NDUFS4 KO	Kruse *et al.* (2008)	CI only	Death by 7 weeks of age (ie prior to prostate maturation)
NDUFS4 cd-KO	Quintana *et al.* (2010) Choi *et al.* (2017)	CI only	Death by 7 weeks of age. Tissue-specific to neurons and astroglial cell, dominergic neurons
NDUFS4 knock-in	Ingraham *et al.* (2009)	CI only	Embryonic lethality of homozygous mice
mtDNA defects			
Trans-mitochondrial cybrid mice	McKenzie *et al.* (2004) Fan *et al.* (2008) Hashizume *et al.* (2012)	Mt-Nd6, m.13997G>A [CI] *COXI* (T6589C/V421A) [CIV]	Technically challenging. Useful for studying threshold effects of mutant mtDNA heteroplasmy on the same nuclear background.
Conplastic strains	Yu *et al.* (2009)	Multiple	Takes 4-5 years to establish conplastic strains by multiple back-crosses.
Mitochondrial-Nuclear eXchange (MNX) mice	Kesterson *et al.* (2016) Examples: Feeley *et al.* (2015) Vivian *et al.* (2017)	Multiple	Pronuclear transfer. Limited by mtDNA polymorphisms seen in mice, due to current limitations in designing mtDNA polymorphisms observed in humans.
Proteins involved in mtDNA stability and repair			
TFAM knockout	Larsson *et al.* (1998) in cardiomyocytes	Multiple	Reduced mitochondrial copy number, severe OXPHOS defects and abnormal mitochondrial morphology. Others - skeletal muscle, pancreatic endocrine tissue, brain.
Polg (D457A) mutator mice	Trifunovic *et al.* (2004) Kujoth *et al.* (2005)	Multiple	Described in **Table 6-2**.
mSUV helicase mice	Chen *et al.* (2013a)	Multiple	Overt metastasis.

Table 6-1: Mouse models of mitochondrial dysfunction and associated phenotypes.

6.1.3 Spontaneous tumour development in mouse models of mitochondrial dysfunction

Wild-type mice do not spontaneously develop PCa (Lamb and Zhang, 2005). Spontaneous tumour initiation has been reported in two mouse models of mitochondrial dysfunction: *mSuv*$^{+/-}$ mice and m.13997A>G trans-mitochondrial mice.

Suv3 is a mitochondrially-localised nuclear-encoded ATP-dependent DNA/RNA helicase, where it forms part of the RNA degradosome. Inactivation of Suv3 in *mSuv*$^{+/-}$ mice results in accumulation of aberrant transcripts, truncated transcripts, and excised group I introns, eventually disrupting mitochondrial dysfunction associated with reduced mtDNA copy number and reduced OXPHOS protein synthesis. Homozygous *mSuv3*$^{-/-}$ mice demonstrate embryonic lethality, whereas *mSuv3*$^{+/-}$ mice developed multiple tumours, including lymphoma and lung adenocarcinomas. MtDNA mutations from tumour-bearing *mSuv3*$^{+/-}$ mice were maternally transmitted to wild-type *mSuv3*$^{+/+}$ offspring, which also developed tumours and had a significantly reduced lifespan (Chen *et al.*, 2013a). However, this model had a physiologically catastrophic burden of mtDNA mutations leading to unsustainable metabolism and rapid death, limiting its clinical relevance.

Trans-mitochondrial cybrid mice (also known as “mito-mice”) generated by introduction of m.13997A>G (ND6 of Complex I) in C57BL/6J (B6) mouse embryonic fibroblasts (MEF) spontaneously developed lymphomas, but with no change in lifespan (Hashizume *et al.*, 2012).

Notably, spontaneous development of prostate tumours was not reported in either of these models and is rarely observed in any established laboratory mouse strains (Suwa *et al.*, 2002; Szymanska *et al.*, 2014). Both Chen & Wu papers used the C57BL/6J (B6) genetic background, which is pre-disposed to development of lymphoma (Ward, 2006). Therefore, the observed tumour initiation may be due to the genetic background rather than mitochondrial dysfunction. Consistent with this hypothesis, lymphoma formation was not observed when m.13977A>G mito-mice were generated over a A/J nuclear genomic background (Hashizume *et al.*, 2015).

6.1.4 The Polg mutator mouse model

The Polg mutator mouse model has been extensively used in the study of ageing research as it closely models age-related phenotypes observed in humans. DNA polymerase gamma is an enzyme comprising of a catalytic subunit encoded by the *POLG* gene (Mouse *Polg*: Chr 7; Human *POLG1*: Chr 15) and two accessory subunits encoded by *POLG2* gene (Mouse *Polg2:* Chr 11; Human POLG2: Chr 17), that plays a critical role in proof-reading during mtDNA replication (Vanderstraeten *et al.*, 1998). The catalytic unit comprises of DNA polymerase, a 3'-5' exonuclease and 5' lysase activity, whereas the accessory subunits comprises of a DNA binding factor enabling high processivity by increasing affinity to the DNA template (Hudson and Chinnery, 2006).

Mice lacking both copies of the catalytic domain of *Polg* ($Polg^{-/-}$) lose both polymerase and exonuclease activity resulting in a dramatic decrease in mtDNA levels and absence of COX activity (Hance *et al.*, 2005), and consequently demonstrate embryonic lethality.

In contrast, *Polg*-mutator mice ($Polg^{mut/mut}$) have a knock-in mutation in exon 3 of the exonuclease domain of DNA polymerase ɣ (Pol-g) leading to leading to loss of mtDNA proof-reading during DNA replication due to loss of exonuclease activity, but preservation of polymerase activity. This leads to accumulation of mtDNA mutations over time, resulting in mitochondrial dysfunction (Trifunovic *et al.*, 2004; Kujoth *et al.*, 2005). Homozygous *Polg* mutator mice, henceforth referred to as 'Polg-HOM' mice, develop an accelerated ageing phenotype as described in **Table 6-2**, as a consequence of approximately 2,500 times greater rate of mtDNA mutations (Vermulst *et al.*, 2007). In comparison, mice with heterozygous Polg mutation ($Polg^{wt/mut}$), henceforth referred to as 'Polg-HET' mice, develop a lower burden of mtDNA mutations with no overt phenotypes. The mutational frequency in young Polg-HET mice (2-3 months of age) is 500 times that of age-matched wild-type mice, and 29 times higher than older wild-type mice (24-33 months of age, (Vermulst *et al.*, 2007)). Baines *et al.* (2014) reported a comparable pattern of clonally expanded somatic mtDNA mutations in Polg-HET mouse colons, as compared to ageing human colons. Notably, prostate tissue from Polg mutator mice has previously not been evaluated.

Organ system	Phenotype	Reference
Systemic	Weight loss Reduced subcutaneous fat Alopecia & premature greying Reduced life span	Trifunovic *et al.* (2004) Kujoth *et al.* (2005)
Genito-urinary	Testicular atrophy Reduced spermatogenesis Reduced fertility Reduced ovarian function	Trifunovic *et al.* (2004) Kujoth *et al.* (2005) Jiang *et al.* (2017) Faraci *et al.* (2018)
Immune system	Activation of innate immune response Immune cell infiltration Decreased IL-1b secretion Reduced B-cells	Martinez *et al.* (2018)
Gastrointestinal	Malabsorption Stunted intestinal crypts	Trifunovic *et al.* (2004) Kujoth *et al.* (2005)
Cardiovascular	Cardiomyopathy	Dai *et al.* (2010)
Musculoskeletal	Kyphosis Osteoporosis Sarcopaenia	Trifunovic *et al.* (2004) Kujoth *et al.* (2005) Hiona *et al.* (2010)
Endocrine	Reduced testosterone Reduced appetite	Fox *et al.* (2012)
Haematological	Erythroid dysplasia, megaloblastic anaemia, and impaired lymphopoiesis Reduced haematopoesis	Chen *et al.* (2009) Norddahl *et al.* (2011)
Others	Presbycusis (age-related hearing loss)	Yamasoba *et al.* (2007)
Cellular	Increased apoptosis	Kujoth *et al.* (2005) Hiona *et al.* (2010)

Table 6-2: Phenotypes observed in Polg-HOM mutator mice.

Given that mitotic tissues stochastically accumulate mtDNA mutations with advancing age and a similar age-related increase in stochastic mtDNA mutations is observed in human prostate cancer (Hopkins *et al.*, 2017), the Polg model provides an opportunity to model age-related accumulation of mtDNA mutations and evaluate the impact of consequent systemic and local mitochondrial dysfunction on cancer initiation and progression.

6.1.5 Chapter aims

In this chapter, I aim to evaluate the potential consequences of age-related mtDNA mutations focussing at development of OXPHOS defects and impact on prostate cancer initiation. Broadly, the key objectives of this chapter are therefore to:

1. Characterise the Polg mutator mouse prostate, as a model of age-related mitochondrial dysfunction.
2. Measure burden of mitochondrial OXPHOS defects in Polg mouse prostate tissue, and age-matched wild-type control tissue.
3. Evaluate transcriptomic changes associated with age-related accumulation of mitochondrial DNA mutations.

6.2 Results

6.2.1 Reduced lifespan in Polg-HOM mice

As per previous reports, Polg-HOM mice have reduced lifespan, ranging from median survival of 329 days (Trifunovic *et al.* (2004), C57Bl/6N background) to 425 days (Kujoth *et al.* (2005), C57Bl/6J background). Also, in keeping with published data, Polg-HOM mice were found to display severe age-related pathologies at clinical end points, including kyphosis, anaemia and significant weight loss. Polg-HOM mice used in this study were derived from animals kindly donated by Professor Thomas Prolla (Kujoth *et al.*, 2005). Based on previous lifespan data, these animals were sacrificed at 11 months (330 days) of age, to minimise animal distress. A small number of mice were sacrificed at earlier timepoints due to development of severe anal prolapse, significant weight loss, or clinical features of anaemia.

Variation in median survival between different colonies may be attributed to variation in genetic backgrounds, local pathogens and animal husbandry practices. In light of this, experimental and control mice from the same colony have been used for all subsequent comparisons.

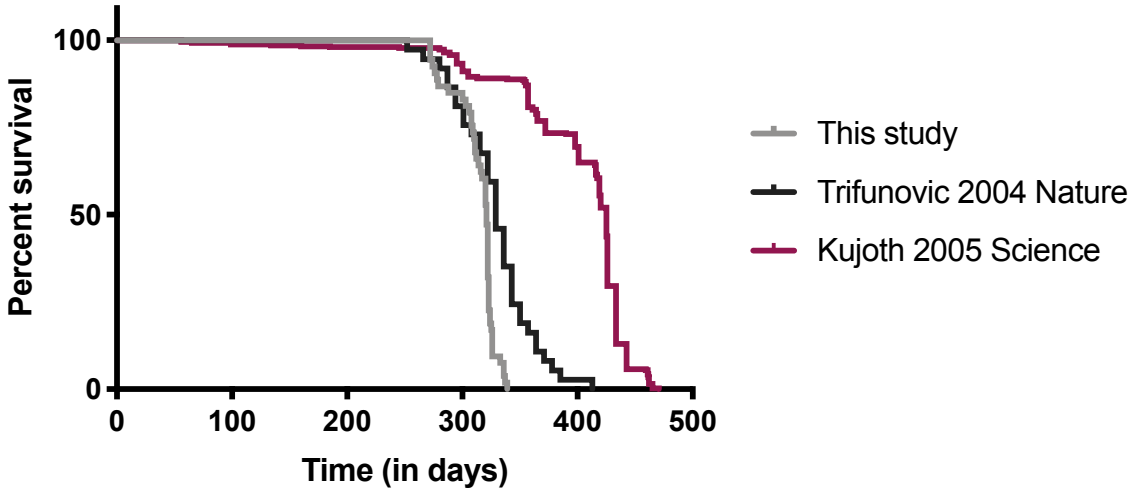

Figure 6-1: Variation in survival across different Polg-HOM mouse cohorts. Data from Polg-HOM mice used in this study (n=54) were compared with previously published data from Trifunovic *et al.* (2004)(C57Bl/6N background, n=37) and Kujoth *et al.* (2005)(C57Bl/6J background, n=230).

6.2.2 Polg-HOM mice have smaller urogenitals compared to age-matched wild-type controls

Wild-type, Polg-HET and Polg-HOM mice were sacrificed, weighed, and their organs harvested at 4, 7, and 11 months of age (dissection protocol described in section 2.4) to study age-related changes. Organ weights are reported as percentage of total body weight to adjust for age and genotype related variation in body weights. Polg-HOM mice had a relatively smaller urogenitus and testes by 11 months of age (**Figure 6-2**). In comparison to age-matched wild-type controls, Polg-HOM mice had lower body weight and testicular weight at 7 months and 11 months of age (**Figure 6-3**), as previously reported (Trifunovic *et al.*, 2004; Jiang *et al.*, 2017). Body and testicular weights amongst Polg-HET mice were similar to age-matched wild-type mice.

Prostate lobes were micro-dissected, weighed and normalised to body weight. Though normalised total prostate weight did not differ between different genotypes, normalised anterior and ventral prostate weights were lower in Polg-HOM mice at 11 months of age, in comparison to age-matched wild-type controls (**Figure 6-3**).

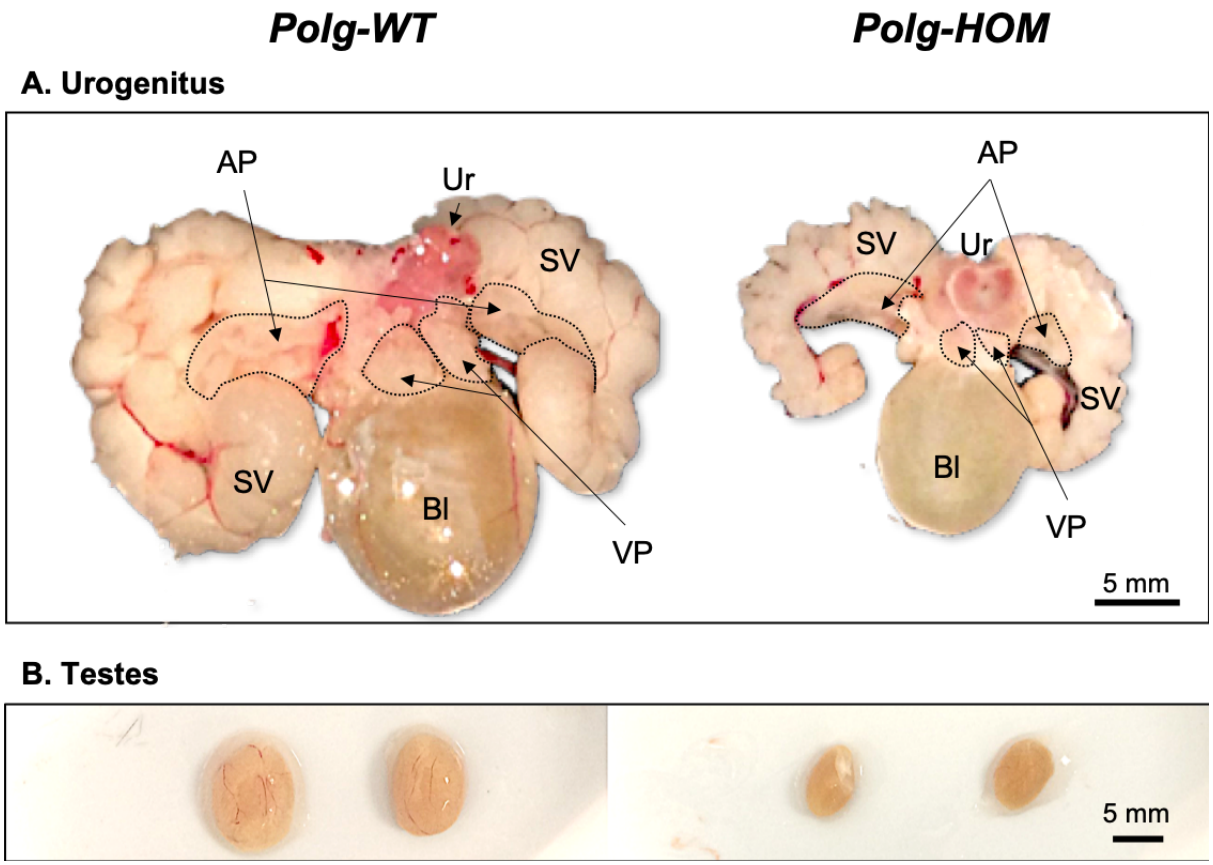

Figure 6-2: Urogenitus and testis size. **(A)** Urogenital and **(B)** testicular hypoplasia was observed in Polg-HOM mice, as compared to wild-type mice. AP: Anterior prostate, Bl: Bladder, SV: Seminar vesicle, Ur: Urethra, VP: Ventral prostate.

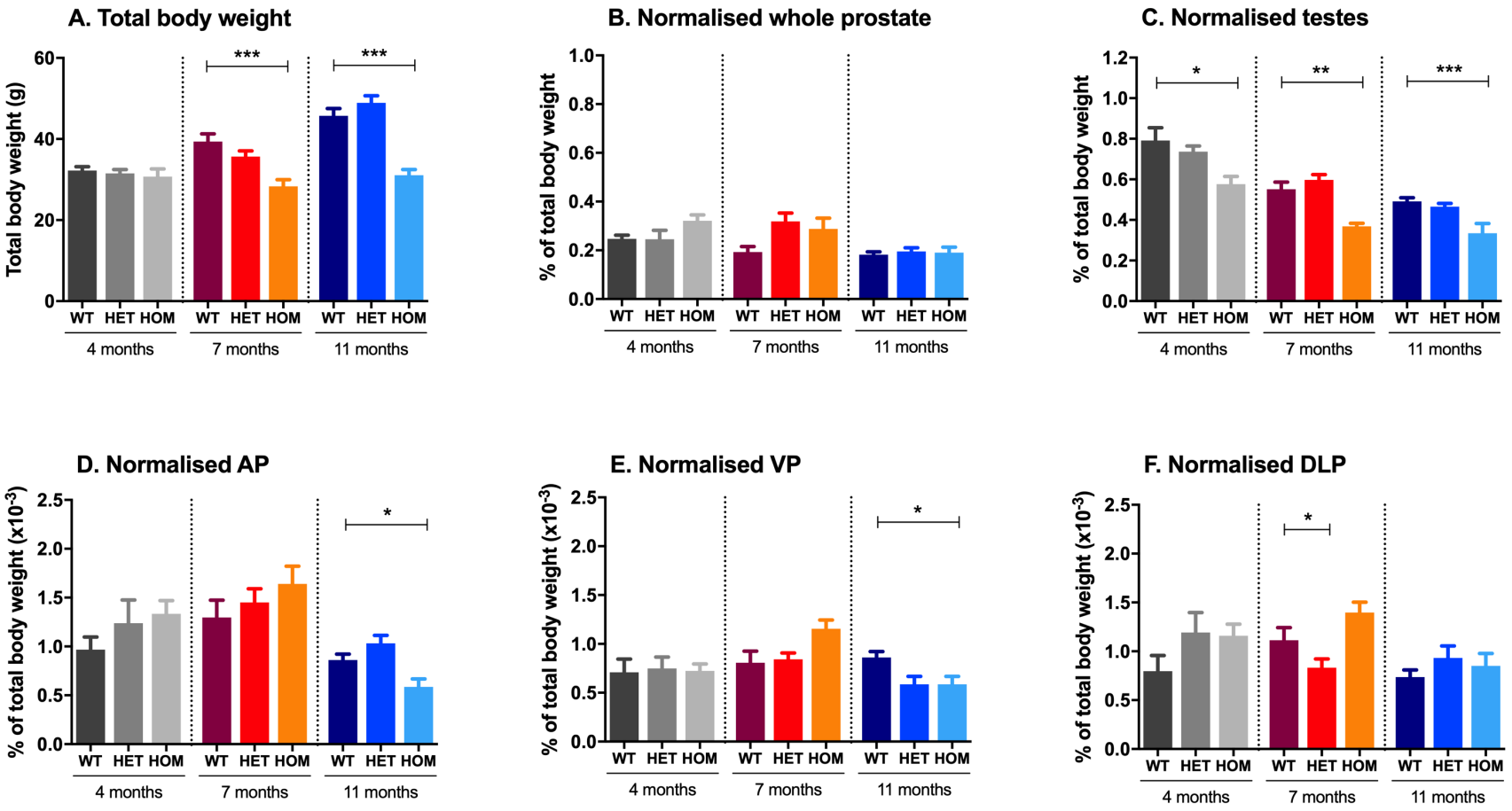

Figure 6-3: Morphometric data for Polg mouse colony. Weight data for Polg-WT, Polg-HET and Polg-HOM mice at ages 4, 7 and 11 months. Minimum of 5 mice included in each group. Amongst Polg-HOM mice, these data demonstrate age-related **(A)** loss of body weight; **(B)** No change in total prostate weight; **(C)** loss of testicular, **(D)** anterior prostate and **(E)** ventral prostate weight weight; **(F)** No change in dorsolateral prostate weight. *P* values determined by one-way ANOVA and Dunnet's multiple comparison tests are reported as *, **, *** and represent <0.05, <0.01, and <0.001, respectively.

6.2.3 Polg-HOM mice develop atypical hyperplasia, but not invasive adenocarcinoma.

Histologically, Polg-HOM prostate tissue was comparable to age-matched wild-type controls with normal epithelial morphology observed across both genotypes.

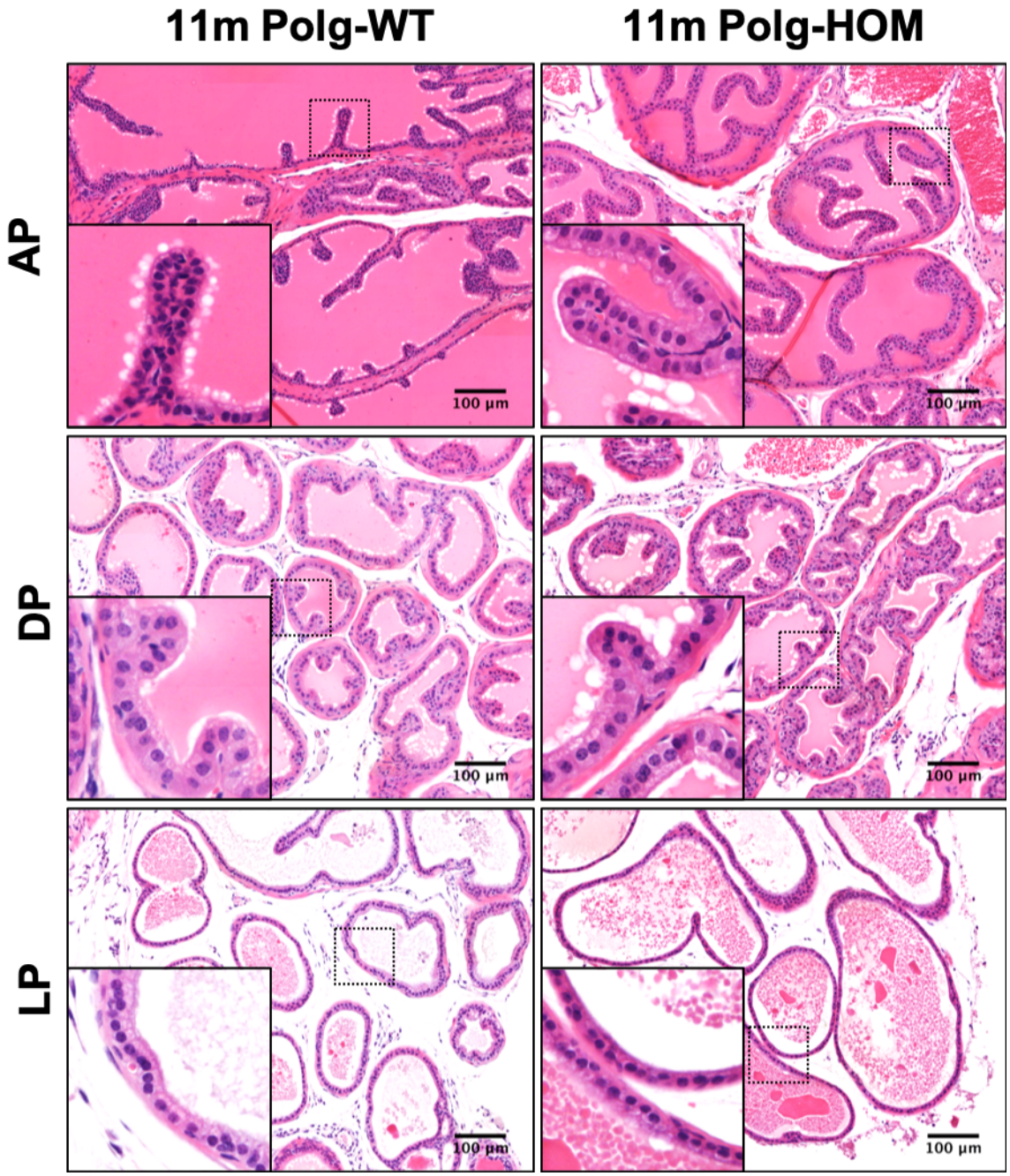

Figure 6-4: Haemotoxylin and eosin stained mouse prostate tissue. Representative regions of anterior (AP), dorsal (DP) and lateral (LP) prostate lobes from 11-month Polg-HOM and wild-type control cohorts. Scale bars represent 100 µm.

Scattered hyperplastic glands were observed in 11-month Polg-HOM mice (**Figure 6-5**), but not amongst younger Polg-HOM mice or age-matched wild-type controls. However, these lesions were relatively rare (approx. median 1-2 atypical glands per mouse) and not restricted to any particular prostate lobe. Epithelial hyperplasia is a non-neoplastic proliferation characterised by an increase in glandular spaces or increase in epithelial cells within normal-appearing glands, which may appear as stratified epithelial cells, either focally or uniformly throughout the prostate. This may occasionally be accompanied by minimal atypia, including nuclear enlargement, pleomorphism, prominent nucleoli and chromatin abnormalities.

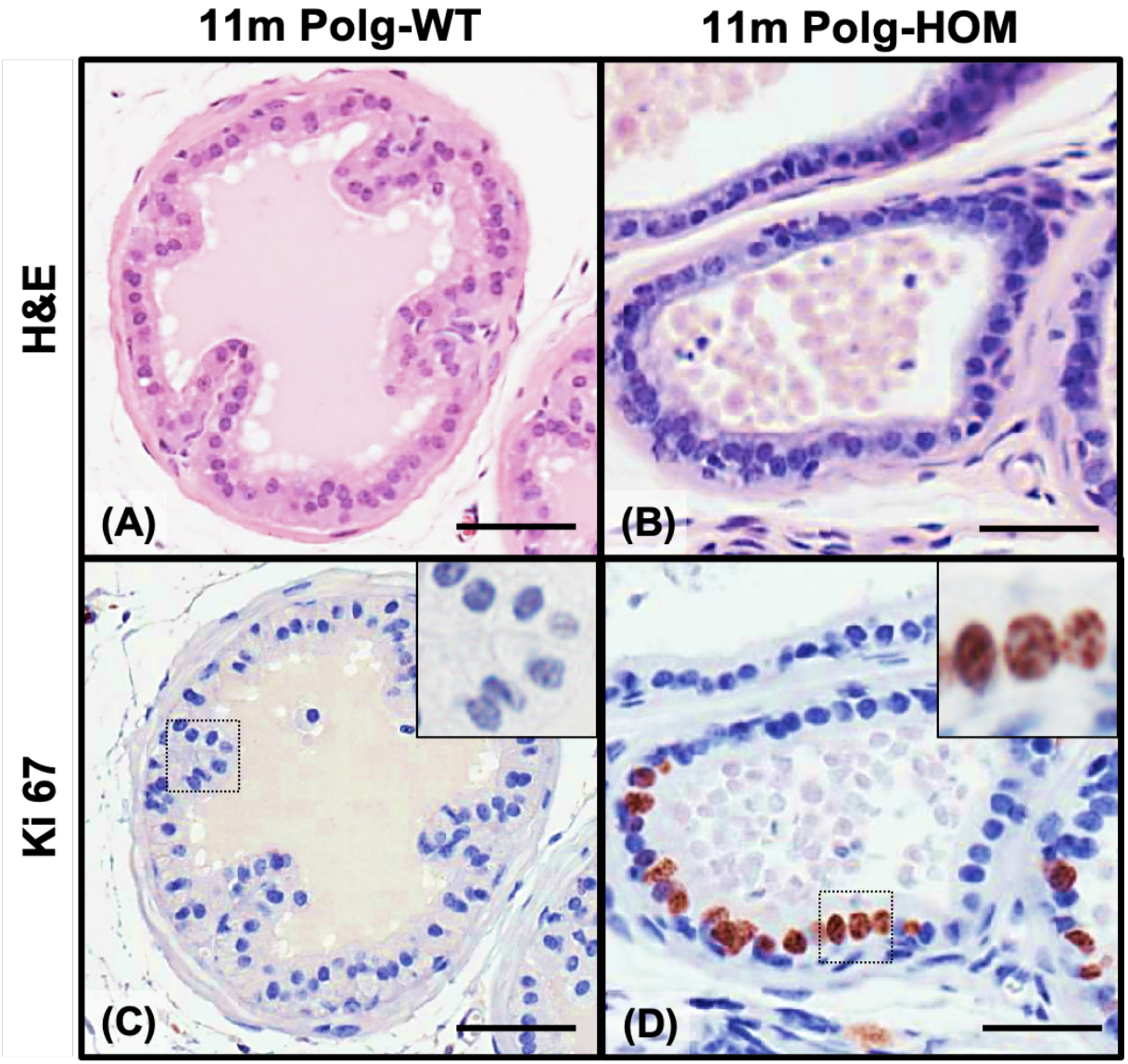

Figure 6-5: Prostate hyperplasia in Polg-HOM mouse model. Representative H&E and Ki-67 immunostaining of prostate tissue sections from 11-month wild-type and Polg-HOM mouse prostates. Rare areas of epithelial hyperplasia, with increased frequency of Ki-67 positive cells and nuclear atypia (*inset*), were observed in prostate tissue from Polg-HOM mice. Scale bars represent 100 µm.

6.2.4 Impaired spermatogenesis in aged Polg-HOM mice

Consistent with morphometric data in section 6.2, testicular atrophy was observed in Polg-HOM mouse testes by 7-months of age, in keeping with previous reports (Trifunovic *et al.*, 2004; Jiang *et al.*, 2017). Histologically, 7-month old Polg-HOM testes displayed tubular degeneration with reduced spermatids, as previously noted by Trifunovic *et al.* (2004), who also reported a complete absence of sperm by 40 weeks.

In keeping with this finding, decreased serum testosterone has previously been reported in Polg mice (Fox *et al.*, 2012). Jiang *et al.* (2017) have also reported profoundly reduced fertility in Polg-HOM mice, despite normal mating behaviour, associated with significantly lower sperm counts, lower percentage of motile sperm and morphological abnormal sperm head and tail abnormalities, in comparison to wild type controls. OXPHOS defects were observed also in spermatids from Polg-HOM mice in this study, which was partially rescued by TFAM overexpression via an increase in absolute mtDNA copy number.

Since mice aged 4-9 months of age are frequently used in colony maintenance and mtDNA mutations are maternally inherited, Polg-HOM mice with reduced fertility could not be used for breeding purposes. The Polg colony was therefore maintained using Polg-HET mice.

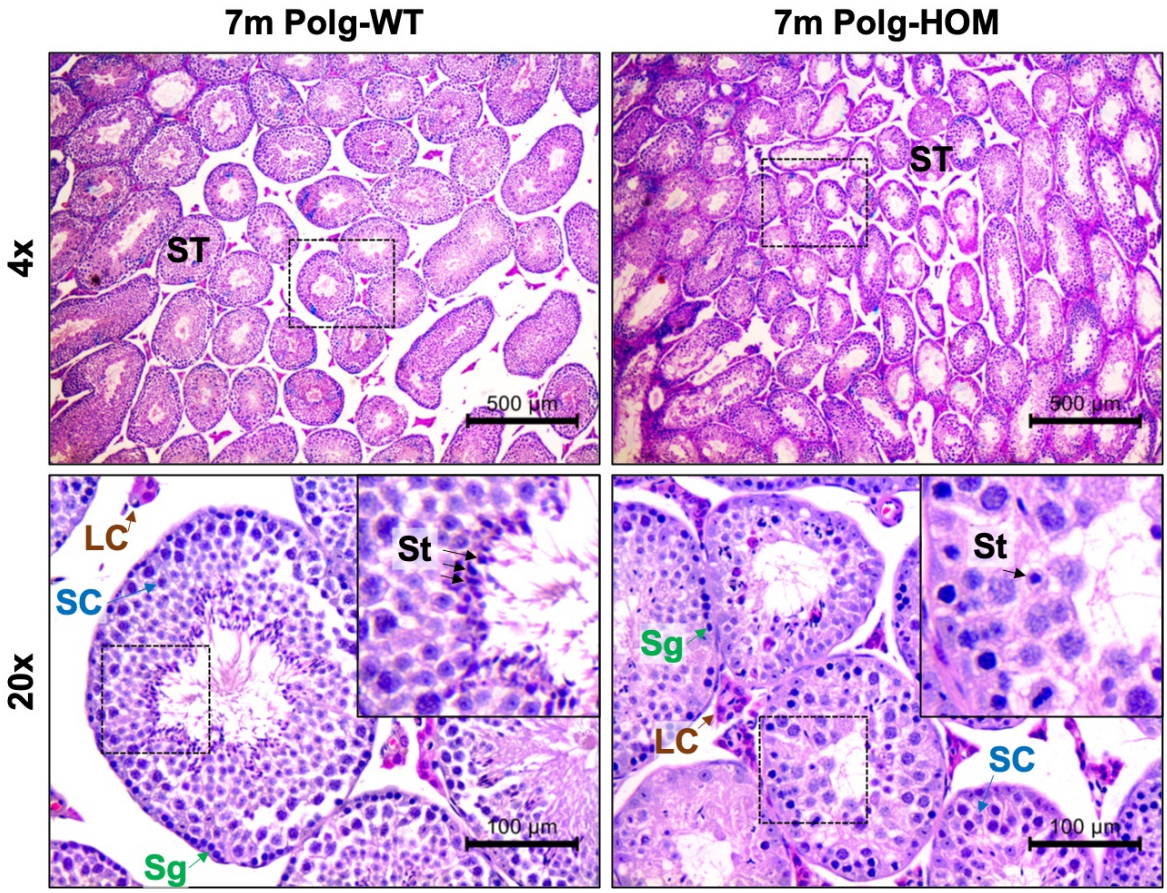

Figure 6-6: Impaired spermatogenesis in Polg-HOM mouse model. Representative H&E stained tissue sections from 7-month wild-type and Polg-HOM mouse testes. Severe testicular tubular degeneration with reduced spermatids (St) noted in Polg-HOM mouse testes (*inset*). ST: Seminiferous tubube; SC: Sertoli cell; Sg: Spermatogonia; St: Spermatid; LC: Leydig cell. Scale bars represent 500 µm (4x objective, *top panels*) and 100 µm (20x objective, *bottom panels*).

6.2.5 COX defects in Polg-HOM mouse prostates

Mitochondrial function was evaluated in snap-frozen mouse prostate tissue sections using the sequential COX/SDH enzyme histochemical assay, as described in section 2.5.1. The rationale underlying this assay is described below.

The presence of functional COX enzyme catalyses the oxidation of 3,3'-diaminobenzamine (an electron donor), leading to the deposition of the brown indamine polymer at mitochondrial cristae, and subsequent saturation of cells with functional COX enzyme. Upon subsequent addition of nitroblue tetrazolium (NBT, an electron acceptor), cells not saturated by brown indamine polymer are visualised by the reduction of NBT by the action of SDH, leading to the deposition of blue formazon crystals. Endogenous levels of cytochrome *c* and sodium succinate are normalised by exogenous supplementation of these reagents in the reaction media. The COX media also supplemented with catalase to minimise contamination by endogenous peroxidases, and sodium azide to terminally inhibit the mitochondrial respiratory chain. Phenazine methosulphate (PMS) is included in the SDH medium as an intermediate electron carrier. Both sodium azide and PMS thereby help increase the formation of the final reaction products.

Cells lacking a functional COX enzyme are therefore stained blue, whereas those with COX-defects are stained brown. An increased frequency of COX-deficient cells has previously been reported in multiple Polg-HOM mouse tissues, including heart, intestine, liver and skeletal muscle. An exponential increase in proportion of COX-deficient cells was noted in Polg-HOM mice (R^2 0.99), as compared to a slow linear increase in Polg-HET prostates (R^2 0.97). Scant COX-deficient cells were observed in aged 11-month Polg-WT mouse prostates. Similarly, an age-related increase in COX-deficient cells has also been reported in human organs, including prostate tissue (Blackwood *et al.*, 2011), intestine (Taylor *et al.*, 2003; Greaves *et al.*, 2010), and brain (Cottrell *et al.*, 2001).

The COX/SDH assay predominantly highlights cells with loss of complex IV of the electron transport chain. Since Polg-HOM mice are driven by a proof-reading defect, leading to a stochastic accumulation of mtDNA mutations across the mitochondrial genome, it is likely that these mice may also harbour alterations in other OXPHOS complexes. This raises the possibility that the true burden of OXPHOS defects may not have been adequately captured in this small study using COX/SDH enzyme histochemistry.

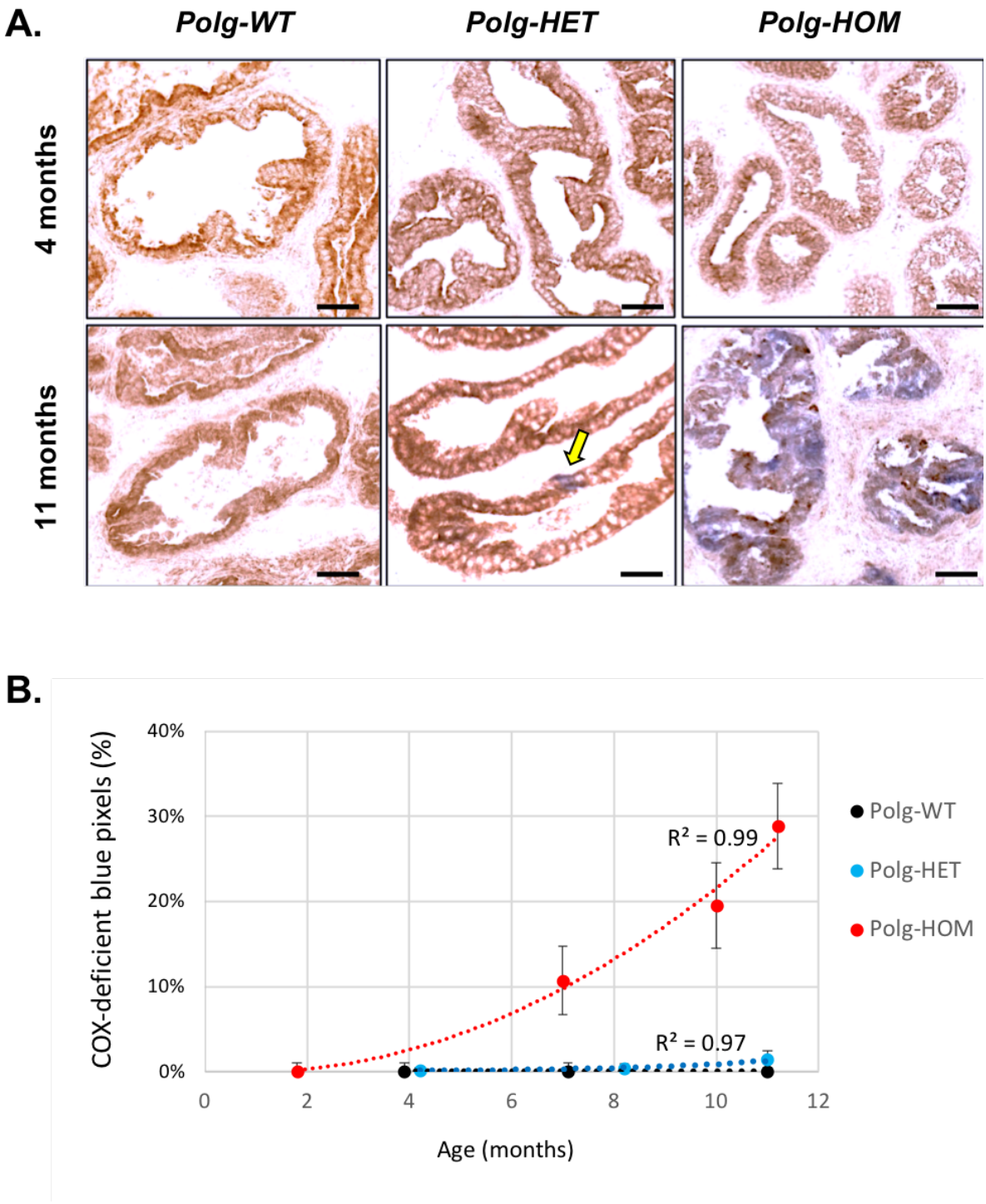

Figure 6-7: COX-SDH enzyme histochemistry. (A) Representative images of sequential COX-SDH enzyme histochemistry performed on frozen prostate tissue sections from an ageing series of Polg-WT and Polg-HOM mice. COX-deficient cells (counterstained blue) are observed in 11-month Polg-HET (*arrow*) and more frequently in 11-month Polg-HOM mouse prostate tissue. Scale bar represents 50µm. **(B)** Quantification of COX-deficient blue pixels. Each point represents an individual mouse. Error bars represent standard deviation. Trends lines representing exponential increase best fit age-related increase in COX-deficient blue pixels in COX-SDH images from Polg-HOM mice (R^2 0.99), whereas a small linear increase in blue pixels was observed in Polg-HET (R^2 0.97) and Polg-WT mice.

6.2.6 Frequency and magnitude of OXPHOS defects is greater in older Polg-HOM mouse prostates, as compared to age-matched wild-type controls

6.2.6.1 Chromogenic immunohistochemistry

Since both Polg-HOM mice (Ma *et al.*, 2018) and human prostate tissues (Chapter 3), frequently accumulated mtDNA mutations in complex I & IV, we evaluated these complexes in formalin-fixed prostate tissue using chromogenic immunohistochemistry with established antibody markers *NDUFB8* and *MTCO1*, respectively. Protein defects in *NDUFB8* (complex I subunit) and *MTCO1* (complex IV subunit) were noted in adjacent glands in 11-month Polg-HOM prostates. However, adaptive increase in mitochondrial biogenesis as a response to OXPHOS defects, may lead to cellular heterogeneity in mitochondrial mass, and consequently underestimate true OXPHOS defects (relative defects), while only highlighting absolute OXPHOS defects through the absence of chromogen.

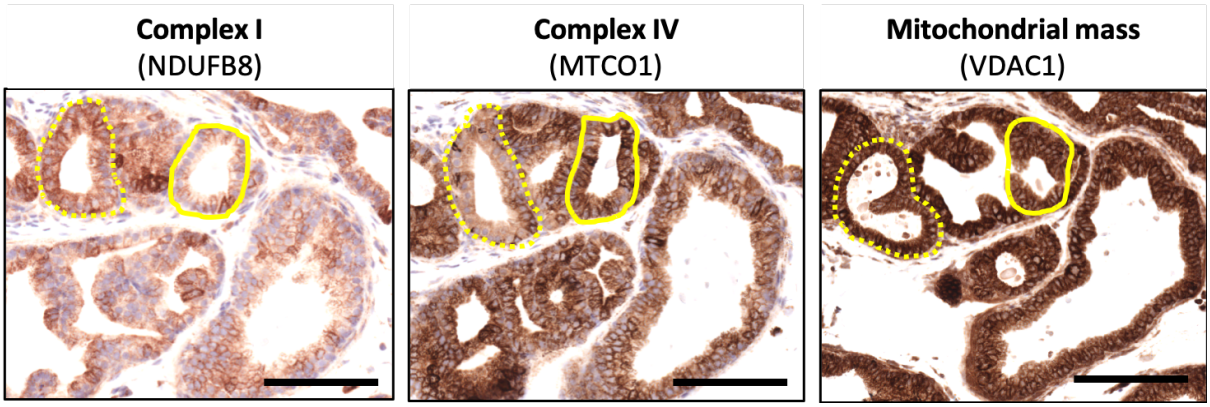

Figure 6-8: OXPHOS defects in Polg mouse prostate tissue: Chromogenic immunohistochemistry. Immunohistochemical staining of serial sections of 11-month Polg-HOM mouse using **(A)** *NDUFB8*, **(B)** *MTCO1*, and **(C)** *VDAC1* antibodies. Solid line highlights a Complex I deficient gland, Dotted line highlights a Complex IV deficient gland. Scale bars represent 100µm.

6.2.6.2 Quantitative immunofluorescence

In order to overcome bias due to variability in mitochondrial mass, a quantitative quadruple immunofluorescence-based method was employed. This is similar to the manual method used in the estimation of OXPHOS defects in human prostate tissue (section 4.2.5). FFPE mouse prostate tissue sections from 4 and 11-month-old mice from wild-type and Polg-HOM genotypes (n=2-5 per cohort) were labelled for markers of complex I (*NDUFB8*), complex IV (*MTCO1*), mitochondrial mass (*VDAC1*) and epithelial cells (β-catenin). *VDAC1* (Voltage dependent anion-specific channel 1), is an ion channel located at the outer mitochondrial membrane and an established marker of mitochondrial mass (Rocha *et al.*, 2015). B-catenin was used as an epithelial cell marker, since this is expressed on the cell membranes of benign prostate epithelial cells and can therefore be used to demarcate individual epithelial cells. Up to 10 randomly selected regions of interest were acquired from each sample using a 40x objective, and a minimum of 50 cells were manually demarcated per ROI. Single cell level optical density data were acquired. Together with a single cell analysis pipeline and the use of a mitochondrial mass marker, abundance of complex I and IV was normalised for inter-cellular variation in mitochondrial mass, thus providing comparable measures of mitochondrial OXPHOS complex abundance. Data from prostate epithelial cells from 4-month Polg-WT mice was used as control, and z-scores for complex I, IV and mitochondria mass were estimated. These were plot on a mitochondrial respiratory chain (MRC) plot to visually assess the relationship between complex I, IV and mitochondrial mass z-scores.

Since the 4-month Polg-WT prostate samples were used as controls, the z-scores for all mitochondrial markers were expectedly within 3 standard deviations of the mean. This was based on the assumption that that OXPHOS defects arise only at very low frequency and magnitude by 4 months of age, consistent with a recent report of absence of mtDNA mutations in young wild-type heart and liver tissue (Ma *et al.*, 2018). In contrast, a proportionate decrease in complex I and complex IV z-scores was noted in wild-type mice by 11 months of age (**Figure 6-10**), with a speckled morphology of mitochondria on confocal imaging (**Figure 6-9**).

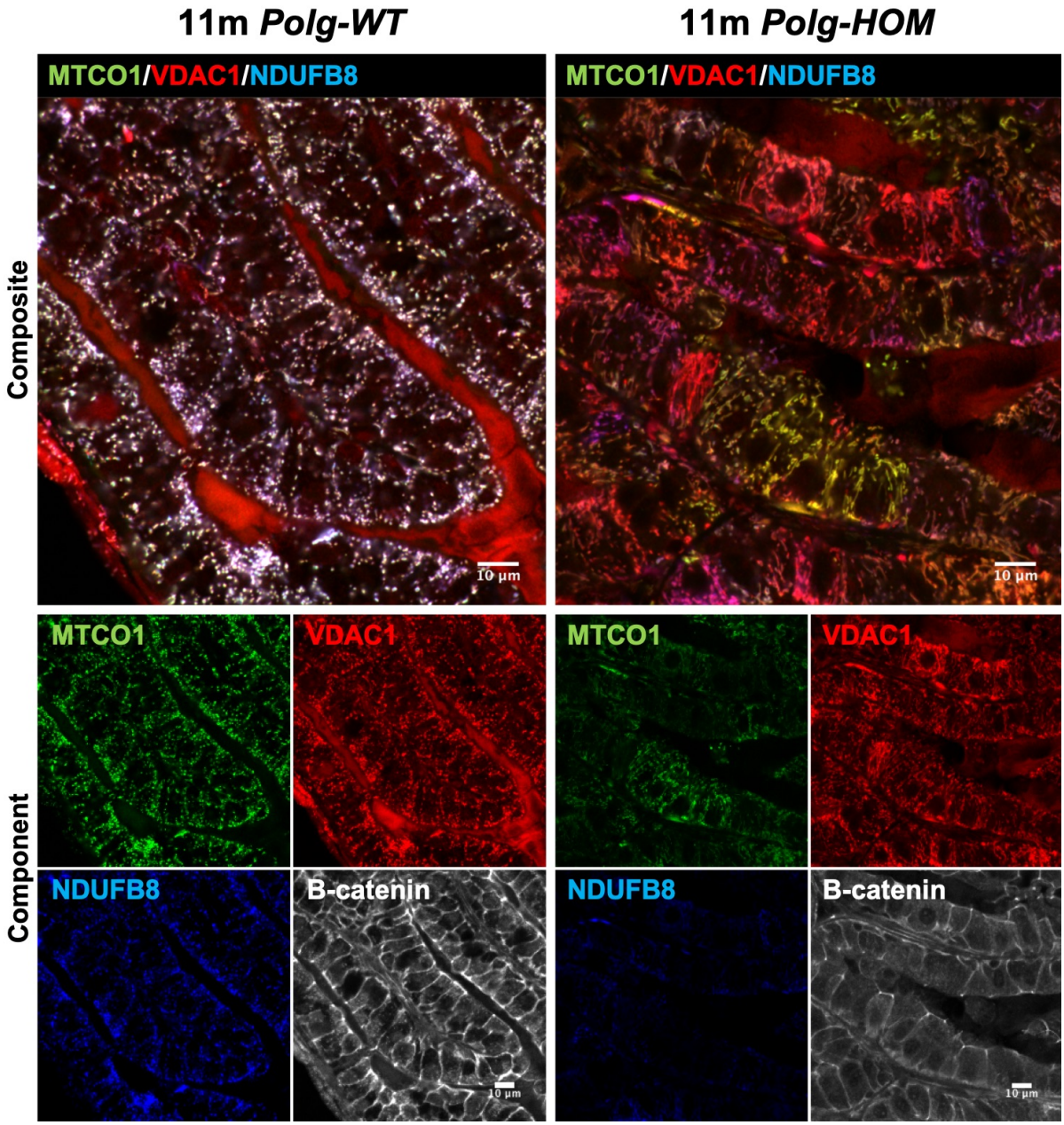

Figure 6-9: OXPHOS protein alterations in Polg-HOM mouse prostate tissue. Quadruple immunofluorescence assay targeting *NDUFB8* (complex I subunit, blue, AlexaFluor 647), *MTCO1* (complex IV subunit, green, AlexaFluor 488), *VDAC1* (mitochondrial mass marker, red, AlexaFluor 546), and β-catenin (as epithelial cell membrane marker, grey, AlexaFluor 405) demonstrates areas of reduced *NDUFB8* expression, *MTCO1* expression and increased *VDAC1* expression in Polg-HOM mouse prostate tissue, in comparison to an age-matched wild-type control (*top panels*). Note alteration in mitochondrial morphology with speckled appearance in Polg-WT as compared to the fused appearance of mitochondria in Polg-HOM mouse prostate tissue. The bottom panels are individual component images forming the multiplex image above. Scale bars represent 10 µm.

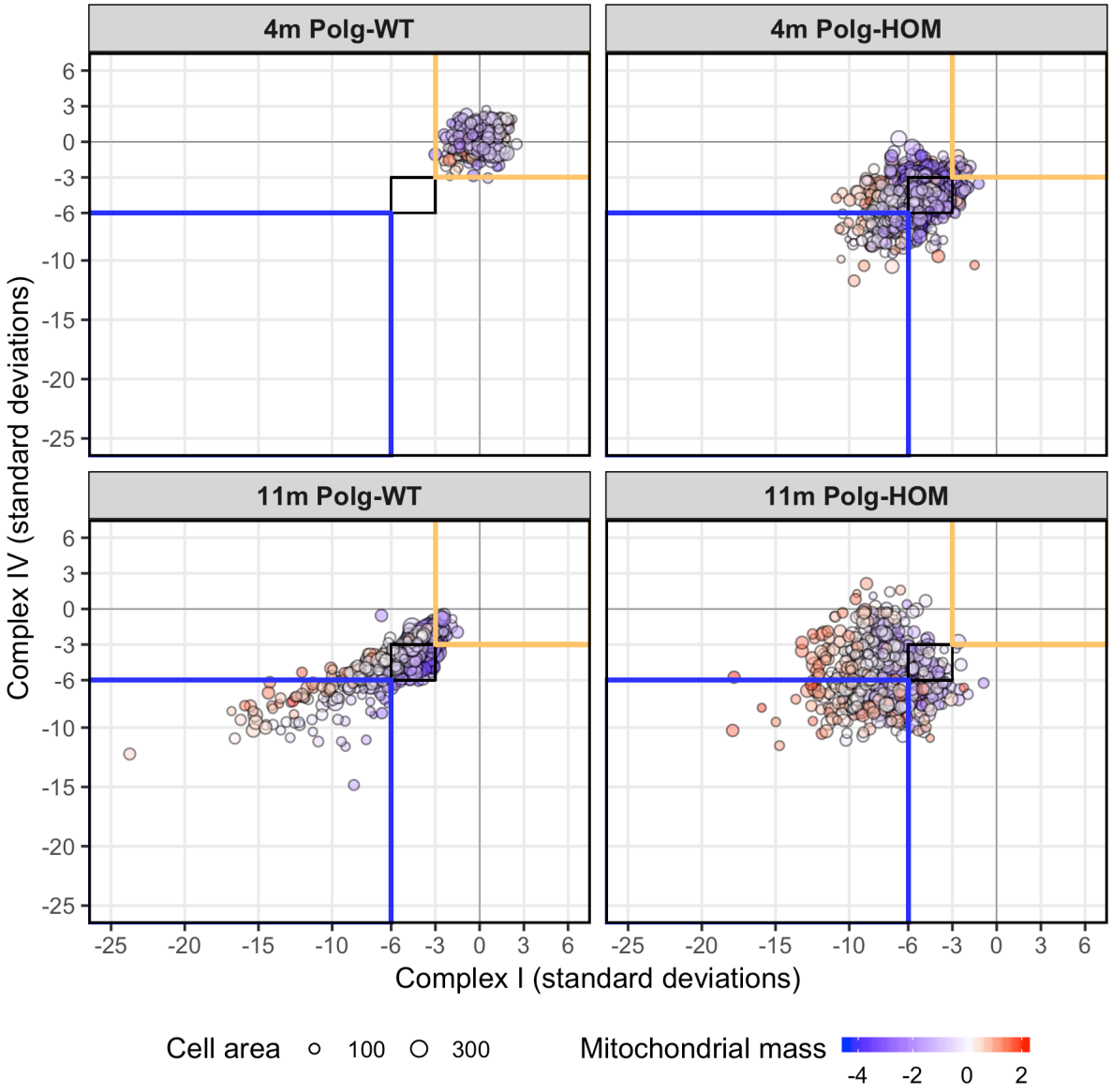

Figure 6-10: Mitochondrial respiratory chain graphs. Each point represents complex I and IV z-scores, whereas the size of each point represents cell area for each individual cell. **(A)** 4m Polg-WT prostates (n=2) used as control, with all z-scores within 3 s.d. **(B)** 4m Polg-HOM mice (n=5) had wide variation in complex I & IV z-scores. **(C)** Proportional decrease in complex I and IV z-scores amongst 11m Polg-WT mice (n=4). **(D)** Random scatter of complex I & IV z-scores reflecting stochastic accumulation of OXPHOS defects in 11m Polg-HOM mouse prostates (n=3). Note the greater frequency and magnitude of OXPHOS defects as compared to 4m Polg-HOM prostates.

Prostate epithelial cells from both 4-month and 11-month Polg-HOM mice were found to have a wide variation in complex I and IV abundance (**Figure 6-10**). This may be explained by the stochastic nature of accumulation of mtDNA mutations, secondary to absence of Polg-mediated proof-reading. Polg-HOM prostates had lower median complex I and complex IV abundance, as compared to age-matched wild-type controls at both time points (**Figure 6-11**).

By 4 months of age, frequency of complex I and IV defects in Polg-HOM prostates were comparable to 11-month Polg-WT controls (**Figure 6-14**). By 11 months of age, 96% epithelial cells in Polg-HOM prostates were complex I deficient, whereas 41% were complex IV deficient and comparable to the 30% COX-deficient cells estimated using the COX/SDH assay in section 6.2.5. Isolated complex I defects were observed across all genotypes but were most frequent in aged Polg-HOM prostates (53%, vs 18% in 11-month Polg-WT, Δ -35%, p=0.003). Isolated complex IV defects were rarely observed. This may reflect the larger number of complex I subunits in mtDNA, resulting in more frequent mtDNA mutations in associated genes.

Compared to the speckled appearance of mitochondrial in 11-month wild-type epithelial cells, mitochondria appeared more fused in age-matched Polg-HOM prostates (**Figure 6-9**), consistent with previous reports of alterations in mitochondrial morphology in cells with mitochondrial defects (Larsson *et al.*, 1998; West *et al.*, 2015). However, this subjective finding of increased mitochondrial fusion was not evaluated quantitatively.

Increased mitochondrial mass was noted in Polg-HOM at 11 months (mean *VDAC1* z-score -0.35 vs -0.92 in Polg-WT, Δ 0.57, p<0.001). This was further explored by evaluating mitochondrial mass at the single cell level and stratification based upon Complex I and IV status (**Figure 6-12**). Across all genotypes and age groups, cells with defects in complexes I and IV had increased mitochondrial mass (p<0.01 for all comparisons). Potential explanations for this phenomenon may include (1) reduced mitophagy, whereby dysfunctional mitochondria are not degraded, or (2) increased mitochondrial biogenesis, as an adaptive response to partially restore mitochondrial function.

These data therefore validate age-related loss of complex I and complex IV abundance in the Polg-HOM mouse prostate, with an associated increase in mitochondrial mass in cells with OXPHOS defects.

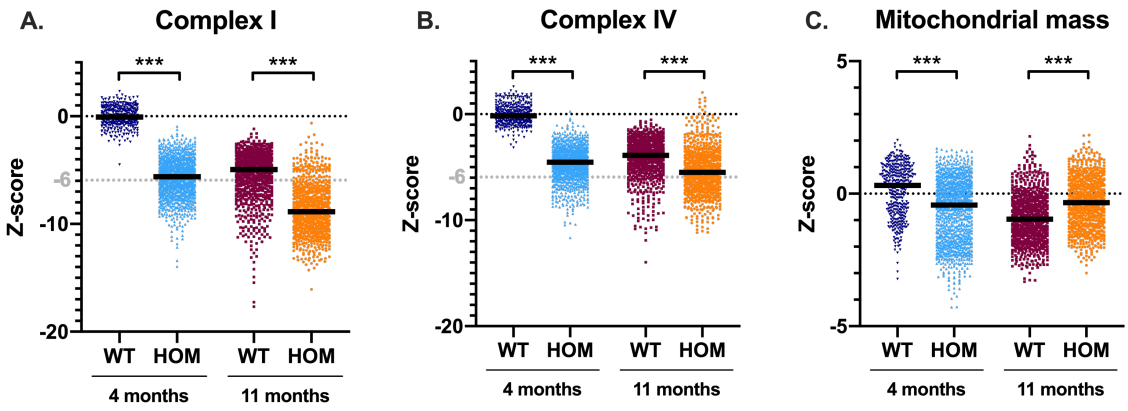

Figure 6-11: OXPHOS protein abundance in Polg-HOM mouse prostates. Complex I and IV abundance, and mitochondrial mass in Polg-HOM mouse prostates at 4 months and 11 months of age, represented as z-scores. Horizontal lines denote median z-scores for each group. *P* values were determined using one-way t test, with *** denoting $p<0.001$.

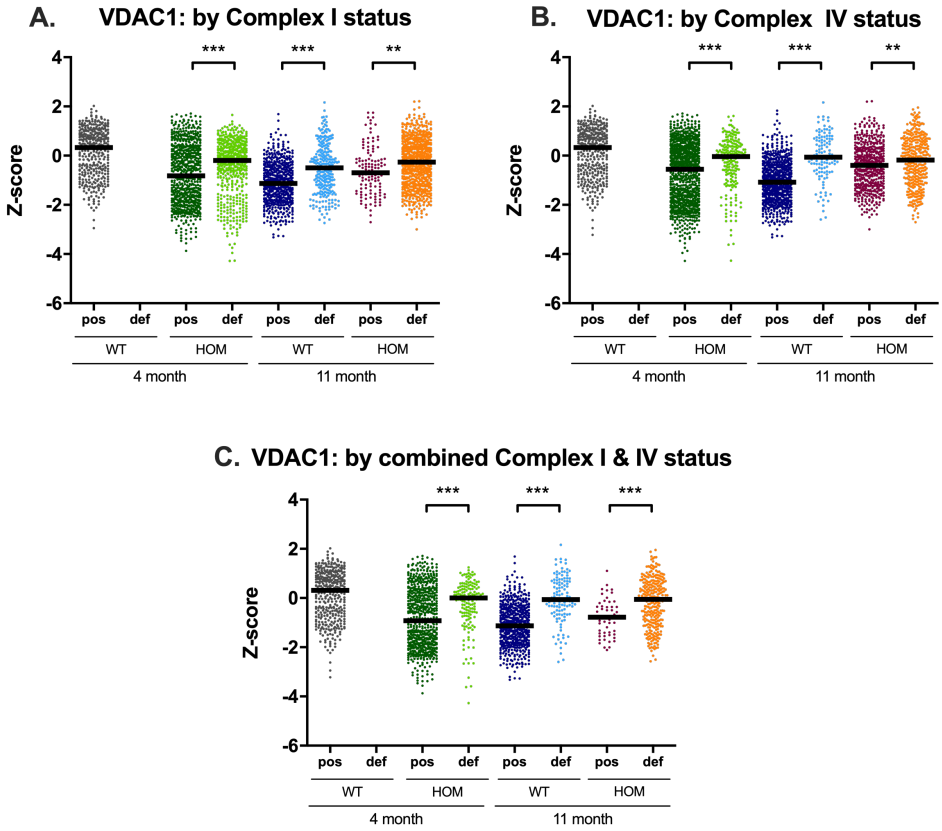

Figure 6-12: Increased mitochondrial mass in cells with OXPHOS defects. VDAC1 abundance quantified by **(A)** Complex I status, **(B)** Complex IV status, and **(C)** combined complex I & IV status. Cells with OXPHOS defects had increased VDAC1-OD in all ages and genotypes. Each point represents an individual cell. Two-tailed t-test (Mann Whitney) with *** and ** denoting $p<0.001$ and $p<0.01$, respectively. Defect defined as z-score < -6.

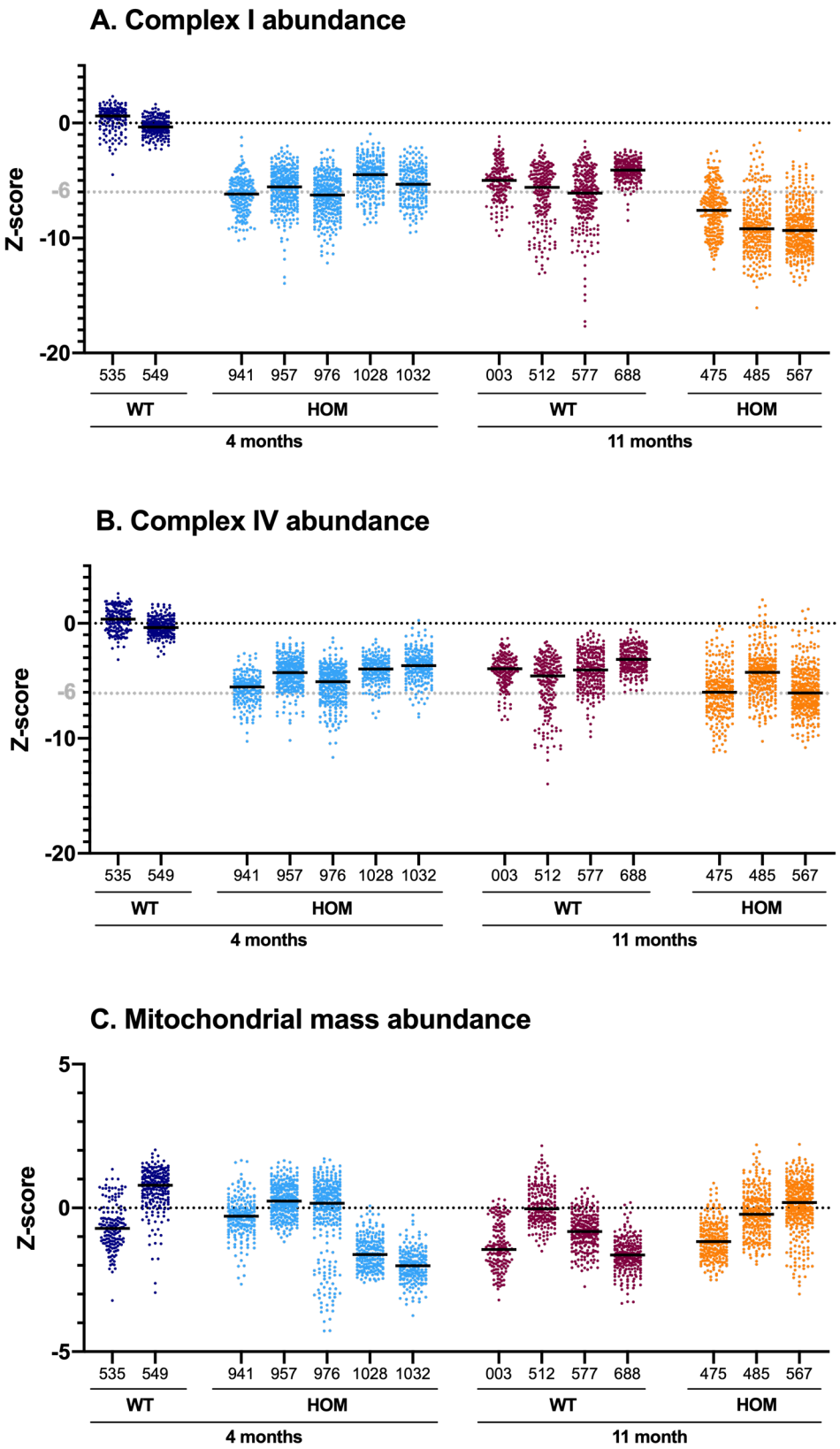

Figure 6-13: OXPHOS protein abundance in mouse prostate tissue – by sample. Z-scores for markers of **(A)** complex I (NDUFB8), **(B)** complex IV, and **(C)** mitochondrial mass are presented. Each dot represents a single cell. Colour represents mouse age group and genotype. For complex I and IV, cells with z-score < -6 were deemed to have an OXPHOS defect.

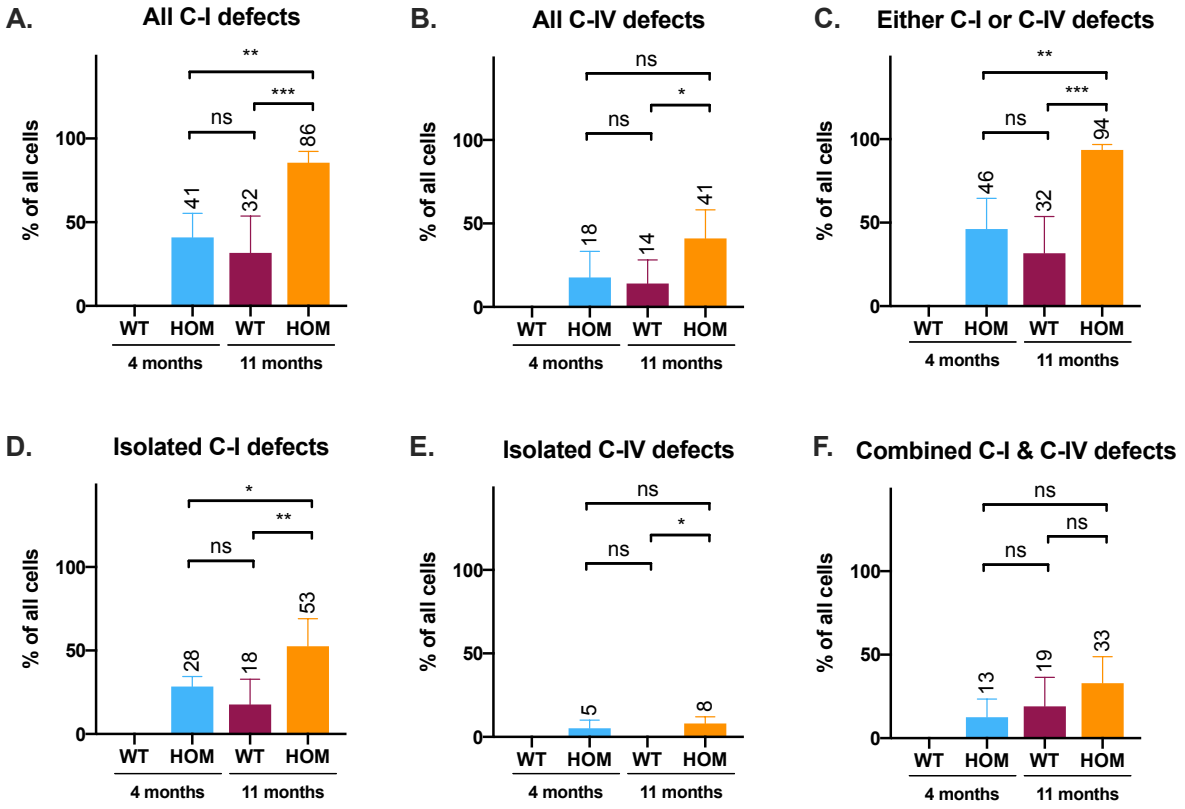

Figure 6-14: Frequency of OXPHOS defects in Polg-HOM mouse prostates. Frequency of cells with complex I (C-I) and complex IV (C-IV) defects are reported for Polg-HOM and Polg-WT controls at 4 months and 11 months of age (n=2-5 pooled for each cohort). Cells with z-score <-6 were classified as '*deficient*', whereas cells with z-score >-6 were classified as '*proficient*'. *P* values were determined using one-way t test, with ***, **, *, and 'ns' denoting $p<0.001$, $p<0.01$, $p<0.05$, and not significant, respectively.

6.2.7 Transcriptomic alterations

Potential functional effects of age-related accumulation of mitochondrial OXPHOS defects, as modelled in the Polg mouse prostate, on gene expression were assessed using RNA sequencing. This approach provides an exploratory assessment of transcriptomic alterations which may impact progression of PCa, by altering the tissue microenvironment.

Transcriptomic alterations associated with mitochondrial dysfunction were evaluated by mRNA sequencing of 11-month Polg-HOM ventral prostates, and age-matched Polg-WT control tissue. Since prostate cancer initiation was not observed in 11-month Polg-HOM mouse prostates, the aim of this work was to identify the potential impact of altered gene expression on cellular processes, which may subsequently impact tumour progression. Dysregulation of signalling pathways due to mitochondrial dysfunction may either attenuate or exacerbate age-associated disease progression. Prior to the submission of this thesis, validation experiments evaluating transcripts identified from this study had not been completed. Thus, the results from RNA sequencing are preliminary in nature, with the aim of generating potential hypotheses for future work.

RNA was extracted from 11-month Polg-HOM and age-matched Polg-WT ventral prostate tissue (n=4 in each group), and underwent library preparation, sequencing and initial quality checks at Eurofins Genomics (Ebersberg, Germany). Subsequent bioinformatic analyses through to generating a list of differentially regulated genes (DEGs) was performed by Dr Rebecca Steele under the supervision of Professor Ian Mills at Queens' University Belfast, as described in section 2.7.1.8. Principal component analysis identified two outlier samples (one from each genotypes), which were excluded from subsequent analysis. Therefore, data from 3 samples/genotype were used for subsequent analysis.

In total, 25,150 transcripts were annotated, of which 459 (1.8%) differentially expressed genes were identified. Amongst these, 262 genes were associated with a fold-change (FC) >+2 (64 upregulated genes) or FC<-2 (198 downregulated genes).

6.2.7.1 Mitochondrial OXPHOS subunits

Consistent with widespread loss in complex I & IV expression noted in Polg-HOM prostate tissue, five of 13 mitochondrial-encoded OXPHOS genes and six nuclear-encoded OXPHOS genes were significantly downregulated (**Figure 6-15**). Notably, a number of assembly factors were also downregulated. *Mt-Nd6* was the most downregulated amongst all mitochondrial-encoded Complex I genes. This may be in keeping with a potentially high burden of *mt-Nd6* mutations, given that *mt-Nd6* is the last of the complex I genes to be replicated and therefore most prone to *Polg*-mediated proofreading errors (Tapper and Clayton, 1981; Bai and Attardi, 1998). However, this hypothesis requires confirmation by mitochondrial genome sequencing.

These findings are consistent with previous data from colonic crypts isolated from Polg-HET mice. RNA sequencing of laser capture micro-dissected COX-deficient and COX-positive colonic crypts noted downregulation of OXPHOS genes in COX-deficient crypts (Baines, 2014). However, reduced mitochondrial-encoded gene expression is in contrast to observations from 25-week Polg-HOM mouse liver, where increased expression of *mt-Nd1*, *mt-Nd5* and *mt-Co2* was noted (Edgar *et al.*, 2009). Potential explanations for this disparity may include tissue-specific differences and post-translational effects, as previously observed in Polg mouse brains (Hauser *et al.*, 2014).

Intriguingly, in the present study, genes involved in mitochondrial transcription, *mt-Rnr1* and *mt-Rnr2*, were downregulated, whereas two genes involved in translation (*mt-Tt*, *mt-Tm*) were upregulated in Polg-HOM prostate tissues. This suggests an imbalance between mitochondrial translation and transcription, which may be a consequence of severe OXPHOS defects, in an attempt to drive protein synthesis and restore OXPHOS function.

Mitochondrial-encoded tRNA methionine (*mt-Tm*) was notably one of the top 10 upregulated genes in Polg-HOM mice. There are two distinct forms of tRNA-met in the eukaryotic cystosol for use in either initiation (tRNAi-met) or elongation (tRNA-met). In contrast, mitochondrial tRNA-met is used in both initiation and elongation stages of protein synthesis (Pearce *et al.*, 2017). Overexpression of tRNAs has been associated with increased cell proliferation and invasion amongst multiple cancers, including breast, lung and AR-positive PCa (Huang *et al.*, 2018; Zhang *et al.*, 2018). This has been hypothesised to be a consequence of increased translation, activation of *PSK2/MSK2* signalling pathway, and driving protein synthesis in an attempt to overcome OXPHOS defects. Indeed, inhibition of mitochondrial translation has been posed as a novel cancer therapy (Skrtic *et al.*, 2011).

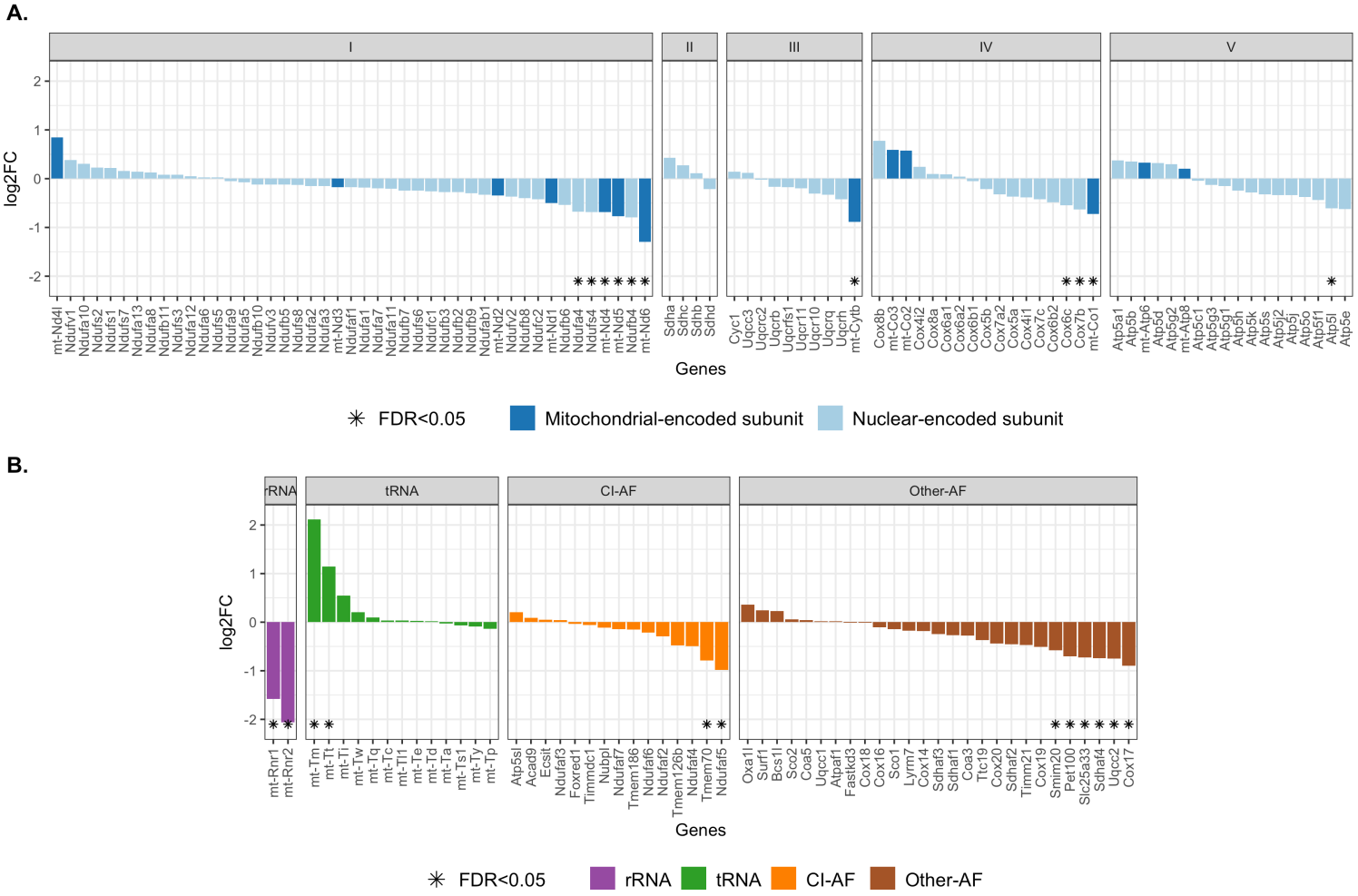

Figure 6-15: Transcriptomic alterations in genes encoding OXPHOS subunits. RNA sequencing of 11-month Polg-HOM mouse ventral prostates, and age-matched wild-type controls. Results reported as log2 fold change (log2FC) in Polg-HOM prostates. **(A)** OXPHOS subunit genes categorised by complexes I-V, **(B)** mt-rRNA, mt-tRNAs, complex I assembly factors (CI-AF) and other assembly factors (Other-AF). Transcripts with false discovery rate (FDR) <0.05 are highlighted with an asterisk.

Gene	log2FC	*p* value	MGI Description	Complex
OXPHOS subunits				
mt-Nd6	-1.30	6.2E-07	mitochondrially encoded NADH dehydrogenase 6	I
mt-Cytb	-0.88	2.7E-04	mitochondrially encoded cytochrome b	III
Ndufb4	-0.79	0.028	NADH:ubiquinone oxidoreductase subunit B4	I
mt-Nd5	-0.77	0.011	mitochondrially encoded NADH dehydrogenase 5	I
mt-Co1	-0.72	0.011	mitochondrially encoded cytochrome c oxidase I	IV
mt-Nd4	-0.69	8.6E-03	mitochondrially encoded NADH dehydrogenase 4	I
Ndufs4	-0.68	7.7E-03	NADH dehydrogenase Fe-S protein 4	I
Ndufa4	-0.68	0.014	NADH dehydrogenase 1 alpha subcomplex, 4	I
Cox7b	-0.63	0.018	cytochrome c oxidase subunit VIIb	IV
Atp5l	-0.61	0.025	F1F0-ATP synthase g subunit	V
Cox6c	-0.54	0.022	cytochrome c oxidase subunit 6C	IV
Other mitochondrial encoded genes				
mt-Rnr2	-2.06	1.7E-13	mitochondrially encoded 16S rRNA	rRNA
mt-Rnr1	-1.58	0.002	mitochondrially encoded 12S rRNA	rRNA
mt-Tt	1.14	0.027	mitochondrially encoded tRNA threonine	tRNA
mt-Tm	2.11	1.7E-13	mitochondrially encoded tRNA methionine	tRNA
Assembly factors				
Tmem70	-0.79	0.002	transmembrane protein 70	CI-AF
Uqcc2	-0.75	0.015	ubiquinol-cytochrome c reductase complex assembly factor 2	Other-AF
Pet100	-0.70	0.016	PET100 homolog	Other-AF
Smim20	-0.58	0.027	small integral membrane protein 20	Other-AF
Sdhaf4	-0.74	0.020	succinate dehydrogenase complex assembly factor 4	Other-AF
Slc25a33	-0.72	0.017	solute carrier family 25, member 33	Other-AF
Ndufaf5	-0.98	0.008	NADH:ubiquinone oxidoreductase complex assembly factor 5	CI-AF
Cox17	-0.89	0.043	cytochrome c oxidase assembly protein 17, copper chaperone	Other-AF

Table 6-3: Differentially altered mitochondrial genes in 11-month Polg-HOM ventral prostates. Log-transformed fold-change and false-discovery rate adjusted *p*-values are reported.

6.2.7.2 Mitochondrially-localised transcripts

Other potential effects on mitochondrial function were evaluated by identifying mitochondrially-localised transcripts using MRC MitoMiner 4.0 (Smith and Robinson, 2019) and Mouse MitoCarta 2.0 (Calvo *et al.*, 2016) gene lists. Two mitochondrial transcripts were upregulated (*Acacb*, *Sardh*), and four were downregulated (*Gimap3*, *Mthfd2l*, *Immp1l*, *mt-Nd6*; **Figure 6-16**).

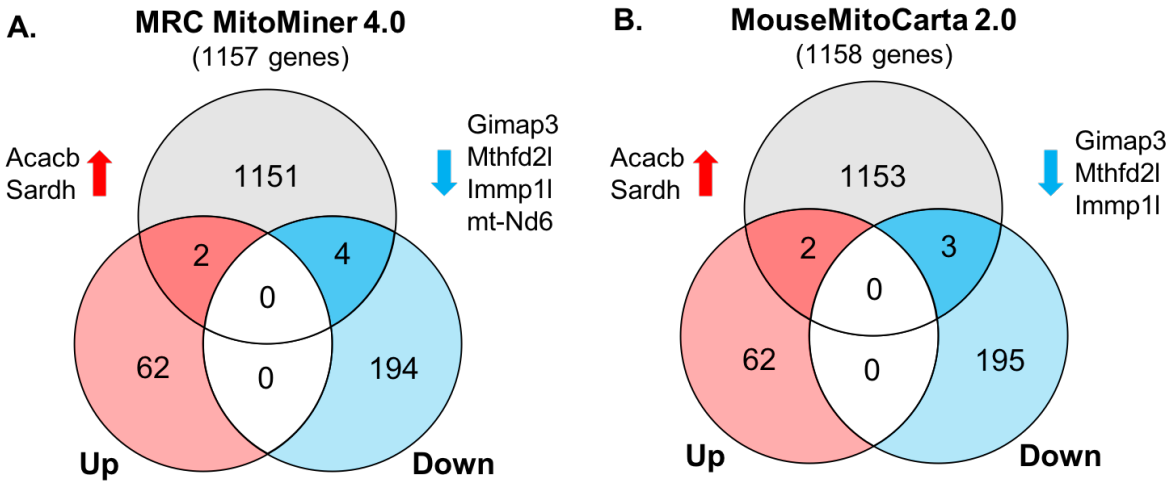

Figure 6-16: Mitochondria-associated differentially expressed genes in Polg-HOM ventral prostates. (A) MRC MitoMiner 4.0 gene list, **(B)** MouseMitoCarta 2.0 gene list. Notable genes are annotated and described in **Table 6-4**.

Gene	log2FC	*p* value	MGI Description
Upregulated in Polg-HOM ventral prostate			
Sardh	1.10	0.004	Sarcosine dehydrogenase
Acacb	1.35	0.006	Acetyl-Coenzyme A carboxylase beta
Downregulated in Polg-HOM ventral prostate			
Gimap3	-1.71	3E-05	GTPase, IMAP family member 3
Mthfd2l	-1.14	0.001	Methylenetetrahydrofolate dehydrogenase (NADP+ dependent) 2-like
Immp1l	-1.07	5E-05	IMP1 inner mitochondrial membrane peptidase-like
mt-Nd6	-1.30	6E-07	NADH:ubiquinone oxidoreductase core subunit 6

Table 6-4: Altered mitochondrial-localised transcripts in Polg-HOM ventral prostates. Log-transformed fold-change and false-discovery rate adjusted *p*-values are reported.

***Sardh*:** Sarcosine is a derivative of the amino acid glycine, formed upon methylation by the enzyme glycin N-methyltransferase (*Gnmt*). Sarcosine dehydrogenase (*Sardh*) reduces sarcosine back into glycine. Metabolomic profiling of PCa specimens identified increasing sarcosine levels with PCa progression (Sreekumar *et al.*, 2009). Sarcosine pathway is regulated by AR and ERG, whereby androgen treatment leads to reduction in SARDH and over-expression of ERG is associated with increased sarcosine concentration. SARDH is often downregulated in human PCa (Khan *et al.*, 2013), however, exogenous sarcosine supplementation increases invasive potential (Sreekumar *et al.*, 2009)and upregulates cell cycle progression in metastatic PCa models (Heger *et al.*, 2016). Upregulated *Sardh* in Polg-HOM prostates may thereby contribute to suppressing tumour progression.

***Acacb*:** Acetyl-CoA carboxylase (*Acac*) catalyses the conversion of acetyl Co-A to malonyl CoA and is the most highly regulated enzyme in the fatty acid biosynthesis pathway (Currie *et al.*, 2013). Phosphorylation of *Acac* by *AMPK* and other kinases leads to its inactivation. It has two isoforms: *Acaca* and *Acacb*. *Acaca* is highly enriched in lipogenic tissues and serves as a substrate for fatty acid synthesis. *Acacb* occurs in oxidative tissues and inhibits the carnitine-palmitoyl-CoA transferase I (CPT1) fatty acid transporter, thereby suppressing fatty acid entry into mitochondria and thus suppressing fatty acid degradation. Reduced *Acacb* and increased *Acaca* expression is observed in human PCa tissue (Tessem *et al.*, 2016). Knockdown of *Acaca* by siRNA (Brusselmans *et al.*, 2005) or chemical inhibition (Beckers *et al.*, 2007) in *in vitro* PCa models induces apoptosis and growth arrest. Notably, Acac inactivation upon AMPK-mediated phosphorylation has been hypothesised as a potential mechanism underlying anti-tumour effect of metformin treatment. Upregulation of *Acacb* in the Polg-HOM prostate was not associated with alterations in other markers of fatty acid synthesis frequently observed in human PCa (Wu *et al.*, 2014), including *Acaca* (log2FC 0.25, p 0.5), *Fasn* (log2FC 0.69, p 0.08), and *Acly* (log2FC 0.46, p 0.1). This suggests that *Acacb*-mediated inhibition of fatty acid oxidation in Polg-HOM prostates may be occurring independent of alteration in fatty acid biosynthesis and is therefore likely to have a tumour-inhibitory effect.

***Mthfd2l*:** *Mthfd2l* is the mitochondrial counterpart of MTHFD2 participating in one carbon metabolism and thereby contributing to NADPH production in the mitochondria (Tedeschi *et al.*, 2013). *Mthfd2l* expression was reduced in Polg-HOM mice. This may putatively be a consequence of severe Complex I defects, resulting in a negative feedback loop to suppress mitochondrial NADPH production, which is the substrate of Complex I activity. Consistent with

this finding, reduced expression of complex I subunits, including *mt-Nd6*, was also observed (**Figure 6-15**).

Gimap3: *Gimap3* is a murine orthologue of *GIMAP5*, which supports T cell survival by inactivating *GSB3β* activity (Patterson *et al.*, 2018). In keeping with this mechanism, *GSK3β* inhibitors are under investigation for treatment of a variety of diseases, including cancer, Alzheimer's dementia and diabetes mellitus (MacAulay and Woodgett, 2008; Kramer *et al.*, 2012). *GIMAP5* inhibition, however, upregulates constitutive *GSK3β* activity which constrains *c-Myc* induction and in combination with increased DNA damage limits productive $CD4^+$ T cell proliferation. Indeed, mice with combined *Gimap3* and *Gimap5* loss have severe defects in cellularity of $CD4^+$ and $CD8^+$ T cells (Yano *et al.*, 2014). Data linking *Gimap3* levels to specific alterations in immune cell function and cancer progression are, however, currently lacking.

Immp1l: Inner mitochondrial membrane peptidase subunit 1 forms part of the inner mitochondrial membrane peptidase (*IMMP*) that cleaves the mitochondrial targeting pre-sequence of nuclear-encoded proteins, thereby creating mature proteins at the mitochondrial inter-membrane space (Burri *et al.*, 2005). At present, the functional impact of *Immp1l* deficiency, as observed in Polg-HOM mice, remains unclear (Lu *et al.*, 2008; Ma *et al.*, 2011); however, low *Immp2l* expression has been shown to contribute to mitochondrial dysfunction and leads to cancer-related fatigue amongst PCa patients receiving external beam radiotherapy (Hsiao *et al.*, 2013).

6.2.7.3 Top 10 and bottom 10 differentially expressed genes

Top 10 and bottom ten DEGs are annotated in **Figure 6-17** and described in **Table 6-5**.

Upregulated transcripts included genes involved translation (*mt-Tm*, as discussed in section 6.2.7.1), RNA export from the nucleus (*Nxf7*)(Vanmarsenille *et al.*, 2013), arachidonic acid metabolism (*Alox12*), and platelet function (*Vwf*, *Fgl1*). Notably, upregulation of *Alox12* metabolises the conversion of arachidonic acid to hydroxy eicosatetraenoic acids (12(S)-HETE). *Alox12* is over-expressed in human PCa (Gao *et al.*, 1995), where it stimulates tumour progression by upregulating angiogenesis via expression of VEGF (Nie *et al.*, 1998), chemotaxis of neutrophils (Turner *et al.*, 1975) and expression of MMP9 via activation of the Nk-kB pathway (Dilly *et al.*, 2013). Therefore, increased *Alox12* expression in Polg-HOM mice may potentially have a pro-tumourigenic effect.

Downregulated transcripts included genes involved in protein translation (Spermine binding protein, *Sbp*) and immune function. Reduced expression of *Sbp* may be a consequence of reduced serum testosterone levels, as observed following castration (Chang *et al.*, 1987; Mills *et al.*, 1987). Indeed, pathway analysis of DEGs with adjusted *p*-value <0.01 using PANTHER (Mi *et al.*, 2019) enriched for pathways associated with immune function and cell cycle. These pathways are therefore evaluated later in this chapter.

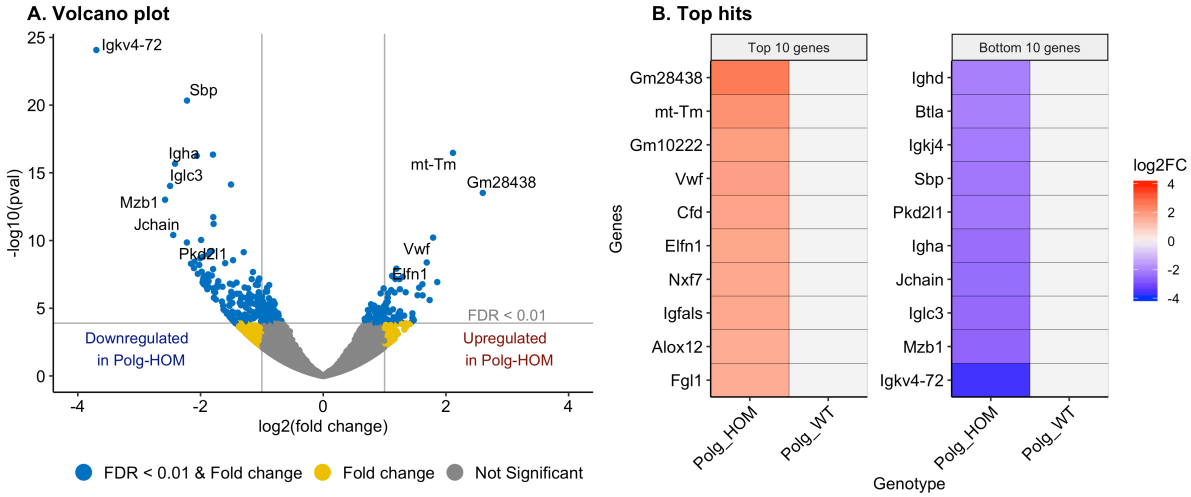

Figure 6-17: Transcriptomic alterations in Polg-HOM ventral prostates. RNA sequencing of 11-month Polg-HOM mouse ventral prostates, and age-matched wild-type controls. Results reported as log2 fold change (log2FC) in Polg-HOM prostates and represented as **(A)** a volcano plot, and **(B)** heat map. Top 10 and bottom 10 transcripts with false discovery rate (FDR) <0.01 are annotated.

Gene	log2FC	*p* value	MGI Description
Top 10 genes			
Gm28438	2.60	8E-11	predicted gene 28438
mt-Tm	2.11	3E-13	mitochondrially encoded tRNA methionine
Gm10222	1.86	6E-05	predicted gene 10222
Vwf	1.79	1E-07	Von Willebrand factor
Cfd	1.73	6E-04	complement factor D (adipsin)
Elfn1	1.69	4E-06	leucine rich repeat and fibronectin type III, extracellular 1
Nxf7	1.62	3E-04	nuclear RNA export factor 7
Igfals	1.62	7E-05	insulin-like growth factor binding protein, acid labile subunit
Alox12	1.56	1E-04	arachidonate 12-lipoxygenase
Fgl1	1.54	3E-04	fibrinogen-like protein 1
Bottom 10 genes			
Ighd	-2.10	4E-06	immunoglobulin heavy constant delta
Btla	-2.11	1E-05	B and T lymphocyte associated
Igkj4	-2.16	5E-06	immunoglobulin kappa joining 4
Pkd2l1	-2.22	2E-07	polycystic kidney disease 2-like 1
Sbp	-2.22	6E-17	spermine binding protein
Igha	-2.41	9E-13	immunoglobulin heavy constant alpha
Jchain	-2.44	8E-08	immunoglobulin joining chain
Iglc3	-2.50	3E-11	immunoglobulin lambda constant 3
Mzb1	-2.58	2E-10	marginal zone B and B1 cell-specific protein 1
Igkv4-72	-3.70	2E-20	immunoglobulin kappa chain variable 4-72

Table 6-5: Top 10 and bottom 10 differentially expressed genes in 11 month Polg-HOM vs Polg-WT ventral prostate tissue. Log-transformed fold change and false-discovery adjusted *p* values are reported.

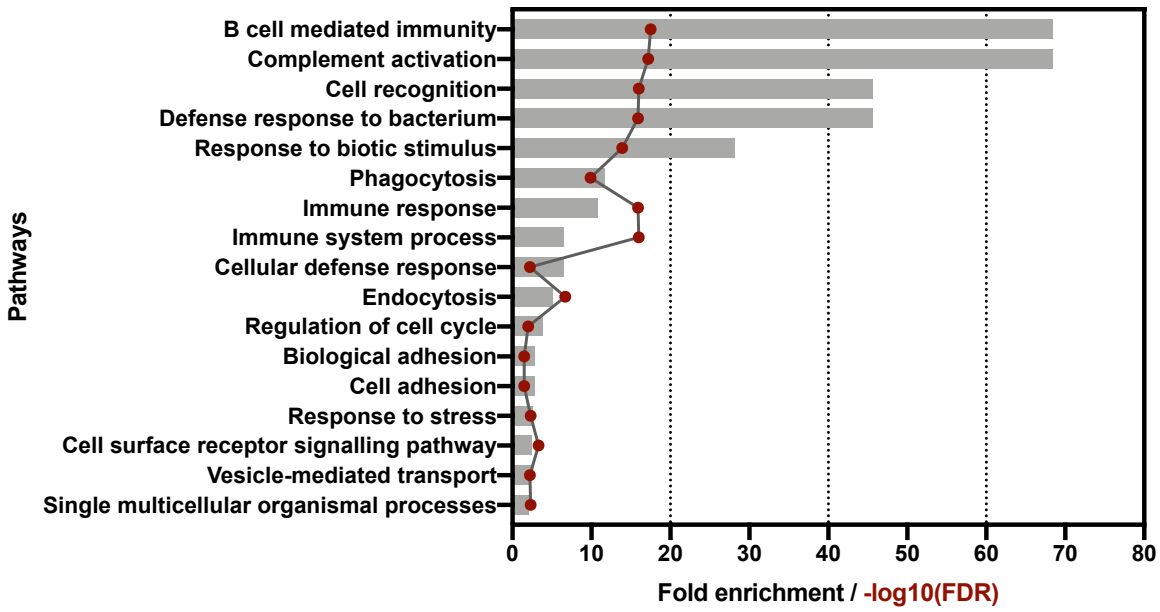

Figure 6-18: Gene set enrichment analysis of 11-month Polg-HOM ventral prostates and Polg-WT controls. Fold enrichment (grey bars) and log-transferred FDR adjusted *p*-values (red) are reported.

6.2.7.4 Immune signalling pathways

Since immune signalling pathways were enriched, markers of innate and adaptive immunity were evaluated in fixed prostate specimens from 11-month Polg-HOM and Polg-WT mice, in collaboration with Dr Debayan Mukherjee at the University of Manchester. CD11b and CD8 were used as markers of macrophages (innate immunity) and cytotoxic T cells (adaptive immunity), respectively. Frequency of $CD11b^+$ and $CD8^+$ cells were evaluated in three samples from each genotype using QuPath v0.1 and found to be comparable across both 11-month wild-type and Polg-HOM prostate tissues (**Figure 6-19**).

These findings are in contrast to age-related alterations in prostate microenvironment observe in wild-type C57BL/6 mice at 4 and 20-24 months of age, where $F4/80^+$ macrophages, $CD3^+$ T-cells and $B220^+$ B-cells were noted to increase with advancing age (Bianchi-Frias *et al.*, 2010). The high frequency of OXPHOS defects in Polg-HOM mice are likely to contribute to immune cell exhaustion and thereby lead to cell death, which may therefore suggest a comparable immune cell frequency. It is also possible that a true difference in immune cell frequency may have been missed due to the small sample size (n=3 per genotype) used in the evaluation of Polg-HOM prostates and increasing the sample size may help reach more precise estimates.

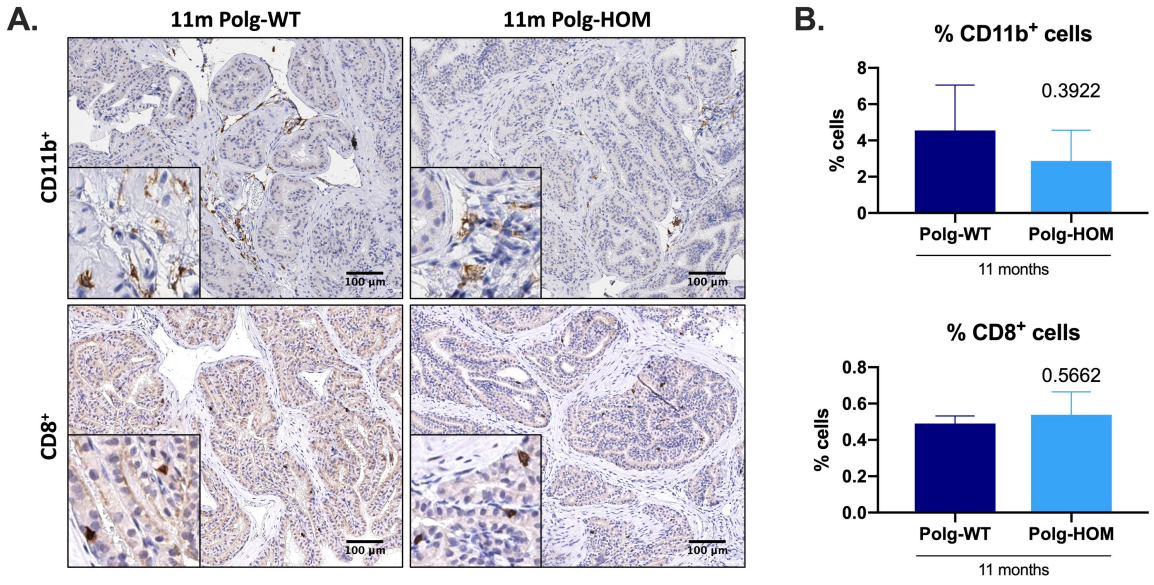

Figure 6-19: Immune cell phenotypes in Polg mouse prostates. (A) Immunohistochemistry for cytotoxic T-cell marker $CD8^+$ cells, and myeloid derived suppressor cell marker $CD11b^+$ in 11-month Polg-WT and Polg-HOM mice were evaluated (n=3 in each cohort). **(B)** Quantification of $CD8^+$ and $CD11b^+$ cells in n=3 mouse prostates from each cohort. *P* values using two-way t-test are reported.

Notably, genes involved in antigen presentation (*H2-DMb2*), interleukin-1 signalling (*Illrap*), and lymphocyte recruitment (*Itgb7*) have previously been found to be downregulated in COX-deficient colonic crypts (Baines, 2014), further supporting potential alterations in immune signalling pathway as a consequence of mitochondrial dysfunction.

6.2.7.5 Comparison with gene expression in *PbCre4⁺Ptenᶠˡ/ᶠˡ* mouse prostate tumours

Next, transcriptomic alterations observed in the Polg-HOM mice were compared against those observed in an established transgenic mouse model, using the *PbCre4⁺Ptenᶠˡ/ᶠˡ* model, which is based upon prostate-specific activation of the Pi3k/Akt signalling pathway, and leads to the development of mPIN by 6 weeks of age and invasive adenocarcinoma from approximately 4-6 months of age (Trotman *et al.*, 2003; Wang *et al.*, 2003; Chen *et al.*, 2005). It was hypothesised that genes with discordant alterations, as compared to *PbCre4⁺Ptenᶠˡ/ᶠˡ* prostate tissue, may potentially suppress tumour progression through opposing mechanisms.

DEG lists from RNA sequencing data from individual prostate lobes from the *PbCre4⁺Ptenᶠˡ/ᶠˡ* model were kindly provided by Professor Ian Mills (Queen's University Belfast). Transcripts with FDR < 0.01 and log2FC > 1 or <-1 were compared with the DEG list from Polg-HOM mouse prostates to identify discordant changes (**Figure 6-20**, **Table 6-6**).

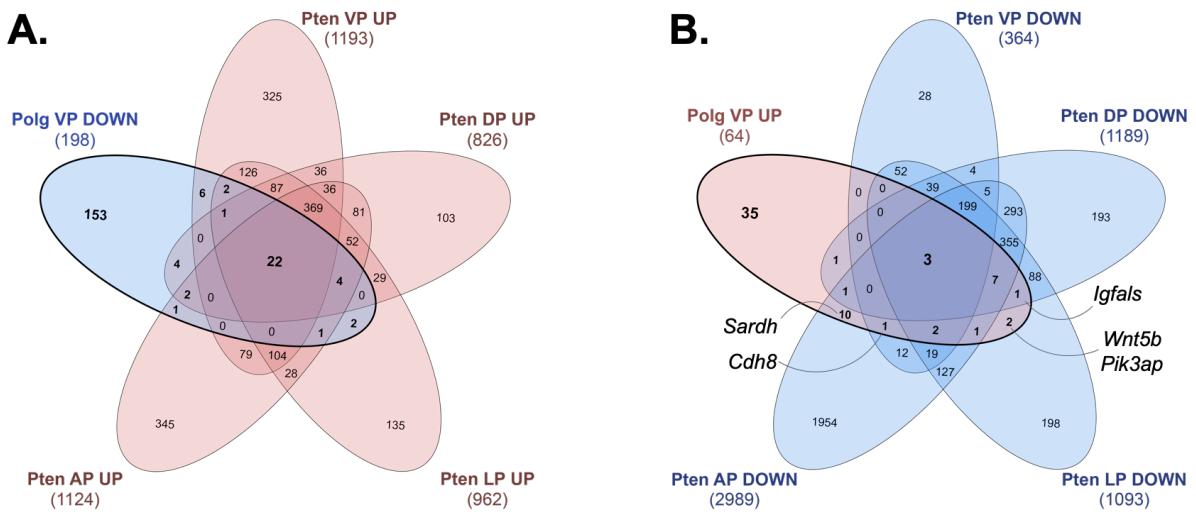

Figure 6-20: Comparison of differentially expressed genes in Polg-HOM ventral prostates vs various *PbCre4⁺Ptenᶠˡ/ᶠˡ* mouse prostate lobes. (A) Genes upregulated in Pten-HOM mice and downregulated in Polg-HOM mice, **(B)** Genes downregulated in Pten-HOM mice and upregulated in Polg-HOM mice. Notable genes not uniformly expressed across all Pten-HOM prostate lobes are annotated. VP: ventral prostate; AP: Anterior prostate; DP: Dorsal prostate; LP: Lateral prostate.

Gene	log2FC	*p* value	MGI Description
Genes upregulated in PbCre4^{+}Pten$^{fl/fl}$ mouse prostate and downregulated in Polg-HOM prostates			
Pclaf	-2.02	3.6E-06	Proliferating Cell Nuclear Antigen-associated factor
Pbk	-1.87	8.7E-07	Lymphokine-activated killer T-cell-originated protein kinase
Serpina3g	-1.78	1.1E-04	Serine protease inhibitor A3G
Esco2	-1.73	6.3E-05	N-acetyltransferase ESCO2
Ckap2	-1.53	6.6E-04	Cytoskeleton-associated protein 2
Knstrn	-1.53	3.0E-04	Small kinetochore-associated protein
Kif11	-1.53	2.4E-04	Kinesin-like protein KIF11
Mki67	-1.52	4.1E-05	Proliferation marker protein Ki-67
Birc5	-1.48	1.5E-03	Baculoviral IAP repeat-containing protein 5
Trim59	-1.47	2.1E-03	Tripartite motif-containing protein 59
Cdkn3	-1.43	5.9E-03	Cyclin-dependent kinase inhibitor 3
Ect2	-1.40	1.9E-03	Protein ECT2
Nuf2	-1.39	7.1E-03	Kinetochore protein Nuf2
Shcbp1	-1.39	6.1E-03	SHC SH2 domain-binding protein 1
Ccnb1	-1.37	6.8E-03	G2/mitotic-specific cyclin-B1
Cxcr4	-1.37	2.1E-03	C-X-C chemokine receptor type 4
Ccna2	-1.37	2.7E-03	Cyclin-A2
Aurkb	-1.32	8.9E-03	Aurora kinase B
Nusap1	-1.26	7.7E-03	Nucleolar and spindle-associated protein 1
Cdca3	-1.21	9.7E-03	Cell division cycle-associated protein 3
Prc1	-1.17	7.7E-03	Protein regulator of cytokinesis 1
2200002D01Rik	-1.04	9.8E-03	MCG22941, Immortalization-Upregulated Protein
Genes downregulated in PbCre4^{+}Pten$^{fl/fl}$ mouse prostate and upregulated in Polg-HOM prostates			
Arhgef37	1.23	1.9E-03	Rho guanine nucleotide exchange factor 37
Sh3gl2	1.20	3.5E-03	Endophilin-A1
Kcnk3	1.05	4.5E-04	Potassium channel subfamily K member 3

Table 6-6: Table of differentially-expressed genes in Polg-HOM ventral prostate tissue with discordant direction of change in expression, as compared with *PbCre4^{+}Pten$^{fl/fl}$* prostate tissue. *P* values adjusted for false discovery rate.

PANTHER gene ontology analysis was used to evaluate statistical over-representation of discordant genes, using the Fisher's exact test and adjustment for false discovery rate. Discordant downregulated transcripts in Polg-HOM mice were statistically over-represented for cell cycle related biological processes (GO:0022402 cell cycle process, p=0.0031; GO:0051726 regulation of cell cycle, p=0.02) and molecular processes including cyclin-dependent serine/threonine kinase activity (GO:0004693, p=0.006) and microtubule binding (GO:0008017, p=0.003).

6.2.7.6 Cell proliferation

Discordant genes in **Table 6-6** predominantly reflect alterations in cell proliferation, which is upregulated in the *PbCre4*$^{+}$*Pten*$^{fl/fl}$ model but downregulated in Polg-HOM mouse prostate tissue. In keeping with this, reduced expression of the associated Mki67 transcript (log2FC Mki67 -1.52, FDR-adjusted p=0.0004), and reduced expression of multiple genes included in the cell cycle progression (CCP) gene signature (Cuzick *et al.*, 2011; Jurmeister *et al.*, 2018) were noted.

A balance between cell proliferation and apoptosis is required for maintenance of homeostasis. The loss of balance between these physiological phenomena results in altered growth dynamics. Notably, Kujoth *et al.* (2005) reported increased apoptosis in multiple organs from Polg-HOM mice with predominantly high cell turnover (liver, testis, muscle, duodenum and thymus, but not brain) with no change in cellular proliferation compared to age-matched wild-type controls. In contrast, no significantly altered transcriptomic changes in apoptotic transcripts were noted in Polg-HOM prostates and immunohistochemistry revealed very low incidence of apoptotic cells across both Polg-HOM and Polg-WT prostate tissue. A potential explanation for these phenomena may be the low mitotic rate of non-malignant prostate tissue.

Gene	log2FC	*p* value		MGI Description
2810417H13Rik	-2.02	3.61E-06	*	PCNA clamp associated factor
Pbk	-1.87	8.73E-07	*	PDZ binding kinase
Kif11	-1.53	2.45E-04	*	kinesin family member 11
Birc5	-1.48	1.54E-03	*	baculoviral IAP repeat-containing 5
Dtl	-1.45	3.94E-03	*	denticleless E3 ubiquitin protein ligase
Cdkn3	-1.43	5.88E-03	*	cyclin-dependent kinase inhibitor 3
Nusap1	-1.26	7.67E-03	*	nucleolar and spindle associated protein 1
Cdca3	-1.21	9.70E-03	*	cell division cycle associated 3
Dlgap5	-1.19	0.020	*	DLG associated protein 5
Prc1	-1.17	0.008	*	protein regulator of cytokinesis 1
Cenpf	-1.11	0.013	*	centromere protein F
Kif20a	-1.04	0.035	*	kinesin family member 20A
Cep55	-1.02	0.06		centrosomal protein 55
Aspm	-0.98	0.08		abnormal spindle microtubule assembly
Ska1	-0.98	0.07		spindle and kinetochore associated complex subunit 1
Cdca8	-0.80	0.14		cell division cycle associated 8
Rrm2	-0.80	0.01	*	ribonucleotide reductase M2
Rad51	-0.79	0.13		RAD51 recombinase
Bub1b	-0.75	0.10		BUB1B, mitotic checkpoint serine/threonine kinase
Cdk1	-0.74	0.19		cyclin-dependent kinase 1
Asf1b	-0.66	0.19		anti-silencing function 1B histone chaperone
Cdc20	-0.61	0.28		cell division cycle 20
Foxm1	-0.58	0.31		forkhead box M1
Tk1	-0.55	0.26		thymidine kinase 1
Orc6	-0.54	0.10		origin recognition complex, subunit 6
Top2a	-0.53	0.18		topoisomerase (DNA) II alpha
Rad54l	-0.44	0.51		RAD54 like (S. cerevisiae)
Plk1	-0.42	0.52		polo like kinase 1
Cenpm	-0.36	0.58		centromere protein M
Mcm10	0.12	0.86		minichromosome maintenance 10 replication initiation factor
Pttg1	0.19	0.59		pituitary tumor-transforming gene 1

Table 6-7: Expression of cell cycle progression genes in Polg-HOM ventral prostate tissue. Log-transformed fold change and false-discovery adjusted *p*-values are reported. Asterisk denotes $p<0.05$.

The potential impact of OXPHOS defects on cell proliferation was further evaluated at the protein level in fixed mouse prostate tissues using chromogenic immunohistochemistry labelling of the proliferative marker Ki67 by Miss Karolina Habrajska (MSc student). $Ki67^+$ cells were identified using Aperio ImageScope Positive Pixel Count algorithm. By 11 months of age, Polg-HOM mice had fewer $Ki\text{-}67^+$ cells in ventral prostates as compared to Polg-WT controls (Polg-HOM 0.78% vs Polg-WT 2.48%, Δ -1.70%, p=0.01). Consistent but statistically insignificant trends were also noted in anterior (Polg-HOM 0.70% vs Polg-WT 1.62%, Δ -0.92%, p=0.18) and dorsolateral prostate lobes (Polg-HOM 0.77% vs Polg-WT 0.98%, Δ -0.20%, p=0.4).

These results are consistent with attenuated cell proliferation observed in a drosophila model of complex I defects, with cell cycle arrest at the G1-S checkpoint (Owusu-Ansah *et al.*, 2008). Using fluorescent MT-CO1 immunohistochemical labelling, COX-I deficient intestinal crypts in an ageing human cohort are also reported to have reduced proliferation, increased apoptosis and shortened crypt length (Nooteboom *et al.*, 2010).

In contrast, the proliferation and apoptosis rate in COX-deficient and COX-proficient human prostate epithelial cells has been reported to be comparable (Moad *et al.*, 2017). Potential explanations for these discrepancies may include variability in frequency and magnitude of complex I and complex IV defects on cell cycle kinetics in different organs. Furthermore, Moad *et al.* (2017) employed sequential COX/SDH enzyme histochemistry to identify COX-deficient epithelial cells, which would identify cells lacking mitochondrial complex IV, and fail to identify cells with isolated complex I defects. Further work evaluating employing multiplex evaluation of mitochondrial markers with cell cycle markers is therefore warranted.

Therefore, it is plausible to hypothesise that mitochondrial defects may lead to a cascade of effects which may eventually suppress cell proliferation in Polg-HOM mouse prostate tissue.

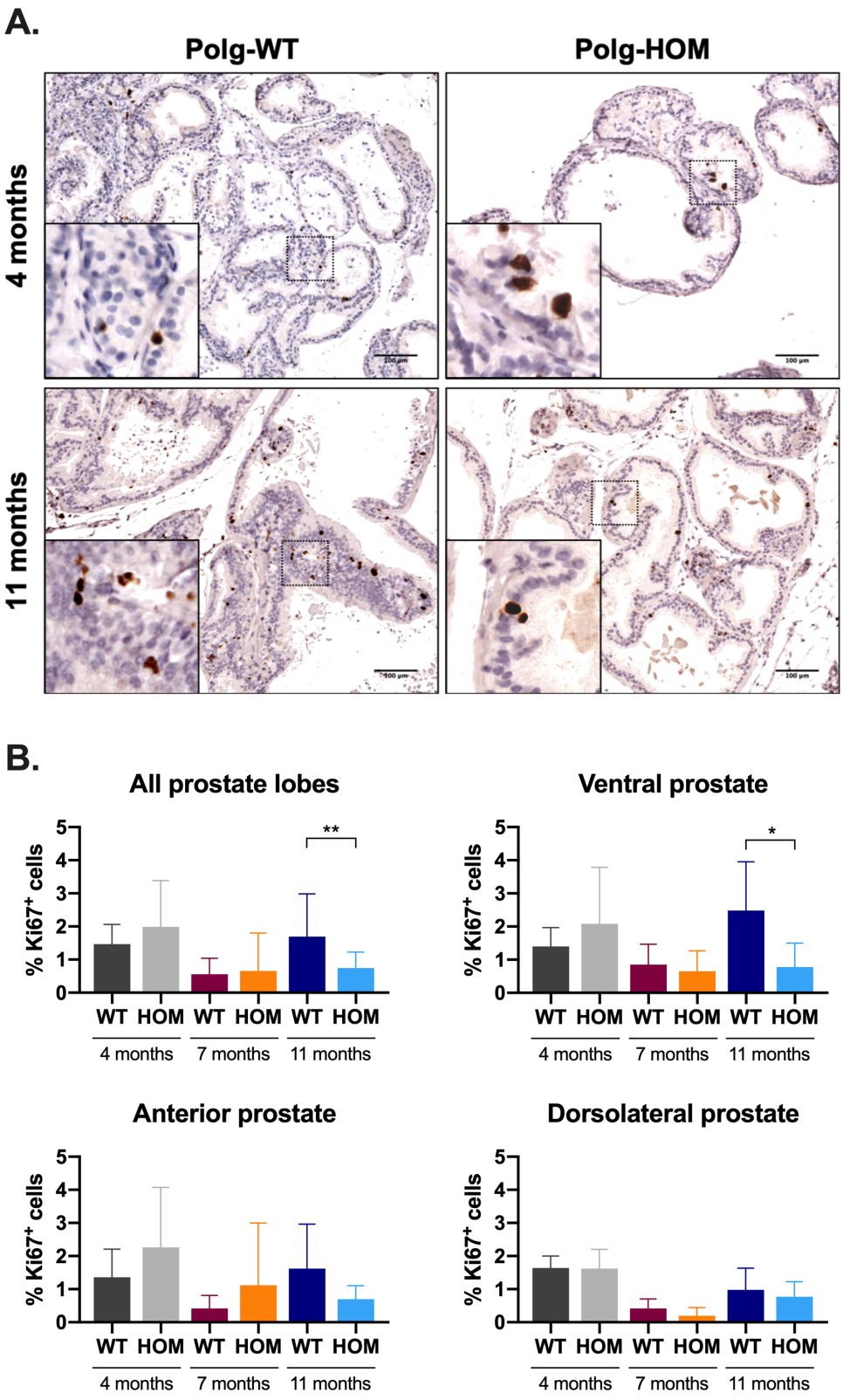

Figure 6-21: Reduced cell proliferation in Polg-HOM ventral prostates. **(A)** Representative images of prostate tissue from Polg-HOM mice, and age-matched wild-type controls labelled for Ki67$^+$ cells using chromogenic immunohistochemistry. Scale bars represent 100 µm. **(B)** Quantitative analysis of Ki67$^+$ cells, include data for at least n=5 mice in each group. *P* values were determined using one-way t test, with ** and * denoting $p<0.01$ and $p<0.05$, respectively.

6.3 Discussion

Mitochondrial DNA mutations and associated OXPHOS defects are frequently observed in human prostate cancer. However, the *in vivo* functional consequences of these mitochondrial alterations on prostate cancer initiation and progression remain largely unknown. In this chapter, the use of transgenic animal models facilitated the assessment of phenotypic alterations associated with mitochondrial dysfunction. As such, a detailed assessment of OXPHOS defects and transcriptomic alterations in prostate tissue from Polg-HOM mouse model have been reported.

6.3.1 Polg-HOM mice are a suitable model to study impact of OXPHOS defects in prostate tissue

Polg-HOM mice develop a significant burden of OXPHOS defects by 11 months of age, as quantified by COX/SDH enzyme histochemistry and quantitative multiplex immunofluorescence. In keeping with high frequency of Complex I and IV mutations observed in human PCa studies (chapter 3), defects in complex I and IV were observed in 86% and 41% of 11-month Polg-HOM epithelial cells, respectively. Isolated complex IV defects were rarely observed. Though mtDNA sequencing of prostate tissue was not performed on Polg-HOM mouse prostate tissue, a recent study by Ma *et al.* (2018) observed high frequency of mutations in Complex I and mitochondrial rRNAs from old Polg-HOM mice, as compared to younger Polg-HOM mice. This suggests that mutations in complex I increase with age, rather than being lost through clonal selection pressures.

Replication errors account for stochastic occurrence of mtDNA mutations in the Polg-HOM mouse, which are rarely shared amongst mice from the same litter (Ameur *et al.*, 2011; Ma *et al.*, 2018). Consistent with human ageing, neither wild-type nor Polg-HOM mice develop transversion mutations, thus questioning the role of oxidative stress as the major cause of mtDNA mutations. These results are also in line with findings reported in Chapter 3, where transversions mutations were rarely observed in human prostate cancer.

Single cell analysis demonstrated higher VDAC1 levels (marker of mitochondrial mass) in cells with OXPHOS defects, as compared to cells without OXPHOS defects at all ages and in all genotypes, which may represent compensatory upregulation of mitochondrial biogenesis. This phenomenon was also observed in human prostate cancer tissue (Chapter 5), whereby low complex I abundance and high mitochondrial mass were found to be features of aggressive prostate cancer.

The use of the Polg-HOM mutator mouse model differs from traditional gene targeted transgenic models for two mains reasons: (a) stochastic accumulation of highly heterogenous mtDNA mutations (while still at low heteroplasmy), which helps capture tumour heterogeneity as observed in human PCa; and (b) constitutive loss of Polg fidelity leads to systemic development of mitochondrial dysfunction, again more closely modelling systemic changes associated with human ageing. Thus, these features of the Polg mouse model help address established limitations of transgenic models, including limited heterogeneity and include the impact of systemic age-related changes in determining phenotype.

6.3.2 OXPHOS defects do not lead to malignant transformation in Polg-HOM mouse prostates

In comparison to age-matched wild-type controls, Polg-HOM prostates are smaller with occasional hyperplastic lesions but no gross evidence of PIN or invasive adenocarcinoma. Globally, reduced cell proliferation was also noted, which is likely to have a tumour suppressive effect following extrinsic tumour initiation. Due to a reduced lifespan of Polg-HOM mice (11 months, versus 2-3 years in Polg-WT mice) associated with age-related pathologies in other organ systems, the progression of hyperplastic lesions within the Polg-HOM prostates into early invasive adenocarcinoma may be missed. This may be overcome by one of two ways: (a) the development of prostate tissue specific models of mitochondrial dysfunction to overcome the reduced lifespan associated with systemic mitochondrial dysfunction, for the study of tumour initiation, or (b) generating a cross between Polg-HOM mice and established models of prostate cancer to study the additive effect of systemic mitochondrial dysfunction on tumour progression, as reported in the chapter 7.

Though Polg-HET mouse tissues were harvested, OXPHOS defects in prostates from these mice have thus far not been evaluated. Young Polg-HET (2-3 month) heart and brain tissue bears a 200-500 times higher burden of mtDNA mutations, as compared to age-matched wild-type controls, and 30 times higher burden of mtDNA mutations as compared to older wild-type controls (23-33 months) (Vermulst *et al.*, 2007). Notably, Polg-HET mice do not demonstrate overt age-related phenotypes and have a lifespan comparable to wild-type mice. Furthermore, the burden of OXPHOS defects in Polg-HET intestinal tissue is reportedly comparable to normal ageing human intestinal tissue (Baines *et al.*, 2014). Thus, further work aiming to estimate the burden of OXPHOS defects and assess histological changes in prostate tissue from old Polg-HET mice may help evaluate the impact of a more gradual accumulation of mitochondrial dysfunction at later time points.

Reduced expression of OXPHOS subunits was also evident in Polg-HOM mouse prostates tissue at the transcriptomic level. Pathways analysis revealed alterations in cell cycle and immune response. Reduced cell proliferation was confirmed at the proteomic level using Ki67 immunohistochemistry, which may be a consequence of reduced availability of ATP due to OXPHOS defects. In contrast, the frequency of $CD8^+$ or $CD11b^+$ immune cells were comparable in prostate tissue from 11-month Polg-HOM and age-matched Polg-WT controls. Further functional experiments assessing activation status of various components of the immune system are however required.

6.3.3 Potential limitations of Polg-HOM mice as a model of age-related mitochondrial dysfunction

Polg-HOM mice were found to have smaller testes and a smaller urogenitus, as compared to age-matched wild-types. A potential explanation for these phenomena may be low serum testosterone levels, as previously reported (Fox *et al.*, 2012; Jiang *et al.*, 2017). Since prostate cancers are initially testosterone dependent, reduced testosterone levels in Polg-HOM mice implies that prostate tumour suppression may be suppressed. However, this model may provide useful insights in the study of prostate cancer, following the development of castrate-resistance, as observed in *PTEN*-deficient prostate cancer.

Impaired spermatogenesis was also noted in aged Polg-HOM mice. This results in impaired fertility and small litter sizes (Trifunovic *et al.*, 2004; Jiang *et al.*, 2017) and necessitates the maintenance of multiple breeding cages or, preferably, the use of Polg-HET mice for breeding.

Though Polg-HOM mice display phenotypic features of human ageing, there are several differences in comparison to human ageing. Polg-HOM mice start to accumulate mtDNA mutations in the earliest stages of embryonic development in a small number of progenitor cells. This leads to high levels of mtDNA mutations in most if not all organs, which may clonally expand to orders of magnitude above the mutational frequency observed in normal human ageing (Khrapko *et al.*, 2006). Thus, unlike human ageing, mtDNA mutations in Polg-HOM mice do not accumulate in a slow and tissue-specific pattern.

6.3.4 Future work

This study has focussed on the characterisation of epithelial cells in Polg-HOM prostate tissue. However, since benign prostate hyperplasia is frequently observed in prostate tissue from older human prostate tissue, age-related alterations may also occur in the stromal

compartment. Bianchi-Frias *et al.* (2010) have previously reported subjective stromal changes in older C57B/6 mouse prostates (20-24 months), as compared to younger mice at 4 months of age, including increased thickness of glandular-adjacent cellular stroma in DP and AP, rounded and less elongated appearance of smooth-muscle cells in a disordered orientation, and increased frequency of inflammatory cell infiltration in aged prostate tissues. Thus, future work should include characterisation of the stromal compartment in Polg-HOM mouse prostate tissue. This work would also help assess whether Polg-HOM mice develop histological changes observed in normal ageing human prostate tissue, including benign prostatic hyperplasia (BPH), for which suitable animal models are lacking (Hieble, 2011).

Characterisation of mtDNA mutations observed in mouse prostate epithelial cells may help validate OXPHOS status determined by COX/SDH and multiplex fluorescence assays. This work may shed light upon potential clonal dynamics in ageing prostate tissue, including whether individual mtDNA mutations impact positive or negative selection processes.

In this study, Polg-HOM mouse prostates were initially characterised in *en bloc* embedded tissues, as per expert guidelines (Ittmann *et al.*, 2013). However, lobe-specific differences across the four mouse prostate lobes have previously been reported (Berquin *et al.*, 2005), with no consensus on which lobe is most comparable to human prostate tissue. A tissue micro-array consisting of micro-dissected individual prostate lobes from an ageing series of wild-type, Polg-HET and Polg-HOM mouse prostates has therefore be constructed (716 cores from 76 mice). This may subsequently be employed for protein-level validation of transcriptomic alterations identified in section 0, and supplement results of validation experiments using quantitative PCR.

6.4 Conclusion

Polg-HOM mice accumulate mtDNA mutations with advancing age and replicate phenotypic features of human ageing across multiple organ systems. In this study, Polg-HOM mouse prostate tissue was found to develop a high burden of OXPHOS defects by 11 months of age, as determined by sequential COX/SDH enzyme histochemistry and a quantitative single cell multiplex immunofluorescence assay. The vast majority of prostate epithelial cells developed complex I defects, whereas approximately 50% cells developed combined complex I and IV defects.

Pre-invasive and invasive prostate lesions were not observed in Polg-HOM mouse prostates, suggesting that age-related mitochondrial dysfunction may not be implicated in prostate tumour initiation. On the contrary, Polg-HOM mice demonstrated reduced prostate epithelial cell proliferation as evaluated by Ki67 immunohistochemistry and expression of cell cycle progression genes. A diverse range of transcriptomic alterations, predominantly involving immune signalling pathways, were also observed, which require further validation using proteomic or functional assays.

Since tumour initiation was not observed in Polg-HOM mouse prostate tissue, subsequent work using this model should focus on evaluating the role of mitochondrial dysfunction on tumour progression, by breeding Polg-HOM mice with established transgenic models of prostate cancer. However, such studies employing Polg-HOM mouse model would be limited by the observation that these mice develop testicular atrophy and have previously been shown to have significantly reduced serum testosterone levels, akin to the aim of surgical castration or androgen deprivation therapy in the management of clinical prostate cancer. Thus, the Polg-HOM model may provide a suitable model for the study of mitochondrial dysfunction in the context of castrate resistant prostate cancer (as modelled by the *PbCre4*$^{+}$*Pten*$^{fl/fl}$ model), which remains an area of significant unmet clinical need.

Chapter 7 Impact of OXPHOS defects on tumour progression in a mouse models of prostate cancer

7.1 Introduction

7.1.1 Background

Despite emerging data supporting an association between mtDNA mutations, mitochondrial dysfunction and adverse prostate cancer outcome, the functional impact of mitochondrial alterations on cancer progression, whether as drivers (i.e. conferring a fitness advantage), passengers (i.e. conferring no fitness advantage) or tumour suppressors, remains unclear.

Trans-mitochondrial cytoplasmic hybrid (cybrid) cell lines have been used to evaluate the impact of specific mtDNA mutations on cancer progression, as described in section 1.7.3. Cybrid lines are established by depleting mtDNA in immortalised cell lines using ethidium bromide, which are then fused with cytoplasts from donor cell lines harbouring characterised mtDNA mutations. The resulting cybrids (cytoplasmic hybrids) therefore contain the nuclear genomic background of tumourigenic cell lines and pathogenic donor mtDNA mutations. Xenografts of prostate cancer (PC3 cell line) (Petros *et al.*, 2005) and osteosarcoma (Arnold *et al.*, 2015) cybrid lines with donor mtDNA from a patient with Leigh syndrome (*MT-ATP6* m.8993T>G mutation) demonstrated accelerated tumour progression, in comparison to cybrids harbouring wild-type mtDNA. Intriguingly, complex I cybrid lines with varying degrees of OXPHOS impairment demonstrated a tumour suppressive effect (Iommarini *et al.*, 2013), with greatest effect observed amongst mutations that resulted in severe OXPHOS defects. These findings are, however, in contrast to the pro-tumourigenic effect of complex I defects noted using primary clinical tissue in Chapter 5.

Though cybrid experiments have helped elucidate potential underlying mechanisms for mtDNA-mediated tumour progression, this approach remains technically challenging, low-throughput and requires suitable patient-derived donor mtDNA cell lines. These models also fail to adequately recapitulate systemic and local tumour-related changes, which impact clinical cancer progression, in addition to modelling only a small range of mtDNA mutations, as opposed to the stochastic nature of mutations observed in both benign human ageing prostate tissues and clinical prostate cancer. Given the above limitations, suitable tumourigenic *in vivo* models of mitochondrial dysfunction are required.

7.1.2 *PTEN*-deficient prostate cancer

Phosphatase and tensin homolog (*PTEN*), is a tumour suppressor gene, encoding a lipid/protein phosphatase that negatively regulates the Pi3k/Akt signalling pathway by dephosphorylating phosphatidylinositol (3,4,5)-trisphosphates (*PIP3*) back to phosphatidylinositol 4,5-bisphosphates (*PIP2*). It is implicated in 40-70% of patients with prostate cancer (Cairns *et al.*, 1997; Suzuki *et al.*, 1998; Wang *et al.*, 1998; Jamaspishvili *et al.*, 2018). As described in section 1.4, alterations in the *Pi3k/Akt*, *MAPK* and *p53* signalling pathways are frequently observed in human prostate cancer (Taylor *et al.*, 2010). Genetic manipulation of these pathways using transgenic models has consequently provided key insights into the complex interplay between established features of prostate tumourigenesis and cellular phenomena.

7.1.3 Mouse models of prostate cancer

Though spontaneous PCa is uncommon in the mouse, transgenic mouse models have been extensively employed in the study of human prostate carcinogenesis. This is due to similarities in mouse and human genomes, relative ease of genetic modification in the mouse, their short period of gestation and small size allowing greater affordability (Valkenburg and Williams, 2011).

The majority of PCa in mouse models arise in the dorsolateral lobe, which was previously thought to most closely resemble the peripheral zone of the human prostate. However, according to revised expert opinion, there is no direct relationship between any one mouse lobe and any particular zone of the human prostate (Shappell *et al.*, 2004).

The ideal mouse model would exhibit all stages of human PCa, sequentially including low-grade PIN, high-grade PIN, locally-invasive adenocarcinoma, locally-advanced adenocarcinoma, metastasis and, finally, castrate-resistance (Valkenburg and Williams, 2011). It would temporally mimic molecular changes associated with human PCa progression, and recapitulate metastasis to the bone and lymph nodes, as seen in human disease. By mimicking response to therapeutics in early stages of human PCa, the ideal model would initially respond to anti-androgen therapies, and subsequently develop androgen-resistant disease.

7.1.4 Constitutive *Pten*-deficient mouse models

Historically, constitutive models were used to model molecular changes in every cell of the transgenic animal, such as the *Polg* mutator mouse (Trifunovic *et al.*, 2004; Kujoth *et al.*, 2005) described in Chapter 6. However, these models may be limited by embryonic lethality if genes essential to normal development were ablated.

Using homologous recombination, Di Cristofano *et al.* (1998) created a mouse model with constitutive *Pten* inactivation. $Pten^{-/-}$ mice demonstrated embryonic lethality by embryonic day 7.5, whereas $Pten^{+/-}$ mice demonstrated shorter lifespan (6-14 weeks) with pre-neoplastic changes in the prostate, in addition to other organs. Conversely, more recently, a transgenic mouse with elevated *Pten* expression was generated, and found to be cancer resistant upon injection of chemical carcinogens (Garcia-Cao *et al.*, 2012). These experiments using constitutive transgenic *Pten* mouse models have confirmed the role of *PTEN* as a tumour suppressor gene.

7.1.5 Generating tissue-specific *Pten*-deficient mouse models using *Cre-lox* technology

The use of *Cre-loxP* technology now allows the generation of target-specific inducible transgenic models, which help circumvent embryonic lethality and test the consequence of gene manipulation in the organ of interest at a chosen time point (Valkenburg and Williams, 2011).

The *Cre* ("cyclisation recombination") gene catalyses site-specific DNA recombination in genes which are flanked by two synthetic 34-base pair sequences knowns as '*Lox-P*' sites (locus of cross-over of P1 bacteriophage). Upon recombination, the target-gene previously flanked (or 'floxed') by the two *Lox-P* sites is excised (**Figure 7-1**). A single *loxP* now remains in the linear DNA, whereas the target gene, now attached with the remaining *loxP* sequence, forms a circular DNA fragment, which is rapidly degraded.

The expression of *Cre*-recombinase is typically under the control of a tissue-specific promoter, which enables DNA recombination in a tissue-specific manner, either by constitutive activation of the promoter (eg probasin production upon reaching puberty) or following the delivery of an induction agent (eg Tamoxifen administration).

The *Cre-loxP* system has been successfully employed to devise a prostate-specific *Pten* knockdown mouse model ($PbCre4^{+};Pten^{fl/fl}$) using the $ARR_2Probasin$-*Cre* transgenic line (*PbCre4*), in which the *Cre*-recombinase is under the control of a modified rat probasin (*Pb*)

promoter encompassing two androgen receptor response (ARR) elements (Wu *et al.*, 2001). Probasin is only expressed in luminal cells of the mouse prostate and reaches highest level of expression by puberty at 8 weeks, leading to formation of Cre-recombinase in prostate luminal cells. This ensures prostate luminal cell-specific knockdown of *Pten*. *Cre*-recombinase expression was reported to vary between the different prostatic lobes (lateral > ventral > dorsal > anterior lobe), however, in a subsequent study, all lobes were found express *Cre*-recombinase equally by 8 months of age (Powell *et al.*, 2003).

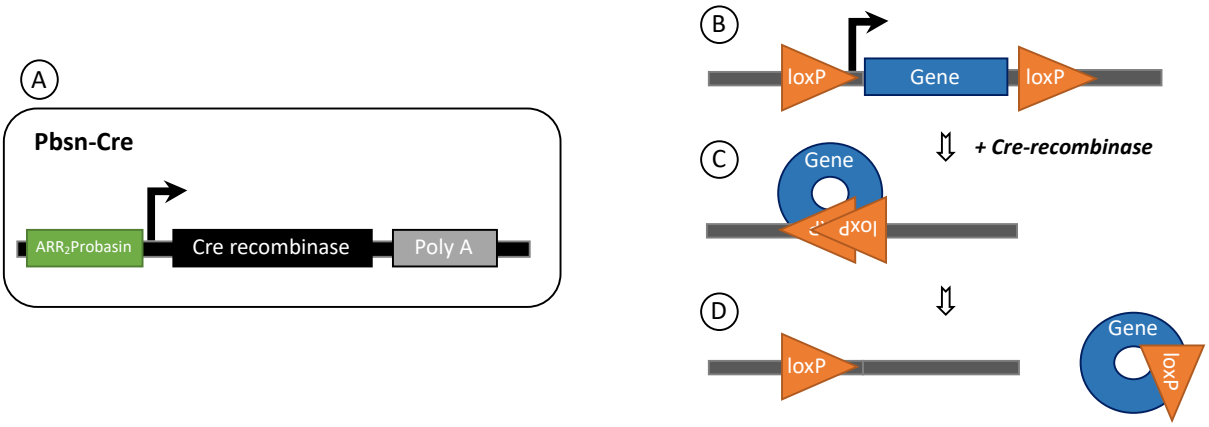

Figure 7-1: Schematic demonstrating the Cre-loxP system for gene ablation. (A) Activation of the ARR_2Probasin promoter by androgen production at puberty results in transcription of Cre recombinase in mice with a Probsin-Cre allele. **(B)** The gene of interest is flanked by two loxP sites. **(C)** Recombination of the two loxP sites by the action of Cre-recombinase leads to **(D)** the formation of mutant sequence with single remaining loxP site and the circular DNA fragment containing the ablated gene of interest.

7.1.6 Isolated *Pten*-loss results in prostate cancer initiation

Prostate-specific loss of *PTEN* and consequent activation of the *Pi3k/Akt* signalling pathway has been modelled in *PbCre4*$^{+}$*;Pten*$^{fl/fl}$ mice. Heterozygous *PbCre4*$^{+}$*;Pten*$^{fl/+}$ mice develop prostate intra-epithelial neoplasia (PIN) by 12-16 months of age, whereas homozygous *Pten*-loss results in PIN by 6 weeks with full penetrance and invasive adenocarcinoma at 9-27 weeks (Wang *et al.*, 2003). A subsequent report by Trotman *et al.* (2003) reported a dose-dependent effect of targeted *Pten* depletion on prostate cancer progression.

Castration of *PbCre4*$^{+}$*Pten*$^{fl/fl}$ mice transiently increases apoptosis, with subsequent adaptation of *Pten*-deficient cells (Wang *et al.*, 2003)., emergence of castrate-resistance and increased *Pi3k/Akt* signalling through inhibition of the androgen receptor transcription factor activity (Mulholland *et al.*, 2011). Progression to metastatic disease has been reported by Wang *et al.*

(2003) with 50% penetrance by 6 months of age. However, subsequent studies have failed to demonstrate metastatic lesions in *PbCre4*$^{+}$*Pten*$^{fl/fl}$ mice (Ratnacaram *et al.*, 2008; Kwak *et al.*, 2013) and highlight the potential need for additional oncogenic events in driving metastatic spread, despite spontaneous development of castrate-resistance disease in this model.

7.1.7 Double mutant mice develop features of advanced prostate cancer:

Activated *MAPK* signalling and *p53* alterations have been demonstrated in 90% and 50% metastatic cases, respectively (Taylor *et al.*, 2010; Robinson *et al.*, 2015). These events may frequently co-occur with activated *Pi3k*/*Akt* signalling in advanced stages of prostate cancer as discussed in section 1.4.4 (Zou *et al.*, 2017; Hamid *et al.*, 2019). Transgenic models of either *MAPK* activation (Mulholland *et al.*, 2012; Jefferies *et al.*, 2017) or *p53* alterations alone (Chen *et al.*, 2005; Couto *et al.*, 2009; Wang *et al.*, 2014) do not spontaneously develop invasive prostate cancer. However, upon *Pten* ablation, both *Kras* and *p53* alterations result in aggressive prostate cancer with high penetrance. Thus, double mutant mice are thought to more accurately recapitulate stages of prostate cancer progression.

Pten-loss activates a *p53*-mediated senescence programme, which permanently halts cell proliferation and promotes immune surveillance of pre-invasive and invasive prostate lesions in *PbCre4*$^{+}$*;Pten*$^{fl/fl}$ mice (Chen *et al.*, 2005; Parisotto *et al.*, 2018). A reciprocal cooperation between *PTEN* and *p53* is therefore proposed, whereby *Pten* regulates *p53* stability and *p53* in turn enhances *PTEN* transcription. Inactivation of *p53* by deletion of *p53* alleles in *PbCre4*$^{+}$*;Pten*$^{fl/fl}$*;p53*$^{fl/fl}$ mice overcomes cellular senescence and results in progression to aggressive dedifferentiated sarcomatoid prostate tumours (Martin *et al.*, 2011), lymph node deposits and cancer-related mortality by 7 months of age (Chen *et al.*, 2005; Wang *et al.*, 2014). *Pten*-deficient heterozygous *p53* mutants develop an intermediate phenotype with a reduced lifespan in comparison to *PbCre4*$^{+}$*;Pten*$^{fl/fl}$ mice (Chen *et al.*, 2005).

Heterozygous mutant *Kras*^{V12} allele results in increased *MAPK* signalling (Guerra *et al.*, 2003), which alone cannot initiate prostate carcinogenesis (Mulholland *et al.*, 2012; Jefferies *et al.*, 2017), though early PIN is observed in aged mice with oncogenic *Kras*^{G12D} (Mulholland *et al.*, 2012) or *Kras*^{G12V} mutations (Pearson *et al.*, 2009). Cross-talk between *MAPK* signalling and *Pi3k*/*Akt* signalling is well established (Mulholland *et al.*, 2012; Wang *et al.*, 2012; Rozengurt *et al.*, 2014) and co-activation of these pathways promotes epithelial to mesenchymal

transition and subsequent development of metastases (Mulholland *et al.*, 2012; Jefferies *et al.*, 2017). In keeping with this phenomenon, *PbCre4*$^{+}$*;Pten*$^{fl/fl}$*;Kras-V12*$^{fl/+}$ mice develop micro-invasive adenocarcinoma by 100 days and retroperitoneal lymph node metastasis at clinical end points by approximately 240 days of age (Jefferies *et al.*, 2017). In comparison, the mutant *Kras*^{G12D} allele leads to a more aggressive phenotype with invasive adenocarcinoma by 30 days, macrometastatic lesions in the lung and liver with 100% penetrance and cancer-related mortality by 150 days of age (Mulholland *et al.*, 2012).

7.1.8 Chapter aims

In Chapter 5, I reported reduced Complex I protein abundance and increased mitochondrial mass in primary tissue samples from patients with prostate cancer. Molecular stratification of patients demonstrated reduced overall survival in *PTEN*-low patients with reduced complex I abundance. It was therefore hypothesised that mitochondrial dysfunction mediated by age-associated accumulation of mtDNA mutations would accelerate prostate cancer progression.

In order to test this hypothesis, I aimed to generate a tumourigenic prostate-specific *Pten*-deficient mouse model that constitutively accumulated mtDNA mutations with advancing age. Two exploratory colonies with additional oncogenic alterations in *Kras* and *p53* were also set up.

The objectives of this chapter are therefore to:

1. Use *in vitro* models of PCa to evaluate the impact of *Pten* loss on OXPHOS protein abundance and metabolic phenotype
2. Generate novel mouse models to mimic constitutively mutant *PolgA*-mediated mitochondrial dysfunction on prostate-specific tumourigenic backgrounds based upon *Pten*-loss alone, or combined with either oncogenic *Kras* or *p53* alterations.
3. Evaluate histopathological and immunohistochemical markers of tumour progression at age-matched clinical endpoints.

7.2 Results

7.2.1 *PTEN* loss upregulates glycolytic ATP production

Previous data using mouse embryonic fibroblasts (Goo *et al.*, 2012) and PCa cell lines (Weber *et al.*, 2018) has reported that *PTEN* ablation increased mitochondrial respiratory capacity with increased succinate accumulation, driven by a switch from mitochondrial NADH-linked pathway (where protons enter ETC via Complex I) to a succinate-linked pathway (where protons enter ETC via Complex II). Similarly, *PTEN* overexpression has been associated with increased mitochondrial ATP production (Garcia-Cao *et al.*, 2012). Conversely, *PTEN* loss is associated with upregulation of glycolytic pathways (Zhou *et al.*, 2019). However, it is unclear whether ATP production in *PTEN*-deficient cells is driven by upregulation of glycolysis or increased mitochondrial oxidative phosphorylation (OXPHOS).

In order to characterise the impact of *PTEN* loss on the metabolic phenotype, the PC3-PTEN cell line model was used (Maxwell *et al.*, 2013), where administration of doxycycline leads to transgenic expression of *PTEN* and inactivation of *Pi3k/Akt* signalling. *PTEN* expression and consequent reduction of *pAkt* expression in this cell line was first validated following 24, 48 and 72 hours of doxycycline administration (**Figure 7-2**). Mitochondrial protein expression was comparable across both DOX- and DOX+ conditions across all time points.

Since doxycycline has been thought to impair mito-nuclear protein balance at the 1µm/ml range (Moullan *et al.*, 2015), the lowest dose of doxycycline enabling *PTEN* expression and inhibiting *pAkt* expression was titrated down to 10 ng/ml, with no substantial alteration in alteration in expression of mitochondrial proteins *NDUFB8* (complex I subunit) and *MTCO1* (complex IV subunit). A potential limitation of this work is the low basal expression of *NDUFB8* in the PC3 cell line and lack of technical replicates, which makes it challenging to determine the true magnitude of effect of doxycycline on mitochondrial protein abundance in this model. Therefore, validation of these data using alternative PCa cell lines and additional technical replicates is warranted.

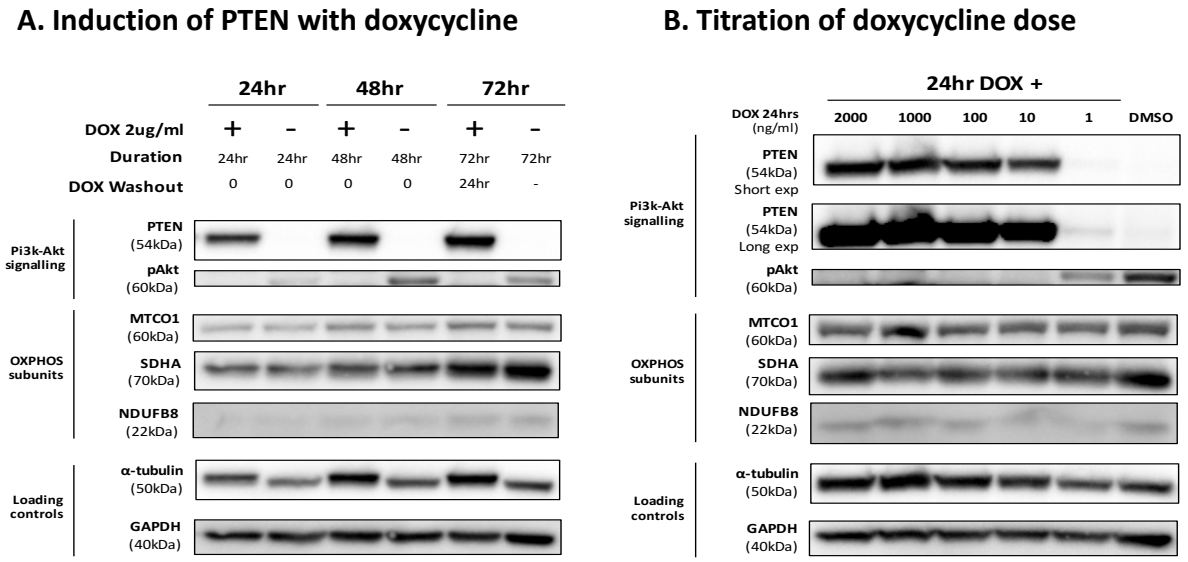

Figure 7-2: Western blot analysis of DOX-inducible PC3-PTEN cell line. Induction of *PTEN* was assessed using **(A)** 2µg/ml doxycycline at various time points, and **(B)** a range of doses were titrated at the 24-hour time point. Membranes were probed for *PTEN* and its downstream effector phospho-Akt (*pAkt*), OXPHOS subunits (*MTCO1*, *SDHA*, and *NDUFB8*) and loading controls (α-tubulin and *GAPDH*).

The functional impact of *PTEN* expression of mitochondrial metabolism was subsequently evaluated using the mitochondrial stress test on the Seahorse Flux analyser. Following 72 hours of incubation in culture media containing either DOX 10ng/ml, DOX 1µg/ml or DMSO 1µg/ml, PC3-PTEN cells were placed in a CO_2-free incubator for serial measurements of oxygen consumption rate (OCR) and extra-cellular acidification rate (ECAR). These variables were measured at baseline, and following administration of complex III inhibitor oligomycin, mitochondrial uncoupler carbonyl cyanide-4-phenylhydrazone (FCCP), and combined inhibition of complexes I and V, using rotenone and antimycin A, respectively (**Figure 7-3**).

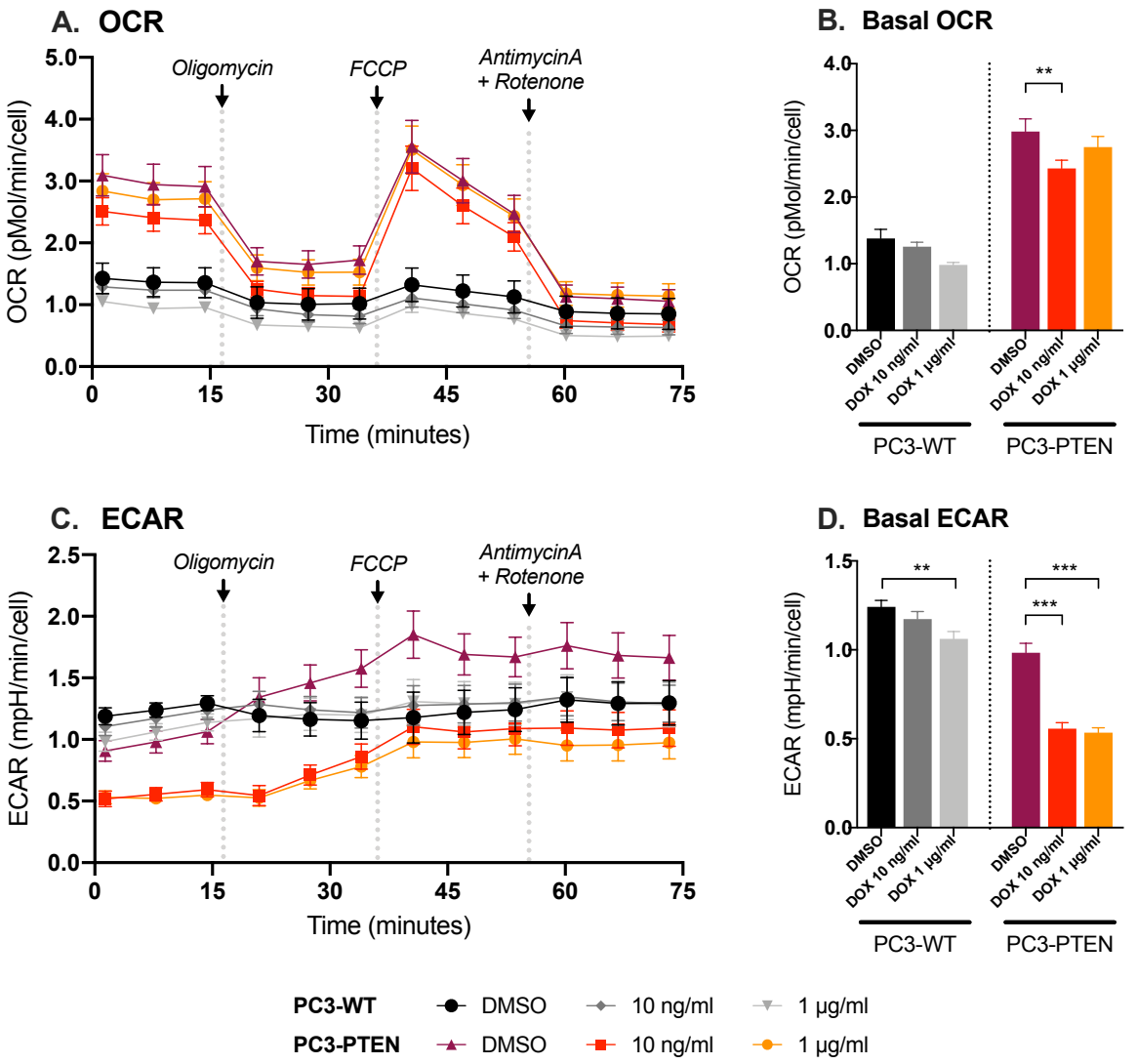

Figure 7-3: Seahorse metabolic flux analysis of doxycycline-inducible PC3-PTEN cell line using the mitochondrial stress test. Parental PC3-WT cell line and doxycycline-inducible PC3-PTEN cell line were cultured with either DMSO or doxycycline at 10ng/ml or 1µg/ml for 72 hours. **(A-B)** Oxygen consumption rate and **(C-D)** Extracellular acidification rate (ECAR) were measured after introduction of mitochondrial OXPHOS complex inhibitors oligomycin, FCCP, antimycin A and rotenone. Results of three biological replicates are presented with standard error of measurement. Mean basal rates were compared using Fisher's exact test, with *p* values reported as *, **, and ***, representing $p<0.05$, $p<0.01$, and $p<0.001$, respectively.

As compared to the wild-type PC3 cell line, basal expression of OCR was higher and ECAR expression was lower in the transgenic PC3-PTEN cell line across all conditions. In the presence of doxycycline, ECAR was reduced in the PC3-PTEN cell line at both 10µg/ml (Δ-0.43 mpH/min/cell, $p<0.001$) and 1µg/ml (Δ-0.45 mpH/min/cell, $p<0.001$), and also in the PC3-WT cell line at 1µg/ml (Δ-0.18 mpH/min/cell, $p=0.004$). However, since extra-cellular acidification results from both glycolytic lactate production and respiratory CO_2 production, differential

modes of ATP production were estimated (Mookerjee *et al.*, 2015). ATP production via OXPHOS was comparable across all conditions (p>0.4), whereas *PTEN* induction in the PC3-*PTEN* cell line in the presence of doxycycline led to a reduction of glycolytic ATP production (**Figure 7-4**, DOX 10µg/ml:Δ-7.8 pmol/min/cell, p<0.001; DOX 1µg/ml:Δ-7.3 pmol/min/cell, p=0.002).

Therefore, these data suggest that *PTEN* re-expression in the *PTEN*-deficient PC3 cell line results in reduced glycolytic ATP production without affecting OXPHOS mediated ATP production. Conversely, these data would suggest that *PTEN* loss upon removal of doxycycline-mediated *PTEN* expression results in an increase in glycolytic ATP production, without altering OXPHOS-driven ATP production. Notably, only mitochondrial ATP production was evaluated in this work. Thus, it is plausible that *Pi3k/Akt* signalling in *PTEN*-deficient PCa may influence non-metabolic functions of mitochondria, such as ROS signalling (Koundouros and Poulogiannis, 2018), which were not evaluated in this study. Furthermore, the use of *in vitro* models, rather than comparison of systemic alterations in *PTEN*-deficient mouse models may not accurately model the interaction between prostate cancer cells and the host microenvironment, and its potential impact on cancer cell metabolism.

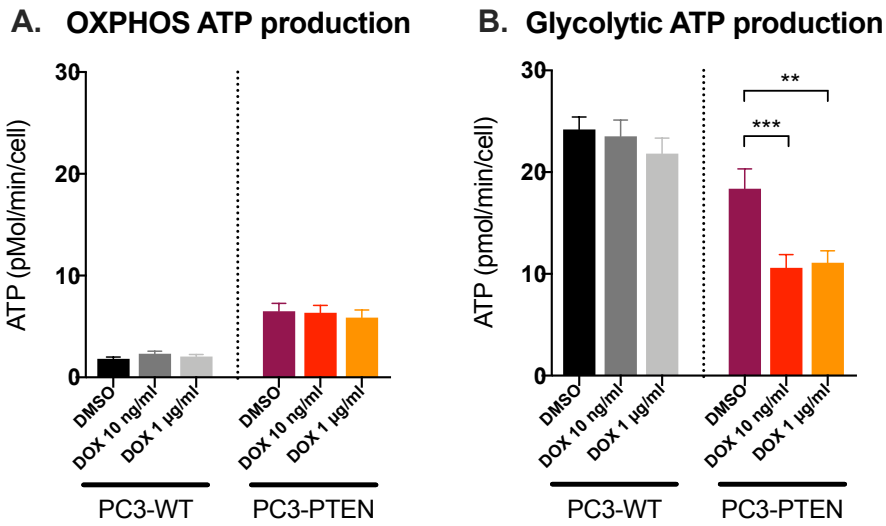

Figure 7-4: Impact of *PTEN* status on ATP production tested by the mitochondrial stress test using doxycycline-inducible PC3-*PTEN* cell line. (A-B) After adjusting for CO_2 produced as part of respiration, ATP production from **(C)** glycolysis and **(D)** OXPHOS was estimated. Results of three biological replicates are presented with standard error of measurement. Mean basal rates were compared using Fisher's exact test, with p-values reported as *, **, and ***, representing p<0.05, p<0.01, and p<0.001, respectively. These results demonstrate that induction of PTEN leads to upregulation of glycolysis, with no change in OXPHOS.

7.2.2 Generation of mouse model of mitochondrial dysfunction and prostate carcinogenesis

The Polg mutator model was established at the European Cancer Stem Cell Institute (Cardiff University) in collaboration with Dr Boris Shorning, Professor Matthew Smalley and Professor Alan Clarke. Female founder Polg-HET mice from the Newcastle colony (characterised in Chapter 6) were crossed with tumourigenic models of *Pten*-deficient prostate cancer over a mixed genetic background, to set up the *PbCre4*$^{+}$*;Pten*$^{fl/fl}$ colony. In order to recapitulate more advanced stage disease, two exploratory cohorts with additional oncogenic alterations in *MAPK* (*PbCre4*$^{+}$*;Pten*$^{fl/fl}$*;Kras*$^{V12/wt}$ colony) and *p53* signalling (*PbCre4*$^{+}$*;Pten*$^{fl/fl}$*;p53*$^{mut/wt}$ colony) were also established. Breeding schemes used to generate these models are outlined in section 2.3.3, and resulting genotypes are listed in **Table 7-1**.

Colony	*PbCre4*$^{+}$*Pten*	*Kras-V12*	*p53-mut*	*Polg*
Background				
Polg-WT	wt/wt	wt/wt	wt/wt	wt/wt
Polg-HET				mut/wt
Polg-HOM				mut/mut
***PbCre4*$^{+}$*;Pten*$^{fl/fl}$**				
Pten-HOM; Polg-WT	fl/fl	wt/wt	wt/wt	wt/wt
Pten-HOM; Polg-HET				mut/wt
Pten-HOM; Polg-HOM				mut/mut
***PbCre4*$^{+}$*;Pten*$^{fl/fl}$*; Kras*$^{V12/wt}$**				
Pten-HOM; Kras-HET; Polg-WT	fl/fl	fl/wt	wt/wt	wt/wt
Pten-HOM; Kras-HET; Polg-HET				mut/wt
Pten-HOM; Kras-HET; Polg-HOM				mut/mut
***PbCre4*$^{+}$*;Pten*$^{fl/fl}$*; p53*$^{mut/wt}$**				
Pten-HOM; p53-HET; Polg-WT	fl/fl	wt/wt	fl/wt	wt/wt
Pten-HOM; p53-HET; Polg-HET				mut/wt
Pten-HOM; p53-HET; Polg-HOM				mut/mut

Table 7-1: Genotypes of established mouse models.

Mice were monitored for age and tumour-related phenotypes and subsequently culled at humane endpoints for lifespan studies. Once median lifespans for Polg-HOM mice were determined in each colony, a minimum of four mice were culled at an age-matched time point at a median age of 200 days. At harvest, body weight and prostate weight were noted. All organs were harvested for assessment of metastatic spread. Prostate tumours were bisected for formalin-fixation and cryopreservation for molecular studies. Formalin fixed paraffin embedded tissues were evaluated by H&E staining and immunohistochemical markers of OXPHOS protein abundance, *Pi3k*/*Akt* signalling, cell proliferation and apoptosis.

7.2.2.1 Tumourigenic mouse models

Baseline lifespan data for tumourigenic mouse models and wild-type mice at Cardiff are reported in **Figure 7-5**. Wild-type control mice were followed up to a maximum of 500 days for logistical reasons. As previously observed in Chapter 6, Polg-HOM mice demonstrated reduced lifespan with a median survival of 201.5 days, succumbing to age-related pathologies including anaemia, reduced thermogenesis and anal prolapse, necessitating early euthanasia. Only *PbCre4*$^{+}$*;Pten*$^{fl/fl}$*;Kras*$^{V12/+}$ mice had similar lifespan as Polg-HOM mice (201 vs 201.5 days, log rank test, p=0.510), whereas relatively increased lifespan was noted in both *PbCre4*$^{+}$*;Pten*$^{fl/fl}$ and *PbCre4*$^{+}$*;Pten*$^{fl/fl}$*;p53*$^{mut/+}$ mice (log rank test, p<0.001).

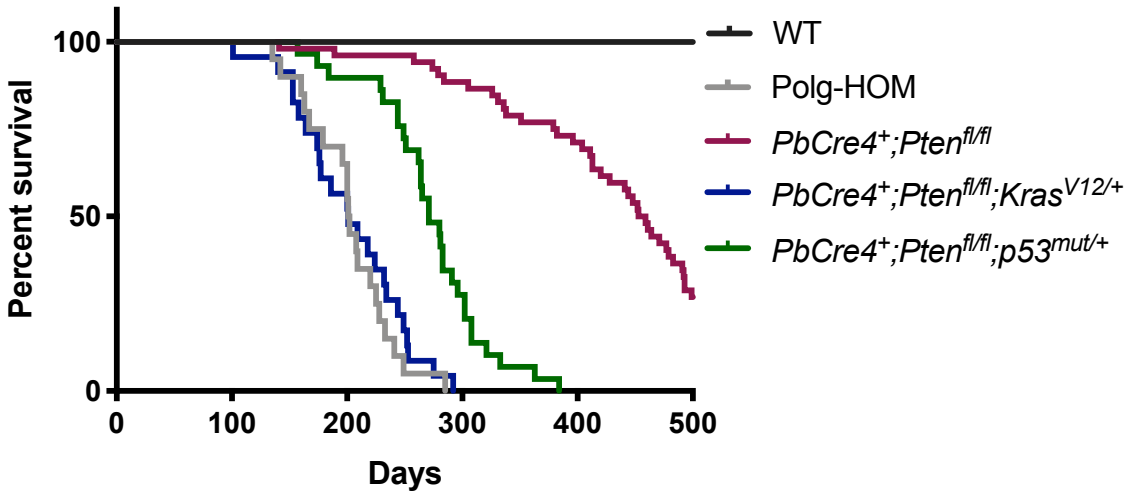

Genotype	N	Median survival (days)	*p* value (log rank test) vs Polg-HOM
WT	15	500	<0.001
Polg-HOM	20	201.5	
***PbCre4*$^{+}$*; Pten*$^{fl/fl}$**	52	456	<0.001
***PbCre4*$^{+}$*; Pten*$^{fl/fl}$*; Kras*$^{V12/+}$**	23	201	0.510
***PbCre4*$^{+}$*; Pten*$^{fl/fl}$*; p53*$^{mut/+}$**	29	271	<0.001

Figure 7-5: Kaplan-Meier survival curves for tumourigenic mouse colonies at Cardiff. For comparison, lifespan data for Polg-HOM mice and wild-type mice at Cardiff are included. Number of mice, median survival and results of log-rank test are reported, using the Cardiff Polg-HOM mouse cohort as reference.

7.2.3 Immunohistochemical validation

7.2.3.1 OXPHOS defects

Since Polg-mediated mtDNA mutations are expected to result in defects in mitochondrial-encoded OXPHOS complexes, the OXPHOS protein abundance was evaluated in randomly selected regions of interest from prostate tissue from at least four mice from each genotype using the quantitative multiplex immunofluorescence assay described in section 4.2.5. Z-scores were calculated in comparison to prostate epithelial cells from a cohort of age-matched wild-type mice using single cell level optical density data, normalised for inter-cellular variation in mitochondrial mass and corrected for background signal.

Summary results from the genetic background cohort, and tumourigenic *PbCre4*$^{+}$*;Pten*$^{fl/fl}$ and *PbCre4*$^{+}$*Pten*$^{fl/fl}$*;Kras*$^{V12/+}$ colonies are reported in **Figure 7-6**. Representative composite and z-score pseudo-images are presented in **Figure 7-7**, **Figure 7-8** and **Figure 7-9**. At the time of writing, OXPHOS data were not available for mice from the *PbCre4*$^{+}$*;Pten*$^{fl/fl}$*;p53*$^{mut/+}$ colony.

Across all cohorts, a high frequency of cells with either complex I or complex IV defects were observed in Polg-HOM mice, in comparison to age-matched Polg-WT controls (**Figure 7-6**, one-way ANOVA test, $p<0.001$). A compensatory increase in mitochondrial mass was noted in both tumourigenic cohorts, but not the genetic background colony. Cohort-specific age-matched Polg-WT mouse prostate tissue was used as controls to define 'normal' mitochondrial function, rather than younger 4-month Polg-WT mice (as in Chapter 6), resulting in a relatively conservative estimates of proportion of cells with OXPHOS defects.

Though Polg-HET mice were not included in these analyses, sequencing of Polg-HET mouse tissue has previously noted an increased frequency of mtDNA mutations as compared to age-matched wild-type controls (Vermulst *et al.*, 2008). Thus, Polg-HET mouse prostate tissue is expected to bear a higher frequency of OXPHOS defects as compared to age-matched controls, but lower than Polg-HOM tissue. These assumptions would, however, require validation at the genomic and proteomic level in murine prostate tissue, which had not been completed at the time of submission of this thesis.

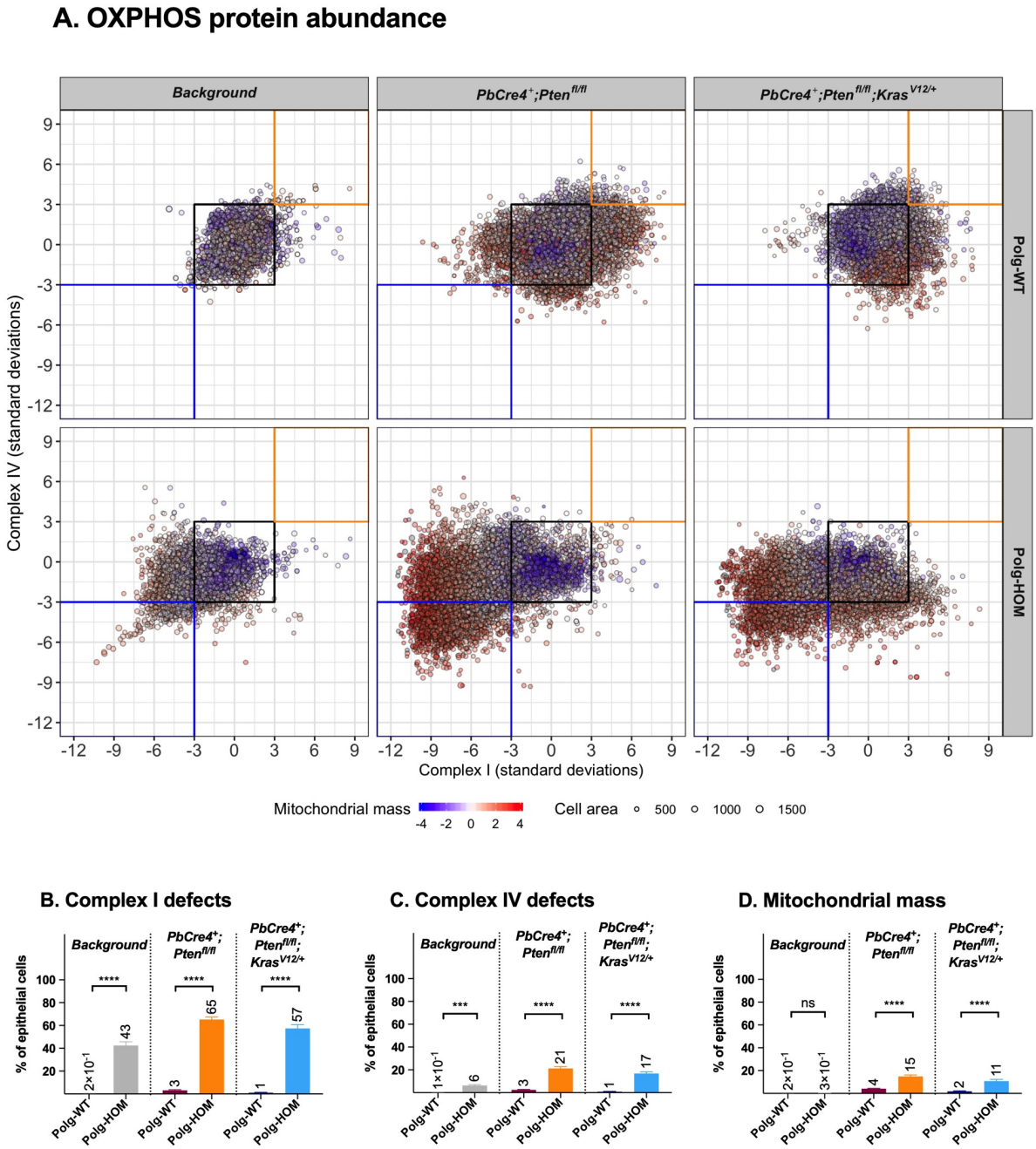

Figure 7-6: OXPHOS protein abundance in mouse prostate tissue. **(A)** Mitochondrial respiratory chain graphs highlight OXPHOS alterations in complex I, IV and mitochondrial mass across 10,000 randomly sampled cells per genotype, by quantified immunofluorescence for NDUFB8, MTCO1 and TOMM20 respectively. Each point represents results for an individual epithelial cell, with size presenting cell area and colour representing TOMM20 z-score. Quantification of OXPHOS alterations within randomly-selected regions of interest (ROIs) was performed by calculating the percentage of cells with **(B)** complex I and **(C)** complex IV z-scores below -3 standard deviations (s.d), or **(D)** an increase in mitochondrial mass as defined as z-score above +2 s.d. Mean percentage of cells with OXPHOS alteration are reported above each bar plot. Data from a median of 22 ROIs from at least 4 mice per genotype were included in each cohort. Error bars represent standard error of measurement. Student's t test was used and *p*-values are represented with **** and *** representing $p<0.0001$ and $p<0.001$ respectively.

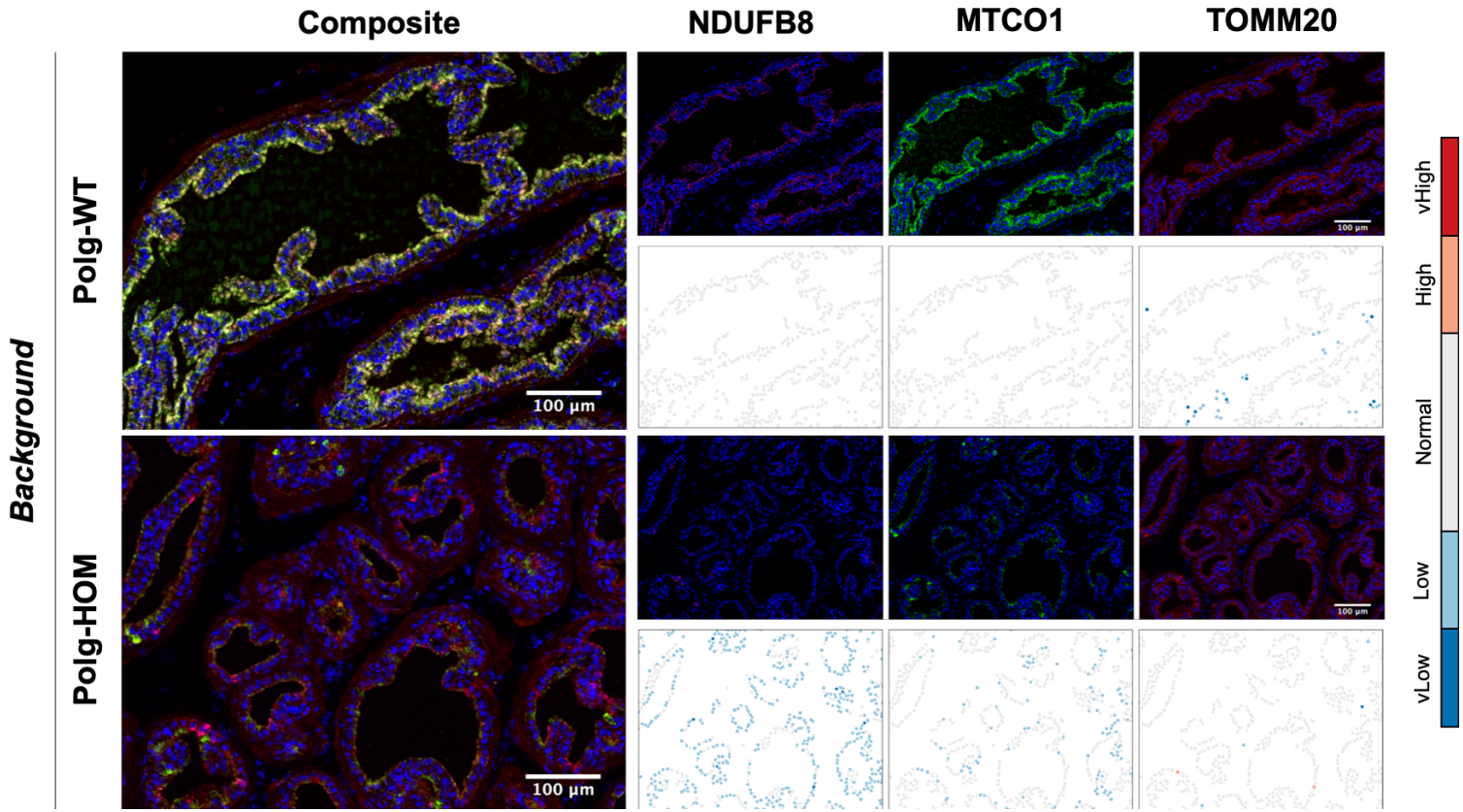

Figure 7-7: OXPHOS defects in mouse prostate tissue from the non-tumourigenic genetic background cohort. Representative multiplex fluorescence images (left) with single channel images (top right panels) with colours representing *NDUFB8* (complex I, magenta), *MTCO1* (complex IV, green) and *TOMM20* (mitochondrial mass, red). Corresponding bottom panels represent pseudo-images (bottom right panels) demonstrating high frequency of epithelial cells with low complex I abundance in Polg-HOM prostate tissue. Across all pseudo-images, each point represents a single cell with colours denoting z-scores for complexes I and IV categorised into very low (vLow, <-6 s.d), low (-6 to -3 s.d.), normal (-3 to 3 s.d.), high (+3 to +6 s.d.), and very high (>+6 s.d.) with respect to age-matched Polg-WT tissue. Z-scores for mitochondrial mass used thresholds for -3, -2, +2, and +3 s.d. to categorise cells into very low, low, normal, high and very high groups. Colour scales are denoted on the right and scale bars represent 100 µm.

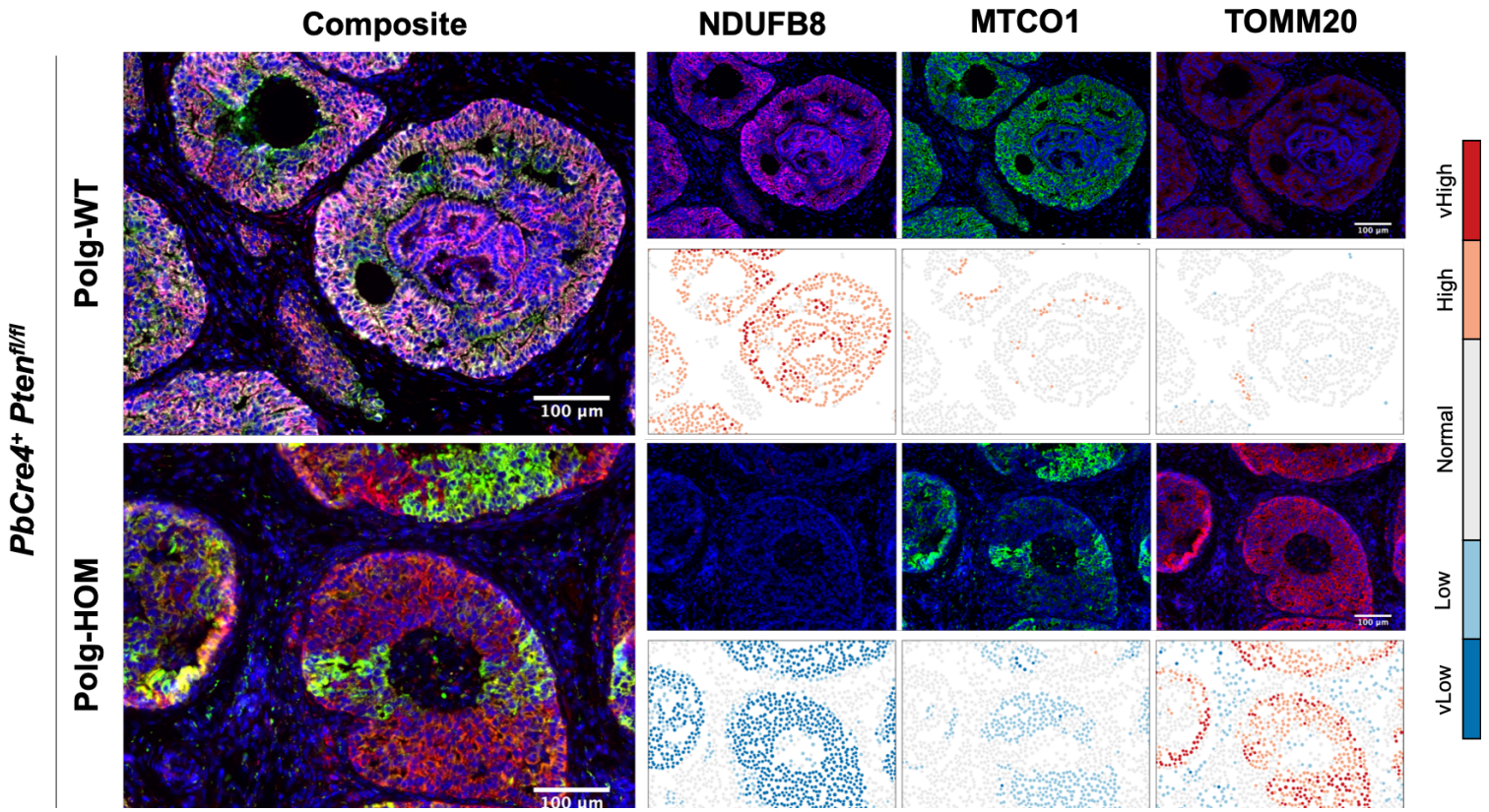

Figure 7-8: OXPHOS defects in mouse prostate tissue from the *PbCre4*$^{+}$*;Pten*$^{fl/fl}$ cohort. Representative multiplex fluorescence images (left) with single channel images (top right panels) with colours representing *NDUFB8* (complex I, magenta), *MTCO1* (complex IV, green) and *TOMM20* (mitochondrial mass, red). Corresponding bottom panels represent pseudo-images (bottom right panels) demonstrating high frequency of epithelial cells with low complex I abundance in Polg-HOM prostate tissue. Across all pseudo-images, each point represents a single cell with colours denoting Z-scores for complexes I and IV categorised into very low (vLow, <-6 s.d.), low (-6 to -3 s.d.), normal (-3 to 3 s.d.), high (+3 to +6 s.d.), and very high (>+6 s.d.) with respect to age-matched Polg-WT tissue. Z-scores for mitochondrial mass used thresholds for -3, -2, +2, and +3 s.d. to categorise cells into very low, low, normal, high and very high groups. Colour scales are denoted on the right and scale bars represent 100 µm.

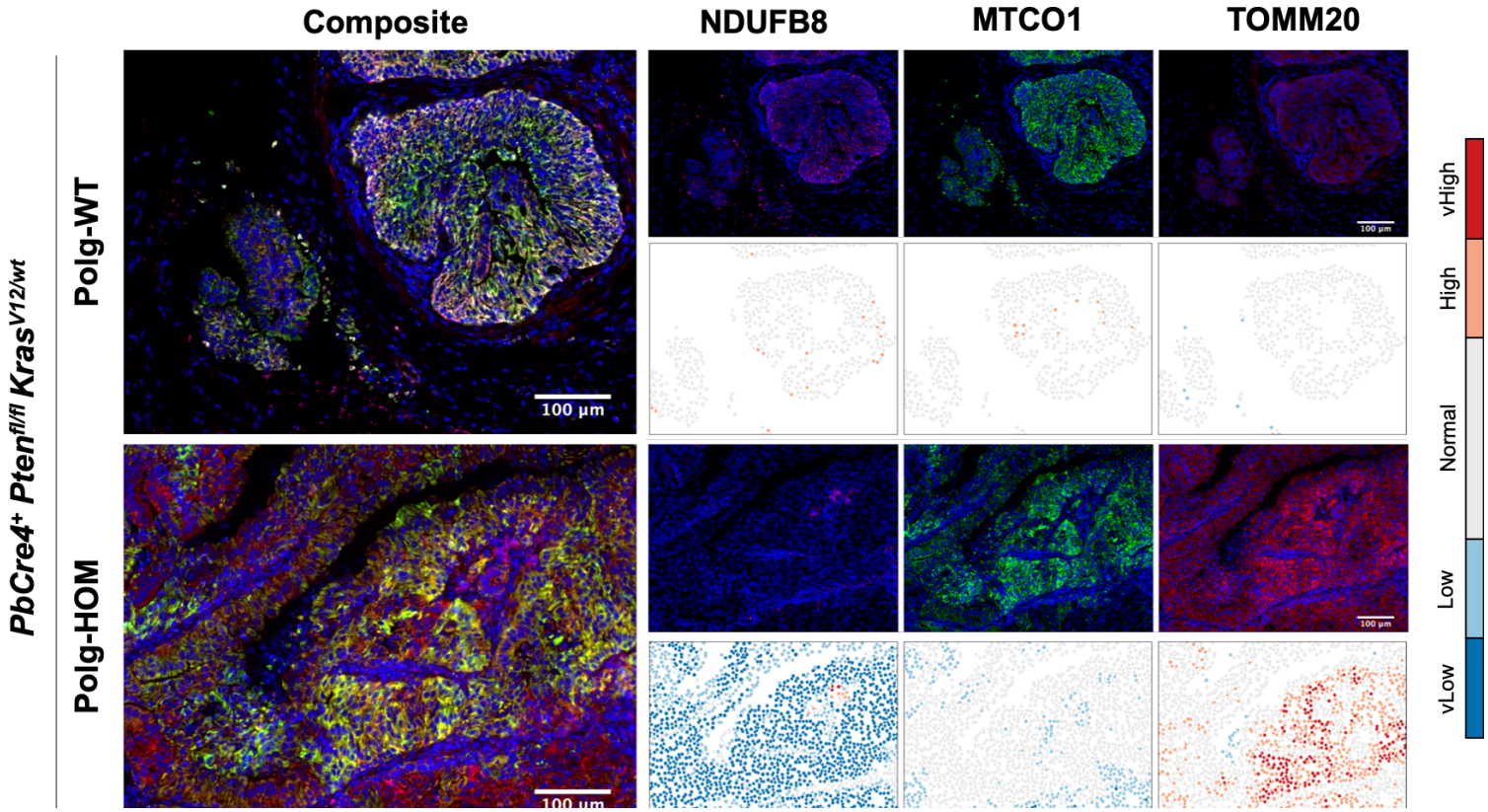

Figure 7-9: OXPHOS defects in mouse prostate tissue from the *PbCre4*$^{+}$*;Pten*$^{fl/fl}$*;Kras*$^{V12/+}$ cohort. Representative multiplex fluorescence images (left) with single channel images (top right panels) with colours representing *NDUFB8* (complex I, magenta), *MTCO1* (complex IV, green) and *TOMM20* (mitochondrial mass, red). Corresponding bottom panels represent pseudo-images (bottom right panels) demonstrating high frequency of epithelial cells with low complex I abundance in Polg-HOM prostate tissue. Across all pseudo-images, each point represents a single cell with colours denoting Z-scores for complexes I and IV categorised into very low (vLow, <-6 s.d.), low (-6 to -3 s.d.), normal (-3 to 3 s.d.), high (+3 to +6 s.d.), and very high (>+6 s.d.) with respect to age-matched Polg-WT tissue. Z-scores for mitochondrial mass used thresholds for -3, -2, +2, and +3 s.d. to categorise cells into very low, low, normal, high and very high groups. Colour scales are denoted on the right and scale bars represent 100 µm.

7.2.3.2 Activation of tumour signalling pathways

***Pi3k-Akt* signalling pathway:** Loss of *PTEN* results in activation of *Pi3k*/*Akt* signalling via phosphorylation of *Akt* at serine 473 and threonine 307, and downstream phosphorylation of ribosomal protein S6 (*RpS6*) at serine 240-244 (Jamaspishvili *et al.*, 2018). As expected, mice with proficient *Pten* (ie lacking the *PbCre4*$^{+}$*;Pten*$^{fl/fl}$ genotype) had normal *Pten*, low phosphorylated-*Akt*^{S473} (p-*Akt*^{S473}) and low phosphorylated-*RpS6*$^{S240\text{-}244}$ (p-*RpS6*$^{S240\text{-}244}$) protein expression, across both Polg-WT and Polg-HOM genotypes (**Figure 7-10**). Conversely, Pten-deficient mice across all tumourigenic backgrounds (ie *PbCre4*$^{+}$*;Pten*$^{fl/fl}$, *PbCre4*$^{+}$*;Pten*$^{fl/fl}$*;Kras*$^{V12/+}$, *PbCre4*$^{+}$*;Pten*$^{fl/fl}$*;p53*$^{mut/+}$ genotypes) demonstated weak epithelial *Pten* expression, with associated increased p-*Akt*^{S473} and p-*RpS6*$^{S240\text{-}244}$ expression across both Polg-WT and Polg-HOM genotypes (**Figure 7-11**, **Figure 7-12**). These data thus confirm *Pten*-loss with subsequent activation of the *Pi3k*/*Akt* signalling pathway at the protein level in mouse models described in this chapter.

Notably, *in vivo* activation of *Pi3k*/*Akt* signalling was not observed in Polg-HOM mouse prostate tissue from the genetic background cohort. This finding is in contrast to previous *in vitro* data based upon cybrid experiments (Pelicano *et al.*, 2006) and mtDNA depleted cell lines (Moro *et al.*, 2009) where mitochondrial defects were reported to lead to activation of this pathway.

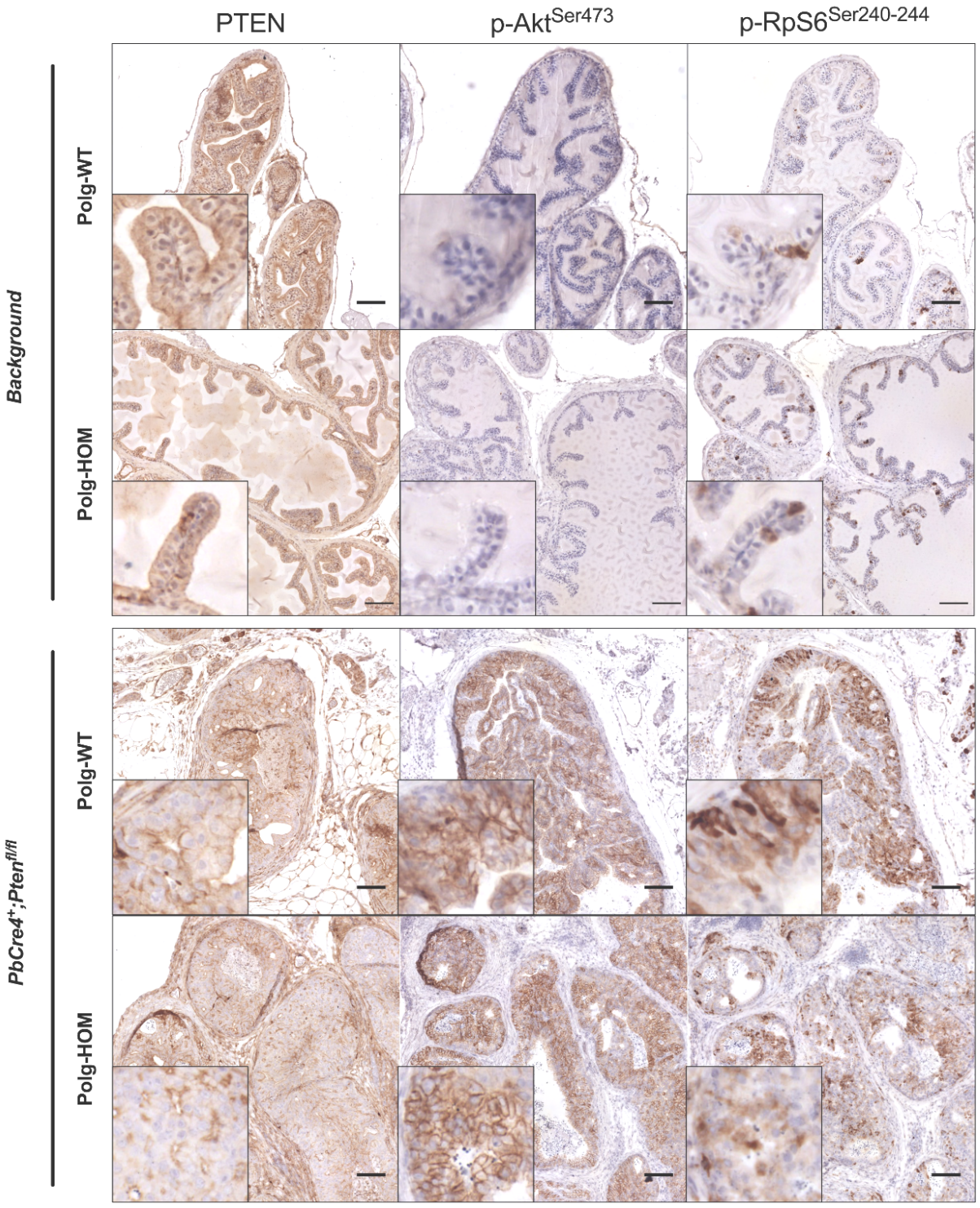

Figure 7-10: Representative immunohistochemical validation of *PTEN* status and downstream effectors of the *Pi3k/Akt* signalling pathway in the genetic background and *PbCre4*$^{+}$*;Pten*$^{fl/fl}$ cohorts. Cytoplasmic *Pten* expression is preserved in epithelial cells in the genetic background cohort, but reduced in the *PbCre4*$^{+}$*;Pten*$^{fl/fl}$ cohort. *Pten* expression is observed in stromal cells across both cohorts. *Pten* loss is associated with phosphorylation of downstream effectors *Akt*^{Ser473} and *RpS6*$^{Ser240-244}$. Higher magnification of representative regions are highlighted within the inset. Scale bars represent 100 µm.

MAPK signalling pathway: Over-expression of the mutated *Kras*^{V12} allele results in the activation of both the *MAPK* signalling pathway and concurrent activation of the *Pi3k*/*Akt* signalling pathway. Activated *MAPK* signalling results in downstream phosphorylation of *MEK1/2* and *ERK1/2* (or *MAPK*). Notably, activated Kras also leads to Pi3k/Akt pathway activation (Castellano and Downward, 2011). Collaborators have previously demonstrated activation of MAPK signalling in the *PbCre4*$^{+}$*;Pten*$^{fl/fl}$*;Kras*$^{V12/+}$ mouse prostate tissue used in this study (Jefferies *et al.*, 2017). Similar findings are reported in prostate tissue from mice with a mutated *Kras*^{G12D} allele in a *PbCre4*$^{+}$*;Pten*$^{fl/fl}$ model (Mulholland *et al.*, 2012). However, the impact of Polg-HOM mediated mitochondrial dysfunction of *MAPK* signalling is currently unknown and merits further evaluation.

P53 signalling pathway: Loss of *Pten* results in *p53*-mediated senescence which restricts prostate tumour progression in *PbCre4*$^{+}$*;Pten*$^{fl/fl}$ mice. Deletion of *p53* results in loss of *p53* protein expression and thereby removes the senescence block and facilitates progression to lethality (Chen *et al.*, 2005). At the time of writing, the impact of Polg-HOM mediated mitochondrial dysfunction on *p53* signalling in *PbCre4*$^{+}$*;Pten*$^{fl/fl}$*;p53*$^{mut/+}$ mice had not been evaluated, and merits further investigation.

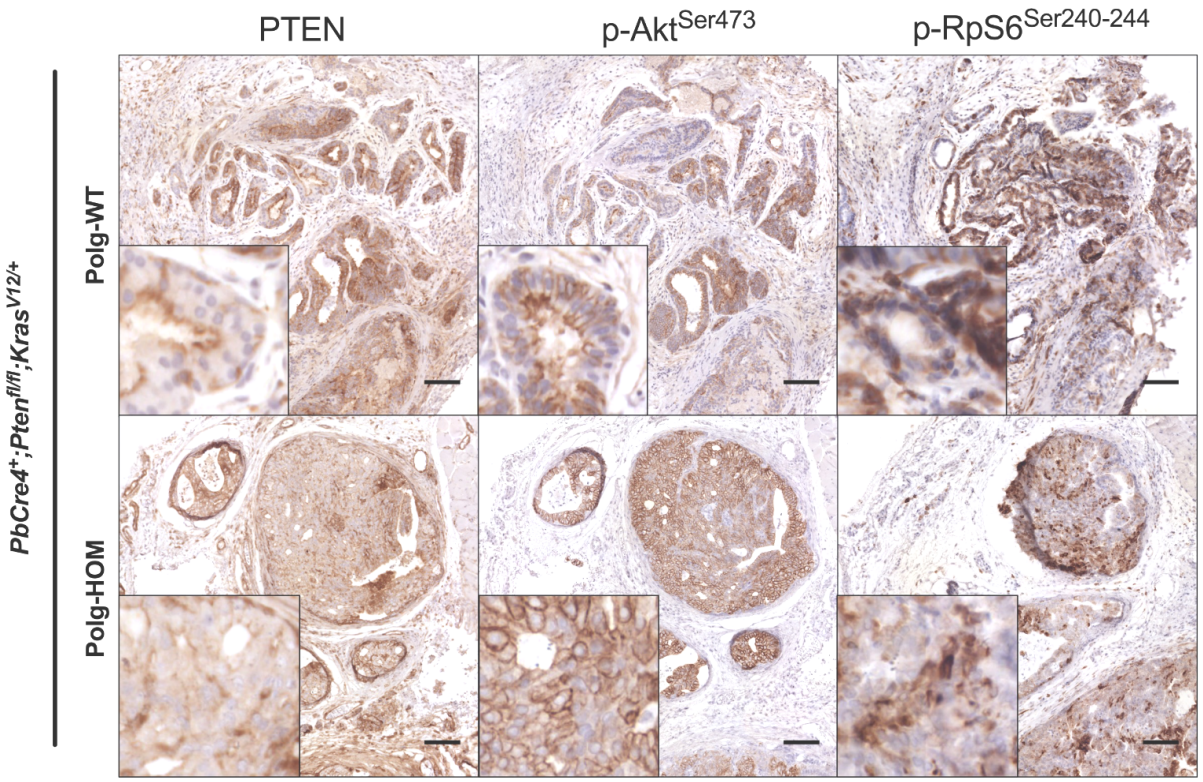

Figure 7-11: Representative immunohistochemical validation of *PTEN* status and downstream effectors of the *Pi3k/Akt* signalling pathway in the *PbCre4*$^{+}$*;Pten*$^{fl/fl}$*;Kras*$^{V12/+}$cohort. Higher magnification images of representative regions are highlighted within the inset. Scale bars represent 100 µm.

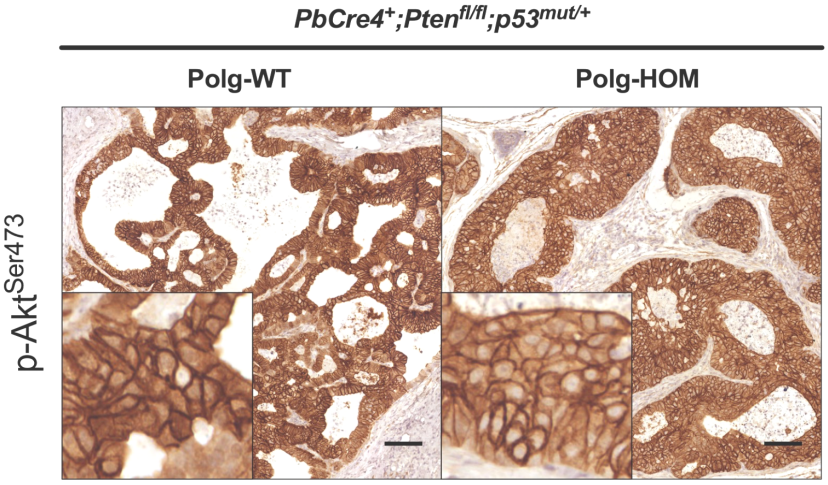

Figure 7-12: Representative immunohistochemical validation of *PTEN* status and downstream effectors of the *Pi3k/Akt* signalling pathway in the *PbCre4*$^{+}$*;Pten*$^{fl/fl}$*;p53*$^{mut/+}$cohort. Higher magnification images of representative regions are highlighted within the inset. Scale bars represent 100 µm.

7.2.4 Survival outcomes

7.2.4.1 Double mutants

Neither *Pten* haploinsufficiency nor biallelic *Pten*-loss influenced lifespan in Polg-HOM mice (**Figure 7-13A**). Reduced lifespan in Polg-HOM mice with either wild-type PTEN, monoallelic or biallelic PTEN loss was predominantly associated with severe age-related systemic phenotypes, rather than prostate tumour-related clinical endpoints. Conversely, lifespan of mice with a *PbCre4*$^{+}$*;Pten*$^{fl/fl}$ tumourigenic background was significantly shorter in Polg-HOM vs Polg-HET genotypes (p=2x10^{-8}), and Polg-HET vs Polg-WT genotypes (p=4x10^{-8}, **Figure 7-13B**), suggesting that increasing burden of mitochondrial defects contributed to reduced lifespan. Thus, these data do not demonstrate either an adverse or a favourable impact of mitochondrial defects on cancer-related survival.

7.2.4.2 Triple mutants

Two exploratory cohorts of triple mutant mice were generated to assess the impact of mitochondrial dysfunction over a more aggressive tumourigenic background. Notably, penile warts were observed in a small number of *PbCre4*$^{+}$*;Pten*$^{fl/fl}$*;Kras*$^{V12/+}$ mice, reflecting leaky *PbCre4*$^{+}$-mediated recombination, some of which were humanely euthanised when penile warts exceeded 5mm in size, as per local animal husbandry practices and project license. Only mice culled due to development of clinical signs of prostate cancer or age-related end points were therefore used for survival analyses.

Amongst the *PbCre4*$^{+}$*;Pten*$^{fl/fl}$*;Kras*$^{V12/+}$ colony (**Figure 7-14A**), Polg-WT and Polg-HOM mice had comparable median survival (Polg-WT: 201 days vs Polg-HOM: 199 days, p=0.260) whereas Polg-HET mice demonstrated a non-significantly reduced median lifespan of 161 days (vs Polg-WT, p=0.05; vs Polg-HOM, p=0.610). These data suggest that both Polg-WT and Polg-HOM mice in this cohort succumbed to *PbCre4*$^{+}$*;Pten*$^{fl/fl}$*;Kras*$^{V12/+}$ prostate tumour related lethality at comparable time points, rather than due to accelerated ageing-related pathologies.

Amongst the *PbCre4*$^{+}$*;Pten*$^{fl/fl}$*;p53*$^{mut/+}$ colony (**Figure 7-14B**), Polg-HOM mice had reduced survival (218.5 days) as compared to both Polg-WT mice (271 days, p=8x10^{-5}) and Polg-HET mice (275 days, p=0.001). These data reflect early mortality due to advanced age-related systemic phenotypes, rather than prostate tumour-related endpoints.

Thus, these data were again unable to ascertain the impact of *Polg* mediated OXPHOS defects on cancer-related survival outcomes in more aggressive tumour models due to early development of clinically significant age-related phenotypes. Furthermore, robust statistical analyses are limited by the small sample size of triple mutant mice with Polg-HOM genotypes.

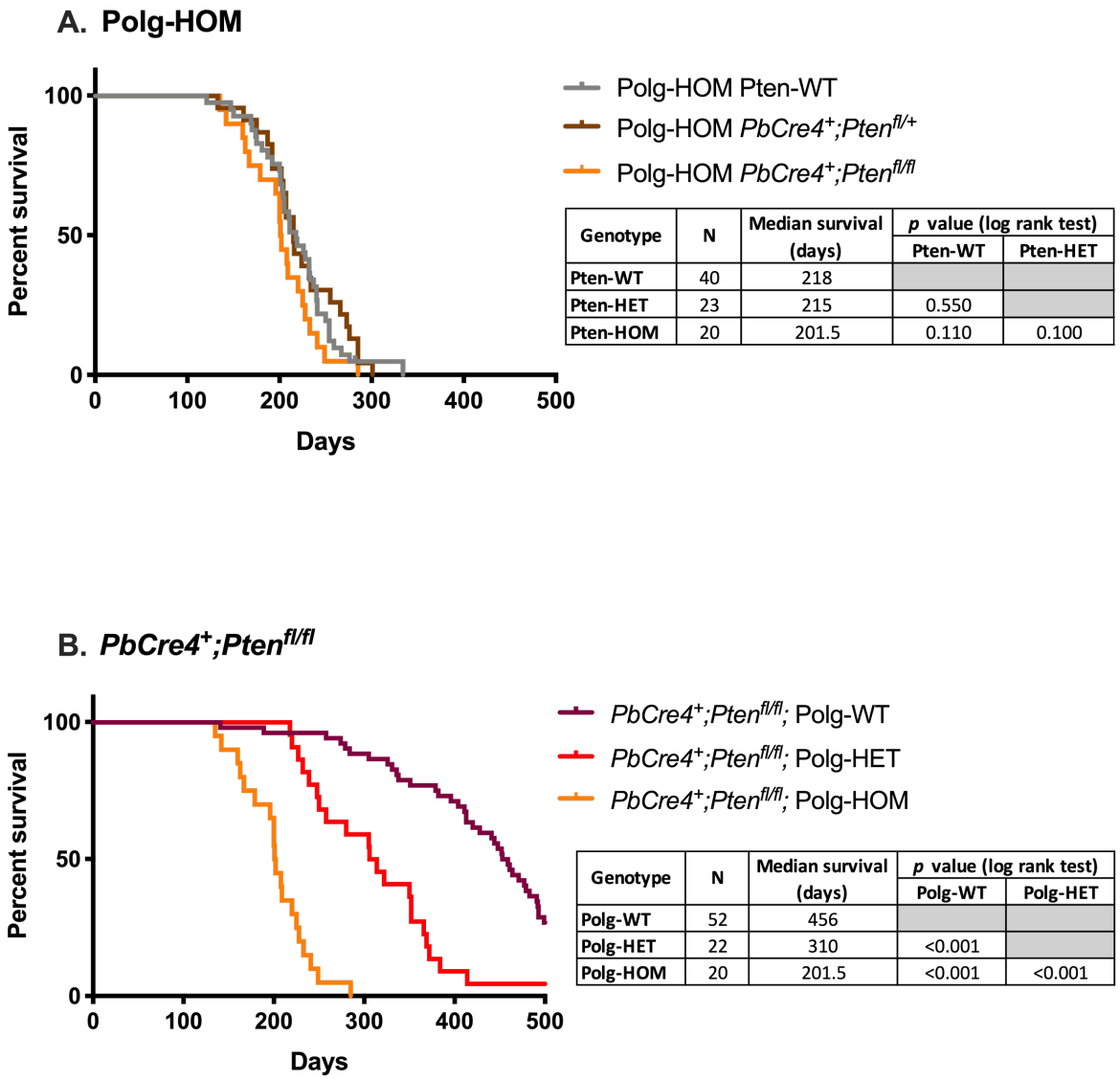

Genotype	N	Median survival (days)	*p* value (log rank test)	
			Pten-WT	Pten-HET
Pten-WT	40	218		
Pten-HET	23	215	0.550	
Pten-HOM	20	201.5	0.110	0.100

Genotype	N	Median survival (days)	*p* value (log rank test)	
			Polg-WT	Polg-HET
Polg-WT	52	456		
Polg-HET	22	310	<0.001	
Polg-HOM	20	201.5	<0.001	<0.001

Figure 7-13: Survival outcomes of (A) Polg-HOM and (B) *PbCre4*$^{+}$*;Pten*$^{fl/fl}$ mouse cohorts. Inset table reports sample size, median survival, and results of the log rank test for within-cohort comparisons.

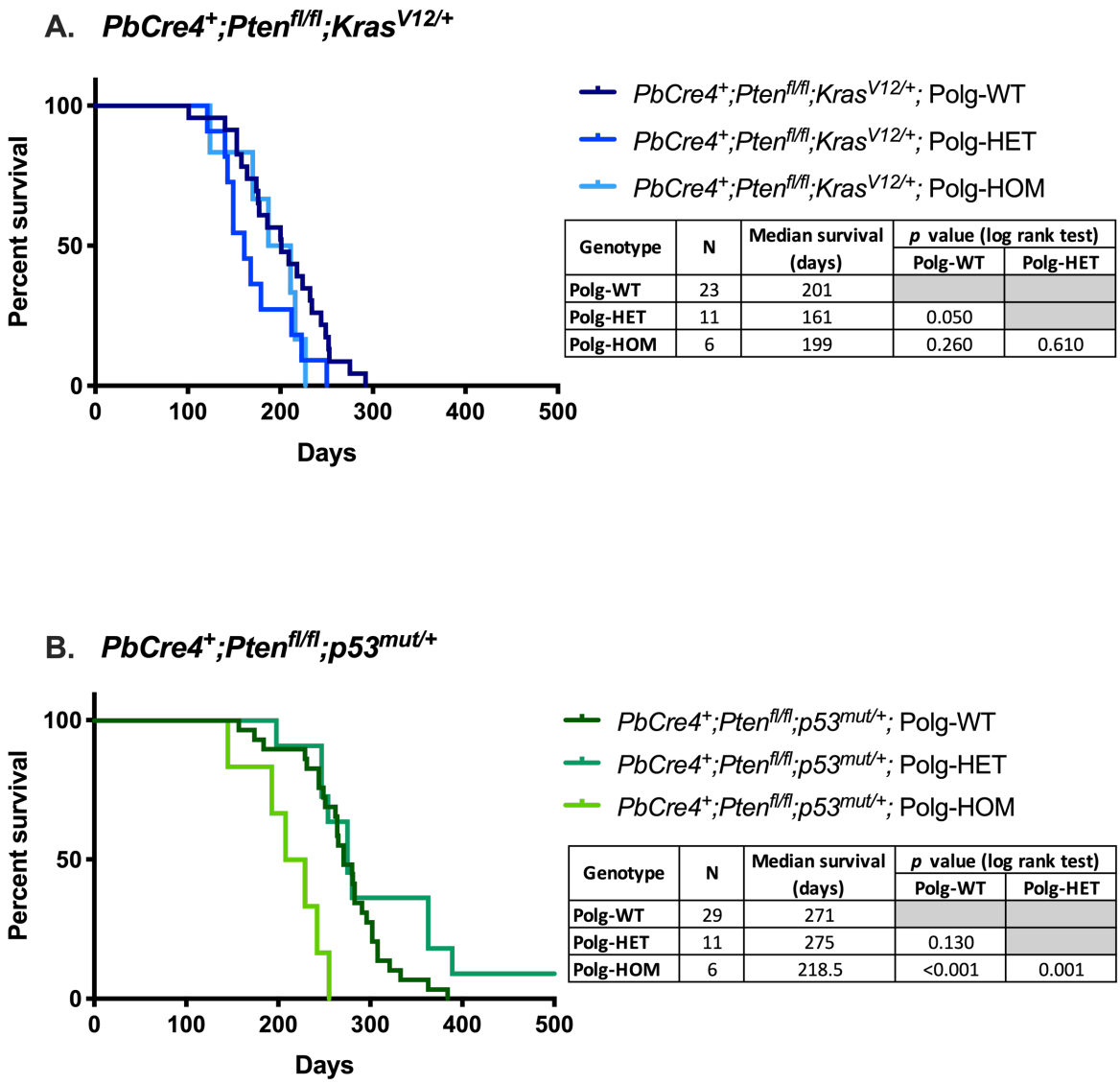

Genotype	N	Median survival (days)	*p* value (log rank test)	
			Polg-WT	Polg-HET
Polg-WT	23	201		
Polg-HET	11	161	0.050	
Polg-HOM	6	199	0.260	0.610

Genotype	N	Median survival (days)	*p* value (log rank test)	
			Polg-WT	Polg-HET
Polg-WT	29	271		
Polg-HET	11	275	0.130	
Polg-HOM	6	218.5	<0.001	0.001

Figure 7-14: Survival outcomes of exploratory mouse cohorts. (A) *PbCre4*$^{+}$*;Pten*$^{fl/fl}$*;Kras*$^{V12/+}$ and **(B)** *PbCre4*$^{+}$*;Pten*$^{fl/f}$*;p53*$^{mut/+}$ genetic backgrounds. Inset table reports sample size, median survival, and results of the log rank test for within-cohort comparisons.

7.2.5 Morphometric analysis

7.2.5.1 Body weight of Polg-HOM mice decreases across all tumourigenic backgrounds

Since Polg-HOM mice developed severe age-related phenotypes leading to early death, an earlier time point of median 200 days was selected to evaluate age-matched cohorts. At this age, Polg-HOM mice had lower body weight, as compared to age-matched Polg-WT controls across all cohorts (**Figure 7-15**). These findings are in keeping with results in section 6.2.2 based upon the Polg mouse colony at Newcastle, and previously published data (Trifunovic *et al.*, 2004; Kujoth *et al.*, 2005).

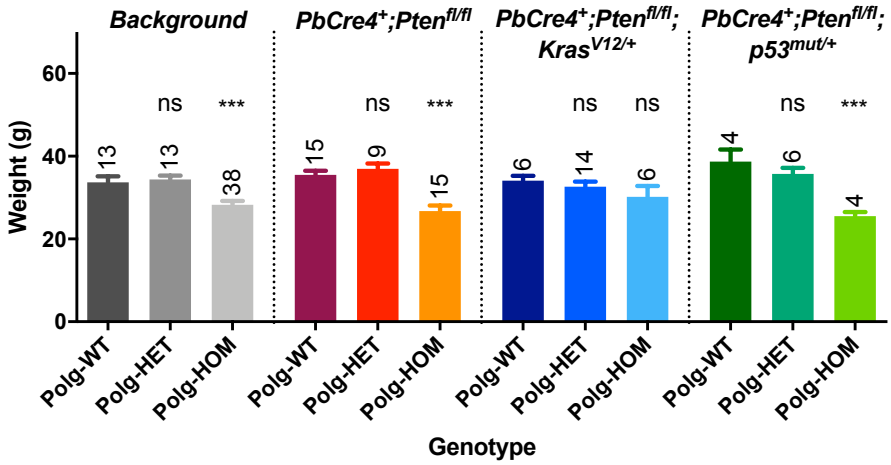

Figure 7-15: Body weight of mice aged 200 days in (A) genetic background, (B) *PbCre4⁺;Ptenᶠˡ/ᶠˡ*, (C) *PbCre4⁺;Ptenᶠˡ/ᶠˡ;Krasᵛ¹²/⁺* and (D) *PbCre4⁺;Ptenᶠˡ/ᶠ;p53ᵐᵘᵗ/⁺* mouse cohorts. Results of one-way ANOVA, in comparison to within-cohort Polg-WT control group, are reported with ***, **, *, and 'ns' denoting $p<0.001$, $p<0.01$, $p<0.05$, and not significant, respectively. Number of mice reported in each cohort are reported above each bar plot. Error bars represent standard error of measurement.

7.2.5.2 Polg-HOM reduces prostate tumour weight in the *PbCre4⁺;Ptenᶠˡ/ᶠˡ;p53ᵐᵘᵗ/⁺* model

PbCre4⁺;Ptenᶠˡ/ᶠˡ;p53ᵐᵘᵗ/⁺ mice had higher tumour weight as compared to all other tumourigenic backgrounds ($p<0.0001$, one-way ANOVA test). Mouse prostate weight was comparable across all Polg genotypes in all cohorts, except the *PbCre4⁺;Ptenᶠˡ/ᶠˡ;p53ᵐᵘᵗ/⁺* cohort where prostate tumours from both Polg-HET (7.3% vs Polg-WT 11.7%, Δ -4.4%, $p=0.005$) and Polg-HOM mice (4.2% vs Polg-WT 11.8%, Δ -7.6%, $p=5\times10^{-6}$) weighed significantly less as compared to Polg-WT mouse tumours.

These data suggest that mitochondrial dysfunction in Polg-HOM mice from the *PbCre4*$^{+}$;*Pten*$^{fl/fl}$;*p53*$^{mut/+}$ may suppress macroscopic prostate tumour growth. Of note, due to missing body weight data in the Polg-WT cohort, median age-matched body weight was used to normalise prostate weight in both *PbCre4*$^{+}$;*Pten*$^{fl/fl}$;*p53*$^{mut/+}$ and *PbCre4*$^{+}$;*Pten*$^{fl/fl}$;*Kras*$^{V12/+}$ cohorts, which may potentially bias these results. However, raw prostate weight was also lower in Polg-HOM mice, as compared to Polg-WT mice, in the *PbCre4*$^{+}$;*Pten*$^{fl/fl}$;*p53*$^{mut/+}$ cohort (median weight in Polg-HOM: 0.7g vs Polg WT: 3.4g, Δ -2.7g, p=0.017). Raw prostate weights were comparable across all three genotypes in the two remaining tumourigenic cohorts (see data in Appendix D, **Figure D-2**).

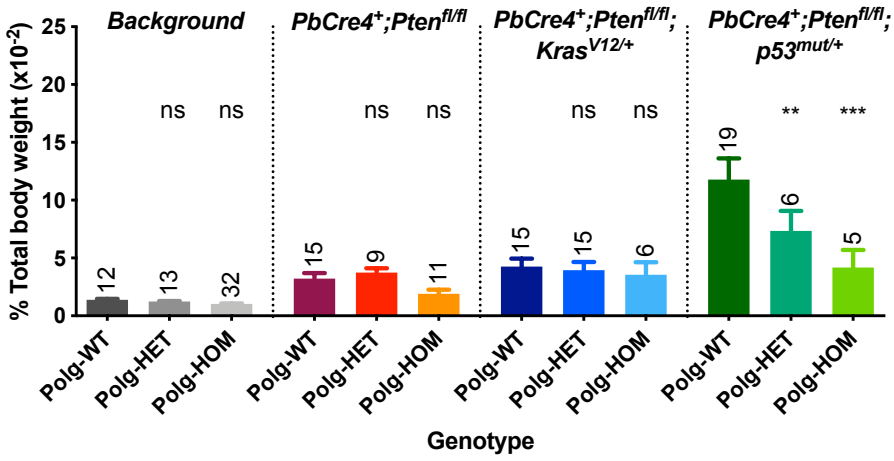

Figure 7-16: Normalised prostate weight of mice aged 200 days in (A) genetic background, (B) *PbCre4*$^{+}$;*Pten*$^{fl/fl}$, (C) *PbCre4*$^{+}$;*Pten*$^{fl/fl}$;*Kras*$^{V12/+}$ and (D) *PbCre4*$^{+}$;*Pten*$^{fl/f}$;*p53*$^{mut/+}$ mouse cohorts. Prostate weights were normalised to the body weight by calculating proportion of total body weight. Number of mice reported in each cohort are reported above each bar plot. Note: where body weight data were unavailable in the two triple mutant mouse cohorts, prostate weight was normalised using body weight data from genotype-specific age-matched mice. Error bars represent standard error of measurement. Results of one-way ANOVA, in comparison to within-cohort Polg-WT control group, are reported with ***, **, *, and 'ns' denoting p<0.001, p<0.01, p<0.05, and not significant, respectively.

7.2.6 Mitochondrial OXPHOS defects suppress histological prostate cancer progression

Mouse prostate tissue histopathology was reviewed by Dr Boris Shorning (Cardiff University) blinded to the genotype and according to the criteria detailed below, based upon consensus guidelines (Shappell *et al.*, 2004; Ittmann *et al.*, 2013). Each mouse was categorised into one of the following histopathological categories based upon highest grade disease focus identified within the H&E stained prostate tissue.

- **Epithelial hyperplasia** is a non-neoplastic increase in the number of epithelial cells. It may range from simple (single layer of epithelial cells) to more complex architecture, including tufting, papillary or cribriform patterns. Minimal, but not marked, nuclear atypia may also be observed.
- **Prostate epithelial neoplasia (PIN)** is a neoplastic proliferation of atypical epithelial cells within pre-existing glandular spaces, but without frank invasion. mPIN is often associated with stratified epithelial cells with marked nuclear atypia and tufting, micropapillary, or cribriform growth.
- **Micro-invasive adenocarcinoma** is a neoplastic proliferation characterised by the penetration of cytologically atypical malignant cells through the basement membrane of PIN-involved glands into the thin rim of surrounding stroma. This may be associated with focally desmoplastic (or 'reactive') stroma, adjacent to the invasive focus, rather than being present uniformly throughout the prostate.
- **Invasive adenocarcinoma** is a malignant epithelial neoplasm characterised by destructive growth in prostate parenchyma, with increased size or extent of the invasive focus, as compared to micro-invasive adenocarcinoma. This includes extension into widened stroma, connective tissue or peri-prostatic fat, and focus size greater than 1mm. These lesions may be associated with metastatic spread, due to the presence of lymphatics, vessels and nerves in adjacent stroma. In order to simplify grading, both micro-invasive and invasive adenocarcinoma have been combined for quantitiative analyses in this chapter.
- **Sarcomatoid carcinoma** is a malignant neoplasm characterised by the presence of highly atypical spindle cells admixed with, or adjacent to, invasive adenocarcinoma, further supported by markers of epithelial-to-mesenchymal transition.

Representative images are presented in **Figure 7-17** and **Figure 7-18**.

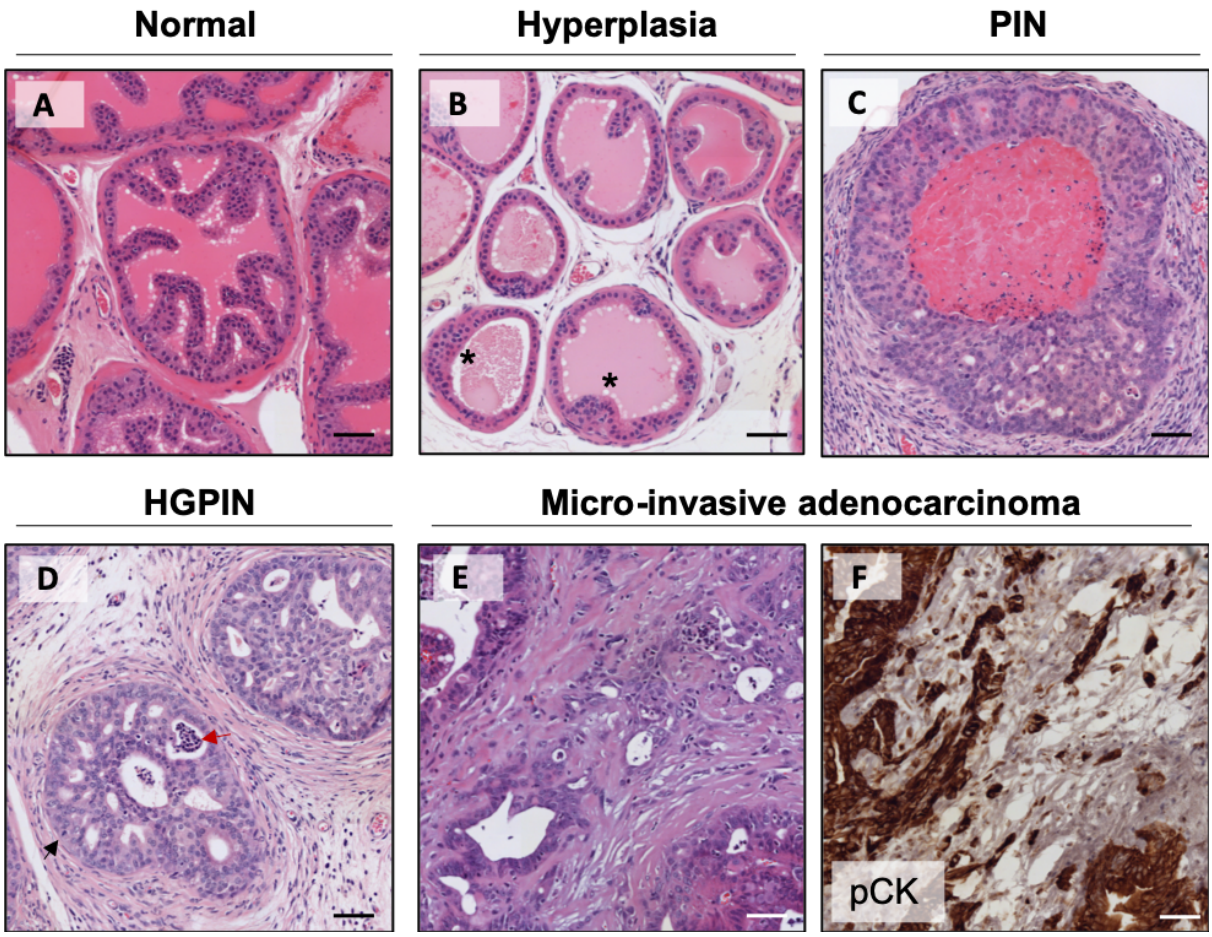

Figure 7-17: Representative prostate histopathological disease stages in development of prostate adenocarcinoma. Images of prostate tissue from **(A)** normal, **(B)** epithelial hyperplasia (asterisk highlights tufting epithelium), **(C)** prostate intra-epithelial neoplasia, PIN, with characteristic cribriform pattern which progresses to **(D)** high-grade PIN, HGPIN, filling the gland lumen with nuclear atypia (black arrow) and apoptotic cell bodies (red arrow). Prostate tissue in images A-E was stained with haematoxylin & eosin. **(E)** Micro-invasive adenocarcinoma characterised by invasive individual or small groups of epithelial cells upon pan-cytokeratin immunohistochemistry **(F)**. Scale bars represent 100 µm.

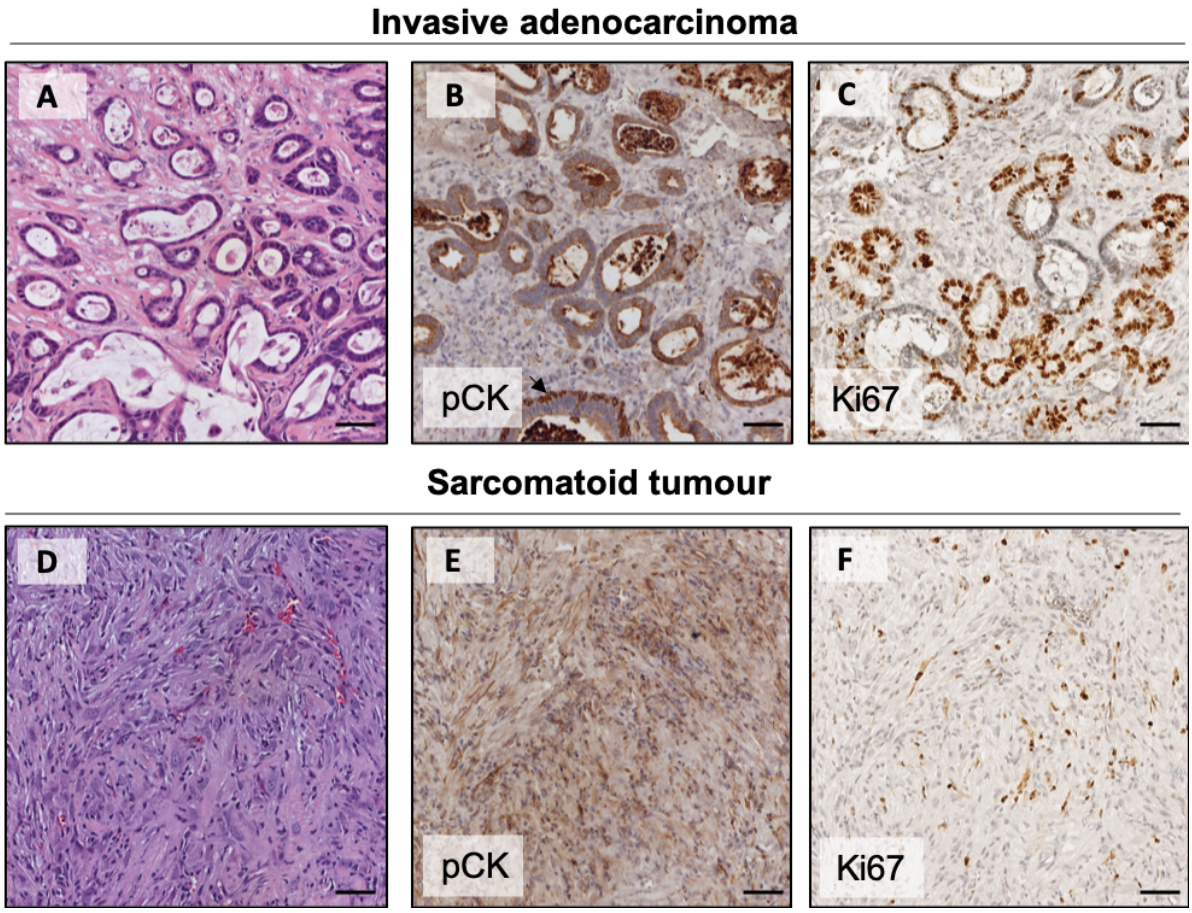

Figure 7-18: Representative images of (A-C) invasive adenocarcinoma and (D-F) sarcomatoid tumour. Haematoxylin and eosin staining (A, D), pan-cytokeratin (B, E) and Ki-67 (C, F) immunohistochemical staining of prostate tissue demonstrates gradual loss of pan-cytokeratin staining during epithelial-to-mesenchymal transition in progression to a sarcomatoid tumour. Ki-67 staining (C, F) demonstrates increased proliferation of tumour cells. Scale bars represent 100 µm.

Results of histopathological evaluation of mouse prostate tissue are summarised in **Figure 7-19** with a breakdown of results reported in appendix D (iii). As previously noted in Chapter 6, hyperplastic lesions were noted in only 2 of 27 Polg-HOM mice, with no evidence of tumour initiation observed over the baseline genetic background. Amongst *PbCre4*$^{+}$*;Pten*$^{fl/fl}$ mice, invasive adenocarcinoma was observed at comparable frequency across all three Polg genotypes (Polg-WT: 60%, Polg-HET: 22%, Polg-HOM: 36%, p=0.25, Chi-square test for trend), implying mitochondrial dysfunction does not impact histopathological progression in this model.

Sarcomatoid differentiation of PCa is a marker of progression to advanced disease, and rarely observed in human PCa (Hansel and Epstein, 2006). Increasing dose of mutant Polg allele was associated with a lower frequency of invasive or sarcomatoid histology in *PbCre4*$^{+}$*;Pten*$^{fl/fl}$*;p53*$^{mut/+}$ background (Polg-WT: 96%, 27/28 mice; Polg-HET: 57%, 4/7 mice; Polg-HOM: 20%, 1/5 mice; p=1.9x10^{-5}, Chi-square test for trend) but not in mice with either *PbCre4*$^{+}$*;Pten*$^{fl/fl}$ (Polg-WT: 60%, Polg-HET: 22%, Polg-HOM: 36%, p=0.19) or *PbCre4*$^{+}$*;Pten*$^{fl/fl}$*;Kras*$^{V12/+}$ background (Polg-WT: 75%, Polg-HET: 83%, Polg-HOM: 80%, p=0.78).

These data suggest that mitochondrial dysfunction suppresses histopathology tumour progression in *PbCre4*$^{+}$*;Pten*$^{fl/fl}$*;p53*$^{mut/+}$ background, with no measurable histopathological change in *PbCre4*$^{+}$*;Pten*$^{fl/fl}$ and *PbCre4*$^{+}$*;Pten*$^{fl/fl}$*;Kras*$^{V12/+}$ backgrounds.

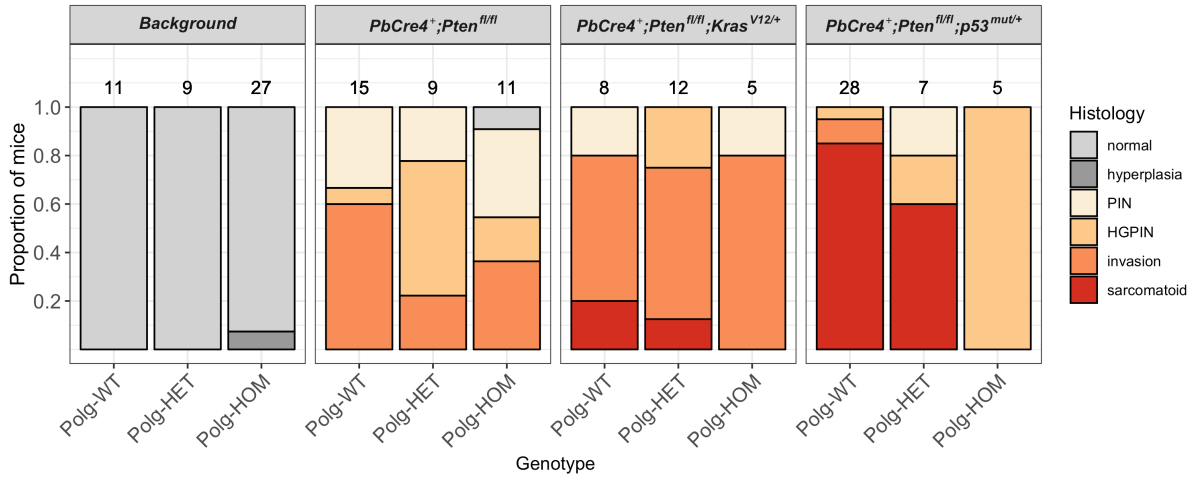

Figure 7-19: Histochemical evaluation of mouse prostates at 200 days of age. The highest reported histopathological grade is reported as a proportion of total mice in each cohort. Total number of mice included in each cohort are reported above each bar plot.

7.2.7 Mitochondrial dysfunction influences cell cycle kinetics in tumourigenic models

Immunohistochemical evaluation of cell cycle kinetics was performed on at least 3 mice from each genotype targeting cell proliferation marker Ki67 and apoptotic marker cleaved caspase 3 (CC3). Percentage of marker positive cells was determined in epithelial regions using QuPath software and compared across Polg-WT and Polg-HOM genotypes using the one-way ANOVA test.

Proliferation: Consistent with previous reports (Chen *et al.*, 2005; Jefferies *et al.*, 2017), double mutant tumourigenic mice were noted to have increased cell proliferation, as compared to *PbCre4*$^{+}$*;Pten*$^{fl/fl}$ mice (**Figure 7-20**). Reduced cell proliferation observed in the Polg-HOM mice at Newcastle (refer to section 6.2.7.6), was not reproduced in the Cardiff cohort which may be due to the relatively reduced lifespan of the Polg-HOM mouse colony at Cardiff. . However, Polg-HOM mice across all tumourigenic backgrounds were noted to have a lower frequency of Ki67^{+} proliferative cells, as compared to age-matched Polg-WT control mice. The greatest magnitude of difference in frequency of Ki67^{+} proliferative cells was noted in *PbCre4*$^{+}$*;Pten*$^{fl/fl}$*;p53*$^{mut/+}$ mice (Polg-WT 23.1% vs Polg-HOM 12.6%, Δ 10.5%, p=4 x 10^{-8}), whereas the smallest magnitude of difference was noted in *PbCre4*$^{+}$*;Pten*$^{fl/fl}$ mice (Polg-WT 4.2% vs Polg-HOM 1.7%, Δ 2.5%, p=0.04, one-way ANOVA test).

Apoptosis: Consistent with previous reports (Ma *et al.*, 2005; Jefferies *et al.*, 2017), frequency of CC3^{+} apoptotic bodies was similar across wild-type, *PbCre4*$^{+}$*;Pten*$^{fl/fl}$, and *PbCre4*$^{+}$*;Pten*$^{fl/fl}$*;Kras*$^{V12/+}$ mice (**Figure 7-21**). However, contrary to previous reports (Chen *et al.*, 2005), *PbCre4*$^{+}$*;Pten*$^{fl/fl}$*;p53*$^{mut/+}$ mouse prostates were found to have a slight increase in CC3^{+} apoptotic bodies, as compared to *PbCre4*$^{+}$*;Pten*$^{fl/fl}$ mice. Increased frequency of CC3^{+} apoptotic bodies was observed in Polg-HOM mice in *PbCre4*$^{+}$*;Pten*$^{fl/fl}$ (Polg-WT: 0.09% vs Polg-HOM: 0.93%, Δ 0.84%, p=0.02) and *PbCre4*$^{+}$*;Pten*$^{fl/fl}$*;p53*$^{mut/+}$ colonies (Polg-WT: 1.8% vs Polg-HOM: 3.2%, Δ 1.4%, p=0.002), with no difference observed in the *PbCre4*$^{+}$*;Pten*$^{fl/fl}$*;Kras*$^{V12/+}$ colony (Polg-WT: 0.47% vs Polg-HOM: 0.44%, Δ -0.03%, p=0.94).

These data suggest that Polg-HOM mediated mitochondrial dysfunction results in decreased cell proliferation across all tumourigenic backgrounds studied, and increased apoptosis in both *PbCre4*$^{+}$*;Pten*$^{fl/fl}$ and *PbCre4*$^{+}$*;Pten*$^{fl/fl}$*;p53*$^{mut/+}$ mice.

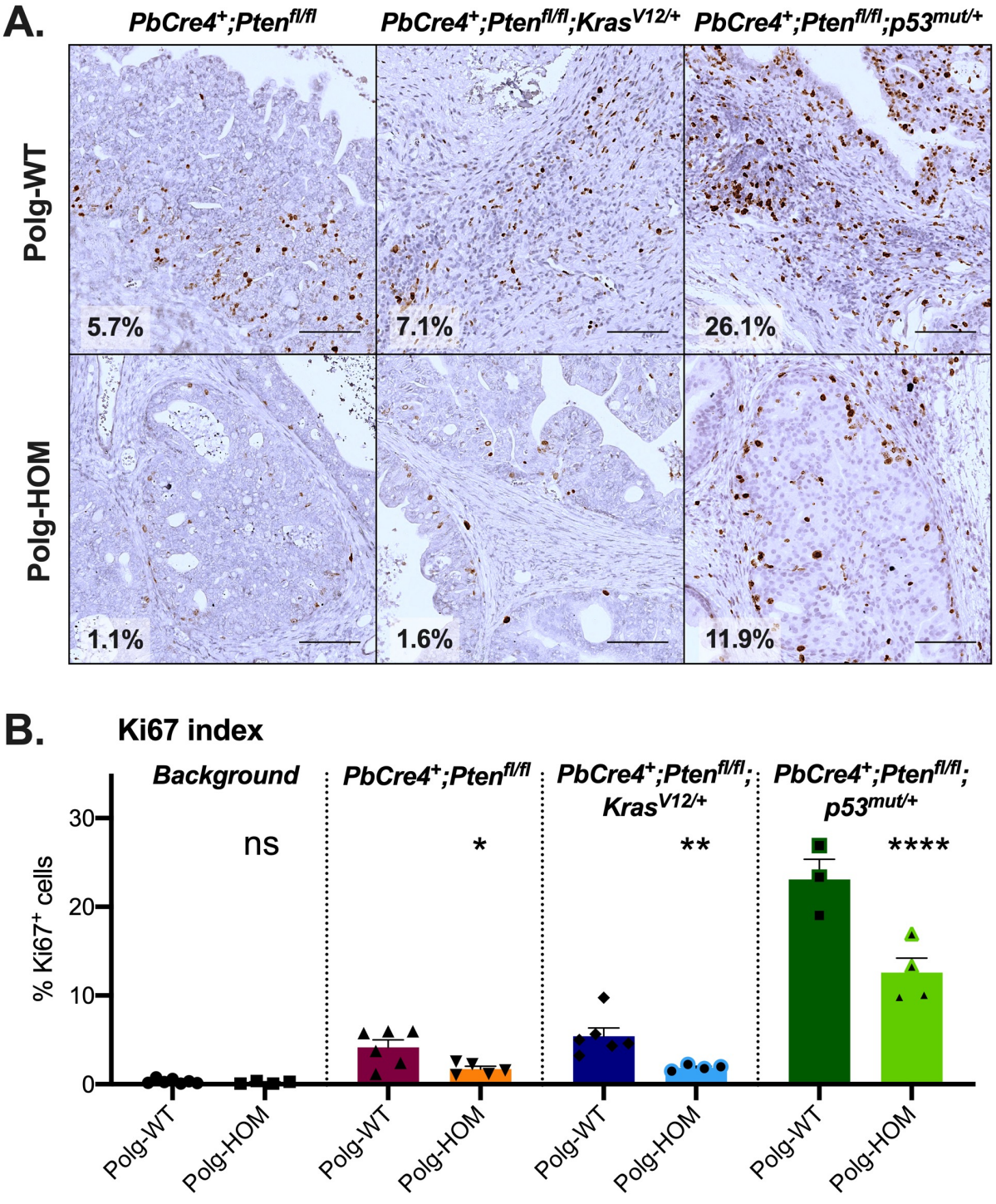

Figure 7-20: Immunohistochemistry for Ki67$^+$ proliferative cells in murine prostate tissue. **(A)** Representative IHC images from Polg-WT and Polg-HOM mouse prostates across three tumourigenic genetic backgrounds. Scale bar is 100µm. The number in the inset represents the percentage of Ki67$^+$ cells in the region of interest shown. **(B)** Quantified results. Each point represents an individual mouse. Data were included for a minimum of 3 mice per cohort. Error bars denote standard error of measurement. Results of one-way ANOVA, in comparison to within-cohort Polg-WT control group, are reported with ****, **, *, and 'ns' denoting p<0.0001, p<0.01, p<0.05, and not significant, respectively.

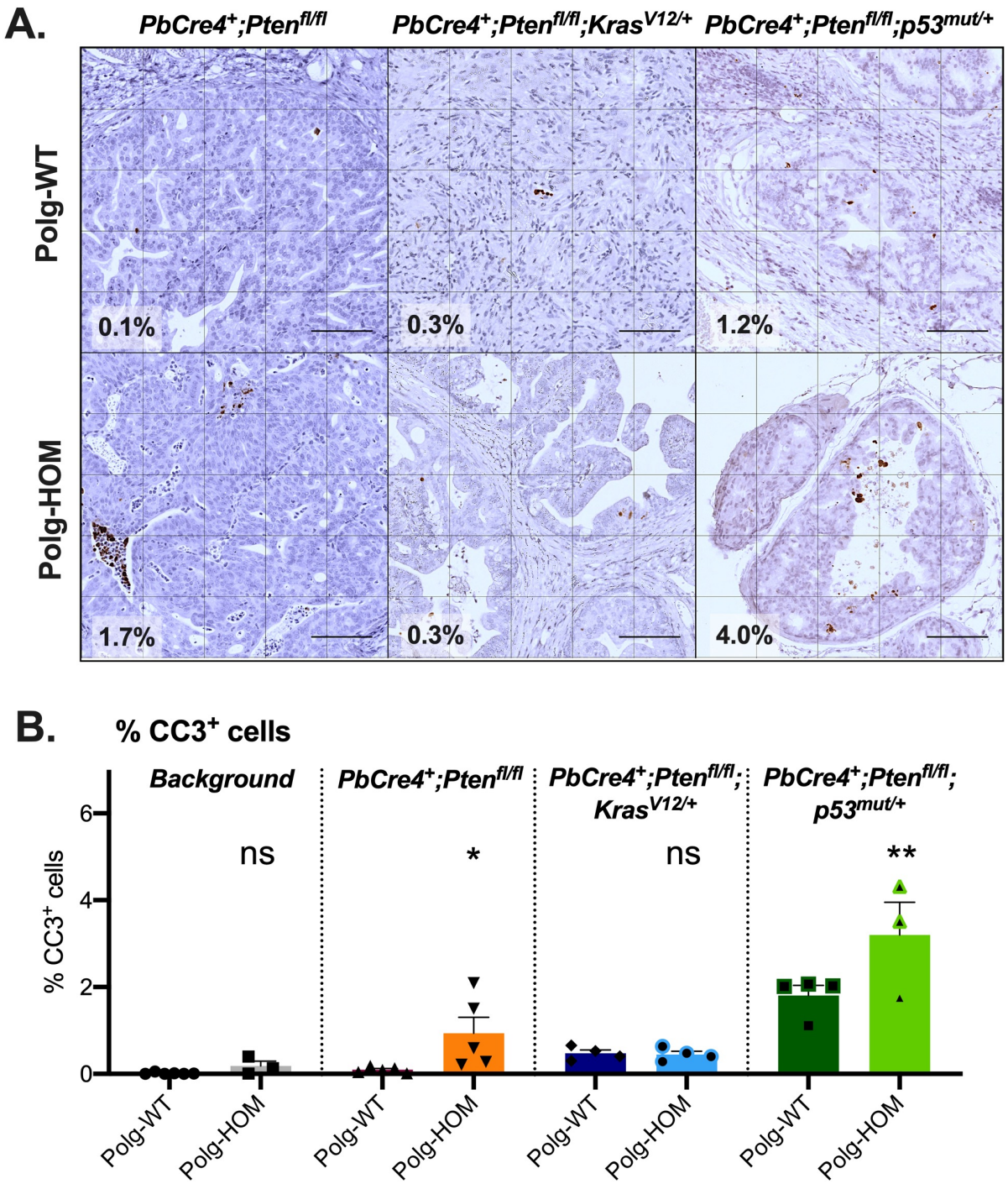

Figure 7-21: Immunohistochemistry for CC3⁺ apoptotic bodies in murine prostate tissue. (A) Representative IHC images from Polg-WT and Polg-HOM mouse prostates across three tumourigenic genetic backgrounds. Scale bar is 100µm. The number in the inset represents the percentage of CC3⁺ cells in the region of interest shown. **(B)** Quantified results. Each point represents an individual mouse. Data were included for a minimum of 3 mice per cohort. Error bars denote standard error of measurement. Results of one-way ANOVA, in comparison to within-cohort Polg-WT control group, are reported with **, *, and 'ns' denoting $p<0.01$, $p<0.05$, and not significant, respectively.

7.2.8 Mitochondrial dysfunction may suppress progression to metastasis

All harvested organs and lumbar lymph nodes were evaluated for histological evidence of metastases by H&E staining. Where metastatic lesions were suspected, confirmatory immunohistochemical staining for pan-cytokeratin (epithelial cell marker) and androgen receptor were performed.

In total, metastatic lesions were noted in regional lymph nodes from 7 mice, which included 5 mice from the *PbCre4*$^{+}$*;Pten*$^{fl/fl}$*;Kras*$^{V12/+}$ colony (four Polg-WT and one Polg-HOM), and two Polg-WT mouse from the *PbCre4*$^{+}$*;Pten*$^{fl/fl}$*;p53*$^{mut/+}$ colony (**Figure 7-22**). Notably one Polg-WT mouse from the *PbCre4*$^{+}$*;Pten*$^{fl/fl}$*;Kras*$^{V12/+}$ colony developed a lung metastatic lesion with variable androgen receptor expression and lacking pan-cytokeratin expression at a later time point at 253 days. It is suspected that the absence of pan-cytokeratin expression represents a feature of epithelial-to-mesenchymal transition, though further immunohistochemical characterisation of this sample for an expected increase in expression of mesenchymal markers and *Pten* loss is warranted. Furthermore, it is important to note that no gross bone metastases were observed, though sub-clinical micro-metastases may have been overlooked since bone marrow from femurs was not routinely flushed and subject to flow cytometry.

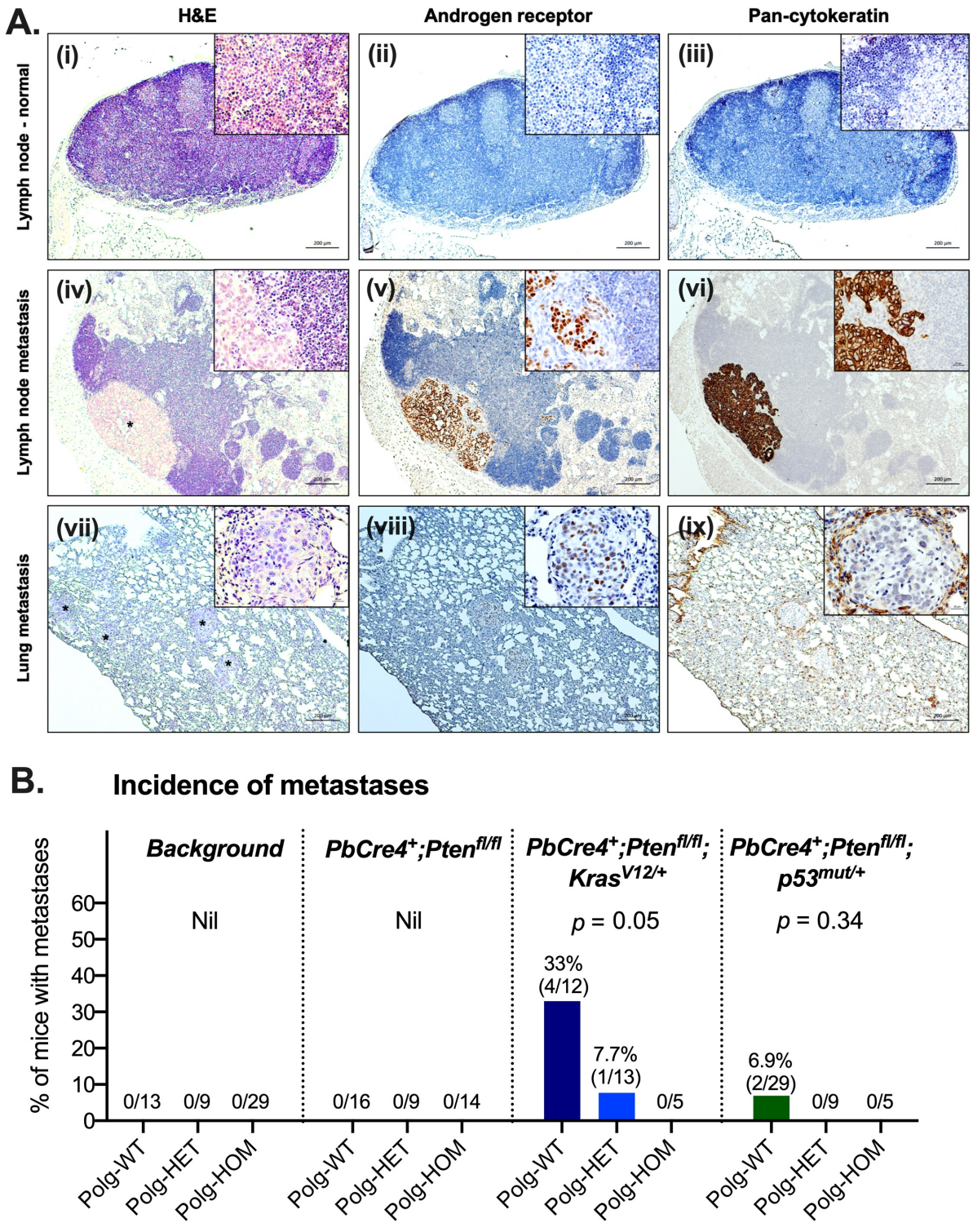

Figure 7-22: Metastatic lesions in tumourigenic mouse models. **(A)** Representative histopathological images of (i-iii) normal lymph node, (iv-vi) lymph node metastasis, and (vii) lung metastasis. H&E and immunohistochemical staining for androgen receptor and pan-cytokeratin to confirm presence of metastatic lesions. **(B)** Frequency of metastases in various genetic backgrounds, with annotations denoting number of mice with metastatic lesions and total number of mice per genotype. Results of Chi-square test for trend are reported as *p*-values.

7.3 Discussion

Since complex I defects were found to be most prognostic amongst patients with *PTEN*-deficient human prostate cancer in Chapter 5, this chapter aimed to evaluate the impact of OXPHOS defects on prostate cancer progression using prostate-specific *Pten*-deficient mouse models. Upregulation of glycolytic ATP production, but not OXPHOS production, was first confirmed using *in vitro* PCa models. Three novel *Pten*-deficient prostate cancer mouse models were successfully generated using the Polg-HOM mutator mouse model described in Chapter 6 and validated using immunohistochemical assays for OXPHOS defects and *Pten*-loss driven activation of the *Pi3k*/*Akt* signalling pathway. These models encompassed the spectrum of prostate carcinogenesis, including the development of invasive adenocarcinoma (*PbCre4*$^{+}$*;Pten*$^{fl/fl}$), progression to sarcomatoid features through epithelial-to-mesenchymal transition (*PbCre4*$^{+}$*;Pten*$^{fl/fl}$*;p53*$^{mut/+}$), and metastatic spread (*PbCre4*$^{+}$*;Pten*$^{fl/fl}$*;Kras*$^{V12/+}$). Lifespan across all three tumourigenic models with Polg-HOM genotype was limited by accelerated development of age-related phenotypes necessitating early euthanasia, and thereby limiting the assessment of cancer-related survival outcomes. Mouse tissue collected at earlier age-matched time points were therefore evaluated for markers of tumour progression.

7.3.1 Mitochondrial dysfunction suppresses tumour progression in *in vivo* models of advanced prostate cancer

Though mitochondrial dysfunction was initially hypothesised to accelerated prostate cancer progression, the evaluation of age-matched cohorts at 200 days of age noted reduced tumour weight, reduced histological progression to sarcomatoid disease, reduced cell proliferation and increased apoptosis in the *PbCre4*$^{+}$*;Pten*$^{fl/fl}$*;p53*$^{mut/+}$ cohort. However, tumour weight and histological grade remained unchanged in both *PbCre4*$^{+}$*;Pten*$^{fl/fl}$ and *PbCre4*$^{+}$*;Pten*$^{fl/fl}$*;Kras*$^{V12/+}$ cohorts, despite decrease in cell proliferation in both cohorts and a slight increase in apoptosis in *PbCre4*$^{+}$*;Pten*$^{fl/fl}$ prostate tissue. Metastatic disease progression was suppressed in both *PbCre4*$^{+}$*;Pten*$^{fl/fl}$*;Kras*$^{V12/+}$ and *PbCre4*$^{+}$*;Pten*$^{fl/fl}$*;p53*$^{mut/+}$ cohorts with metastatic lesions not observed in Polg-HOM mice in either cohort. Results are summarised in **Table 7-2**.

Polg-HOM vs WT	*PbCre4^{+};Pten$^{fl/fl}$*	*PbCre4^{+};Pten$^{fl/fl}$; Kras$^{V12/+}$*	*PbCre4^{+};Pten$^{fl/fl}$; p53$^{mut/+}$*
Lifespan	↓	↔	↓
Tumour weight	↔	↔	↓ ↓
Histopathological progression	↔	↔	↓
Cell proliferation	↓	↓↓	↓↓↓
Apoptosis	↑	↔	↑↑
Metastatic spread	Not observed	↓/↔	↔

Table 7-2: Summary of results for the three tumourigenic cohorts. ↑, ↓ and ↔ represent increased, decreased, and unchanged.

7.3.2 Supporting evidence

The tumour suppressive effect of mitochondrial dysfunction has been evaluated using tumourigenic mouse models based upon alterations in *Pten*, *Kras* and *p53* previously, and lend support to findings reported above.

Pten model: Mitochondrial heat shock proteins, including *Hsp90* and its homolog TNF-receptor associated protein (*Trap1*), are upregulated in metastatic prostate cancer (Leav 2010), where they play a key role in regulating gene expression, protein translation, protein folding and a host of metabolic pathways. Lisanti *et al.* (2014) generated a constitutive mouse model of *Trap1* deletion (*Trap1$^{-/-}$*) which confirmed reduced oxidative metabolism and a compensatory increase in glycolysis, associated with a reduced incidence of age-related pathologies as compared to wild-type mice. These mice were then crossed with constitutively *Pten*-haploinsufficient mice to generate *Pten$^{+/-}$;Trap1$^{-/-}$* mice, which demonstrated a reduced incidence of invasive prostate adenocarcinoma, as compared to *Pten$^{+/-}$;Trap1$^{+/+}$* controls. The reciprocal hypothesis was tested by generating prostate-specific transgenic *TRAP1* over-expressing mice (*PbsnTrap1^{tg}*), which preserved folding of key regulators of OXPHOS, membrane permeability and redox balance (Lisanti *et al.*, 2016). Upon crossing *PbsnTrap1^{tg}* mice with tumourigenic constitutive *Pten$^{+/-}$* mice, increased incidence of invasive prostate adenocarcinoma, increased cell proliferation and reduced apoptosis were noted in *Pten$^{+/-}$; PbsnTrap1^{tg}* mice, as compared to *Pten$^{+/-}$* mice. Together, these data suggest that *TRAP1*-mediated loss of OXPHOS protein folding exerts a tumour suppressive effect on prostate carcinogenesis. Comparable to these findings, the *PbCre4^{+};Pten$^{fl/fl}$;Polg$^{mut/mut}$* mouse model

described in this chapter (with complete prostate-specific *Pten* loss rather than constitutive *Pten*-haploinsufficiency) also demonstrated consistent changes in cell cycle markers, though suppression of histological disease progression was not observed. The lack of histological impact may be attributed to the reduced lifespan of Polg-HOM mice.

***P53* models:** *P53* plays a key role in regulating mitochondrial function via transactivation of Synthesis of Cytochrome Oxidase (*SCO2*), a downstream target required for assembly of cytochrome *c* oxidase (COX). Whereas *p53* loss leads to reduced *SCO2* levels and emergence of COX defects resulting in upregulation of aerobic glycolysis (Matoba *et al.*, 2006), gain-of-function *p53* mutations result in increased transcriptional regulation of *SCO2* and *TFAM*, thereby resulting in increased mitochondrial function and oxidative metabolism (Wang *et al.*, 2013). This may be a potential explanation for the greatest magnitude of tumour suppressive effect of Polg-HOM mediated mitochondrial dysfunction in $PbCre4^{+};Pten^{fl/fl};p53^{mut/+}$ mice, where *Pten* mediated increase in aerobic glycolysis is supplemented by *p53*-deletion mediated increase in oxidative phosphorylation.

Additional support for these data comes from a study of Li Fraumeni syndrome (LFS), which is an autosomal dominant cancer predisposition syndrome characterised by germline gain-of-function mutations in the *p53* gene resulting in a variety of early sarcomas and carcinomas. LFS patients and *p53* mutant mouse models demonstrate increased oxidative metabolism via mitochondrial function (Wang *et al.*, 2013). The pro-tumourigenic impact of p53 alterations is also observed in cancer patients more widely (Nath and Chan, 2016). Given the upregulation of oxidative metabolism in *p53*-related cancers, inhibition of mitochondrial function has been porposed as a potential therapeutic option. Wang *et al.* (2017) tested this hypothesis by crossing a $p53^{172H/H}$ mouse model of LFS with Polg mutator mice, akin to the $PbCre4^{+};Pten^{fl/fl};p53^{mut/+};Polg^{mut/mut}$ model described in this chapter. The authors noted increased autophagy and inhibition of aberrant *p53*-driven proliferation signalling, resulting in tumour suppression and improved cancer-free survival in mutant *Polg* mice. Similar results were also achieved upon pharmacological inhibition of complex I by metformin supplementation in both $p53^{172H/H}$ mice and patients with LFS. Furthermore, comparable suppressed prostate cancer progression has also been reported in the RapidCap $Pten^{fl/fl}p53^{fl/fl}$ mouse model of prostate cancer upon systemic administration of a complex I inhibitor, deguelin (Naguib *et al.*, 2018). Taken together, these findings are in keeping with findings from

the *PbCre4*$^{+}$*;Pten*$^{fl/fl}$*;p53*$^{mut/+}$ cohort reported in this chapter and highlight a metabolic vulnerability of *p53*-related cancers.

Mutant Kras models: The MAPK signalling pathway regulates mitochondrial biogenesis by selectively stimulating *PGC-1ß* expression (Gao *et al.*, 2011), resulting in increased oxidative phosphorylation to prime cells for rapid proliferation (Yao *et al.*, 2019). Oncogenic *Kras* mutations result in activation of MAPK signalling and development of low-grade PIN lesions without progression to overt malignancy. However, lung-specific *LSL-Kras*$^{G12D\text{-}fl/+}$ mutant mice develop lung adenocarcinoma. Weinberg *et al.* (2010) therefore evaluated the impact of mitochondrial dysfunction on lung tumourigenesis by crossing *LSL-KrasG12D*$^{fl/+}$ mutant mice with *Tfam*$^{fl/fl}$ mice. Since *TFAM* plays a critical role in mtDNA replication, *TFAM*-deficient mice display severe mtDNA depletion and OXPHOS defects (Larsson *et al.*, 1998). The authors noted severely reduced frequency of tumourigenic lung lesions, and smaller lung tumours with reduced cell proliferation in *LSL-Kras*$^{G12D\text{-}fl/+}$*;Tfam*$^{fl/fl}$ mice, consistent with the tumour suppressive phenotype observed in *PbCre4*$^{+}$*;Pten*$^{fl/fl}$*;Kras*$^{V12/+}$ mice in this chapter. Therapeutic inhibition of mitochondrial function is therefore already under investigation across a number of different *Kras*-driven cancers (Weinberg *et al.*, 2010; Viale *et al.*, 2014; Boyle *et al.*, 2018; Moro *et al.*, 2018).

7.3.3 Limitations

Since, based upon clinical data in Chapter 5, it was initially hypothesised that Polg-HOM would result in accelerated prostate cancer progression, tumourigenic models resulting in early invasive disease were employed, rather than more aggressive metastatic disease and shorter lifespans. Amongst the three baseline tumourigenic models employed, the *PbCre4*$^{+}$*;Pten*$^{fl/fl}$*;Kras*$^{V12/+}$ model had the shortest median lifespan at 201 days. Since Polg-HOM mice succumbed to age-related humane endpoints by this age, it is possible that a potential improvement in survival associated with mitochondrial dysfunction may have been masked by age-related phenotypes.

Polg-HOM mice display reduced fertility, in keeping with reduced sperm count, immotile spermatozoa, and decreased female fecundity (Trifunovic *et al.*, 2004; Jiang *et al.*, 2017), resulting in small litter sizes. Polg-HET mice were thus preferentially used in each generation of the breeding strategy. Furthermore, as previously reported (Birbach, 2013), paternal

transmission of the *PbCre4*$^{+}$ allele is required to avoid non-specific mosaic expression of the *lox-P* flanked allele. Together, these issues result in a low 1:64 Mendelian yield of triple mutant Polg-HOM mice and thus limit experiments to small sample sizes. Though we attempted to cross the mutant *Polg* allele into a more aggressive *PbCre4*$^{+}$*;Pten*$^{fl/fl}$*;p53*$^{mut/mut}$ model with a median survival of 150 days (Chen *et al.*, 2005), no Polg-HOM mice were generated in this background, in keeping with an extremely low predicted Mendelian yield of 1:128. However, a small number of *PbCre4*$^{+}$*;Pten*$^{fl/fl}$*;p53*$^{mut/+}$*;*Polg-HET (n=3) mice were generated, tissues from which merit further investigation.

The disparity in impact of systemic mitochondrial alterations (as modelled herein) and local mitochondrial alterations (as evaluated using human data in chapters 3 and 5) is discussed in section 8.1.5.

7.3.4 Future work

Further characterisation experiments are required to validate alterations in OXPHOS protein abundance (in the *PbCre4*$^{+}$*;Pten*$^{fl/fl}$*;p53*$^{mut/+}$ cohort, and Polg-HET mice from all cohorts), *p53* alterations and *MAPK* signalling targets in the three mouse models generated. These may be supplemented by mtDNA sequencing and western blotting of tissue lysates.

In light of the relatively low frequency of apoptotic bodies noted in the triple mutant Polg-HOM mice, it is expected that cells have switched to alternative metabolic pathways, rather than succumbing to cell death. RNA sequencing of frozen prostate tissue specimens may therefore help identify potential alternative metabolic pathways which may be upregulated to compensate for OXPHOS defects and enable cell survival. Pathways associated with glycolysis, fatty acid oxidation and one carbon metabolism may be expected to be altered leads in this context. Furthermore, transcriptomic studies may identify tumour signalling pathways, including hypoxic signalling, which may help identify potential underlying mechanisms for the observed tumour suppressive effect of mitochondrial dysfunction. Cross-species meta-analysis using curated clinically annotated databases would help identify associated features observed in human prostate cancer studies, with a view to determining potential therapeutic targets for further study. Similarly, laser capture microdissection for mtDNA sequencing and OXPHOS immunohistochemistry of primary prostate tumours and metastatic lesions observed in lymph nodes and lung tissue of *PbCre4*$^{+}$*;Pten*$^{fl/fl}$*;Kras*$^{V12/+}$ mice

may provide valuable insights into adaptive metabolic alterations and the role of mitochondrial dysfunction in disease dissemination.

Since defects in Complex I were frequently observed in this stochastic model of age-related mitochondrial dysfunction, either tissue-specific Complex I loss or pharmacological inhibition of complex I in tumourigenic mouse models with wild-type *Polg* genotype may provide further confirmation of this potential target.

These results should also be validated using functional studies and perturbation experiments using established *in vitro* models of prostate cancer. Characterisation of *de novo* mitochondrial alterations in prostate cancer cell lines would, however, be necessary prior to embarking on this work.

7.4 Conclusion

In this chapter, I described the development and characterisation of three novel mouse models of prostate tumourigenesis based upon alterations in *PTEN*, *p53* and *MAPK* signalling pathways crossed with *Polg* mutator mice characterised in Chapter 6. Tumour progression was evaluated by morphological measurements, histopathological evaluation, immunohistochemical assessment of markers of cell proliferation and apoptosis in mouse prostate tissue, and assessment for metastatic lesions. Contrary to the pro-tumourigenic effect of local mitochondrial defects observed in clinical data (Chapter 5), systemic mitochondrial defects modelled in the novel models characterised in this chapter were found to suppress prostate cancer progression. Further analysis of archived mouse tissue samples by next generation sequencing may help elucidate the underlying mechanisms for these observations and identify potential targets for subsequent functional *in vitro* validation studies.

Chapter 8 General Discussion

Large scale multi-institution molecular studies have helped vastly improve our understanding of nuclear genomic alterations in prostate carcinogenesis, enabling molecular stratification of patients with prostate cancer (PCa). Recent work has further shed light upon potential molecularly stratified therapeutic options for patients, such as the use of olaparib for patients with DNA repair defects (Mateo *et al.*, 2015). Similarly, a multitude of trials focussing on agents targeting androgen receptor signalling have recently shown promising results (see section 1.3).

Nevertheless, limited clarity exists regarding metabolic alterations associated with prostate cancer progression, which is further complicated by the unique metabolism of normal prostate epithelial cells, contributing to a mixed Warburg phenotype during early prostate transformation. The more conventional Warburg shift from oxidative phosphorylation (OXPHOS) to reliance on a predominantly glycolytic phenotype is most evident upon progression to advanced stages of PCa (Pertega-Gomes *et al.*, 2015). Mitochondrial alterations have been proposed as a potential mechanism underlying the Warburg effect (Senyilmaz and Teleman, 2015). Thus, a better understanding of mitochondrial molecular alterations and their association with PCa progression may help develop prognostic markers of aggressive disease, and therapeutic targets aiming to supress disease progression. Thus, I hypothesised that mitochondrial dysfunction accelerates prostate cancer progression and aimed to evaluate the impact of mitochondrial alterations on prostate cancer progression using both primary prostate cancer samples and development of novel transgenic mouse models.

8.1 Key findings

8.1.1 Transcriptomic signature of mitochondrial dysfunction is associated with aggressive PCa

Given that (a) recurrent driver nuclear genomic alterations are observed in PCa at low frequency, and (b) DNA polymerase-gamma fidelity results in stochastic mitochondrial DNA (mtDNA) mutations, mtDNA mutations in publicly available PCa data were first evaluated in ***Chapter 3***. Consistent with previous reports (Ju *et al.*, 2014; Stewart *et al.*, 2015; Grandhi *et al.*, 2017), mtDNA mutations were observed across the whole mitochondrial genome, but seemed to be under clonal selection pressures. Notably, mutations in tRNA genes and the control regions appeared to be positively selected, whereas those affecting complexes I and

V of the mitochondrial respiratory chain appeared to be negatively selected, suggest that complexes I and V may be crucial for cancer cell proliferation. In keeping with these observations, Hopkins et al recently reported a diverse range of prognostic consequences associated with mutant gene loci (Hopkins *et al.*, 2017). However, the low frequency of these individual mtDNA mutations affecting protein coding regions, coupled with the likely diverse range of downstream functional consequences associated with positively selected tRNA genes, raises the possibility that the true burden of mitochondrial functional alterations may not be fully captured by mtDNA sequencing alone. Assessment of mitochondrial copy number alterations from two separate cohorts provided inconsistent results. However, founded on the dual genomic origin of the OXPHOS subunits, a transcriptomic signature of OXPHOS defects was curated, based upon increased nuclear and decreased mitochondrial gene expression score. This OXPHOS defect score correlated with established PCa risk features and increased risk of biochemical recurrence. In addition, increased OXPHOS defect scores were associated with molecular subgroups of PCa, including *PTEN*-loss and *TMPRSS2:ERG* fusion, and other gene expression signatures including cell cycle progression and hypoxia signalling. However, the translational impact of these data is limited by (a) the primarily low and intermediate risk cohort of patients who subsequently underwent radical treatment of PCa, and (b) the use of biochemical recurrence as the primary endpoint of this study. Further validation of this curated signature in independent datasets is therefore warranted.

8.1.2 Development of a multiplex spatial proteomic assay for evaluating mitochondrial alterations

Mitochondrial functional status cannot be reliably inferred from transcriptomic data, and ideally requires the use of metabolomic or functional assays of fresh tissue. Given the need for long-term follow-up of PCa patients to determine impact of mitochondrial alterations on overall survival, logistic reasons frequently necessitate the use of proteomic surrogate markers in archived formalin-fixed paraffin-embedded (FFPE) tissue samples. Rocha *et al.* (2015) recently described a multiplex quantitative immunofluorescence-based assay to evaluate alterations in complex I and IV of the electron transport chain and normalise these data for heterogeneity in mitochondrial mass. The authors reported high accuracy in quantifying the abundance of mitochondrial OXPHOS complexes, when applied to fresh-frozen muscle biopsy tissue from patients with genetically confirmed mitochondrial disease. In order to improve the throughput of this approach and enable its use with archived FFPE tissue, I developed an automated assay in ***Chapter 4***, employing automated staining, imaging,

and quantification protocols. Application of this technique to tissue samples collected 15-20 years ago confirmed adequate preservation of mitochondrial epitopes, while maintaining high reproducibility. The automated workflow reduced staining time from 2 days to 13 hours, and imaging time from 7.5 hours hands-on time to 1 hour of set-up time for overnight batch processing. The image analysis pipeline allowed the assessment of spatial proteomic heterogeneity and provided single cell level data for downstream analysis. Though multiplexing was limited to 5 epitopes, the assay can be adapted to use with alternative cell type markers for a diverse range of applications. However, it would be beneficial to validate the specificity and sensitivity of this approach with other methods, such as mtDNA sequencing or traditional enzyme histochemical approaches.

8.1.3 Mitochondrial proteomic alterations are associated with aggressive PCa

The spatial proteomic assay described above was applied to a clinically annotated tissue microarray comprising 506 PCa patients from two centres in ***Chapter 5***, comprising a diverse range of PCa risk features, and tissue sources including radical prostatectomy (RP), transurethral resection of prostate (TURP) and prostate biopsy tissue. In comparison to normal-adjacent tissue cores, tumour cores had increased mitochondrial mass, but comparable Complex I and IV abundance. OXPHOS markers were not found to be associated with advancing age, which may be due to the low number of young patients in these cohorts. High PCa risk features were associated with reduced Complex I abundance and increased mitochondrial mass. Widespread intra-patient heterogeneity in complex I abundance and mitochondrial mass were also observed. Upon adjustment for established PCa risk features, low complex I and increased mitochondrial mass were found to be independently predictive of reduced overall survival at 20-year follow-up. Molecular stratification by *PTEN* and *ERG* status further found complex I abundance to be most prognostic in patients with $PTEN^{-}$ ERG^{+} PCa, whereas increased Complex IV and mitochondrial mass were predictive of increased overall survival amongst $PTEN^{+}ERG^{-}$ PCa. These data suggest that metabolic dependency of PCa may vary by molecular subgroup. Subsequent work should first aim to validate these findings in other independent cohorts, and then evaluate associations with other relevant molecular subgroups.

8.1.4 Age-associated systemic accumulation of mtDNA mutations suppresses cancer progression in transgenic mouse models of *Pten*-deficient prostate cancer

Both transcriptomic (Chapter 3) and proteomic (Chapter 5) assays on primary PCa tissue highlighted an association between mitochondrial alterations and PCa progression. Given that advancing age is the strong risk factor for PCa (Bostwick *et al.*, 2004) , and frequency of mtDNA mutations also increases with advancing age (Hopkins *et al.*, 2017), these associations were further tested using transgenic mouse models. In ***Chapter 6***, I characterised prostate tissue from the *Polg* mutator mouse model, an established model of systemic age-related accumulation of mtDNA mutations, which acquire systemic features of accelerated ageing and demonstrate reduced lifespan. Polg-HOM mouse prostates developed a high burden of OXPHOS defects, with Complex I and Complex IV defects observed in 86% and 41% of epithelial cells, respectively. OXPHOS features were associated with increased mitochondrial mass, suggestive of compensatory mitochondrial biogenesis. Polg-HOM prostates were macroscopically smaller than age-matched wild-type controls, with infrequent atypical hyperplastic lesions, but no overt histopathological features of invasive PCa. Transcriptomic features of reduced cell cycle progression, downregulation of mitochondrial gene expression, and upregulation of innate immune pathways were also observed. However, immunohistochemical assays noted reduced cell proliferation in Polg-HOM prostate tissues, with comparable $CD8^+$ and $CD11b^+$ immune cell types.

Based upon the above data, OXPHOS defects do not appear to spontaneously initiate PCa. Thus, the impact of OXPHOS defects on PCa progression was evaluated in ***Chapter 7***. *Pten*-deficient mice were crossed with *Polg* mutator mice, to model age-related systemic accumulation of OXPHOS defects over a tumourigenic background. Since Polg-HOM mice develop testicular atrophy and reduced testosterone levels with advancing age (Trifunovic *et al.*, 2004; Fox *et al.*, 2012; Jiang *et al.*, 2017), *Pten*-deficient mice were specifically selected as the tumourigenic background, given that this model recapitulates castrate-resistant prostate cancer (Carver *et al.*, 2011), and tumour progression in this model would be agnostic to Polg-HOM mediated testosterone depletion. Two additional exploratory cohorts with additional oncogenic *Kras* overexpression or *p53* deletion, associated with progression to more advanced stage disease, were also established. In comparison to cohort-matched wild-type controls, Polg-HOM mice succumbed to early mortality due to accelerated systemic age-related phenotypes. In comparison to age-matched control mice, Polg-HOM tended to be associated with reduced cell proliferation, increased apoptosis, reduced frequency of

sarcomatoid differentiation and reduced incidence of distant metastases. However, progression to invasive adenocarcinoma across both genotypes were comparable. These data suggest that mitochondrial defects suppress PCa progression but not tumour initiation in *Pten*-deficient PCa.

8.1.5 Systemic versus local effects of mitochondrial function on tumour progression

These pre-clinical results conflict with the initial hypothesis of a pro-tumourigenic effect of mitochondrial dysfunction and clinical findings reported in chapters 3 and 5, where the OXPHOS defect gene expression signature and complex I defects in primary prostate cancer tissue cores was an independent prognostic marker of poor outcome. This discrepancy may be accounted for a number of possible hypotheses including:

(1) Mitochondrial defects may occur early in prostate cancer development (Lindberg *et al.*, 2013) and clonally expand by neutral drift (Coller *et al.*, 2001; Elson *et al.*, 2001; Nekhaeva *et al.*, 2002; Salk and Horwitz, 2010) during progression to aggressive prostate cancer. This may result in a detectable increase in the burden of passenger mitochondrial defects associated with increased cancer cell proliferation, which may thereby act as a marker of aggressive disease, rather than driving disease progression itself.

(2) Mitochondrial dysfunction may exert an oncojanus effect on tumour progression (Leone *et al.*, 2018), whereby at low frequency and severity, mitochondrial defects result in oxidative stress mediated by DNA damage and stabilisation of *HIF1α* leading to a pro-tumourigenic phenotype; whereas at high frequency result in accumulation of TCA cycle intermediates (NADH and α-ketoglutarate) and impede *HIF1α* stabilisation to exert a tumour suppressive effect (Iommarini *et al.*, 2013; Cruz-Bermúdez *et al.*, 2015). In keeping with this hypothesis, the tumour suppressive effect of the tumourigenic models described in chapter 7 may be a consequence of a high burden of *Polg*-HOM mediated mitochondrial defects, whereas a relatively lower burden of mitochondrial defects in primary human prostate cancer tissue, as observed in chapter 5, may result in a pro-tumourigenic phenotype.

(3) There may exist an interplay between the diverse effects of systemic versus local mitochondrial dysfunction on tumour progression. This hypothesis is discussed further below.

The *Polg* mutator mouse has a constitutive knock-in mutation in *Polg* resulting in systemic features of mitochondrial dysfunction, that manifest in an accelerated ageing phenotype. Therefore, it is expected that systemic features of mitochondrial dysfunction occurring across multiple organ systems, such as impacting immune cell function through known haematopoetic stem cell dysfunction (Ahlqvist *et al.*, 2012), which may contribute to the observed attenuation in tumour progression in the tumourigenic models generated in Chapter 7.

This hypothesis is supported by previous studies using tissue-specific and constitutive ablation of other key regulators of mitochondrial function, which allows independent study of local and systemic effects of mitochondrial dysfunction, respectively. Woo *et al.* (2012) generated a constitutive $Apc^{min/+};Tfam^{+/-}$ model of heterozygous *TFAM* loss using an established *Apc*-driven mouse model of intestinal tumourigenesis. *TFAM* fidelity resulted in mtDNA instability, increased mitochondrial ROS production and accelerated tumour progression in comparison to control $Apc^{min/+};Tfam^{+/+}$ mice. In a reciprocal experiment, ROS-mediated intestinal tumour progression was abrogated by over-expression of ROS-scavenging catalase (Woo *et al.*, 2012). In contrast, tissue-specific *TFAM* haploinsufficiency did not alter *Apc*-driven tumourigenesis in *Vil-cre;* $Apc^{fl/fl};Tfam^{fl/+}$ mice, whereas, homozygous *TFAM* loss drastically reduced adenoma formation in *Vil-cre;* $Apc^{fl/fl};TFAM^{fl/fl}$ mice (Wen *et al.*, 2019).

Taken together, these results suggest that mitochondrial dysfunction may have diverse effects on cancer progression at a local versus a systemic level. This warrants further investigation, which may be designed by crossing a prostate-specific mouse model of prostate cancer with tissue-specific knock-out of a key regulator of mitochondrial function. This could involve the use of either the $Tfam^{fl/fl}$ model described above, a $Cox10^{fl/fl}$ model (Diaz *et al.*, 2005) recently used to demonstrate the tumour suppressive role of endothelial oxidative phosphorylation in prostate cancer (Zahalka *et al.*, 2017), or the $Ndufs4^{fl/fl}$ model (Kruse *et al.*, 2008).

8.2 Emerging hypotheses and translational opportunities

8.2.1 Mitochondrial alterations herald aggressive prostate cancer

Local mitochondrial alterations in primary prostate tissue at both transcriptomic (Chapter 3) and proteomic level (Chapter 5) were found to be associated with features of both clinical and genomic features of unfavourable prostate cancer. These features include hypoxia, genomic

instability, and senescence, which were recently described as “nimbosus” (“gathering of storm clouds” in latin), which may herald the development of lethal disease. This is supported by recent findings by Bhandari *et al.* (2019a), who report an association between mtDNA mutations with tumour hypoxia in PCa. Using the transcriptomic signature curated in Chapter 3, it would be beneficial to evaluate the association of mitochondrial alterations and cribriform and intra-ductal PCa, which has recently been evaluated in the TCGA-PRAD cohort (Bottcher *et al.*, 2018), and form part of the constellation of nimbosus features. Future work may focus on further dissecting these relationships at the transcriptomic and proteomic level and validating these findings in independent cohorts, such as the CPC-GENE cohort (where transcriptomic data has recently been made publicly available, Chen *et al.* (2019)) with a view to developing mitochondrial-based biomarkers and mitochondrial targeted therapies.

The mechanistic basis driving mitochondrial defects during progression to advanced PCa is unknown. However, these features may be associated with alterations in *Pi3k/Akt* (Moro *et al.*, 2009; Ghosh *et al.*, 2015; Koundouros and Poulogiannis, 2018), *AR* receptor (Bajpai *et al.*, 2019), and ROS (Khandrika *et al.*, 2009; Afanas'ev, 2011) signalling which previously have been implicated in both mitochondrial dysfunction and PCa.

8.2.2 Predictive, prognostic and therapeutic potential of mitochondrial complex I defects

Reduced Complex I abundance and increased mitochondrial mass were identified as independent prognostic markers of lethal PCa. Together these features suggest loss of dependency on Complex I mediated OXPHOS in early PCa, with compensatory increase in mitochondrial mass to support Complex II shuttled entry of protons into ETC, as has recently also been proposed by others (Weber *et al.*, 2018). Thus, validation of these findings in independent cohorts is warranted, to further investigate the use of complex I abundance as a prognostic PCa tissue biomarker.

In contrast, systemic mitochondrial dysfunction in transgenic mouse models was found to suppress tumour progression in Chapter 5. Consistent with this observation, systemic complex I inhibition has been proposed as a potential adjuvant therapeutic option. Since the anti-diabetic drug metformin has complex I inhibitory properties, arm J of the ongoing STAMPEDE trial (Gillessen *et al.*, 2016) aims to evaluate the use of metformin, in addition to current standard of care therapies, to minimise toxicity associated with androgen deprivation therapy and also suppress tumour progression. If the anti-tumour effect of metformin is indeed driven

by its complex I inhibitory effect in malignant cells, it may be hypothesised that metformin treatment may be beneficial amongst patients with abundant complex I in their primary tumour tissues. If this hypothesis is borne out in prospective studies, it would make a case for further developing mitochondrial-targeted agents, such as mitochondrial-targeted metformin ('mito-metformin')(Cheng *et al.*, 2016), to further improve drug efficacy and minimise potential dose-related systemic toxicity (Heinz *et al.*, 2017), such as lactic acidosis. Other mitochondrial-targeted agents have also been proposed (Ashton *et al.*, 2018), though the vast majority have been evaluated in the context of *PTEN*-deficient PCa. Since different molecular subgroups may have varying metabolic vulnerabilities (Yuneva *et al.*, 2012; Gaude and Frezza, 2016), evaluation of the impact of OXPHOS in other molecular subgroups of PCa is warranted.

Surrogate tissue biomarkers of mitochondrial function may also predict response to radiotherapy (Tang *et al.*, 2018) and chemotherapeutic regimens (Fan *et al.*, 2019). For instance, docetaxel resistant cells become more reliant on OXPHOS (Ippolito *et al.*, 2016), whereas reduced mitochondrial copy number makes malignant cells more responsive to chemotherapy (Mei *et al.*, 2015). Complex I inhibitors, such as metformin, have also been shown to improve radiosensitivity of prostate cancer (Spratt *et al.*, 2013; Zannella *et al.*, 2013). Similarly, the use of gold nanoparticles accentuates mtDNA damage upon irradiation and results in mitochondrial damage and eventual cell death (Taggart *et al.*, 2014).

Thus, assessment of complex I abundance, using methods developed in Chapter 4, may assist in molecular stratification of a subgroup of patients who may either benefit from adjuvant metformin therapy and/or respond to chemoradiotherapeutic regimens.

8.2.3 Adjunctive utility of mitochondrial imaging biomarkers to improve diagnostic accuracy of conventional imaging modalities

Though recent level 1 data has highlighted the accuracy of multi-parametric MRI (mpMRI) to detect clinically significant prostate cancer (Ahmed *et al.*, 2017a; Kasivisvanathan *et al.*, 2018), approximately 20% of clinically-significant lesions are invisible on conventional mpMRI (Johnson *et al.*, 2019) and may harbour aggressive genomic characteristics (Houlahan *et al.*, 2019; Parry *et al.*, 2019; Shoag *et al.*, 2019). The accurate identification of these MRI invisible but clinically or genomically aggressive PCa lesions may be improved by combining metabolic imaging modalities with conventional imaging platforms. A growing understanding of mitochondrial alterations over the course of PCa progression therefore lends itself to the development and interpretation of novel adjunct imaging biomarkers. The most established

metabolic imaging molality is ^{18}F-fluorodeoxyglucose-positron emission tomography (FDG-PET), which is often used to locate cancer foci as part of diagnostic and surveillance protocols. However, the use of FDG-PET has proven to be challenging in prostate cancer due to the mixed Warburg phenotype of PCa and the pooling of renally excreted tracer within the bladder and results in difficulty in accurately determining uptake in the abutting prostate (Jadvar, 2016). However, since Gleason score >7 PCa demonstrates high FDG uptake, FDG-PET may still have a role in staging and prognostication amongst patients with established PCa, if the above challenges can be overcome. As FDG-PET is primarily based on evaluating glycolytic tumours, the use of hyperpolarised [1-^{13}C]Pyruvate has recently also been proposed to evaluate metabolic alterations in PCa more comprehensively, as an adjunct to conventional mpMRI platforms (Nelson *et al.*, 2013). Such a more comprehensive metabolic phenotype may include novel radiotracers including radiolabelled oxygen (Knowles *et al.*, 2019), and markers of Complex I, which this thesis posits as a potential prognostic biomarker, with a variety of relevant mitochondrial-targeted radiotracers already in development (Li *et al.*, 2017).

8.2.4 Unravelling the mechanistic basis of tumour suppression mediated by systemic mitochondrial dysfunction

The tumour suppressive phenotype of systemic accumulation of age-related mitochondrial over *Pten*-deficient tumourigenic backgrounds are in contrast to the increased frequency of aggressive PCa detected in older men in epidemiological studies. This was likely due to lead time bias, whereby older men are more likely to present at a later stage, following the onset of clinical symptoms of advanced PCa, whereas younger men are more likely to undergo PSA testing and consequently present with early stage prostate cancer. The systemic effects of mitochondrial dysfunction in transgenic models devised in Chapter 7 suggests that age-related changes may suppress tumour progression, and further highlight the need to balance the risks of prostate-cancer mortality against other-cause mortality amongst older patients with PCa.

The mechanistic basis of this observation, is however, unclear at present. RNA sequencing of Polg-HOM mice in Chapter 6 noted upregulation of innate immune pathways, which were not validated in preliminary immunohistochemical assays of *CD8*$^{+}$ and *CD11b*$^{+}$ cells. In light of growing understanding of diverse metabolic dependencies of various immune cell phenotypes, it is hypothesised that systemic mitochondrial dysfunction in these models may result in immunomodulation that can impact tumour progression. Indeed, metabolic alterations in immune cell phenotypes have been previously observed in the tumour

microenvironment (Bianchi-Frias *et al.*, 2010; Bianchi-Frias *et al.*, 2018; Garcia-Canaveras *et al.*, 2019), but were not explored in this thesis. Thus, future work focussing on metabolic dependencies of components of the tumour microenvironment and their impact on tumour progression are warranted. Furthermore, transcriptomic evaluation of tumourigenic transgenic models devised in Chapter 7 may shed light on potential mechanisms of tumour suppression for further evaluation. In support of this goal, I have characterised baseline mitochondrial alterations and associated metabolic phenotypes in *in vitro* models of prostate cancer (see Appendix E) which may be utilised to plan perturbation experiments.

8.3 Final conclusions

Consistent with the Warburg effect, age-related mitochondrial alterations were hypothesised to accelerate prostate cancer progression. This hypothesis was supported by transcriptomic and proteomic evaluation of primary prostate cancer tissue, where complex I defects and increased mitochondrial mass were independent prognostic markers of poor overall survival. Molecular stratification revealed a strong association between these local surrogate markers of mitochondrial function with *PTEN*-deficient prostate cancer. However, contrary to the initial hypothesis, age-related systemic accumulation of mitochondrial mutations suppressed cancer progression in transgenic *Pten*-deficient mouse models.

Thus, mitochondrial alterations exert diverse systemic and local effects on *PTEN*-deficient prostate cancer progression. Leveraging mitochondrial tissue biomarkers and mitochondrial-targeted systemic therapies may provide a novel approach for identifying aggressive prostate cancer and suppressing progression to lethal disease.

Appendix A Supplementary data for Chapter 3

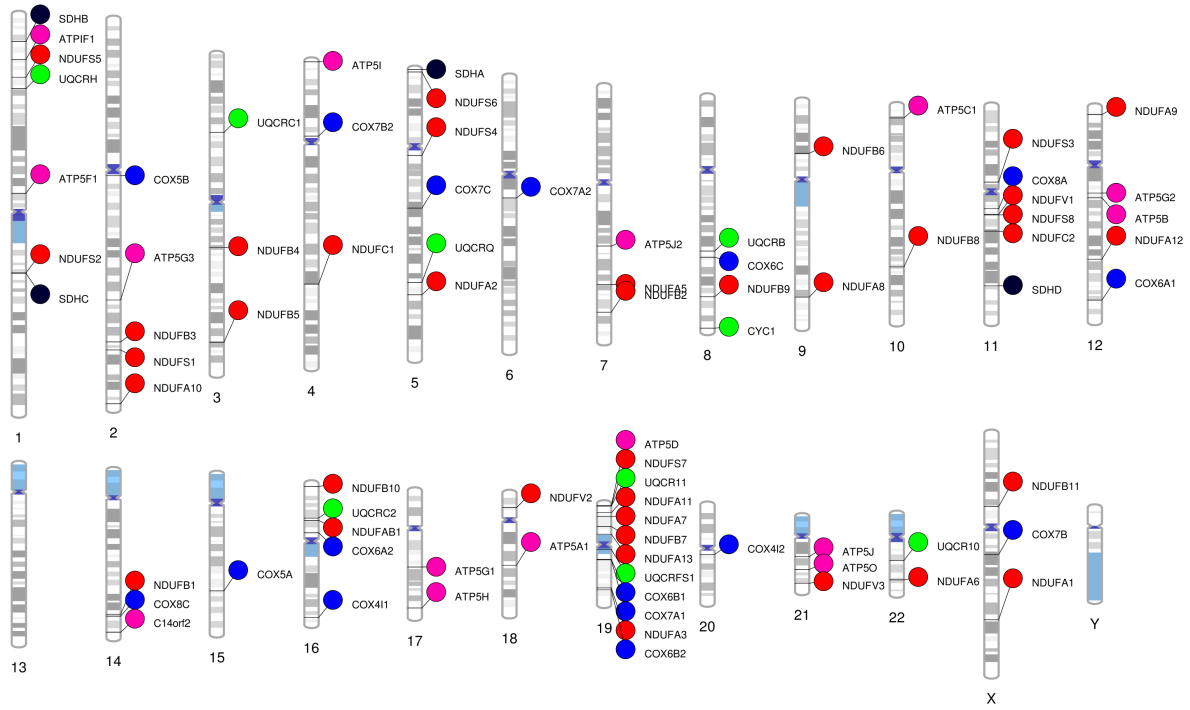

Figure A-1: Gene loci of nuclear-encoded OXPHOS subunits. Gene positions were obtained from ensembl.org and annotated to chromosomes. Colors represent associated OXPHOS complexes.

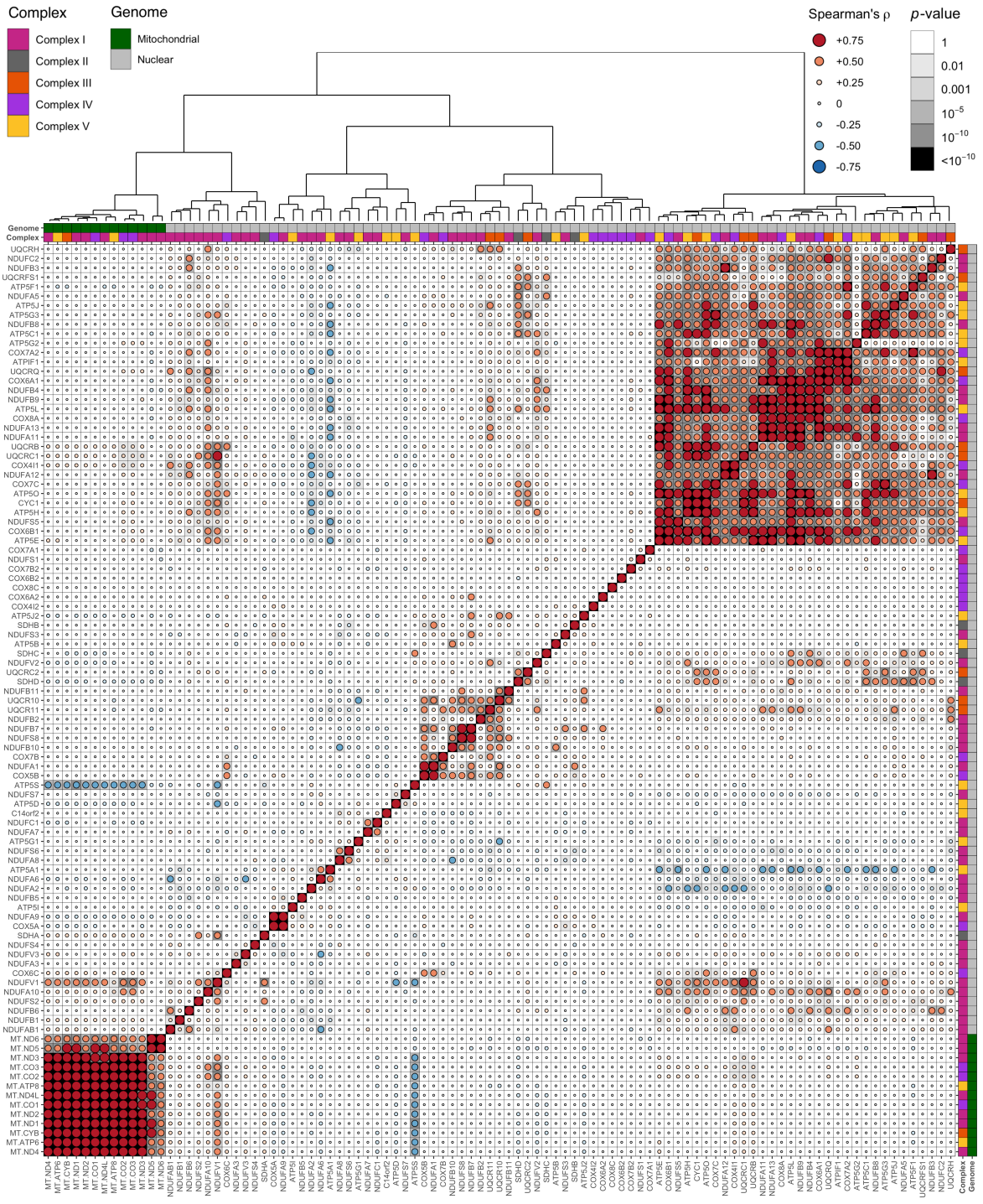

Figure A-2: Relationship between gene expression of nuclear-encoded and mitochondrial-encoded OXPHOS subunits in TCGA-PRAD normal samples. TCGA-PRAD cohort (mt-RNA expression data available for 48 normal-adjacent samples) from Reznik *et al.* (2017). Spearman correlation, FDR adjusted *p*-values, Ward.D2 method of calculating distances.

Appendix B Supplementary data for Chapter 4

B (i). Use of the H-score to summarise single cell level data

In order to summarise the cell population within a region of interest (ROI), each cell may first be categorised on a scale of “very low”, “low”, “normal”, and “high” intensity, based upon Z-scores cut-offs for each individual marker, as described in chapter 4. Proportions of cells in each of these categories can be used to calculate a cumulative histological score (or, H-score). The H-score is a semi-quantitative method frequently used in evaluation of stained tissue sections following chromogenic IHC, and is calculated using the following equation:

H-score = (0 x % ‘very low’ intensity cells)
+ (1 x % ‘low’ intensity cells)
+ (2 x % ‘normal’ intensity cells)
+ (3 x % ‘high’ intensity cells)

Using categorical Z-score data, the abundance of a particular protein in a ROI can therefore be summarised by their H-score. This method demonstrated greater spatial heterogeneity in relative OXPHOS protein abundance in PCa tissue, as compared to benign tissue.

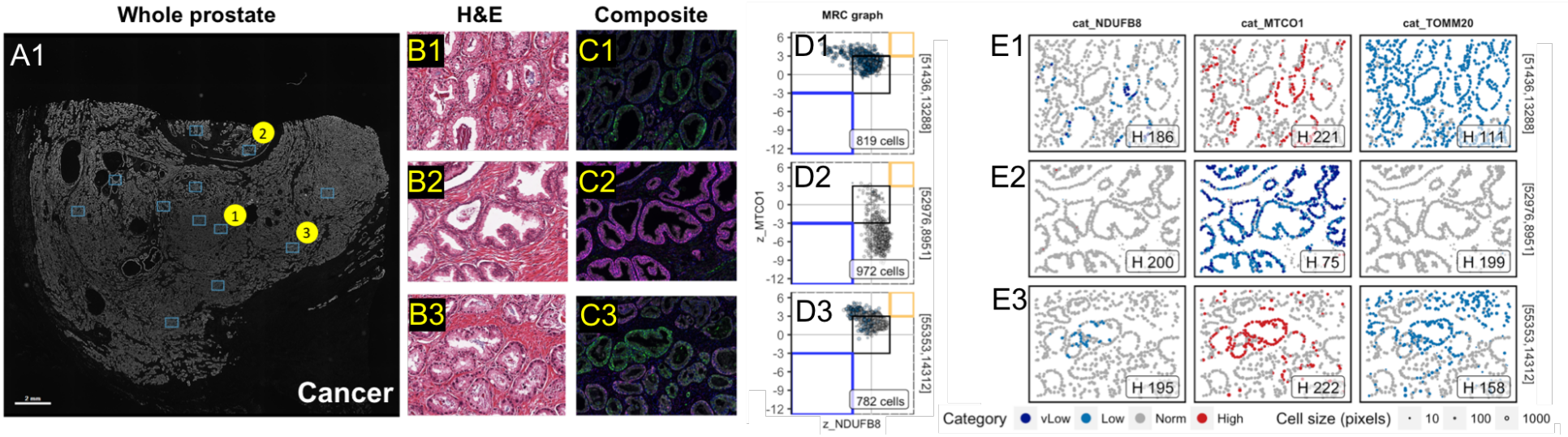

Figure B-1: Spatial heterogeneity in OXPHOS abundance in PCa tissue. (A) Cytokeratin map of whole tissue section from (A1) malignant prostate tissue, marked with distinct regions of interest. **(B)** Malignant histopathology was noted upon haematoxylin and eosin staining in regions 1 and 3. **(C)** Associated unmixed composite images and **(D)** mitochondrial respiratory chain (MRC) graphs plotting z-scores for NDUFB8 vs MTCO1 for individual cells. **(E)** Pseudo-image with categorised Z-scores demonstrates more frequently altered OXPHOS protein abundance in malignant (E1-3) tissue. H-scores reported in inset.

B (ii). A comparison of data reduction methods

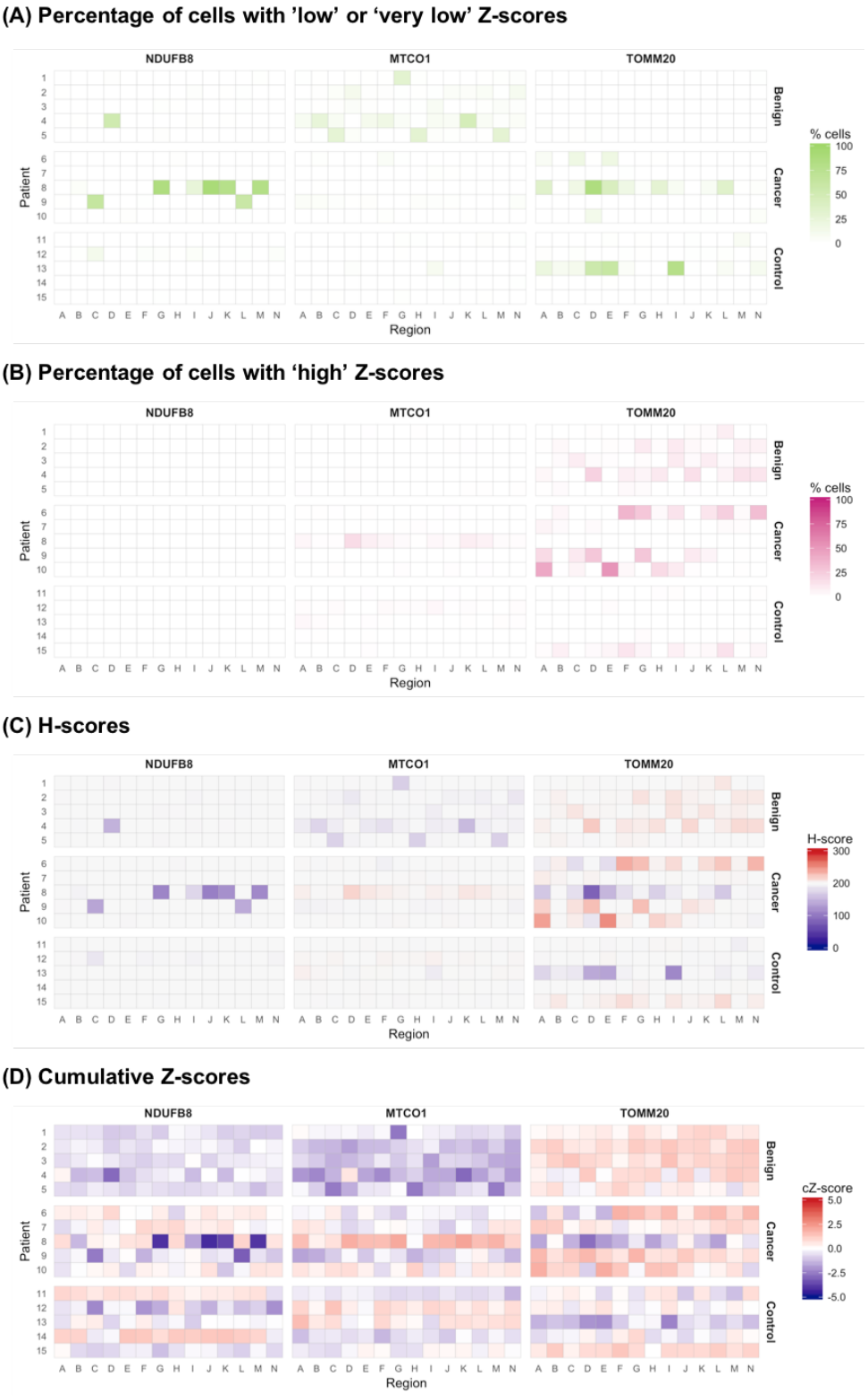

Figure B-2: Comparison of data reduction methods across all cells per core confirmed the use of Z-scores to maintain greatest dynamic range of measurement.

B (iii). Mean Z-score correlates well with H-score (core level)

Good correlation between was noted between cumulative Z-scores and H-scores for NDUFB8 (R 0.692), MTCO1 (R 0.691) and TOMM20 (0.783). However, dynamic range is lost when using H-scores (**Figure B-3**).

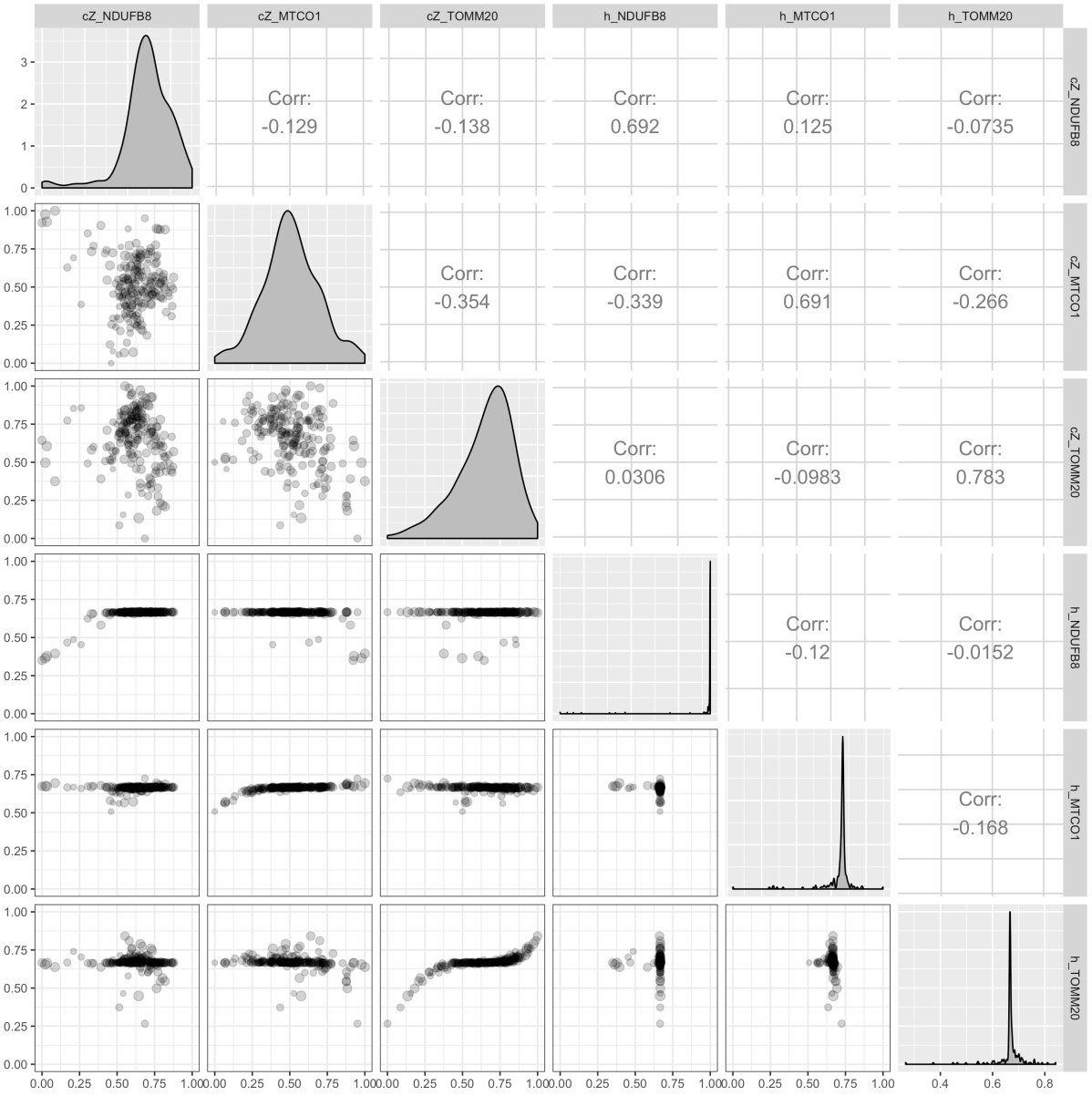

Figure B-3: Correlation between mean Z-score and H-score on a per core basis. Each point represents and individual core. cZ: Cumulative Z-score;

Appendix C Supplementary data for Chapter 5

C (i). Prognostic impact of unadjusted mean Z-scores

		HR (univariable, 95% CI)	HR (multivariable, 95% CI)
All patients			
Unadjusted	high	-	-
***NDUFB8*-max**	low	0.95 (0.75-1.20, *p*=0.690)	1.02 (0.77-1.35, *p*=0.904)
Unadjusted	high	-	-
***NDUFB8*-mean**	low	1.37 (1.07-1.75, *p*=0.012)	1.36 (1.03-1.81, *p*=0.033) *
Unadjusted	high	-	-
***NDUFB8*-min**	low	1.64 (1.28-2.11, *p*<0.001)	1.58 (1.18-2.13, *p*=0.002) **
Unadjusted	high	-	-
***MTCO1*-max**	low	0.80 (0.64-1.01, *p*=0.064)	0.82 (0.62-1.08, *p*=0.153)
Unadjusted	high	-	-
***MTCO1*-mean**	low	0.93 (0.70-1.23, *p*=0.603)	0.90 (0.64-1.26, *p*=0.545)
Unadjusted	high	-	-
***MTCO1*-min**	low	1.04 (0.82-1.30, *p*=0.764)	1.01 (0.77-1.33, *p*=0.917)
ERG positive			
Unadjusted	high	-	-
***NDUFB8*-min**	low	2.62 (1.55-4.43, *p*<0.001)	1.76 (0.97-3.19, *p*=0.063)
Unadjusted	high	-	-
***MTCO1*-max**	low	0.55 (0.35-0.86, *p*=0.009)	0.70 (0.41-1.19, *p*=0.189)
ERG negative			
Unadjusted	high	-	-
***NDUFB8*-min**	low	1.13 (0.73-1.74, *p*=0.593)	1.34 (0.80-2.25, *p*=0.263)
Unadjusted	high	-	-
***MTCO1*-max**	low	0.51 (0.33-0.80, *p*=0.003)	0.44 (0.26-0.74, *p*=0.002) **
PTEN-proficient			
Unadjusted	high	-	-
***NDUFB8*-min**	low	1.54 (1.00-2.35, *p*=0.048)	1.25 (0.78-2.01, *p*=0.347)
Unadjusted	high	-	-
***MTCO1*-max**	low	0.63 (0.43-0.92, *p*=0.017)	0.78 (0.50-1.21, *p*=0.269)
PTEN-deficient			
Unadjusted	high	-	-
***NDUFB8*-min**	low	1.77 (1.16-2.70, *p*=0.008)	2.00 (1.21-3.30, *p*=0.007)
Unadjusted	high	-	-
***MTCO1*-max**	low	0.56 (0.37-0.86, *p*=0.009)	0.51 (0.31-0.85, *p*=0.010)

Table C-1: Cox regression models of unadjusted OXPHOS marker metrics for overall survival (n=360). Three metrics were calculated for each marker based upon mean z-scores across all tumour cores (mean), a single core with the lowest mean marker z-score (min), and a single core with the highest mean marker z-score (max). Note: Z-scores for NDUBF8 and MTCO1 were not normalised for variation in mitochondrial mass (TOMM20 z-score). Hazard ratios (HR) reported with 95% confidence interval (CI), using the high-expression group as reference. Multivariable Cox regression model adjusted for age at diagnosis, log-10 PSA at diagnosis, Gleason group, clinical tumour stage, and presence of metastasis. False-discovery rate (FDR) adjusted *p*-values calculated using multivariable Cox regression are represented as * <0.05, ** < 0.01, and *** < 0.001.

		HR (univariable, 95% CI)	HR (multivariable, 95% CI)
***PTEN*-proficient *ERG*-positive prostate cancer (n=61)**			
Unadjusted	high	-	-
***NDUFB8*-min**	low	2.88 (1.26-6.58, *p*=0.012)	2.09 (0.77-5.68, *p*=0.146)
Unadjusted	high	-	-
***MTCO1*-max**	low	0.65 (0.38-1.13, *p*=0.130)	0.93 (0.45-1.94, *p*=0.847)
***PTEN*-proficient *ERG*-negative prostate cancer (n=60)**			
Unadjusted	high	-	-
***NDUFB8*-min**	low	1.04 (0.57-1.91, *p*=0.898)	1.02 (0.46-2.23, *p*=0.968)
Unadjusted	high	-	-
***MTCO1*-max**	low	0.47 (0.25-0.89, *p*=0.019)	0.33 (0.15-0.74, *p*=0.007) **
***PTEN*-deficient *ERG*-positive prostate cancer (n= 35)**			
Unadjusted	high	-	-
***NDUFB8*-min**	low	2.76 (1.31-5.84, *p*=0.008) **	1.27 (0.45-3.59, *p*=0.649)
Unadjusted	high	-	-
***MTCO1*-max**	low	0.42 (0.19-0.91, *p*=0.028) *	0.29 (0.10-0.89, *p*=0.020) *
***PTEN*-deficient *ERG*-negative prostate cancer (n=34)**			
Unadjusted	high	-	-
***NDUFB8*-min**	low	1.18 (0.61-2.31, *p*=0.619)	1.69 (0.64-4.47, *p*=0.286)
Unadjusted	high	-	-
***MTCO1*-max**	low	0.57 (0.29-1.15, *p*=0.115)	0.44 (0.17-1.16, *p*=0.099)

Table C-2: Cox regression models for unadjusted OXPHOS marker metrics based upon *PTEN* and *ERG* status amongst 190 patients. Hazard ratios (HR) reported with 95% confidence interval (CI), using the high-expression group as reference. Multivariable Cox regression model adjusted for age, PSA at diagnosis, Gleason group, clinical tumour stage, and presence of metastasis. *PTEN* status unavailable for 4 *ERG*-low cases. ERG status unavailable for 16 *PTEN*-high and 27 *PTEN*-low cases. *P* values calculated using Cox regression are represented as * $p<0.05$, ** $p<0.01$, and *** $p<0.001$.

C (ii). Comparison with proteomic studies

Mean data from tumour samples and normal-adjacent controls were available from a previous studying evaluating the proteome of primary prostate cancer (Iglesias-Gato *et al.*, 2016). Tumour samples had increased TOMM20 and MTCO1, and decreased NDUFB8 protein.

	Raw values			Normalised to TOMM20		
	Σ Intensity L (C)	**Σ Intensity L (T)**	**T/C**	**Σ Intensity L (C)**	**Σ Intensity L (T)**	**T/C**
NDUFB8	4.52×10^9	2.58×10^{10}	5.71	20.5	15.5	0.76
MTCO1	2.37×10^8	2.71×10^9	11.43	0.0524	0.105	2.00
TOMM20	2.21×10^8	1.66×10^9	7.55	-	-	-

Table C-3: Validation of OXPHOS alterations in primary proteome of prostate cancer. Proteomic data for *NDUFB8*, *MTCO1* and *TOMM20* from tumour and control prostate tissue reported both as raw values and normalised to mitochondrial mass marker *TOMM20*. Data from Iglesias-Gato *et al*. (2016).

Appendix D Supplementary data for Chapter 7

D (i). Additional lifespan data

As compared to published literature, the Polg-HOM colony at Cardiff had a significantly shorter lifespan, with a median survival of 201.5 days (**Figure D-1**). Polg-HOM mice at Newcastle were, in contrast, maintained up to planned humane euthanasia at 11 months of age (median 321 days) based on lifespan data from prior studies. The reduced lifespan of Polg-HOM mice observed in the Cardiff cohort may be due to variation in animal husbandry practices (conventional cages at Cardiff and individually ventilated cages at Newcastle), diet, environmental pathogens, and genetic backgrounds across different laboratories. Thus, all subsequent comparisons are based upon mice bred at Cardiff, to minimise any such potential biases.

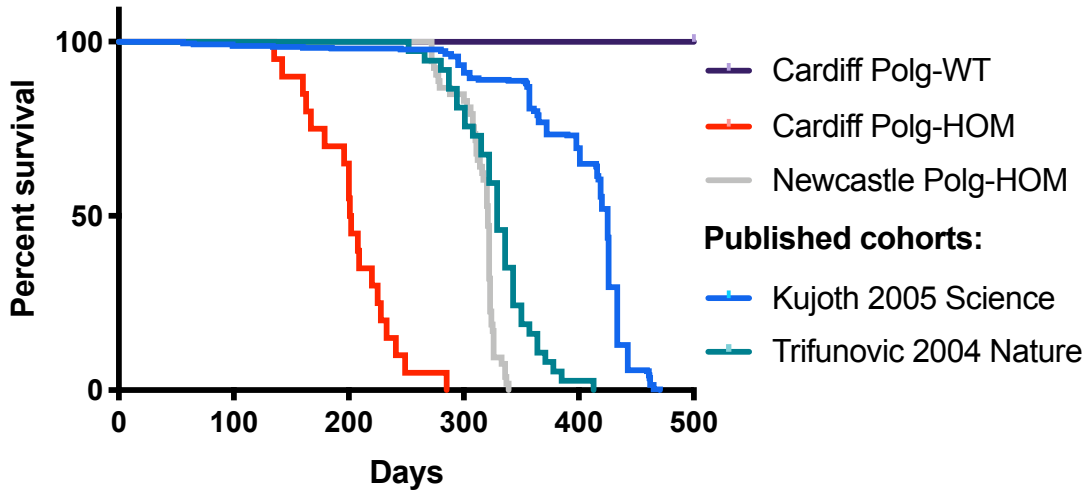

Polg-HOM mice	N	p value	Median survival
Cardiff cohort	20	-	201.5 days
Newcastle cohort	53	<0.001	321 days
Trifunovic 2004 Nature	37	<0.001	329 days
Kujoth 2005 Science	230	<0.001	416 days

Figure D-1: Kaplan-Meier survival curves for Polg mutator mouse colonies at Cardiff and Newcastle. For comparison, lifespan data for Polg-HOM mice in previously published cohorts from Kujoth *et al.* (2005) and Trifunovic *et al.* (2004) are included. Number of mice, median survival and results of log-rank test are reported, using the Cardiff *Polg*-HOM mouse cohort as reference.

D (ii). Raw prostate weights at 200 days

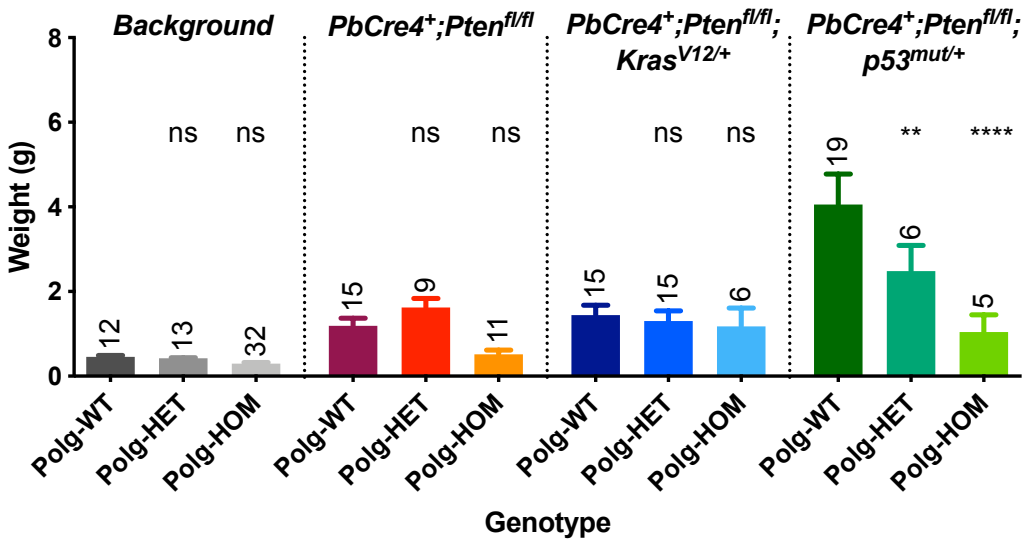

Figure D-2: Raw weights of transgenic mouse cohorts at 200 days.

D (iii). Histopathology at 200 days

Genetic background	Polg genotype	Total	Normal	Hyperplasia	PIN	HGPIN	Invasion	Sarcomatoid
Background	Polg-WT	11	100% (11/11)					
	Polg-HET	9	100% (9/9)					
	Polg-HOM	27	93% (25/27)	7% (2/27)				
PbCre4+;Ptenfl/fl	Polg-WT	15			33% (5/15)	7% (1/15)	60% (9/15)	
	Polg-HET	9			22% (2/9)	56% (5/9)	22% (2/9)	
	Polg-HOM	11	9% (1/11)		36% (4/11)	18% (2/11)	36% (4/11)	
PbCre4+;Ptenfl/fl; KrasV12/+	Polg-WT	8			25% (2/8)		50% (4/8)	25% (2/8)
	Polg-HET	12				17% (2/12)	75% (9/12)	8% (1/12)
	Polg-HOM	5			20% (1/5)		80% (4/5)	
PbCre4+;Ptenfl/fl; p53mut/+	Polg-WT	28				4% (1/28)	14% (4/28)	82% (23/28)
	Polg-HET	7		14% (1/7)	14% (1/7)	14% (1/7)		57% (4/7)
	Polg-HOM	5			20% (1/5)	60% (3/5)	20% (1/5)	

Table D-4: Histopathology of transgenic mouse cohorts at 200 days.

D (iv). Mitochondrial dysfunction may suppress metastases – raw data points

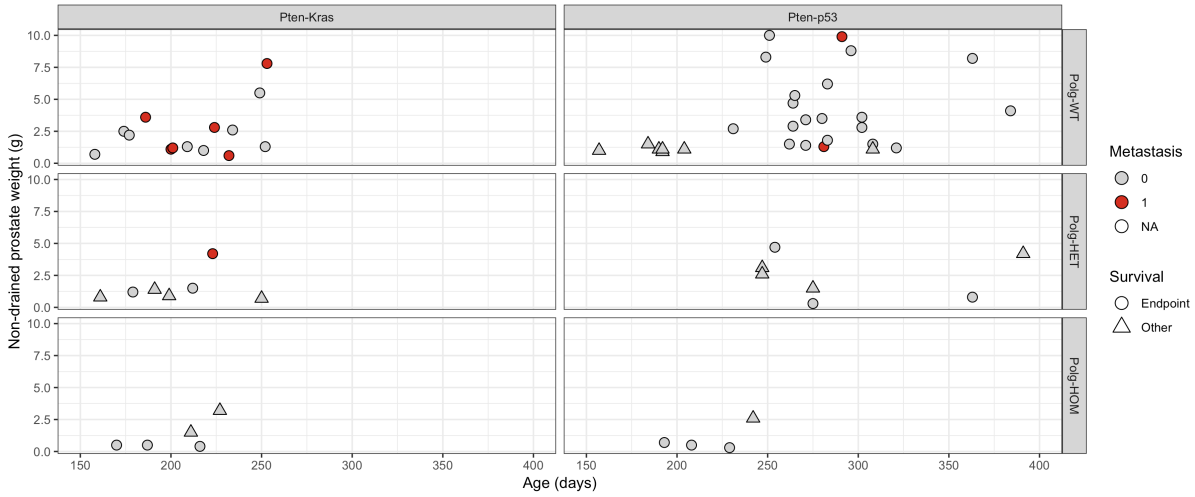

Figure D-3: Incidence of metastasis in tumourigenic mouse models, with advancing chronological age. (A) *PbCre4*$^{+}$*;Pten*$^{fl/fl}$*;Kras*$^{V12/+}$ and (B) *PbCre4*$^{+}$*;Pten*$^{fl/fl}$*; p53*$^{mut/+}$ mouse cohorts.

Appendix E Characterising mitochondrial alterations in prostate cell lines

Mitochondrial function in frequently used prostate cancer cell lines (PC3, LNCaP, 22Rv1, and VCaP), SV40-immortalised prostate epithelial cell lines (PNT1a and PNT2c2) and the experimental PC3 cell line with inducible-*PTEN* (PC3-PTEN, used in chapter 7) were characterised, to evaluate baseline mitochondrial characteristics for future perturbation experiments. This included probing cell lysates for OXPHOS protein abundance, mitochondrial stress test using the Seahorse Flux Analyser, long-range PCR of the mitochondrial genome and next generation mtDNA sequencing using the Ion Torrent Personal Genome machine. Nuclear and mitochondrial encoded OXPHOS gene mutations were also extracted from the Cancer Cell Line Encyclopaedia (Ghandi *et al.*, 2019) to validate results of mtDNA sequencing.

E (i). mtDNA deletions

Long-range PCR or prostate cell lines found no long-range mtDNA deletions (**Figure E-1**).

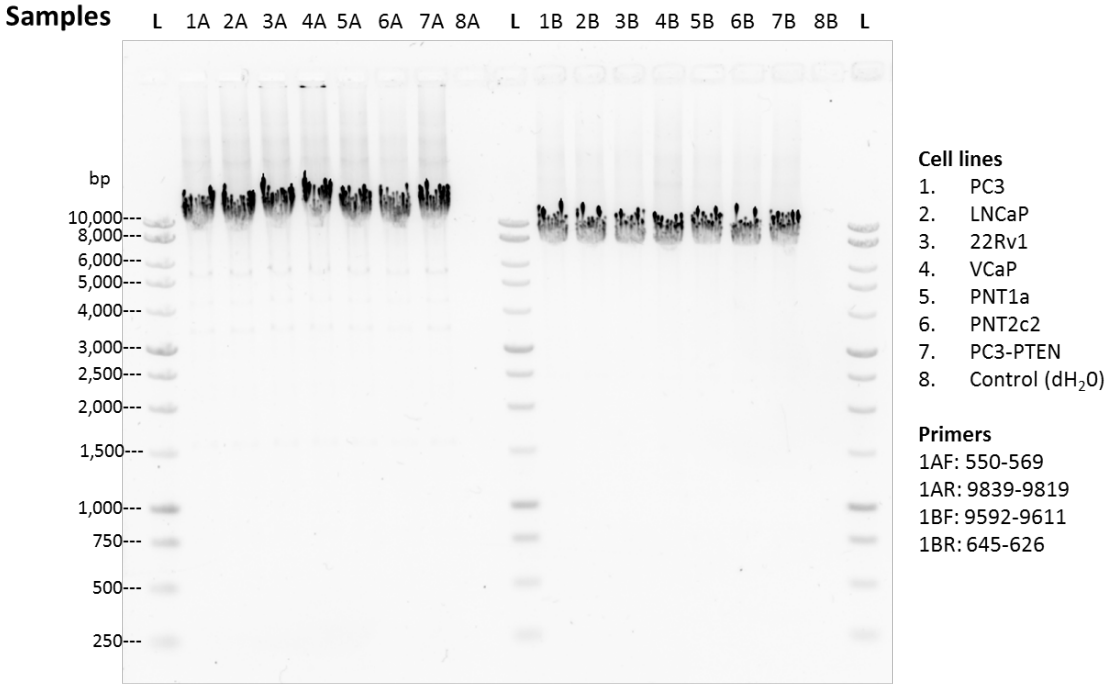

Figure E-1: Long-range PCR of prostate cell lines. These data confirm the absence of mtDNA deletions across all cell lines.

E (ii). mtDNA mutations in prostate cell lines

Non-synonymous mtDNA mutations					% Homoplasmy in prostate epithelial cell lines							Number of mutated cell lines
Mutation	Gene	Amino acid change	Polymorphic frequency	MutPred2 score	PC3	PC3-PTEN	LNCaP	22Rv1	VCaP	PNT1a	PNT2c2	
Complex I												
m.4216T>C	MT-ND1	Tyr304His	9.9%	0.094							100	1
m.4732A>G	MT-ND2	Asn88Ser	0.7%	0.148				99.8				1
m.10398A>C	MT-ND3	Thr114Pro	0.0%	0.447					99.8			1
m.10398A>G	MT-ND3	Thr114Ala	44.2%	0.203							99.9	1
m.10550A>C	MT-ND4L	Met27Ile	0.0%	0.483					99.9			1
m.11120T>C	MT-ND4	Phe121Leu	0.0%	0.091	99.6	99.7						2
m.11467A>C	MT-ND4	Leu236Phe	0.0%	0.623					99.9			1
m.13708G>A	MT-ND5	Ala458Thr	6.9%	0.067							99.5	1
m.13802C>T	MT-ND5	Thr489Met	0.1%	0.081	99.2	99.6						2
m.13879T>C	MT-ND5	Ser515Pro	0.8%	0.199				99.4		100		2
m.13966A>G	MT-ND5	Thr544Ala	1.4%	0.249				99.4				1
m.14138T>C	MT-ND5	Leu601Pro	0.0%	0.573				73.2		74.8		2
Complex III												
m.14766C>T	MT-CYB	Thr7Ile	76.0%	0.064	99.7	99.8	99.8	99.9		99.8	99.8	6
m.14793A>G	MT-CYB	His16Arg	2.3%	0.224	99.6	99.8						2
m.14798T>C	MT-CYB	Phe18Leu	7.4%	0.127					99.8		99.3	2
m.15218A>G	MT-CYB	Thr158Ala	2.0%	0.169	99.9	99.9						2
m.15326A>C	MT-CYB	Thr194Pro	0.0%	0.164					99.8			1
m.15326A>G	MT-CYB	Thr194Ala	98.9%	0.097	100	99.9	100	100		100	100	6
m.15452C>A	MT-CYB	Leu236Ile	9.2%	0.086							99.9	1
m.15672T>C	MT-CYB	Met309Thr	0.1%	0.054				99.8		99.9		2
Complex IV												
m.5985G>A	MT-CO1	Val28Ile	0.1%	0.089				99.6				1
m.8239C>A	MT-CO2	Ile218Met	0.0%	0.071		12.8						1
m.9247G>A	MT-CO3	Ser14Asn	0.0%	0.224				99.7				1
m.9477G>A	MT-CO3	Val91Ile	4.2%	0.328	99.7	99.8		100				3
Complex V												
m.8860A>G	MT-ATP6	Thr112Ala	99.0%	0.288	100	100	99.9	99.9	99.8	100	99.8	7
m.9055G>A	MT-ATP6	Ala177Thr	5.0%	0.297					99.7			1
tRNA												
m.15900T>C	MT-TT	-	0.1%	-							100	1
m.15916T>C	MT-TT	-	0.0%	-							99.9	1
Total non-synonymous mutations					8	9	3	11	7	6	10	54
						Legend:	>80% Homoplasmic mutation			<80% Heteroplasmic mutation		

Table E-1: Non-synonymous mtDNA mutations identified in prostate cell lines. Associated amino acid change, polymorphic frequency, MutPred2 score and heteroplasmy are reported. Only the following mutations were also observed in the human TCMA-PRAD cohort (Chapter 3): m.13708G>A (*MT-ND5*, PNT2c2), m.9247G>A (*MT-CO3*, 22Rv1), and m.9055G>A (*MT-ATP6*, VCaP).

Cell line	Complex	Gene	Mutation	Protein Change	Validated
PC3_PROSTATE	I	MT-ND4	m.11120T>C	p.F121L	Y
PC3_PROSTATE	I	MT-ND5	m.13802C>T	p.T489I	Y
PC3_PROSTATE	III	MT-CYB	m.14793A>G	p.H16R	Y
PC3_PROSTATE	III	MT-CYB	m.15218A>G	p.T158A	Y
LNCAPCLONEFGC_PROSTATE	III	MT-CYB	m.15497G>A	p.G251S	N
LNCAPCLONEFGC_PROSTATE	V	MT-ATP6	m.8940C>G	p.I138M	N (8860)
22RV1_PROSTATE	I	MT-ND2	m.4732A>G	p.N88S	Y
22RV1_PROSTATE	I	MT-ND5	m.13637A>G	p.Q434R	N
22RV1_PROSTATE	IV	MT-CO3	m.9477G>A	p.V91I	Y
22RV1_PROSTATE	IV	MT-CO1	m.5985G>A	p.V28I	Y
22RV1_PROSTATE	IV	MT-CO3	m.9247G>A	p.S14N	Y
22RV1_PROSTATE	IV	MT-CO2	m.7768A>G	p.I61M	N
VCAP_PROSTATE	III	MT-CYB	m.15884G>A	p.A380T	N
VCAP_PROSTATE	III	MT-CYB	m.14766C>T	p.T7I	Y

Table E-2: Non-synonymous mtDNA mutations validated using previous data. Data from Cancer Cell Line Encyclopaedia (Ghandi *et al.*, 2019).

Mutations in nuclear-encoded OXPHOS subunits in prostate cancer cell lines

Complex	Gene	PC3		LNCaP		22Rv1		VCaP		DU145		MDAPCA2B		NCIH660	
		MUT	mRNA	MUT	mRNA	MUT	mRNA	MUT	mRNA	MUT	mRNA	MUT	mRNA	MUT	mRNA
Complex I	NDUFA1														
	NDUFA10														DOWN
	NDUFA11								DOWN						
	NDUFA12														
	NDUFA13														
	NDUFA2														
	NDUFA3												UP		DOWN
	NDUFA5				UP		UP		UP						
	NDUFA6														
	NDUFA7														
	NDUFA8														
	NDUFA9														DOWN
	NDUFAB1														
	NDUFB1												UP		
	NDUFB10						UP						UP		
	NDUFB11														
	NDUFB2						UP								
	NDUFB3														
	NDUFB4											HOMDEL			
	NDUFB5														
	NDUFB6														
	NDUFB7										DOWN				
	NDUFB8			HOMDEL											DOWN
	NDUFB9	AMP	UP												UP
	NDUFC1												UP		
	NDUFC2								UP				UP		
	NDUFS1														
	NDUFS2				UP		UP						UP		
	NDUFS3														
	NDUFS4														
	NDUFS5														
	NDUFS6														
	NDUFS7														
	NDUFS8							AMP	UP						
	NDUFV1							AMP	UP						
	NDUFV2	AMP													
	NDUFV3														
Complex II	SDHA									AMP					
	SDHB			HOMDEL											
	SDHC						UP								
	SDHD														
Complex III	CYC1	AMP	UP				UP						UP		
	UQCR10														
	UQCR11														
	UQCRB	AMP	UP						UP				UP		
	UQCRC1		UP												
	UQCRC2														
	UQCRFS1														
	UQCRH														
	UQCRQ														
Complex IV	COX4I1							HOMDEL	DOWN						DOWN
	COX4I2														
	COX5A														
	COX5B														
	COX6A1														
	COX6A2														
	COX6B1														UP
	COX6B2														
	COX6C	AMP	UP										UP		UP
	COX7A1														
	COX7A2						UP								
	COX7B														
	COX7B2														
	COX7C	AMP													
	COX8A						UP	AMP	UP	AMP					
	COX8C														
Complex V	ATP5A1														
	ATP5B						UP								
	ATP5C1														
	ATP5D														
	ATP5E														
	ATP5F1					HOMDEL									
	ATP5G1	AMP													
	ATP5G2						UP								
	ATP5G3					HOMDEL									
	ATP5H	AMP													
	ATP5I														
	ATP5J														
	ATP5J2						UP								
	ATP5L														
	ATP5L2														
	ATP5O														
	ATPIF1				UP		UP								UP

Legend: AMP Gene amplification; HOMDEL Deep deletion; UP mRNA upregulation; DOWN mRNA downregulation

Table E-3: Non-synonymous nuclear-encoded OXPHOS mutations and mRNA alterations in prostate cell lines. Data from Cancer Cell Line Encyclopaedia (Ghandi *et al.*, 2019).

E (iii). OXPHOS protein abundance in prostate cell lines

Cell lysates from prostate cell lines were probed for subunits of OXPHOS complexes by western blotting (**Figure E-2**), with markers for Complex I (*NDUFB8*) and IV (*MTCO1*) quantified and normalised for mitochondrial mass (*SDHA*).

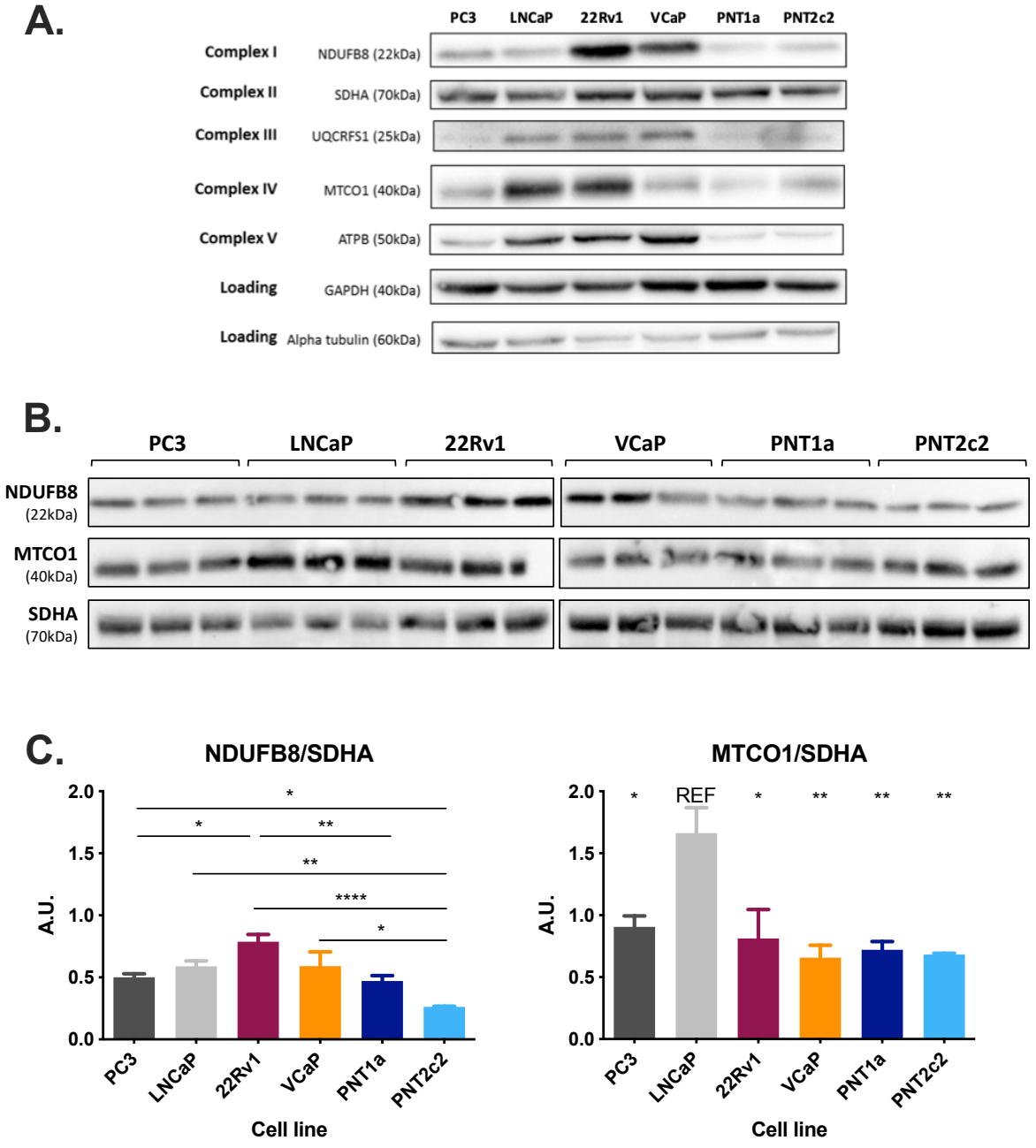

Figure E-2: OXPHOS protein abundance in prostate cell lines. (A) Western blots probing OXPHOS complexes and loading controls. **(B)** Western blots used for quantification of protein abundance. **(C)** Protein abundance of Complex I (*NDUFB8*) and Complex IV (*MTCO1*) normalised to mitochondrial mass (*SDHA*). Error bars denote standard error of measurement.

E (iv). Metabolic phenotypes of prostate cell lines

Prostate cell lines were subjected to the mitochondrial stress test on the Seahorse metabolic flux analyser, after incubating for 72 hours in RPMI growth media. The resulting data were used to estimate ATP production through glycolysis and OXPHOS (**Figure E-3**). PNT2C2 cell line was found to be most metabolically active, with greater total ATP production as compared to both LNCaP and 22Rv1 lines. Glycolytic ATP production was greater than OXPHOS ATP production in the PC3 cell line. OXPHOS ATP production was comparable across all cell lines, whereas glycolytic ATP production was greatest in PNT2c2 and PC3 cell lines, in comparison to the remaining lines. Complex I protein abundance was inversely associated with glycolytic ATP production (**Figure E-4**).

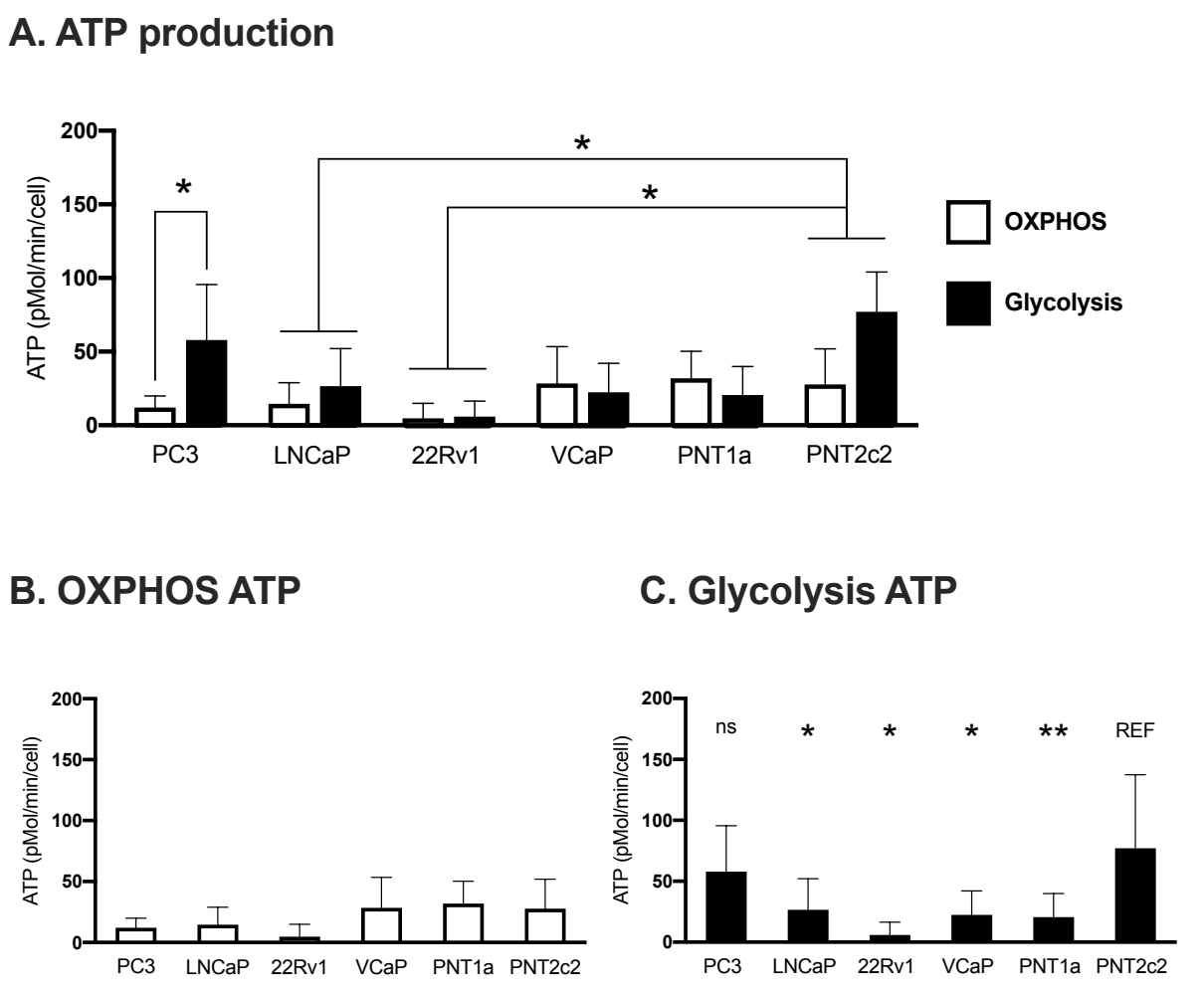

Figure E-3: Metabolic phenotype of prostate cell lines. ATP production vai OXPHOS and glycolysis were compared using one-way ANOVA test. Error bars denote standard deviation. P values denoted as * and **, represent $p<0.05$ and $p<0.01$, respectively. REF: reference cell line; ns: not significant.

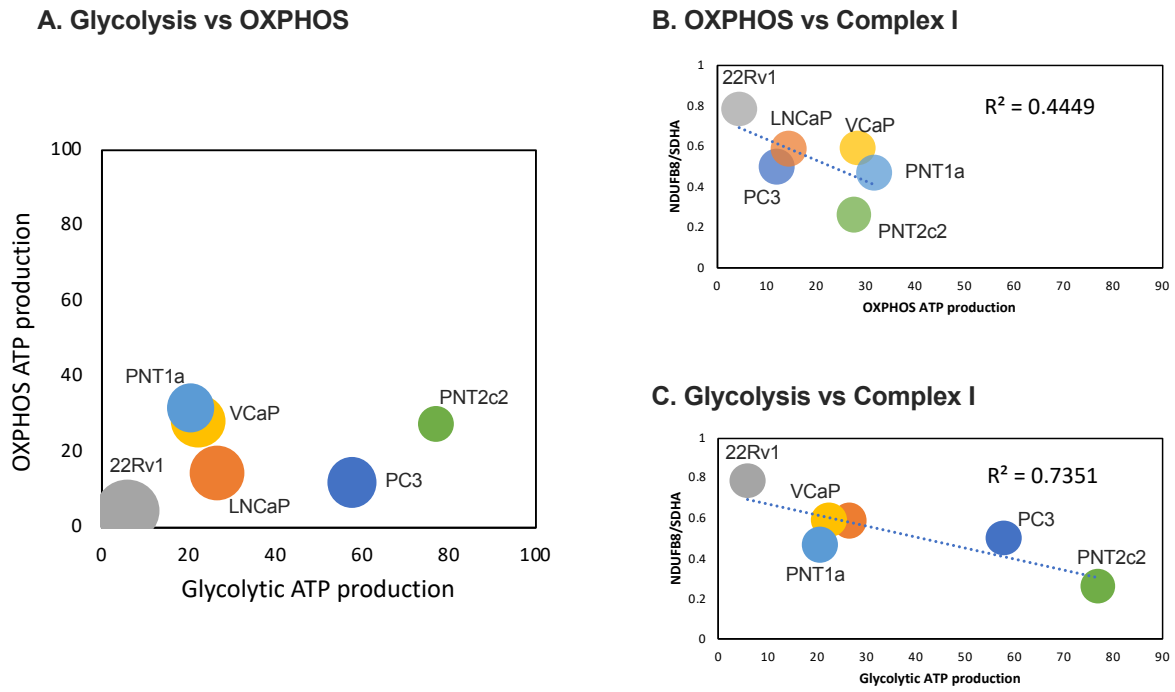

Figure E-4: Impact of Complex I protein abundance on metabolic phenotype of prostate cell lines. **(A)** ATP production using glycolysis vs OXPHOS. Bubble size represents *NDUFB8*/*SDHA* abundance (N=3 replicates). **(B)** ATP production using OXPHOS vs *NDUFB8*/*SDHA* abundance. **(C)** ATP production using glycolysis vs *NDUFB8*/*SDHA* abundance. Cell lines names are annotated. R^2 value of linear regression trend lines in panels B and C are reported. Units used for ATP production were pmol/min/cell.

Bibliography

Aaron, L., Franco, O.E. and Hayward, S.W. (2016) 'Review of Prostate Anatomy and Embryology and the Etiology of Benign Prostatic Hyperplasia', *Urol Clin North Am*, 43(3), pp. 279-88.

Abida, W., Cyrta, J., Heller, G., Prandi, D., Armenia, J., Coleman, I., Cieslik, M., Benelli, M., Robinson, D., Van Allen, E.M., Sboner, A., Fedrizzi, T., Mosquera, J.-M., Robinson, B.D., De Sarkar, N., Kunju, L.P., Tomlins, S., Wu, Y.-M., Nava Rodrigues, D., Loda, M., Gopalan, A., Reuter, V.E., Pritchard, C.C., Mateo, J., Bianchini, D., Miranda, S., Carreira, S., Rescigno, P., Filipenko, J., Vinson, J., Montgomery, R.B., Beltran, H., Heath, E.I., Scher, H.I., Kantoff, P.W., Taplin, M.-E., Schultz, N., deBono, J.S., Demichelis, F., Nelson, P.S., Rubin, M.A., Chinnaiyan, A.M. and Sawyers, C.L. (2019) 'Genomic correlates of clinical outcome in advanced prostate cancer.', *Proceedings of the National Academy of Sciences of the United States of America*, 116(23), pp. 11428-11436.

Abouassaly, R., Tan, N., Moussa, A. and Jones, J.S. (2008) 'Risk of prostate cancer after diagnosis of atypical glands suspicious for carcinoma on saturation and traditional biopsies', *J Urol*, 180(3), pp. 911-4; discussion 914.

Abramowitz, M.C., Li, T., Buyyounouski, M.K., Ross, E., Uzzo, R.G., Pollack, A. and Horwitz, E.M. (2008) 'The Phoenix definition of biochemical failure predicts for overall survival in patients with prostate cancer', *Cancer*, 112(1), pp. 55-60.

Afanas'ev, I. (2011) 'Reactive oxygen species signaling in cancer: comparison with aging', *Aging Dis*, 2(3), pp. 219-30.

Ahearn, T.U., Pettersson, A., Ebot, E.M., Gerke, T., Graff, R.E., Morais, C.L., Hicks, J.L., Wilson, K.M., Rider, J.R., Sesso, H.D., Fiorentino, M., Flavin, R., Finn, S., Giovannucci, E.L., Loda, M., Stampfer, M.J., De Marzo, A.M., Mucci, L.A. and Lotan, T.L. (2016) 'A Prospective Investigation of PTEN Loss and ERG Expression in Lethal Prostate Cancer', *J Natl Cancer Inst*, 108(2), p. djv346.

Ahlqvist, K.J., Hamalainen, R.H., Yatsuga, S., Uutela, M., Terzioglu, M., Gotz, A., Forsstrom, S., Salven, P., Angers-Loustau, A., Kopra, O.H., Tyynismaa, H., Larsson, N.G., Wartiovaara, K., Prolla, T., Trifunovic, A. and Suomalainen, A. (2012) 'Somatic progenitor cell vulnerability to mitochondrial DNA mutagenesis underlies progeroid phenotypes in Polg mutator mice', *Cell Metab*, 15(1), pp. 100-9.

Ahmed, H.U., El-Shater Bosaily, A., Brown, L.C., Gabe, R., Kaplan, R., Parmar, M.K., Collaco-Moraes, Y., Ward, K., Hindley, R.G., Freeman, A., Kirkham, A.P., Oldroyd, R., Parker, C., Emberton, M. and group, P.s. (2017a) 'Diagnostic accuracy of multi-parametric MRI and TRUS biopsy in prostate cancer (PROMIS): a paired validating confirmatory study', *Lancet*, 389(10071), pp. 815-822.

Ahmed, S.T., Alston, C.L., Hopton, S., He, L., Hargreaves, I.P., Falkous, G., Olahova, M., McFarland, R., Turnbull, D.M., Rocha, M.C. and Taylor, R.W. (2017b) 'Using a quantitative quadruple immunofluorescent assay to diagnose isolated mitochondrial Complex I deficiency', *Sci Rep*, 7(1), p. 15676.

Akinyemiju, T., Sakhuja, S., Waterbor, J., Pisu, M. and Altekruse, S.F. (2018) 'Racial/ethnic disparities in de novo metastases sites and survival outcomes for patients with primary breast, colorectal, and prostate cancer', *Cancer Med*, 7(4), pp. 1183-1193.

Akram, M. (2014) 'Citric acid cycle and role of its intermediates in metabolism', *Cell Biochem Biophys*, 68(3), pp. 475-8.

Al Kadhi, O., Traka, M.H., Melchini, A., Troncoso-Rey, P., Jurkowski, W., Defernez, M., Pachori, P., Mills, R.D., Ball, R.Y. and Mithen, R.F. (2017) 'Increased transcriptional and metabolic capacity for lipid metabolism in the peripheral zone of the prostate may underpin its increased susceptibility to cancer', *Oncotarget*, 8(49), pp. 84902-84916.

Alexander, G.A. and Brawley, O.W. (1998) 'Prostate cancer treatment outcome in blacks and whites: a summary of the literature', *Semin Urol Oncol*, 16(4), pp. 232-4.

Alexandrov, L.B., Nik-Zainal, S., Wedge, D.C., Aparicio, S.A., Behjati, S., Biankin, A.V., Bignell, G.R., Bolli, N., Borg, A., Borresen-Dale, A.L., Boyault, S., Burkhardt, B., Butler, A.P., Caldas, C., Davies, H.R., Desmedt, C., Eils, R., Eyfjord, J.E., Foekens, J.A., Greaves, M., Hosoda, F., Hutter, B., Ilicic, T., Imbeaud, S., Imielinski, M., Jager, N., Jones, D.T., Jones, D., Knappskog, S., Kool, M., Lakhani, S.R., Lopez-Otin, C., Martin, S., Munshi, N.C., Nakamura, H., Northcott, P.A., Pajic, M., Papaemmanuil, E., Paradiso, A., Pearson, J.V., Puente, X.S., Raine, K., Ramakrishna, M., Richardson, A.L., Richter, J., Rosenstiel, P., Schlesner, M., Schumacher, T.N., Span, P.N., Teague, J.W., Totoki, Y., Tutt, A.N., Valdes-Mas, R., van Buuren, M.M., van 't Veer, L., Vincent-Salomon, A., Waddell, N., Yates, L.R., Australian Pancreatic Cancer Genome, I., Consortium, I.B.C., Consortium, I.M.-S., PedBrain, I., Zucman-Rossi, J., Futreal, P.A., McDermott, U., Lichter, P., Meyerson, M., Grimmond, S.M., Siebert, R., Campo, E., Shibata, T., Pfister, S.M., Campbell, P.J. and Stratton, M.R. (2013) 'Signatures of mutational processes in human cancer', *Nature*, 500(7463), pp. 415-21.

Alexeyev, M., Shokolenko, I., Wilson, G. and LeDoux, S. (2013) 'The maintenance of mitochondrial DNA integrity--critical analysis and update', *Cold Spring Harb Perspect Biol*, 5(5), p. a012641.

Ali, A.T., Boehme, L., Carbajosa, G., Seitan, V.C., Small, K.S. and Hodgkinson, A. (2019) 'Nuclear genetic regulation of the human mitochondrial transcriptome', *Elife*, 8.

Allott, E.H., Geradts, J., Sun, X., Cohen, S.M., Zirpoli, G.R., Khoury, T., Bshara, W., Chen, M., Sherman, M.E., Palmer, J.R., Ambrosone, C.B., Olshan, A.F. and Troester, M.A. (2016) 'Intratumoral heterogeneity as a source of discordance in breast cancer biomarker classification', *Breast Cancer Res*, 18(1), p. 68.

Ameur, A., Stewart, J.B., Freyer, C., Hagstrom, E., Ingman, M., Larsson, N.G. and Gyllensten, U. (2011) 'Ultra-deep sequencing of mouse mitochondrial DNA: mutational patterns and their origins', *PLoS Genet*, 7(3), p. e1002028.

Amin, M.M., Jeyaganth, S., Fahmy, N., Begin, L., Aronson, S., Jacobson, S., Tanguay, S. and Aprikian, A.G. (2007) 'Subsequent prostate cancer detection in patients with prostatic intraepithelial neoplasia or atypical small acinar proliferation', *Can Urol Assoc J*, 1(3), pp. 245-9.

Anders, S., Pyl, P.T. and Huber, W. (2015) 'HTSeq--a Python framework to work with high-throughput sequencing data', *Bioinformatics*, 31(2), pp. 166-9.

Anderson, S., Bankier, A.T., Barrell, B.G., de Bruijn, M.H., Coulson, A.R., Drouin, J., Eperon, I.C., Nierlich, D.P., Roe, B.A., Sanger, F., Schreier, P.H., Smith, A.J., Staden, R. and Young, I.G. (1981) 'Sequence and organization of the human mitochondrial genome', *Nature*, 290(5806), pp. 457-65.

Angajala, A., Lim, S., Phillips, J.B., Kim, J.H., Yates, C., You, Z. and Tan, M. (2018) 'Diverse Roles of Mitochondria in Immune Responses: Novel Insights Into Immuno-Metabolism', *Front Immunol*, 9, p. 1605.

Angelo, M., Bendall, S.C., Finck, R., Hale, M.B., Hitzman, C., Borowsky, A.D., Levenson, R.M., Lowe, J.B., Liu, S.D., Zhao, S., Natkunam, Y. and Nolan, G.P. (2014) 'Multiplexed ion beam imaging of human breast tumors', *Nat Med*, 20(4), pp. 436-42.

Armenia, J., Wankowicz, S.A.M., Liu, D., Gao, J., Kundra, R., Reznik, E., Chatila, W.K., Chakravarty, D., Han, G.C., Coleman, I., Montgomery, B., Pritchard, C., Morrissey, C., Barbieri, C.E., Beltran, H., Sboner, A., Zafeiriou, Z., Miranda, S., Bielski, C.M., Penson, A.V., Tolonen, C., Huang, F.W., Robinson, D., Wu, Y.M., Lonigro, R., Garraway, L.A., Demichelis, F., Kantoff, P.W., Taplin, M.E., Abida, W., Taylor, B.S., Scher, H.I., Nelson, P.S., de Bono, J.S., Rubin, M.A., Sawyers, C.L., Chinnaiyan, A.M., Team, P.S.C.I.P.C.D., Schultz, N. and Van Allen, E.M. (2018) 'The long tail of oncogenic drivers in prostate cancer', *Nat Genet*, 50(5), pp. 645-651.

Arnold, R.S., Fedewa, S.A., Goodman, M., Osunkoya, A.O., Kissick, H.T., Morrissey, C., True, L.D. and Petros, J.A. (2015) 'Bone metastasis in prostate cancer: Recurring mitochondrial DNA mutation reveals selective pressure exerted by the bone microenvironment', *Bone*, 78, pp. 81-6.

Arnold, R.S., Sun, C.Q., Richards, J.C., Grigoriev, G., Coleman, I.M., Nelson, P.S., Hsieh, C.L., Lee, J.K., Xu, Z., Rogatko, A., Osunkoya, A.O., Zayzafoon, M., Chung, L. and Petros, J.A. (2009) 'Mitochondrial DNA mutation stimulates prostate cancer growth in bone stromal environment', *Prostate*, 69(1), pp. 1-11.

Ashtiani, Z.O., Heidari, M., Hasheminasab, S.M., Ayati, M. and Rakhshani, N. (2012) 'Mitochondrial D-Loop polymorphism and microsatellite instability in prostate cancer and benign hyperplasia patients', *Asian Pac J Cancer Prev*, 13(8), pp. 3863-8.

Ashton, T.M., McKenna, W.G., Kunz-Schughart, L.A. and Higgins, G.S. (2018) 'Oxidative Phosphorylation as an Emerging Target in Cancer Therapy', *Clin Cancer Res*, 24(11), pp. 2482-2490.

Assel, M., Dahlin, A., Ulmert, D., Bergh, A., Stattin, P., Lilja, H. and Vickers, A.J. (2018) 'Association Between Lead Time and Prostate Cancer Grade: Evidence of Grade Progression from Long-term Follow-up of Large Population-based Cohorts Not Subject to Prostate-specific Antigen Screening', *Eur Urol*, 73(6), pp. 961-967.

Attard, G., Reid, A.H., Yap, T.A., Raynaud, F., Dowsett, M., Settatree, S., Barrett, M., Parker, C., Martins, V., Folkerd, E., Clark, J., Cooper, C.S., Kaye, S.B., Dearnaley, D., Lee, G. and de Bono, J.S. (2008) 'Phase I clinical trial of a selective inhibitor of CYP17, abiraterone acetate, confirms that castration-resistant prostate cancer commonly remains hormone driven', *J Clin Oncol*, 26(28), pp. 4563-71.

Attard, G., Swennenhuis, J.F., Olmos, D., Reid, A.H., Vickers, E., A'Hern, R., Levink, R., Coumans, F., Moreira, J., Riisnaes, R., Oommen, N.B., Hawche, G., Jameson, C., Thompson, E., Sipkema, R., Carden, C.P., Parker, C., Dearnaley, D., Kaye, S.B., Cooper, C.S., Molina, A., Cox, M.E., Terstappen, L.W. and de Bono, J.S. (2009) 'Characterization of ERG, AR and PTEN gene status in circulating tumor cells from patients with castration-resistant prostate cancer', *Cancer Res*, 69(7), pp. 2912-8.

Awwad, H.M., Geisel, J. and Obeid, R. (2012) 'The role of choline in prostate cancer', *Clin Biochem*, 45(18), pp. 1548-53.

Ayala, A.G., Ro, J.Y., Babaian, R., Troncoso, P. and Grignon, D.J. (1989) 'The prostatic capsule: does it exist? Its importance in the staging and treatment of prostatic carcinoma', *Am J Surg Pathol*, 13(1), pp. 21-7.

Bai, Y. and Attardi, G. (1998) 'The mtDNA-encoded ND6 subunit of mitochondrial NADH dehydrogenase is essential for the assembly of the membrane arm and the respiratory function of the enzyme', *EMBO J*, 17(16), pp. 4848-58.

Baines, H. (2014) *Using mouse models to learn about mitochondrial DNA point mutations in ageing and disease*. Newcastle University.

Baines, H.L., Stewart, J.B., Stamp, C., Zupanic, A., Kirkwood, T.B., Larsson, N.G., Turnbull, D.M. and Greaves, L.C. (2014) 'Similar patterns of clonally expanded somatic mtDNA mutations in the colon of heterozygous mtDNA mutator mice and ageing humans', *Mech Ageing Dev*, 139, pp. 22-30.

Bajpai, P., Koc, E., Sonpavde, G., Singh, R. and Singh, K.K. (2019) 'Mitochondrial localization, import, and mitochondrial function of the androgen receptor', *J Biol Chem*, 294(16), pp. 6621-6634.

Balk, S.P., Ko, Y.J. and Bubley, G.J. (2003) 'Biology of prostate-specific antigen', *J Clin Oncol*, 21(2), pp. 383-91.

Baradaran, R., Berrisford, J.M., Minhas, G.S. and Sazanov, L.A. (2013) 'Crystal structure of the entire respiratory complex I', *Nature*, 494(7438), pp. 443-8.

Barbieri, C.E., Baca, S.C., Lawrence, M.S., Demichelis, F., Blattner, M., Theurillat, J.P., White, T.A., Stojanov, P., Van Allen, E., Stransky, N., Nickerson, E., Chae, S.S., Boysen, G., Auclair, D., Onofrio, R.C., Park, K., Kitabayashi, N., MacDonald, T.Y., Sheikh, K., Vuong, T., Guiducci, C., Cibulskis, K., Sivachenko, A., Carter, S.L., Saksena, G., Voet, D., Hussain, W.M., Ramos, A.H., Winckler, W., Redman, M.C., Ardlie, K., Tewari, A.K., Mosquera, J.M., Rupp, N., Wild, P.J., Moch, H., Morrissey, C., Nelson, P.S., Kantoff, P.W., Gabriel, S.B., Golub, T.R., Meyerson, M., Lander, E.S., Getz, G., Rubin, M.A. and Garraway, L.A. (2012) 'Exome sequencing identifies recurrent SPOP, FOXA1 and MED12 mutations in prostate cancer', *Nat Genet*, 44(6), pp. 685-9.

Bardella, C., Pollard, P.J. and Tomlinson, I. (2011) 'SDH mutations in cancer', *Biochim Biophys Acta*, 1807(11), pp. 1432-43.

Barshad, G., Blumberg, A., Cohen, T. and Mishmar, D. (2018) 'Human primitive brain displays negative mitochondrial-nuclear expression correlation of respiratory genes', *Genome Res*, 28(7), pp. 952-967.

Baughman, J.M., Perocchi, F., Girgis, H.S., Plovanich, M., Belcher-Timme, C.A., Sancak, Y., Bao, X.R., Strittmatter, L., Goldberger, O., Bogorad, R.L., Koteliansky, V. and Mootha, V.K. (2011) 'Integrative genomics identifies MCU as an essential component of the mitochondrial calcium uniporter', *Nature*, 476(7360), pp. 341-5.

Bayona-Bafaluy, M.P., Manfredi, G. and Moraes, C.T. (2003) 'A chemical enucleation method for the transfer of mitochondrial DNA to rho(o) cells', *Nucleic Acids Res*, 31(16), p. e98.

Bechis, S.K., Carroll, P.R. and Cooperberg, M.R. (2011) 'Impact of age at diagnosis on prostate cancer treatment and survival', *J Clin Oncol*, 29(2), pp. 235-41.

Beckers, A., Organe, S., Timmermans, L., Scheys, K., Peeters, A., Brusselmans, K., Verhoeven, G. and Swinnen, J.V. (2007) 'Chemical inhibition of acetyl-CoA carboxylase induces growth arrest and cytotoxicity selectively in cancer cells', *Cancer Res*, 67(17), pp. 8180-7.

Begley, L.A., Kasina, S., MacDonald, J. and Macoska, J.A. (2008) 'The inflammatory microenvironment of the aging prostate facilitates cellular proliferation and hypertrophy', *Cytokine*, 43(2), pp. 194-9.

Bell, K.J., Del Mar, C., Wright, G., Dickinson, J. and Glasziou, P. (2015) 'Prevalence of incidental prostate cancer: A systematic review of autopsy studies', *Int J Cancer*, 137(7), pp. 1749-57.

Beltran, H., Prandi, D., Mosquera, J.M., Benelli, M., Puca, L., Cyrta, J., Marotz, C., Giannopoulou, E., Chakravarthi, B.V., Varambally, S., Tomlins, S.A., Nanus, D.M., Tagawa, S.T., Van Allen, E.M., Elemento, O., Sboner, A., Garraway, L.A., Rubin, M.A. and Demichelis, F. (2016) 'Divergent clonal evolution of castration-resistant neuroendocrine prostate cancer', *Nat Med*, 22(3), pp. 298-305.

Berg, K.D., Vainer, B., Thomsen, F.B., Roder, M.A., Gerds, T.A., Toft, B.G., Brasso, K. and Iversen, P. (2014) 'ERG protein expression in diagnostic specimens is associated with increased risk of progression during active surveillance for prostate cancer', *Eur Urol*, 66(5), pp. 851-60.

Berquin, I.M., Min, Y., Wu, R., Wu, H. and Chen, Y.Q. (2005) 'Expression signature of the mouse prostate', *J Biol Chem*, 280(43), pp. 36442-51.

Betz, C., Stracka, D., Prescianotto-Baschong, C., Frieden, M., Demaurex, N. and Hall, M.N. (2013) 'Feature Article: mTOR complex 2-Akt signaling at mitochondria-associated endoplasmic reticulum membranes (MAM) regulates mitochondrial physiology', *Proc Natl Acad Sci U S A*, 110(31), pp. 12526-34.

Bhandari, V., Hoey, C., Liu, L.Y., Lalonde, E., Ray, J., Livingstone, J., Lesurf, R., Shiah, Y.J., Vujcic, T., Huang, X., Espiritu, S.M.G., Heisler, L.E., Yousif, F., Huang, V., Yamaguchi, T.N., Yao, C.Q., Sabelnykova, V.Y., Fraser, M., Chua, M.L.K., van der Kwast, T., Liu, S.K., Boutros, P.C. and Bristow, R.G. (2019a) 'Molecular landmarks of tumor hypoxia across cancer types', *Nat Genet*, 51(2), pp. 308-318.

Bhandari, V., Li, C.H., Bristow, R.G. and Boutros, P.C. (2019b) 'Divergent mutational processes distinguish hypoxic and normoxic tumours', *bioRxiv*.

Bianchi-Frias, D., Damodarasamy, M., Hernandez, S.A., Gil da Costa, R.M., Vakar-Lopez, F., Coleman, I., Reed, M.J. and Nelson, P.S. (2018) 'The Aged Microenvironment Influences the Tumorigenic Potential of Malignant Prostate Epithelial Cells.', *Molecular cancer research : MCR*, p. molcanres.0522.2018.

Bianchi-Frias, D., Vakar-Lopez, F., Coleman, I.M., Plymate, S.R., Reed, M.J. and Nelson, P.S. (2010) 'The effects of aging on the molecular and cellular composition of the prostate microenvironment', *PLoS One*, 5(9).

Biesterfeld, S., Kraus, H.L., Reineke, T., Muys, L., Mihalcea, A.M. and Rudlowski, C. (2003) 'Analysis of the reliability of manual and automated immunohistochemical staining procedures. A pilot study.', *Analytical and quantitative cytology and histology*, 25(2), pp. 90-96.

Bill-Axelson, A., Holmberg, L., Garmo, H., Rider, J.R., Taari, K., Busch, C., Nordling, S., Haggman, M., Andersson, S.O., Spangberg, A., Andren, O., Palmgren, J., Steineck, G., Adami, H.O. and Johansson, J.E. (2014) 'Radical prostatectomy or watchful waiting in early prostate cancer', *N Engl J Med*, 370(10), pp. 932-42.

Birbach, A. (2013) 'Use of PB-Cre4 mice for mosaic gene deletion.', *PLoS ONE*, 8(1), p. e53501.

Blackwood, J.K., Williamson, S.C., Greaves, L.C., Wilson, L., Rigas, A.C., Sandher, R., Pickard, R.S., Robson, C.N., Turnbull, D.M., Taylor, R.W. and Heer, R. (2011) 'In situ lineage tracking of human prostatic epithelial stem cell fate reveals a common clonal origin for basal and luminal cells', *J Pathol*, 225(2), pp. 181-8.

Blattner, M., Liu, D., Robinson, B.D., Huang, D., Poliakov, A., Gao, D., Nataraj, S., Deonarine, L.D., Augello, M.A., Sailer, V., Ponnala, L., Ittmann, M., Chinnaiyan, A.M., Sboner, A., Chen, Y., Rubin, M.A. and Barbieri, C.E. (2017) 'SPOP Mutation Drives Prostate Tumorigenesis In Vivo through Coordinate Regulation of PI3K/mTOR and AR Signaling.', *Cancer Cell*, 31(3), pp. 436-451.

Bodenmiller, B. (2016) 'Multiplexed Epitope-Based Tissue Imaging for Discovery and Healthcare Applications', *Cell Syst*, 2(4), pp. 225-38.

Bogenhagen, D. and Clayton, D.A. (1977) 'Mouse L cell mitochondrial DNA molecules are selected randomly for replication throughout the cell cycle', *Cell*, 11(4), pp. 719-27.

Booker, L.M., Habermacher, G.M., Jessie, B.C., Sun, Q.C., Baumann, A.K., Amin, M., Lim, S.D., Fernandez-Golarz, C., Lyles, R.H., Brown, M.D., Marshall, F.F. and Petros, J.A. (2006) 'North American white mitochondrial haplogroups in prostate and renal cancer', *J Urol*, 175(2), pp. 468-72; discussion 472-3.

Bostwick, D.G., Burke, H.B., Djakiew, D., Euling, S., Ho, S.M., Landolph, J., Morrison, H., Sonawane, B., Shifflett, T., Waters, D.J. and Timms, B. (2004) 'Human prostate cancer risk factors', *Cancer*, 101(10 Suppl), pp. 2371-490.

Bottcher, R., Kweldam, C.F., Livingstone, J., Lalonde, E., Yamaguchi, T.N., Huang, V., Yousif, F., Fraser, M., Bristow, R.G., van der Kwast, T., Boutros, P.C., Jenster, G. and van Leenders, G. (2018) 'Cribriform and intraductal prostate cancer are associated with increased genomic instability and distinct genomic alterations', *BMC Cancer*, 18(1), p. 8.

Boutros, P.C., Fraser, M., Harding, N.J., de Borja, R., Trudel, D., Lalonde, E., Meng, A., Hennings-Yeomans, P.H., McPherson, A., Sabelnykova, V.Y., Zia, A., Fox, N.S., Livingstone, J., Shiah, Y.J., Wang, J., Beck, T.A., Have, C.L., Chong, T., Sam, M., Johns, J., Timms, L., Buchner, N., Wong, A., Watson, J.D., Simmons, T.T., P'ng, C., Zafarana, G., Nguyen, F., Luo, X., Chu, K.C., Prokopec, S.D., Sykes, J., Dal Pra, A., Berlin, A., Brown, A., Chan-Seng-Yue, M.A., Yousif, F., Denroche, R.E., Chong, L.C., Chen, G.M., Jung, E., Fung, C., Starmans, M.H., Chen, H., Govind, S.K., Hawley, J., D'Costa, A., Pintilie, M., Waggott, D., Hach, F., Lambin, P., Muthuswamy, L.B., Cooper, C., Eeles, R., Neal, D., Tetu, B., Sahinalp, C., Stein, L.D., Fleshner, N., Shah, S.P., Collins, C.C., Hudson, T.J., McPherson, J.D., van der Kwast, T. and Bristow, R.G. (2015) 'Spatial genomic heterogeneity within localized, multifocal prostate cancer', *Nat Genet*, 47(7), pp. 736-45.

Bowen, C., Bubendorf, L., Voeller, H.J., Slack, R., Willi, N., Sauter, G., Gasser, T.C., Koivisto, P., Lack, E.E., Kononen, J., Kallioniemi, O.-P. and Gelmann, E.P. (2000) 'Loss of NKX3.1 Expression in Human Prostate Cancers Correlates with Tumor Progression1,2', *Cancer Research*, 60(21), pp. 6111-6115.

Boyle, K.A., Van Wickle, J., Hill, R.B., Marchese, A., Kalyanaraman, B. and Dwinell, M.B. (2018) 'Mitochondria-targeted drugs stimulate mitophagy and abrogate colon cancer cell proliferation.', *Journal of Biological Chemistry*, 293(38), pp. 14891-14904.

Bratic, A. and Larsson, N.-G. (2013) 'The role of mitochondria in aging.', *Journal of Clinical Investigation*, 123(3), pp. 951-957.

Bratt, O., Drevin, L., Akre, O., Garmo, H. and Stattin, P. (2016) 'Family History and Probability of Prostate Cancer, Differentiated by Risk Category: A Nationwide Population-Based Study', *J Natl Cancer Inst*, 108(10).

Broad Institute TCGA Genome Data Analysis Center (2016) 'Broad Institute TCGA Genome Data Analysis Center'.

Brusselmans, K., De Schrijver, E., Verhoeven, G. and Swinnen, J.V. (2005) 'RNA interference-mediated silencing of the acetyl-CoA-carboxylase-alpha gene induces growth inhibition and apoptosis of prostate cancer cells', *Cancer Res*, 65(15), pp. 6719-25.

Bubendorf, L., Schopfer, A., Wagner, U., Sauter, G., Moch, H., Willi, N., Gasser, T.C. and Mihatsch, M.J. (2000) 'Metastatic patterns of prostate cancer: an autopsy study of 1,589 patients', *Hum Pathol*, 31(5), pp. 578-83.

Buffa, F.M., Harris, A.L., West, C.M. and Miller, C.J. (2010) 'Large meta-analysis of multiple cancers reveals a common, compact and highly prognostic hypoxia metagene', *Br J Cancer*, 102(2), pp. 428-35.

Burri, L., Strahm, Y., Hawkins, C.J., Gentle, I.E., Puryer, M.A., Verhagen, A., Callus, B., Vaux, D. and Lithgow, T. (2005) 'Mature DIABLO/Smac is produced by the IMP protease complex on the mitochondrial inner membrane', *Mol Biol Cell*, 16(6), pp. 2926-33.

Cairns, P., Okami, K., Halachmi, S., Halachmi, N., Esteller, M., Herman, J.G., Jen, J., Isaacs, W.B., Bova, G.S. and Sidransky, D. (1997) 'Frequent inactivation of PTEN/MMAC1 in primary prostate cancer', *Cancer Res*, 57(22), pp. 4997-5000.

Calvo, S.E., Clauser, K.R. and Mootha, V.K. (2016) 'MitoCarta2.0: an updated inventory of mammalian mitochondrial proteins', *Nucleic Acids Res*, 44(D1), pp. D1251-7.

Camp, R.L., Chung, G.G. and Rimm, D.L. (2002) 'Automated subcellular localization and quantification of protein expression in tissue microarrays', *Nat Med*, 8(11), pp. 1323-7.

Cancer Genome Atlas Research, N. (2015) 'The Molecular Taxonomy of Primary Prostate Cancer', *Cell*, 163(4), pp. 1011-25.

Cancer Research UK (2019) *Prostate cancer*. Available at: https://www.cancerresearchuk.org/health-professional/cancer-statistics/statistics-by-cancer-type/prostate-cancer (Accessed: 21 September 2019).

Canter, J.A., Kallianpur, A.R. and Fowke, J.H. (2006) 'Re: North American white mitochondrial haplogroups in prostate and renal cancer', *J Urol*, 176(5), pp. 2308-9; author reply 2309.

Carstens, J.L., Correa de Sampaio, P., Yang, D., Barua, S., Wang, H., Rao, A., Allison, J.P., LeBleu, V.S. and Kalluri, R. (2017) 'Spatial computation of intratumoral T cells correlates with survival of patients with pancreatic cancer', *Nat Commun*, 8, p. 15095.

Carver, B.S., Chapinski, C., Wongvipat, J., Hieronymus, H., Chen, Y., Chandarlapaty, S., Arora, V.K., Le, C., Koutcher, J., Scher, H., Scardino, P.T., Rosen, N. and Sawyers, C.L. (2011) 'Reciprocal feedback regulation of PI3K and androgen receptor signaling in PTEN-deficient prostate cancer', *Cancer Cell*, 19(5), pp. 575-86.

Carver, B.S., Tran, J., Gopalan, A., Chen, Z., Shaikh, S., Carracedo, A., Alimonti, A., Nardella, C., Varmeh, S., Scardino, P.T., Cordon-Cardo, C., Gerald, W. and Pandolfi, P.P. (2009) 'Aberrant ERG expression cooperates with loss of PTEN to promote cancer progression in the prostate.', *Nature genetics*, 41(5), pp. 619-624.

Castellano, E. and Downward, J. (2011) 'RAS Interaction with PI3K: More Than Just Another Effector Pathway', *Genes Cancer*, 2(3), pp. 261-74.

Castro, E., Goh, C., Leongamornlert, D., Saunders, E., Tymrakiewicz, M., Dadaev, T., Govindasami, K., Guy, M., Ellis, S., Frost, D., Bancroft, E., Cole, T., Tischkowitz, M., Kennedy, M.J., Eason, J., Brewer, C., Evans, D.G., Davidson, R., Eccles, D., Porteous, M.E., Douglas, F., Adlard, J., Donaldson, A., Antoniou, A.C., Kote-Jarai, Z., Easton, D.F., Olmos, D. and Eeles, R. (2015) 'Effect of BRCA Mutations on Metastatic Relapse and Cause-specific Survival After Radical Treatment for Localised Prostate Cancer', *Eur Urol*, 68(2), pp. 186-93.

Castro, E., Goh, C., Olmos, D., Saunders, E., Leongamornlert, D., Tymrakiewicz, M., Mahmud, N., Dadaev, T., Govindasami, K., Guy, M., Sawyer, E., Wilkinson, R., Ardern-Jones, A., Ellis, S., Frost, D., Peock, S., Evans, D.G., Tischkowitz, M., Cole, T., Davidson, R., Eccles, D., Brewer, C., Douglas, F., Porteous, M.E., Donaldson, A., Dorkins, H., Izatt, L., Cook, J., Hodgson, S., Kennedy, M.J., Side, L.E., Eason, J., Murray, A., Antoniou, A.C., Easton, D.F., Kote-Jarai, Z. and Eeles, R. (2013) 'Germline BRCA mutations are associated with higher risk of nodal involvement, distant metastasis, and poor survival outcomes in prostate cancer', *J Clin Oncol*, 31(14), pp. 1748-57.

Cerami, E., Gao, J., Dogrusoz, U., Gross, B.E., Sumer, S.O., Aksoy, B.A., Jacobsen, A., Byrne, C.J., Heuer, M.L., Larsson, E., Antipin, Y., Reva, B., Goldberg, A.P., Sander, C. and Schultz, N. (2012) 'The cBio cancer genomics portal: an open platform for exploring multidimensional cancer genomics data', *Cancer Discov*, 2(5), pp. 401-4.

Chang, C.S., Saltzman, A.G., Hiipakka, R.A., Huang, I.Y. and Liao, S.S. (1987) 'Prostatic spermine-binding protein. Cloning and nucleotide sequence of cDNA, amino acid sequence, and androgenic control of mRNA level', *J Biol Chem*, 262(6), pp. 2826-31.

Chang, J.Y., Yi, H.S., Kim, H.W. and Shong, M. (2017) 'Dysregulation of mitophagy in carcinogenesis and tumor progression', *Biochim Biophys Acta Bioenerg*, 1858(8), pp. 633-640.

Chatterjee, A., Mambo, E. and Sidransky, D. (2006) 'Mitochondrial DNA mutations in human cancer', *Oncogene*, 25(34), pp. 4663-74.

Chaudhary, A.K., Bhat, T.A., Kumar, S., Kumar, A., Kumar, R., Underwood, W., Koochekpour, S., Shourideh, M., Yadav, N., Dhar, S. and Chandra, D. (2016) 'Mitochondrial dysfunction-mediated apoptosis resistance associates with defective heat shock protein response in African-American men with prostate cancer', *Br J Cancer*, 114(10), pp. 1090-100.

Chaux, A., Albadine, R., Toubaji, A., Hicks, J., Meeker, A., Platz, E.A., De Marzo, A.M. and Netto, G.J. (2011) 'Immunohistochemistry for ERG expression as a surrogate for TMPRSS2-ERG fusion detection in prostatic adenocarcinomas', *Am J Surg Pathol*, 35(7), pp. 1014-20.

Chen, F., Zhang, Y., Gibbons, D.L., Deneen, B., Kwiatkowski, D.J., Ittmann, M. and Creighton, C.J. (2018) 'Pan-Cancer Molecular Classes Transcending Tumor Lineage Across 32 Cancer Types, Multiple Data Platforms, and over 10,000 Cases', *Clinical Cancer Research*, 24(9), pp. 2182-2193.

Chen, G., Gharib, T.G., Huang, C.C., Taylor, J.M., Misek, D.E., Kardia, S.L., Giordano, T.J., Iannettoni, M.D., Orringer, M.B., Hanash, S.M. and Beer, D.G. (2002a) 'Discordant protein and mRNA expression in lung adenocarcinomas', *Mol Cell Proteomics*, 1(4), pp. 304-13.

Chen, J.Z., Gokden, N., Greene, G.F., Green, B. and Kadlubar, F.F. (2003) 'Simultaneous generation of multiple mitochondrial DNA mutations in human prostate tumors suggests mitochondrial hyper-mutagenesis', *Carcinogenesis*, 24(9), pp. 1481-7.

Chen, J.Z., Gokden, N., Greene, G.F., Mukunyadzi, P. and Kadlubar, F.F. (2002b) 'Extensive somatic mitochondrial mutations in primary prostate cancer using laser capture microdissection', *Cancer Res*, 62(22), pp. 6470-4.

Chen, M.L., Logan, T.D., Hochberg, M.L., Shelat, S.G., Yu, X., Wilding, G.E., Tan, W., Kujoth, G.C., Prolla, T.A., Selak, M.A., Kundu, M., Carroll, M. and Thompson, J.E. (2009) 'Erythroid dysplasia, megaloblastic anemia, and impaired lymphopoiesis arising from mitochondrial dysfunction.', *Blood*, 114(19), pp. 4045-4053.

Chen, N., Wen, S., Sun, X., Fang, Q., Huang, L., Liu, S., Li, W. and Qiu, M. (2016) 'Elevated Mitochondrial DNA Copy Number in Peripheral Blood and Tissue Predict the Opposite Outcome of Cancer: A Meta-Analysis', *Sci Rep*, 6, p. 37404.

Chen, P.L., Chen, C.F., Chen, Y., Guo, X.E., Huang, C.K., Shew, J.Y., Reddick, R.L., Wallace, D.C. and Lee, W.H. (2013a) 'Mitochondrial genome instability resulting from SUV3 haploinsufficiency leads to tumorigenesis and shortened lifespan', *Oncogene*, 32(9), pp. 1193-201.

Chen, S., Huang, V., Xu, X., Livingstone, J., Soares, F., Jeon, J., Zeng, Y., Hua, J.T., Petricca, J., Guo, H., Wang, M., Yousif, F., Zhang, Y., Donmez, N., Ahmed, M., Volik, S., Lapuk, A., Chua, M.L.K., Heisler, L.E., Foucal, A., Fox, N.S., Fraser, M., Bhandari, V., Shiah, Y.J., Guan, J., Li, J., Orain, M., Picard, V., Hovington, H., Bergeron, A., Lacombe, L., Fradet, Y., Tetu, B., Liu, S., Feng, F., Wu, X., Shao, Y.W., Komor, M.A., Sahinalp, C., Collins, C., Hoogstrate, Y., de Jong, M., Fijneman, R.J.A., Fei, T., Jenster, G., van der Kwast, T., Bristow, R.G., Boutros, P.C. and He, H.H. (2019) 'Widespread and Functional RNA Circularization in Localized Prostate Cancer', *Cell*, 176(4), pp. 831-843 e22.

Chen, Y., Chi, P., Rockowitz, S., Iaquinta, P.J., Shamu, T., Shukla, S., Gao, D., Sirota, I., Carver, B.S., Wongvipat, J., Scher, H.I., Zheng, D. and Sawyers, C.L. (2013b) 'ETS factors reprogram the androgen receptor cistrome and prime prostate tumorigenesis in response to PTEN loss', *Nature Medicine*, 19(8), pp. 1023-1029.

Chen, Z., Trotman, L.C., Shaffer, D., Lin, H.K., Dotan, Z.A., Niki, M., Koutcher, J.A., Scher, H.I., Ludwig, T., Gerald, W., Cordon-Cardo, C. and Pandolfi, P.P. (2005) 'Crucial role of p53-dependent cellular senescence in suppression of Pten-deficient tumorigenesis', *Nature*, 436(7051), pp. 725-30.

Cheng, G., Zielonka, J., Ouari, O., Lopez, M., McAllister, D., Boyle, K., Barrios, C.S., Weber, J.J., Johnson, B.D., Hardy, M., Dwinell, M.B. and Kalyanaraman, B. (2016) 'Mitochondria-Targeted Analogues of Metformin Exhibit Enhanced Antiproliferative and Radiosensitizing Effects in Pancreatic Cancer Cells', *Cancer Research*, 76(13), pp. 3904-3915.

Choi, W.S., Kim, H.W., Tronche, F., Palmiter, R.D., Storm, D.R. and Xia, Z. (2017) 'Conditional deletion of Ndufs4 in dopaminergic neurons promotes Parkinson's disease-like non-motor symptoms without loss of dopamine neurons', *Sci Rep*, 7, p. 44989.

Christian, B.E. and Spremulli, L.L. (2009) 'Evidence for an active role of IF3mt in the initiation of translation in mammalian mitochondria', *Biochemistry*, 48(15), pp. 3269-78.

Chung, J.H., Dewal, N., Sokol, E., Mathew, P., Whitehead, R., Millis, S.Z., Frampton, G.M., Bratslavsky, G., Pal, S.K., Lee, R.J., Necchi, A., Gregg, J.P., Lara, P., Jr., Antonarakis, E.S., Miller, V.A., Ross, J.S., Ali, S.M. and Agarwal, N. (2019) 'Prospective Comprehensive Genomic Profiling of Primary and Metastatic Prostate Tumors', *JCO Precis Oncol*, 3.

Clay Montier, L.L., Deng, J.J. and Bai, Y. (2009) 'Number matters: control of mammalian mitochondrial DNA copy number.', *Journal of genetics and genomics = Yi chuan xue bao*, 36(3), pp. 125-131.

Clayton, D.A. (1982) 'Replication of animal mitochondrial DNA', *Cell*, 28(4), pp. 693-705.

Cluntun, A.A., Lukey, M.J., Cerione, R.A. and Locasale, J.W. (2017) 'Glutamine Metabolism in Cancer: Understanding the Heterogeneity', *Trends Cancer*, 3(3), pp. 169-180.

Clutter, M.R., Heffner, G.C., Krutzik, P.O., Sachen, K.L. and Nolan, G.P. (2010) 'Tyramide signal amplification for analysis of kinase activity by intracellular flow cytometry', *Cytometry A*, 77(11), pp. 1020-31.

Cohen, R.J., Shannon, B.A., Phillips, M., Moorin, R.E., Wheeler, T.M. and Garrett, K.L. (2008) 'Central zone carcinoma of the prostate gland: a distinct tumor type with poor prognostic features', *J Urol*, 179(5), pp. 1762-7; discussion 1767.

Cole, L.W. (2016) 'The Evolution of Per-cell Organelle Number', *Front Cell Dev Biol*, 4, p. 85.

Coller, H.A., Khrapko, K., Bodyak, N.D., Nekhaeva, E., Herrero-Jimenez, P. and Thilly, W.G. (2001) 'High frequency of homoplasmic mitochondrial DNA mutations in human tumors can be explained without selection', *Nat Genet*, 28(2), pp. 147-50.

Conde-Perez, A., Gros, G., Longvert, C., Pedersen, M., Petit, V., Aktary, Z., Viros, A., Gesbert, F., Delmas, V., Rambow, F., Bastian, B.C., Campbell, A.D., Colombo, S., Puig, I., Bellacosa, A., Sansom, O., Marais, R., Van Kempen, L.C. and Larue, L. (2015) 'A caveolin-dependent and PI3K/AKT-independent role of PTEN in beta-catenin transcriptional activity', *Nat Commun*, 6, p. 8093.

Conteduca, V., Oromendia, C., Eng, K.W., Bareja, R., Sigouros, M., Molina, A., Faltas, B.M., Sboner, A., Mosquera, J.M., Elemento, O., Nanus, D.M., Tagawa, S.T., Ballman, K.V. and Beltran, H. (2019) 'Clinical features of neuroendocrine prostate cancer', *European Journal of Cancer*, 121, pp. 7-18.

Cookson, M.S., Aus, G., Burnett, A.L., Canby-Hagino, E.D., D'Amico, A.V., Dmochowski, R.R., Eton, D.T., Forman, J.D., Goldenberg, S.L., Hernandez, J., Higano, C.S., Kraus, S.R., Moul, J.W., Tangen, C., Thrasher, J.B. and Thompson, I. (2007) 'Variation in the definition of biochemical recurrence in patients treated for localized prostate cancer: the American Urological Association Prostate Guidelines for Localized Prostate Cancer Update Panel report and recommendations for a standard in the reporting of surgical outcomes', *J Urol*, 177(2), pp. 540-5.

Cooper, C.S., Eeles, R., Wedge, D.C., Van Loo, P., Gundem, G., Alexandrov, L.B., Kremeyer, B., Butler, A., Lynch, A.G., Camacho, N., Massie, C.E., Kay, J., Luxton, H.J., Edwards, S., Kote-Jarai, Z., Dennis, N., Merson, S., Leongamornlert, D., Zamora, J., Corbishley, C., Thomas, S., Nik-Zainal, S., O'Meara, S., Matthews, L., Clark, J., Hurst, R., Mithen, R., Bristow, R.G., Boutros, P.C., Fraser, M., Cooke, S., Raine, K., Jones, D., Menzies, A., Stebbings, L., Hinton, J., Teague, J., McLaren, S., Mudie, L., Hardy, C., Anderson, E., Joseph, O., Goody, V., Robinson, B., Maddison, M., Gamble, S., Greenman, C., Berney, D., Hazell, S., Livni, N., Group, I.P., Fisher, C., Ogden, C., Kumar, P., Thompson, A., Woodhouse, C., Nicol, D., Mayer, E., Dudderidge, T., Shah, N.C., Gnanapragasam, V., Voet, T., Campbell, P., Futreal, A., Easton, D., Warren, A.Y., Foster, C.S., Stratton, M.R., Whitaker, H.C., McDermott, U., Brewer, D.S. and Neal, D.E. (2015) 'Analysis of the genetic phylogeny of multifocal prostate cancer identifies multiple independent clonal expansions in neoplastic and morphologically normal prostate tissue', *Nat Genet*, 47(4), pp. 367-372.

Cooper, G.M. (2000) *Bioenergetics and Metabolism - Mitochondria, Chloroplasts, and Peroxisomes*. 2nd edn. Sinauer Associates.

Cortopassi, G.A. and Arnheim, N. (1990) 'Detection of a specific mitochondrial DNA deletion in tissues of older humans', *Nucleic Acids Res*, 18(23), pp. 6927-33.

Costa, R., Peruzzo, R., Bachmann, M., Monta, G.D., Vicario, M., Santinon, G., Mattarei, A., Moro, E., Quintana-Cabrera, R., Scorrano, L., Zeviani, M., Vallese, F., Zoratti, M., Paradisi, C., Argenton, F., Brini, M., Cali, T., Dupont, S., Szabo, I. and Leanza, L. (2019) 'Impaired Mitochondrial ATP Production Downregulates Wnt Signaling via ER Stress Induction', *Cell Rep*, 28(8), pp. 1949-1960 e6.

Costello, L.C. and Franklin, R.B. (2006) 'The clinical relevance of the metabolism of prostate cancer; zinc and tumor suppression: connecting the dots', *Mol Cancer*, 5, p. 17.

Costello, L.C., Franklin, R.B. and Feng, P. (2005) 'Mitochondrial function, zinc, and intermediary metabolism relationships in normal prostate and prostate cancer', *Mitochondrion*, 5(3), pp. 143-53.

Costello, L.C., Franklin, R.B. and Narayan, P. (1999) 'Citrate in the diagnosis of prostate cancer', *Prostate*, 38(3), pp. 237-45.

Costello, L.C., Liu, Y., Franklin, R.B. and Kennedy, M.C. (1997) 'Zinc inhibition of mitochondrial aconitase and its importance in citrate metabolism of prostate epithelial cells', *J Biol Chem*, 272(46), pp. 28875-81.

Cottrell, D.A., Blakely, E.L., Johnson, M.A., Ince, P.G., Borthwick, G.M. and Turnbull, D.M. (2001) 'Cytochrome c oxidase deficient cells accumulate in the hippocampus and choroid plexus with age', *Neurobiol Aging*, 22(2), pp. 265-72.

Couto, S.S., Cao, M., Duarte, P.C., Banach-Petrosky, W., Wang, S., Romanienko, P., Wu, H., Cardiff, R.D., Abate-Shen, C. and Cunha, G.R. (2009) 'Simultaneous haploinsufficiency of Pten and Trp53 tumor suppressor genes accelerates tumorigenesis in a mouse model of prostate cancer.', *Differentiation; research in biological diversity*, 77(1), pp. 103-111.

Couvillion, M.T., Soto, I.C., Shipkovenska, G. and Churchman, L.S. (2016) 'Synchronized mitochondrial and cytosolic translation programs.', *Nature*, 533(7604), pp. 499-503.

Creed, J., Klotz, L., Harbottle, A., Maggrah, A., Reguly, B., George, A. and Gnanapragasm, V. (2018) 'A single mitochondrial DNA deletion accurately detects significant prostate cancer in men in the PSA 'grey zone'', *World J Urol*, 36(3), pp. 341-348.

Cruz-Bermúdez, A., Vallejo, C.G., Vicente-Blanco, R.J., Gallardo, M.E., Fernández-Moreno, M.Á., Quintanilla, M. and Garesse, R. (2015) 'Enhanced tumorigenicity by mitochondrial DNA mild mutations.', *Oncotarget*, 6(15), pp. 13628-13643.

Culp, M.B., Soerjomataram, I., Efstathiou, J.A., Bray, F. and Jemal, A. (2019) 'Recent Global Patterns in Prostate Cancer Incidence and Mortality Rates', *Eur Urol*.

Cunha, G.R. (2008) 'Mesenchymal-epithelial interactions: past, present, and future', *Differentiation*, 76(6), pp. 578-86.

Cunha, G.R., Ricke, W., Thomson, A., Marker, P.C., Risbridger, G., Hayward, S.W., Wang, Y.Z., Donjacour, A.A. and Kurita, T. (2004) 'Hormonal, cellular, and molecular regulation of normal and neoplastic prostatic development', *J Steroid Biochem Mol Biol*, 92(4), pp. 221-36.

Currie, E., Schulze, A., Zechner, R., Walther, T.C. and Farese, R.V., Jr. (2013) 'Cellular fatty acid metabolism and cancer', *Cell Metab*, 18(2), pp. 153-61.

Cussenot, O., Berthon, P., Berger, R., Mowszowicz, I., Faille, A., Hojman, F., Teillac, P., Le Duc, A. and Calvo, F. (1991) 'Immortalization of human adult normal prostatic epithelial cells by liposomes containing large T-SV40 gene', *J Urol*, 146(3), pp. 881-6.

Cuzick, J., Swanson, G.P., Fisher, G., Brothman, A.R., Berney, D.M., Reid, J.E., Mesher, D., Speights, V.O., Stankiewicz, E., Foster, C.S., Moller, H., Scardino, P., Warren, J.D., Park, J., Younus, A., Flake, D.D., 2nd, Wagner, S., Gutin, A., Lanchbury, J.S., Stone, S. and Transatlantic Prostate, G. (2011) 'Prognostic value of an RNA expression signature derived from cell cycle proliferation genes in patients with prostate cancer: a retrospective study', *Lancet Oncol*, 12(3), pp. 245-55.

Cyll, K., Ersvaer, E., Vlatkovic, L., Pradhan, M., Kildal, W., Avranden Kjaer, M., Kleppe, A., Hveem, T.S., Carlsen, B., Gill, S., Loffeler, S., Haug, E.S., Waehre, H., Sooriakumaran, P. and Danielsen, H.E. (2017) 'Tumour heterogeneity poses a significant challenge to cancer biomarker research', *Br J Cancer*, 117(3), pp. 367-375.

Dai, D.F., Chen, T., Wanagat, J., Laflamme, M., Marcinek, D.J., Emond, M.J., Ngo, C.P., Prolla, T.A. and Rabinovitch, P.S. (2010) 'Age-dependent cardiomyopathy in mitochondrial mutator mice is attenuated by overexpression of catalase targeted to mitochondria', *Aging Cell*, 9(4), pp. 536-44.

Davis, I.D., Martin, A.J., Stockler, M.R., Begbie, S., Chi, K.N., Chowdhury, S., Coskinas, X., Frydenberg, M., Hague, W.E., Horvath, L.G., Joshua, A.M., Lawrence, N.J., Marx, G., McCaffrey, J., McDermott, R., McJannett, M., North, S.A., Parnis, F., Parulekar, W., Pook, D.W., Reaume, M.N., Sandhu, S.K., Tan, A., Tan, T.H., Thomson, A., Tu, E., Vera-Badillo, F., Williams, S.G., Yip, S., Zhang, A.Y., Zielinski, R.R., Sweeney, C.J., Investigators, E.T., the, A., New Zealand, U. and Prostate Cancer Trials, G. (2019) 'Enzalutamide with Standard First-Line Therapy in Metastatic Prostate Cancer', *N Engl J Med*, 381(2), pp. 121-131.

De Stefani, D., Raffaello, A., Teardo, E., Szabo, I. and Rizzuto, R. (2011) 'A forty-kilodalton protein of the inner membrane is the mitochondrial calcium uniporter', *Nature*, 476(7360), pp. 336-40.

Di Cristofano, A., Pesce, B., Cordon-Cardo, C. and Pandolfi, P.P. (1998) 'Pten is essential for embryonic development and tumour suppression', *Nat Genet*, 19(4), pp. 348-55.

Diaz, F., Garcia, S., Hernandez, D., Regev, A., Rebelo, A., Oca-Cossio, J. and Moraes, C.T. (2008) 'Pathophysiology and fate of hepatocytes in a mouse model of mitochondrial hepatopathies', *Gut*, 57(2), pp. 232-42.

Diaz, F., Thomas, C.K., Garcia, S., Hernandez, D. and Moraes, C.T. (2005) 'Mice lacking COX10 in skeletal muscle recapitulate the phenotype of progressive mitochondrial myopathies associated with cytochrome c oxidase deficiency.', *Human Molecular Genetics*, 14(18), pp. 2737-2748.

Dilly, A.K., Ekambaram, P., Guo, Y., Cai, Y., Tucker, S.C., Fridman, R., Kandouz, M. and Honn, K.V. (2013) 'Platelet-type 12-lipoxygenase induces MMP9 expression and cellular invasion via activation of PI3K/Akt/NF-kappaB', *Int J Cancer*, 133(8), pp. 1784-91.

Dimmen, M., Vlatkovic, L., Hole, K.H., Nesland, J.M., Brennhovd, B. and Axcrona, K. (2012) 'Transperineal prostate biopsy detects significant cancer in patients with elevated prostate-specific antigen (PSA) levels and previous negative transrectal biopsies', *BJU Int*, 110(2 Pt 2), pp. E69-75.

Director's Challenge Consortium for the Molecular Classification of Lung, A., Shedden, K., Taylor, J.M., Enkemann, S.A., Tsao, M.S., Yeatman, T.J., Gerald, W.L., Eschrich, S., Jurisica, I., Giordano, T.J., Misek, D.E., Chang, A.C., Zhu, C.Q., Strumpf, D., Hanash, S., Shepherd, F.A., Ding, K., Seymour, L., Naoki, K., Pennell, N., Weir, B., Verhaak, R., Ladd-Acosta, C., Golub, T., Gruidl, M., Sharma, A., Szoke, J., Zakowski, M., Rusch, V., Kris, M., Viale, A., Motoi, N., Travis, W., Conley, B., Seshan, V.E., Meyerson, M., Kuick, R., Dobbin, K.K., Lively, T., Jacobson, J.W. and Beer, D.G. (2008) 'Gene expression-based survival prediction in lung adenocarcinoma: a multi-site, blinded validation study', *Nat Med*, 14(8), pp. 822-7.

Dixon, A.R., Bathany, C., Tsuei, M., White, J., Barald, K.F. and Takayama, S. (2015) 'Recent developments in multiplexing techniques for immunohistochemistry.', *Expert review of molecular diagnostics*, 15(9), pp. 1171-1186.

Dobin, A., Davis, C.A., Schlesinger, F., Drenkow, J., Zaleski, C., Jha, S., Batut, P., Chaisson, M. and Gingeras, T.R. (2013) 'STAR: ultrafast universal RNA-seq aligner', *Bioinformatics*, 29(1), pp. 15-21.

Dobson, P.F., Rocha, M.C., Grady, J.P., Chrysostomou, A., Hipps, D., Watson, S., Greaves, L.C., Deehan, D.J. and Turnbull, D.M. (2016) 'Unique quadruple immunofluorescence assay demonstrates mitochondrial respiratory chain dysfunction in osteoblasts of aged and PolgA(-/-) mice', *Sci Rep*, 6, p. 31907.

Donovan, J.L., Hamdy, F.C., Lane, J.A., Mason, M., Metcalfe, C., Walsh, E., Blazeby, J.M., Peters, T.J., Holding, P., Bonnington, S., Lennon, T., Bradshaw, L., Cooper, D., Herbert, P., Howson, J., Jones, A., Lyons, N., Salter, E., Thompson, P., Tidball, S., Blaikie, J., Gray, C., Bollina, P., Catto, J., Doble, A., Doherty, A., Gillatt, D., Kockelbergh, R., Kynaston, H., Paul, A., Powell, P., Prescott, S., Rosario, D.J., Rowe, E., Davis, M., Turner, E.L., Martin, R.M., Neal, D.E. and Protec, T.S.G. (2016) 'Patient-Reported Outcomes after Monitoring, Surgery, or Radiotherapy for Prostate Cancer', *N Engl J Med*, 375(15), pp. 1425-1437.

Drost, F.H., Osses, D.F., Nieboer, D., Steyerberg, E.W., Bangma, C.H., Roobol, M.J. and Schoots, I.G. (2019) 'Prostate MRI, with or without MRI-targeted biopsy, and systematic biopsy for detecting prostate cancer', *Cochrane Database Syst Rev*, 4, p. CD012663.

Drummond, F.J., Carsin, A.E., Sharp, L. and Comber, H. (2009) 'Factors prompting PSA-testing of asymptomatic men in a country with no guidelines: a national survey of general practitioners', *BMC Fam Pract*, 10, p. 3.

Eckel-Passow, J.E., Lohse, C.M., Sheinin, Y., Crispen, P.L., Krco, C.J. and Kwon, E.D. (2010) 'Tissue microarrays: one size does not fit all', *Diagn Pathol*, 5(1), p. 48.

Edgar, D., Shabalina, I., Camara, Y., Wredenberg, A., Calvaruso, M.A., Nijtmans, L., Nedergaard, J., Cannon, B., Larsson, N.G. and Trifunovic, A. (2009) 'Random point mutations with major effects on protein-coding genes are the driving force behind premature aging in mtDNA mutator mice', *Cell Metab*, 10(2), pp. 131-8.

Edlind, M.P. and Hsieh, A.C. (2014) 'PI3K-AKT-mTOR signaling in prostate cancer progression and androgen deprivation therapy resistance', *Asian J Androl*, 16(3), pp. 378-86.

Efremov, R.G., Baradaran, R. and Sazanov, L.A. (2010) 'The architecture of respiratory complex I', *Nature*, 465(7297), pp. 441-5.

Eidelman, E., Twum-Ampofo, J., Ansari, J. and Siddiqui, M.M. (2017) 'The Metabolic Phenotype of Prostate Cancer', *Front Oncol*, 7, p. 131.

Ellinger, J., Muller, D.C., Muller, S.C., Hauser, S., Heukamp, L.C., von Ruecker, A., Bastian, P.J. and Walgenbach-Brunagel, G. (2012) 'Circulating mitochondrial DNA in serum: a universal diagnostic biomarker for patients with urological malignancies', *Urol Oncol*, 30(4), pp. 509-15.

Ellinger, J., Poss, M., Bruggemann, M., Gromes, A., Schmidt, D., Ellinger, N., Tolkach, Y., Dietrich, D., Kristiansen, G. and Muller, S.C. (2017) 'Systematic Expression Analysis of Mitochondrial Complex I Identifies NDUFS1 as a Biomarker in Clear-Cell Renal-Cell Carcinoma', *Clin Genitourin Cancer*, 15(4), pp. e551-e562.

Elson, J.L., Samuels, D.C., Turnbull, D.M. and Chinnery, P.F. (2001) 'Random intracellular drift explains the clonal expansion of mitochondrial DNA mutations with age', *Am J Hum Genet*, 68(3), pp. 802-6.

Epstein, J.I., Egevad, L., Amin, M.B., Delahunt, B., Srigley, J.R., Humphrey, P.A. and Grading, C. (2016a) 'The 2014 International Society of Urological Pathology (ISUP) Consensus Conference on Gleason Grading of Prostatic Carcinoma: Definition of Grading Patterns and Proposal for a New Grading System', *Am J Surg Pathol*, 40(2), pp. 244-52.

Epstein, J.I., Zelefsky, M.J., Sjoberg, D.D., Nelson, J.B., Egevad, L., Magi-Galluzzi, C., Vickers, A.J., Parwani, A.V., Reuter, V.E., Fine, S.W., Eastham, J.A., Wiklund, P., Han, M., Reddy, C.A., Ciezki, J.P., Nyberg, T. and Klein, E.A. (2016b) 'A Contemporary Prostate Cancer Grading System: A Validated Alternative to the Gleason Score.', *European Urology*, 69(3), pp. 428-435.

Eriksson, M., Ambroise, G., Ouchida, A.T., Lima Queiroz, A., Smith, D., Gimenez-Cassina, A., Iwanicki, M.P., Muller, P.A., Norberg, E. and Vakifahmetoglu-Norberg, H. (2017) 'Effect of Mutant p53 Proteins on Glycolysis and Mitochondrial Metabolism', *Mol Cell Biol*, 37(24).

Esgueva, R., Perner, S., C, J.L., Scheble, V., Stephan, C., Lein, M., Fritzsche, F.R., Dietel, M., Kristiansen, G. and Rubin, M.A. (2010) 'Prevalence of TMPRSS2-ERG and SLC45A3-ERG gene fusions in a large prostatectomy cohort', *Mod Pathol*, 23(4), pp. 539-46.

Espiritu, S.M.G., Liu, L.Y., Rubanova, Y., Bhandari, V., Holgersen, E.M., Szyca, L.M., Fox, N.S., Chua, M.L.K., Yamaguchi, T.N., Heisler, L.E., Livingstone, J., Wintersinger, J., Yousif, F., Lalonde, E., Rouette, A., Salcedo, A., Houlahan, K.E., Li, C.H., Huang, V., Fraser, M., van der Kwast, T., Morris, Q.D., Bristow, R.G. and Boutros, P.C. (2018) 'The Evolutionary Landscape of Localized Prostate Cancers Drives Clinical Aggression', *Cell*, 173(4), pp. 1003-1013 e15.

Falkenberg, M. (2018) 'Mitochondrial DNA replication in mammalian cells: overview of the pathway', *Essays Biochem*, 62(3), pp. 287-296.

Falkenberg, M., Gaspari, M., Rantanen, A., Trifunovic, A., Larsson, N.G. and Gustafsson, C.M. (2002) 'Mitochondrial transcription factors B1 and B2 activate transcription of human mtDNA', *Nat Genet*, 31(3), pp. 289-94.

Fan, S., Tian, T., Chen, W., Lv, X., Lei, X., Zhang, H., Sun, S., Cai, L., Pan, G., He, L., Ou, Z., Lin, X., Wang, X., Perez, M.F., Tu, Z., Ferrone, S., Tannous, B.A. and Li, J. (2019) 'Mitochondrial miRNA Determines Chemoresistance by Reprogramming Metabolism and Regulating Mitochondrial Transcription', *Cancer Res*, 79(6), pp. 1069-1084.

Fan, W., Waymire, K.G., Narula, N., Li, P., Rocher, C., Coskun, P.E., Vannan, M.A., Narula, J., Macgregor, G.R. and Wallace, D.C. (2008) 'A mouse model of mitochondrial disease reveals germline selection against severe mtDNA mutations', *Science*, 319(5865), pp. 958-62.

Fan, Y., Dickman, K.G. and Zong, W.X. (2010) 'Akt and c-Myc differentially activate cellular metabolic programs and prime cells to bioenergetic inhibition', *J Biol Chem*, 285(10), pp. 7324-33.

Faraci, C., Annis, S., Jin, J., Li, H., Khrapko, K. and Woods, D.C. (2018) 'Impact of exercise on oocyte quality in the POLG mitochondrial DNA mutator mouse', *Reproduction*, 156(2), pp. 185-194.

Fawcett, D.W. (1975) 'The mammalian spermatozoon', *Dev Biol*, 44(2), pp. 394-436.

Fedchenko, N. and Reifenrath, J. (2014) 'Different approaches for interpretation and reporting of immunohistochemistry analysis results in the bone tissue - a review', *Diagn Pathol*, 9, p. 221.

Feeley, K.P., Bray, A.W., Westbrook, D.G., Johnson, L.W., Kesterson, R.A., Ballinger, S.W. and Welch, D.R. (2015) 'Mitochondrial Genetics Regulate Breast Cancer Tumorigenicity and Metastatic Potential', *Cancer Res*, 75(20), pp. 4429-36.

Feng, Z., Bethmann, D., Kappler, M., Ballesteros-Merino, C., Eckert, A., Bell, R.B., Cheng, A., Bui, T., Leidner, R., Urba, W.J., Johnson, K., Hoyt, C., Bifulco, C.B., Bukur, J., Wickenhauser, C., Seliger, B. and Fox, B.A. (2017) 'Multiparametric immune profiling in HPV- oral squamous cell cancer', *JCI Insight*, 2(14).

Fisher, R.P., Lisowsky, T., Parisi, M.A. and Clayton, D.A. (1992) 'DNA wrapping and bending by a mitochondrial high mobility group-like transcriptional activator protein', *J Biol Chem*, 267(5), pp. 3358-67.

Fizazi, K., Shore, N., Tammela, T.L., Ulys, A., Vjaters, E., Polyakov, S., Jievaltas, M., Luz, M., Alekseev, B., Kuss, I., Kappeler, C., Snapir, A., Sarapohja, T., Smith, M.R. and Investigators, A. (2019) 'Darolutamide in Nonmetastatic, Castration-Resistant Prostate Cancer', *N Engl J Med*, 380(13), pp. 1235-1246.

Fizazi, K., Tran, N., Fein, L., Matsubara, N., Rodriguez-Antolin, A., Alekseev, B.Y., Ozguroglu, M., Ye, D., Feyerabend, S., Protheroe, A., De Porre, P., Kheoh, T., Park, Y.C., Todd, M.B., Chi, K.N. and Investigators, L. (2017) 'Abiraterone plus Prednisone in Metastatic, Castration-Sensitive Prostate Cancer', *N Engl J Med*, 377(4), pp. 352-360.

Ford, W.C. and Harrison, A. (1984) 'The role of citrate in determining the activity of calcium ions in human semen', *Int J Androl*, 7(3), pp. 198-202.

Fox, R.G., Magness, S., Kujoth, G.C., Prolla, T.A. and Maeda, N. (2012) 'Mitochondrial DNA polymerase editing mutation, PolgD257A, disturbs stem-progenitor cell cycling in the small intestine and restricts excess fat absorption', *Am J Physiol Gastrointest Liver Physiol*, 302(9), pp. G914-24.

Fraser, M., Sabelnykova, V.Y., Yamaguchi, T.N., Heisler, L.E., Livingstone, J., Huang, V., Shiah, Y.J., Yousif, F., Lin, X., Masella, A.P., Fox, N.S., Xie, M., Prokopec, S.D., Berlin, A., Lalonde, E., Ahmed, M., Trudel, D., Luo, X., Beck, T.A., Meng, A., Zhang, J., D'Costa, A., Denroche, R.E., Kong, H., Espiritu, S.M., Chua, M.L., Wong, A., Chong, T., Sam, M., Johns, J., Timms, L., Buchner, N.B., Orain, M., Picard, V.,

Hovington, H., Murison, A., Kron, K., Harding, N.J., P'ng, C., Houlahan, K.E., Chu, K.C., Lo, B., Nguyen, F., Li, C.H., Sun, R.X., de Borja, R., Cooper, C.I., Hopkins, J.F., Govind, S.K., Fung, C., Waggott, D., Green, J., Haider, S., Chan-Seng-Yue, M.A., Jung, E., Wang, Z., Bergeron, A., Dal Pra, A., Lacombe, L., Collins, C.C., Sahinalp, C., Lupien, M., Fleshner, N.E., He, H.H., Fradet, Y., Tetu, B., van der Kwast, T., McPherson, J.D., Bristow, R.G. and Boutros, P.C. (2017) 'Genomic hallmarks of localized, non-indolent prostate cancer', *Nature*, 541(7637), pp. 359-364.

Freedland, S.J., Sutter, M.E., Dorey, F. and Aronson, W.J. (2003) 'Defining the ideal cutpoint for determining PSA recurrence after radical prostatectomy. Prostate-specific antigen', *Urology*, 61(2), pp. 365-9.

Frenzel, M., Rommelspacher, H., Sugawa, M.D. and Dencher, N.A. (2010) 'Ageing alters the supramolecular architecture of OxPhos complexes in rat brain cortex', *Exp Gerontol*, 45(7-8), pp. 563-72.

Gabaldon, T. and Huynen, M.A. (2003) 'Reconstruction of the proto-mitochondrial metabolism', *Science*, 301(5633), p. 609.

Gammage, P.A. and Frezza, C. (2019) 'Mitochondrial DNA: the overlooked oncogenome?', *BMC Biol*, 17(1), p. 53.

Gandaglia, G., Karakiewicz, P.I., Briganti, A., Passoni, N.M., Schiffmann, J., Trudeau, V., Graefen, M., Montorsi, F. and Sun, M. (2015) 'Impact of the Site of Metastases on Survival in Patients with Metastatic Prostate Cancer', *Eur Urol*, 68(2), pp. 325-34.

Gao, M., Wang, J., Lu, N., Fang, F., Liu, J. and Wong, C.W. (2011) 'Mitogen-activated protein kinase kinases promote mitochondrial biogenesis in part through inducing peroxisome proliferator-activated receptor gamma coactivator-1beta expression', *Biochim Biophys Acta*, 1813(6), pp. 1239-44.

Gao, X., Grignon, D.J., Chbihi, T., Zacharek, A., Chen, Y.Q., Sakr, W., Porter, A.T., Crissman, J.D., Pontes, J.E., Powell, I.J. and et al. (1995) 'Elevated 12-lipoxygenase mRNA expression correlates with advanced stage and poor differentiation of human prostate cancer', *Urology*, 46(2), pp. 227-37.

Garcia-Canaveras, J.C., Chen, L. and Rabinowitz, J.D. (2019) 'The Tumor Metabolic Microenvironment: Lessons from Lactate', *Cancer Res*, 79(13), pp. 3155-3162.

Garcia-Cao, I., Song, M.S., Hobbs, R.M., Laurent, G., Giorgi, C., de Boer, V.C., Anastasiou, D., Ito, K., Sasaki, A.T., Rameh, L., Carracedo, A., Vander Heiden, M.G., Cantley, L.C., Pinton, P., Haigis, M.C. and Pandolfi, P.P. (2012) 'Systemic elevation of PTEN induces a tumor-suppressive metabolic state', *Cell*, 149(1), pp. 49-62.

Gasparre, G., Hervouet, E., de Laplanche, E., Demont, J., Pennisi, L.F., Colombel, M., Mege-Lechevallier, F., Scoazec, J.Y., Bonora, E., Smeets, R., Smeitink, J., Lazar, V., Lespinasse, J., Giraud, S., Godinot, C., Romeo, G. and Simonnet, H. (2008) 'Clonal expansion of mutated mitochondrial DNA is associated with tumor formation and complex I deficiency in the benign renal oncocytoma', *Hum Mol Genet*, 17(7), pp. 986-95.

Gaude, E. and Frezza, C. (2014) 'Defects in mitochondrial metabolism and cancer', *Cancer Metab*, 2(1), p. 10.

Gaude, E. and Frezza, C. (2016) 'Tissue-specific and convergent metabolic transformation of cancer correlates with metastatic potential and patient survival', *Nat Commun*, 7, p. 13041.

Gerdes, M.J., Sevinsky, C.J., Sood, A., Adak, S., Bello, M.O., Bordwell, A., Can, A., Corwin, A., Dinn, S., Filkins, R.J., Hollman, D., Kamath, V., Kaanumalle, S., Kenny, K., Larsen, M., Lazare, M., Li, Q., Lowes, C., McCulloch, C.C., McDonough, E., Montalto, M.C., Pang, Z., Rittscher, J., Santamaria-Pang, A., Sarachan, B.D., Seel, M.L., Seppo, A., Shaikh, K., Sui, Y., Zhang, J. and Ginty, F. (2013) 'Highly multiplexed single-cell analysis of formalin-fixed, paraffin-embedded cancer tissue', *Proc Natl Acad Sci U S A*, 110(29), pp. 11982-7.

Gerhauser, C., Favero, F., Risch, T., Simon, R., Feuerbach, L., Assenov, Y., Heckmann, D., Sidiropoulos, N., Waszak, S.M., Hubschmann, D., Urbanucci, A., Girma, E.G., Kuryshev, V., Klimczak, L.J., Saini, N., Stutz, A.M., Weichenhan, D., Bottcher, L.M., Toth, R., Hendriksen, J.D., Koop, C., Lutsik, P., Matzk, S., Warnatz, H.J., Amstislavskiy, V., Feuerstein, C., Raeder, B., Bogatyrova, O., Schmitz, E.M., Hube-Magg, C., Kluth, M., Huland, H., Graefen, M., Lawerenz, C., Henry, G.H., Yamaguchi, T.N., Malewska, A., Meiners, J., Schilling, D., Reisinger, E., Eils, R., Schlesner, M., Strand, D.W., Bristow, R.G., Boutros, P.C., von Kalle, C., Gordenin, D., Sultmann, H., Brors, B., Sauter, G., Plass, C., Yaspo, M.L., Korbel, J.O., Schlomm, T. and Weischenfeldt, J. (2018) 'Molecular Evolution of Early-Onset Prostate Cancer Identifies Molecular Risk Markers and Clinical Trajectories', *Cancer Cell*, 34(6), pp. 996-1011 e8.

Gerner, M.Y., Kastenmuller, W., Ifrim, I., Kabat, J. and Germain, R.N. (2012) 'Histo-cytometry: a method for highly multiplex quantitative tissue imaging analysis applied to dendritic cell subset microanatomy in lymph nodes', *Immunity*, 37(2), pp. 364-76.

Ghandi, M., Huang, F.W., Jane-Valbuena, J., Kryukov, G.V., Lo, C.C., McDonald, E.R., 3rd, Barretina, J., Gelfand, E.T., Bielski, C.M., Li, H., Hu, K., Andreev-Drakhlin, A.Y., Kim, J., Hess, J.M., Haas, B.J., Aguet, F., Weir, B.A., Rothberg, M.V., Paolella, B.R., Lawrence, M.S., Akbani, R., Lu, Y., Tiv, H.L., Gokhale, P.C., de Weck, A., Mansour, A.A., Oh, C., Shih, J., Hadi, K., Rosen, Y., Bistline, J., Venkatesan, K., Reddy, A., Sonkin, D., Liu, M., Lehar, J., Korn, J.M., Porter, D.A., Jones, M.D., Golji, J., Caponigro, G., Taylor, J.E., Dunning, C.M., Creech, A.L., Warren, A.C., McFarland, J.M., Zamanighomi, M., Kauffmann, A., Stransky, N., Imielinski, M., Maruvka, Y.E., Cherniack, A.D., Tsherniak, A., Vazquez, F., Jaffe, J.D., Lane, A.A., Weinstock, D.M., Johannessen, C.M., Morrissey, M.P., Stegmeier, F., Schlegel, R., Hahn, W.C., Getz, G., Mills, G.B., Boehm, J.S., Golub, T.R., Garraway, L.A. and Sellers, W.R. (2019) 'Next-generation characterization of the Cancer Cell Line Encyclopedia', *Nature*, 569(7757), pp. 503-508.

Ghosh, J.C., Siegelin, M.D., Vaira, V., Faversani, A., Tavecchio, M., Chae, Y.C., Lisanti, S., Rampini, P., Giroda, M., Caino, M.C., Seo, J.H., Kossenkov, A.V., Michalek, R.D., Schultz, D.C., Bosari, S., Languino, L.R. and Altieri, D.C. (2015) 'Adaptive mitochondrial reprogramming and resistance to PI3K therapy', *J Natl Cancer Inst*, 107(3), pp. 1-9.

Gibbons, D.L. and Creighton, C.J. (2017) 'Pan-cancer survey of epithelial-mesenchymal transition markers across the Cancer Genome Atlas', *Developmental Dynamics*, 247(3), pp. 555-564.

Giesen, C., Wang, H.A.O., Schapiro, D., Zivanovic, N., Jacobs, A., Hattendorf, B., Schüffler, P.J., Grolimund, D., Buhmann, J.M., Brandt, S., Varga, Z., Wild, P.J., Günther, D. and Bodenmiller, B. (2014) 'Highly multiplexed imaging of tumor tissues with subcellular resolution by mass cytometry.', *Nature methods*, 11(4), pp. 417-422.

Gillessen, S., Gilson, C., James, N., Adler, A., Sydes, M.R., Clarke, N. and Group, S.T.M. (2016) 'Repurposing Metformin as Therapy for Prostate Cancer within the STAMPEDE Trial Platform', *Eur Urol*, 70(6), pp. 906-908.

Giorgi, C., Romagnoli, A., Pinton, P. and Rizzuto, R. (2008) 'Ca2+ signaling, mitochondria and cell death', *Curr Mol Med*, 8(2), pp. 119-30.

Giorgi, E.E., Li, Y., Caberto, C.P., Beckman, K.B., Lum-Jones, A., Haiman, C.A., Le Marchand, L., Stram, D.O., Saxena, R. and Cheng, I. (2016) 'No Association between the Mitochondrial Genome and Prostate Cancer Risk: The Multiethnic Cohort', *Cancer Epidemiology Biomarkers & Prevention*, 25(6), pp. 1001-1003.

Giunchi, F., Fiorentino, M. and Loda, M. (2019) 'The Metabolic Landscape of Prostate Cancer', *Eur Urol Oncol*, 2(1), pp. 28-36.

Gomez, L.A. and Hagen, T.M. (2012) 'Age-related decline in mitochondrial bioenergetics: does supercomplex destabilization determine lower oxidative capacity and higher superoxide production?', *Semin Cell Dev Biol*, 23(7), pp. 758-67.

Gomez, L.A., Monette, J.S., Chavez, J.D., Maier, C.S. and Hagen, T.M. (2009) 'Supercomplexes of the mitochondrial electron transport chain decline in the aging rat heart', *Arch Biochem Biophys*, 490(1), pp. 30-5.

Goo, C.K., Lim, H.Y., Ho, Q.S., Too, H.P., Clement, M.V. and Wong, K.P. (2012) 'PTEN/Akt signaling controls mitochondrial respiratory capacity through 4E-BP1', *PLoS One*, 7(9), p. e45806.

Gopal, R.K., Calvo, S.E., Shih, A.R., Chaves, F.L., McGuone, D., Mick, E., Pierce, K.A., Li, Y., Garofalo, A., Van Allen, E.M., Clish, C.B., Oliva, E. and Mootha, V.K. (2018) 'Early loss of mitochondrial complex I and rewiring of glutathione metabolism in renal oncocytoma', *Proceedings of the National Academy of Sciences*, 115(27), pp. E6283-E6290.

Gorris, M.A.J., Halilovic, A., Rabold, K., van Duffelen, A., Wickramasinghe, I.N., Verweij, D., Wortel, I.M.N., Textor, J.C., de Vries, I.J.M. and Figdor, C.G. (2018) 'Eight-Color Multiplex Immunohistochemistry for Simultaneous Detection of Multiple Immune Checkpoint Molecules within the Tumor Microenvironment', *J Immunol*, 200(1), pp. 347-354.

Gottlob, K., Majewski, N., Kennedy, S., Kandel, E., Robey, R.B. and Hay, N. (2001) 'Inhibition of early apoptotic events by Akt/PKB is dependent on the first committed step of glycolysis and mitochondrial hexokinase', *Genes Dev*, 15(11), pp. 1406-18.

Grandhi, S., Bosworth, C., Maddox, W., Sensiba, C., Akhavanfard, S., Ni, Y. and LaFramboise, T. (2017) 'Heteroplasmic shifts in tumor mitochondrial genomes reveal tissue-specific signals of relaxed and positive selection.', *Human Molecular Genetics*, 26(15), pp. 2912-2922.

Grasso, C.S., Wu, Y.M., Robinson, D.R., Cao, X., Dhanasekaran, S.M., Khan, A.P., Quist, M.J., Jing, X., Lonigro, R.J., Brenner, J.C., Asangani, I.A., Ateeq, B., Chun, S.Y., Siddiqui, J., Sam, L., Anstett, M., Mehra, R., Prensner, J.R., Palanisamy, N., Ryslik, G.A., Vandin, F., Raphael, B.J., Kunju, L.P., Rhodes, D.R., Pienta, K.J., Chinnaiyan, A.M. and Tomlins, S.A. (2012) 'The mutational landscape of lethal castration-resistant prostate cancer', *Nature*, 487(7406), pp. 239-43.

Greaves, L.C., Barron, M.J., Plusa, S., Kirkwood, T.B., Mathers, J.C., Taylor, R.W. and Turnbull, D.M. (2010) 'Defects in multiple complexes of the respiratory chain are present in ageing human colonic crypts', *Exp Gerontol*, 45(7-8), pp. 573-9.

Groelz, D., Viertler, C., Pabst, D., Dettmann, N. and Zatloukal, K. (2018) 'Impact of storage conditions on the quality of nucleic acids in paraffin embedded tissues', *PLoS One*, 13(9), p. e0203608.

Grummet, J.P., Weerakoon, M., Huang, S., Lawrentschuk, N., Frydenberg, M., Moon, D.A., O'Reilly, M. and Murphy, D. (2014) 'Sepsis and 'superbugs': should we favour the transperineal over the transrectal approach for prostate biopsy?', *BJU Int*, 114(3), pp. 384-8.

Grupp, K., Jedrzejewska, K., Tsourlakis, M.C., Koop, C., Wilczak, W., Adam, M., Quaas, A., Sauter, G., Simon, R., Izbicki, J.R., Graefen, M., Huland, H., Schlomm, T., Minner, S. and Steurer, S. (2013) 'High mitochondria content is associated with prostate cancer disease progression.', *Molecular Cancer*, 12(1), p. 145.

Guerra, C., Mijimolle, N., Dhawahir, A., Dubus, P., Barradas, M., Serrano, M., Campuzano, V. and Barbacid, M. (2003) 'Tumor induction by an endogenous K-ras oncogene is highly dependent on cellular context.', *Cancer Cell*, 4(2), pp. 111-120.

Guo, T., Li, L., Zhong, Q., Rupp, N.J., Charmpi, K., Wong, C.E., Wagner, U., Rueschoff, J.H., Jochum, W., Fankhauser, C.D., Saba, K., Poyet, C., Wild, P.J., Aebersold, R. and Beyer, A. (2018) 'Multi-region proteome analysis quantifies spatial heterogeneity of prostate tissue biomarkers', *Life Sci Alliance*, 1(2), p. e201800042.

Gurel, B., Ali, T.Z., Montgomery, E.A., Begum, S., Hicks, J., Goggins, M., Eberhart, C.G., Clark, D.P., Bieberich, C.J., Epstein, J.I. and De Marzo, A.M. (2010) 'NKX3.1 as a marker of prostatic origin in metastatic tumors', *Am J Surg Pathol*, 34(8), pp. 1097-105.

Gustafsson, A.B. and Dorn, G.W., 2nd (2019) 'Evolving and Expanding the Roles of Mitophagy as a Homeostatic and Pathogenic Process', *Physiol Rev*, 99(1), pp. 853-892.

Haas, G.P., Delongchamps, N., Brawley, O.W., Wang, C.Y. and de la Roza, G. (2008) 'The worldwide epidemiology of prostate cancer: perspectives from autopsy studies', *Can J Urol*, 15(1), pp. 3866-71.

Hagerhall, C. (1997) 'Succinate: quinone oxidoreductases. Variations on a conserved theme', *Biochim Biophys Acta*, 1320(2), pp. 107-41.

Haider, S., McIntyre, A., van Stiphout, R.G., Winchester, L.M., Wigfield, S., Harris, A.L. and Buffa, F.M. (2016) 'Genomic alterations underlie a pan-cancer metabolic shift associated with tumour hypoxia', *Genome Biol*, 17(1), p. 140.

Hamamah, S. and Gatti, J.L. (1998) 'Role of the ionic environment and internal pH on sperm activity', *Hum Reprod*, 13 Suppl 4, pp. 20-30.

Hamdy, F.C., Donovan, J.L., Lane, J.A., Mason, M., Metcalfe, C., Holding, P., Davis, M., Peters, T.J., Turner, E.L., Martin, R.M., Oxley, J., Robinson, M., Staffurth, J., Walsh, E., Bollina, P., Catto, J., Doble, A., Doherty, A., Gillatt, D., Kockelbergh, R., Kynaston, H., Paul, A., Powell, P., Prescott, S., Rosario, D.J., Rowe, E., Neal, D.E. and Protec, T.S.G. (2016) '10-Year Outcomes after Monitoring, Surgery, or Radiotherapy for Localized Prostate Cancer', *N Engl J Med*, 375(15), pp. 1415-1424.

Hamid, A.A., Gray, K.P., Shaw, G., MacConaill, L.E., Evan, C., Bernard, B., Loda, M., Corcoran, N.M., Van Allen, E.M., Choudhury, A.D. and Sweeney, C.J. (2019) 'Compound Genomic Alterations of TP53, PTEN, and RB1 Tumor Suppressors in Localized and Metastatic Prostate Cancer', *Eur Urol*, 76(1), pp. 89-97.

Hanahan, D. and Weinberg, R.A. (2011) 'Hallmarks of cancer: the next generation', *Cell*, 144(5), pp. 646-74.

Hance, N., Ekstrand, M.I. and Trifunovic, A. (2005) 'Mitochondrial DNA polymerase gamma is essential for mammalian embryogenesis', *Hum Mol Genet*, 14(13), pp. 1775-83.

Hansel, D.E. and Epstein, J.I. (2006) 'Sarcomatoid carcinoma of the prostate: a study of 42 cases', *Am J Surg Pathol*, 30(10), pp. 1316-21.

Hansen, A.F., Sandsmark, E., Rye, M.B., Wright, A.J., Bertilsson, H., Richardsen, E., Viset, T., Bofin, A.M., Angelsen, A., Selnæs, K.M., Bathen, T.F. and Tessem, M.-B. (2016) 'Presence of TMPRSS2-ERG is associated with alterations of the metabolic profile in human prostate cancer', *Oncotarget*, 7(27), pp. 42071-42085.

Harder, N., Athelogou, M., Hessel, H., Brieu, N., Yigitsoy, M., Zimmermann, J., Baatz, M., Buchner, A., Stief, C.G., Kirchner, T., Binnig, G., Schmidt, G. and Huss, R. (2018) 'Tissue Phenomics for prognostic biomarker discovery in low- and intermediate-risk prostate cancer', *Sci Rep*, 8(1), p. 4470.

Hargreaves, I.P., Duncan, A.J., Wu, L., Agrawal, A., Land, J.M. and Heales, S.J. (2007) 'Inhibition of mitochondrial complex IV leads to secondary loss complex II-III activity: implications for the pathogenesis and treatment of mitochondrial encephalomyopathies', *Mitochondrion*, 7(4), pp. 284-7.

Harman, D. (1972) 'The biologic clock: the mitochondria?', *J Am Geriatr Soc*, 20(4), pp. 145-7.

Hartmann, A., Blaszyk, H., McGovern, R.M., Schroeder, J.J., Cunningham, J., De Vries, E.M., Kovach, J.S. and Sommer, S.S. (1995) 'p53 gene mutations inside and outside of exons 5-8: the patterns differ in breast and other cancers', *Oncogene*, 10(4), pp. 681-8.

Hashizume, O., Shimizu, A., Yokota, M., Sugiyama, A., Nakada, K., Miyoshi, H., Itami, M., Ohira, M., Nagase, H., Takenaga, K. and Hayashi, J. (2012) 'Specific mitochondrial DNA mutation in mice regulates diabetes and lymphoma development', *Proc Natl Acad Sci U S A*, 109(26), pp. 10528-33.

Hashizume, O., Yamanashi, H., Taketo, M.M., Nakada, K. and Hayashi, J. (2015) 'A specific nuclear DNA background is required for high frequency lymphoma development in transmitochondrial mice with G13997A mtDNA', *PLoS One*, 10(3), p. e0118561.

Hauser, D.N., Dillman, A.A., Ding, J., Li, Y. and Cookson, M.R. (2014) 'Post-Translational Decrease in Respiratory Chain Proteins in the Polg Mutator Mouse Brain', *PLoS ONE*, 9(4), p. e94646.

Heger, Z., Merlos Rodrigo, M.A., Michalek, P., Polanska, H., Masarik, M., Vit, V., Plevova, M., Pacik, D., Eckschlager, T., Stiborova, M. and Adam, V. (2016) 'Sarcosine Up-Regulates Expression of Genes Involved in Cell Cycle Progression of Metastatic Models of Prostate Cancer', *PLoS One*, 11(11), p. e0165830.

Heinz, S., Freyberger, A., Lawrenz, B., Schladt, L., Schmuck, G. and Ellinger-Ziegelbauer, H. (2017) 'Mechanistic Investigations of the Mitochondrial Complex I Inhibitor Rotenone in the Context of Pharmacological and Safety Evaluation.', *Scientific Reports*, 7(1), p. 45465.

Henry, G.H., Malewska, A., Joseph, D.B., Malladi, V.S., Lee, J., Torrealba, J., Mauck, R.J., Gahan, J.C., Raj, G.V., Roehrborn, C.G., Hon, G.C., MacConmara, M.P., Reese, J.C., Hutchinson, R.C., Vezina, C.M. and Strand, D.W. (2018) 'A Cellular Anatomy of the Normal Adult Human Prostate and Prostatic Urethra.', *Cell Reports*, 25(12), pp. 3530-3542.e5.

Herrmann, P.C., Gillespie, J.W., Charboneau, L., Bichsel, V.E., Paweletz, C.P., Calvert, V.S., Kohn, E.C., Emmert-Buck, M.R., Liotta, L.A. and Petricoin, E.F., 3rd (2003) 'Mitochondrial proteome: altered cytochrome c oxidase subunit levels in prostate cancer', *Proteomics*, 3(9), pp. 1801-10.

Hieble, J.P. (2011) 'Animal models for benign prostatic hyperplasia', *Handb Exp Pharmacol*, (202), pp. 69-79.

Hieronymus, H., Murali, R., Tin, A., Yadav, K., Abida, W., Moller, H., Berney, D., Scher, H., Carver, B., Scardino, P., Schultz, N., Taylor, B., Vickers, A., Cuzick, J. and Sawyers, C.L. (2018) 'Tumor copy number alteration burden is a pan-cancer prognostic factor associated with recurrence and death', *Elife*, 7, p. 1.

Hieronymus, H., Schultz, N., Gopalan, A., Carver, B.S., Chang, M.T., Xiao, Y., Heguy, A., Huberman, K., Bernstein, M., Assel, M., Murali, R., Vickers, A., Scardino, P.T., Sander, C., Reuter, V., Taylor, B.S. and Sawyers, C.L. (2014) 'Copy number alteration burden predicts prostate cancer relapse', *Proceedings of the National Academy of Sciences*, 111(30), pp. 11139-11144.

Hiona, A., Sanz, A., Kujoth, G.C., Pamplona, R., Seo, A.Y., Hofer, T., Someya, S., Miyakawa, T., Nakayama, C., Samhan-Arias, A.K., Servais, S., Barger, J.L., Portero-Otin, M., Tanokura, M., Prolla, T.A. and Leeuwenburgh, C. (2010) 'Mitochondrial DNA mutations induce mitochondrial dysfunction, apoptosis and sarcopenia in skeletal muscle of mitochondrial DNA mutator mice', *PLoS One*, 5(7), p. e11468.

Ho, H.Y., Lin, Y.T., Lin, G., Wu, P.R. and Cheng, M.L. (2017) 'Nicotinamide nucleotide transhydrogenase (NNT) deficiency dysregulates mitochondrial retrograde signaling and impedes proliferation', *Redox Biol*, 12, pp. 916-928.

Hoffman, R.M., Gilliland, F.D., Eley, J.W., Harlan, L.C., Stephenson, R.A., Stanford, J.L., Albertson, P.C., Hamilton, A.S., Hunt, W.C. and Potosky, A.L. (2001) 'Racial and ethnic differences in advanced-stage prostate cancer: the Prostate Cancer Outcomes Study', *J Natl Cancer Inst*, 93(5), pp. 388-95.

Holmstrom, B., Johansson, M., Bergh, A., Stenman, U.H., Hallmans, G. and Stattin, P. (2009) 'Prostate specific antigen for early detection of prostate cancer: longitudinal study', *BMJ*, 339, p. b3537.

Holt, I.J., Lorimer, H.E. and Jacobs, H.T. (2000) 'Coupled leading- and lagging-strand synthesis of mammalian mitochondrial DNA', *Cell*, 100(5), pp. 515-24.

Hong, M.K., Macintyre, G., Wedge, D.C., Van Loo, P., Patel, K., Lunke, S., Alexandrov, L.B., Sloggett, C., Cmero, M., Marass, F., Tsui, D., Mangiola, S., Lonie, A., Naeem, H., Sapre, N., Phal, P.M., Kurganovs, N., Chin, X., Kerger, M., Warren, A.Y., Neal, D., Gnanapragasam, V., Rosenfeld, N., Pedersen, J.S., Ryan, A., Haviv, I., Costello, A.J., Corcoran, N.M. and Hovens, C.M. (2015) 'Tracking the origins and drivers of subclonal metastatic expansion in prostate cancer', *Nat Commun*, 6, p. 6605.

Hopkins, J.F., Sabelnykova, V.Y., Weischenfeldt, J., Simon, R., Aguiar, J.A., Alkallas, R., Heisler, L.E., Zhang, J., Watson, J.D., Chua, M.L.K., Fraser, M., Favero, F., Lawerenz, C., Plass, C., Sauter, G., McPherson, J.D., van der Kwast, T., Korbel, J., Schlomm, T., Bristow, R.G. and Boutros, P.C. (2017) 'Mitochondrial mutations drive prostate cancer aggression', *Nat Commun*, 8(1), p. 656.

Hoppins, S., Lackner, L. and Nunnari, J. (2007) 'The machines that divide and fuse mitochondria', *Annu Rev Biochem*, 76, pp. 751-80.

Horning, A.M., Wang, Y., Lin, C.-K., Louie, A.D., Jadhav, R.R., Hung, C.-N., Wang, C.-M., Lin, C.-L., Kirma, N.B., Liss, M.A., Kumar, A.P., Sun, L., Liu, Z., Chao, W.-T., Wang, Q., Jin, V.X., Chen, C.-L. and Huang, T.H.M. (2018) 'Single-Cell RNA-seq Reveals a Subpopulation of Prostate Cancer Cells with Enhanced Cell-Cycle–Related Transcription and Attenuated Androgen Response', *Cancer Research*, 78(4), pp. 853-864.

Horoszewicz, J.S., Leong, S.S., Kawinski, E., Karr, J.P., Rosenthal, H., Chu, T.M., Mirand, E.A. and Murphy, G.P. (1983) 'LNCaP model of human prostatic carcinoma', *Cancer Res*, 43(4), pp. 1809-18.

Hosios, A.M., Hecht, V.C., Danai, L.V., Johnson, M.O., Rathmell, J.C., Steinhauser, M.L., Manalis, S.R. and Vander Heiden, M.G. (2016) 'Amino Acids Rather than Glucose Account for the Majority of Cell Mass in Proliferating Mammalian Cells', *Dev Cell*, 36(5), pp. 540-9.

Hothorn, T. and Lausen, B. (2003) 'On the exact distribution of maximally selected rank statistics', *Computational Statistics & Data Analysis*, 43(2), pp. 121-137.

Houlahan, K.E., Salmasi, A., Sadun, T.Y., Pooli, A., Felker, E.R., Livingstone, J., Huang, V., Raman, S.S., Ahuja, P., Sisk, A.E., Jr., Boutros, P.C. and Reiter, R.E. (2019) 'Molecular Hallmarks of Multiparametric Magnetic Resonance Imaging Visibility in Prostate Cancer', *Eur Urol*, 76(1), pp. 18-23.

Hoyle, A.P., Ali, A., James, N.D., Cook, A., Parker, C.C., de Bono, J.S., Attard, G., Chowdhury, S., Cross, W.R., Dearnaley, D.P., Brawley, C.D., Gilson, C., Ingleby, F., Gillessen, S., Aebersold, D.M., Jones, R.J., Matheson, D., Millman, R., Mason, M.D., Ritchie, A.W.S., Russell, M., Douis, H., Parmar, M.K.B., Sydes, M.R., Clarke, N.W. and Investigators, S. (2019) 'Abiraterone in "High-" and "Low-risk" Metastatic Hormone-sensitive Prostate Cancer', *Eur Urol*.

Hsiao, C.P., Wang, D., Kaushal, A. and Saligan, L. (2013) 'Mitochondria-related gene expression changes are associated with fatigue in patients with nonmetastatic prostate cancer receiving external beam radiation therapy', *Cancer Nurs*, 36(3), pp. 189-97.

Hu, L., Yao, X. and Shen, Y. (2016) 'Altered mitochondrial DNA copy number contributes to human cancer risk: evidence from an updated meta-analysis', *Sci Rep*, 6, p. 35859.

Huang, S.Q., Sun, B., Xiong, Z.P., Shu, Y., Zhou, H.H., Zhang, W., Xiong, J. and Li, Q. (2018) 'The dysregulation of tRNAs and tRNA derivatives in cancer', *J Exp Clin Cancer Res*, 37(1), p. 101.

Hudson, G. and Chinnery, P.F. (2006) 'Mitochondrial DNA polymerase-gamma and human disease', *Hum Mol Genet*, 15 Spec No 2(suppl_2), pp. R244-52.

Huggins, C. and Hodges, C. (1941) 'Studies on prostatic cancer. II. The effects of castration on advanced carcinoma of the prostate gland', *Arch Surg* 43, p. 209.

Hunyady, B., Krempels, K., Harta, G. and Mezey, E. (1996) 'Immunohistochemical signal amplification by catalyzed reporter deposition and its application in double immunostaining.', *Journal of Histochemistry & Cytochemistry*, 44(12), pp. 1353-1362.

Hussain, M., Fizazi, K., Saad, F., Rathenborg, P., Shore, N., Ferreira, U., Ivashchenko, P., Demirhan, E., Modelska, K., Phung, Krivoshik, A. and Sternberg, C.N. (2018) 'Enzalutamide in Men with Nonmetastatic, Castration-Resistant Prostate Cancer', *N Engl J Med*, 378(26), pp. 2465-2474.

Iglesias-Gato, D., Thysell, E., Tyanova, S., Crnalic, S., Santos, A., Lima, T.S., Geiger, T., Cox, J., Widmark, A., Bergh, A., Mann, M., Flores-Morales, A. and Wikström, P. (2018) 'The Proteome of Prostate Cancer

Bone Metastasis Reveals Heterogeneity with Prognostic Implications.', *Clinical Cancer Research*, 24(21), pp. 5433-5444.

Iglesias-Gato, D., Wikstrom, P., Tyanova, S., Lavallee, C., Thysell, E., Carlsson, J., Hagglof, C., Cox, J., Andren, O., Stattin, P., Egevad, L., Widmark, A., Bjartell, A., Collins, C.C., Bergh, A., Geiger, T., Mann, M. and Flores-Morales, A. (2016) 'The Proteome of Primary Prostate Cancer', *Eur Urol*, 69(5), pp. 942-52.

Ilic, D., Djulbegovic, M., Jung, J.H., Hwang, E.C., Zhou, Q., Cleves, A., Agoritsas, T. and Dahm, P. (2018) 'Prostate cancer screening with prostate-specific antigen (PSA) test: a systematic review and meta-analysis', *BMJ*, 362, p. k3519.

Ingraham, C.A., Burwell, L.S., Skalska, J., Brookes, P.S., Howell, R.L., Sheu, S.S. and Pinkert, C.A. (2009) 'NDUFS4: creation of a mouse model mimicking a Complex I disorder', *Mitochondrion*, 9(3), pp. 204-10.

Iommarini, L., Calvaruso, M.A., Kurelac, I., Gasparre, G. and Porcelli, A.M. (2013) 'Complex I impairment in mitochondrial diseases and cancer: parallel roads leading to different outcomes', *Int J Biochem Cell Biol*, 45(1), pp. 47-63.

Ippolito, L., Marini, A., Cavallini, L., Morandi, A., Pietrovito, L., Pintus, G., Giannoni, E., Schrader, T., Puhr, M., Chiarugi, P. and Taddei, M.L. (2016) 'Metabolic shift toward oxidative phosphorylation in docetaxel resistant prostate cancer cells', *Oncotarget*, 7(38), pp. 61890-61904.

Irwin, M.H., Parameshwaran, K. and Pinkert, C.A. (2013) 'Mouse models of mitochondrial complex I dysfunction', *Int J Biochem Cell Biol*, 45(1), pp. 34-40.

Ittmann, M., Huang, J., Radaelli, E., Martin, P., Signoretti, S., Sullivan, R., Simons, B.W., Ward, J.M., Robinson, B.D., Chu, G.C., Loda, M., Thomas, G., Borowsky, A. and Cardiff, R.D. (2013) 'Animal models of human prostate cancer: the consensus report of the New York meeting of the Mouse Models of Human Cancers Consortium Prostate Pathology Committee.', *Cancer Research*, 73(9), pp. 2718-2736.

Jadvar, H. (2016) 'Is There Use for FDG-PET in Prostate Cancer?', *Semin Nucl Med*, 46(6), pp. 502-506.

Jamaspishvili, T., Berman, D.M., Ross, A.E., Scher, H.I., De Marzo, A.M., Squire, J.A. and Lotan, T.L. (2018) 'Clinical implications of PTEN loss in prostate cancer', *Nat Rev Urol*, 15(4), pp. 222-234.

James, N.D., de Bono, J.S., Spears, M.R., Clarke, N.W., Mason, M.D., Dearnaley, D.P., Ritchie, A.W.S., Amos, C.L., Gilson, C., Jones, R.J., Matheson, D., Millman, R., Attard, G., Chowdhury, S., Cross, W.R., Gillessen, S., Parker, C.C., Russell, J.M., Berthold, D.R., Brawley, C., Adab, F., Aung, S., Birtle, A.J., Bowen, J., Brock, S., Chakraborti, P., Ferguson, C., Gale, J., Gray, E., Hingorani, M., Hoskin, P.J., Lester, J.F., Malik, Z.I., McKinna, F., McPhail, N., Money-Kyrle, J., O'Sullivan, J., Parikh, O., Protheroe, A., Robinson, A., Srihari, N.N., Thomas, C., Wagstaff, J., Wylie, J., Zarkar, A., Parmar, M.K.B., Sydes, M.R. and Investigators, S. (2017) 'Abiraterone for Prostate Cancer Not Previously Treated with Hormone Therapy', *N Engl J Med*, 377(4), pp. 338-351.

James, N.D., Spears, M.R., Clarke, N.W., Dearnaley, D.P., De Bono, J.S., Gale, J., Hetherington, J., Hoskin, P.J., Jones, R.J., Laing, R., Lester, J.F., McLaren, D., Parker, C.C., Parmar, M.K.B., Ritchie, A.W.S., Russell, J.M., Strebel, R.T., Thalmann, G.N., Mason, M.D. and Sydes, M.R. (2015) 'Survival with Newly Diagnosed Metastatic Prostate Cancer in the "Docetaxel Era": Data from 917 Patients in the Control Arm of the STAMPEDE Trial (MRC PR08, CRUK/06/019)', *Eur Urol*, 67(6), pp. 1028-1038.

James, N.D., Spears, M.R., Clarke, N.W., Dearnaley, D.P., Mason, M.D., Parker, C.C., Ritchie, A.W., Russell, J.M., Schiavone, F., Attard, G., de Bono, J.S., Birtle, A., Engeler, D.S., Elliott, T., Matheson, D., O'Sullivan, J., Pudney, D., Srihari, N., Wallace, J., Barber, J., Syndikus, I., Parmar, M.K., Sydes, M.R. and Investigators, S. (2016) 'Failure-Free Survival and Radiotherapy in Patients With Newly Diagnosed Nonmetastatic Prostate Cancer: Data From Patients in the Control Arm of the STAMPEDE Trial', *JAMA Oncol*, 2(3), pp. 348-57.

Jedroszka, D., Orzechowska, M., Hamouz, R., Gorniak, K. and Bednarek, A.K. (2017) 'Markers of epithelial-to-mesenchymal transition reflect tumor biology according to patient age and Gleason score in prostate cancer', *PLoS One*, 12(12), p. e0188842.

Jefferies, M.T., Cox, A.C., Shorning, B.Y., Meniel, V., Griffiths, D., Kynaston, H.G., Smalley, M.J. and Clarke, A.R. (2017) 'PTEN loss and activation of K-RAS and beta-catenin cooperate to accelerate prostate tumourigenesis', *J Pathol*, 243(4), pp. 442-456.

Jeronimo, S.M., Teixeira, M.J., Sousa, A., Thielking, P., Pearson, R.D. and Evans, T.G. (2000) 'Natural history of Leishmania (Leishmania) chagasi infection in Northeastern Brazil: long-term follow-up', *Clin Infect Dis*, 30(3), pp. 608-9.

Jessen, K., Sondergaard, J., Larsen, P.V. and Thomsen, J.L. (2013) 'Danish General Practitioners' Use of Prostate-Specific Antigen in Opportunistic Screening for Prostate Cancer: A Survey Comprising 174 GPs', *Int J Family Med*, 2013, p. 540707.

Jessie, B.C., Sun, C.Q., Irons, H.R., Marshall, F.F., Wallace, D.C. and Petros, J.A. (2001) 'Accumulation of mitochondrial DNA deletions in the malignant prostate of patients of different ages', *Exp Gerontol*, 37(1), pp. 169-74.

Jha, G.G., Anand, V., Soubra, A. and Konety, B.R. (2014) 'Challenges of managing elderly men with prostate cancer', *Nat Rev Clin Oncol*, 11(6), pp. 354-64.

Jiang, M., Kauppila, T.E.S., Motori, E., Li, X., Atanassov, I., Folz-Donahue, K., Bonekamp, N.A., Albarran-Gutierrez, S., Stewart, J.B. and Larsson, N.G. (2017) 'Increased Total mtDNA Copy Number Cures Male Infertility Despite Unaltered mtDNA Mutation Load', *Cell Metab*, 26(2), pp. 429-436 e4.

Johnson, D.C., Raman, S.S., Mirak, S.A., Kwan, L., Bajgiran, A.M., Hsu, W., Maehara, C.K., Ahuja, P., Faiena, I., Pooli, A., Salmasi, A., Sisk, A., Felker, E.R., Lu, D.S.K. and Reiter, R.E. (2019) 'Detection of Individual Prostate Cancer Foci via Multiparametric Magnetic Resonance Imaging', *Eur Urol*, 75(5), pp. 712-720.

Johnson, J.M., Lai, S.Y., Cotzia, P., Cognetti, D., Luginbuhl, A., Pribitkin, E.A., Zhan, T., Mollaee, M., Domingo-Vidal, M., Chen, Y., Campling, B., Bar-Ad, V., Birbe, R., Tuluc, M., Martinez Outschoorn, U. and Curry, J. (2015) 'Mitochondrial Metabolism as a Treatment Target in Anaplastic Thyroid Cancer', *Semin Oncol*, 42(6), pp. 915-22.

Johnson, M.A., Hernandez, I., Wei, Y. and Greenberg, N. (2000) 'Isolation and characterization of mouse probasin: An androgen-regulated protein specifically expressed in the differentiated prostate.', *The Prostate*, 43(4), pp. 255-262.

Jones, D., Friend, C., Dreher, A., Allgar, V. and Macleod, U. (2018) 'The diagnostic test accuracy of rectal examination for prostate cancer diagnosis in symptomatic patients: a systematic review', *BMC Fam Pract*, 19(1), p. 79.

Jones, S.F. and Infante, J.R. (2015) 'Molecular Pathways: Fatty Acid Synthase', *Clin Cancer Res*, 21(24), pp. 5434-8.

Jonkers, J., Meuwissen, R., van der Gulden, H., Peterse, H., van der Valk, M. and Berns, A. (2001) 'Synergistic tumor suppressor activity of BRCA2 and p53 in a conditional mouse model for breast cancer', *Nat Genet*, 29(4), pp. 418-25.

Jornayvaz, F.R. and Shulman, G.I. (2010) 'Regulation of mitochondrial biogenesis', *Essays Biochem*, 47, pp. 69-84.

Jouaville, L.S., Pinton, P., Bastianutto, C., Rutter, G.A. and Rizzuto, R. (1999) 'Regulation of mitochondrial ATP synthesis by calcium: evidence for a long-term metabolic priming', *Proc Natl Acad Sci U S A*, 96(24), pp. 13807-12.

Ju, Y.S., Alexandrov, L.B., Gerstung, M., Martincorena, I., Nik-Zainal, S., Ramakrishna, M., Davies, H.R., Papaemmanuil, E., Gundem, G., Shlien, A., Bolli, N., Behjati, S., Tarpey, P.S., Nangalia, J., Massie, C.E., Butler, A.P., Teague, J.W., Vassiliou, G.S., Green, A.R., Du, M.Q., Unnikrishnan, A., Pimanda, J.E., Teh, B.T., Munshi, N., Greaves, M., Vyas, P., El-Naggar, A.K., Santarius, T., Collins, V.P., Grundy, R., Taylor, J.A., Hayes, D.N., Malkin, D., Group, I.B.C., Group, I.C.M.D., Group, I.P.C., Foster, C.S., Warren, A.Y., Whitaker, H.C., Brewer, D., Eeles, R., Cooper, C., Neal, D., Visakorpi, T., Isaacs, W.B., Bova, G.S., Flanagan, A.M., Futreal, P.A., Lynch, A.G., Chinnery, P.F., McDermott, U., Stratton, M.R. and Campbell, P.J. (2014) 'Origins and functional consequences of somatic mitochondrial DNA mutations in human cancer', *Elife*, 3, pp. 415-28.

Jurmeister, S., Ramos-Montoya, A., Sandi, C., Pertega-Gomes, N., Wadhwa, K., Lamb, A.D., Dunning, M.J., Attig, J., Carroll, J.S., Fryer, L.G., Felisbino, S.L. and Neal, D.E. (2018) 'Identification of potential therapeutic targets in prostate cancer through a cross-species approach', *EMBO Mol Med*, 10(3), pp. e8274-18.

Kadenbach, B., Münscher, C., Frank, V., Müller-Höcker, J. and Napiwotzki, J. (1995) 'Human aging is associated with stochastic somatic mutations of mitochondrial DNA', *Mutation Research/DNAging*, 338(1-6), pp. 161-172.

Kaguni, L.S. (2004) 'DNA polymerase gamma, the mitochondrial replicase', *Annu Rev Biochem*, 73, pp. 293-320.

Kaighn, M.E., Narayan, K.S., Ohnuki, Y., Lechner, J.F. and Jones, L.W. (1979) 'Establishment and characterization of a human prostatic carcinoma cell line (PC-3)', *Invest Urol*, 17(1), pp. 16-23.

Kalsbeek, A.M., Chan, E.F., Grogan, J., Petersen, D.C., Jaratlerdsiri, W., Gupta, R., Lyons, R.J., Haynes, A.M., Horvath, L.G., Kench, J.G., Stricker, P.D. and Hayes, V.M. (2016) 'Mutational load of the mitochondrial genome predicts pathological features and biochemical recurrence in prostate cancer', *Aging (Albany NY)*, 8(11), pp. 2702-2712.

Kalsbeek, A.M.F., Chan, E.K.F., Corcoran, N.M., Hovens, C.M. and Hayes, V.M. (2017) 'Mitochondrial genome variation and prostate cancer: a review of the mutational landscape and application to clinical management.', *Oncotarget*, 8(41), pp. 71342-71357.

Kalsbeek, A.M.F., Chan, E.K.F., Grogan, J., Petersen, D.C., Jaratlerdsiri, W., Gupta, R., Lyons, R.J., Haynes, A.M., Horvath, L.G., Kench, J.G., Stricker, P.D. and Hayes, V.M. (2018) 'Altered mitochondrial genome content signals worse pathology and prognosis in prostate cancer', *Prostate*, 78(1), pp. 25-31.

Karlberg, O., Canback, B., Kurland, C.G. and Andersson, S.G. (2000) 'The dual origin of the yeast mitochondrial proteome', *Yeast*, 17(3), pp. 170-87.

Kasivisvanathan, V., Rannikko, A.S., Borghi, M., Panebianco, V., Mynderse, L.A., Vaarala, M.H., Briganti, A., Budäus, L., Hellawell, G., Hindley, R.G., Roobol, M.J., Eggener, S., Ghei, M., Villers, A., Bladou, F., Villeirs, G.M., Virdi, J., Boxler, S., Robert, G., Singh, P.B., Venderink, W., Hadaschik, B.A., Ruffion, A., Hu, J.C., Margolis, D., Crouzet, S., Klotz, L., Taneja, S.S., Pinto, P., Gill, I., Allen, C., Giganti, F., Freeman, A., Morris, S., Punwani, S., Williams, N.R., Brew-Graves, C., Deeks, J., Takwoingi, Y., Emberton, M., Moore, C.M. and Collaborators, P.S.G. (2018) 'MRI-Targeted or Standard Biopsy for Prostate-Cancer Diagnosis.', *New England Journal of Medicine*, 378(19), pp. 1767-1777.

Kelly, R.S., Sinnott, J.A., Rider, J.R., Ebot, E.M., Gerke, T., Bowden, M., Pettersson, A., Loda, M., Sesso, H.D., Kantoff, P.W., Martin, N.E., Giovannucci, E.L., Tyekucheva, S., Heiden, M.V. and Mucci, L.A. (2016) 'The role of tumor metabolism as a driver of prostate cancer progression and lethal disease: results from a nested case-control study', *Cancer Metab*, 4(1), p. 22.

Kenney, M.C., Chwa, M., Atilano, S.R., Falatoonzadeh, P., Ramirez, C., Malik, D., Tarek, M., Del Carpio, J.C., Nesburn, A.B., Boyer, D.S., Kuppermann, B.D., Vawter, M.P., Jazwinski, S.M., Miceli, M.V., Wallace, D.C. and Udar, N. (2014) 'Molecular and bioenergetic differences between cells with African versus

European inherited mitochondrial DNA haplogroups: implications for population susceptibility to diseases', *Biochim Biophys Acta*, 1842(2), pp. 208-19.

Kesterson, R.A., Johnson, L.W., Lambert, L.J., Vivian, J.L., Welch, D.R. and Ballinger, S.W. (2016) 'Generation of Mitochondrial-nuclear eXchange Mice via Pronuclear Transfer', *Bio Protoc*, 6(20).

Khan, A.P., Rajendiran, T.M., Ateeq, B., Asangani, I.A., Athanikar, J.N., Yocum, A.K., Mehra, R., Siddiqui, J., Palapattu, G., Wei, J.T., Michailidis, G., Sreekumar, A. and Chinnaiyan, A.M. (2013) 'The role of sarcosine metabolism in prostate cancer progression', *Neoplasia*, 15(5), pp. 491-501.

Khandrika, L., Kumar, B., Koul, S., Maroni, P. and Koul, H.K. (2009) 'Oxidative stress in prostate cancer', *Cancer Lett*, 282(2), pp. 125-36.

Khani, F., Mosquera, J.M., Park, K., Blattner, M., O'Reilly, C., MacDonald, T.Y., Chen, Z., Srivastava, A., Tewari, A.K., Barbieri, C.E., Rubin, M.A. and Robinson, B.D. (2014) 'Evidence for molecular differences in prostate cancer between African American and Caucasian men', *Clin Cancer Res*, 20(18), pp. 4925-34.

Khrapko, K., Kraytsberg, Y., de Grey, A.D., Vijg, J. and Schon, E.A. (2006) 'Does premature aging of the mtDNA mutator mouse prove that mtDNA mutations are involved in natural aging?', *Aging Cell*, 5(3), pp. 279-82.

Kicinski, M., Vangronsveld, J. and Nawrot, T.S. (2011) 'An epidemiological reappraisal of the familial aggregation of prostate cancer: a meta-analysis', *PLoS One*, 6(10), p. e27130.

Kim, K.K., Abelman, S., Yano, N., Ribeiro, J.R., Singh, R.K., Tipping, M. and Moore, R.G. (2015) 'Tetrathiomolybdate inhibits mitochondrial complex IV and mediates degradation of hypoxia-inducible factor-1alpha in cancer cells', *Sci Rep*, 5, p. 14296.

King, J.C., Xu, J., Wongvipat, J., Hieronymus, H., Carver, B.S., Leung, D.H., Taylor, B.S., Sander, C., Cardiff, R.D., Couto, S.S., Gerald, W.L. and Sawyers, C.L. (2009) 'Cooperativity of TMPRSS2-ERG with PI3-kinase pathway activation in prostate oncogenesis', *Nat Genet*, 41(5), pp. 524-6.

Kirches, E. (2009) 'Mitochondrial and nuclear genes of mitochondrial components in cancer', *Curr Genomics*, 10(4), pp. 281-93.

Kirichok, Y., Krapivinsky, G. and Clapham, D.E. (2004) 'The mitochondrial calcium uniporter is a highly selective ion channel', *Nature*, 427(6972), pp. 360-4.

Klezovitch, O., Risk, M., Coleman, I., Lucas, J.M., Null, M., True, L.D., Nelson, P.S. and Vasioukhin, V. (2008) 'A causal role for ERG in neoplastic transformation of prostate epithelium', *Proc Natl Acad Sci U S A*, 105(6), pp. 2105-10.

Kloss-Brandstätter, A., Schäfer, G., Erhart, G., Hüttenhofer, A., Coassin, S., Seifarth, C., Summerer, M., Bektic, J., Klocker, H. and Kronenberg, F. (2010) 'Somatic mutations throughout the entire mitochondrial genome are associated with elevated PSA levels in prostate cancer patients.', *American journal of human genetics*, 87(6), pp. 802-812.

Knoblaugh, S. and True, L. (2012) 'Male Reproductive System', in Treuting, P., Dintzis, S. and Montine, K.S. (eds.) *Comparative Anatomy and Histology*. 1st edn. Academic Press.

Knowles, B.R., Friedrich, F., Fischer, C., Paech, D. and Ladd, M.E. (2019) 'Beyond T2 and 3T: New MRI techniques for clinicians', *Clin Transl Radiat Oncol*, 18, pp. 87-97.

Koochekpour, S., Marlowe, T., Singh, K.K., Attwood, K. and Chandra, D. (2013) 'Reduced mitochondrial DNA content associates with poor prognosis of prostate cancer in African American men', *PLoS One*, 8(9), p. e74688.

Korenchuk, S., Lehr, J.E., L, M.C., Lee, Y.G., Whitney, S., Vessella, R., Lin, D.L. and Pienta, K.J. (2001) 'VCaP, a cell-based model system of human prostate cancer', *In Vivo*, 15(2), pp. 163-8.

Korhonen, J.A., Gaspari, M. and Falkenberg, M. (2003) 'TWINKLE Has 5' -> 3' DNA helicase activity and is specifically stimulated by mitochondrial single-stranded DNA-binding protein', *J Biol Chem*, 278(49), pp. 48627-32.

Kote-Jarai, Z., Leongamornlert, D., Saunders, E., Tymrakiewicz, M., Castro, E., Mahmud, N., Guy, M., Edwards, S., O'Brien, L., Sawyer, E., Hall, A., Wilkinson, R., Dadaev, T., Goh, C., Easton, D., Collaborators, U., Goldgar, D. and Eeles, R. (2011) 'BRCA2 is a moderate penetrance gene contributing to young-onset prostate cancer: implications for genetic testing in prostate cancer patients', *Br J Cancer*, 105(8), pp. 1230-4.

Koundouros, N. and Poulogiannis, G. (2018) 'Phosphoinositide 3-Kinase/Akt Signaling and Redox Metabolism in Cancer', *Front Oncol*, 8, p. 160.

Kramer, T., Schmidt, B. and Lo Monte, F. (2012) 'Small-Molecule Inhibitors of GSK-3: Structural Insights and Their Application to Alzheimer's Disease Models', *Int J Alzheimers Dis*, 2012, p. 381029.

Krauss, D., Kestin, L., Ye, H., Brabbins, D., Ghilezan, M., Gustafson, G., Vicini, F. and Martinez, A. (2011) 'Lack of benefit for the addition of androgen deprivation therapy to dose-escalated radiotherapy in the treatment of intermediate- and high-risk prostate cancer', *Int J Radiat Oncol Biol Phys*, 80(4), pp. 1064-71.

Krishnan, K.J., Greaves, L.C., Reeve, A.K. and Turnbull, D. (2007) 'The ageing mitochondrial genome', *Nucleic Acids Res*, 35(22), pp. 7399-405.

Kruse, S.E., Watt, W.C., Marcinek, D.J., Kapur, R.P., Schenkman, K.A. and Palmiter, R.D. (2008) 'Mice with mitochondrial complex I deficiency develop a fatal encephalomyopathy', *Cell Metab*, 7(4), pp. 312-20.

Kujoth, G.C., Hiona, A., Pugh, T.D., Someya, S., Panzer, K., Wohlgemuth, S.E., Hofer, T., Seo, A.Y., Sullivan, R., Jobling, W.A., Morrow, J.D., Van Remmen, H., Sedivy, J.M., Yamasoba, T., Tanokura, M., Weindruch, R., Leeuwenburgh, C. and Prolla, T.A. (2005) 'Mitochondrial DNA mutations, oxidative stress, and apoptosis in mammalian aging.', *Science*, 309(5733), pp. 481-484.

Kupelian, P.A., Ciezki, J., Reddy, C.A., Klein, E.A. and Mahadevan, A. (2008) 'Effect of increasing radiation doses on local and distant failures in patients with localized prostate cancer', *Int J Radiat Oncol Biol Phys*, 71(1), pp. 16-22.

Kurita, T., Medina, R.T., Mills, A.A. and Cunha, G.R. (2004) 'Role of p63 and basal cells in the prostate', *Development*, 131(20), pp. 4955-64.

Kurosaki, T. and Maquat, L.E. (2016) 'Nonsense-mediated mRNA decay in humans at a glance', *J Cell Sci*, 129(3), pp. 461-7.

Kuser-Abali, G., Alptekin, A., Lewis, M., Garraway, I.P. and Cinar, B. (2015) 'YAP1 and AR interactions contribute to the switch from androgen-dependent to castration-resistant growth in prostate cancer', *Nat Commun*, 6, p. 8126.

Kuzmenko, A., Atkinson, G.C., Levitskii, S., Zenkin, N., Tenson, T., Hauryliuk, V. and Kamenski, P. (2014) 'Mitochondrial translation initiation machinery: conservation and diversification', *Biochimie*, 100, pp. 132-40.

Kwabi-Addo, B., Chung, W., Shen, L., Ittmann, M., Wheeler, T., Jelinek, J. and Issa, J.-P.J. (2007) 'Age-related DNA methylation changes in normal human prostate tissues.', *Clinical Cancer Research*, 13(13), pp. 3796-3802.

Kwak, M.K., Johnson, D.T., Zhu, C., Lee, S.H., Ye, D.W., Luong, R. and Sun, Z. (2013) 'Conditional deletion of the Pten gene in the mouse prostate induces prostatic intraepithelial neoplasms at early ages but a slow progression to prostate tumors', *PLoS One*, 8(1), p. e53476.

Laderman, K.A., Penny, J.R., Mazzucchelli, F., Bresolin, N., Scarlato, G. and Attardi, G. (1996) 'Aging-dependent functional alterations of mitochondrial DNA (mtDNA) from human fibroblasts transferred into mtDNA-less cells', *J Biol Chem*, 271(27), pp. 15891-7.

Lamb, D.J. and Zhang, L. (2005) 'Challenges in prostate cancer research: animal models for nutritional studies of chemoprevention and disease progression', *J Nutr*, 135(12 Suppl), pp. 3009S-3015S.

Lang, M., Vocke, C.D., Merino, M.J., Schmidt, L.S. and Linehan, W.M. (2015) 'Mitochondrial DNA mutations distinguish bilateral multifocal renal oncocytomas from familial Birt-Hogg-Dube tumors', *Mod Pathol*, 28(11), pp. 1458-69.

Larsson, N.G., Wang, J., Wilhelmsson, H., Oldfors, A., Rustin, P., Lewandoski, M., Barsh, G.S. and Clayton, D.A. (1998) 'Mitochondrial transcription factor A is necessary for mtDNA maintenance and embryogenesis in mice', *Nat Genet*, 18(3), pp. 231-6.

Latonen, L., Afyounian, E., Jylha, A., Nattinen, J., Aapola, U., Annala, M., Kivinummi, K.K., Tammela, T.T.L., Beuerman, R.W., Uusitalo, H., Nykter, M. and Visakorpi, T. (2018) 'Integrative proteomics in prostate cancer uncovers robustness against genomic and transcriptomic aberrations during disease progression', *Nat Commun*, 9(1), p. 1176.

Lazarou, M., Thorburn, D.R., Ryan, M.T. and McKenzie, M. (2009) 'Assembly of mitochondrial complex I and defects in disease', *Biochim Biophys Acta*, 1793(1), pp. 78-88.

Lee, J.J., Thomas, I.C., Nolley, R., Ferrari, M., Brooks, J.D. and Leppert, J.T. (2015) 'Biologic differences between peripheral and transition zone prostate cancer', *Prostate*, 75(2), pp. 183-90.

Legisi, L., DeSa, E. and Qureshi, M.N. (2016) 'Use of the Prostate Core Mitomic Test in Repeated Biopsy Decision-Making: Real-World Assessment of Clinical Utility in a Multicenter Patient Population', *Am Health Drug Benefits*, 9(9), pp. 497-502.

Lei, Q., Jiao, J., Xin, L., Chang, C.J., Wang, S., Gao, J., Gleave, M.E., Witte, O.N., Liu, X. and Wu, H. (2006) 'NKX3.1 stabilizes p53, inhibits AKT activation, and blocks prostate cancer initiation caused by PTEN loss', *Cancer Cell*, 9(5), pp. 367-78.

Lenaz, G., Bovina, C., Castelluccio, C., Fato, R., Formiggini, G., Genova, M.L., Marchetti, M., Pich, M.M., Pallotti, F., Parenti Castelli, G. and Biagini, G. (1997) 'Mitochondrial complex I defects in aging.', *Molecular and cellular biochemistry*, 174(1-2), pp. 329-333.

Leone, G., Abla, H., Gasparre, G., Porcelli, A.M. and Iommarini, L. (2018) 'The Oncojanus Paradigm of Respiratory Complex I', *Genes*, 9(5), p. 243.

Leongamornlert, D., Mahmud, N., Tymrakiewicz, M., Saunders, E., Dadaev, T., Castro, E., Goh, C., Govindasami, K., Guy, M., O'Brien, L., Sawyer, E., Hall, A., Wilkinson, R., Easton, D., Collaborators, U., Goldgar, D., Eeles, R. and Kote-Jarai, Z. (2012) 'Germline BRCA1 mutations increase prostate cancer risk', *Br J Cancer*, 106(10), pp. 1697-701.

Levenson, R.M., Borowsky, A.D. and Angelo, M. (2015) 'Immunohistochemistry and mass spectrometry for highly multiplexed cellular molecular imaging', *Lab Invest*, 95(4), pp. 397-405.

Li, C., Li, Y., He, L., Agarwal, A.R., Zeng, N., Cadenas, E. and Stiles, B.L. (2013a) 'PI3K/AKT signaling regulates bioenergetics in immortalized hepatocytes', *Free Radic Biol Med*, 60, pp. 29-40.

Li, J., Lu, J. and Zhou, Y. (2017) 'Mitochondrial-Targeted Molecular Imaging in Cardiac Disease', *Biomed Res Int*, 2017, p. 5246853.

Li, N., Zhao, J., Ma, Y., Roy, B., Liu, R., Kristiansen, K. and Gao, Q. (2018) 'Dissecting the expression landscape of mitochondrial genes in lung squamous cell carcinoma and lung adenocarcinoma', *Oncol Lett*, 16(3), pp. 3992-4000.

Li, Y., He, L., Zeng, N., Sahu, D., Cadenas, E., Shearn, C., Li, W. and Stiles, B.L. (2013b) 'Phosphatase and tensin homolog deleted on chromosome 10 (PTEN) signaling regulates mitochondrial biogenesis and respiration via estrogen-related receptor alpha (ERRalpha)', *J Biol Chem*, 288(35), pp. 25007-24.

Liberzon, A., Birger, C., Thorvaldsdottir, H., Ghandi, M., Mesirov, J.P. and Tamayo, P. (2015) 'The Molecular Signatures Database (MSigDB) hallmark gene set collection', *Cell Syst*, 1(6), pp. 417-425.

Lilja, H., Oldbring, J., Rannevik, G. and Laurell, C.B. (1987) 'Seminal vesicle-secreted proteins and their reactions during gelation and liquefaction of human semen', *J Clin Invest*, 80(2), pp. 281-5.

Lin, J.R., Izar, B., Wang, S., Yapp, C., Mei, S., Shah, P.M., Santagata, S. and Sorger, P.K. (2018) 'Highly multiplexed immunofluorescence imaging of human tissues and tumors using t-CyCIF and conventional optical microscopes', *Elife*, 7, p. 545.

Lindberg, J., Mills, I.G., Klevebring, D., Liu, W., Neiman, M., Xu, J., Wikstrom, P., Wiklund, P., Wiklund, F., Egevad, L. and Gronberg, H. (2013) 'The mitochondrial and autosomal mutation landscapes of prostate cancer', *Eur Urol*, 63(4), pp. 702-8.

Lippolis, G., Edsjo, A., Stenman, U.H. and Bjartell, A. (2013) 'A high-density tissue microarray from patients with clinically localized prostate cancer reveals ERG and TATI exclusivity in tumor cells', *Prostate Cancer Prostatic Dis*, 16(2), pp. 145-50.

Lisanti, S., Garlick, D.S., Bryant, K.G., Tavecchio, M., Mills, G.B., Lu, Y., Kossenkov, A.V., Showe, L.C., Languino, L.R. and Altieri, D.C. (2016) 'Transgenic Expression of the Mitochondrial Chaperone TNFR-associated Protein 1 (TRAP1) Accelerates Prostate Cancer Development', *J Biol Chem*, 291(48), pp. 25247-25254.

Lisanti, S., Tavecchio, M., Chae, Y.C., Liu, Q., Brice, A.K., Thakur, M.L., Languino, L.R. and Altieri, D.C. (2014) 'Deletion of the mitochondrial chaperone TRAP-1 uncovers global reprogramming of metabolic networks.', *Cell Reports*, 8(3), pp. 671-677.

Liu, J., Lichtenberg, T., Hoadley, K.A., Poisson, L.M., Lazar, A.J., Cherniack, A.D., Kovatich, A.J., Benz, C.C., Levine, D.A., Lee, A.V., Omberg, L., Wolf, D.M., Shriver, C.D., Thorsson, V., Cancer Genome Atlas Research, N. and Hu, H. (2018) 'An Integrated TCGA Pan-Cancer Clinical Data Resource to Drive High-Quality Survival Outcome Analytics', *Cell*, 173(2), pp. 400-416 e11.

Liu, Y. (2006) 'Fatty acid oxidation is a dominant bioenergetic pathway in prostate cancer', *Prostate Cancer Prostatic Dis*, 9(3), pp. 230-4.

Liu, Y., Beyer, A. and Aebersold, R. (2016) 'On the Dependency of Cellular Protein Levels on mRNA Abundance', *Cell*, 165(3), pp. 535-50.

Lloyd, S.M., Arnold, J. and Sreekumar, A. (2015) 'Metabolomic profiling of hormone-dependent cancers: a bird's eye view', *Trends Endocrinol Metab*, 26(9), pp. 477-85.

Lombardi, A., Silvestri, E., Cioffi, F., Senese, R., Lanni, A., Goglia, F., de Lange, P. and Moreno, M. (2009) 'Defining the transcriptomic and proteomic profiles of rat ageing skeletal muscle by the use of a cDNA array, 2D- and Blue native-PAGE approach', *J Proteomics*, 72(4), pp. 708-21.

Lopez-Otin, C., Blasco, M.A., Partridge, L., Serrano, M. and Kroemer, G. (2013) 'The hallmarks of aging', *Cell*, 153(6), pp. 1194-217.

Lorente, D., Mateo, J., Perez-Lopez, R., de Bono, J.S. and Attard, G. (2015) 'Sequencing of agents in castration-resistant prostate cancer', *Lancet Oncol*, 16(6), pp. e279-92.

Lotan, T.L., Heumann, A., Rico, S.D., Hicks, J., Lecksell, K., Koop, C., Sauter, G., Schlomm, T. and Simon, R. (2017) 'PTEN loss detection in prostate cancer: comparison of PTEN immunohistochemistry and PTEN FISH in a large retrospective prostatectomy cohort', *Oncotarget*, 8(39), pp. 65566-65576.

Lott, M.T., Leipzig, J.N., Derbeneva, O., Xie, H.M., Chalkia, D., Sarmady, M., Procaccio, V. and Wallace, D.C. (2013) 'mtDNA Variation and Analysis Using Mitomap and Mitomaster', *Curr Protoc Bioinformatics*, 44, pp. 1 23 1-26.

Love, M.I., Huber, W. and Anders, S. (2014) 'Moderated estimation of fold change and dispersion for RNA-seq data with DESeq2', *Genome Biol*, 15(12), p. 550.

Lu, B., Poirier, C., Gaspar, T., Gratzke, C., Harrison, W., Busija, D., Matzuk, M.M., Andersson, K.E., Overbeek, P.A. and Bishop, C.E. (2008) 'A mutation in the inner mitochondrial membrane peptidase 2-like gene (Immp2l) affects mitochondrial function and impairs fertility in mice', *Biol Reprod*, 78(4), pp. 601-10.

Ma, H., Lee, Y., Hayama, T., Van Dyken, C., Marti-Gutierrez, N., Li, Y., Ahmed, R., Koski, A., Kang, E., Darby, H., Gonmanee, T., Park, Y., Wolf, D.P., Jai Kim, C. and Mitalipov, S. (2018) 'Germline and somatic mtDNA mutations in mouse aging', *PLoS One*, 13(7), p. e0201304.

Ma, X., Ziel-van der Made, A.C., Autar, B., van der Korput, H.A., Vermeij, M., van Duijn, P., Cleutjens, K.B., de Krijger, R., Krimpenfort, P., Berns, A., van der Kwast, T.H. and Trapman, J. (2005) 'Targeted biallelic inactivation of Pten in the mouse prostate leads to prostate cancer accompanied by increased epithelial cell proliferation but not by reduced apoptosis', *Cancer Res*, 65(13), pp. 5730-9.

Ma, Y., Mehta, S.L., Lu, B. and Li, P.A. (2011) 'Deficiency in the inner mitochondrial membrane peptidase 2-like (Immp21) gene increases ischemic brain damage and impairs mitochondrial function', *Neurobiol Dis*, 44(3), pp. 270-6.

MacAulay, K. and Woodgett, J.R. (2008) 'Targeting glycogen synthase kinase-3 (GSK-3) in the treatment of Type 2 diabetes', *Expert Opin Ther Targets*, 12(10), pp. 1265-74.

Macintosh, C.A., Stower, M., Reid, N. and Maitland, N.J. (1998) 'Precise microdissection of human prostate cancers reveals genotypic heterogeneity', *Cancer Res*, 58(1), pp. 23-8.

Mahad, D.J., Ziabreva, I., Campbell, G., Laulund, F., Murphy, J.L., Reeve, A.K., Greaves, L., Smith, K.J. and Turnbull, D.M. (2009) 'Detection of cytochrome c oxidase activity and mitochondrial proteins in single cells', *J Neurosci Methods*, 184(2), pp. 310-9.

Mak, M.P., Tong, P., Diao, L., Cardnell, R.J., Gibbons, D.L., William, W.N., Skoulidis, F., Parra, E.R., Rodriguez-Canales, J., Wistuba, I.I., Heymach, J.V., Weinstein, J.N., Coombes, K.R., Wang, J. and Byers, L.A. (2016) 'A Patient-Derived, Pan-Cancer EMT Signature Identifies Global Molecular Alterations and Immune Target Enrichment Following Epithelial-to-Mesenchymal Transition', *Clinical Cancer Research*, 22(3), pp. 609-620.

Maki, J., Robinson, K., Reguly, B., Alexander, J., Wittock, R., Aguirre, A., Diamandis, E.P., Escott, N., Skehan, A., Prowse, O., Thayer, R.E., Froberg, M.K., Wilson, M.J., Maragh, S., Jakupciak, J.P., Wagner, P.D., Srivastava, S., Dakubo, G.D. and Parr, R.L. (2008) 'Mitochondrial genome deletion aids in the identification of false- and true-negative prostate needle core biopsy specimens', *Am J Clin Pathol*, 129(1), pp. 57-66.

Mansfield, J.R. (2014) 'Multispectral imaging: a review of its technical aspects and applications in anatomic pathology', *Vet Pathol*, 51(1), pp. 185-210.

Mao, P., Nakao, K. and Angrist, A. (1966) 'Human prostatic carcinoma: an electron microscope study', *Cancer Res*, 26(5), pp. 955-73.

Maragh, S., Veltri, R.W., Lund, S.P., Mangold, L., Isharwal, S., Christudass, C.S., Partin, A.W., Humphreys, E.B., Sorbara, L., Srivastava, S. and Wagner, P.D. (2015) 'Evaluation of two mitochondrial DNA biomarkers for prostate cancer detection', *Cancer Biomark*, 15(6), pp. 763-73.

Martin, P., Liu, Y.N., Pierce, R., Abou-Kheir, W., Casey, O., Seng, V., Camacho, D., Simpson, R.M. and Kelly, K. (2011) 'Prostate epithelial Pten/TP53 loss leads to transformation of multipotential progenitors and epithelial to mesenchymal transition', *Am J Pathol*, 179(1), pp. 422-35.

Martin, R.M., Donovan, J.L., Turner, E.L., Metcalfe, C., Young, G.J., Walsh, E.I., Lane, J.A., Noble, S., Oliver, S.E., Evans, S., Sterne, J.A.C., Holding, P., Ben-Shlomo, Y., Brindle, P., Williams, N.J., Hill, E.M., Ng, S.Y., Toole, J., Tazewell, M.K., Hughes, L.J., Davies, C.F., Thorn, J.C., Down, E., Davey Smith, G., Neal, D.E., Hamdy, F.C. and Group, C.A.P.T. (2018) 'Effect of a Low-Intensity PSA-Based Screening Intervention on Prostate Cancer Mortality: The CAP Randomized Clinical Trial', *JAMA*, 319(9), pp. 883-895.

Martinez, C.G., Lei, Y. and West, P. (2018) 'Defining how mitochondrial DNA stress regulates innate immune responses', *The Journal of Immunology*, 200(1 Supplement), p. 169.14.

Mashima, T., Seimiya, H. and Tsuruo, T. (2009) 'De novo fatty-acid synthesis and related pathways as molecular targets for cancer therapy', *Br J Cancer*, 100(9), pp. 1369-72.

Mason, M.D., Parulekar, W.R., Sydes, M.R., Brundage, M., Kirkbride, P., Gospodarowicz, M., Cowan, R., Kostashuk, E.C., Anderson, J., Swanson, G., Parmar, M.K., Hayter, C., Jovic, G., Hiltz, A., Hetherington, J., Sathya, J., Barber, J.B., McKenzie, M., El-Sharkawi, S., Souhami, L., Hardman, P.D., Chen, B.E. and Warde, P. (2015) 'Final Report of the Intergroup Randomized Study of Combined Androgen-Deprivation Therapy Plus Radiotherapy Versus Androgen-Deprivation Therapy Alone in Locally Advanced Prostate Cancer', *J Clin Oncol*, 33(19), pp. 2143-50.

Mateo, J., Carreira, S., Sandhu, S., Miranda, S., Mossop, H., Perez-Lopez, R., Nava Rodrigues, D., Robinson, D., Omlin, A., Tunariu, N., Boysen, G., Porta, N., Flohr, P., Gillman, A., Figueiredo, I., Paulding, C., Seed, G., Jain, S., Ralph, C., Protheroe, A., Hussain, S., Jones, R., Elliott, T., McGovern, U., Bianchini, D., Goodall, J., Zafeiriou, Z., Williamson, C.T., Ferraldeschi, R., Riisnaes, R., Ebbs, B., Fowler, G., Roda, D., Yuan, W., Wu, Y.M., Cao, X., Brough, R., Pemberton, H., A'Hern, R., Swain, A., Kunju, L.P., Eeles, R., Attard, G., Lord, C.J., Ashworth, A., Rubin, M.A., Knudsen, K.E., Feng, F.Y., Chinnaiyan, A.M., Hall, E. and de Bono, J.S. (2015) 'DNA-Repair Defects and Olaparib in Metastatic Prostate Cancer', *N Engl J Med*, 373(18), pp. 1697-708.

Mateo, J., Fizazi, K., Gillessen, S., Heidenreich, A., Perez-Lopez, R., Oyen, W.J.G., Shore, N., Smith, M., Sweeney, C., Tombal, B., Tomlins, S.A. and de Bono, J.S. (2019) 'Managing Nonmetastatic Castration-resistant Prostate Cancer', *Eur Urol*, 75(2), pp. 285-293.

Matoba, S., Kang, J.-G., Patino, W.D., Wragg, A., Boehm, M., Gavrilova, O., Hurley, P.J., Bunz, F. and Hwang, P.M. (2006) 'p53 regulates mitochondrial respiration.', *Science*, 312(5780), pp. 1650-1653.

Maxwell, P.J., Coulter, J., Walker, S.M., McKechnie, M., Neisen, J., McCabe, N., Kennedy, R.D., Salto-Tellez, M., Albanese, C. and Waugh, D.J. (2013) 'Potentiation of inflammatory CXCL8 signalling sustains cell survival in PTEN-deficient prostate carcinoma', *Eur Urol*, 64(2), pp. 177-88.

Mayr, J.A., Meierhofer, D., Zimmermann, F., Feichtinger, R., Kogler, C., Ratschek, M., Schmeller, N., Sperl, W. and Kofler, B. (2008) 'Loss of complex I due to mitochondrial DNA mutations in renal oncocytoma', *Clin Cancer Res*, 14(8), pp. 2270-5.

McCabe, A., Dolled-Filhart, M., Camp, R.L. and Rimm, D.L. (2005) 'Automated quantitative analysis (AQUA) of in situ protein expression, antibody concentration, and prognosis', *J Natl Cancer Inst*, 97(24), pp. 1808-15.

McCabe, N., Hanna, C., Walker, S.M., Gonda, D., Li, J., Wikstrom, K., Savage, K.I., Butterworth, K.T., Chen, C., Harkin, D.P., Prise, K.M. and Kennedy, R.D. (2015) 'Mechanistic Rationale to Target PTEN-Deficient Tumor Cells with Inhibitors of the DNA Damage Response Kinase ATM', *Cancer Res*, 75(11), pp. 2159-65.

McCormack, J.G., Halestrap, A.P. and Denton, R.M. (1990) 'Role of calcium ions in regulation of mammalian intramitochondrial metabolism', *Physiol Rev*, 70(2), pp. 391-425.

McCrow, J.P., Petersen, D.C., Louw, M., Chan, E.K., Harmeyer, K., Vecchiarelli, S., Lyons, R.J., Bornman, M.S. and Hayes, V.M. (2016) 'Spectrum of mitochondrial genomic variation and associated clinical presentation of prostate cancer in South African men', *Prostate*, 76(4), pp. 349-58.

McIlwain, D.R., Berger, T. and Mak, T.W. (2013) 'Caspase functions in cell death and disease', *Cold Spring Harb Perspect Biol*, 5(4), p. a008656.

McKenzie, M., Trounce, I.A., Cassar, C.A. and Pinkert, C.A. (2004) 'Production of homoplasmic xenomitochondrial mice', *Proc Natl Acad Sci U S A*, 101(6), pp. 1685-90.

McNeal, J.E. (1981) 'The zonal anatomy of the prostate', *Prostate*, 2(1), pp. 35-49.

McNeal, J.E. and Bostwick, D.G. (1986) 'Intraductal dysplasia: a premalignant lesion of the prostate', *Hum Pathol*, 17(1), pp. 64-71.

McNeal, J.E., Redwine, E.A., Freiha, F.S. and Stamey, T.A. (1988) 'Zonal distribution of prostatic adenocarcinoma. Correlation with histologic pattern and direction of spread', *Am J Surg Pathol*, 12(12), pp. 897-906.

Meeks, J.J. and Schaeffer, E.M. (2011) 'Genetic regulation of prostate development', *J Androl*, 32(3), pp. 210-7.

Mei, H., Sun, S., Bai, Y., Chen, Y., Chai, R. and Li, H. (2015) 'Reduced mtDNA copy number increases the sensitivity of tumor cells to chemotherapeutic drugs', *Cell Death Dis*, 6, p. e1710.

Meller, S., Meyer, H.A., Bethan, B., Dietrich, D., Maldonado, S.G., Lein, M., Montani, M., Reszka, R., Schatz, P., Peter, E., Stephan, C., Jung, K., Kamlage, B. and Kristiansen, G. (2016) 'Integration of tissue metabolomics, transcriptomics and immunohistochemistry reveals ERG- and gleason score-specific metabolomic alterations in prostate cancer', *Oncotarget*, 7(2), pp. 1421-38.

Mengel-From, J., Thinggaard, M., Dalgard, C., Kyvik, K.O., Christensen, K. and Christiansen, L. (2014) 'Mitochondrial DNA copy number in peripheral blood cells declines with age and is associated with general health among elderly', *Hum Genet*, 133(9), pp. 1149-59.

Mermel, C.H., Schumacher, S.E., Hill, B., Meyerson, M.L., Beroukhim, R. and Getz, G. (2011) 'GISTIC2.0 facilitates sensitive and confident localization of the targets of focal somatic copy-number alteration in human cancers', *Genome Biol*, 12(4), p. R41.

Metallo, C.M., Gameiro, P.A., Bell, E.L., Mattaini, K.R., Yang, J., Hiller, K., Jewell, C.M., Johnson, Z.R., Irvine, D.J., Guarente, L., Kelleher, J.K., Vander Heiden, M.G., Iliopoulos, O. and Stephanopoulos, G. (2011) 'Reductive glutamine metabolism by IDH1 mediates lipogenesis under hypoxia', *Nature*, 481(7381), pp. 380-4.

Mi, H., Muruganujan, A., Ebert, D., Huang, X. and Thomas, P.D. (2019) 'PANTHER version 14: more genomes, a new PANTHER GO-slim and improvements in enrichment analysis tools', *Nucleic Acids Res*, 47(D1), pp. D419-D426.

Millis, S.Z., Jardim, D.L., Albacker, L., Ross, J.S., Miller, V.A., Ali, S.M. and Kurzrock, R. (2019) 'Phosphatidylinositol 3-kinase pathway genomic alterations in 60,991 diverse solid tumors informs targeted therapy opportunities.', *Cancer*, 125(7), pp. 1185-1199.

Mills, J.S., Needham, M. and Parker, M.G. (1987) 'Androgen regulated expression of a spermine binding protein gene in mouse ventral prostate', *Nucleic Acids Res*, 15(19), pp. 7709-24.

Minner, S., Enodien, M., Sirma, H., Luebke, A.M., Krohn, A., Mayer, P.S., Simon, R., Tennstedt, P., Müller, J., Scholz, L., Brase, J.C., Liu, A.Y., Schlüter, H., Pantel, K., Schumacher, U., Bokemeyer, C., Steuber, T., Graefen, M., Sauter, G. and Schlomm, T. (2011) 'ERG Status Is Unrelated to PSA Recurrence in Radically Operated Prostate Cancer in the Absence of Antihormonal Therapy', *Clinical Cancer Research*, 17(18), pp. 5878-5888.

Mizumachi, T., Muskhelishvili, L., Naito, A., Furusawa, J., Fan, C.Y., Siegel, E.R., Kadlubar, F.F., Kumar, U. and Higuchi, M. (2008) 'Increased distributional variance of mitochondrial DNA content associated with prostate cancer cells as compared with normal prostate cells', *Prostate*, 68(4), pp. 408-17.

Moad, M., Hannezo, E., Buczacki, S.J., Wilson, L., El-Sherif, A., Sims, D., Pickard, R., Wright, N.A., Williamson, S.C., Turnbull, D.M., Taylor, R.W., Greaves, L., Robson, C.N., Simons, B.D. and Heer, R. (2017) 'Multipotent Basal Stem Cells, Maintained in Localized Proximal Niches, Support Directed Long-Ranging Epithelial Flows in Human Prostates', *Cell Rep*, 20(7), pp. 1609-1622.

Montoya, J., Christianson, T., Levens, D., Rabinowitz, M. and Attardi, G. (1982) 'Identification of initiation sites for heavy-strand and light-strand transcription in human mitochondrial DNA', *Proc Natl Acad Sci U S A*, 79(23), pp. 7195-9.

Mookerjee, S.A., Goncalves, R.L.S., Gerencser, A.A., Nicholls, D.G. and Brand, M.D. (2015) 'The contributions of respiration and glycolysis to extracellular acid production', *Biochim Biophys Acta*, 1847(2), pp. 171-181.

Moore, A., Lan, Q., Hofmann, J.N., Liu, C.-S., Cheng, W.-L., Lin, T.-T. and Berndt, S.I. (2017) 'A prospective study of mitochondrial DNA copy number and the risk of prostate cancer.', *Cancer causes & control : CCC*, 28(6), pp. 529-538.

Moro, L., Arbini, A.A., Yao, J.L., di Sant'Agnese, P.A., Marra, E. and Greco, M. (2009) 'Mitochondrial DNA depletion in prostate epithelial cells promotes anoikis resistance and invasion through activation of PI3K/Akt2', *Cell Death Differ*, 16(4), pp. 571-83.

Moro, M., Caiola, E., Ganzinelli, M., Zulato, E., Rulli, E., Marabese, M., Centonze, G., Busico, A., Pastorino, U., de Braud, F.G., Vernieri, C., Simbolo, M., Bria, E., Scarpa, A., Indraccolo, S., Broggini, M., Sozzi, G. and Garassino, M.C. (2018) 'Metformin Enhances Cisplatin-Induced Apoptosis and Prevents Resistance to Cisplatin in Co-mutated KRAS/LKB1 NSCLC', *J Thorac Oncol*, 13(11), pp. 1692-1704.

Morrish, F. and Hockenbery, D. (2014) 'MYC and mitochondrial biogenesis', *Cold Spring Harb Perspect Med*, 4(5).

Mottet, N., Peneau, M., Mazeron, J.J., Molinie, V. and Richaud, P. (2012) 'Addition of radiotherapy to long-term androgen deprivation in locally advanced prostate cancer: an open randomised phase 3 trial', *Eur Urol*, 62(2), pp. 213-9.

Mottet, N., van den Bergh, R., Briers, E., Bourke, L., Cornford, P., De Santis, M., Gillessen, S., Govorov, A., Grummet, J., Henry, A., Lam, T., Mason, M., van der Poel, H., van der Kwast, T., Rouvière, O., Wiegel, T., Van den Broeck, T., Cumberbatch, M., Fossati, N., Gross, T., Lardas, M., Liew, M., Moris, L., Schoots, I. and Willemse, P. (2018) *EAU - ESTRO - ESUR - SIOG Guidelines on Prostate Cancer*. Copenhagen: European Association of Urology.

Moullan, N., Mouchiroud, L., Wang, X., Ryu, D., Williams, E.G., Mottis, A., Jovaisaite, V., Frochaux, M.V., Quiros, P.M., Deplancke, B., Houtkooper, R.H. and Auwerx, J. (2015) 'Tetracyclines Disturb Mitochondrial Function across Eukaryotic Models: A Call for Caution in Biomedical Research', *Cell Rep*, 10(10), pp. 1681-1691.

Mouse Genome Sequencing, C., Waterston, R.H., Lindblad-Toh, K., Birney, E., Rogers, J., Abril, J.F., Agarwal, P., Agarwala, R., Ainscough, R., Alexandersson, M., An, P., Antonarakis, S.E., Attwood, J., Baertsch, R., Bailey, J., Barlow, K., Beck, S., Berry, E., Birren, B., Bloom, T., Bork, P., Botcherby, M., Bray, N., Brent, M.R., Brown, D.G., Brown, S.D., Bult, C., Burton, J., Butler, J., Campbell, R.D., Carninci, P., Cawley, S., Chiaromonte, F., Chinwalla, A.T., Church, D.M., Clamp, M., Clee, C., Collins, F.S., Cook, L.L., Copley, R.R., Coulson, A., Couronne, O., Cuff, J., Curwen, V., Cutts, T., Daly, M., David, R., Davies, J., Delehaunty, K.D., Deri, J., Dermitzakis, E.T., Dewey, C., Dickens, N.J., Diekhans, M., Dodge, S., Dubchak, I., Dunn, D.M., Eddy, S.R., Elnitski, L., Emes, R.D., Eswara, P., Eyras, E., Felsenfeld, A., Fewell, G.A., Flicek, P., Foley, K., Frankel, W.N., Fulton, L.A., Fulton, R.S., Furey, T.S., Gage, D., Gibbs, R.A., Glusman, G., Gnerre, S., Goldman, N., Goodstadt, L., Grafham, D., Graves, T.A., Green, E.D., Gregory, S., Guigo, R., Guyer, M., Hardison, R.C., Haussler, D., Hayashizaki, Y., Hillier, L.W., Hinrichs, A., Hlavina, W., Holzer, T., Hsu, F., Hua, A., Hubbard, T., Hunt, A., Jackson, I., Jaffe, D.B., Johnson, L.S., Jones, M., Jones, T.A., Joy, A., Kamal, M., et al. (2002) 'Initial sequencing and comparative analysis of the mouse genome', *Nature*, 420(6915), pp. 520-62.

Mulholland, D.J., Kobayashi, N., Ruscetti, M., Zhi, A., Tran, L.M., Huang, J., Gleave, M. and Wu, H. (2012) 'Pten loss and RAS/MAPK activation cooperate to promote EMT and metastasis initiated from prostate cancer stem/progenitor cells.', *Cancer Research*, 72(7), pp. 1878-1889.

Mulholland, D.J., Tran, L.M., Li, Y., Cai, H., Morim, A., Wang, S., Plaisier, S., Garraway, I.P., Huang, J., Graeber, T.G. and Wu, H. (2011) 'Cell autonomous role of PTEN in regulating castration-resistant prostate cancer growth', *Cancer Cell*, 19(6), pp. 792-804.

Müller-Höcker, J., Aust, D., Rohrbach, H., Napiwotzky, J., Reith, A., Link, T.A., Seibel, P., Hölzel, D. and Kadenbach, B. (1997) 'Defects of the respiratory chain in the normal human liver and in cirrhosis during aging.', *Hepatology (Baltimore, Md.)*, 26(3), pp. 709-719.

Murphy, J.L., Ratnaike, T.E., Shang, E., Falkous, G., Blakely, E.L., Alston, C.L., Taivassalo, T., Haller, R.G., Taylor, R.W. and Turnbull, D.M. (2012) 'Cytochrome c oxidase-intermediate fibres: importance in understanding the pathogenesis and treatment of mitochondrial myopathy', *Neuromuscul Disord*, 22(8), pp. 690-8.

Murphy, M.P. (2009) 'How mitochondria produce reactive oxygen species', *Biochem J*, 417(1), pp. 1-13.

Naguib, A., Mathew, G., Reczek, C.R., Watrud, K., Ambrico, A., Herzka, T., Salas, I.C., Lee, M.F., El-Amine, N., Zheng, W., Di Francesco, M.E., Marszalek, J.R., Pappin, D.J., Chandel, N.S. and Trotman, L.C. (2018) 'Mitochondrial Complex I Inhibitors Expose a Vulnerability for Selective Killing of Pten-Null Cells', *Cell Rep*, 23(1), pp. 58-67.

Narendra, D., Tanaka, A., Suen, D.F. and Youle, R.J. (2008) 'Parkin is recruited selectively to impaired mitochondria and promotes their autophagy', *J Cell Biol*, 183(5), pp. 795-803.

Nath, A. and Chan, C. (2016) 'Genetic alterations in fatty acid transport and metabolism genes are associated with metastatic progression and poor prognosis of human cancers', *Sci Rep*, 6(1), p. 18669.

National Institute for Health and Care Excellence (2019) *Radical treatment for localised or locally advanced prostate cancer*.National Institute for Health and Care Excellence. [Online]. Available at: http://pathways.nice.org.uk/pathways/prostate-cancer.

Navarro, A. and Boveris, A. (2007) 'The mitochondrial energy transduction system and the aging process', *American Journal of Physiology-Cell Physiology*, 292(2), pp. C670-C686.

Nekhaeva, E., Bodyak, N.D., Kraytsberg, Y., McGrath, S.B., Van Orsouw, N.J., Pluzhnikov, A., Wei, J.Y., Vijg, J. and Khrapko, K. (2002) 'Clonally expanded mtDNA point mutations are abundant in individual cells of human tissues.', *Proceedings of the National Academy of Sciences*, 99(8), pp. 5521-5526.

Nelson, S.J., Kurhanewicz, J., Vigneron, D.B., Larson, P.E., Harzstark, A.L., Ferrone, M., van Criekinge, M., Chang, J.W., Bok, R., Park, I., Reed, G., Carvajal, L., Small, E.J., Munster, P., Weinberg, V.K., Ardenkjaer-Larsen, J.H., Chen, A.P., Hurd, R.E., Odegardstuen, L.I., Robb, F.J., Tropp, J. and Murray, J.A. (2013) 'Metabolic imaging of patients with prostate cancer using hyperpolarized [1-(1)(3)C]pyruvate', *Sci Transl Med*, 5(198), p. 198ra108.

Nicholls, T.J. and Minczuk, M. (2014) 'In D-loop: 40 years of mitochondrial 7S DNA', *Exp Gerontol*, 56, pp. 175-81.

Nie, D., Hillman, G.G., Geddes, T., Tang, K., Pierson, C., Grignon, D.J. and Honn, K.V. (1998) 'Platelet-type 12-lipoxygenase in a human prostate carcinoma stimulates angiogenesis and tumor growth', *Cancer Res*, 58(18), pp. 4047-51.

Nie, H., Shu, H., Vartak, R., Milstein, A.C., Mo, Y., Hu, X., Fang, H., Shen, L., Ding, Z., Lu, J. and Bai, Y. (2013) 'Mitochondrial common deletion, a potential biomarker for cancer occurrence, is selected against in cancer background: a meta-analysis of 38 studies', *PLoS One*, 8(7), p. e67953.

Nitta, H., Tsuta, K., Yoshida, A., Ho, S.N., Kelly, B.D., Murata, L.B., Kosmeder, J., White, K., Ehser, S., Towne, P., Schemp, C., McElhinny, A., Ranger-Moore, J., Bieniarz, C., Singh, S., Tsuda, H. and Grogan, T.M. (2013) 'New methods for ALK status diagnosis in non-small-cell lung cancer: an improved ALK immunohistochemical assay and a new, Brightfield, dual ALK IHC-in situ hybridization assay', *J Thorac Oncol*, 8(8), pp. 1019-31.

Nooteboom, M., Johnson, R., Taylor, R.W., Wright, N.A., Lightowlers, R.N., Kirkwood, T.B., Mathers, J.C., Turnbull, D.M. and Greaves, L.C. (2010) 'Age-associated mitochondrial DNA mutations lead to small but significant changes in cell proliferation and apoptosis in human colonic crypts', *Aging Cell*, 9(1), pp. 96-9.

Norddahl, G.L., Pronk, C.J., Wahlestedt, M., Sten, G., Nygren, J.M., Ugale, A., Sigvardsson, M. and Bryder, D. (2011) 'Accumulating mitochondrial DNA mutations drive premature hematopoietic aging phenotypes distinct from physiological stem cell aging', *Cell Stem Cell*, 8(5), pp. 499-510.

Nyberg, T., Frost, D., Barrowdale, D., Evans, D.G., Bancroft, E., Adlard, J., Ahmed, M., Barwell, J., Brady, A.F., Brewer, C., Cook, J., Davidson, R., Donaldson, A., Eason, J., Gregory, H., Henderson, A., Izatt, L., Kennedy, M.J., Miller, C., Morrison, P.J., Murray, A., Ong, K.R., Porteous, M., Pottinger, C., Rogers, M.T., Side, L., Snape, K., Walker, L., Tischkowitz, M., Eeles, R., Easton, D.F. and Antoniou, A.C. (2019) 'Prostate Cancer Risks for Male BRCA1 and BRCA2 Mutation Carriers: A Prospective Cohort Study', *Eur Urol*.

O'Toole, J.F., Patel, H.V., Naples, C.J., Fujioka, H. and Hoppel, C.L. (2010) 'Decreased cytochrome c mediates an age-related decline of oxidative phosphorylation in rat kidney mitochondria', *Biochem J*, 427(1), pp. 105-12.

Ojala, D., Montoya, J. and Attardi, G. (1981) 'tRNA punctuation model of RNA processing in human mitochondria', *Nature*, 290(5806), pp. 470-4.

Old, S.L. and Johnson, M.A. (1989) 'Methods of microphotometric assay of succinate dehydrogenase and cytochrome c oxidase activities for use on human skeletal muscle', *Histochem J*, 21(9-10), pp. 545-55.

Oldfors, A., Larsson, N.G., Holme, E., Tulinius, M., Kadenbach, B. and Droste, M. (1992) 'Mitochondrial DNA deletions and cytochrome c oxidase deficiency in muscle fibres', *J Neurol Sci*, 110(1-2), pp. 169-77.

Orrenius, S. and Zhivotovsky, B. (2005) 'Cardiolipin oxidation sets cytochrome c free', *Nat Chem Biol*, 1(4), pp. 188-9.

Ott, M., Gogvadze, V., Orrenius, S. and Zhivotovsky, B. (2007) 'Mitochondria, oxidative stress and cell death', *Apoptosis*, 12(5), pp. 913-22.

Owusu-Ansah, E., Yavari, A., Mandal, S. and Banerjee, U. (2008) 'Distinct mitochondrial retrograde signals control the G1-S cell cycle checkpoint', *Nat Genet*, 40(3), pp. 356-61.

Page, E.C., Bancroft, E.K., Brook, M.N., Assel, M., Hassan Al Battat, M., Thomas, S., Taylor, N., Chamberlain, A., Pope, J., Raghallaigh, H.N., Evans, D.G., Rothwell, J., Mahle, L., Grindedal, E.M.M., James, P., Mascarenhas, L., McKinley, J., Side, L., Thomas, T., van Asperen, C., Vasen, H., Kiemeney, L.A., Ringelberg, J., Jensen, T.D., Osther, P.J.S., Helfand, B.T., Genova, E., Oldenburg, R.A., Cybulski, C., Wokolorczyk, D., Ong, K.R., Huber, C., Lam, J., Taylor, L., Salinas, M., Feliubadalo, L., Oosterwijk, J.C., van Zelst-Stams, W., Cook, J., Rosario, D.J., Domchek, S., Powers, J., Buys, S., O'Toole, K., Ausems, M., Schmutzler, R.K., Rhiem, K., Izatt, L., Tripathi, V., Teixeira, M.R., Cardoso, M., Foulkes, W.D., Aprikian, A., van Randeraad, H., Davidson, R., Longmuir, M., Ruijs, M.W.G., Helderman van den Enden, A., Adank, M., Williams, R., Andrews, L., Murphy, D.G., Halliday, D., Walker, L., Liljegren, A., Carlsson, S., Azzabi, A., Jobson, I., Morton, C., Shackleton, K., Snape, K., Hanson, H., Harris, M., Tischkowitz, M., Taylor, A., Kirk, J., Susman, R., Chen-Shtoyerman, R., Spigelman, A., Pachter, N., Ahmed, M., Ramon, Y.C.T., Zgajnar, J., Brewer, C., Gadea, N., Brady, A.F., van Os, T., Gallagher, D., Johannsson, O., Donaldson, A., Barwell, J., Nicolai, N., Friedman, E., Obeid, E., Greenhalgh, L., Murthy, V., Copakova, L., Saya, S.,

McGrath, J., Cooke, P., et al. (2019) 'Interim Results from the IMPACT Study: Evidence for Prostate-specific Antigen Screening in BRCA2 Mutation Carriers', *Eur Urol*.

Paradkar, P.N., Zumbrennen, K.B., Paw, B.H., Ward, D.M. and Kaplan, J. (2009) 'Regulation of mitochondrial iron import through differential turnover of mitoferrin 1 and mitoferrin 2', *Mol Cell Biol*, 29(4), pp. 1007-16.

Parisotto, M., Grelet, E., El Bizri, R., Dai, Y., Terzic, J., Eckert, D., Gargowitsch, L., Bornert, J.M. and Metzger, D. (2018) 'PTEN deletion in luminal cells of mature prostate induces replication stress and senescence in vivo', *J Exp Med*, 215(6), pp. 1749-1763.

Parisotto, M. and Metzger, D. (2013) 'Genetically engineered mouse models of prostate cancer', *Mol Oncol*, 7(2), pp. 190-205.

Park, K., Tomlins, S.A., Mudaliar, K.M., Chiu, Y.-L., Esgueva, R., Mehra, R., Suleman, K., Varambally, S., Brenner, J.C., MacDonald, T., Srivastava, A., Tewari, A.K., Sathyanarayana, U., Nagy, D., Pestano, G., Kunju, L.P., Demichelis, F., Chinnaiyan, A.M. and Rubin, M.A. (2010) 'Antibody-based detection of ERG rearrangement-positive prostate cancer.', *Neoplasia (New York, N.Y.)*, 12(7), pp. 590-598.

Parker, C.C., James, N.D., Brawley, C.D., Clarke, N.W., Hoyle, A.P., Ali, A., Ritchie, A.W.S., Attard, G., Chowdhury, S., Cross, W., Dearnaley, D.P., Gillessen, S., Gilson, C., Jones, R.J., Langley, R.E., Malik, Z.I., Mason, M.D., Matheson, D., Millman, R., Russell, J.M., Thalmann, G.N., Amos, C.L., Alonzi, R., Bahl, A., Birtle, A., Din, O., Douis, H., Eswar, C., Gale, J., Gannon, M.R., Jonnada, S., Khaksar, S., Lester, J.F., O'Sullivan, J.M., Parikh, O.A., Pedley, I.D., Pudney, D.M., Sheehan, D.J., Srihari, N.N., Tran, A.T.H., Parmar, M.K.B., Sydes, M.R. and Systemic Therapy for Advanced or Metastatic Prostate cancer: Evaluation of Drug Efficacy, i. (2018) 'Radiotherapy to the primary tumour for newly diagnosed, metastatic prostate cancer (STAMPEDE): a randomised controlled phase 3 trial', *Lancet*, 392(10162), pp. 2353-2366.

Parra, E.R., Uraoka, N., Jiang, M., Cook, P., Gibbons, D., Forget, M.A., Bernatchez, C., Haymaker, C., Wistuba, II and Rodriguez-Canales, J. (2017) 'Validation of multiplex immunofluorescence panels using multispectral microscopy for immune-profiling of formalin-fixed and paraffin-embedded human tumor tissues', *Sci Rep*, 7(1), p. 13380.

Parry, M.A., Srivastava, S., Ali, A., Cannistraci, A., Antonello, J., Barros-Silva, J.D., Ubertini, V., Ramani, V., Lau, M., Shanks, J., Nonaka, D., Oliveira, P., Hambrock, T., Leong, H.S., Dhomen, N., Miller, C., Brady, G., Dive, C., Clarke, N.W., Marais, R. and Baena, E. (2019) 'Genomic Evaluation of Multiparametric Magnetic Resonance Imaging-visible and -nonvisible Lesions in Clinically Localised Prostate Cancer', *Eur Urol Oncol*, 2(1), pp. 1-11.

Patterson, A.R., Endale, M., Lampe, K., Aksoylar, H.I., Flagg, A., Woodgett, J.R., Hildeman, D., Jordan, M.B., Singh, H., Kucuk, Z., Bleesing, J. and Hoebe, K. (2018) 'Gimap5-dependent inactivation of GSK3beta is required for CD4(+) T cell homeostasis and prevention of immune pathology', *Nat Commun*, 9(1), p. 430.

Pearce, S.F., Rebelo-Guiomar, P., D'Souza, A.R., Powell, C.A., Van Haute, L. and Minczuk, M. (2017) 'Regulation of Mammalian Mitochondrial Gene Expression: Recent Advances', *Trends Biochem Sci*, 42(8), pp. 625-639.

Pearson, H.B., Phesse, T.J. and Clarke, A.R. (2009) 'K-ras and Wnt signaling synergize to accelerate prostate tumorigenesis in the mouse', *Cancer Res*, 69(1), pp. 94-101.

Pelicano, H., Xu, R.H., Du, M., Feng, L., Sasaki, R., Carew, J.S., Hu, Y., Ramdas, L., Hu, L., Keating, M.J., Zhang, W., Plunkett, W. and Huang, P. (2006) 'Mitochondrial respiration defects in cancer cells cause activation of Akt survival pathway through a redox-mediated mechanism', *J Cell Biol*, 175(6), pp. 913-23.

Perales-Clemente, E., Fernandez-Vizarra, E., Acin-Perez, R., Movilla, N., Bayona-Bafaluy, M.P., Moreno-Loshuertos, R., Perez-Martos, A., Fernandez-Silva, P. and Enriquez, J.A. (2010) 'Five entry points of the

mitochondrially encoded subunits in mammalian complex I assembly', *Mol Cell Biol*, 30(12), pp. 3038-47.

Permuth-Wey, J., Boulware, D., Valkov, N., Livingston, S., Nicosia, S., Lee, J.H., Sutphen, R., Schildkraut, J., Narod, S., Parker, A., Coppola, D., Sellers, T. and Pal, T. (2009) 'Sampling strategies for tissue microarrays to evaluate biomarkers in ovarian cancer', *Cancer Epidemiol Biomarkers Prev*, 18(1), pp. 28-34.

Pertega-Gomes, N., Felisbino, S., Massie, C.E., Vizcaino, J.R., Coelho, R., Sandi, C., Simoes-Sousa, S., Jurmeister, S., Ramos-Montoya, A., Asim, M., Tran, M., Oliveira, E., Lobo da Cunha, A., Maximo, V., Baltazar, F., Neal, D.E. and Fryer, L.G. (2015) 'A glycolytic phenotype is associated with prostate cancer progression and aggressiveness: a role for monocarboxylate transporters as metabolic targets for therapy', *J Pathol*, 236(4), pp. 517-30.

Petros, J.A., Baumann, A.K., Ruiz-Pesini, E., Amin, M.B., Sun, C.Q., Hall, J., Lim, S., Issa, M.M., Flanders, W.D., Hosseini, S.H., Marshall, F.F. and Wallace, D.C. (2005) 'mtDNA mutations increase tumorigenicity in prostate cancer.', *Proceedings of the National Academy of Sciences*, 102(3), pp. 719-724.

Philley, J.V., Kannan, A., Qin, W., Sauter, E.R., Ikebe, M., Hertweck, K.L., Troyer, D.A., Semmes, O.J. and Dasgupta, S. (2016) 'Complex-I Alteration and Enhanced Mitochondrial Fusion Are Associated With Prostate Cancer Progression.', *Journal of Cellular Physiology*, 231(6), pp. 1364-1374.

Pinton, P., Giorgi, C., Siviero, R., Zecchini, E. and Rizzuto, R. (2008) 'Calcium and apoptosis: ER-mitochondria Ca2+ transfer in the control of apoptosis', *Oncogene*, 27(50), pp. 6407-18.

Ploussard, G., Gandaglia, G., Borgmann, H., de Visschere, P., Heidegger, I., Kretschmer, A., Mathieu, R., Surcel, C., Tilki, D., Tsaur, I., Valerio, M., van den Bergh, R., Ost, P., Briganti, A. and Group, E.-Y.P.C.W. (2019) 'Salvage Lymph Node Dissection for Nodal Recurrent Prostate Cancer: A Systematic Review', *Eur Urol*, 76(4), pp. 493-504.

Poluri, R.T.K. and Audet-Walsh, E. (2018) 'Genomic Deletion at 10q23 in Prostate Cancer: More Than PTEN Loss?', *Front Oncol*, 8, p. 246.

Potter, G.A., Barrie, S.E., Jarman, M. and Rowlands, M.G. (1995) 'Novel steroidal inhibitors of human cytochrome P45017 alpha (17 alpha-hydroxylase-C17,20-lyase): potential agents for the treatment of prostatic cancer', *J Med Chem*, 38(13), pp. 2463-71.

Poulose, N., Mills, I.G. and Steele, R.E. (2018) 'The impact of transcription on metabolism in prostate and breast cancers', *Endocr Relat Cancer*, 25(9), pp. R435-R452.

Pound, C.R., Partin, A.W., Eisenberger, M.A., Chan, D.W., Pearson, J.D. and Walsh, P.C. (1999) 'Natural history of progression after PSA elevation following radical prostatectomy', *JAMA*, 281(17), pp. 1591-7.

Powell, I.J., Bock, C.H., Ruterbusch, J.J. and Sakr, W. (2010) 'Evidence supports a faster growth rate and/or earlier transformation to clinically significant prostate cancer in black than in white American men, and influences racial progression and mortality disparity', *J Urol*, 183(5), pp. 1792-6.

Powell, W.C., Cardiff, R.D., Cohen, M.B., Miller, G.J. and Roy-Burman, P. (2003) 'Mouse strains for prostate tumorigenesis based on genes altered in human prostate cancer', *Curr Drug Targets*, 4(3), pp. 263-79.

Preisser, F., Chun, F.K.H., Pompe, R.S., Heinze, A., Salomon, G., Graefen, M., Huland, H. and Tilki, D. (2019a) 'Persistent Prostate-Specific Antigen After Radical Prostatectomy and Its Impact on Oncologic Outcomes', *Eur Urol*, 76(1), pp. 106-114.

Preisser, F., Mazzone, E., Knipper, S., Nazzani, S., Bandini, M., Shariat, S.F., Tian, Z., Saad, F., Montorsi, F., Zorn, K.C., Graefen, M., Tilki, D. and Karakiewicz, P.I. (2019b) 'Rates of Positive Surgical Margins and Their Effect on Cancer-specific Mortality at Radical Prostatectomy for Patients With Clinically Localized Prostate Cancer', *Clin Genitourin Cancer*, 17(1), pp. e130-e139.

Prichard, J.W. (2014) 'Overview of automated immunohistochemistry', *Arch Pathol Lab Med*, 138(12), pp. 1578-82.

Public Health England (2016) *Prostate cancer risk management programme (PCRMP): benefits and risks of PSA testing*.Public Health England. [Online]. Available at: https://www.gov.uk/government/publications/prostate-cancer-risk-management-programme-psa-test-benefits-and-risks/prostate-cancer-risk-management-programme-pcrmp-benefits-and-risks-of-psa-testing

Purysko, A.S., Magi-Galluzzi, C., Mian, O.Y., Sittenfeld, S., Davicioni, E., du Plessis, M., Buerki, C., Bullen, J., Li, L., Madabhushi, A., Stephenson, A. and Klein, E.A. (2019) 'Correlation between MRI phenotypes and a genomic classifier of prostate cancer: preliminary findings', *Eur Radiol*, 29(9), pp. 4861-4870.

Quintana, A., Kruse, S.E., Kapur, R.P., Sanz, E. and Palmiter, R.D. (2010) 'Complex I deficiency due to loss of Ndufs4 in the brain results in progressive encephalopathy resembling Leigh syndrome', *Proc Natl Acad Sci U S A*, 107(24), pp. 10996-1001.

Radford, N.B., Wan, B., Richman, A., Szczepaniak, L.S., Li, J.L., Li, K., Pfeiffer, K., Schagger, H., Garry, D.J. and Moreadith, R.W. (2002) 'Cardiac dysfunction in mice lacking cytochrome-c oxidase subunit VIaH', *Am J Physiol Heart Circ Physiol*, 282(2), pp. H726-33.

Rahman, S., Lake, B.D., Taanman, J.W., Hanna, M.G., Cooper, J.M., Schapira, A.H. and Leonard, J.V. (2000) 'Cytochrome oxidase immunohistochemistry: clues for genetic mechanisms', *Brain*, 123 Pt 3, pp. 591-600.

Ratnacaram, C.K., Teletin, M., Jiang, M., Meng, X., Chambon, P. and Metzger, D. (2008) 'Temporally controlled ablation of PTEN in adult mouse prostate epithelium generates a model of invasive prostatic adenocarcinoma.', *Proceedings of the National Academy of Sciences of the United States of America*, 105(7), pp. 2521-2526.

Ray, A.M., Zuhlke, K.A., Levin, A.M., Douglas, J.A., Cooney, K.A. and Petros, J.A. (2009) 'Sequence variation in the mitochondrial gene cytochrome c oxidase subunit I and prostate cancer in African American men', *Prostate*, 69(9), pp. 956-60.

Remark, R., Merghoub, T., Grabe, N., Litjens, G., Damotte, D., Wolchok, J.D., Merad, M. and Gnjatic, S. (2016) 'In-depth tissue profiling using multiplexed immunohistochemical consecutive staining on single slide', *Sci Immunol*, 1(1), p. aaf6925.

Reznik, E., Miller, M.L., Şenbabaoğlu, Y., Riaz, N., Sarungbam, J., Tickoo, S.K., Al-Ahmadie, H.A., Lee, W., Seshan, V.E., Hakimi, A.A. and Sander, C. (2016) 'Mitochondrial DNA copy number variation across human cancers.', *eLife*, 5, p. 483.

Reznik, E., Wang, Q., La, K., Schultz, N. and Sander, C. (2017) 'Mitochondrial respiratory gene expression is suppressed in many cancers', *Elife*, 6, p. 1.

Robin, E.D. and Wong, R. (1988) 'Mitochondrial DNA molecules and virtual number of mitochondria per cell in mammalian cells', *J Cell Physiol*, 136(3), pp. 507-13.

Robinson, D., Van Allen, E.M., Wu, Y.M., Schultz, N., Lonigro, R.J., Mosquera, J.M., Montgomery, B., Taplin, M.E., Pritchard, C.C., Attard, G., Beltran, H., Abida, W., Bradley, R.K., Vinson, J., Cao, X., Vats, P., Kunju, L.P., Hussain, M., Feng, F.Y., Tomlins, S.A., Cooney, K.A., Smith, D.C., Brennan, C., Siddiqui, J., Mehra, R., Chen, Y., Rathkopf, D.E., Morris, M.J., Solomon, S.B., Durack, J.C., Reuter, V.E., Gopalan, A., Gao, J., Loda, M., Lis, R.T., Bowden, M., Balk, S.P., Gaviola, G., Sougnez, C., Gupta, M., Yu, E.Y., Mostaghel, E.A., Cheng, H.H., Mulcahy, H., True, L.D., Plymate, S.R., Dvinge, H., Ferraldeschi, R., Flohr, P., Miranda, S., Zafeiriou, Z., Tunariu, N., Mateo, J., Perez-Lopez, R., Demichelis, F., Robinson, B.D., Schiffman, M., Nanus, D.M., Tagawa, S.T., Sigaras, A., Eng, K.W., Elemento, O., Sboner, A., Heath, E.I., Scher, H.I., Pienta, K.J., Kantoff, P., de Bono, J.S., Rubin, M.A., Nelson, P.S., Garraway, L.A., Sawyers, C.L. and Chinnaiyan, A.M. (2015) 'Integrative clinical genomics of advanced prostate cancer', *Cell*, 161(5), pp. 1215-1228.

Robinson, K., Creed, J., Reguly, B., Powell, C., Wittock, R., Klein, D., Maggrah, A., Klotz, L., Parr, R.L. and Dakubo, G.D. (2010) 'Accurate prediction of repeat prostate biopsy outcomes by a mitochondrial DNA deletion assay', *Prostate Cancer Prostatic Dis*, 13(2), pp. 126-31.

Rocha, M.C., Grady, J.P., Grunewald, A., Vincent, A., Dobson, P.F., Taylor, R.W., Turnbull, D.M. and Rygiel, K.A. (2015) 'A novel immunofluorescent assay to investigate oxidative phosphorylation deficiency in mitochondrial myopathy: understanding mechanisms and improving diagnosis', *Sci Rep*, 5, p. 15037.

Rorbach, J. and Minczuk, M. (2012) 'The post-transcriptional life of mammalian mitochondrial RNA', *Biochem J*, 444(3), pp. 357-73.

Rorbach, J., Soleimanpour-Lichaei, R., Lightowlers, R.N. and Chrzanowska-Lightowlers, Z.M. (2007) 'How do mammalian mitochondria synthesize proteins?', *Biochem Soc Trans*, 35(Pt 5), pp. 1290-1.

Ross, J.M. (2011) 'Visualization of mitochondrial respiratory function using cytochrome c oxidase/succinate dehydrogenase (COX/SDH) double-labeling histochemistry', *J Vis Exp*, (57), p. e3266.

Rozengurt, E., Soares, H.P. and Sinnet-Smith, J. (2014) 'Suppression of feedback loops mediated by PI3K/mTOR induces multiple overactivation of compensatory pathways: an unintended consequence leading to drug resistance', *Mol Cancer Ther*, 13(11), pp. 2477-88.

Rybak, A.P., Bristow, R.G. and Kapoor, A. (2015) 'Prostate cancer stem cells: deciphering the origins and pathways involved in prostate tumorigenesis and aggression', *Oncotarget*, 6(4), pp. 1900-19.

Sagan, L. (1967) 'On the origin of mitosing cells', *J Theor Biol*, 14(3), pp. 255-74.

Sakr, W.A., Grignon, D.J., Crissman, J.D., Heilbrun, L.K., Cassin, B.J., Pontes, J.J. and Haas, G.P. (1994) 'High grade prostatic intraepithelial neoplasia (HGPIN) and prostatic adenocarcinoma between the ages of 20-69: an autopsy study of 249 cases', *In Vivo*, 8(3), pp. 439-43.

Sakr, W.A., Grignon, D.J., Haas, G.P., Heilbrun, L.K., Pontes, J.E. and Crissman, J.D. (1996) 'Age and racial distribution of prostatic intraepithelial neoplasia', *Eur Urol*, 30(2), pp. 138-44.

Salami, S.S., Hovelson, D.H., Kaplan, J.B., Mathieu, R., Udager, A.M., Curci, N.E., Lee, M., Plouffe, K.R., de la Vega, L.L., Susani, M., Rioux-Leclercq, N., Spratt, D.E., Morgan, T.M., Davenport, M.S., Chinnaiyan, A.M., Cyrta, J., Rubin, M.A., Shariat, S.F., Tomlins, S.A. and Palapattu, G.S. (2018) 'Transcriptomic heterogeneity in multifocal prostate cancer', *JCI Insight*, 3(21), pp. 3-14.

Salk, J.J. and Horwitz, M.S. (2010) 'Passenger mutations as a marker of clonal cell lineages in emerging neoplasia', *Seminars in Cancer Biology*, 20(5), pp. 294-303.

Sanchez-Caballero, L., Guerrero-Castillo, S. and Nijtmans, L. (2016) 'Unraveling the complexity of mitochondrial complex I assembly: A dynamic process', *Biochim Biophys Acta*, 1857(7), pp. 980-90.

Sazanov, L.A. (2015) 'A giant molecular proton pump: structure and mechanism of respiratory complex I', *Nat Rev Mol Cell Biol*, 16(6), pp. 375-88.

Schon, E.A., DiMauro, S. and Hirano, M. (2012) 'Human mitochondrial DNA: roles of inherited and somatic mutations', *Nat Rev Genet*, 13(12), pp. 878-90.

Schriner, S.E., Linford, N.J., Martin, G.M., Treuting, P., Ogburn, C.E., Emond, M., Coskun, P.E., Ladiges, W., Wolf, N., Van Remmen, H., Wallace, D.C. and Rabinovitch, P.S. (2005) 'Extension of murine life span by overexpression of catalase targeted to mitochondria', *Science*, 308(5730), pp. 1909-11.

Schroder, F.H., Hugosson, J., Roobol, M.J., Tammela, T.L., Zappa, M., Nelen, V., Kwiatkowski, M., Lujan, M., Maattanen, L., Lilja, H., Denis, L.J., Recker, F., Paez, A., Bangma, C.H., Carlsson, S., Puliti, D., Villers, A., Rebillard, X., Hakama, M., Stenman, U.H., Kujala, P., Taari, K., Aus, G., Huber, A., van der Kwast, T.H., van Schaik, R.H., de Koning, H.J., Moss, S.M., Auvinen, A. and Investigators, E. (2014) 'Screening and prostate cancer mortality: results of the European Randomised Study of Screening for Prostate Cancer (ERSPC) at 13 years of follow-up', *Lancet*, 384(9959), pp. 2027-35.

Schulz, D., Zanotelli, V.R.T., Fischer, J.R., Schapiro, D., Engler, S., Lun, X.-K., Jackson, H.W. and Bodenmiller, B. (2018) 'Simultaneous Multiplexed Imaging of mRNA and Proteins with Subcellular Resolution in Breast Cancer Tissue Samples by Mass Cytometry.', *Cell Systems*, 6(1), pp. 25-36.e5.

Scosyrev, E., Messing, E.M., Mohile, S., Golijanin, D. and Wu, G. (2012) 'Prostate cancer in the elderly: frequency of advanced disease at presentation and disease-specific mortality', *Cancer*, 118(12), pp. 3062-70.

Scott, T.A., Arnold, R. and Petros, J.A. (2012) 'Mitochondrial Cytochrome c Oxidase subunit 1 Sequence Variation in Prostate Cancer', *Scientifica (Cairo)*, 2012, p. 701810.

Seidel-Rogol, B.L. and Shadel, G.S. (2002) 'Modulation of mitochondrial transcription in response to mtDNA depletion and repletion in HeLa cells', *Nucleic Acids Res*, 30(9), pp. 1929-34.

Selman, S.H. (2011) 'The McNeal prostate: a review', *Urology*, 78(6), pp. 1224-8.

Senyilmaz, D. and Teleman, A.A. (2015) 'Chicken or the egg: Warburg effect and mitochondrial dysfunction', *F1000Prime Rep*, 7, p. 41.

Shadel, G.S. and Horvath, T.L. (2015) 'Mitochondrial ROS signaling in organismal homeostasis', *Cell*, 163(3), pp. 560-9.

Shah, R.B., Bentley, J., Jeffery, Z. and DeMarzo, A.M. (2015) 'Heterogeneity of PTEN and ERG expression in prostate cancer on core needle biopsies: implications for cancer risk stratification and biomarker sampling', *Human Pathology*, 46(5), pp. 698-706.

Shappell, S.B., Thomas, G.V., Roberts, R.L., Herbert, R., Ittmann, M.M., Rubin, M.A., Humphrey, P.A., Sundberg, J.P., Rozengurt, N., Barrios, R., Ward, J.M. and Cardiff, R.D. (2004) 'Prostate pathology of genetically engineered mice: definitions and classification. The consensus report from the Bar Harbor meeting of the Mouse Models of Human Cancer Consortium Prostate Pathology Committee', *Cancer Res*, 64(6), pp. 2270-305.

Sharma, L.K., Lu, J. and Bai, Y. (2009) 'Mitochondrial respiratory complex I: structure, function and implication in human diseases', *Curr Med Chem*, 16(10), pp. 1266-77.

Shen, L., Attimonelli, M., Bai, R., Lott, M.T., Wallace, D.C., Falk, M.J. and Gai, X. (2018) 'MSeqDR mvTool: A mitochondrial DNA Web and API resource for comprehensive variant annotation, universal nomenclature collation, and reference genome conversion', *Hum Mutat*, 39(6), pp. 806-810.

Shen, M.M. and Abate-Shen, C. (2010) 'Molecular genetics of prostate cancer: new prospects for old challenges', *Genes Dev*, 24(18), pp. 1967-2000.

Shen, P.F., Zhu, Y.C., Wei, W.R., Li, Y.Z., Yang, J., Li, Y.T., Li, D.M., Wang, J. and Zeng, H. (2012) 'The results of transperineal versus transrectal prostate biopsy: a systematic review and meta-analysis', *Asian J Androl*, 14(2), pp. 310-5.

Shoag, J.E., Tosoian, J.J., Salami, S.S. and Barbieri, C.E. (2019) 'Unraveling Prostate Cancer Genomics, Pathology, and Magnetic Resonance Imaging Visibility', *Eur Urol*, 76(1), pp. 24-26.

Sicheritz-Ponten, T., Kurland, C.G. and Andersson, S.G. (1998) 'A phylogenetic analysis of the cytochrome b and cytochrome c oxidase I genes supports an origin of mitochondria from within the Rickettsiaceae', *Biochim Biophys Acta*, 1365(3), pp. 545-51.

Siegel, R.L., Miller, K.D. and Jemal, A. (2019) 'Cancer statistics, 2019', *CA Cancer J Clin*, 69(1), pp. 7-34.

Simonnet, H., Demont, J., Pfeiffer, K., Guenaneche, L., Bouvier, R., Brandt, U., Schagger, H. and Godinot, C. (2003) 'Mitochondrial complex I is deficient in renal oncocytomas', *Carcinogenesis*, 24(9), pp. 1461-6.

Singh, K.B. and Singh, S.V. (2017) 'Fatty Acid Synthesis Intermediates Represent Novel Noninvasive Biomarkers of Prostate Cancer Chemoprevention by Phenethyl Isothiocyanate', *Cancer Prev Res (Phila)*, 10(5), pp. 279-289.

Sinnott, J.A., Rider, J.R., Carlsson, J., Gerke, T., Tyekucheva, S., Penney, K.L., Sesso, H.D., Loda, M., Fall, K., Stampfer, M.J., Mucci, L.A., Pawitan, Y., Andersson, S.O. and Andren, O. (2015) 'Molecular differences in transition zone and peripheral zone prostate tumors', *Carcinogenesis*, 36(6), pp. 632-8.

Skrtic, M., Sriskanthadevan, S., Jhas, B., Gebbia, M., Wang, X., Wang, Z., Hurren, R., Jitkova, Y., Gronda, M., Maclean, N., Lai, C.K., Eberhard, Y., Bartoszko, J., Spagnuolo, P., Rutledge, A.C., Datti, A., Ketela, T., Moffat, J., Robinson, B.H., Cameron, J.H., Wrana, J., Eaves, C.J., Minden, M.D., Wang, J.C., Dick, J.E., Humphries, K., Nislow, C., Giaever, G. and Schimmer, A.D. (2011) 'Inhibition of mitochondrial translation as a therapeutic strategy for human acute myeloid leukemia', *Cancer Cell*, 20(5), pp. 674-88.

Smith, A.C. and Robinson, A.J. (2019) 'MitoMiner v4.0: an updated database of mitochondrial localization evidence, phenotypes and diseases', *Nucleic Acids Res*, 47(D1), pp. D1225-D1228.

Smith, M.R., Saad, F., Chowdhury, S., Oudard, S., Hadaschik, B.A., Graff, J.N., Olmos, D., Mainwaring, P.N., Lee, J.Y., Uemura, H., Lopez-Gitlitz, A., Trudel, G.C., Espina, B.M., Shu, Y., Park, Y.C., Rackoff, W.R., Yu, M.K., Small, E.J. and Investigators, S. (2018) 'Apalutamide Treatment and Metastasis-free Survival in Prostate Cancer', *N Engl J Med*, 378(15), pp. 1408-1418.

Sobin, L., Gospodariwicz, M. and Wittekind, C. (2009) *TNM classification of malignant tumors. UICC International Union Against Cancer*. 7th edn. Wiley-Blackwell.

Soleimanpour-Lichaei, H.R., Kuhl, I., Gaisne, M., Passos, J.F., Wydro, M., Rorbach, J., Temperley, R., Bonnefoy, N., Tate, W., Lightowlers, R. and Chrzanowska-Lightowlers, Z. (2007) 'mtRF1a is a human mitochondrial translation release factor decoding the major termination codons UAA and UAG', *Mol Cell*, 27(5), pp. 745-57.

Song, S., Pursell, Z.F., Copeland, W.C., Longley, M.J., Kunkel, T.A. and Mathews, C.K. (2005) 'DNA precursor asymmetries in mammalian tissue mitochondria and possible contribution to mutagenesis through reduced replication fidelity', *Proc Natl Acad Sci U S A*, 102(14), pp. 4990-5.

Spratt, D.E., Zhang, C., Zumsteg, Z.S., Pei, X., Zhang, Z. and Zelefsky, M.J. (2013) 'Metformin and prostate cancer: reduced development of castration-resistant disease and prostate cancer mortality', *Eur Urol*, 63(4), pp. 709-16.

Sramkoski, R.M., Pretlow, T.G., 2nd, Giaconia, J.M., Pretlow, T.P., Schwartz, S., Sy, M.S., Marengo, S.R., Rhim, J.S., Zhang, D. and Jacobberger, J.W. (1999) 'A new human prostate carcinoma cell line, 22Rv1', *In Vitro Cell Dev Biol Anim*, 35(7), pp. 403-9.

Sreekumar, A., Poisson, L.M., Rajendiran, T.M., Khan, A.P., Cao, Q., Yu, J., Laxman, B., Mehra, R., Lonigro, R.J., Li, Y., Nyati, M.K., Ahsan, A., Kalyana-Sundaram, S., Han, B., Cao, X., Byun, J., Omenn, G.S., Ghosh, D., Pennathur, S., Alexander, D.C., Berger, A., Shuster, J.R., Wei, J.T., Varambally, S., Beecher, C. and Chinnaiyan, A.M. (2009) 'Metabolomic profiles delineate potential role for sarcosine in prostate cancer progression', *Nature*, 457(7231), pp. 910-914.

Srihari, S., Kwong, R., Tran, K., Simpson, R., Tattam, P. and Smith, E. (2018) 'Metabolic deregulation in prostate cancer', *Mol Omics*, 14(5), pp. 320-329.

Stamey, T.A., Kabalin, J.N., McNeal, J.E., Johnstone, I.M., Freiha, F., Redwine, E.A. and Yang, N. (1989) 'Prostate specific antigen in the diagnosis and treatment of adenocarcinoma of the prostate. II. Radical prostatectomy treated patients', *J Urol*, 141(5), pp. 1076-83.

Stehling, O., Sheftel, A.D. and Lill, R. (2009) 'Chapter 12 Controlled expression of iron-sulfur cluster assembly components for respiratory chain complexes in mammalian cells', *Methods Enzymol*, 456, pp. 209-31.

Stewart, J.B., Alaei-Mahabadi, B., Sabarinathan, R., Samuelsson, T., Gorodkin, J., Gustafsson, C.M. and Larsson, E. (2015) 'Simultaneous DNA and RNA Mapping of Somatic Mitochondrial Mutations across Diverse Human Cancers', *PLoS Genet*, 11(6), p. e1005333.

Stewart, J.B. and Larsson, N.G. (2014) 'Keeping mtDNA in shape between generations', *PLoS Genet*, 10(10), p. e1004670.

Stocco, D.M., Cascarano, J. and Wilson, M.A. (1977) 'Quantitation of mitochondrial DNA, RNA, and protein in starved and starved-refed rat liver', *J Cell Physiol*, 90(2), pp. 295-306.

Stroud, D.A., Surgenor, E.E., Formosa, L.E., Reljic, B., Frazier, A.E., Dibley, M.G., Osellame, L.D., Stait, T., Beilharz, T.H., Thorburn, D.R., Salim, A. and Ryan, M.T. (2016) 'Accessory subunits are integral for assembly and function of human mitochondrial complex I', *Nature*, 538(7623), pp. 123-126.

Su, C.-Y., Chang, Y.-C., Yang, C.-J., Huang, M.-S. and Hsiao, M. (2016) 'The opposite prognostic effect of NDUFS1 and NDUFS8 in lung cancer reflects the oncojanus role of mitochondrial complex I', *Scientific Reports*, 6(1), p. 85.

Subramanian, A., Tamayo, P., Mootha, V.K., Mukherjee, S., Ebert, B.L., Gillette, M.A., Paulovich, A., Pomeroy, S.L., Golub, T.R., Lander, E.S. and Mesirov, J.P. (2005) 'Gene set enrichment analysis: a knowledge-based approach for interpreting genome-wide expression profiles', *Proc Natl Acad Sci U S A*, 102(43), pp. 15545-50.

Sun, M., Choueiri, T.K., Hamnvik, O.P., Preston, M.A., De Velasco, G., Jiang, W., Loeb, S., Nguyen, P.L. and Trinh, Q.D. (2016) 'Comparison of Gonadotropin-Releasing Hormone Agonists and Orchiectomy: Effects of Androgen-Deprivation Therapy', *JAMA Oncol*, 2(4), pp. 500-7.

Sun, X., Liao, N.K. and Yu, J.J. (2012) 'Prognostic value of a mitochondrial functional score in prostate cancer', *J Int Med Res*, 40(1), pp. 371-6.

Suwa, T., Nyska, A., Haseman, J.K., Mahler, J.F. and Maronpot, R.R. (2002) 'Spontaneous lesions in control B6C3F1 mice and recommended sectioning of male accessory sex organs.', *Toxicologic pathology*, 30(2), pp. 228-234.

Suzuki, A., Yamaguchi, M.T., Ohteki, T., Sasaki, T., Kaisho, T., Kimura, Y., Yoshida, R., Wakeham, A., Higuchi, T., Fukumoto, M., Tsubata, T., Ohashi, P.S., Koyasu, S., Penninger, J.M., Nakano, T. and Mak, T.W. (2001) 'T cell-specific loss of Pten leads to defects in central and peripheral tolerance.', *Immunity*, 14(5), pp. 523-534.

Suzuki, H., Freije, D., Nusskern, D.R., Okami, K., Cairns, P., Sidransky, D., Isaacs, W.B. and Bova, G.S. (1998) 'Interfocal heterogeneity of PTEN/MMAC1 gene alterations in multiple metastatic prostate cancer tissues', *Cancer Res*, 58(2), pp. 204-9.

Suzuki, T., Nagao, A. and Suzuki, T. (2011) 'Human mitochondrial tRNAs: biogenesis, function, structural aspects, and diseases', *Annu Rev Genet*, 45, pp. 299-329.

Sweeney, C.J., Chen, Y.H., Carducci, M., Liu, G., Jarrard, D.F., Eisenberger, M., Wong, Y.N., Hahn, N., Kohli, M., Cooney, M.M., Dreicer, R., Vogelzang, N.J., Picus, J., Shevrin, D., Hussain, M., Garcia, J.A. and DiPaola, R.S. (2015) 'Chemohormonal Therapy in Metastatic Hormone-Sensitive Prostate Cancer', *N Engl J Med*, 373(8), pp. 737-46.

Sydes, M.R., Spears, M.R., Mason, M.D., Clarke, N.W., Dearnaley, D.P., de Bono, J.S., Attard, G., Chowdhury, S., Cross, W., Gillessen, S., Malik, Z.I., Jones, R., Parker, C.C., Ritchie, A.W.S., Russell, J.M., Millman, R., Matheson, D., Amos, C., Gilson, C., Birtle, A., Brock, S., Capaldi, L., Chakraborti, P., Choudhury, A., Evans, L., Ford, D., Gale, J., Gibbs, S., Gilbert, D.C., Hughes, R., McLaren, D., Lester, J.F., Nikapota, A., O'Sullivan, J., Parikh, O., Peedell, C., Protheroe, A., Rudman, S.M., Shaffer, R., Sheehan, D., Simms, M., Srihari, N., Strebel, R., Sundar, S., Tolan, S., Tsang, D., Varughese, M., Wagstaff, J., Parmar, M.K.B., James, N.D. and Investigators, S. (2018) 'Adding abiraterone or docetaxel to long-term

hormone therapy for prostate cancer: directly randomised data from the STAMPEDE multi-arm, multi-stage platform protocol', *Ann Oncol*, 29(5), pp. 1235-1248.

Szymanska, H., Lechowska-Piskorowska, J., Krysiak, E., Strzalkowska, A., Unrug-Bielawska, K., Grygalewicz, B., Skurzak, H.M., Pienkowska-Grela, B. and Gajewska, M. (2014) 'Neoplastic and nonneoplastic lesions in aging mice of unique and common inbred strains contribution to modeling of human neoplastic diseases', *Vet Pathol*, 51(3), pp. 663-79.

Taggart, L.E., McMahon, S.J., Currell, F.J., Prise, K.M. and Butterworth, K.T. (2014) 'The role of mitochondrial function in gold nanoparticle mediated radiosensitisation', *Cancer Nanotechnol*, 5(1), p. 5.

Tanaka, M., Kovalenko, S.A., Gong, J.S., Borgeld, H.J., Katsumata, K., Hayakawa, M., Yoneda, M. and Ozawa, T. (1996) 'Accumulation of deletions and point mutations in mitochondrial genome in degenerative diseases', *Ann N Y Acad Sci*, 786, pp. 102-11.

Tang, L., Wei, F., Wu, Y., He, Y., Shi, L., Xiong, F., Gong, Z., Guo, C., Li, X., Deng, H., Cao, K., Zhou, M., Xiang, B., Li, X., Li, Y., Li, G., Xiong, W. and Zeng, Z. (2018) 'Role of metabolism in cancer cell radioresistance and radiosensitization methods', *J Exp Clin Cancer Res*, 37(1), p. 87.

Tapper, D.P. and Clayton, D.A. (1981) 'Mechanism of replication of human mitochondrial DNA. Localization of the 5' ends of nascent daughter strands', *J Biol Chem*, 256(10), pp. 5109-15.

Tayari, N., Heerschap, A., Scheenen, T.W.J. and Kobus, T. (2017) 'In vivo MR spectroscopic imaging of the prostate, from application to interpretation', *Anal Biochem*, 529, pp. 158-170.

Taylor, B.S., Schultz, N., Hieronymus, H., Gopalan, A., Xiao, Y., Carver, B.S., Arora, V.K., Kaushik, P., Cerami, E., Reva, B., Antipin, Y., Mitsiades, N., Landers, T., Dolgalev, I., Major, J.E., Wilson, M., Socci, N.D., Lash, A.E., Heguy, A., Eastham, J.A., Scher, H.I., Reuter, V.E., Scardino, P.T., Sander, C., Sawyers, C.L. and Gerald, W.L. (2010) 'Integrative genomic profiling of human prostate cancer', *Cancer Cell*, 18(1), pp. 11-22.

Taylor, R.A., Fraser, M., Livingstone, J., Espiritu, S.M., Thorne, H., Huang, V., Lo, W., Shiah, Y.J., Yamaguchi, T.N., Sliwinski, A., Horsburgh, S., Meng, A., Heisler, L.E., Yu, N., Yousif, F., Papargiris, M., Lawrence, M.G., Timms, L., Murphy, D.G., Frydenberg, M., Hopkins, J.F., Bolton, D., Clouston, D., McPherson, J.D., van der Kwast, T., Boutros, P.C., Risbridger, G.P. and Bristow, R.G. (2017) 'Germline BRCA2 mutations drive prostate cancers with distinct evolutionary trajectories', *Nat Commun*, 8, p. 13671.

Taylor, R.A., Fraser, M., Rebello, R.J., Boutros, P.C., Murphy, D.G., Bristow, R.G. and Risbridger, G.P. (2019) 'The influence of BRCA2 mutation on localized prostate cancer', *Nat Rev Urol*, 16(5), pp. 281-290.

Taylor, R.W., Barron, M.J., Borthwick, G.M., Gospel, A., Chinnery, P.F., Samuels, D.C., Taylor, G.A., Plusa, S.M., Needham, S.J., Greaves, L.C., Kirkwood, T.B. and Turnbull, D.M. (2003) 'Mitochondrial DNA mutations in human colonic crypt stem cells', *J Clin Invest*, 112(9), pp. 1351-60.

Tedeschi, P.M., Markert, E.K., Gounder, M., Lin, H., Dvorzhinski, D., Dolfi, S.C., Chan, L.L., Qiu, J., DiPaola, R.S., Hirshfield, K.M., Boros, L.G., Bertino, J.R., Oltvai, Z.N. and Vazquez, A. (2013) 'Contribution of serine, folate and glycine metabolism to the ATP, NADPH and purine requirements of cancer cells', *Cell Death Dis*, 4, p. e877.

Tessem, M.B., Bertilsson, H., Angelsen, A., Bathen, T.F., Drablos, F. and Rye, M.B. (2016) 'A Balanced Tissue Composition Reveals New Metabolic and Gene Expression Markers in Prostate Cancer', *PLoS One*, 11(4), p. e0153727.

Tolis, G., Ackman, D., Stellos, A., Mehta, A., Labrie, F., Fazekas, A.T., Comaru-Schally, A.M. and Schally, A.V. (1982) 'Tumor growth inhibition in patients with prostatic carcinoma treated with luteinizing hormone-releasing hormone agonists', *Proc Natl Acad Sci U S A*, 79(5), pp. 1658-62.

Tomlins, S.A., Laxman, B., Varambally, S., Cao, X., Yu, J., Helgeson, B.E., Cao, Q., Prensner, J.R., Rubin, M.A., Shah, R.B., Mehra, R. and Chinnaiyan, A.M. (2008) 'Role of the TMPRSS2-ERG gene fusion in prostate cancer', *Neoplasia*, 10(2), pp. 177-88.

Tomlins, S.A., Rhodes, D.R., Perner, S., Dhanasekaran, S.M., Mehra, R., Sun, X.W., Varambally, S., Cao, X., Tchinda, J., Kuefer, R., Lee, C., Montie, J.E., Shah, R.B., Pienta, K.J., Rubin, M.A. and Chinnaiyan, A.M. (2005) 'Recurrent fusion of TMPRSS2 and ETS transcription factor genes in prostate cancer', *Science*, 310(5748), pp. 644-8.

Torrano, V., Valcarcel-Jimenez, L., Cortazar, A.R., Liu, X., Urosevic, J., Castillo-Martin, M., Fernández-Ruiz, S., Morciano, G., Caro-Maldonado, A., Guiu, M., Zúñiga-García, P., Graupera, M., Bellmunt, A., Pandya, P., Lorente, M., Martín-Martín, N., Sutherland, J.D., Sanchez-Mosquera, P., Bozal-Basterra, L., Zabala-Letona, A., Arruabarrena-Aristorena, A., Berenguer, A., Embade, N., Ugalde-Olano, A., Lacasa-Viscasillas, I., Loizaga-Iriarte, A., Unda-Urzaiz, M., Schultz, N., Aransay, A.M., Sanz-Moreno, V., Barrio, R., Velasco, G., Pinton, P., Cordon-Cardo, C., Locasale, J.W., Gomis, R.R. and Carracedo, A. (2016) 'The metabolic co-regulator PGC1α suppresses prostate cancer metastasis.', *Nature Cell Biology*, 18(6), pp. 645-656.

Toth, Z.E. and Mezey, E. (2007) 'Simultaneous visualization of multiple antigens with tyramide signal amplification using antibodies from the same species', *J Histochem Cytochem*, 55(6), pp. 545-54.

Tran, C., Ouk, S., Clegg, N.J., Chen, Y., Watson, P.A., Arora, V., Wongvipat, J., Smith-Jones, P.M., Yoo, D., Kwon, A., Wasielewska, T., Welsbie, D., Chen, C.D., Higano, C.S., Beer, T.M., Hung, D.T., Scher, H.I., Jung, M.E. and Sawyers, C.L. (2009) 'Development of a second-generation antiandrogen for treatment of advanced prostate cancer', *Science*, 324(5928), pp. 787-90.

Trifunovic, A., Wredenberg, A., Falkenberg, M., Spelbrink, J.N., Rovio, A.T., Bruder, C.E., Bohlooly, Y.M., Gidlof, S., Oldfors, A., Wibom, R., Tornell, J., Jacobs, H.T. and Larsson, N.G. (2004) 'Premature ageing in mice expressing defective mitochondrial DNA polymerase', *Nature*, 429(6990), pp. 417-23.

Trotman, L.C., Niki, M., Dotan, Z.A., Koutcher, J.A., Di Cristofano, A., Xiao, A., Khoo, A.S., Roy-Burman, P., Greenberg, N.M., Van Dyke, T., Cordon-Cardo, C. and Pandolfi, P.P. (2003) 'Pten dose dictates cancer progression in the prostate', *PLoS Biol*, 1(3), p. E59.

Trounce, I., Neill, S. and Wallace, D.C. (1994) 'Cytoplasmic transfer of the mtDNA nt 8993 T-->G (ATP6) point mutation associated with Leigh syndrome into mtDNA-less cells demonstrates cosegregation with a decrease in state III respiration and ADP/O ratio', *Proc Natl Acad Sci U S A*, 91(18), pp. 8334-8.

Tsui, K.H., Chang, P.L. and Juang, H.H. (2006) 'Zinc blocks gene expression of mitochondrial aconitase in human prostatic carcinoma cells', *Int J Cancer*, 118(3), pp. 609-15.

Tsujikawa, T., Kumar, S., Borkar, R.N., Azimi, V., Thibault, G., Chang, Y.H., Balter, A., Kawashima, R., Choe, G., Sauer, D., El Rassi, E., Clayburgh, D.R., Kulesz-Martin, M.F., Lutz, E.R., Zheng, L., Jaffee, E.M., Leyshock, P., Margolin, A.A., Mori, M., Gray, J.W., Flint, P.W. and Coussens, L.M. (2017) 'Quantitative Multiplex Immunohistochemistry Reveals Myeloid-Inflamed Tumor-Immune Complexity Associated with Poor Prognosis', *Cell Rep*, 19(1), pp. 203-217.

Tsukihara, T., Aoyama, H., Yamashita, E., Tomizaki, T., Yamaguchi, H., Shinzawa-Itoh, K., Nakashima, R., Yaono, R. and Yoshikawa, S. (1996) 'The whole structure of the 13-subunit oxidized cytochrome c oxidase at 2.8 A', *Science*, 272(5265), pp. 1136-44.

Turkbey, B., Huang, R., Vourganti, S., Trivedi, H., Bernardo, M., Yan, P., Benjamin, C., Pinto, P. and Choyke, P. (2012) 'Age related changes in prostate zonal volume as measured by high resolution prostate MRI: a cross sectional study in over 500 patients', *BJU International*, 110(11), pp. 1642-1647.

Turner, S.R., Campbell, J.A. and Lynn, W.S. (1975) 'Polymorphonulcear leukocyte chemotaxis toward oxidized lipid components of cell membranes', *J Exp Med*, 141(6), pp. 1437-41.

Turrens, J.F. and Boveris, A. (1980) 'Generation of superoxide anion by the NADH dehydrogenase of bovine heart mitochondria', *Biochem J*, 191(2), pp. 421-7.

Valkenburg, K.C. and Williams, B.O. (2011) 'Mouse models of prostate cancer', *Prostate Cancer*, 2011, p. 895238.

Valko, M., Leibfritz, D., Moncol, J., Cronin, M.T., Mazur, M. and Telser, J. (2007) 'Free radicals and antioxidants in normal physiological functions and human disease', *Int J Biochem Cell Biol*, 39(1), pp. 44-84.

Van den Broeck, T., van den Bergh, R.C.N., Arfi, N., Gross, T., Moris, L., Briers, E., Cumberbatch, M., De Santis, M., Tilki, D., Fanti, S., Fossati, N., Gillessen, S., Grummet, J.P., Henry, A.M., Lardas, M., Liew, M., Rouviere, O., Pecanka, J., Mason, M.D., Schoots, I.G., van Der Kwast, T.H., van Der Poel, H.G., Wiegel, T., Willemse, P.M., Yuan, Y., Lam, T.B., Cornford, P. and Mottet, N. (2019) 'Prognostic Value of Biochemical Recurrence Following Treatment with Curative Intent for Prostate Cancer: A Systematic Review', *Eur Urol*, 75(6), pp. 967-987.

van der Kwast, T.H., Amin, M.B., Billis, A., Epstein, J.I., Griffiths, D., Humphrey, P.A., Montironi, R., Wheeler, T.M., Srigley, J.R., Egevad, L., Delahunt, B. and Group, I.P.C. (2011) 'International Society of Urological Pathology (ISUP) Consensus Conference on Handling and Staging of Radical Prostatectomy Specimens. Working group 2: T2 substaging and prostate cancer volume', *Mod Pathol*, 24(1), pp. 16-25.

Van Heusden, J., de Jong, P., Ramaekers, F., Bruwiere, H., Borgers, M. and Smets, G. (1997) 'Fluorescein-labeled tyramide strongly enhances the detection of low bromodeoxyuridine incorporation levels.', *Journal of Histochemistry & Cytochemistry*, 45(2), pp. 315-319.

Vander Heiden, M.G., Cantley, L.C. and Thompson, C.B. (2009) 'Understanding the Warburg effect: the metabolic requirements of cell proliferation', *Science*, 324(5930), pp. 1029-33.

Vanderstraeten, S., Van den Brule, S., Hu, J. and Foury, F. (1998) 'The role of 3'-5' exonucleolytic proofreading and mismatch repair in yeast mitochondrial DNA error avoidance', *J Biol Chem*, 273(37), pp. 23690-7.

Vanmarsenille, L., Verbeeck, J., Belet, S., Roebroek, A.J., Van de Putte, T., Nevelsteen, J., Callaerts-Vegh, Z., D'Hooge, R., Marynen, P. and Froyen, G. (2013) 'Generation and characterization of an Nxf7 knockout mouse to study NXF5 deficiency in a patient with intellectual disability', *PLoS One*, 8(5), p. e64144.

Vermulst, M., Bielas, J.H., Kujoth, G.C., Ladiges, W.C., Rabinovitch, P.S., Prolla, T.A. and Loeb, L.A. (2007) 'Mitochondrial point mutations do not limit the natural lifespan of mice', *Nat Genet*, 39(4), pp. 540-3.

Vermulst, M., Wanagat, J., Kujoth, G.C., Bielas, J.H., Rabinovitch, P.S., Prolla, T.A. and Loeb, L.A. (2008) 'DNA deletions and clonal mutations drive premature aging in mitochondrial mutator mice', *Nat Genet*, 40(4), pp. 392-4.

Vernooij, R.W.M., van Oort, I., de Reijke, T.M. and Aben, K.K.H. (2019) 'Nationwide treatment patterns and survival of older patients with prostate cancer', *J Geriatr Oncol*, 10(2), pp. 252-258.

Viale, A., Pettazzoni, P., Lyssiotis, C.A., Ying, H., Sánchez, N., Marchesini, M., Carugo, A., Green, T., Seth, S., Giuliani, V., Kost-Alimova, M., Muller, F., Colla, S., Nezi, L., Genovese, G., Deem, A.K., Kapoor, A., Yao, W., Brunetto, E., Kang, Y.a., Yuan, M., Asara, J.M., Wang, Y.A., Heffernan, T.P., Kimmelman, A.C., Wang, H., Fleming, J.B., Cantley, L.C., DePinho, R.A. and Draetta, G.F. (2014) 'Oncogene ablation-resistant pancreatic cancer cells depend on mitochondrial function.', *Nature*, 514(7524), pp. 628-632.

Villers, A., McNeal, J.E., Freiha, F.S. and Stamey, T.A. (1992) 'Multiple cancers in the prostate. Morphologic features of clinically recognized versus incidental tumors', *Cancer*, 70(9), pp. 2313-8.

Vivian, C.J., Brinker, A.E., Graw, S., Koestler, D.C., Legendre, C., Gooden, G.C., Salhia, B. and Welch, D.R. (2017) 'Mitochondrial Genomic Backgrounds Affect Nuclear DNA Methylation and Gene Expression', *Cancer Res*, 77(22), pp. 6202-6214.

Vogel, C. and Marcotte, E.M. (2012) 'Insights into the regulation of protein abundance from proteomic and transcriptomic analyses', *Nat Rev Genet*, 13(4), pp. 227-32.

Vogel, R.O., Janssen, R.J., Ugalde, C., Grovenstein, M., Huijbens, R.J., Visch, H.J., van den Heuvel, L.P., Willems, P.H., Zeviani, M., Smeitink, J.A. and Nijtmans, L.G. (2005) 'Human mitochondrial complex I assembly is mediated by NDUFAF1', *FEBS J*, 272(20), pp. 5317-26.

Wallace, D.C. (2012) 'Mitochondria and cancer', *Nat Rev Cancer*, 12(10), pp. 685-98.

Wang, J., Kobayashi, T., Floc'h, N., Kinkade, C.W., Aytes, A., Dankort, D., Lefebvre, C., Mitrofanova, A., Cardiff, R.D., McMahon, M., Califano, A., Shen, M.M. and Abate-Shen, C. (2012) 'B-Raf Activation Cooperates with PTEN Loss to Drive c-Myc Expression in Advanced Prostate Cancer', *Cancer Research*, 72(18), pp. 4765-4776.

Wang, J. and Pantopoulos, K. (2011) 'Regulation of cellular iron metabolism', *Biochem J*, 434(3), pp. 365-81.

Wang, L., Xiong, H., Wu, F., Zhang, Y., Wang, J., Zhao, L., Guo, X., Chang, L.-J., Zhang, Y., You, M.J., Koochekpour, S., Saleem, M., Huang, H., Lu, J. and Deng, Y. (2014) 'Hexokinase 2-mediated Warburg effect is required for PTEN- and p53-deficiency-driven prostate cancer growth.', *Cell Reports*, 8(5), pp. 1461-1474.

Wang, P.Y., Li, J., Walcott, F.L., Kang, J.G., Starost, M.F., Talagala, S.L., Zhuang, J., Park, J.H., Huffstutler, R.D., Bryla, C.M., Mai, P.L., Pollak, M., Annunziata, C.M., Savage, S.A., Fojo, A.T. and Hwang, P.M. (2017) 'Inhibiting mitochondrial respiration prevents cancer in a mouse model of Li-Fraumeni syndrome', *J Clin Invest*, 127(1), pp. 132-136.

Wang, P.Y., Ma, W., Park, J.Y., Celi, F.S., Arena, R., Choi, J.W., Ali, Q.A., Tripodi, D.J., Zhuang, J., Lago, C.U., Strong, L.C., Talagala, S.L., Balaban, R.S., Kang, J.G. and Hwang, P.M. (2013) 'Increased oxidative metabolism in the Li-Fraumeni syndrome', *N Engl J Med*, 368(11), pp. 1027-32.

Wang, S., Gao, J., Lei, Q., Rozengurt, N., Pritchard, C., Jiao, J., Thomas, G.V., Li, G., Roy-Burman, P., Nelson, P.S., Liu, X. and Wu, H. (2003) 'Prostate-specific deletion of the murine Pten tumor suppressor gene leads to metastatic prostate cancer', *Cancer Cell*, 4(3), pp. 209-21.

Wang, S.I., Parsons, R. and Ittmann, M. (1998) 'Homozygous deletion of the PTEN tumor suppressor gene in a subset of prostate adenocarcinomas', *Clin Cancer Res*, 4(3), pp. 811-5.

Wang, X.S., Shankar, S., Dhanasekaran, S.M., Ateeq, B., Sasaki, A.T., Jing, X., Robinson, D., Cao, Q., Prensner, J.R., Yocum, A.K., Wang, R., Fries, D.F., Han, B., Asangani, I.A., Cao, X., Li, Y., Omenn, G.S., Pflueger, D., Gopalan, A., Reuter, V.E., Kahoud, E.R., Cantley, L.C., Rubin, M.A., Palanisamy, N., Varambally, S. and Chinnaiyan, A.M. (2011) 'Characterization of KRAS rearrangements in metastatic prostate cancer', *Cancer Discov*, 1(1), pp. 35-43.

Warburg, O. (1956) 'On respiratory impairment in cancer cells', *Science*, 124(3215), pp. 269-70.

Ward, J.M. (2006) 'Lymphomas and leukemias in mice', *Exp Toxicol Pathol*, 57(5-6), pp. 377-81.

Waris, G. and Ahsan, H. (2006) 'Reactive oxygen species: role in the development of cancer and various chronic conditions', *J Carcinog*, 5, p. 14.

Weber, A., Klocker, H., Oberacher, H., Gnaiger, E., Neuwirt, H., Sampson, N. and Eder, I.E. (2018) 'Succinate Accumulation Is Associated with a Shift of Mitochondrial Respiratory Control and HIF-1alpha Upregulation in PTEN Negative Prostate Cancer Cells', *Int J Mol Sci*, 19(7), p. 2129.

Wedge, D.C., Gundem, G., Mitchell, T., Woodcock, D.J., Martincorena, I., Ghori, M., Zamora, J., Butler, A., Whitaker, H., Kote-Jarai, Z., Alexandrov, L.B., Van Loo, P., Massie, C.E., Dentro, S., Warren, A.Y.,

Verrill, C., Berney, D.M., Dennis, N., Merson, S., Hawkins, S., Howat, W., Lu, Y.J., Lambert, A., Kay, J., Kremeyer, B., Karaszi, K., Luxton, H., Camacho, N., Marsden, L., Edwards, S., Matthews, L., Bo, V., Leongamornlert, D., McLaren, S., Ng, A., Yu, Y., Zhang, H., Dadaev, T., Thomas, S., Easton, D.F., Ahmed, M., Bancroft, E., Fisher, C., Livni, N., Nicol, D., Tavare, S., Gill, P., Greenman, C., Khoo, V., Van As, N., Kumar, P., Ogden, C., Cahill, D., Thompson, A., Mayer, E., Rowe, E., Dudderidge, T., Gnanapragasam, V., Shah, N.C., Raine, K., Jones, D., Menzies, A., Stebbings, L., Teague, J., Hazell, S., Corbishley, C., Group, C.S., de Bono, J., Attard, G., Isaacs, W., Visakorpi, T., Fraser, M., Boutros, P.C., Bristow, R.G., Workman, P., Sander, C., Consortium, T., Hamdy, F.C., Futreal, A., McDermott, U., Al-Lazikani, B., Lynch, A.G., Bova, G.S., Foster, C.S., Brewer, D.S., Neal, D.E., Cooper, C.S. and Eeles, R.A. (2018) 'Sequencing of prostate cancers identifies new cancer genes, routes of progression and drug targets', *Nat Genet*, 50(5), pp. 682-692.

Weinberg, F., Hamanaka, R., Wheaton, W.W., Weinberg, S., Joseph, J., Lopez, M., Kalyanaraman, B., Mutlu, G.M., Budinger, G.R.S. and Chandel, N.S. (2010) 'Mitochondrial metabolism and ROS generation are essential for Kras-mediated tumorigenicity.', *Proceedings of the National Academy of Sciences of the United States of America*, 107(19), pp. 8788-8793.

Weischenfeldt, J., Simon, R., Feuerbach, L., Schlangen, K., Weichenhan, D., Minner, S., Wuttig, D., Warnatz, H.J., Stehr, H., Rausch, T., Jager, N., Gu, L., Bogatyrova, O., Stutz, A.M., Claus, R., Eils, J., Eils, R., Gerhauser, C., Huang, P.H., Hutter, B., Kabbe, R., Lawerenz, C., Radomski, S., Bartholomae, C.C., Falth, M., Gade, S., Schmidt, M., Amschler, N., Hass, T., Galal, R., Gjoni, J., Kuner, R., Baer, C., Masser, S., von Kalle, C., Zichner, T., Benes, V., Raeder, B., Mader, M., Amstislavskiy, V., Avci, M., Lehrach, H., Parkhomchuk, D., Sultan, M., Burkhardt, L., Graefen, M., Huland, H., Kluth, M., Krohn, A., Sirma, H., Stumm, L., Steurer, S., Grupp, K., Sultmann, H., Sauter, G., Plass, C., Brors, B., Yaspo, M.L., Korbel, J.O. and Schlomm, T. (2013) 'Integrative genomic analyses reveal an androgen-driven somatic alteration landscape in early-onset prostate cancer', *Cancer Cell*, 23(2), pp. 159-70.

Wen, Y.A., Xiong, X., Scott, T., Li, A.T., Wang, C., Weiss, H.L., Tan, L., Bradford, E., Fan, T.W.M., Chandel, N.S., Barrett, T.A. and Gao, T. (2019) 'The mitochondrial retrograde signaling regulates Wnt signaling to promote tumorigenesis in colon cancer', *Cell Death Differ*, 26(10), pp. 1955-1969.

West, A.P., Khoury-Hanold, W., Staron, M., Tal, M.C., Pineda, C.M., Lang, S.M., Bestwick, M., Duguay, B.A., Raimundo, N., MacDuff, D.A., Kaech, S.M., Smiley, J.R., Means, R.E., Iwasaki, A. and Shadel, G.S. (2015) 'Mitochondrial DNA stress primes the antiviral innate immune response', *Nature*, 520(7548), pp. 553-7.

Westphal, D., Dewson, G., Czabotar, P.E. and Kluck, R.M. (2011) 'Molecular biology of Bax and Bak activation and action', *Biochim Biophys Acta*, 1813(4), pp. 521-31.

White, C.W., Xie, J.H. and Ventura, S. (2013) 'Age-related changes in the innervation of the prostate gland: implications for prostate cancer initiation and progression', *Organogenesis*, 9(3), pp. 206-15.

Widmark, A., Klepp, O., Solberg, A., Damber, J.E., Angelsen, A., Fransson, P., Lund, J.A., Tasdemir, I., Hoyer, M., Wiklund, F., Fossa, S.D., Scandinavian Prostate Cancer Group, S. and Swedish Association for Urological, O. (2009) 'Endocrine treatment, with or without radiotherapy, in locally advanced prostate cancer (SPCG-7/SFUO-3): an open randomised phase III trial', *Lancet*, 373(9660), pp. 301-8.

Williams, H. and Powell, I.J. (2009) 'Epidemiology, pathology, and genetics of prostate cancer among African Americans compared with other ethnicities', *Methods Mol Biol*, 472, pp. 439-53.

Wilt, T.J., Jones, K.M., Barry, M.J., Andriole, G.L., Culkin, D., Wheeler, T., Aronson, W.J. and Brawer, M.K. (2017) 'Follow-up of Prostatectomy versus Observation for Early Prostate Cancer', *N Engl J Med*, 377(2), pp. 132-142.

Winter, S.C., Buffa, F.M., Silva, P., Miller, C., Valentine, H.R., Turley, H., Shah, K.A., Cox, G.J., Corbridge, R.J., Homer, J.J., Musgrove, B., Slevin, N., Sloan, P., Price, P., West, C.M. and Harris, A.L. (2007) 'Relation of a hypoxia metagene derived from head and neck cancer to prognosis of multiple cancers', *Cancer Res*, 67(7), pp. 3441-9.

Woo, D.K., Green, P.D., Santos, J.H., D'Souza, A.D., Walther, Z., Martin, W.D., Christian, B.E., Chandel, N.S. and Shadel, G.S. (2012) 'Mitochondrial genome instability and ROS enhance intestinal tumorigenesis in APC(Min/+) mice.', *The American Journal of Pathology*, 180(1), pp. 24-31.

Wu, X., Daniels, G., Lee, P. and Monaco, M.E. (2014) 'Lipid metabolism in prostate cancer', *Am J Clin Exp Urol*, 2(2), pp. 111-20.

Wu, X., Wu, J., Huang, J., Powell, W.C., Zhang, J., Matusik, R.J., Sangiorgi, F.O., Maxson, R.E., Sucov, H.M. and Roy-Burman, P. (2001) 'Generation of a prostate epithelial cell-specific Cre transgenic mouse model for tissue-specific gene ablation.', *Mechanisms of development*, 101(1-2), pp. 61-69.

Xie, W., Regan, M.M., Buyse, M., Halabi, S., Kantoff, P.W., Sartor, O., Soule, H., Clarke, N.W., Collette, L., Dignam, J.J., Fizazi, K., Paruleker, W.R., Sandler, H.M., Sydes, M.R., Tombal, B., Williams, S.G., Sweeney, C.J. and Group, I.C.W. (2017) 'Metastasis-Free Survival Is a Strong Surrogate of Overall Survival in Localized Prostate Cancer', *J Clin Oncol*, 35(27), pp. 3097-3104.

Xu, J., Chang, W.S., Tsai, C.W., Bau, D.T., Davis, J.W., Thompson, T.C., Logothetis, C.J. and Gu, J. (2019) 'Mitochondrial DNA copy number in peripheral blood leukocytes is associated with biochemical recurrence in prostate cancer patients in African Americans', *Carcinogenesis*.

Yamasoba, T., Someya, S., Yamada, C., Weindruch, R., Prolla, T.A. and Tanokura, M. (2007) 'Role of mitochondrial dysfunction and mitochondrial DNA mutations in age-related hearing loss', *Hear Res*, 226(1-2), pp. 185-93.

Yang, L., Roberts, D., Takhar, M., Erho, N., Bibby, B.A.S., Thiruthaneeswaran, N., Bhandari, V., Cheng, W.C., Haider, S., McCorry, A.M.B., McArt, D., Jain, S., Alshalalfa, M., Ross, A., Schaffer, E., Den, R.B., Jeffrey Karnes, R., Klein, E., Hoskin, P.J., Freedland, S.J., Lamb, A.D., Neal, D.E., Buffa, F.M., Bristow, R.G., Boutros, P.C., Davicioni, E., Choudhury, A. and West, C.M.L. (2018) 'Development and Validation of a 28-gene Hypoxia-related Prognostic Signature for Localized Prostate Cancer', *EBioMedicine*, 31, pp. 182-189.

Yano, K., Carter, C., Yoshida, N., Abe, T., Yamada, A., Nitta, T., Ishimaru, N., Takada, K., Butcher, G.W. and Takahama, Y. (2014) 'Gimap3 and Gimap5 cooperate to maintain T-cell numbers in the mouse', *Eur J Immunol*, 44(2), pp. 561-72.

Yao, C.H., Wang, R., Wang, Y., Kung, C.P., Weber, J.D. and Patti, G.J. (2019) 'Mitochondrial fusion supports increased oxidative phosphorylation during cell proliferation', *Elife*, 8, p. 279.

Yasukawa, T., Reyes, A., Cluett, T.J., Yang, M.Y., Bowmaker, M., Jacobs, H.T. and Holt, I.J. (2006) 'Replication of vertebrate mitochondrial DNA entails transient ribonucleotide incorporation throughout the lagging strand', *EMBO J*, 25(22), pp. 5358-71.

Yates, B., Braschi, B., Gray, K.A., Seal, R.L., Tweedie, S. and Bruford, E.A. (2017) 'Genenames.org: the HGNC and VGNC resources in 2017', *Nucleic Acids Res*, 45(D1), pp. D619-D625.

Ye, K., Lu, J., Ma, F., Keinan, A. and Gu, Z. (2014) 'Extensive pathogenicity of mitochondrial heteroplasmy in healthy human individuals.', *Proceedings of the National Academy of Sciences of the United States of America*, 111(29), pp. 10654-10659.

Yoshida, M., Muneyuki, E. and Hisabori, T. (2001) 'ATP synthase--a marvellous rotary engine of the cell', *Nat Rev Mol Cell Biol*, 2(9), pp. 669-77.

Yoshimoto, M., Joshua, A.M., Cunha, I.W., Coudry, R.A., Fonseca, F.P., Ludkovski, O., Zielenska, M., Soares, F.A. and Squire, J.A. (2008) 'Absence of TMPRSS2:ERG fusions and PTEN losses in prostate cancer is associated with a favorable outcome', *Mod Pathol*, 21(12), pp. 1451-60.

Yossepowitch, O., Briganti, A., Eastham, J.A., Epstein, J., Graefen, M., Montironi, R. and Touijer, K. (2014) 'Positive surgical margins after radical prostatectomy: a systematic review and contemporary update', *Eur Urol*, 65(2), pp. 303-13.

Yu, J.J. and Yan, T. (2010) 'Effect of mtDNA mutation on tumor malignant degree in patients with prostate cancer', *Aging Male*, 13(3), pp. 159-65.

Yu, X., Gimsa, U., Wester-Rosenlof, L., Kanitz, E., Otten, W., Kunz, M. and Ibrahim, S.M. (2009) 'Dissecting the effects of mtDNA variations on complex traits using mouse conplastic strains', *Genome Res*, 19(1), pp. 159-65.

Yuan, Y., Ju, Y.S., Kim, Y., Li, J., Wang, Y., Yang, Y., Martincorena, I., Creighton, C.J., Weinstein, J.N., Xu, Y., Han, L., Kim, H.-L., Nakagawa, H., Park, K., Campbell, P.J. and Liang, H. (2017) 'Comprehensive Molecular Characterization of Mitochondrial Genomes in Human Cancers', *bioRxiv*, p. 161356.

Yuneva, M.O., Fan, T.W., Allen, T.D., Higashi, R.M., Ferraris, D.V., Tsukamoto, T., Mates, J.M., Alonso, F.J., Wang, C., Seo, Y., Chen, X. and Bishop, J.M. (2012) 'The metabolic profile of tumors depends on both the responsible genetic lesion and tissue type', *Cell Metab*, 15(2), pp. 157-70.

Yusoff, A.A.M., Abdullah, W.S.W., Khair, S. and Radzak, S.M.A. (2019) 'A comprehensive overview of mitochondrial DNA 4977-bp deletion in cancer studies', *Oncol Rev*, 13(1), p. 409.

Zahalka, A.H., Arnal-Estapé, A., Maryanovich, M., Nakahara, F., Cruz, C.D., Finley, L.W.S. and Frenette, P.S. (2017) 'Adrenergic nerves activate an angio-metabolic switch in prostate cancer.', *Science*, 358(6361), pp. 321-326.

Zannella, V.E., Dal Pra, A., Muaddi, H., McKee, T.D., Stapleton, S., Sykes, J., Glicksman, R., Chaib, S., Zamiara, P., Milosevic, M., Wouters, B.G., Bristow, R.G. and Koritzinsky, M. (2013) 'Reprogramming metabolism with metformin improves tumor oxygenation and radiotherapy response', *Clin Cancer Res*, 19(24), pp. 6741-50.

Zaorsky, N.G., Davis, B.J., Nguyen, P.L., Showalter, T.N., Hoskin, P.J., Yoshioka, Y., Morton, G.C. and Horwitz, E.M. (2017) 'The evolution of brachytherapy for prostate cancer', *Nat Rev Urol*, 14(7), pp. 415-439.

Zarrella, E.R., Coulter, M., Welsh, A.W., Carvajal, D.E., Schalper, K.A., Harigopal, M., Rimm, D.L. and Neumeister, V.M. (2016) 'Automated measurement of estrogen receptor in breast cancer: a comparison of fluorescent and chromogenic methods of measurement', *Lab Invest*, 96(9), pp. 1016-25.

Zhang, B., Wang, J., Wang, X., Zhu, J., Liu, Q., Shi, Z., Chambers, M.C., Zimmerman, L.J., Shaddox, K.F., Kim, S., Davies, S.R., Wang, S., Wang, P., Kinsinger, C.R., Rivers, R.C., Rodriguez, H., Townsend, R.R., Ellis, M.J., Carr, S.A., Tabb, D.L., Coffey, R.J., Slebos, R.J., Liebler, D.C. and Nci, C. (2014) 'Proteogenomic characterization of human colon and rectal cancer', *Nature*, 513(7518), pp. 382-7.

Zhang, J., Baran, J., Cros, A., Guberman, J.M., Haider, S., Hsu, J., Liang, Y., Rivkin, E., Wang, J., Whitty, B., Wong-Erasmus, M., Yao, L. and Kasprzyk, A. (2011) 'International Cancer Genome Consortium Data Portal--a one-stop shop for cancer genomics data', *Database (Oxford)*, 2011, p. bar026.

Zhang, W., Hubbard, A., Jones, T., Racolta, A., Bhaumik, S., Cummins, N., Zhang, L., Garsha, K., Ventura, F., Lefever, M.R., Lu, Z., Hurley, J.K., Day, W.A., Pestic-Dragovich, L., Morrison, L.E. and Tang, L. (2017) 'Fully automated 5-plex fluorescent immunohistochemistry with tyramide signal amplification and same species antibodies', *Lab Invest*, 97(7), pp. 873-885.

Zhang, Z., Ye, Y., Gong, J., Ruan, H., Liu, C.J., Xiang, Y., Cai, C., Guo, A.Y., Ling, J., Diao, L., Weinstein, J.N. and Han, L. (2018) 'Global analysis of tRNA and translation factor expression reveals a dynamic landscape of translational regulation in human cancers', *Commun Biol*, 1, p. 234.

Zhou, X., Yang, X., Sun, X., Xu, X., Li, X., Guo, Y., Wang, J., Li, X., Yao, L., Wang, H. and Shen, L. (2019) 'Effect of PTEN loss on metabolic reprogramming in prostate cancer cells', *Oncol Lett*, 17(3), pp. 2856-2866.

Zhu, J., Vinothkumar, K.R. and Hirst, J. (2016) 'Structure of mammalian respiratory complex I', *Nature*, 536(7616), pp. 354-358.

Zingiryan, A., Farina, N.H., Finstad, K.H., Stein, J.L., Lian, J.B. and Stein, G.S. (2016) 'Dissection of Individual Prostate Lobes in Mouse Models of Prostate Cancer to Obtain High Quality RNA', *Journal of Cellular Physiology*, 232(1), pp. 14-18.

Zong, Y., Xin, L., Goldstein, A.S., Lawson, D.A., Teitell, M.A. and Witte, O.N. (2009) 'ETS family transcription factors collaborate with alternative signaling pathways to induce carcinoma from adult murine prostate cells', *Proc Natl Acad Sci U S A*, 106(30), pp. 12465-70.

Zou, M., Toivanen, R., Mitrofanova, A., Floch, N., Hayati, S., Sun, Y., Le Magnen, C., Chester, D., Mostaghel, E.A., Califano, A., Rubin, M.A., Shen, M.M. and Abate-Shen, C. (2017) 'Transdifferentiation as a Mechanism of Treatment Resistance in a Mouse Model of Castration-Resistant Prostate Cancer', *Cancer Discovery*, 7(7), pp. 736-749.